MARTIN MARIETTA ENERGY SYSYEMS LIBRARIES

3 4456 0321977 3

ORNL-3016
UC-34 – Physics and Mathematics
TID-4500 (15th ed.)

NEUTRON PHYSICS DIVISION
ANNUAL PROGRESS REPORT
FOR PERIOD ENDING SEPTEMBER 1, 1960

CENTRAL RESEARCH LIBRARY
DOCUMENT COLLECTION
LIBRARY LOAN COPY
DO NOT TRANSFER TO ANOTHER PERSON
If you wish someone else to see this document, send in name with document and the library will arrange a loan.

OAK RIDGE NATIONAL LABORATORY
operated by
UNION CARBIDE CORPORATION
for the
U.S. ATOMIC ENERGY COMMISSION

Printed in USA. Price $4.00. Available from the
Office of Technical Services
Department of Commerce
Washington 25, D.C.

LEGAL NOTICE

This report was prepared as an account of Government sponsored work. Neither the United States, nor the Commission, nor any person acting on behalf of the Commission:

A. Makes any warranty or representation, expressed or implied, with respect to the accuracy, completeness, or usefulness of the information contained in this report, or that the use of any information, apparatus, method, or process disclosed in this report may not infringe privately owned rights; or

B. Assumes any liabilities with respect to the use of, or for damages resulting from the use of any information, apparatus, method, or process disclosed in this report.

As used in the above, "person acting on behalf of the Commission" includes any employee or contractor of the Commission, or employee of such contractor, to the extent that such employee or contractor of the Commission, or employee of such contractor prepares, disseminates, or provides access to, any information pursuant to his employment or contract with the Commission, or his employment with such contractor.

ORNL-3016
UC-34 – Physics and Mathematics

Contract No. W-7405-eng-26

NEUTRON PHYSICS DIVISION ANNUAL PROGRESS REPORT

for Period Ending September 1, 1960

E. P. Blizard, Director

A. D. Callihan, Associate Director
F. C. Maienschein, Associate Director
A. Simon, Associate Director

L. B. Holland, Head, Tower Shielding Facility
F. J. Muckenthaler, Head, Lid Tank Shielding Facility

DATE ISSUED

NOV 23 1960

OAK RIDGE NATIONAL LABORATORY
Oak Ridge, Tennessee
operated by
UNION CARBIDE CORPORATION
for the
U. S. ATOMIC ENERGY COMMISSION

MARTIN MARIETTA ENERGY SYSYEMS LIBRARIES

3 4456 0321977 3

TABLE OF CONTENTS AND SUMMARY

1. RESEARCH FOR LIGHT-WATER-MODERATED REACTORS

1.1 REACTIVITY WORTH OF THE CENTRAL FUEL ELEMENT IN THE BULK SHIELDING REACTOR I

G. deSaussure, K. M. Henry, Jr., and R. Perez-Belles 3

The reactivity worth of a BSR-I fuel element at the center of a critical lattice has been experimentally measured by a pulsed-neutron-source technique. The value obtained for BSR-I loading No. 78 is 6.1 ± 0.5 dollars.

1.2 THE MEASUREMENT OF THE EFFECTIVE DELAYED-NEUTRON FRACTION FOR THE BULK SHIELDING REACTOR I

J. D. Kington, R. Perez-Belles, and G. deSaussure 5

The value of β_{eff}, the effective delayed-neutron fraction, has been measured for a compact loading of the BSR-I by the boron substitution technique. The value obtained was 0.0080 ± 0.0002. By adopting the literature value of the true delayed-neutron fraction, $\beta = 0.0064 \pm 0.0002$, the ratio of the effective delayed-neutron fraction to the true delayed-neutron fraction is found to be 1.25 ± 0.05. When this quantity was computed by a 3-group PDQ code calculation the result was also 1.25, an agreement which indicates the validity of the computational method.

1.3 PULSED-NEUTRON-SOURCE MEASUREMENTS AT THE BULK SHIELDING FACILITY

R. Perez-Belles, G. deSaussure, E. G. Silver, J. D. Kington, E. B. Johnson, and K. M. Henry, Jr. 12

The pulsed-neutron-source technique has been employed to measure the characteristic time, l^*/β_{eff}, for several loadings of the Bulk Shielding Reactor I and one loading of the Puerto Rican Reactor. This technique has also been used to measure the reactivity effect of various control-rod configurations in a 5 × 5 BSR-I loading. Experimental values are compared with values calculated by existing reactor codes. Characteristic times ranged from 8.55 ± 0.28 to 11.2 ± 0.2 msec for BSR-I loadings. Characteristic time for the PRR was 7.75 ± 0.18 msec. Control-rod worths vary over a considerable range, depending on position and number of rods employed.

1.4 DIGITAL COMPUTER REACTOR CALCULATIONS AT THE BULK SHIELDING FACILITY

E. G. Silver, R. Perez-Belles, and B. Bonner 18

The IBM 704 codes PDQ and GNU have been extensively studied in an effort to improve the previously unsatisfactory agreement with experiment in the cases of reactors containing large, unfueled regions, or containing heavily absorbing materials, such as control rods. Agreement with experiment is now of the same order as that previously observed only for compact reactor loadings. The codes have also been applied to a number of problems of immediate practical interest at the BSF.

2. NEW REACTORS FOR THE BULK SHIELDING AND TOWER SHIELDING FACILITIES

2.1 BULK SHIELDING REACTOR II: STATUS REPORT, INCLUDING SPERT TESTS

E. G. Silver and K. M. Henry, Jr. 29

An extensive series of static and dynamic tests of the UO_2–stainless steel core (BSR-II) for the BSF has been completed at the SPERT-I Facility of the National Reactor Testing Station at Arco, Idaho. Static tests included measurements of the reactivity worth of the control system, temperature coefficients, void coefficients, and flux mappings. Transient tests included self-limiting excursions to peak powers of 226 Mw, where some deformation of fuel plates was observed. Controlled transient excursions employing the full control system, as well as others using only the level safety system, completed the program of tests.

The reactor has now been returned to the BSF, and only final Safeguards Committee approval of realistic excess loadings is needed before it will be placed in routine operation.

2.2 TOWER SHIELDING REACTOR II PRELIMINARY EXPERIMENTS

L. B. Holland, V. R. Cain, D. R. Ward, J. L. Hull, T. A. Love, A. D. MacKellar, J. Lewin, and J. H. Wilson 42

The TSR-II preliminary experiments have been completed, and the effects of design changes previously described were determined. The preliminary experiments included measurements of the reactivity worth of the shim and regulating rods for several core configurations, the temperature coefficient of reactivity, the void coefficient of reactivity for voids in each of two regions, the reactivity worth of the lead-boral shell around the core, the reactivity effects of various shield materials outside the reactor pressure vessel, the radial flux through the core, and the prompt-neutron generation time. The heat flux throughout the core has been recalculated on the basis of the measured thermal-flux distribution.

2.3 PULSED-NEUTRON-SOURCE MEASUREMENTS AT THE TSR-II

G. deSaussure, E. G. Silver, and J. D. Kington 54

A pulsed-neutron-source technique has been employed to verify a calibration of the control system of the TSR-II previously obtained by a combination of other methods. The results agree with the previous work. The reactivity worth of the entire control system was -4.77 ± 0.14 dollars. The value of the reduced generation time, l/β_{eff}, obtained by pulsed-neutron methods is 6.61 ± 0.20 msec.

3. CRITICAL EXPERIMENTS

3.1 SOLUTION EXPERIMENTS IN A FLUX-TRAP CRITICAL ASSEMBLY: PRELIMINARY STUDY FOR HIGH FLUX ISOTOPE REACTOR

J. K. Fox, L. W. Gilley, and D. W. Magnuson 59

A study of a flux-trap critical assembly has been made, using a solution of $UO_2(NO_3)_2$ enriched to 93.5 wt % in U^{235} and dissolved in mixtures of D_2O and H_2O. The assembly was a preliminary mockup of the HFIR, and the data was intended to aid in the establishment of design parameters for the HFIR. Critical parameters, relative flux distributions, flux ratios, and the effects of centrally located air- or aluminum-filled "voids" have been obtained.

3.2 HOMOGENEOUS CRITICAL ASSEMBLIES OF 2% U^{235}-ENRICHED UF_4 IN PARAFFIN

J. T. Mihalczo and J. J. Lynn 71

Additional critical experiments have been performed with a homogeneous mixture of 2% U^{235}-enriched UF_4 and paraffin, the $H:U^{235}$ atomic ratio for these later experiments being 501. The results have been combined with those of earlier experiments, in which $H:U^{235}$ ratios of 195, 294, and 404 were used, to present plots of minimum critical masses and volumes.

3.3 CRITICAL DIMENSIONS OF RANDOM ARRAYS OF ThO_2-UO_2 PELLETS

J. K. Fox and L. W. Gilley 72

Several criticality experiments have been performed with assemblies of unclad ThO_2-UO_2 pellets, randomly stacked in aluminum or steel cylinders. Water was added to the cylinders to serve as neutron moderator, and all assemblies were completely water-reflected. The results of these measurements and of preliminary experiments in which the pellets were contained in plastic bottles indicate that the critical dimensions of assemblies of such pellets are extremely sensitive to the degree of neutron moderation.

3.4 CRITICAL PARAMETERS OF BARE AND REFLECTED 93.4 wt % U^{235}-ENRICHED URANIUM METAL SLABS

J. T. Mihalczo and J. J. Lynn 73

The critical parameters of slabs of 93.4 wt % U^{235}-enriched uranium metal have been measured in a series of neutron multiplication experiments. The effect of Plexiglas as a neutron reflector was determined, and a limited number of measurements with graphite and beryllium reflectors were made. The data were extrapolated to give 2.4 in. as the thickness of an infinite, unreflected critical slab, and 0.6 in. as the thickness of an infinite critical slab reflected by 6 in. of Plexiglas.

3.5 CRITICAL EXPERIMENTS WITH PRNC RESEARCH REACTOR FUEL ELEMENTS

E. B. Johnson and K. M. Henry, Jr. 76

A series of critical experiments with Puerto Rico Nuclear Center research reactor fuel elements has been completed in the Pool Critical Assembly of the Bulk Shielding Facility. The experiments validated the computations on which the design fuel-plate loading was based, and they determined the amount of excess reactivity to be expected from three clean, cold loadings proposed by the reactor's designer as operational configurations.

4. EXPERIMENTAL NUCLEAR PHYSICS

4.1 MEASUREMENTS OF η OF U^{233} AND U^{235} BY A MANGANESE-BATH TECHNIQUE

R. L. Macklin, G. deSaussure, J. D. Kington, and W. S. Lyon 81

The final results, including all corrections, of the manganese-bath measurements of η of U^{233} and U^{235} have been obtained. The 2200-m/sec values of η were 2.296 $\pm$ 0.010 for U^{233} and 2.077 $\pm$ 0.010 for U^{235}.

4.2 DETERMINATION OF THE THERMAL VALUE OF η OF U^{233} AND U^{235} BY DIRECT COMPARISON OF CRITICAL PARAMETERS OF AQUEOUS SOLUTIONS

R. Gwin and D. W. Magnuson 81

An experimental determination of the thermal value of η of U^{233} and U^{235}, based on the direct comparison of the critical parameters of dilute aqueous solutions of the uranyl nitrates of U^{233} and U^{235}, has been completed. The average thermal values of η obtained are 2.284 $\pm$ 0.015 for U^{233} and 2.074 $\pm$ 0.015 for U^{235}. The 2200-m/sec values are the same, since the g factor for η is unity in each case.

4.3 THE SPECTRUM OF PROMPT GAMMA RAYS FROM U^{235} FISSION

F. C. Maienschein and R. W. Peelle 82

In the continuing analysis of the experiment to determine the spectrum of gamma rays emitted promptly in the thermal-neutron-induced fission of U^{235}, all experimental work and the combination of data, together with the corrections for all count-rate-sensitive phenomena, have been completed for all energy regions. The source-strength determinations required for spectrometer efficiency measurements have been obtained either by absolute coincidence counting techniques or by use of a 4π high-pressure ionization chamber, and the pair spectrometer efficiency and response to monoenergetic gamma rays have been expressed in a response matrix. The response matrices for the Compton and single-crystal spectrometers, two steps which must precede the final solution for the gamma-ray spectrum, have not yet been formulated.

4.4 GAMMA-GAMMA COINCIDENCE STANDARDIZATION OF SOURCES, WITH APPLICATION TO THE $B^{11}(p,\gamma)C^{12}$ REACTION

R. W. Peelle and F. C. Maienschein 96

Methods are described for determining the disintegration rate of gamma-ray sources by coincidence counting of cascade gamma rays. The equation for the source strength is derived for a moderately complex radionuclide cascade decay scheme and also for the cascade from the $B^{11}(p,\gamma)C^{12}$ reaction. Methods are given for the evaluation of the small correction terms which arise in the formulation. Experimental techniques used for a series of such determinations are described, typical results are given, and the range of applicability of the techniques is discussed.

4.5 GAMMA-RAY INTENSITY RATIOS IN THE DECAY OF 105-DAY Y^{88}

R. W. Peelle 110

A scintillation pair spectrometer and a gamma-gamma coincidence counting apparatus were utilized to obtain the relative intensities of the 2.74-, 1.84-, and 0.90-Mev gamma rays in the decay of Y^{88} to Sr^{88}. The relative intensity of the 2.74- and 1.84-Mev gamma rays was found to be $(5.97 \pm 0.25) \times 10^{-3}$ using pulse-height spectra obtained with a scintillation pair spectrometer together with efficiencies measured with calibrated sources of Na^{24} (2.75 Mev) and Y^{88}. The relative intensity of the 1.8- and 0.90-Mev gamma

transitions was obtained by comparing gamma-gamma coincidence measurements on sources of Y^{88} and Sc^{46} in the same geometry. The intensity ratio $S_{1.8}/S_{0.90}$ was found to be 1.064 ± 0.008.

4.6 DETERMINATION OF THE INTERNAL CONVERSION COEFFICIENT OF THE 279-kev GAMMA RAY IN Tl^{203} BY ABSOLUTE COINCIDENCE TECHNIQUES

R. W. Peelle 116

The total internal conversion coefficient of Tl^{203} for the 279-kev transition in the decay of Hg^{203} was measured using an apparently novel method, involving absolute coincidence counting, to determine separately the rates of emission of the 279-kev gamma rays and the conversion electrons. This measurement was made possible by the encapsulation of the Hg^{203} source within a small plastic scintillator. The 100% efficiency of this arrangement for conversion electrons made possible an almost complete separation between pulse-height ranges corresponding to decay events involving or not involving internal conversion. The value obtained for the *K*-shell internal conversion rate divided by total gamma emission rate was 0.164 ± 0.006, if literature values for the relative internal conversion rates in the various shells are accepted.

5. EXPERIMENTAL REACTOR PHYSICS

5.1 THERMAL-FLUX CALIBRATION IN SLOT 11 OF ORNL STANDARD GRAPHITE PILE

G. M. Estabrook 129

A remeasurement of the thermal-neutron flux in slot 11 of the ORNL Standard Graphite Pile was made. Method and procedure followed those of a previous (1952) measurement. The value of the absolute thermal flux for 2200-m/sec (most probable velocity) neutrons is 635 ± 32 neutrons cm^{-2} sec^{-1}. The value for average-velocity neutrons is 716 ± 36 neutrons cm^{-2} sec^{-1}. The value from the previous calibration was 703 ± 35 neutrons cm^{-2} sec^{-1}.

5.2 A NEUTRON CHOPPER SPECTROMETER FOR THE BULK SHIELDING FACILITY

V. V. Verbinski 130

The preliminary design of a neutron chopper spectrometer for the BSF, to be located underground adjacent to the pool of the BSR, has been completed. The spectrometer will have a flight path of about 10 m, which, with the chopper rotor currently proposed, will give energy resolutions ranging from ~3% for energies below 10 ev, through 10% at 100 ev to ~30% at 1000 ev. A stack of high-pressure BF_3 counters will serve as the detector, with pulses going to a 256-channel time-of-flight analyzer. Readout will be in the form of punched tape coded for the Oracle, which will transform the time-of-flight data to neutron-energy spectra in accordance with factors discussed at length in this report.

5.3 AN APPLICATION OF THE PULSED-NEUTRON TECHNIQUE TO REACTOR STUDY

R. Perez-Belles, G. deSaussure, and E. G. Silver 136

The pulsed-neutron technique has been used to measure the change in the buckling induced when a cadmium control rod was inserted into a beryllium moderating assembly. Measurements were made on various-sized assemblies with slim cylindrical rods, a cruciform rod, and rectangular, hollow boxlike rods fabricated of cadmium sheet. Results were compared with predictions from calculations by the Nordheim-Scalettar method and from PDQ code calculations. Agreement was observed in the simpler cases with the cylindrical rods and, when the Hurwitz-Roe approximation was used to convert to a circular cylinder, in the case of the cruciform rod, but agreement of both Nordheim-Scalettar and PDQ calculations with experiment was poor for the large boxlike rods. Inadequacy of diffusion theory as applied in the case of large rods is suspected, but a possible systematic error in the measurements is not ruled out.

5.4 DETECTOR TECHNIQUES USED IN THE MEASUREMENT OF THE SLOWING DOWN OF FISSION NEUTRONS IN WATER

T. V. Blosser and D. K. Trubey 142

The use of indium foils as detectors in determining the slowing-down distribution in water of neutrons from a fission source has been closely studied. The principal reactions resulting from bombardment of

natural indium by neutrons have been evaluated. Both beta-ray and gamma-ray counting techniques are discussed, and a method by which contributions from indium resonances other than the principal resonance at 1.45 ev may be estimated is given.

6. REACTOR THEORY

6.1 *ON THE VALIDITY OF THE SECOND FUNDAMENTAL THEOREM IN A MEDIUM WITH ANISOTROPIC SCATTERING*

L. Dresner 151

The second fundamental theorem of reactor theory states that a good estimate of the nonleakage probability from a bare reactor is given by the Fourier transform of the infinite-medium kernel evaluated at the asymptotic buckling of the reactor. Inönü has investigated the validity of this theorem for the one-velocity slab reactor with isotropic scattering by means of a variational technique. He finds its use gives very good results even for quite small reactors with dimensions of the order of a few mean free paths. In the present paper the effect of anisotropy in the scattering on the validity of the theorem is investigated by a variation-iteration technique. It is concluded that the theorem is, in general, less reliable the more anisotropic the scattering.

6.2 *COMPARISON THEOREMS FOR THE ESTIMATION OF CRITICALITY IN BARE, ONE-VELOCITY REACTORS*

L. Dresner 154

Several theorems are given for the estimation of the critical multiplication in a bare, one-velocity reactor with isotropic scattering.

6.3 *TIME-DEPENDENT THERMAL-NEUTRON ENERGY SPECTRA IN A MONATOMIC HEAVY GAS*

S. N. Purohit 156

The time-dependent thermal-neutron energy spectra for times greater than the slowing-down time have been calculated for a monatomic heavy gas. The thermalization time constant for the establishment of the final Maxwellian distribution has been estimated, and total thermalization times and diffusion cooling coefficients have been computed for neutrons in both beryllium and graphite.

6.4 *HOMOGENEOUS, INFINITE MEDIUM P_1 CODES*

W. E. Kinney 156

Multigroup codes, utilizing a consistent P_1 approximation to the Boltzmann equation, have been written to compute neutron ages and Fourier transforms. Such codes not only are useful for production of reactor physics data, but will facilitate economical investigation of improvements to multigroup codes. Comparisons of code results with analytic and Monte Carlo results show good agreement.

6.5 *ANISOTROPIC SLOWING-DOWN PARAMETERS FOR CORN PONE*

W. E. Kinney 161

Two codes have been written which permit the inclusion of anisotropic scattering in the center-of-mass system in Corn Pone calculations. The Legendre Polynomial Code employs the coefficients obtained in the expansion of the differential scattering cross section in a series of Legendre polynomials. The Differential Code uses the differential scattering cross sections directly. Input, operating instructions, output, and some typical results are given for each code.

6.6 *ADDITIONS AND CHANGES TO CORN PONE*

W. E. Kinney 166

A version of Corn Pone has been assembled which incorporates codes to compute and use disadvantage factors. This version also includes the boundary conditions requisite to the assumption of isotropic currents entering a void.

6.7 AN EXAMINATION OF SOME FEATURES OF CORN PONE, A MULTIGROUP, MULTIREGION REACTOR CODE

W. E. Kinney 169

Several aspects of the Corn Pone design were evaluated by calculation of a simple reactor model in various ways and by calculation of neutron ages. Comparison of results with Monte Carlo results has assisted in the evaluations. It was indicated that use of the Corn Pone difference equations good to fourth order in the lattice spacing does not significantly improve results over those obtained by use of equations good only to second order. The assumption that the flux is constant over a group, rather than varying linearly, is adequate. Only for light water is there a significant difference between P_1 and diffusion theory results for coarse group structures (31 groups) and isotropic scattering. Differences of the order of 1% in multiplication constants, absorptions, and escapes were noted in comparing Goertzel-Greuling and usual multigroup age slowing-down treatments. A simpler age slowing-down treatment which nevertheless gives better results has been developed.

6.8 AN IBM 704 CODE FOR THE CALCULATION OF MOMENTS

I. M. Happer and W. E. Kinney 183

An IBM 704 code is being written which uses the moments method to compute the even moments, from the zeroth to the tenth, of the flux and the slowing-down distribution of neutrons from a plane source. The portion of the code which computes and stores the kernels has been written and tested. The main code, which solves the group moment equation for the moments of the flux, has been written but not yet tested.

6.9 A TREATMENT OF TIME-DEPENDENT SLOWING-DOWN OF NEUTRONS, USING GROUP THEORY

E. Guth and E. Inönü 187

The Wigner application of group theory to multiple scattering problems has been employed to obtain the distribution function describing the time-dependent slowing-down of neutrons through elastic collisions. For the special case of no absorption and spherically symmetric scattering in the center-of-mass system, the solution reduces to an exact expression.

6.10 THE EFFECT OF THE BOUNDARY REGION IN THE DETERMINATION OF THE EXTRAPOLATION LENGTH FROM EXPERIMENTS WITH CRITICAL CYLINDERS

E. Inönü 188

Experimental determinations of the extrapolation length obtained from vertical traverses in bare homogeneous critical assemblies of aqueous U^{235} solutions have been analyzed. It is shown that the apparent differences between thermal-, epithermal-, and fast-neutron extrapolation lengths are due entirely to boundary region effects. By excluding points within 3 in. of the boundary a consistent, unique extrapolation length is obtained. A similar treatment is successful with fluxes obtained from Corn Pone calculations.

6.11 ON RANDOM WALK INTERPRETATION OF LINEAR BOLTZMANN EQUATIONS

E. Guth and E. Inönü 189

An exact connection between the recurrence relations defining random walks and the linear Boltzmann integrodifferential equations has been demonstrated. Application to problems of neutron transport, Brownian movement, and neutron thermalization is suggested.

6.12 SOLUTION OF THE MONOENERGETIC BOLTZMANN EQUATION IN AN INFINITE HOMOGENEOUS MEDIUM WITH LINEARLY ANISOTROPIC SCATTERING FOR AN ISOTROPIC POINT SOURCE

E. Inönü 190

The monoenergetic Boltzmann equation in an infinite homogeneous medium with linearly anisotropic scattering and an isotropic point source has been solved exactly by the method of Fourier transforms. Results are to be published elsewhere.

6.13 MILNE PROBLEM WITH CAPTURE

S. N. Purohit 191

An approximate method, involving the representation of the nonasymptotic flux by a single exponential, has been used to compute the neutron flux and emergent angular distribution of neutrons in the Milne problem with capture. Parameters governing the exponential representing the nonasymptotic flux were computed for various ratios of absorption to total cross section, and are given in a table.

6.14 NEUTRON THERMALIZATION AND DIFFUSION IN PULSED MEDIA

S. N. Purohit 192

A general formalism for determining the lower time eigenvalues associated with a decaying pulse of neutrons in a finite multiplying or nonmultiplying medium has been developed. The formalism is general and avoids the concept of neutron temperature. A relation was developed which gives an estimate of the thermalization time constant for various moderators. Results from an experiment using a U^{235}-water mixture were analyzed to demonstrate the applicability of the method.

6.15 THE O5R CODE: A GENERAL-PURPOSE MONTE CARLO CODE FOR THE IBM 704

R. R. Coveyou and J. G. Sullivan 193

The O5R code, a general purpose Monte Carlo reactor code for the IBM 704 computer, has been completed and successfully tested on manufactured problems to which the answers were known, age calculations, and, finally, a number of practical problems. It is expected that the main portions of the code will be unaffected by the replacement of the IBM 704 by the IBM 7090, scheduled for December 1960. At that time an improved model for thermal effects will be introduced into the code, and its versatility will be increased to allow a larger number of media and more flexible geometry routines than are presently available.

7. SHIELDING RESEARCH

7.1 LID TANK SHIELDING FACILITY MEASUREMENTS BEHIND THE ML-1 SHIELD MOCKUP

A. D. MacKellar 197

Measurements of thermal-neutron flux, fast-neutron and gamma-ray doses, and gamma-ray dose as a function of time after shutdown have been made behind a mockup of the Aerojet-General Corp. ML-1 shield. The effects on gamma-ray dose rates of various placements of the lead within the mockup configuration were also investigated.

7.2 ANGULAR DISTRIBUTION OF NEUTRONS EMERGING FROM PLANAR SURFACES OF DIFFUSING MEDIA

V. V. Verbinski 202

Measurements of the angular distribution of low-energy neutrons emerging from the surface of hydrogenous slabs indicate that the angular distribution not only follows the $\phi(\mu) = 1 + \sqrt{3}\,\mu$ dependence given by Bethe for pure paraffin but also is independent of the poison content for the range investigated, the slab thickness (after spectral equilibrium is reached), and the angle of incidence of the input neutrons. Measurements for a non-slowing-down medium (lead) indicate that the angular distribution is more strongly peaked in the forward direction when the medium is poisoned.

7.3 EXAMINATION OF THE RANGE OF APPLICABILITY OF CONDITIONAL MONTE CARLO TO DEEP-PENETRATION PROBLEMS

S. K. Penny and C. D. Zerby 209

The conditional Monte Carlo sampling method has been applied to the spatial part of a Monte Carlo calculation of the energy spectra and angular distributions from an isotropic point source of gamma rays in an infinite medium in which energy degradation was permitted. The purpose was to test the applicability of this technique to problems involving several phase-space variables, since the technique had previously been successfully used in a one-dimensional phase-space computation. Differential energy spectra and angular distributions were computed for two cases – a 1-Mev source in water and an 8-Mev source in lead – for penetrations up to 20 mean free paths (mfp). Comparison with existing moments-method results showed agreement to distances of about 10 mfp.

7.4 DESIGN OF A SHIELD FOR THE OAK RIDGE RESEARCH REACTOR SOUTH FACILITY (GCR LOOP NO. 2)

D. K. Trubey 219

Experimental and theoretical programs assisting in the design of a mobile shield for the ORR South Facility are being carried out. The shield is required for the installation of GCR loop No. 2, a test loop for evaluation of gas-cooled-reactor fuel elements. Experimental measurements have been obtained at beam holes HS-1 and HB-2; four IBM 704 codes are being utilized in the theoretical program.

7.5 DESIGN OF A SHIELD FOR THE ORR SOUTH FACILITY: EXPERIMENTAL PROGRAM AT BEAM HOLE HB-2

F. J. Muckenthaler and T. V. Blosser 221

The thermal-neutron flux, fast-neutron and gamma-ray doses, and fast-neutron and gamma-ray spectra from beam hole HB-2 of the ORR have been measured. The data will be used in the design of a portable shield for the ORR South Facility in connection with the installation there of the GCR loop No. 2. Experimental configurations included barytes concrete, iron, lead, polyethylene, and borated polyethylene, used either singly or in various combinations. An attempt was made to evaluate the dose from scattering by these materials. Only a sampling of the data is presented, with the remainder to follow in a later report.

7.6 GRINDER: AN IBM 704 MONTE CARLO PROGRAM FOR ESTIMATING THE SCATTERING OF GAMMA RAYS FROM A CYLINDRICAL BEAM CATCHER

D. K. Trubey and S. K. Penny 226

The energy spectra and dose rates resulting from scattering of a gamma-ray beam incident on a homogeneous right circular cylinder can be obtained from an IBM 704 Monte Carlo program designated Grinder. A maximum of 20 detector positions is permitted. Results are given as energy spectra histograms from which dose is computed. An important feature of the program is that computing time, rather than number of histories, is an input parameter. The code is being used in the design of a shield for the ORR South Facility.

7.7 THE SINGLE-SCATTERING APPROXIMATION TO THE GAMMA-RAY AIR SCATTERING PROBLEM

D. K. Trubey 230

The result of a calculation using the single-scattering approximation, with no exponential attenuation or buildup, has been compared to the result of a Monte Carlo calculation of the dose rate and number flux in air from a monoenergetic gamma-ray source. The comparison shows that the simple approximation is generally adequate for unshielded detectors.

7.8 DEVELOPMENT OF AN IBM 704 ANALYTICAL CODE FOR ANALYSIS OF AXIALLY SYMMETRIC REACTOR SHIELDS

F. B. K. Kam and H. E. Stern 231

Analytic IBM 704 codes, intended to furnish neutron and gamma-ray data applicable to preanalysis of shielding experiments and to general shield design, have been written. Fast-neutron and primary gamma-ray doses outside of an axially symmetric reactor shield can be computed for detector points located along the axis of symmetry. Two subprograms are ready for use; the remaining codes are completed and are being debugged.

7.9 DESIGN OF A REACTOR SHIELD

H. E. Stern and F. B. K. Kam 233

A study of some of the problems inherent in the design of reactor shields for nuclear-powered aircraft has been initiated. Calculational methods for obtaining optimum configurations are being explored. Initial attention has been focused on gamma rays born in a core and has utilized a simple model for some approximate calculations.

7.10 ELECTRON CASCADES: STATUS REPORT

C. D. Zerby and H. S. Moran 234

The study of high-energy electron-photon cascades, a knowledge of which is necessary to design of efficient shielding for high-energy particle accelerators, has continued. A Monte Carlo calculation,

expected to supply all data of interest, is being prepared for automatic computer solution. Codes for determining the requisite cross sections, as well as random selection techniques for determining scattering angles from differential cross sections, are complete. Final assembly of the calculation is in progress.

7.11 CALCULATION OF THE DIFFERENTIAL INELASTIC CROSS SECTION FOR COMPLEX NUCLEI
H. Bertini and C. D. Zerby 235

A program is in progress to calculate the differential energy and angular cross sections for the emission of particles from complex nuclei when the latter are bombarded by pions or nucleons in the energy range from 50 Mev to 30 Bev. These cross sections are needed for the design of shields for high-energy accelerators and rocket vehicles. The lower-energy phase of the program (incident energy range from 50 to 300 Mev) is nearly complete. Some initial results are given and compared with available experimental data.

7.12 NEUTRON YIELDS FROM (α,n) REACTIONS
F. S. Alsmiller and G. M. Estabrook 242

Isotopes decaying by alpha emission and certain light-element impurities may frequently be present in uranium and plutonium materials in sufficient concentrations to give a substantial neutron yield from (α,n) reactions. Calculations of such yields have been made. Since no experimental data could be found concerning the ranges or stopping cross sections of alpha particles in uranium or plutonium, cross sections were computed by an empirical formula, with the parameters determined by a least-squares fit of all available experimental data for $Z > 20$.

7.13 A STUDY OF CONCRETE SAMPLES TAKEN FROM THE TOP SHIELD OF THE ORNL GRAPHITE REACTOR
W. J. Grantham 245

Samples secured during the drilling of experiment holes 70 and 71 in the ORNL Graphite Reactor have been analyzed for water content and compressive strength. At the time of the drilling, the reactor had developed a total power of 4.3×10^8 kwhr. Results indicate a water content consistent with design anticipations, but the compressive strength of both the barytes-haydite and ordinary concretes falls significantly below the design strength of 2.5 ksi.

8. RADIATION-DETECTOR STUDIES

8.1 UNSCRAMBLING OF SCINTILLATION SPECTRA
R. O. Chester and W. R. Burrus 249

A method of automatically processing pulse-height data obtained as the output of a scintillation spectrometer in a spectrum of gamma rays is being developed. The method makes no prior assumptions about the spectrum being examined. Semiempirical functions are used to fit the experimentally determined response of the spectrometer to monoenergetic gamma rays. Simple power-function fits, as a function of energy, to the parameters of the response function are used to develop the response matrix. Solutions to the result-matrix equations are being investigated. Special techniques are necessary to get useful results. Numerical tests using a nonnegativity constraint have been made, and tests are in progress using a smoothing function.

8.2 GAMMA-RAY RESPONSE OF LARGE NaI(Tl) CRYSTALS
G. T. Chapman and T. A. Love 254

The investigations of the gamma-ray response functions of a composite 8-in.-dia by 8-in.-long NaI(Tl) crystal at the Bulk Shielding Facility have continued. Experimental spectra from Cs^{137} and Na^{24} sources have been measured and compared with calculated spectra developed by Monte Carlo codes. The results are encouraging, but additional study of interface effects, reflectors, and background effects is desirable.

8.3 THE EFFECTS OF SCINTILLATOR DIMENSIONS ON PULSE-HEIGHT SPECTRA ESTIMATED BY MONTE CARLO FOR LARGE NaI CRYSTALS

R. W. Peelle 257

An IBM 704 Monte Carlo program has been employed to calculate the pulse-height spectra for large NaI crystals differing in shape, diameter, length, and in whether axial wells had been included. Variations were made about a 9-in.-dia by 10-in.-long crystal, chosen as a standard of comparison. The results clearly demonstrate that a certain degree of control over the photofraction and the shape of the tail spectrum may be achieved by care in the choice of crystal dimensions.

8.4 THE MODEL IV GAMMA-RAY SPECTROMETER: STATUS REPORT

G. T. Chapman 264

Assembly of the model IV gamma-ray spectrometer has been completed, with only final calibration of the positioner and readout system yet to be accomplished. A series of preliminary investigations of the system performance, utilizing a 9-in.-dia, 12-in.-long composite NaI(Tl) scintillator as the gamma-ray detector, is in progress. These experiments will assist in optimizing performance of the spectrometer system. Comparisons with calculations are being used as guides to further improvement.

8.5 EXPERIMENTAL DETERMINATION OF FLUX DEPRESSION AND OTHER CORRECTIONS FOR GOLD FOILS EXPOSED IN WATER

W. Zobel 267

Work has continued on the experimental determination of a correction factor to be applied to thermal-neutron flux measurements with thin gold foils. Results are presented as a plot of correction factor, ϕ_0/ϕ, as a function of foil thickness. Comparison with various calculational approaches to the problem indicates best agreement with recent work of Dalton and Osborn.

8.6 CALCULATION OF PULSE-HEIGHT RESPONSE FUNCTIONS FOR GAMMA-RAY SCINTILLATION COUNTERS

C. D. Zerby and H. S. Moran 269

The IBM 704 Monte Carlo codes for the calculation of the pulse-height response functions for NaI, CsI, and xylene gamma-ray scintillation detectors have been completed with the addition of means for including secondary bremsstrahlung and annihilation radiation. The codes, plus complete operating instructions, have been prepared and are now available to those interested. Comparisons of the results of the NaI code with experimental spectra show excellent agreement when allowance is made for background effects in the experimental spectra.

8.7 SCINTILLATION RESPONSE OF ACTIVATED IONIC CRYSTALS TO CHARGED PARTICLES

A. Meyer and R. B. Murray 275

A simplified phenomenological model of the response of activated inorganic crystals to charged particles has been constructed. It interprets the response in terms of the formation, transport, and capture of energy carriers, under the basic assumptions that the energy carriers are formed by the recombination of electrons and holes, and that the density of carriers is a smooth function of dE/dx. The model predicts scintillator efficiency as a function of dE/dx, concentration-dependent effects, and a diffusion length. Results are consistent with experiment.

8.8 USE OF SILICON SURFACE-BARRIER COUNTERS IN FAST-NEUTRON DETECTION AND SPECTROSCOPY

T. A. Love, R. B. Murray, J. J. Manning, and H. A. Todd 280

A neutron-sensitive semiconductor detector has been constructed by depositing a thin layer of Li^6F between two closely adjacent silicon-gold surface-barrier counters. Neutrons are detected by observing the $\alpha + T$ pair resulting from the $Li^6(n,\alpha)T$ reaction; pulses from the two counters are added and the sum pulse is amplified and recorded on a multichannel analyzer. Experimental pulse-height spectra have been recorded for monoenergetic neutrons ranging from "slow" to 14.7 Mev. Preliminary experiments examining the discrimination of these counters against gamma-ray backgrounds have also been made. It is concluded that these counters may offer advantages of simplicity of construction and operations, small size, and

reasonably good resolution of neutron spectra above 1 or 2 Mev. A disadvantage is the low detection efficiency – present counters giving 3.4×10^{-3} for thermal neutrons and 0.94×10^{-6} for 2-Mev neutrons, both at normal incidence. Some suggestions for improving detection efficiency are offered.

8.9 *THE DISTRIBUTION IN ENERGY OF ALPHA-TRITON PAIRS RESULTING FROM NEUTRON BOMBARDMENT OF LITHIUM FLUORIDE*

F. S. Alsmiller 289

The use of paired silicon-gold surface barrier counters (with an intervening Li^6F layer) to record the sum of the energies of the triton and alpha particle produced in an $Li^6(n,\alpha)T$ reaction as a measure of the incident neutron energy has been described in a previous paper (Sec 8.8). The problem of calculating the shape and width of the distribution in total energy of the pairs reaching the silicon has been investigated and some preliminary results have been obtained.

8.10 *LIGHT OUTPUT OF CsI(Tl) UNDER EXCITATION BY GAMMA RAYS*

R. Gwin and R. B. Murray 293

A series of experiments investigating the light output of CsI(Tl) under excitation by monoenergetic gamma rays has been essentially completed. Results from a range of gamma rays from 10 kev to 2.6 Mev have been obtained and demonstrate that the light output of CsI(Tl) is not a linear function of the energy of the incident gamma ray. The magnitude of the departure from linearity has been measured for the crystal employed. The data will permit a calculation of light output per unit energy for electrons by the methods of Zerby *et al.*

8.11 *COMPARISON OF CALCULATIONS OF SCINTILLATION-COUNTER RESPONSE FUNCTIONS FOR CsI WITH NaI CALCULATIONS AND CsI EXPERIMENTS*

H. S. Moran and C. D. Zerby 297

The IBM 704 codes of Zerby and Moran have been used to compare the responses of CsI and NaI to 0.662-, 1.368-, 2.754-, and 8.0-Mev gamma rays. The calculated response of CsI to 0.662-Mev (Cs^{137}) and 1.368- and 2.754-Mev (Na^{24}) gamma rays has also been compared with experimental results. It is concluded that the advantages of decreased size and weight offered by CsI over NaI may be offset by increased cost. It is also concluded that the comparisons of calculations vs experiment validate the usefulness of the codes.

8.12 *INTRINSIC LINE WIDTH IN NaI(Tl) GAMMA-RAY SPECTROMETERS*

C. D. Zerby, A. Meyer, and R. B. Murray 302

In the use of NaI(Tl) scintillation crystals for gamma-ray spectroscopy it is important to achieve a minimum line width in the pulse-height spectrum resulting from monoenergetic gamma rays. The contribution of the scintillator to the line-width broadening has been studied, and it has been demonstrated that it is the result of the nonlinear response of NaI(Tl) to electrons. A calculation of the intrinsic broadening due to this effect was made, and combined with a semiempirical function describing the broadening due to photomultiplier effects to give a calculated value of the over-all line width. At 661 kev the width was calculated to be 5.5% for a 2.5-in.-dia by 2-in.-high crystal, which is to be compared with experimental values in the range 6–8%. It is pointed out that no account was taken of broadening due to imperfect crystal or optical effects and that the broadening must depend upon source configuration and crystal dimensions, the effects of which have not been investigated.

9. PLASMA PHYSICS THEORY

9.1 FOKKER-PLANCK COEFFICIENTS FOR A PLASMA INCLUDING RADIATION

A. Simon and E. G. Harris 311

The pair-correlation equations, obtained from a generalization of the Rostoker-Rosenbluth expansion to include radiation, have been solved exactly for the special case of a plasma whose zero-order distribution is static, uniformly distributed in space, and with no external magnetic or electric fields. The results are directly interpretable as coefficients of the Fokker-Planck equation.

9.2 DISPERSION RELATIONS FOR PLASMA WAVES IN A FINITE CYLINDRICAL MEDIUM

P. B. Burt 311

A dispersion relation for perturbations of a finite cylindrical shell of plasma has been derived. The external magnetic field is assumed uniform, and for purposes of simplification, perturbation of the magnetic field is neglected. The result of the development is a set of somewhat complicated coupled differential equations in the radial variable. No apparent simplification appears evident.

9.3 EFFECT OF PLASMA POTENTIAL ON DCX STEADY STATE

T. K. Fowler 313

The effect of a plasma potential on the DCX steady state after burnout has been studied. It is concluded that, in comparison with earlier results neglecting the potential, cold electrons flowing through the system drain much less energy from hot ions by collisions.

9.4 A THEORY ON OBTAINING SHORT BURSTS OF IONS FROM A BEAM OF IONS

T. K. Fowler and W. M. Good 313

A study of methods for obtaining short ion bursts by sweeping a steady beam across an aperture has been made. It was shown that shorter bursts can be obtained only at some sacrifice in beam quality, particularly energy spread. Results are subject to the assumptions that collective forces, such as space charge, are negligible and that the sweeping process employs only Hamiltonian forces.

9.5 DENSITY OF IONS OUTSIDE A MAGNETICALLY CONFINED ARC

R. G. Alsmiller, Jr. 313

The nonlinear equations governing the diffusion of ions out of a magnetically confined vacuum arc have been studied. It has not been possible to obtain results for cases of more than one ion species, which would be required for comparison with existing experimental data.

10. THEORETICAL NUCLEAR PHYSICS

10.1 THE ELECTROMAGNETIC PRODUCTION OF PION PAIRS

C. D. Zerby 317

The Pauli-Weisskopf theory of the electromagnetic production of pion pairs has been investigated with the objective of including in it the strong pion-nucleus interaction which ultimately leads to an enhancement of the cross section. This has been accomplished by including the interaction into the rigorous theory in the form of an optical model. Both differential energy spectra and the total pion pair production cross section have been calculated and are presented in graphical form.

10.2 A STATISTICAL MODEL FOR NUCLEAR LEVEL SPACINGS

L. Dresner and E. Inönü 319

An analytical investigation of the effects of a slight generalization of Wigner's simple formula for the distribution of nuclear level spacings has been made. An equation has been derived for the spacing distribution in which the relationship between a given spacing and a preceding spacing is considered. Agreement with the distribution given by the Wigner formula is good, but attempts to compare the new distribution with experimental data were inconclusive.

10.3 AN ANALYSIS OF INELASTIC SCATTERING IN U^{238} BELOW 1 Mev

L. Dresner 321

A semiphenomenological calculation of the partial inelastic scattering cross sections for U^{238}, for bombardment energies from 150 to 1000 kev, has been completed. The method employed was that of Hauser and Feshbach, improved in several important respects, however. The calculated values of the (n,γ) cross section show good agreement with published experimental results.

Part 1

RESEARCH FOR LIGHT-WATER-MODERATED REACTORS

1.1 REACTIVITY WORTH OF THE CENTRAL FUEL ELEMENT IN THE BULK SHIELDING REACTOR I[1]

G. deSaussure K. M. Henry, Jr. R. Perez-Belles[2]

The reactivity worth of a uranium-aluminum alloy Bulk Shielding Reactor I fuel element at the center of a critical lattice has been experimentally determined. This value is of interest for reactor safety considerations, since it determines the initial period by which the reactor power would increase if a fuel element were to be accidentally dropped into an empty channel in the center of a just-critical lattice. The value had not been measured previously because it is too large a reactivity to be measured by the inhour technique. Employment of a pulsed-neutron-source technique made possible the measurement at this time. For the loading used (BSR-I loading No. 78), the reactivity worth of a single fuel element at the center was: $\rho = 6.1 \pm 0.5$ dollars. The corresponding initial multiplication period is $T^+ = 1.5 \pm 0.2$ msec.

Theory

The pulsed-neutron technique permits the determination of large amounts of negative reactivity. The theory of the method is detailed in another section (5.3) of this annual report. In essence, the negative reactivity of a subcritical lattice can be related to the decay constant of the fundamental mode of the neutron population following injection of a burst or pulse of fast neutrons into the lattice. The decay constant is the quantity which is experimentally measured.

Experiment

The procedure consisted essentially of introducing a burst of fast neutrons into one face of a BSR-I loading and observing the decay of the neutrons within the core. The neutron burst was produced by pulsing a deuteron beam onto a tritium-containing zirconium target [the familiar $H^3(d,n)He^4$ reaction] in the BSF 200-kv particle accelerator. Secondary experiments were performed to verify that the decay observed was indeed that of the fundamental mode.

The measurement of the reactivity worth of the central fuel element was made with BSR loading No. 78, shown in Fig. 1.1.1. This loading was chosen because the central fuel element, element No. 135 in position 27, was entirely surrounded by full fuel elements. The

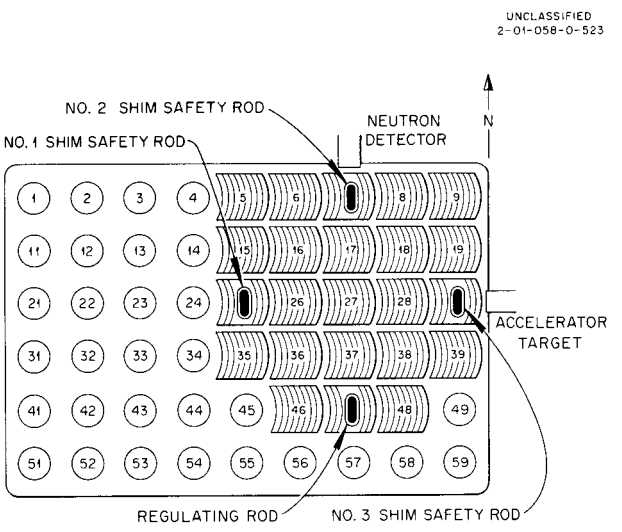

Fig. 1.1.1. BSR-I Loading No. 78.

[1]A detailed version of this paper has been submitted to *Nuclear Sci. and Eng.*

[2]On assignment from Instituto Nacional de Industria, Madrid, Spain.

loading was almost critical with all control rods entirely withdrawn, the negative reactivity, measured by the inhour method, being equal to −0.10 ± 0.01 dollar. All elements were full, 140-g cold elements, except the 4 special ones into which the control rods are inserted, each of which contained only 70 g of fuel.

Results

Decay curves of the prompt-neutron population for three conditions of loading No. 78 are shown in Fig. 1.1.2, and the results of the measurements are summarized in Table 1.1.1.

The reactivity worth of the central fuel element of loading No. 78 is equal to the difference between the reactivity of the full loading, −0.10 ± 0.01 dollar, and the reactivity of the same loading with the central fuel element removed, −6.2 ± 0.5 dollars. The reactivity worth of the central fuel element is therefore 6.1 ± 0.5 dollars. Details of the calculations supporting these results are given elsewhere.[1]

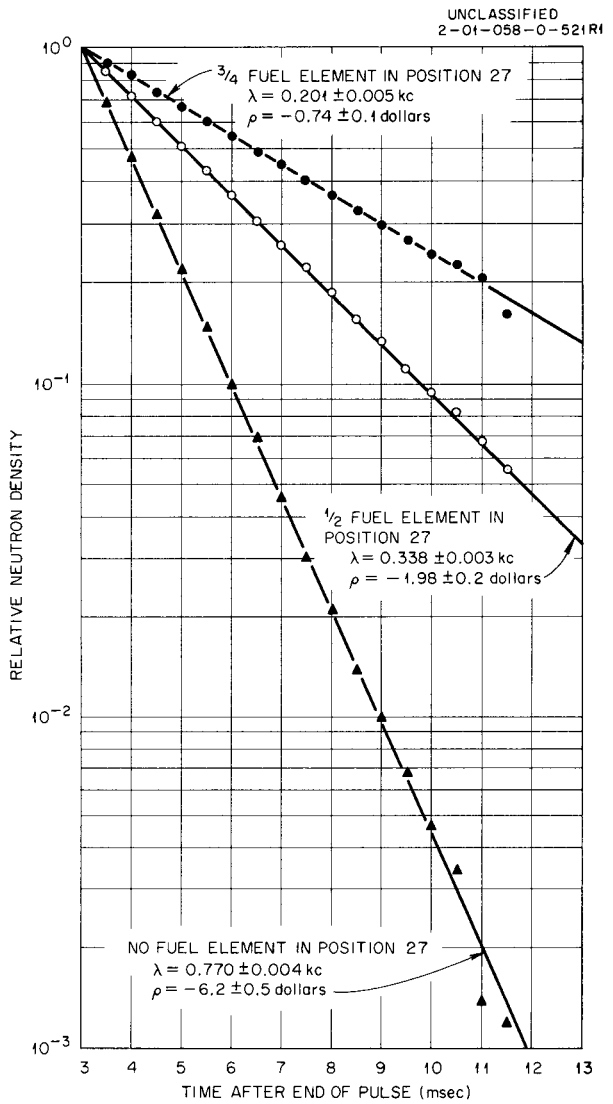

Fig. 1.1.2. Decay of the Neutron Density for Various Fuel Loadings of the Central Position in BSR-I Loading No. 78.

Conclusions

From the data experimentally obtained during this investigation and from other parameters, both experimental and calculated, the initial period of the supercritical reactor resulting from the insertion of a central element has been obtained. If a compact, BSR-type lattice is made critical without the central fuel element, and if a fuel element is then dropped in the central position, the reactor will become supercritical, and its power will initially increase with a period of 1.5 ± 0.2 msec. However, since this time is much shorter than the insertion time of a freely falling element, the initial period in such an accident would be determined by the time of insertion. From a practical point of view, a 5 × 5 lattice of regular BSR-I fuel elements cannot be made critical with a hole in the center. To make such a configuration critical, fuel elements would have to be added. This may change slightly the

reduced generation time, and would decrease the worth of the central fuel element, thus increasing the initial period.

Table 1.1.1. Summary of Results

Element No. in Position 27	Relative Amount of Fuel in Position 27	Prompt-Neutron Decay Constant (kc)	Reactivity of Configuration (dollars)	Reactivity Worth of Element in Position 27	Reactivity per Unit Fuel
None	0	0.770 ± 0.004	−6.2 ± 0.5		
128	½	0.338 ± 0.003	−1.98 ± 0.2	4.2 ± 0.5	1.4
129	¾	0.201 ± 0.005	−0.74 ± 0.1	5.5 ± 0.5	1.2
135	1	Not measured	−0.10 ± 0.01	6.1 ± 0.5	1

1.2 THE MEASUREMENT OF THE EFFECTIVE DELAYED-NEUTRON FRACTION FOR THE BULK SHIELDING REACTOR I

J. D. Kington R. Perez-Belles G. deSaussure

Introduction

Experimental observations of the changes in reactivity associated with perturbations of a delayed-critical reactor may be satisfactorily analyzed with a knowledge of the reactivity in dollars and the ratio of the prompt-neutron generation time to the effective delayed-neutron fraction, β_{eff}. In order to compare such experiments with calculation, however, a knowledge of the value of β_{eff} itself is required. The existence of a large body of experiment and calculation on the Bulk Shielding Reactor I (BSR-I) and similar reactors, therefore, has dictated a need for an accurate measurement of β_{eff} for the BSR-I.

The effective delayed-neutron fraction, β_{eff}, differs from the true delayed-neutron fraction,[1] β, because the delayed neutrons are emitted with a lower average energy than the prompt fission neutrons; thus, their effectiveness in causing new fissions in the reactor core is different. The ratio, γ, of the effective delayed-neutron fraction to the true delayed-neutron fraction is a function of the composition and geometry of the individual reactor.[2]

In order to determine the value of β_{eff} it is necessary to experimentally measure the change in reactivity associated with a perturbation of the reactor whose effect on the reactivity can be

[1] G. R. Keepin, T. F. Wimett, and R. K. Ziegler, *Phys. Rev.* **107**, 1044 (1957).

[2] A. F. Henry, *Nuclear Sci. and Eng.* **3**, 52 (1958).

precisely calculated. The comparison of the measured change in the reactivity ρ, in dollar units, with the calculated change in reactivity, in per cent reactivity, will then give the value of β_{eff}, or, since the dollar is defined as that value of the criticality factor which is just equal to the contribution of the delayed neutrons,[3] the absolute value of the dollar unit.

The technique used for the measurement of β_{eff} was the boron substitution method, which was first developed by Ruane *et al.*,[4] and which has recently also been used by Kaplan and Henry.[5] The BSR-I loading chosen was loading 75, which, because of its symmetry, permitted a minimum of boron substitution measurements.

Theory of the Experiment

We temporarily assume that a neutron poison exists whose scattering and absorption cross sections at every energy are identical with those of the fuel. If a small amount of this poison is substituted for an equivalent amount of fuel in a just-critical reactor ($\rho = 0$) the perturbed reactor will have a reactivity given by[2,6]

$$\beta_{eff}\,\delta\rho_i = -\frac{\iiint_{\tau_i} \Sigma_f(r,E) f(E') \phi(r,E) \phi^+(r,E')\, dE\, dE'\, d^3r}{\iiint_{v} \Sigma_f(r,E) f(E') \phi(r,E) \phi^+(r,E')\, dE\, dE'\, d^3r - \iiint_{\tau_i} \Sigma_f(r,E) f(E') \phi(r,E) \phi^+(r,E')\, dE\, dE'\, d^3r}, \tag{1}$$

where

Σ_f = macroscopic fission cross section,

ϕ = flux,

ϕ^+ = adjoint flux,

$f(E)$ = normalized spectrum of fission neutrons,

and where the integrations are performed over all energies, over the whole core when labeled with a v and over the domain of the poison substitution when labeled with a τ_i. Equation 1 thus is simply the ratio of the change in neutron production (properly weighted) to the total neutron production in the perturbed reactor.

If the substitution of a small amount of poison for an equivalent amount of fuel is repeated successively over the whole fuel-containing region of the reactor, the summation of all the

[3] A. M. Weinberg and E. P. Wigner, *The Physical Theory of Neutron Chain Reactors*, p 595, University of Chicago Press, Chicago, 1958.

[4] T. F. Ruane *et al.*, *Trans. Am. Nuclear Soc.* 1(2), 142 (1958).

[5] S. Kaplan and A. F. Henry, *An Experiment to Measure Effective Delayed-Neutron Fractions*, WAPD-TM-209 (February 1960).

[6] J. Lewin, *Nuclear Sci. and Eng.* 7, 122 (1960).

reactivities measured gives

$$\beta_{\text{eff}} \sum_i \delta\rho_i =$$

$$-\frac{\iiint_v \Sigma_f(r,E) f(E') \phi(r,E) \phi^+(r,E')\, dE\, dE'\, d^3r}{\iiint_v \Sigma_f(r,E) f(E') \phi(r,E) \phi^+(r,E')\, dE\, dE'\, d^3r - \left\langle \iiint_{\tau_i} \Sigma_f(r,E) f(E') \phi(r,E) \phi^+(r,E')\, dE\, dE'\, d^3r \right\rangle} . \tag{2}$$

The angular bracket around the second integral in the denominator indicates that the term in brackets is to be averaged over the various values it assumes for the separate substitutions.

If, for each substitution,

$$\iiint_{\tau_i} \Sigma_f(r,E) f(E') \phi(r,E) \phi^+(r,E')\, dE\, dE'\, d^3r \ll \iiint_v \Sigma_f(r,E) f(E') \phi(r,E) \phi^+(r,E')\, dE\, dE'\, d^3r \ , \tag{3}$$

which is satisfied in a compact reactor loading, provided that the volume τ in which the substitution is performed is much smaller than the core volume, v, then the right side of Eq. 2 is simply equal to -1, and

$$\beta_{\text{eff}} = -\frac{1}{\sum_i \delta\rho_i} . \tag{4}$$

Unfortunately there is no neutron poison available whose scattering and absorption cross sections are identical, at every energy, to those of U^{235}. Since in a reactor such as the BSR-I most of the scattering is done by water, the mismatch in scattering cross sections between poison and fuel does not introduce any appreciable modification to Eq. 4. However, the mismatch in the absorption cross sections does require a correction to Eq. 4. A simple extension of the model which led to Eq. 1 permits the calculation of the change in reactivity associated with the substitution of poison for a portion of the fuel for the condition in which the macroscopic absorption cross section of the fuel, Σ_{aF}, is not the same as that of the poison, Σ_{aP}.

$$\beta_{\text{eff}} \delta\rho_i =$$

$$-\frac{\iiint_{\tau_i} \{ \nu\Sigma_f(r,E) f(E') \phi^+(r,E') - [\Sigma_{aF}(r,E) - \Sigma_{aP}(r,E)] \phi^+(r,E') \delta(E,E') \} \phi(r,E)\, dE\, dE'\, d^3r}{\iiint_v \nu\Sigma_f(r,E) f(E') \phi(r,E) \phi^+(r,E')\, dE\, dE'\, d^3r - \iiint_{\tau_i} \nu\Sigma_f(r,E) f(E') \phi(r,E) \phi^+(r,E')\, dE\, dE'\, d^3r} , \tag{1a}$$

in which $\delta(E,E')$ indicates a delta function.

Provided that the inequality (3) is still met, β_{eff} is given by

$$\beta_{eff} = -\frac{1}{\sum_i \delta\rho_i}\left\{1 - \frac{\iiint_v [\Sigma_{aF}(r,E) - \Sigma_{aP}(r,E)]\phi^+(r,E')\phi(r,E)\, dE\, dE'\, d^3r}{\iiint_v \nu\Sigma_f(r,E)f(E')\phi^+(r,E')\phi(r,E)\, dE\, dE'\, d^3r}\right\} . \quad (4a)$$

If the absorption cross section mismatch is small in comparison with the fuel fission cross section, the second term in the braces in Eq. 4*a* is small, compared to unity, and represents only a small correction to the value of β_{eff} obtained from Eq. 4. This correction can be evaluated to sufficient precision by a multigroup, few-region code computation.

Description of the Experiment

UNCLASSIFIED
2-01-058-0-565

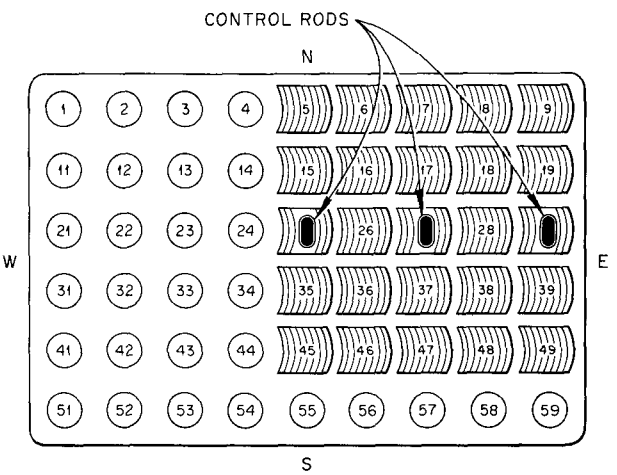

Fig. 1.2.1. Bulk Shielding Reactor Loading No. 75.

Special Fuel Element. – A special BSR-I fuel element, in which 16 of the 18 fuel plates were removable, but which in all other respects was identical with a standard 18-plate BSR-I fuel element, was constructed. This element was successively placed in positions 7, 8, 9, 17, 18, 19, 27, 28, and 29 of loading 75, shown in Fig. 1.2.1. When the special element was placed in positions 27 or 29, which are normally occupied by control-rod-containing half elements (70 g of U^{235}), nine centrally located fuel plates were removed and two aluminum plates were inserted to simulate the control-rod guide plates.

Safety Blade. – A guillotine safety blade, consisting of a thin cadmium sheet between two 12- by 24-in. aluminum plates, was added to one side of loading 75 as an extra safety measure. It was positioned by grooved aluminum guides and supported by electromagnets connected with the scram circuits. The small perturbation induced by the aluminum guides in the otherwise symmetrical loading was considered negligible, in view of the low importance of the reflector.

Poison Plates. – Twenty-two poison plates were fabricated by the Metallurgy Division. The poison plates were identical with standard fuel plates, except that the region normally containing fuel was occupied by the neutron poison. This poison region consisted of a dispersion of B_4C and crystalline Al_2O_3 in type 1100 aluminum, hermetically sealed in type 1100 aluminum by hot rolling. One end of the plates was made 3 in. longer than in the standard plate in order to facilitate handling. The boron content was specified by equating the thermal absorption of the

poison plate to that of an ordinary fuel plate, with 1% tolerance limits permitted for the poison concentration in the finished plates. The B_4C dispersion contained 75.12 wt % B; the boron contained 18.091 wt % B^{10}.

The homogeneity of the B_4C dispersion was verified by photomicrographic examination of selected cross sections under polarized light, and by chemical analysis of typical samples. Test by substitution of one of three plates by another in a given core position showed no variation in the effect upon the reactivity.

Experimental Procedure. – The changes in reactivity produced by the substitution of a poison plate for a fuel plate were measured by a calibrated control rod. The normal all-fuel loading 75 was critical with control rods 1 and 3, in positions 25 and 29, respectively, completely withdrawn, and with rod 2, in position 27, about 15 in. from the bottom of the reactor. With the reactor shut down, a poison plate was substituted for a fuel plate, the reactor brought to critical, and the new position of rod 2 recorded. The changes in reactivity associated with changes in position of rod 2 had previously been determined by an inhour-method calibration. When the special element was used in position 27, measurements were made with rod 3, previously calibrated against rod 2. During all reactivity measurements the temperature of the pool water was checked. It remained almost constant at $26.6 \pm 0.1°C$.

Uncertainties in the Reactivity Measurements. – Two sources of uncertainty exist in the measurement of the change in reactivity caused by the substitution of a poison plate for a fuel plate. The first is a random error associated with the positioning of the fuel plate or poison plate and with the reading of the calibrated control rod. The magnitude of this error was investigated by a reproducibility test. The substitution of a poison plate for a given fuel plate was repeated seven times, using the special element in position 29. In one instance the reactor was completely disassembled and reassembled between substitutions. In every instance the difference (1.12 in.) between the two positions of the control rod was the same within 0.01 in., which corresponds to a reproducibility in the measured change in reactivity of better than 1%. Since only the sum of more than 50 measured changes in reactivity entered into the determination of β_{eff} by Eq. 4, a random 1% error in each measurement introduced an error $<0.2\%$ in β_{eff}.

The second source of uncertainty is derived from the uncertainty in the calibration of the control rod, which is almost entirely due to a 3% uncertainty in determining the period of the supercritical reactor during calibration by the inhour method. The control-rod calibration error introduced a systematic error in all reactivity measurements, resulting in a 1.5% uncertainty in the measured β_{eff}. The error could have been eliminated by an inhour measurement at each substitution of poison for fuel, but such a procedure would have been extremely time-consuming and was rejected.

Additivity Test. – The inequality (3) upon which Eq. 4 is based is only valid if the poison-for-fuel substitution is performed in sufficiently small steps. Since less than one atom in 400 of fuel is replaced by boron when a single poison plate is substituted for a fuel plate, the in-

equality (3) may be assumed to hold. However, to verify the assumption experimentally, an additivity test was performed. Equation 4 is, of course, valid if the changes in reactivity associated with each substitution can be added linearly. A test was made by simultaneously substituting two poison plates for two fuel plates and comparing the resulting change in reactivity with the sum of the changes in reactivity caused by two successive substitutions. The test showed that, within the 1% precision of the reactivity measurements, the reactivity changes were linearly additive.

Absorption-Mismatch Correction

It was earlier pointed out that a correction to the value of β_{eff} given by Eq. 4 must be made in order to account for the inevitable mismatch between the absorption cross sections of fuel and poison. From Eq. 4*a* this correction is

$$\delta A = \frac{\iint_v [\Sigma_{aF}(r,E) - \Sigma_{aP}(r,E)]\phi^+(r,E)\phi(r,E)\, dE\, d^3r}{\iiint_v \nu\Sigma_f(r,E)f(E')\phi^+(r,E')\phi(r,E)\, dE\, dE'\, d^3r} . \tag{5}$$

The value of δA was evaluated by a 3-group, 4-region PDQ calculation, in which

$$\delta A = \frac{\sum_{n=1}^{4}\sum_{i=1}^{3} (\Sigma_{aF} - \Sigma_{aP})_{i,n} \iiint_{v_n} \phi_{i,n}\phi^+_{i,n}\, d^3r}{\sum_{n=1}^{4}\sum_{i=1}^{3} \nu\Sigma_{f_{i,n}} \left(\chi_1 \iiint_{v_n} \phi^+_{1n}\phi_{i,n}\, d^3r + \chi_2 \iiint_{v_n} \phi^+_{2n}\phi_{i,n}\, d^3r \right)} , \tag{5a}$$

where the indexes n and i refer to core regions and energy groups, respectively, and where χ_1 and χ_2 are the normalized contributions of the fission spectrum to the energy groups 1 and 2. The normalized contribution of the third group was assumed to be zero.

The result of the calculation, in which GNU and APC01 codes were used to compute various parameters and weighting factors, was $\delta A = 0.055 \pm 0.017$, in which the 31% error is mostly due to 1% uncertainties in the fuel and poison concentrations and to an 0.8% error in the ratio of the boron thermal-absorption cross section to the fuel thermal-fission cross section.

Results

The change in reactivity due to the substitution of a poison plate for a fuel plate was measured for six plates in each of the nine elements in the positions noted above. Because of

the symmetry of loading 75, these measurements sufficed to give a complete picture of the entire loading. The results are shown in Fig. 1.2.2. The changes in reactivity associated with poison substitution have also been summed for all of the plates of an individual element, and these values are shown in Fig. 1.2.3. The sum of the reactivity changes associated with the substitution of all the fuel plates of the reactor was

$$\sum_i \delta\rho_i = -117.6 \pm 1.8 \text{ dollars} \quad .$$

From this value, and from the value of the absorption-mismatch correction given above, the value of β_{eff} is given by Eq. 4*a*:

$$\beta_{eff} = \frac{1 - 0.055}{117.6} = 0.0080 \pm 0.0002 \quad . \tag{6}$$

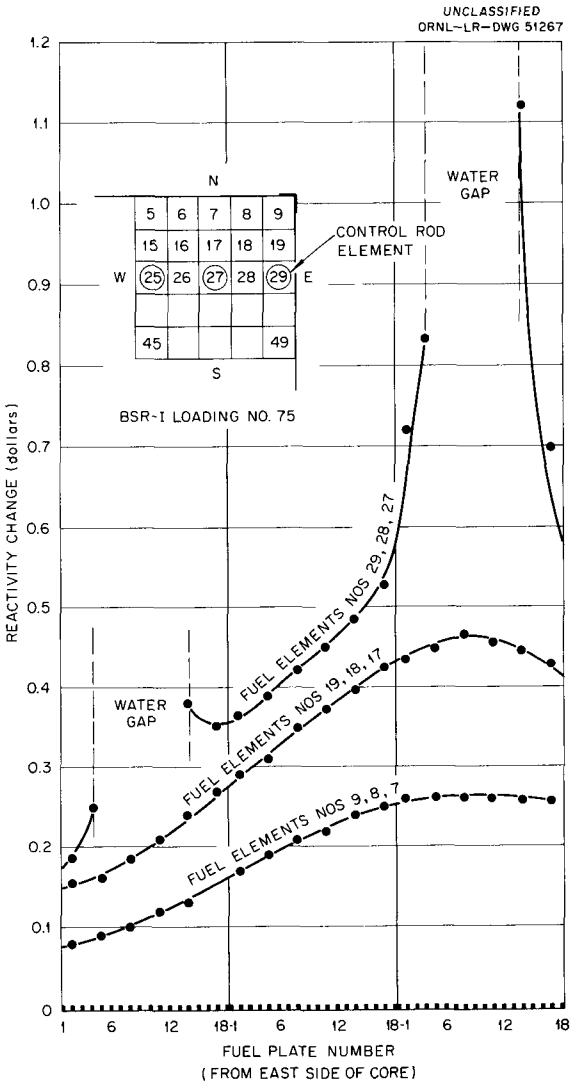

Fig. 1.2.2. Reactivity Changes Produced by the Substitution of a Poison Plate for a Fuel Plate, as a Function of Fuel-Plate Number.

The value of the ratio, γ, of the effective delayed-neutron fraction to the true delayed-neutron fraction, then, is $\gamma = \beta_{eff}/\beta = 1.25 \pm 0.05$, when Keepin's[1] value of β, 0.0064 ± 0.0002, is used.

Theoretical Calculation of γ

For comparison with the experimental value given above, a calculation of the ratio $\gamma = \beta_{eff}/\beta$ was performed, using a 3-group, 4-region model with the PDQ code. Although it is difficult to assign an error to the theoretical calculation, since it largely depends on the

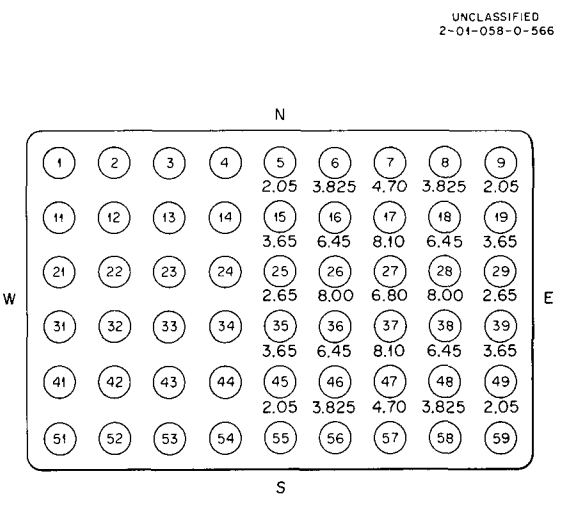

Fig. 1.2.3. Changes in Reactivity Due to the Substitution of Poison for Fuel, in Each Fuel Element.

performance of the code in calculating the space dependence of the flux and its adjoint for the intermediate energy group, the value calculated was $\gamma = 1.25$, in agreement with the experimental value.

Reynolds[7] had previously calculated a value of γ for a 4-by-9 BSR-I loading, in which γ was obtained as the ratio of the delayed-neutron nonleakage probability to the fast-neutron nonleakage probability for a bare equivalent reactor model. His result, $\gamma = 1.22$, is also in agreement with the value obtained from the present work.

A detailed version of this report is to be published elsewhere.

[7] A. B. Reynolds, *Reactivity Effects of Large Voids in the Reflector of a Light-Water-Moderated and Reflected Reactor*, doctoral thesis, Massachusetts Institute of Technology, 1959.

1.3 PULSED-NEUTRON-SOURCE MEASUREMENTS AT THE BULK SHIELDING FACILITY

R. Perez-Belles G. deSaussure E. G. Silver
J. D. Kington E. B. Johnson K. M. Henry, Jr.

Introduction

The pulsed-neutron-source technique[1,2] has been employed at the Bulk Shielding Facility to measure the characteristic time for several loadings of Bulk Shielding Reactor I (BSR-I) fuel elements and one loading of Puerto Rican Research Reactor (PRR) elements. This technique has also been used to measure the reactivity effect of various control-rod configurations in a 5 × 5 BSR-I fuel-element loading. Calculations based on multigroup codes have furnished computed values for comparison with both experiments. The experimental equipment has been described previously.[3] It consisted of the BSF 200-kv particle accelerator, installed on the reactor bridge and producing pulses of fast neutrons by pulsed deuteron bombardment of a tritium target, a thermal-neutron detector, and a time analyzer. The target was at the center of the west face of the reactor core and was connected to the accelerator by a 25-ft-long stainless steel drift tube as shown in Fig. 1.3.1.

[1] E. G. Silver *et al.*, *Neutron Phys. Ann. Prog. Rep. Sept. 1, 1959*, ORNL-2842, p 35.

[2] R. Perez-Belles, *Neutron Phys. Ann. Prog. Rep. Sept. 1, 1959*, ORNL-2842, p 148.

[3] G. deSaussure and E. G. Silver, *Determination of the Neutron Diffusion Parameters in Room-Temperature Beryllium*, ORNL-2641 (Feb. 27, 1959).

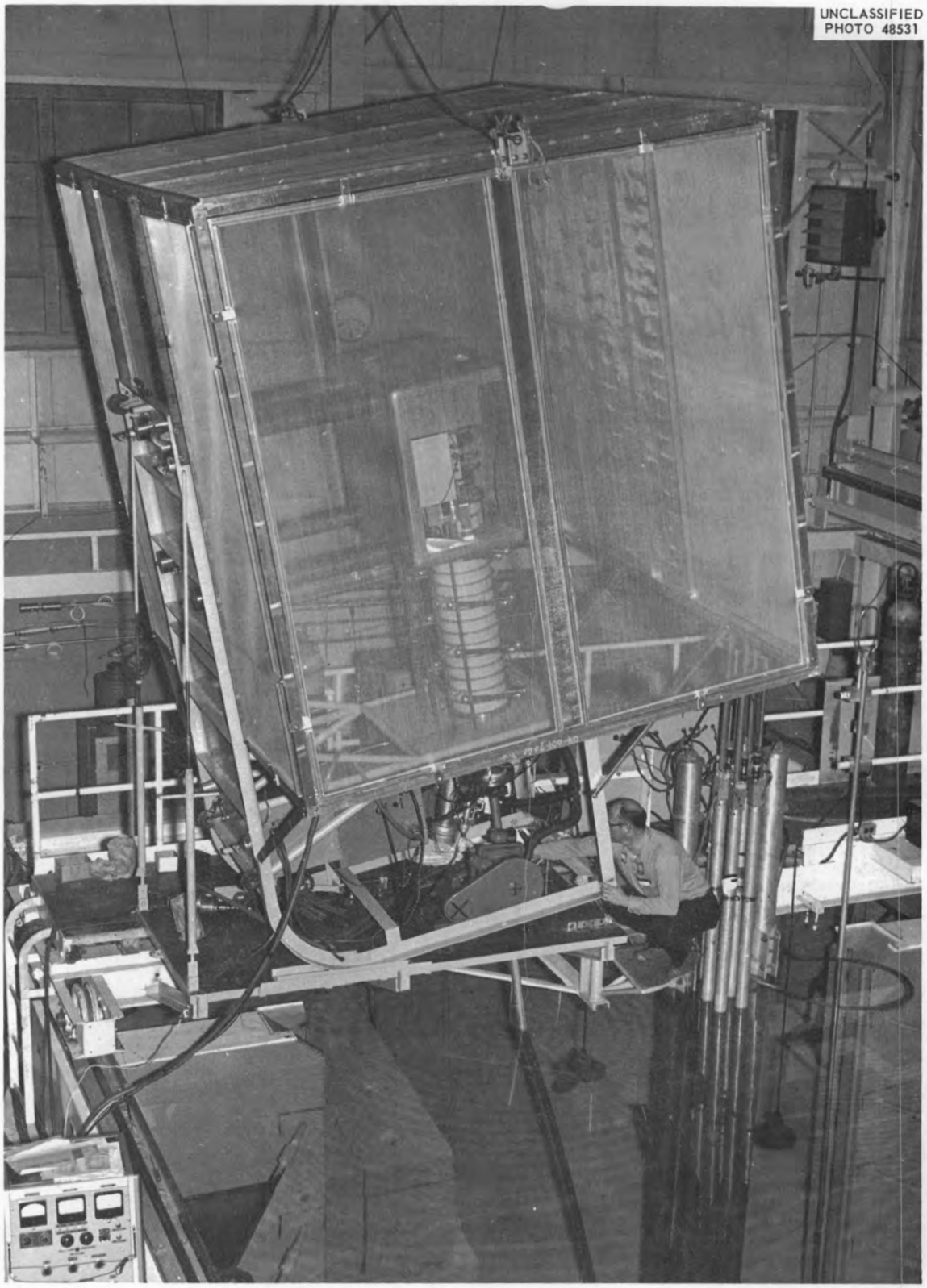

Fig. 1.3.1. Experimental Arrangement.

Measurement of the Characteristic Time

The characteristic time, L, is defined as the ratio of the prompt-neutron generation time to the effective delayed-neutron fraction, or l^*/β_{eff}. This ratio and the ratio of the reactivity, ρ (%), to the effective delayed-neutron fraction are of interest because their values determine the zero-power reactor kinetics. The quantities are related[4] by:

$$\rho^* = \lambda L - 1 \ , \tag{1}$$

where

ρ^* = reactivity (dollars),

λ = decay constant (kc),

$L = l^*/\beta_{eff}$ = characteristic time (msec),

l^* = prompt-neutron generation time (msec),

β_{eff} = effective delayed-neutron fraction.

The characteristic time, L, can be computed from Eq. 1 if ρ^* is known and λ is measured by the pulsed-neutron technique. A previous measurement[1] of L for the BSR-II stainless steel core required a determination of ρ^* by the inhour method, plus the experimental measurement of λ, for solution of Eq. 1. The improved foreground-to-background ratio obtained by use of an accelerator in the present experiment, rather than the chopper previously used, enables measurement of λ at delayed critical ($\rho^* = 0$). Equation 1 then becomes:

$$L = \frac{1}{\lambda_{DC}} \ .$$

This alternate method is thus independent of the inhour determination of the reactivity. However, at critical, since each neutron, in effect, remains in the core, a linearly rising background exists during pulsing. This increasing background limits data-taking runs to about 30 sec, and requires about a 2-min rod insertion to reduce the built-up flux after each 30-sec run. From 100 to 150 such runs are needed for reasonable statistics (1.2×10^5 to 1.5×10^5 counts per channel). Experimental data were analyzed by a method due to Cornell.[5]

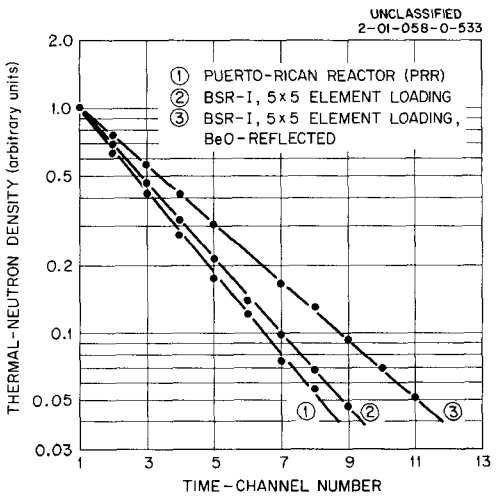

Fig. 1.3.2. Prompt Decay of the Thermal-Neutron Density at Delayed Critical, for Various Pool-Type Reactors.

Figure 1.3.2 shows the decay of the thermal-neutron density (background subtracted) within the BSR-I, both water- and BeO-reflected, and within the PRR. Experimental values of the prompt-neutron decay constant, λ, and the characteristic time, L, for four loadings of the BSR-I and for one loading of the PRR are given in Table 1.3.1.

[4] B. E. Simmons, *Nuclear Sci. and Eng.* 5, 254–56 (1959).

[5] R. G. Cornell, *A New Estimation Procedure for Linear Combinations of Exponentials*, ORNL-2120 (June 21, 1956).

Table 1.3.1. Ratio of the Prompt-Neutron Generation Time, l^*, to the Effective Delayed-Neutron Fraction, β_{eff}, for Various Pool-Type Reactors

Reactor	Configuration	λ, Prompt Decay Constant (kc)	$L = l^*/\beta_{eff}$, Characteristic Time (msec)
BSR-I[a]			
Loading 72	5 × 5, poisoned core	0.112 ± 0.002	8.93 ± 0.18
Loading 75	5 × 5, clean core	0.117 ± 0.004	8.55 ± 0.28
Loading 79	5 × 5, clean, BeO and H_2O reflector	0.089 ± 0.002	11.2 ± 0.2
Loading 73	5 × 5 except 4 corner elements missing, clean core	0.111 ± 0.004	9.00 ± 0.33
PRR	b	0.129 ± 0.003	7.75 ± 0.18

[a]For a complete description of the BSR-I, see, for example, F. C. Maienschein, *A Hazards Summary for Routine Operation of the Bulk Shielding Reactor at One Megawatt*, ORNL-1823 (Dec. 20, 1954).

[b]R. Powell, *Design for U_3O_8 Core Fuel Loading for the Puerto Rico Nuclear Center*, Reactor Engineering Section, AMF Atomics.

Theoretical Calculation of the Characteristic Time

A theoretical calculation of l^*/β_{eff} was performed for a cold, water-reflected, 5 × 5 loading of BSR-I elements. Standard three-group perturbation theory leads to the following expressions for l^* and β_{eff}:

$$l^* = \frac{\sum_{g \text{ groups}} \sum_{\alpha \text{ regions}} \int dr \left\{ (\phi_{g\alpha} \phi^+_{g\alpha})/v_g \right\}}{P} ; \tag{2}$$

$$\beta_{eff} = \gamma\beta = \beta \frac{\sum_{\alpha \text{ regions}} \int dr \left\{ \phi^+_{E\alpha} [(\nu\Sigma_f)_{F\alpha} \phi_{F\alpha} + (\nu\Sigma_f)_{E\alpha} \phi_{E\alpha} + (\nu\Sigma_f)_{S\alpha} \phi_{S\alpha}] \right\}}{P} ; \tag{3}$$

where P, the weighted total neutron production, is given by

$$P = \sum_{\alpha \text{ regions}} \int dr \Big(\left\{ x_F (1-\beta) \phi^+_{F\alpha} + [x_E (1-\beta) + \beta] \phi^+_{E\alpha} \right\} \left\{ (\nu\Sigma_f)_{F\alpha} \phi^+_{F\alpha} + (\nu\Sigma_f)_{E\alpha} \phi_{E\alpha} + (\nu\Sigma_f)_{S\alpha} \phi_{S\alpha} \right\} \Big) , \tag{4}$$

and

$\phi_{g\alpha}$ = neutron flux in group g, region α,

$\phi^+_{g\alpha}$ = adjoint neutron flux in group g, region α,

v = neutron velocity,

ν = neutrons per fission,

Σ_f = macroscopic fission cross section,

x_F = fast fraction of the fission spectrum,

x_E = epithermal fraction of the fission spectrum ($x_E + x_F = 1$),

and the subscripts, F, E, and S refer to fast, epithermal, and slow fluxes, respectively.

The input for the numerical solution of Eqs. 2, 3, and 4 was obtained from the sequence of code computations GNU–PDQ–APC01, applied to the BSR-I 5 × 5 loading. The value of the prompt-neutron generation time, computed from Eq. 2, was found to be $l^* = 74.0$ μsec. By application of Keepin's value[6] of $\beta = 0.0064$ in Eq. 3, $\beta_{eff} = 0.0080$. This value agrees very well with an experimental determination of β_{eff} reported in Sec 1.2, this report.

The ratio l^*/β_{eff} obtained from the calculation is 9.2 msec, which may be compared to the experimentally determined value of 8.55 ± 0.28 msec. It is felt that the 8% disagreement between experiment and calculation could be diminished by improving the adjoint-flux computation.

Measurement of Control-Rod Worth

The accurate measurement of control-rod worth has an obvious importance in reactor technology. Although reactivities ranging from zero at delayed critical to about –2 dollars can be measured by the inhour method, this method is not applicable to multidollar negative reactivities. Large negative reactivities can be measured by the "rod-drop" technique or by the "source-jerk" technique. Both methods, however, involve difficulties associated with measurement of the flux during the transient produced by dropping the rod or removing the external source of neutrons.[7] The pulsed-neutron-source technique, however, is particularly well suited to the measurement of large reactivities. The decay constant, λ, can be measured very accurately (±2%) and the reactivity computed from Eq. 1. The only uncertainty is the change of the characteristic time, L, with reactivity. This is produced by variations in the neutron spectra and flux shape due to insertion of the control rod. It has been experimentally demonstrated[8] that L is insensitive to redistribution of control rods in the reactor core, as long as the reactor remains critical without fuel or moderator changes.

A dependence of L on reactivity, however, is not ruled out, although first-order perturbation calculations now in progress seem to indicate that only a small change takes place for large reactivities ($\rho \geqq 10$ dollars). The pulsed-neutron-source technique was used to measure the reactivity effect of several control rod configurations within a BSR-I 5 × 5 loading. A value of $L = 8.55 \pm 0.28$ msec, previously measured for the loading, was used in Eq. 1 to compute the

---

[6] G. R. Keepin, T. F. Wimett, and R. K. Zeigler, *Phys. Rev.* **107**, 1044 (1957).

[7] W. S. Hogan, "Negative-Reactivity Measurements," to be submitted to *Nuclear Sci. and Eng.*

[8] J. Bengston *et al.*, *Proc. U.N. Intern. Conf. Peaceful Uses Atomic Energy, 2nd, Geneva, 1958* **12**, 63 (1958).

reactivities. The worth of each configuration was computed from:

$$W = \rho_0^\star - \rho^\star \text{ (dollars)} ,$$

where

W = control-rod worth,

$\rho_0^\star$ = positive reactivity with all control rods withdrawn, measured by the positive-period method (= 1.52 dollars),

$\rho^\star$ = actual negative reactivity, computed from Eq. 1.

Figure 1.3.3 shows the experimentally measured decay of the thermal-neutron density (background subtracted) as a function of channel number, for various subcritical conditions in the BSR-I.

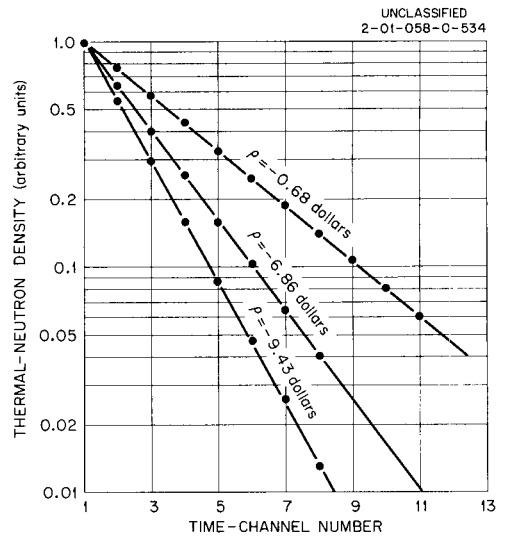

Fig. 1.3.3. Decay of the Thermal-Neutron Density in a BSR-I 5 × 5 Element Loading, for Various Negative Reactivities.

The results of the control-rod-worth measurements are shown in Table 1.3.2, where they are compared with results of parallel PDQ code computations. The PDQ diffusion calculation tends to overestimate the effect of the absorber, a result which was also found in calculations of the bucklings of Be-Cd assemblies, which are reported in Sec 5.3 of this report.

Table 1.3.2. Comparison of Results of Experiments vs Calculations of Control-Rod Worth for the BSR-I

Rod Configuration	λ, Measured Decay Constant (kc)	k_c, Calculated Multiplication[a]	ρ, Measured Reactivity[b] (dollars)	W_c, Calculated Control Rod Worth[c] (dollars)	W_m, Measured Control Rod Worth[d] (dollars)	$100 \times \frac{W_c - W_m}{W_c}$
□ □ □		1.0098	1.52[e]			
□ □ ■	0.197 ± 0.002	0.9898	−0.68 ± 0.04	−2.5	−2.39 ± 0.09	4.4
■ □ ■	0.594 ± 0.020	0.9641	−4.08 ± 0.18	−5.8	−5.79 ± 0.20	0.2
□ ■ □	0.640 ± 0.009	0.9521	−4.47 ± 0.22	−7.5	−6.18 ± 0.23	17.6
■ ■ □	0.919 ± 0.004	0.9252	−7.86 ± 0.64	−11.3	−9.57 ± 0.70	15.3
■ ■ ■	1.220 ± 0.022	0.9033	−9.43 ± 0.69	−14.6	−11.14 ± 1.0	24

[a]Calculation did not include effects of target and detector.

[b]From Eq. 1.

[c]$W_c = (1 - k_c^{-1})\beta_{eff}^{-1}$, where $\beta_{eff} = 0.0080$.

[d]Data from pulsed-neutron-source measurements are corrected by −0.19 dollars to allow for effect of target and detector as measured by inhour method.

[e]Measured by the inhour method.

1.4 DIGITAL COMPUTER REACTOR CALCULATIONS AT THE BULK SHIELDING FACILITY

E. G. Silver R. Perez-Belles B. Bonner[1]

Introduction

The success obtained in the use of the IBM 704 computer codes, PDQ and GNU, at the Bulk Shielding Facility (BSF) for prediction of reactor parameters has previously been reported.[2] It was concluded that these codes agree satisfactorily with experiment for compact loadings. The program of investigation has been continued, both in an attempt to improve the previously unsatisfactory predictions obtained for reactors containing large, nonfueled regions and to improve the treatment for heavily absorbing regions such as control rods, within the reactor, as well as to obtain data for practical application to BSF experimental programs. Some of the calculations are reviewed in other sections of this report and will be touched upon here only to the extent that the calculational techniques are of interest.

Puerto Rican Research Reactor

The Puerto Rican Research Reactor (PRR) calculations have previously been described.[2] As a result of those calculations the fuel content of the PRR elements was increased from 178 g per fuel element, as originally proposed by the designer,[3] to 192 g per element, and the critical experiments for the PRR were performed with the increased content. The multiplication constant, k, computed for PRR loading 5 was 1.0042, while the value obtained from the critical experiment was 1.0002 ± 0.0002, a difference of only 50 cents, based on a value of β_{eff} of 0.0080.

The PDQ calculations for PRR loading 1 were made for 178-g elements. In order to compare calculated multiplications with experimental data obtained with 192-g elements in this loading, a previous GNU calculation of multiplication constant as a function of fuel content per element was utilized. The comparisons are shown in Table 1.4.1 for two conditions, the first with partial elements surrounding the five control rod elements, the second with all full fuel elements. The difference between calculation and experiment is 34 cents with partial elements, and 1.31

[1]On loan, ORINS Summer Student Trainee Program.

[2]E. G. Silver and W. Etzel, *Neutron Phys. Ann. Prog. Rep. Sept. 1, 1959*, ORNL-2842, p 6.

[3]R. Powell, *Design for U_3O_8 Core Fuel Loading for the Puerto Rico Nuclear Center*, Reactor Engineering Section, AMF-Atomics.

Table 1.4.1. Comparison of Calculated Multiplication Constants for PRR Loading 1 with Experiment

Configuration	Calculated Multiplication		Measured Multiplication
	178-g Element	192-g Element	192-g Element
With partial elements	1.0050	1.0233	1.0206
All fully fueled elements	1.0512	1.0704	1.0809

dollars with full elements only. The better agreement in the first instance is probably due to the fact that the k-vs-fuel-content curve used to interpolate to 192-g elements was computed with a loading containing the partial elements.

Bulk Shielding Reactor II

A GNU calculation and a series of PDQ calculations were performed to determine the effect of partial insertion of the control plates in the Bulk Shielding Reactor II (BSR-II). For this purpose the PDQ code was used in R-Z geometry, and the control plates were idealized to an axial hollow cylinder with fuel both inside and outside the poison cylinder. The partially withdrawn poison cylinder projected above the core top, and this projection was explicitly included in the calculations. However, the lower end boxes and grid plate were not included in the calculation. Figure 1.4.1 shows the calculated and measured shapes normalized to the same total worth. The measured curve is the average of curves 3a and 3 of Fig. 2.1.9 in ref 2. The differences in shape between calculation and measurement are attributable to two causes: First, the grid plate, lower end boxes, and the water space left by the rod withdrawals were neglected in the calculation, and second, the measured rod was in the outer row, with a total worth of 63 cents, whereas the calculation was for a central hollow cylinder representing four rods, and worth 9.07 dollars.

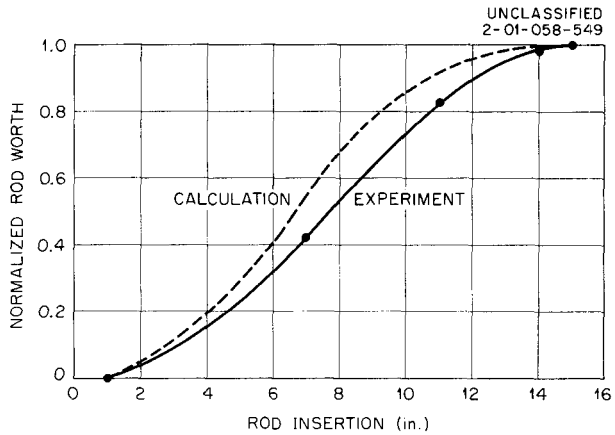

Fig. 1.4.1. BSR-II Rod Worth as a Function of Insertion Distance, Normalized to Unity at Full Insertion. Comparison of experiment with PDQ calculation.

Bulk Shielding Reactor I

The bulk of the calculational work during the past year was done on the Bulk Shielding Reactor I (BSR-I) fuel elements. The work may be divided into two aspects: First, the improvement of input parameters to improve agreement with experimental values, especially in cases containing central water spaces or poison regions; and second, the application of these improved input parameter methods to calculations on specific loadings of practical interest.

Input Improvement. – In a previous paper,[2] a calculation of BSR-I loading 20 was discussed. This loading has a four-element water space in the center of the loading, and the calculated reactivity differed by about 4.4 dollars from the experimental value. Other cases where large spaces existed in the core had also given poor agreement. The calculations were therefore improved in three directions: First, the correct diffusion coefficients for thermal neutrons in water and core were used in the thermal group, rather than the GNU-derived values which

neglect binding effects in the water molecules entirely. Second, new removal cross sections, calculated by an improved method,[4] were used. The older GNU calculation of removal cross sections was based on the mean removal cross section averaged over the few-group lethargy interval. The present method uses the slowing-down out of the bottom of the few-group interval, as shown below:

$$R = \frac{(D_{eg})_j^g + (D_{sb})_j^g + (D_{ino})_j^g}{\phi_j^G} , \tag{1}$$

$$\phi_j^G = \sum_i \left(\Delta U_i \int_{b_{j-1}}^{b_j} \phi_i \, dV \right) \text{vol}^{-1} , \tag{2}$$

where

g = index of lowest multigroup in the Gth few-group interval,

j = index of spherical shell extending from b_{j-1} to b_j,

ΔU_i = lethargy width of ith multigroup,

D_{eg} = degradation out of a group due to elastic scattering from heavy elements,

D_{sb} = degradation out of a group due to elastic scattering from hydrogen,

D_{ino} = inelastic scattering out of a group,

and the index i indicates summation over the multigroup lethargy intervals making up the Gth few-group interval. The new cross sections differed from the earlier values by as much as 40%.

A third change made in the calculational procedure involved the fact that the relative magnitudes of the various multigroup fluxes depend on the proximity of poison or water regions; therefore the fuel region was split into several layers around the poison or water spaces and the few-group parameters calculated separately for each. The following core splitting was employed: (1) inner fuel, a layer about $2\lambda_{tr}$ thick around the water or poison region; (2) fuel region 2, a layer about $5\lambda_{tr}$ thick around the inner fuel; (3) general fuel, fuel regions far from poison, water spaces, or outer boundaries; and (4) outer fuel, a layer about $5\lambda_{tr}$ thick next to the outer water reflector.

Of course, the cross sections in these regions, for the same material composition, differ depending on whether they are adjacent to absorber or water regions.

Loading PCA-20, the four-element-hole loading, and loading PCA-30, a one-element-hole loading, shown in Fig. 1.4.2 were calculated according to the improved method. The comparison of both calculational results with the experimental result is given in Table 1.4.2.

The improved procedure thus gives results differing from experiment by only 59 and 80 cents for the 4- and 1-element gaps, respectively, while under the older procedure the differences were 4.39 and 2.45 dollars. The present procedure obtains agreement of the same order as that

[4]The removal cross section improvements are the work of B. F. Maskewitz and V. E. Anderson of ORGDP.

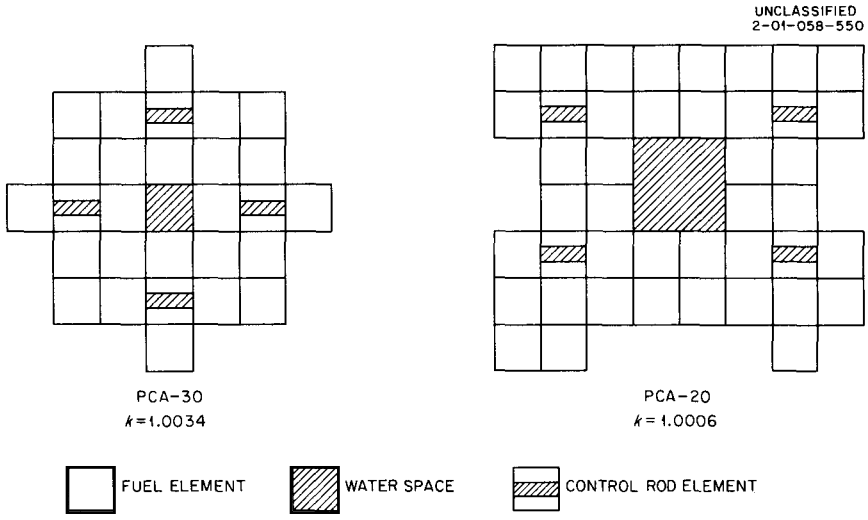

Fig. 1.4.2. PCA Loadings 30 and 20, Both Containing Central Water Spaces.

Table 1.4.2. Comparison of Experimental and Calculated Multiplication Constants for Two BSR-I Loadings Containing Water-Filled Spaces

Configuration	Calculation		Experiment
	Old Method	New Method	
Loading 20 (4-element space)	1.0356	1.0052	1.0006
Loading PCA 30 (1-element space)	1.0230	1.0098	1.0034

previously obtained only for compact loadings. Further improvement would require improvements in basic cross sections and fission parameters and is not planned at this time.

The same improvement program was applied to shutdown-configurations, in order to obtain control-rod worths for comparison with the pulsed-neutron-source measurements reported in Sec 1.3. Loading PCA-26, shown in Fig. 1.4.3, was calculated with all control rods fully withdrawn. The value of the multiplication obtained by the older calculational method was 1.0169; by the new method it was 1.0098, while the experimental value was 1.013. The differences with experiment, amounting to 40 cents for the new method and 49 cents for the old, indicate that for water spaces as small as a control-rod gap there is little practical improvement to be gained by the newer procedure. Table 1.4.3 shows the comparison of the rod-worth calculations with the experimental values deduced

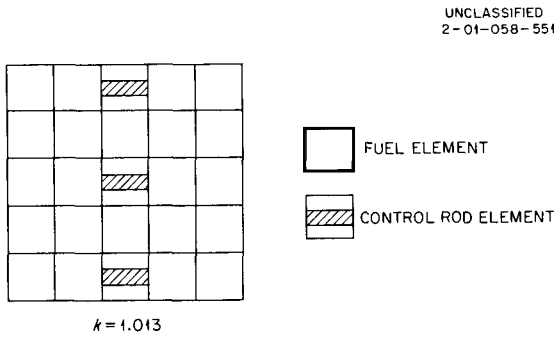

Fig. 1.4.3. PCA Loading 26.

Table 1.4.3. Measured and Computed Multiplication Constants for Various Rod Configurations of Loading PCA-26

Rod Position: □ ≡ Fully out, ■ ≡ Fully in	Experimental Multiplication	Computed Multiplication	
		Old Method	New Method
□ □ □	1.013	1.0169	1.0098
□ ■ □	0.9573	0.9522	0.9521
■ □ ■	0.9674	0.9663	0.9641
■ □ □	0.9961	0.9929	0.9898
■ ■ □	0.9467	0.9274	0.9252
■ ■ ■	0.9263	0.8944	0.9033

from pulsed-neutron measurements. It is apparent that the improvement due to the new calculational methods is not significant. The results of the calculation, even in the most poisoned case, differ by only 2.5% from the k values measured by the pulsed-neutron method; however, this amounts to as much as 17.8% difference in the rod worth. This difference appears to be mostly due to the inherent limitations of diffusion theory in the vicinity of strong absorbers and to the relatively poor geometric approximation to the actual rod shape afforded by a rectangular model. Similar measurements on black absorbers in nonmultiplying one-velocity systems (see below) show similar error magnitudes.

Improvements in rod-worth calculations may be possible by applying transport theory to regions in the vicinity of the absorbers and then suitably adjusting the flux gradients at some fictional rod surface beyond which diffusion theory may be sufficiently rigorous to satisfy the requirements of the calculation.

Applied Calculations. – The PDQ code has been applied to the solution of three problems of practical interest in the Bulk Shielding Facility programs. The first was a calculation of the slab-shaped PCA loading PCA-32, which is being used experimentally for developmental work on the model IV gamma-ray spectrometer.[5] Flux plots were obtained, one of which, the thermal-flux contour plot, is shown as Fig. 1.4.4.

[5]See sec 8.4, this report.

UNCLASSIFIED
2-01-058-552

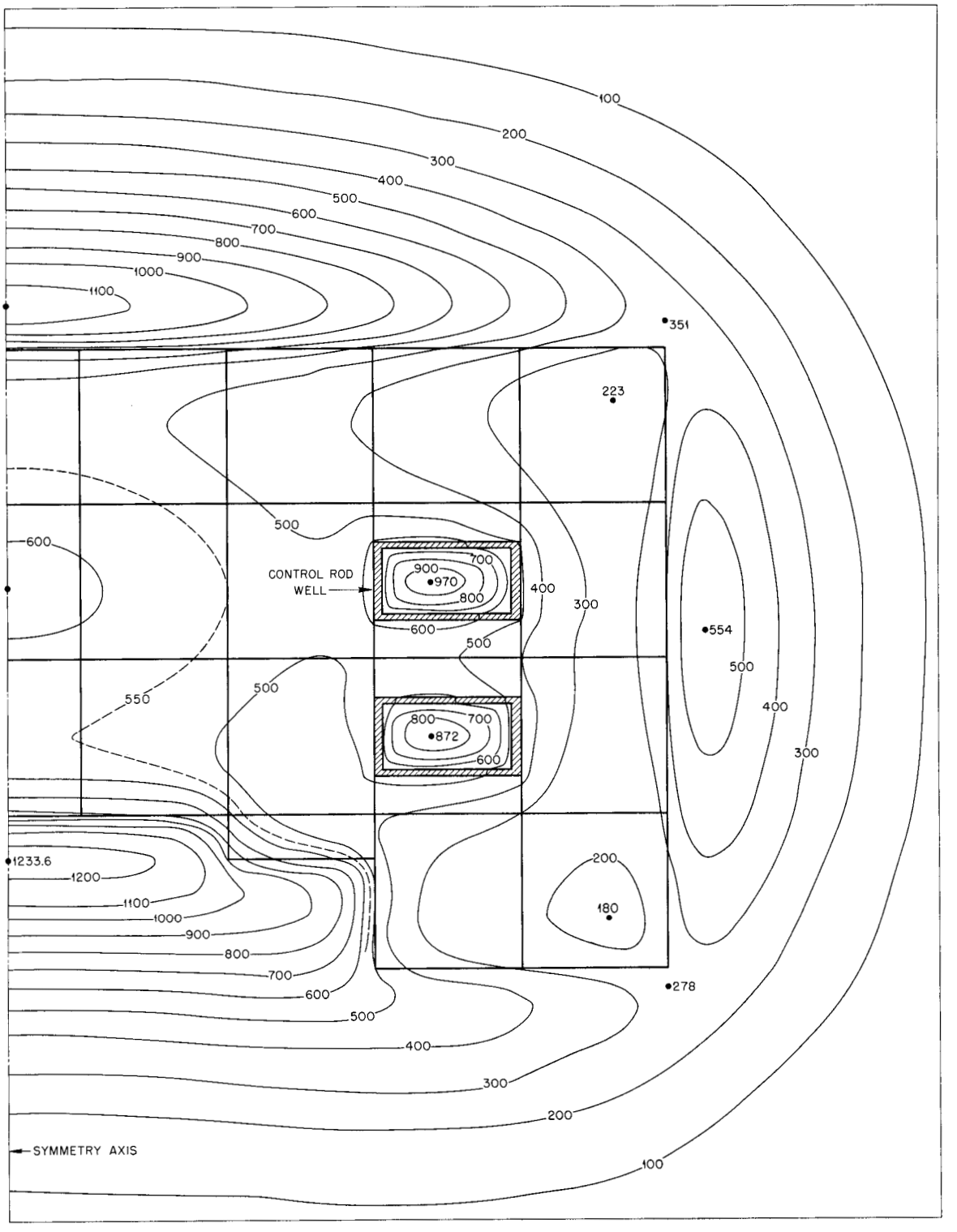

Fig. 1.4.4. Isoflux Contours Calculated by the PDQ Code for the Thermal-Neutron Flux in Loading PCA-32A.

The second problem of practical interest concerned the effect of an accidental close conjunction of two BSR-I-type reactors in the BSF pool. In order to maximize the interaction, the two reactors were assumed as two slab loadings, each 9 by $3\frac{1}{2}$ elements in extent. Critical-mass calculations were performed first for one such loading, then for pairs of such loadings at several separation distances. The results are shown in Fig. 1.4.5. Since at a separation of 3 cm the calculated excess reactivity is 18 dollars, it appears that very close approaches of two BSR-I reactors, even in shutdown condition, could cause a nuclear incident.

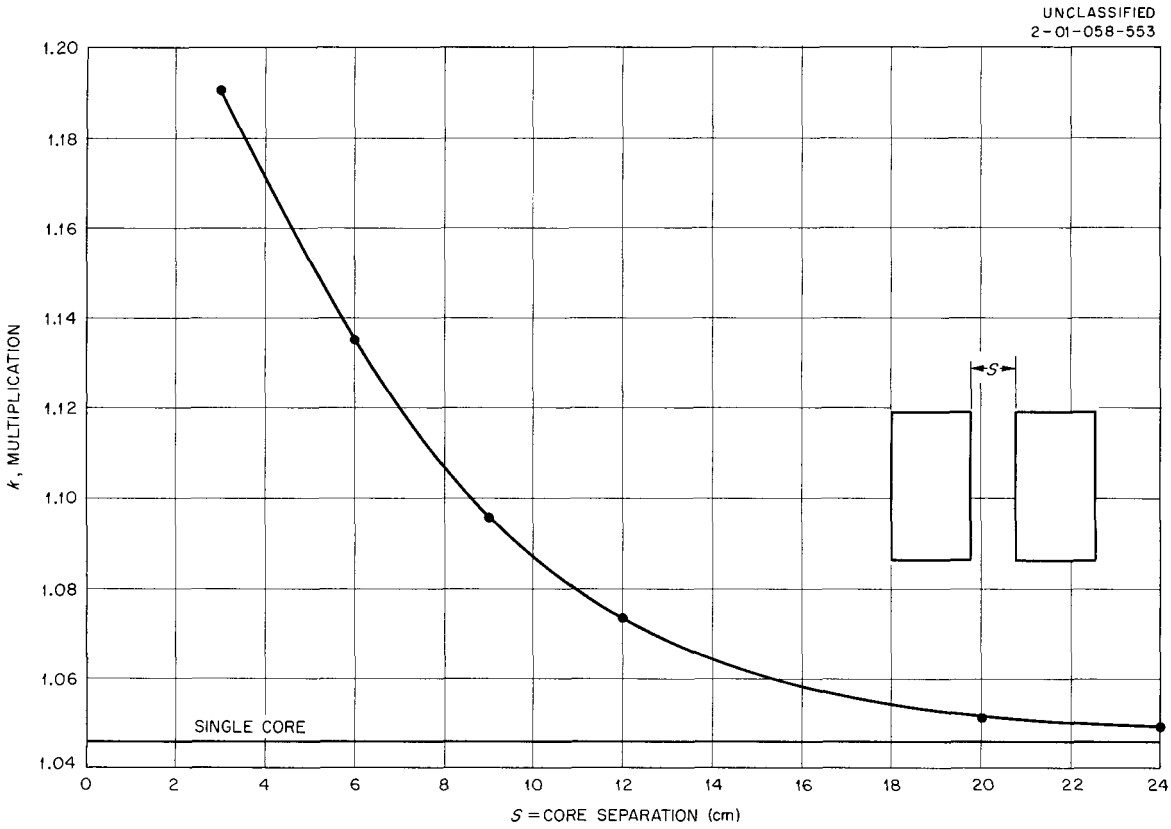

Fig. 1.4.5. Multiplication Constant of Two 9- by $3\frac{1}{2}$-Element BSR-I Reactors as a Function of Their Separation in Water Compared with the Multiplication Constant of an Isolated, Single, Similar Reactor.

The third problem was a calculation of control-rod worth as a function of insertion distance for a central control rod in a water well at the center of an "equivalent-cylinder" BSR-I loading. Figure 1.4.6 shows the results of PDQ calculations in RZ geometry for this configuration, and, for comparison, also shows inhour and pulsed-neutron source measurements for a central rod in PCA loading 26, normalized to the same total worth.

Beryllium Assemblies

In order to predict the one-velocity neutron decay constants that are detailed in Sec 5.3, PDQ calculations have been done on unfueled beryllium assemblies containing inserted cadmium rods. Since two energy groups are the minimum required for PDQ to iterate, a spurious fast group was included with a very large removal cross section, a very small diffusion coefficient,

and a vanishing absorption cross section. This combination of parameters results in immediate localized scattering into the thermal group of all neutrons in the fast group. The decay constant λ is related to the "multiplication" k by the relation $\lambda = v\nu\Sigma_f/k$. By setting $\nu\Sigma_f = 1/v$, one obtains $\lambda = 1/k$. For the cases of unpoisoned beryllium, using the values of $\nu\Sigma_a$ and D obtained from the pulsed-neutron experiments, the calculated and experimental values of $1/k$ agree very well. When cadmium-containing assemblies were considered, disagreement of the order of 10% was evident between the calculated and measured reactivity worths of the poison materials. The explanation, as in the case of the control-rod calculations previously discussed, appears to lie in the basic inadequacy of diffusion theory in the vicinity of strong absorbers. The effect of the choice of flux gradient at the absorber boundary was tested by a series of calculations with this quantity as the parameter, and the result was found to be very insensitive to this variable.

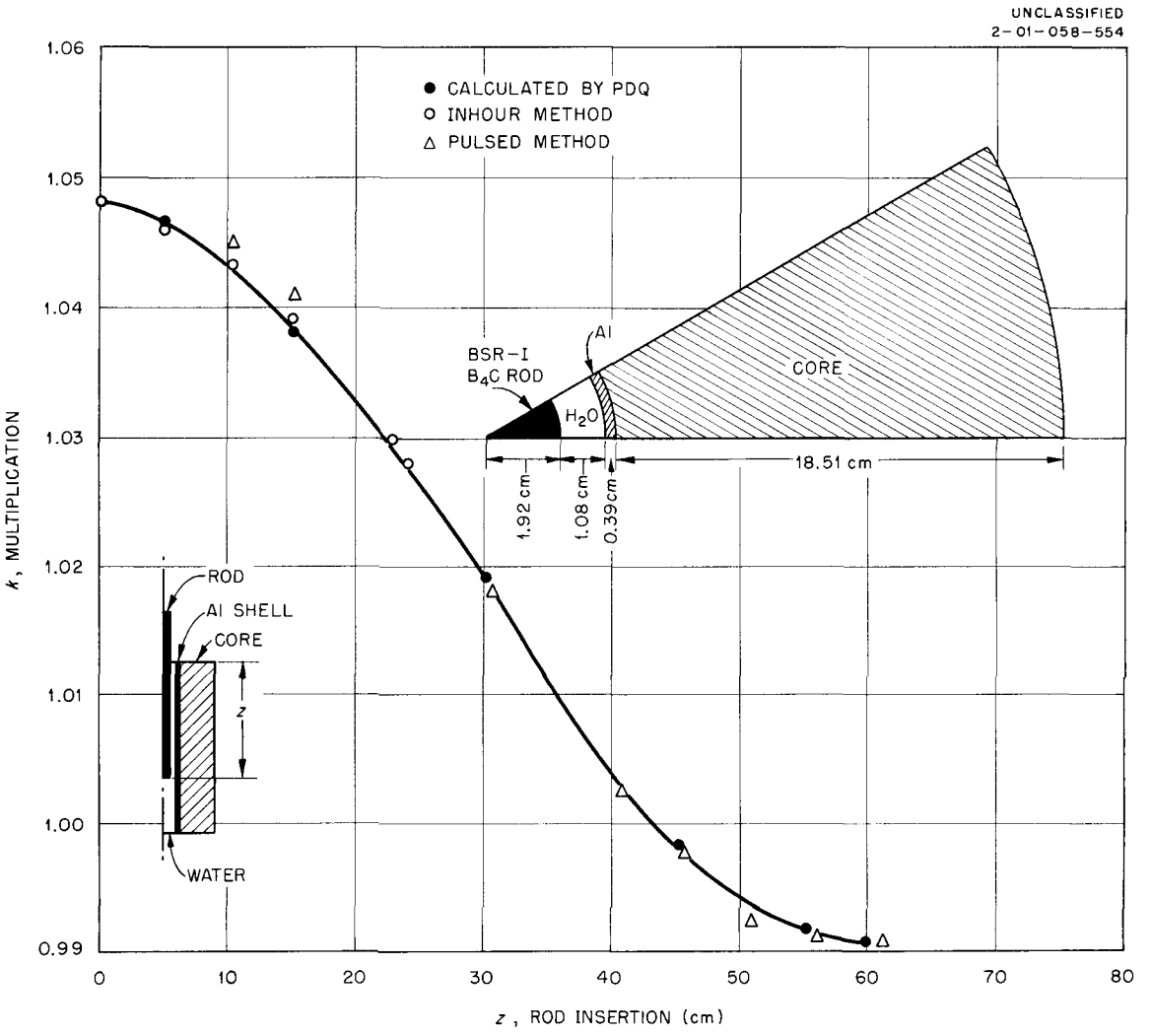

Fig. 1.4.6. Multiplication, k, as a Function of Rod Insertion Distance for a BSR-I B_4C Control Rod on the Axis of a Cylindrical Equivalent of a BSR-I Loading. Values measured by inhour and pulsed-neutron-source methods are shown for comparison.

Part 2

NEW REACTORS FOR THE BULK SHIELDING AND TOWER SHIELDING FACILITIES

2.1 BULK SHIELDING REACTOR II: STATUS REPORT, INCLUDING SPERT TESTS

E. G. Silver K. M. Henry, Jr.

Introduction

The design, fabrication, and assembly of the Bulk Shielding Reactor II (BSR-II), the UO_2–stainless steel reactor core for the Bulk Shielding Facility (BSF), as well as the initial critical experiments with this core, performed at the BSF, have previously been reported.[1-4] At the conclusion of the BSF critical experiments the BSR-II was disassembled and shipped to the National Reactor Testing Station at Arco, Idaho, where it was reassembled in the tank of the SPERT-I Facility for the purpose of performing a number of transient-excursion experiments. Prior to and in preparation for these tests, several static measurements, including measurements of the reactivity worth of the control system, temperature coefficients, void coefficients, and flux shapes, were made. Both the static tests and the transient tests have been completed and are summarized below.

Much of the work described was performed by members of the SPERT staff,[5] and by members of the Reactor Controls Group of the ORNL Instrumentation and Controls Division, who were responsible for the installation and operation of the safety system, and who had a number of objectives additional to those directly concerned with the BSR-II core.

Static Measurements

Control System Reactivity Worth. – The loading configuration of the BSR-II which was employed for the static tests is shown in Fig. 2.1.1. The four pairs of control plates will be referred to as rods Nos. 1, 2, 3, and 4 corresponding to the four control-element positions shown in Fig. 2.1.1. In the transient test program rod No. 1 was used as a regulating rod, both to achieve criticality and to insert the desired amount of excess reactivity for the transients, as will be discussed below. The other three rods, Nos. 2, 3, and 4, were withdrawn to the upper limit at criticality and were scrammed to terminate the excursions. Figure 2.1.2 shows the reactivity worth vs position for rod No. 1, and for rods Nos. 2, 3, and 4 operated as a gang, that is, simultaneously at the same vertical position. The reactivity measurements were made by poisoning the reactor with boron solution in the SPERT tank. This method obviated the need for compensating motion of other poison rods which would have perturbed the flux shape. In each of the two measurements the rod or rods not being evaluated were kept at the upper limit.

---

[1] E. G. Silver and J. Lewin, *Safeguard Report for a Stainless Steel Research Reactor for the BSF (BSR-II)*, ORNL-2470 (1958).

[2] E. G. Silver and J. Lewin, *Appl. Nuclear Phys. Ann. Prog. Rep. Sept. 1, 1957*, ORNL-2389, p 33.

[3] E. G. Silver, *Neutron Phys. Ann. Prog. Rep. Sept. 1, 1958*, ORNL-2609, p 15.

[4] K. M. Henry, E. G. Silver, and E. B. Johnson, *Neutron Phys. Ann. Prog. Rep. Sept. 1, 1959*, ORNL-2842, p 21.

[5] In particular, the foil measurements were made by J. Siegwarth, and the temperature and void coefficients were measured by L. Stephan. The entire SPERT program was supervised by F. L. Bentzen.

UNCLASSIFIED
2-01-058-0-558

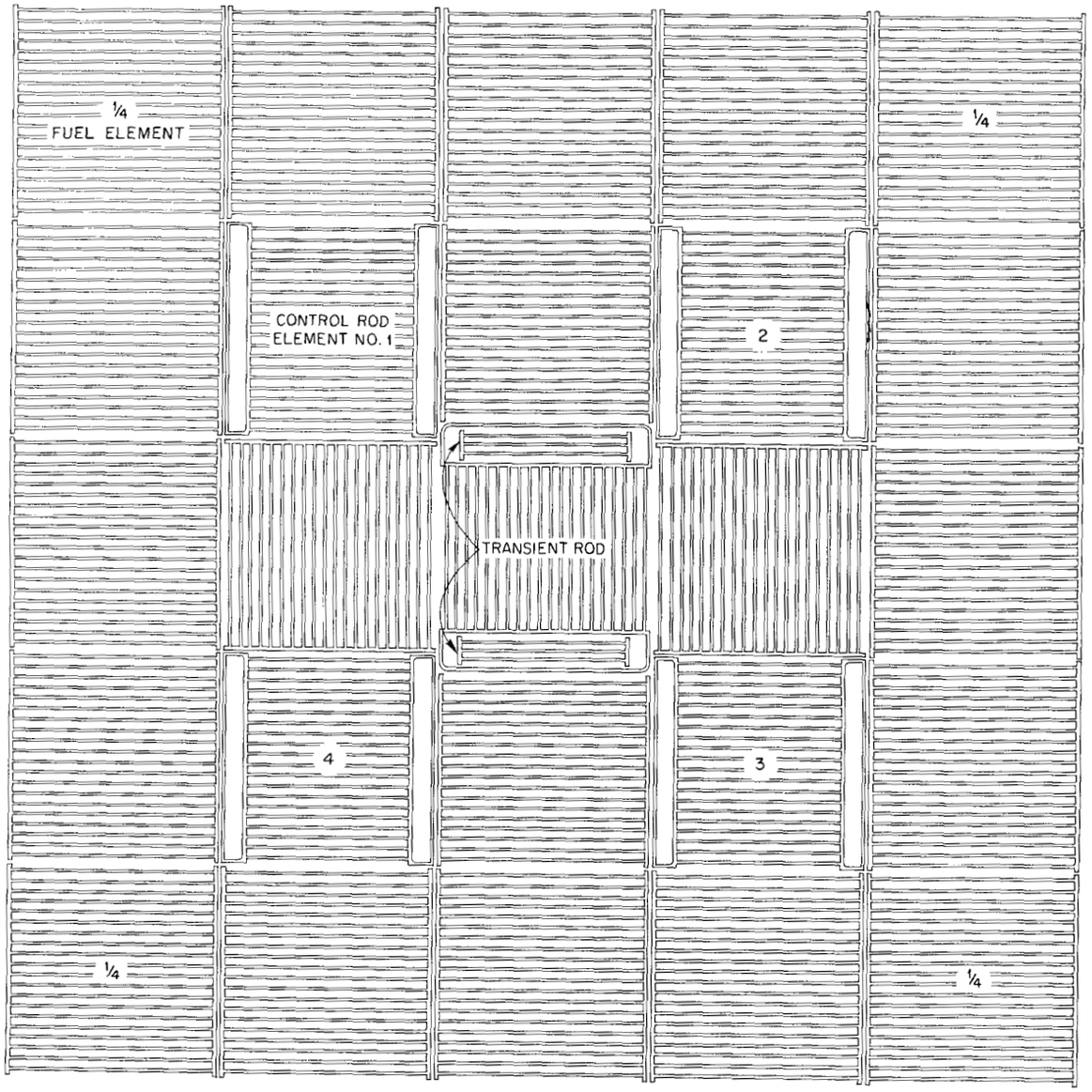

Fig. 2.1.1. Core Configuration Used in Static Tests of the BSR-II at the SPERT-I Facility.

Temperature Coefficient Measurement. – The temperature coefficient of the BSR-II was measured only for the condition of uniform temperature change throughout the core and reflector. This condition was accomplished by the use of electric heaters in the water tank, sufficient time being allowed at each temperature for all of the components to achieve thermal equilibrium. The water was constantly stirred to prevent the formation of temperature gradients in the tank.

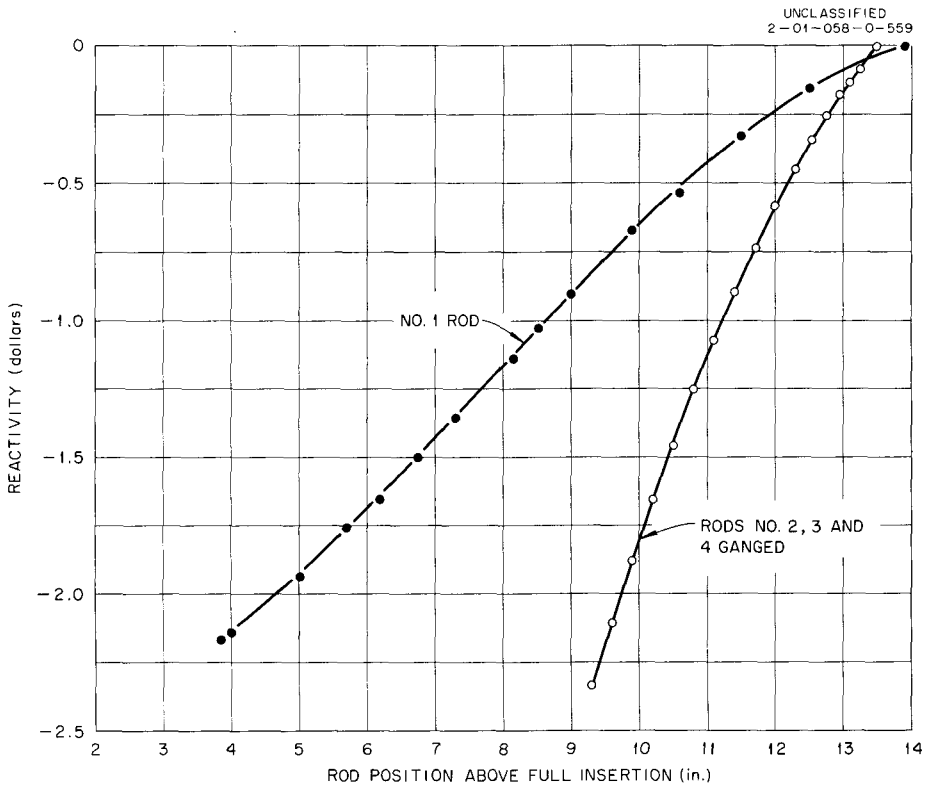

Fig. 2.1.2. Reactivity of No. 1 Control Rod, and of Rods 2, 3, and 4 in Gang, as Functions of Distance Above Full Insertion.

Figure 2.1.3 shows both the reactivity change, referred to 15.0°C, and the temperature coefficient over the range 15.0 to 84.0°C. The coefficient appears to vary linearly with temperature from 15.0 to about 50°C, and then begins to level off. Extrapolation to lower temperature indicates that the coefficient changes sign at about 12°C, becoming positive for temperatures below that value. For comparison, the reactivity change vs temperature in the BSR-I is also shown.[6]

Void Coefficient Measurements. – For this measurement voids were produced in the core by the insertion of magnesium strips, containing 0.2% manganese as the principal impurity, in all fuel elements except the four control elements and the transient-inducing rod element. The magnesium strips were uniformly 0.11 in. thick, 0.52 in. wide, and 15.0 in. long, and for any one measurement the number and distribution of strips in each fuel element were identical. Measurements over a range from zero to a total void fraction of 4% of moderator volume showed a linear dependence, with a measured value of the void coefficient of 8.0×10^{-4} dollar/cm^3 over this range. Since the five control rod and transient elements could not be voided, separate measurements were made with magnesium strips placed adjacent to these elements, and the measured values graphically interpolated across the control elements. The void coefficient of

[6] R. G. Cochran *et al.*, *Reactivity Measurements with the Bulk Shielding Reactor*, ORNL-1682, sec V, p 32–36 (1954).

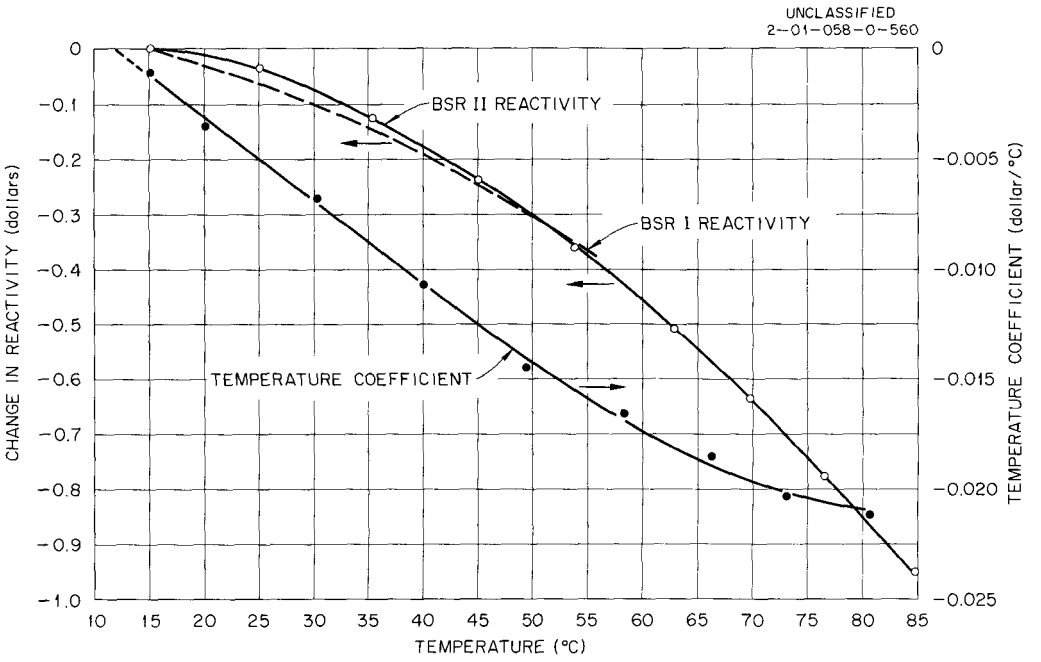

Fig. 2.1.3. Reactivity as a Function of Temperature (Referred to 15°C) and Temperature Coefficient of Reactivity as a Function of Temperature in the BSR-II.

the entire, uniformly voided core was calculated from the sum of the interpolated reactivity worths in the control and transient rod elements and the measured worth of voids uniformly distributed in the remainder of the core. The resulting average void coefficient, for voids produced by magnesium strips, is 11×10^{-4} dollar/cm^3. From the calculated value for the total core moderator volume, 4.2×10^4 cm^3, the void coefficient for voids produced by magnesium strips is thus 0.46 dollar/% of void in the moderator.

In order to evaluate the effect of air voids, a single fuel element was first voided with magnesium strip, and then Styrofoam strips were substituted for magnesium. The volume of air contained in the Styrofoam was computed by weighing the fuel element, immersed in water, with and without the voids and calculating the volume of water displaced.

The reactivity worth of the Styrofoam was found to be 1.3 times that of magnesium. By applying this factor to the magnesium data, a value of 14×10^{-4} dollar/cm^3, or 0.6 dollar/% of void, was found for air-filled voids. No similar measurements for the BSR-I are available for comparison.

Flux Shape Measurements. – The flux shape in the BSR-II was mapped by a total of 186 gold foils exposed in and adjacent to the core. Most of these foils were exposed in vertical stringers positioned in the coolant channels of the fuel elements. The remainder were positioned horizontally out from the face of the reactor along the vertical center line of one face at four different vertical positions. During the foil exposures the reactor was at a power level of about 500 w,

and the four control rods were moved in gang to maintain constant flux level during the exposures. The position of the four rods was about 11 in. above full insertion; thus about 4 in. of the poison plates projected into the core from above. The reactivity insertion device was fully inserted, that is, its fuel portion completely in the core. Figure 2.1.4 gives several representative vertical flux traverses in positions indicated on the small loading diagram on the figure. It will be noted that in those positions close to the control plates the flux peak is shifted below the midplane of the core, as would be expected. There appears to be a considerable amount of scatter in the experimental points, which is apparently not due to actual flux-shape irregularities. The reason for the scatter is not known. The curves drawn through the points are only best fits by eye and should not be considered as possessing any more authority than is lent by the experimental points shown on the figure. All data available for these vertical traverses is shown. The scale of the fluxes is arbitrary, but is the same for all the points so that the relative magnitudes of fluxes in various positions are correctly given.

Figure 2.1.5 is a normalized comparison of the flux shapes determined by the gold foil measurements with those predicted by a calculation using the IBM 704 PDQ code. The curves are the calculation of the flux in the midplane, along the axis shown in the diagram, for two conditions: with the rods fully inserted and again with the rods fully withdrawn. The points are the experimental gold foil data along the axis shown in the diagram but in planes $2\frac{5}{8}$ in. below and $1\frac{7}{8}$ in. above the midplane. Midplane data was not taken. In evaluating this comparison, some significant differences between the calculation and experiment should be noted. The first is the fact that the control rods extended about 4 in. into the core during the experimental measurements. Again, the transient-inducing rod element in the experiment was turned 90° from its position during the calculation. This accounts for the high flux measured at points next to this element, since an extra water space (the clearance space for the transient rod) existed close to the experimental foils but was not existent in the calculation. The lack of agreement beyond the core boundary is probably due to the fact that the PDQ calculations neglected binding effects in water molecules, and thus had a thermal neutron diffusion coefficient in water too large by a factor of 2.2.

The foil data were taken with bare gold foils only and therefore include effects due to fast neutrons. No cadmium differences were measured, but along one vertical traverse alternate bare and cadmium-covered foils were exposed. Figure 2.1.6 shows these data, as well as bare foil data from a diametrically symmetrical element. It appears that the fast-neutron contribution accounts for about 10% of the total activity in the foils of the core, and considerably less outside the core.

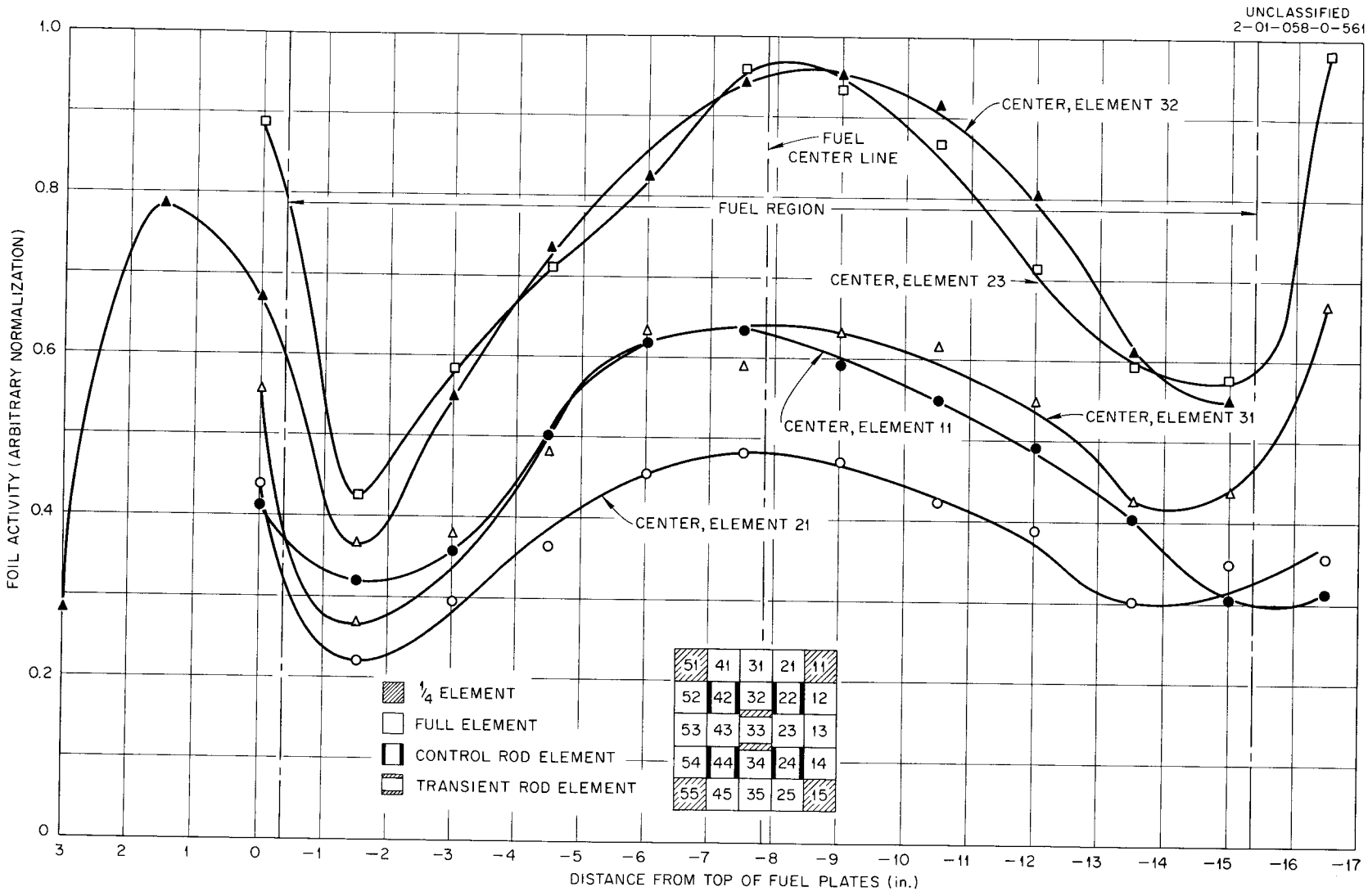

Fig. 2.1.4. Thermal Neutron Flux, Measured by Gold Foils, as a Function of Distance Below Top of Fuel Plate at Various Locations in the BSR-II.

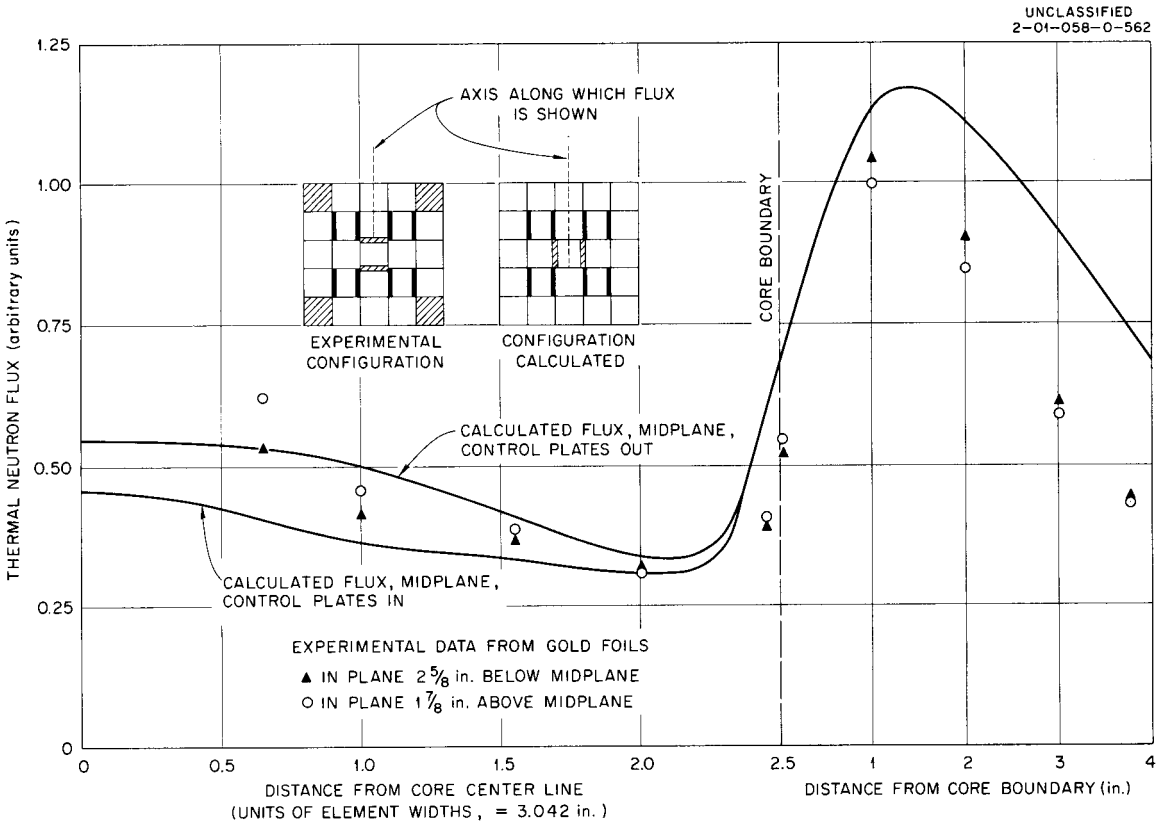

Fig. 2.1.5. Thermal Neutron Flux as a Function of Position in BSR-II: Comparison of Experimental Measurement with Calculation.

Excursion Tests

Methods. – The methods used for initiating and observing the transients were essentially those developed by SPERT during previous transient test programs.[7,8] The procedure was as follows: the three rods used for shutdown and safety (Nos. 2, 3, and 4) were withdrawn to their upper limit position, and the reactor was made critical using only rod No. 1. During this critical setting the transient rod was fully inserted, that is, with its fuel portion in the core. The transient rod was then withdrawn to almost its full length. The reactivity worth of the transient rod is about 5.5 dollars, which is much more than the 2.07 dollars required for the maximum transient.[9] The reactor was thus shut down; it was left without a source in order to allow the neutron flux level to drop as much as possible. After some 10 min the neutron flux would level out at about 1 count/min in the fission chamber. This indicated a power level of about 10^{-7} w,

[7] W. E. Nyer *et al.*, *Experimental Investigations of Reactor Transients*, IDO-16285 (April 1956).

[8] W. E. Nyer *et al.*, *Nucleonics* 14(6), 44 (1956).

[9] K. M. Henry, E. G. Silver, and E. B. Johnson, *op. cit.*, p 33, Fig. 2.1.11.

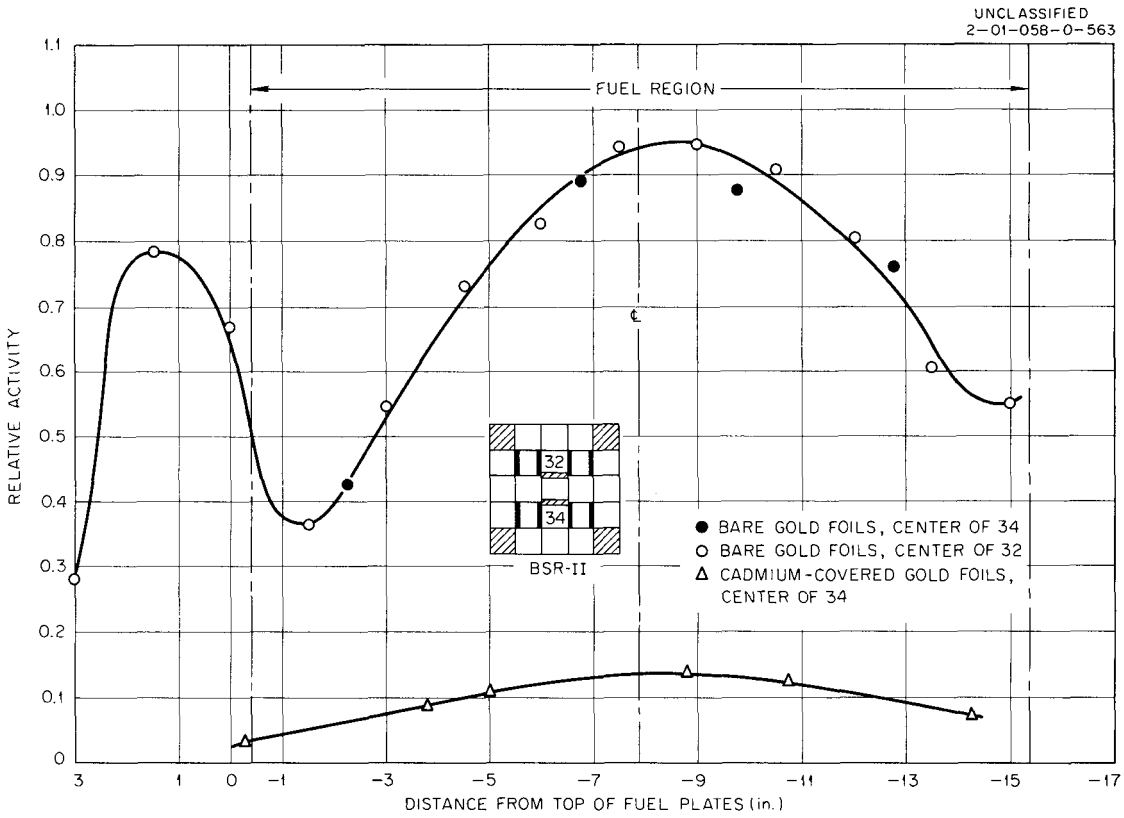

Fig. 2.1.6. Vertical Centerline Traverse with Alternate Cadmium-Covered and Bare Gold Foils in Element 34; Bare Gold Foil Traverse, Element 32.

which really meant that only occasional random fissions took place and that wide variations of the time between fissions occurred. (Evidence for this view is adduced below.) While the flux was decaying, rod No. 1, the regulating rod, was withdrawn a measured amount determined from the reactivity curve (Fig. 2.1.2) and the inhour equation, so as to produce an excursion of the desired period. When the flux had decayed to the very low level noted above, a sequence timer was actuated, which in turn started the two 36-channel oscillograph recorders and released the transient rod. As the transient rod moved down, the reactivity went from negative through critical to the predetermined positive amount, which was reached when the transient rod seated. The transient then occurred when triggered by a random neutron (see below). This procedure allowed the transient rod to accelerate while the reactor was still subcritical, and thus provided the fastest possible reactivity insertion above criticality. Depending upon the type of excursion, the three scram rods would then be released either upon a signal, from the level-scram circuits or from the period-scram circuits, or, to terminate the self-limiting tests, manually. After each run the photographic traces from the oscillograph were developed, and preliminary information about the period and peak power was obtained for use in planning the next experiment.

Self-Limiting Transients. – The first series of dynamic tests involved self-limiting transients. Figure 2.1.7 shows the peak powers recorded in these transients and also, for comparison, the peak powers observed for self-limiting excursions of the APPR P18/19 core, which previously had been tested at SPERT-I. It will be noted that the data points for the two reactors fall essentially along the same curve. This was expected, since the reactors, both highly enriched plate-type reactors made of stainless steel, have closely similar core characteristics as regards metal-to-water ratio, fuel concentration, and value of l^*/β_{eff} (ref 10).

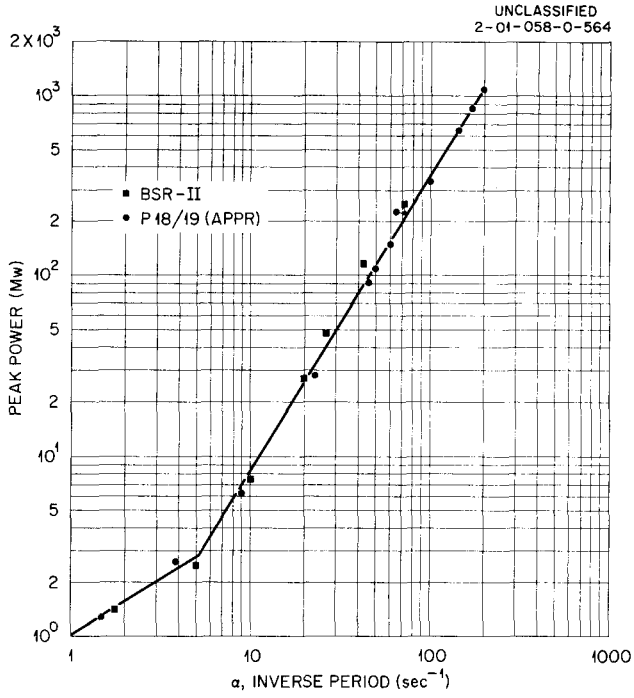

Fig. 2.1.7. Peak Power as a Function of Inverse Period for Self-Limiting Transients in BSR-II and in APPR-P18/19 Core.

This close similarity of the cores and the identical peak-power vs inverse period curves make it possible to extrapolate the BSR-II self-limiting transient data beyond the point tested to the limit to which the P18/19 data were obtained.

The series of self-limiting tests was terminated when an investigation of the core showed that a small permanent warping had occurred in some of the fuel plates located near the center of the reactor. The deformation was in the form of ripples running longitudinally along the plate, with about three nodes along the plate. The appearance suggests that the central portion of the plate, containing the fuel, had expanded against the restraint offered by the cooler side plates and the frame material. The strain so produced had exceeded the elastic limit during the last excursion, and a permanent plastic deformation resulted. No breach of the integrity of the clad appeared to have occurred or to be threatened. The peak power during the transient that caused this deformation was 226 Mw, and the peak temperature recorded by a thermocouple embedded in the clad of a fuel element was 174°C. Accordingly, in all tests following this one the peak power and temperature were kept below this level, and periodic examination of the amplitude of the ripple did not reveal any increase beyond the value of 64 mils measured after the last self-limited excursion.

Control-System-Terminated Excursions. – At about the time that the last self-limited excursion was run the decision was reached that the BSR-II core being tested at SPERT should be

[10] J. D. Siegwarth, p 11 *in Quarterly Progress Report October, November, December 1958 – Reactor Projects Branch*, IDO-16537 (Sept. 1, 1959).

preserved, rather than tested to at least partial destruction as had been the earlier plan. In order to safeguard the core in accordance with these new requirements, a complete second channel of safety instrumentation was installed in the reactor, so as to have the same sort of safety margin against scram system failure that operating reactors are provided with. When this system had been installed the transient testing was resumed. Two types of tests made up the major part of this series. In one type the full safety system was operating; this invariably resulted in the scram being initiated by the period safety system; these tests were called period scrams. In the other type the period safety system was rendered inoperative, and the level safety system alone terminated the excursion. Figure 2.1.8 shows all of the safety-system-terminated excursions, plotted as peak power vs reciprocal period.

The gross features of the graph show a sharp rise in peak power as the reciprocal period passes about 100 sec^{-1}, corresponding to a period of less than 10 msec. The excursions terminated by the level scram system are asymptotic, for small inverse periods, to 100 kw, which is the scram point set on the level scram system. The period safety system is much more effective in the range tested than the level safety system, since a factor of at least 10^3 separates the peak powers for a given inverse period in the two cases. A very few tests are also shown in which either only two or all four of the rods were scrammed rather than the three used in most of the tests. All the 2-rod and 4-rod tests were terminated with the level scram circuits. The effect of adding the fourth rod is seen to decrease the peak power by a factor of about 3, whereas leaving out the third rod only causes an increase in peak power of 1.4. This difference is due to the fact that the fourth rod, which is the regulating rod, started

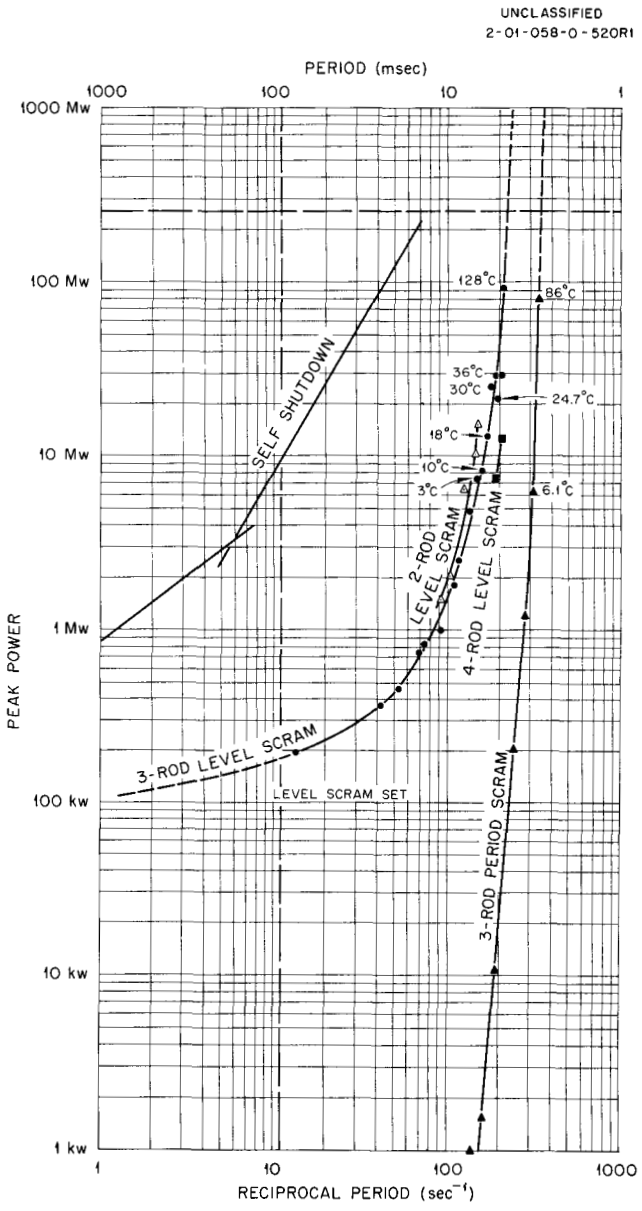

Fig. 2.1.8. Peak Power as a Function of Inverse Period for Controlled Transients in BSR-II.

its motion much further in the core and thus achieved a much higher initial rate of reactivity removal than the other rods, which began their motion at the upper limit, a position of relatively low effectiveness despite the built-in 1-in. preinsertion of the BSR-II control plates. For comparison the curve of peak power vs inverse period for the self-limiting tests is also shown in the figure. It is apparent that, in the range tested, the control system was extremely effective. At the shortest period measured, the peak powers of self-limiting and period-scram-terminated excursions differ by a factor of about 25, and the same ratio for the shortest level-scram-terminated excursion is about 12.

The peak temperatures recorded by the thermocouples are also shown in the figure for those excursions where a significant temperature rise occurred. It will be noted that none of these excursions approached the temperature or peak power attained in the last self-limited excursion.

Power Rise Delay. – One unexpected phenomenon of considerable interest from the safety viewpoint was observed. This was the very variable and occasionally very long interval between the time the transient rod seated, indicating completion of the reactivity insertion, and the time peak power was attained. Table 2.1.1 shows some representative data on this effect.

Table 2.1.1. Period, Peak Power, Elapsed Time Between Transient Rod Seat and Peak Power, and Extrapolated Power at Time of Transient Rod Seat for Some Representative Excursions in the BSR-II

Period (msec)	Peak Power (Mw)	Elapsed Time Between Transient Rod Seat and Peak Power (msec)	Extrapolated "Power" at Time of Transient Rod Seat* (w)
10.9	1.08	321.5	3.4×10^{-7}
8.6	2.06	449.2	1.4×10^{-16}
7.5	4.8	803.0	7.6×10^{-18}
5.0	30.0	735.0	1.2×10^{-56}
5.2	8.3	117.0	3.7×10^{-3}
5.0	12.8	391.0	4.0×10^{-27}
6.7	6.9	119.7	3.4×10^{-1}
4.6	91.7	342.0	1.5×10^{-24}

Note: The average flux level in the reactor at the time the transient was initiated was measured as 10^{-7} w.

*This "power" is *not real.* It is the figure arrived at by extrapolating backward in time from peak power, using the exponential period. See discussion in the body of this report.

As stated above, the apparent power level in the reactor prior to each excursion was about 10^{-7} w. (The calibration was carried out at kilowatt power levels by observing the temperature rise rate in the tank and comparing with the temperature rise with electric heaters of known power.) Table 2.1.1 shows the power level at the instant the transient rod seated, obtained by extrapolating back from peak power using the known period and the known time delay between transient rod seat and peak power.

It is clear that the model of a continuous flux prior to the transient is misleading. (A power level of 1×10^{-7} w is equivalent to a neutron density of ~ 0.2 neutron in the entire core; thus the extrapolated initial powers of 10^{-16} to 10^{-56} w obviously are meaningless.) A more meaningful concept is that the reactor, once it is supercritical, continues to remain at zero flux until by chance a neutron due either to cosmic rays, spontaneous fission, or a (γ,n) process manages to initiate a sustaining fission chain. Since these long times occur, it is clear that in a "cold" reactor it is not necessary that a reactivity insertion occur very rapidly in order to have a severe excursion. A relatively very long time may be available for reactivity changes before the excursion terminates the process; therefore the excursion may be very severe. The importance of a neutron source in a reactor for safety purposes is thus re-emphasized.

Safety Implications. – The performance of the fast safety system used with the BSR-II indicates that it is a good system, one which meets the design specifications and which is probably as good as exists in any comparable reactor. It is also clear from the data that this safety system will protect the reactor from damage in the period range from 10 msec down to about 3 msec, which is a region where self-limited excursions would cause at least some core damage. However, it is also apparent that there is a range at about 2-msec periods where the extrapolated curves of peak power in the self-limiting and scram-limited excursions meet. The power level at which this occurs (about 3000–7000 Mw peak power) also appears to be the threshold for serious catastrophe, including dispersions of at least some fission products. Against such periods the safety system cannot, it appears, provide protection.

One of the basic questions which underlay the BSR-II–SPERT program was this: Is the BSR-II as safe as the BSR-I for use at the BSF? The answer can best be gathered from a consideration of Fig. 2.1.9. This figure shows the peak power vs reactivity curves obtained from the SPERT tests of both the BSR-II and the P17/28 core of SPERT-I. The latter core is an aluminum core with physical characteristics closely approximating those of the BSR-I. The figure also shows the peak powers attained in level-scram and period-scram excursions of the BSR-II. It will be noted that the self-limited peak powers in the BSR-II are higher by about a factor of 3 than those in the BSR-I–type reactor for the same step-reactivity insertion. However, in the region of competence of the control system the peak powers permitted by the system in the BSR-II are considerably lower than the self-limiting excursions in the BSR-I for the same reactivity step. Thus, if reliance on the BSR-II safety system is postulated, the BSR-II is safer than the BSR-I in the reactivity range up to 2.1 dollars of excess reactivity. Beyond this range, where the safety systems of both reactors become of exceedingly limited value, a difference in peak power of a factor of 2 or 3 may be significant but is probably not very decisive.

Present Status

After the completion of the SPERT program the BSR-II was dismantled and shipped, piecemeal, back to ORNL. (Only seven of the irradiated fuel elements could be shipped at a time due

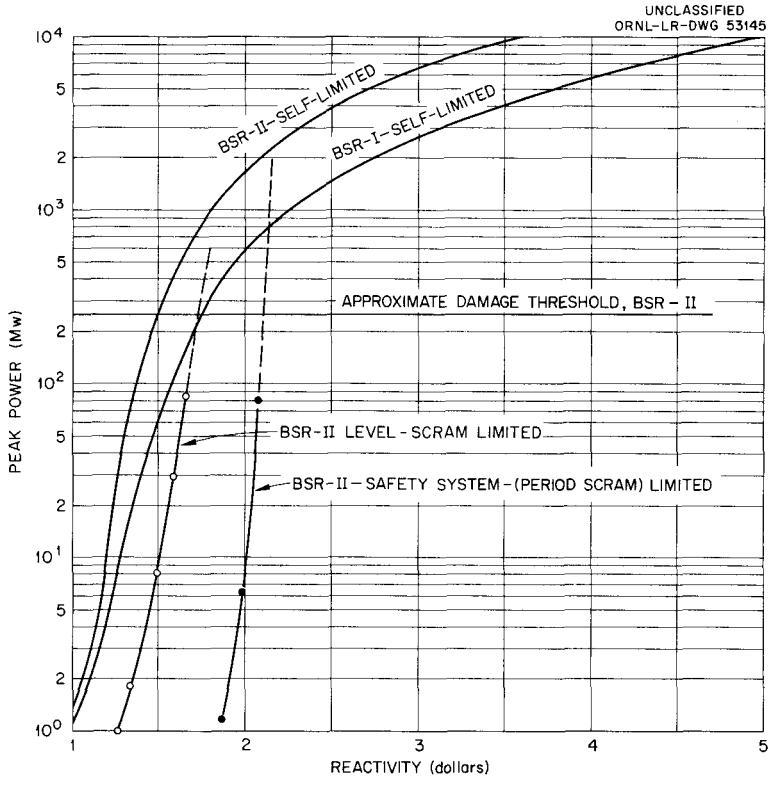

Fig. 2.1.9. Peak Power as a Function of Reactivity for Self-Limiting and Controlled Transients in BSR-I and BSR-II.

to the limitations of the available carrier.) The reactor has now been completely returned and awaits final Safeguard Committee approval before it can be used at the BSF pool. A supplementary Safeguard Report will be submitted to obtain approval by the Committee for power operation using realistic excess reactivity loadings.

Inspection of the fuel elements reveals that in some cases, even in elements never used at SPERT, a certain amount of corrosion has occurred around the brazed joints. This is apparently due to overheating in the process of brazing, and it is the opinion of the responsible persons in the Metallurgy Division that closer temperature control during manufacture will eliminate this corrosion.

2.2 TOWER SHIELDING REACTOR II PRELIMINARY EXPERIMENTS

L. B. Holland D. R. Ward T. A. Love J. Lewin
V. R. Cain J. L. Hull A. D. MacKellar J. H. Wilson[1]

Introduction

The Tower Shielding Reactor II (TSR-II), the spherically symmetric reactor at the Tower Shielding Facility, has previously been described.[2,3] During the past year, construction and assembly of the reactor were completed, and the reactor was first brought to critical at 12:33 AM on Saturday, March 26, 1960. Preliminary experiments, described in detail below, have been completed, and minor component modifications have been made in preparation for operation at 100 kw following final flow studies and cooling system checkout.

Mechanical Design

The TSR-II design as shown in Fig. 2.2.1 remains basically unchanged. However, a second control mechanism housing assembly has been fabricated which differs slightly from the earlier model. The original assembly (see Fig. 2.2.2*a*) has an 11-in.-dia central aluminum ball with 2-in. aluminum plugs extending from the central sphere through the control rods.[4] The control rods are 1-in.-thick dished stainless steel cans filled with B_4C. The second control mechanism housing assembly (Fig. 2.2.2*b*) has an 11½-in.-dia central aluminum ball and does not have the radial aluminum plugs. The unperforated control rods are ½ in. thick and contain approximately the same amount of B_4C as the perforated set. The nominal loading of U^{235} in the spherical cover plates is 233 g, but a second set of plates which contain 116 g was fabricated so that the change in reactivity with fuel loading could be determined.

Regulating-Rod Calibration

The regulating rod was calibrated for each major change in the reactor core or shield assembly. The reactor was made critical with the regulating rod fully inserted (adjacent to the fuel); then the regulating rod was withdrawn a small distance and the resulting positive period was measured. The reactor was then brought back to a critical condition by using the shim-safety rods, and the measurement was repeated for successive increments of regulating-rod withdrawal for the full regulating-rod travel. The period data were used with the inverse hour equation to compute the reactivity change for each increment of movement. Summing these gave the total regulating-rod reactivity worth. Figure 2.2.3 shows the regulating-rod calibration curve

[1]On loan from Lockheed Aircraft Company, Marietta, Ga.

[2]L. B. Holland and C. E. Clifford, *Description of the Tower Shielding Reactor II and Proposed Preliminary Experiments*, ORNL-2747 (1959).

[3]L. B. Holland *et al.*, *Neutron Phys. Ann. Prog. Rep. Sept. 1, 1959*, ORNL-2842, p 39.

[4]Although the dished plates are used for control, they are referred to as rods.

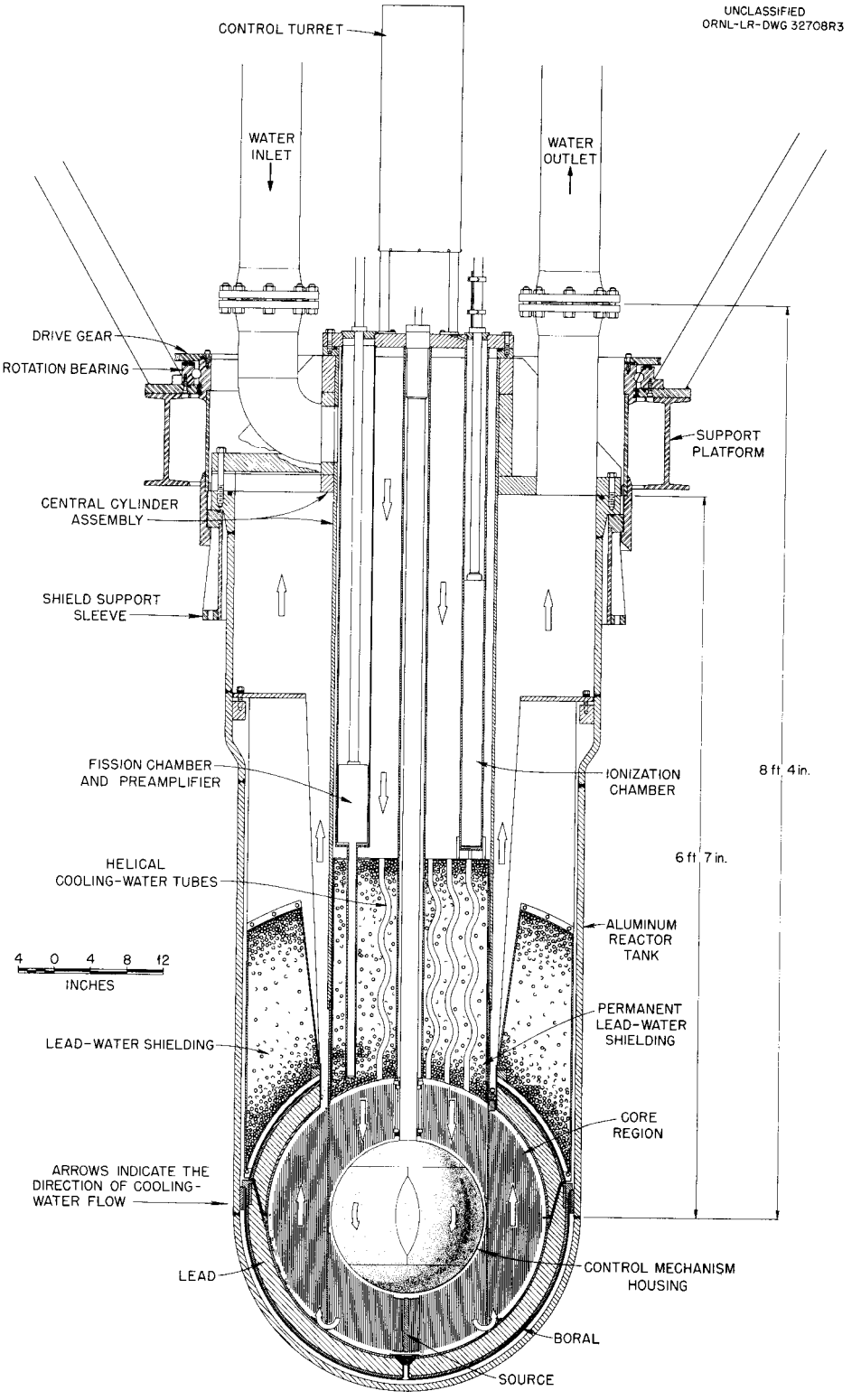

Fig. 2.2.1. TSR-II Design (Vertical Section).

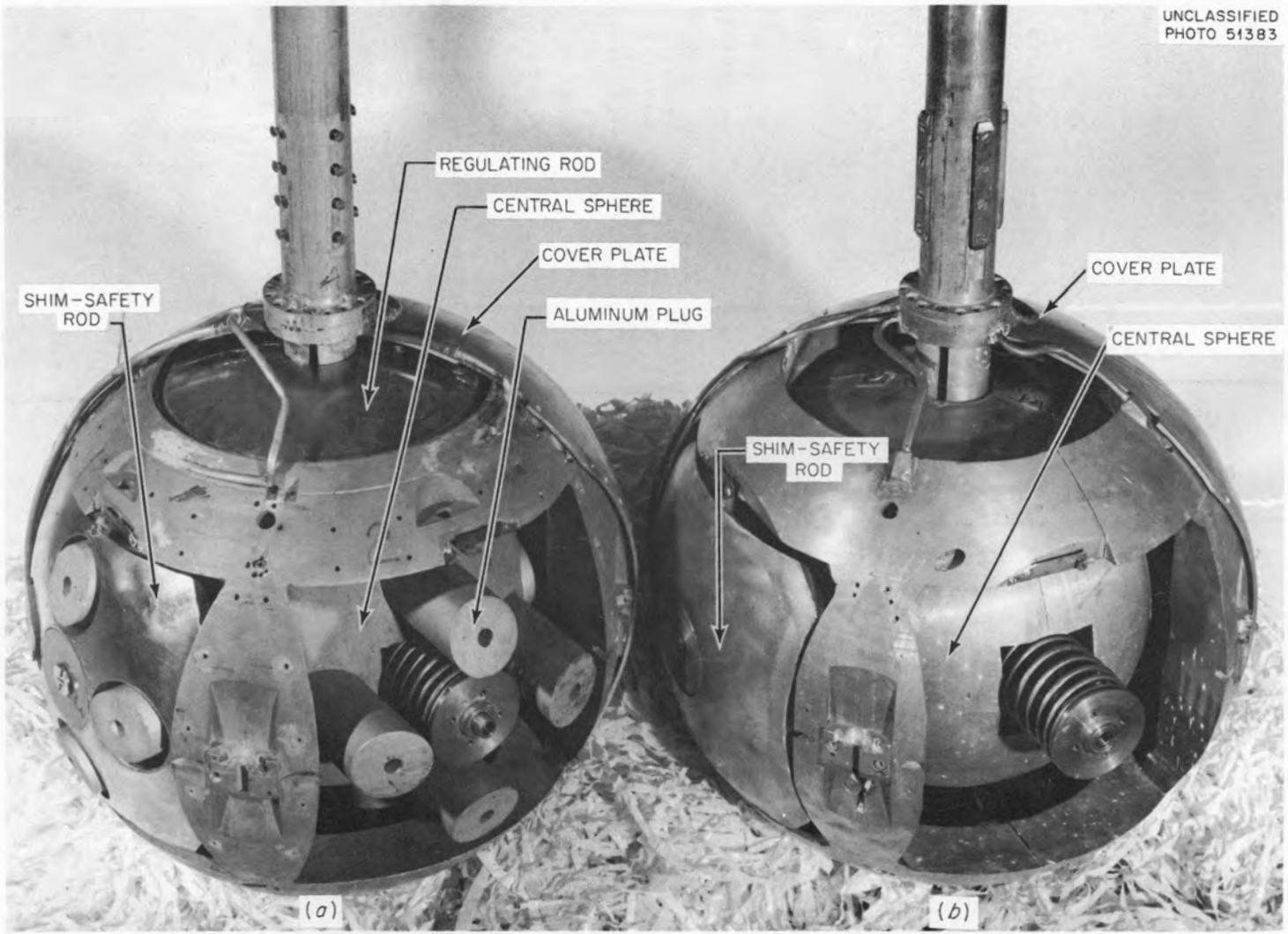

Fig. 2.2.2. TSR-II Control Mechanism Housing with Fuel Cover Plate and Control Plate Removed. (*a*) Model II; (*b*) model III.

obtained for the unperforated ½-in.-thick control rods while using the 233-g cover plates. The modifications to the control housing and cover plates noted above have increased the total worth of the rod from 0.3 to 0.43% $\Delta k/k$.

Shim-Safety Rod Calibration

The shim-safety rod calibration was divided into measurement of the shutdown k and measurement of the excess k. The measurements of the shutdown k of the reactor were made by the pulsed-neutron-source technique, as mentioned in Sec 2.3 of this report. This technique provided not only the total shutdown k but also the shutdown k for intermediate shim-rod positions.

The excess k was measured by adding boric acid to the water until the shim-safety rods could be completely withdrawn. The resulting change in reactivity, computed with the GNU code on the IBM 704 computer, was 1.344% $\Delta k/k$ at 26.5°C. The total excess at 20°C was determined by adding to this amount 0.085% $\Delta k/k$, which was the amount still available in the regulating rod, and 0.048% $\Delta k/k$, which is the temperature correction from 26.5 to 20°C. This gives a total excess of 1.48% $\Delta k/k$ at 20°C.

The excess k was also computed by taking the difference in shutdown k as measured by the pulsed-neutron-source technique with and without a boron solution in the reactor. The excess obtained, assuming a value of 0.008 for β_{eff}, which is the value measured in the BSR-I, was 1.56%. The total shim-rod worth obtained by the pulsed-neutron measurements was 3.82%, as shown in Fig. 2.2.4. The value obtained before the final alterations to the control mechanism housing were made was 2.55% (ref 5).

[5] Holland and Clifford, *op. cit.*, p 19.

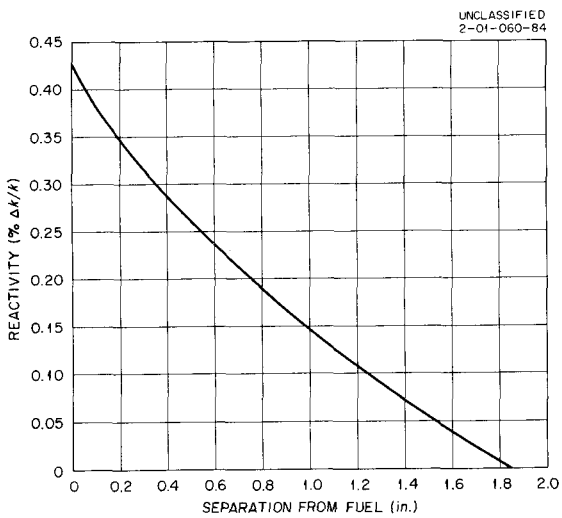

Fig. 2.2.3. Reactivity Worth of the TSR-II Regulating Rod.

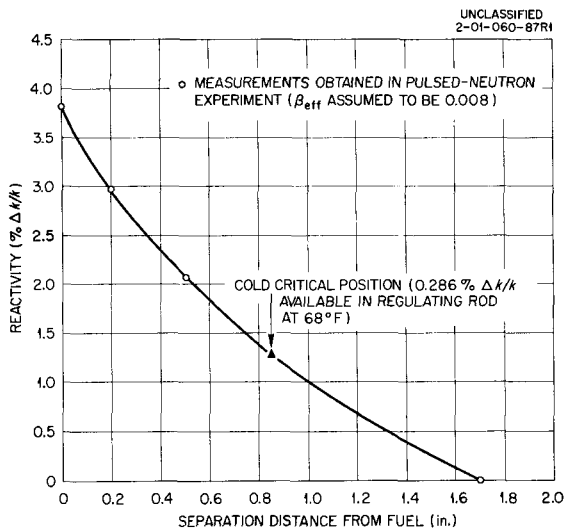

Fig. 2.2.4. Reactivity Worth of All TSR-II Shim Rods.

Temperature Coefficient of Reactivity

For the measurement of the temperature coefficient of reactivity, the water temperature was first lowered by adding ice; then with the reactor operating, the water was circulated through a 40-kw heater and then through the reactor. The control-rod positions were noted as a function of temperature, and the reactivity change was obtained from the control-rod calibration curves. Figure 2.2.5 shows the change in reactivity as a function of temperature. The temperature

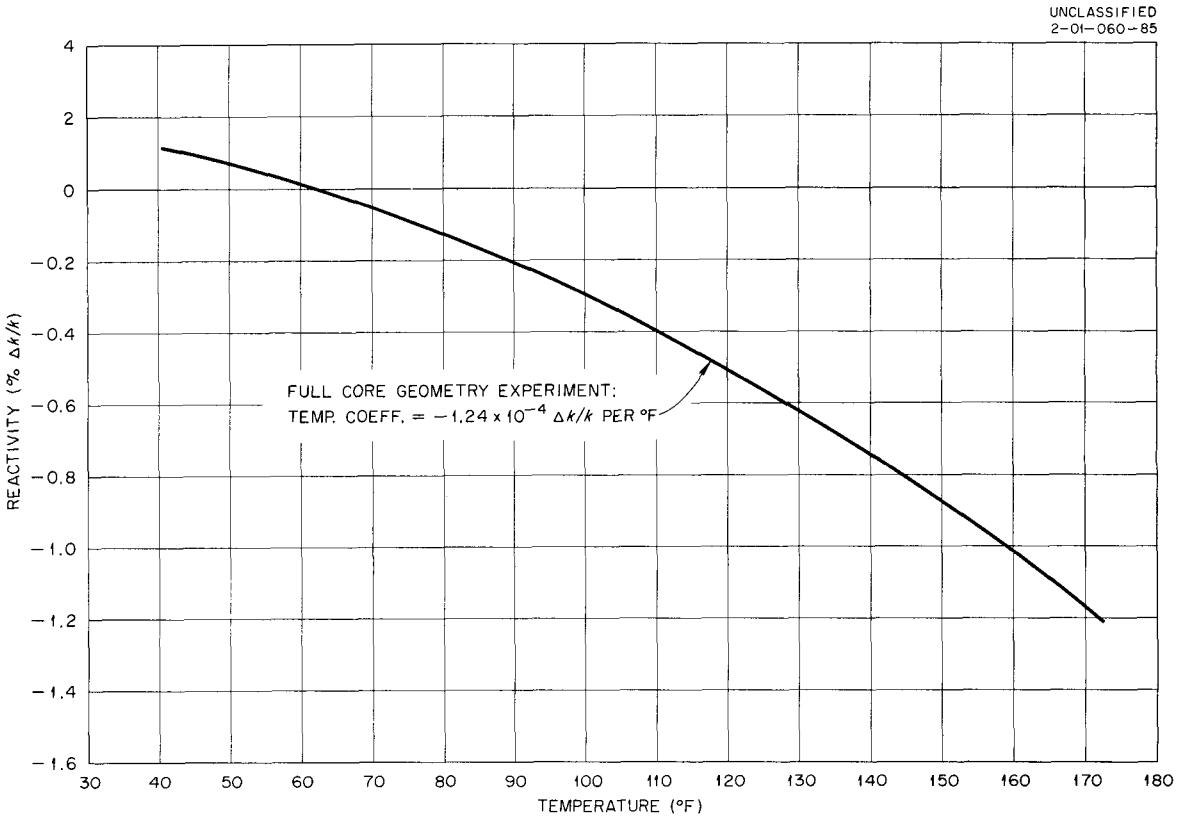

Fig. 2.2.5. Reactivity of the TSR-II as a Function of Water Temperature (Coefficient Stated Is for 140°F Water).

coefficient, for a mean core temperature of 140°F, is $-1.24 \times 10^{-4} \Delta k/k$ per °F. This value agrees quite well with a calculated coefficient of $-1.34 \times 10^{-4} \Delta k/k$ per °F at 140°F, but differs somewhat from a previously reported experimental value[6] of $-8.5 \times 10^{-5} \Delta k/k$ per °F. The difference is probably due to the lesser volume of water in the new control mechanism housing region, a region which has a positive temperature coefficient.

Reactivity Worth of Aluminum Plugs in Control Housing

The reactivity worth of the aluminum plugs in the original control mechanism housing (Fig. 2.2.2*a*) was measured by noting the change in control-rod positions while operating both

[6] L. B. Holland *et al.*, *Neutron Phys. Ann. Prog. Rep. Sept. 1, 1959*, ORNL-2842, p 48.

with and without the aluminum plugs. Twenty aluminum plugs displacing a total water volume of 3966 cc produced a positive reactivity change of 0.3% $\Delta k/k$. The average worth of the aluminum plugs is thus $+7.6 \times 10^{-7} \Delta k/k$ per cc.

Void Coefficient

The coefficient of reactivity was measured for voids both in the water annulus between the control housing and the core region and also for voids in the water pockets behind the control plates inside the control mechanism housing. The reactivity measurements were made by determining the excess k in the reactor both with and without Styrofoam voids and then taking the difference. The coefficient of reactivity is $-6.3 \times 10^{-7} \Delta k/k$ per cc of void outside the control mechanism housing and $+1.06 \times 10^{-6} \Delta k/k$ per cc of void inside the control mechanism housing. The total volume of water inside the control mechanism housing is 20,000 cc.

Prompt-Neutron Generation Time

The measurements to determine the ratio of the prompt-neutron generation time to the effective delayed-neutron fraction, l/β_{eff}, of the TSR-II by the use of the pulsed-neutron-source technique are described in Sec 2.3 of this report. The value of l/β_{eff} was found to be 6.61 ± 0.16 msec. If the value of 0.008 for β_{eff} found for the BSR-I is adopted, the generation time is 53 μsec. The number which had been calculated from macroscopic core constants was previously reported as 50 μsec (ref 7).

Importance of Fuel in Spherical Cover Plates

Calculations had predicted a reactivity change of +0.62% $\Delta k/k$ for an increase in the U^{235} in the spherical cover plates (see Fig. 2.2.1) from 116 g to 233 g. Comparative measurements made with two sets of plates, one of which contained 116 g of U^{235} and the other 233 g, showed a reactivity change of +0.60%. Since the percentage change in mass is 1.5%, the ratio of the percentage change in mass to the reactivity change, $(\Delta M/M)/(\Delta k/k)$, is 2.5. This value indicates that the fuel in the shell region is very important, as would be expected, and thus should have a considerable effect on neutron flux distribution and control-rod worth.

Reactivity Effect of Shields

To evaluate the flexibility of the TSR-II it is necessary to know the reactivity changes that can occur with various changes in shield configurations. Calculations were made for predicting the reactivity change expected for various shield changes and are compared with experimental values in Table 2.2.1.

---

[7] Holland and Clifford, *op. cit.*, p 21.

Table 2.2.1. Reactivity Effect of Shield Variations

Shield Configuration	Reactivity Change (% $\Delta k/k$)	
	Experimental	Calculated*
Normal,** except without water reflector outside reactor pressure vessel	−0.08	−0.26
Lead-boral reflector removed	+0.38	+1.73
Water reflector replaced by beam shield (50% water and 50% lead) adjacent to reactor pressure vessel	+0.17	+0.65
Water removed from beam shield	+0.37	+1.57

*The consistent overestimate evident in the calculated values is believed to be due to an overestimate of the thermal flux in the shield.

**Normal case is as shown in Fig. 2.2.1, except that there is no lead in the lead-water region and there is an essentially infinite water reflector.

The results indicate that the reactor can be operated either unreflected or without the lead-boral shield, and that no dangerous reactivity effects can occur due to shield changes with the presently available shields.

Thermal-Neutron Flux Distribution

Following the substitution of the fuel-containing plates for the original, unfueled cover plates of the control mechanism housing, new calculations of the thermal-neutron flux distribution throughout the core were made. For these calculations the control plates were represented by a continuous boral shell with the boron concentration so adjusted that the transmission of neutrons through the shell was equivalent to the ratio of the area not occupied by the control plates to the total area for the particular control radius under consideration. This approximation resulted in a value of k which was high by 5% and a thermal-neutron flux distribution through the core which agreed in shape with the measured distribution except at the inner surface of the core.

A postexperiment set of calculations has been made with the control region set at the same separation from the fuel as was observed in the experiments and the boron concentration in the control region adjusted to make the calculated flux shape agree with the experimental results. The effective multiplication factor for this case was 1.011. Figure 2.2.6 compares the calculated thermal-neutron flux (curve A) with the measured flux (curve C) for the clean, cold critical condition. The third curve (curve B) shows the calculated thermal-neutron distribution for higher-power operation, that is, when the control plates are withdrawn from 0.85 in. to 1.49 in. to compensate for reactivity losses due to temperature rise and xenon poisoning. In the latter calculation the boron concentration in the control shell has been adjusted to produce a change

UNCLASSIFIED
2-01-060-93

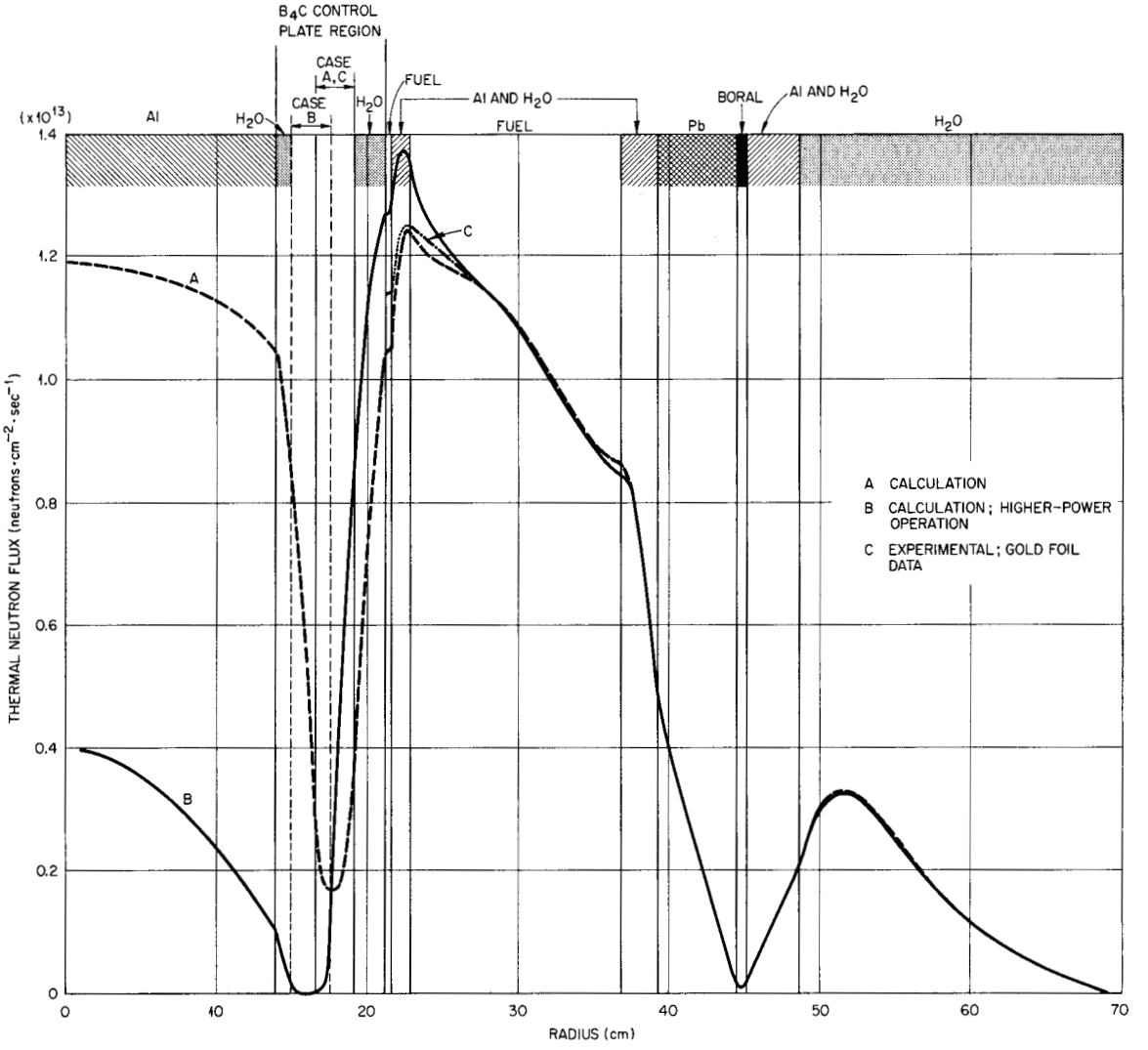

Fig. 2.2.6. Thermal-Flux Distribution in the TSR-II (with Normalized ~~Foil~~ Foil Data).

in k of +1.26%. (The measured change is 1.2%.) The calculated peak value in the thermal-flux distribution in the core is much less than the value obtained in earlier calculations based on unfueled cover plates.[8]

Power Distribution and Heat Flux in the Core

The initial calculations of the power generation distributions throughout the core, which were based on the highly peaked thermal-neutron flux distribution referred to above, were previously presented.[9] Calculated flow rates, for various saturation temperatures and associated

[8] C. E. Clifford and L. B. Holland, *Neutron Phys. Ann. Prog. Rep. Sept. 1, 1958*, ORNL-2609, p 22.

[9] L. B. Holland *et al.*, *Neutron Phys. Ann. Prog. Rep. Sept. 1, 1959*, ORNL-2842, pp 49, 50–51.

pressures, and the measured flow per channel were compared as functions of channel number.[10] The data indicated that the crucial channels were the outermost channels of the annular fuel elements, and that any increase in the power generation in these channels might cause local boiling. Any flattening of the radial thermal-neutron flux through the core would tend to increase the power generation in the outer channels. Therefore the measured flux distribution, which had the flattest profile through the core, was used to compute new values for the power distribution for each fuel plate for a total reactor power of 5 Mw.

Results for several plates in the central fuel element are shown in Fig. 2.2.7, and results for plates in an annular fuel element are shown in Fig. 2.2.8. Integration over fuel plates gives the total power generation in the plate. The total power generated in each fuel plate of a central element is shown in Fig. 2.2.9, and in each plate of an annular element in Fig. 2.2.10. The power generated in the spherical fuel plates in the control mechanism housing is 113 kw for the measured thermal-neutron flux distribution shown as curve *C* of Fig. 2.2.6, but rises to 125 kw for the distribution of curve *B*. The power generated in the single cylindrical element at the lower end of the core is 19.2 kw, and this value changes very little with shifts in the flux distribution.

[10] L. B. Holland *et al.*, *op. cit.*, p 54.

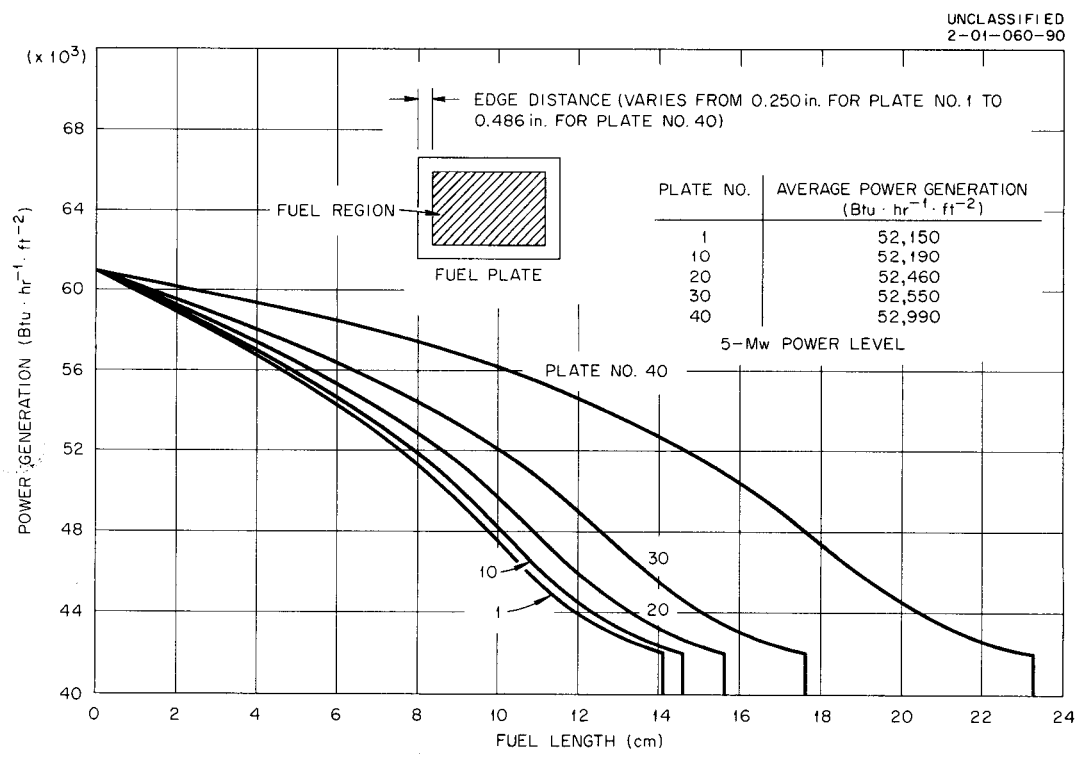

Fig. 2.2.7. Power Generation in the Fuel Plates of a TSR-II Central Element as a Function of the Distance from the Inside Edge of the Fuel.

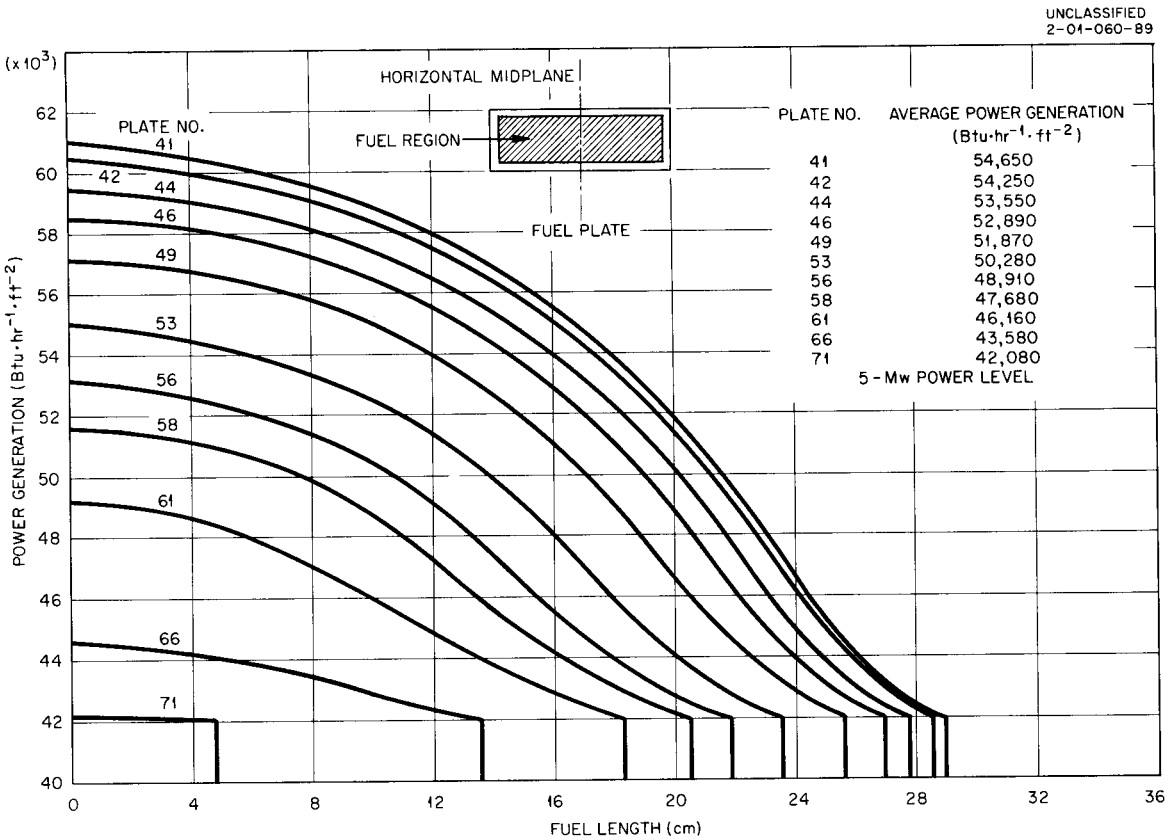

Fig. 2.2.8. Power Generation in the Fuel Plates of a TSR-II Annular Element as a Function of the Distance from the Horizontal Midplane of the Edge of the Fuel.

The results show that the maximum heat flux (one half the power generation) in plate 71 varies from 20,600 Btu hr^{-1} ft^{-2} when the thermal-neutron flux shape in the core is as shown by curve *A* of Fig. 2.2.6 to 21,050 Btu hr^{-1} ft^{-2} when the flux shape is as highly peaked as was previously reported.[9] The average heat flux in the core is 25,120 Btu hr^{-1} ft^{-2}, and the maximum heat flux emitted from the cover plates on the control mechanism housing varies from an initial value of 91,500 to a value of 101,000 Btu hr^{-1} ft^{-2}. The larger value, which will be reached after the reactor has been run several hours at 5 Mw, was derived from the thermal-neutron flux distribution, curve *B* in Fig. 2.2.6. These values exceed the average heat flux by more than a factor of 2 because all the heat is assumed to flow outward from the cover plates. Exclusive of the cover plates, the maximum heat flux in the fuel plates varies from 30,500 to 34,750 Btu hr^{-1} ft^{-2} for the same range of operating conditions.

Flow Distribution Studies

As mentioned above, the power generation in the annular fuel elements changes when the control rods are withdrawn, but the peak values do not approach that which was obtained before

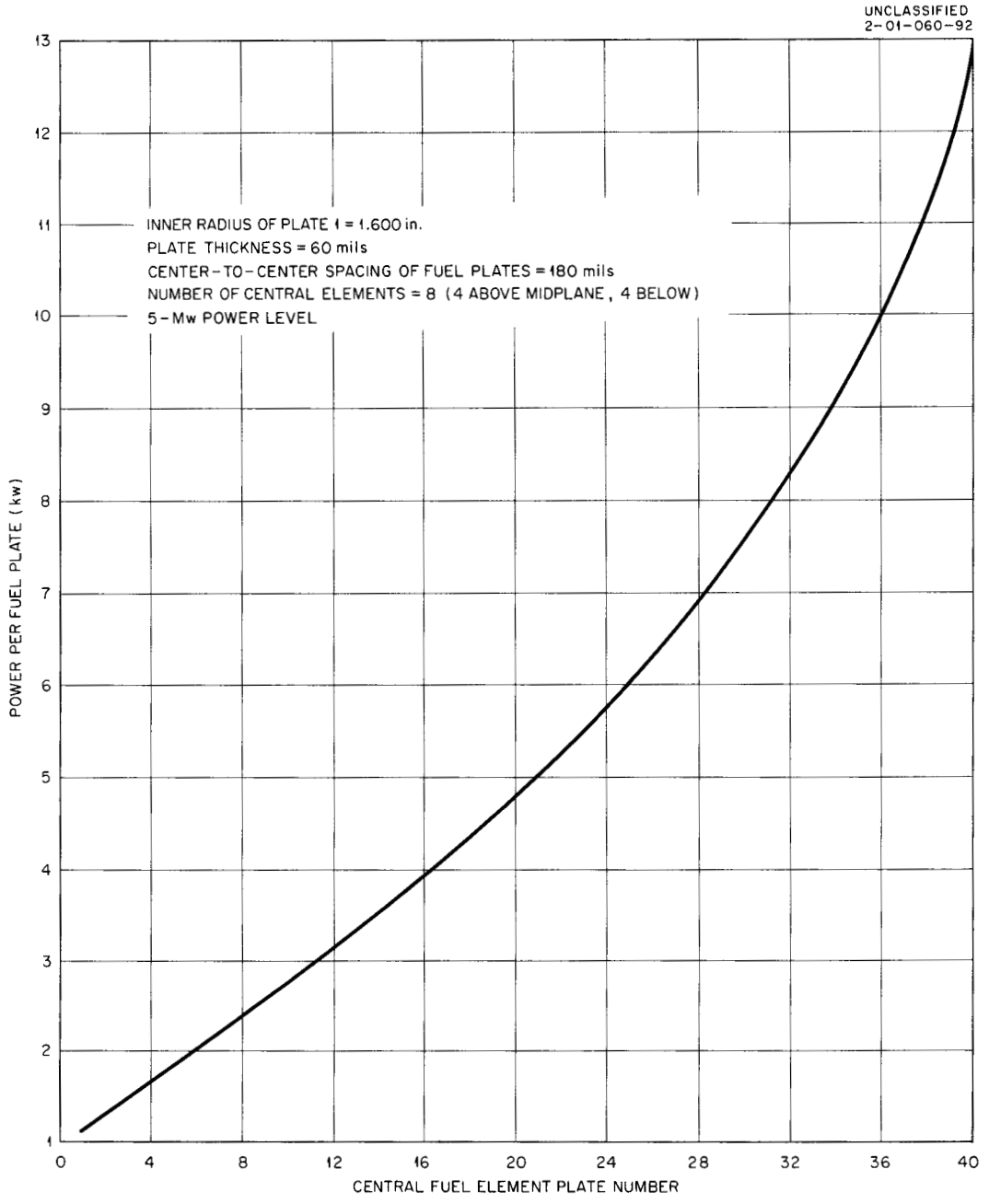

Fig. 2.2.9. Power Generation in the Fuel Plates of a TSR-II Central Fuel Element as a Function of the Fuel Plate Number.

the addition of the U^{235}-loaded cover plates. Since the annular baffle plates were designed for the earlier, more highly peaked power generation distribution, and since the power generation varies so little in the outer fuel plates, these baffle plates should be adequate for the expected range of power generation. The heat flux in the cover plates on the control mechanism housing, however, will go as high as 101,000 Btu hr^{-1} ft^{-2} for operation at high power with the control

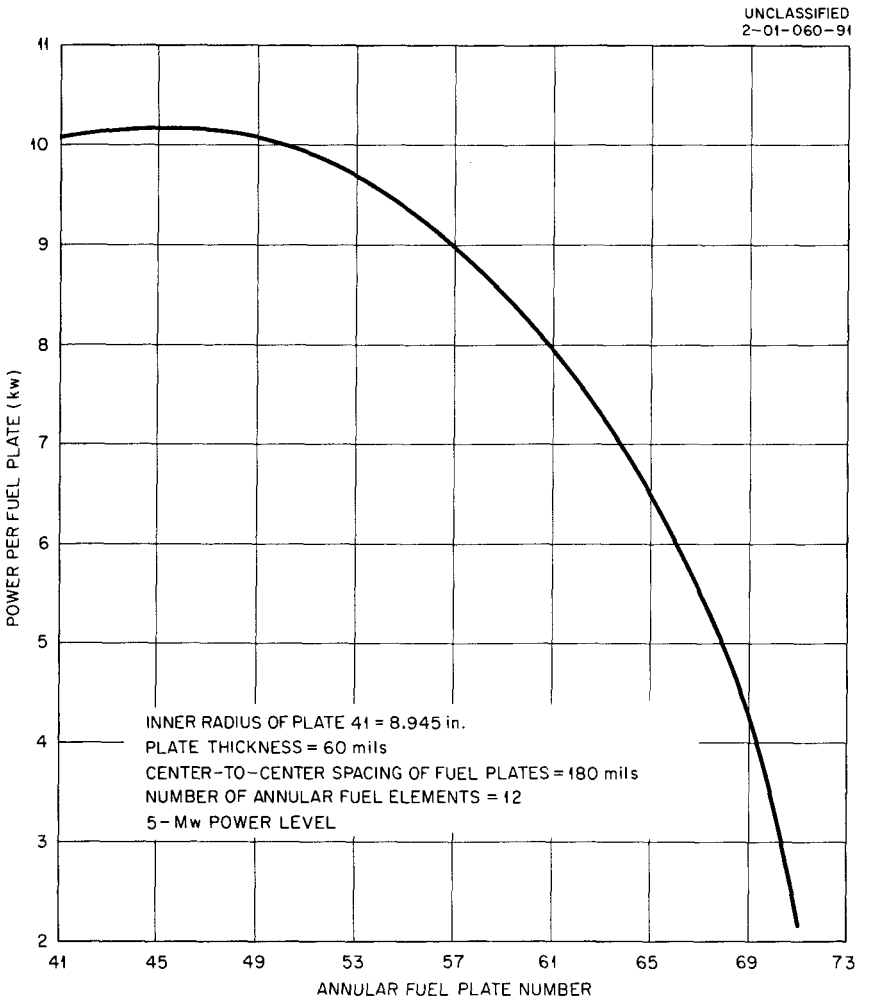

Fig. 2.2.10. Power Generation in the Fuel Plates of a TSR-II Annular Fuel Element as a Function of the Fuel Plate Number.

rods nearly completely withdrawn. The water flow rate over some parts of the cover plates is very high, but further analysis is necessary to determine whether it is adequate over the whole cover-plate surface. The baffle plate design for the lower and upper central elements is not affected by changes in thermal-neutron flux distribution, since a uniform flow distribution suffices in all cases. An acceptable flow distribution has been achieved for these two regions, although studies are continuing in an effort to reduce the pressure drop through the upper fuel baffle plate.

Present Studies

The TSR-II components are undergoing final modification prior to operation at 100 kw. The reactor will be reassembled about October 1, 1960, and final flow studies and water cooling system checkout will be made before the reactor is operated at this level.

2.3 PULSED-NEUTRON-SOURCE MEASUREMENTS AT THE TSR-II

G. deSaussure E. G. Silver J. D. Kington

Introduction

The control rods of the Tower Shielding Reactor-II (TSR-II) have previously been calibrated by a combination of several methods, including inhour, boron-poison, and rod-drop techniques. In order to confirm by a direct method the values previously obtained, the pulsed-neutron-source technique discussed elsewhere in this report has been utilized to repeat the calibration. In addition, the method has also been applied to a determination of the reduced generation time, l/β_{eff}, of the TSR-II.

Experimental Arrangement

The experimental arrangement is diagramed in Fig. 2.3.1. The 300-kv accelerator and the 18-channel time analyzer are those used in previous experiments at the Bulk Shielding Facility

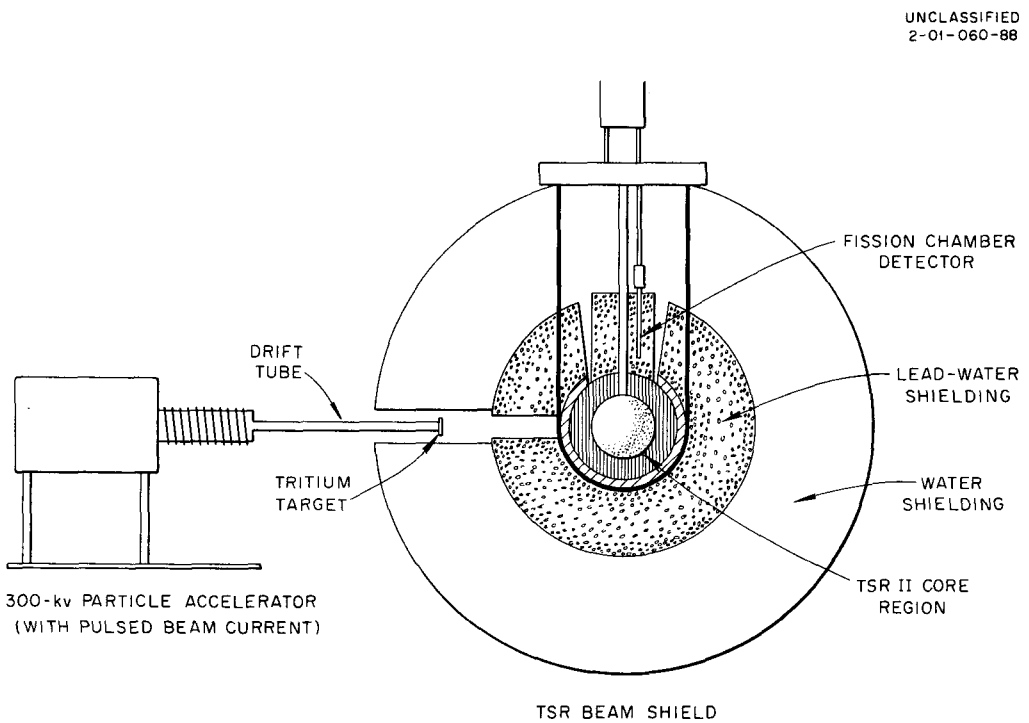

Fig. 2.3.1. Experimental Arrangement Used for Pulsed-Neutron-Source Measurements in the TSR-II.

(BSF), and the procedure was identical with that used in the BSF experiments.[1] The accelerator target was positioned close to the core of the TSR-II through a re-entrant channel through the TSR-II shield, and the decaying neutron pulse was observed with a fission chamber located at

[1] See Sec 1.3 of this report.

the surface of the core about 105° from the target. Pulses from the fission chamber, after amplification and shaping, were fed to the 18-channel time analyzer.

Calibration of TSR-II Control Rods

The check of the TSR-II control-rod calibration curve was accomplished by measuring the negative reactivities accompanying three positions of the control system. With all rods fully inserted, the decay constant, λ, of the prompt-neutron burst was 6.835 ± 0.0030 kc, corresponding to a reactivity of –3.52 ± 0.12 dollars. Negative reactivities were also measured for two other positions of the rod system, and in each case agreement with the previous calibration was good. Figure 2.3.2 shows the data obtained in this experiment plotted on the TSR-II calibration curve previously obtained by other methods.

In order to measure the reactivity worth of a single control rod, the reactor was brought to delayed critical with all rods withdrawn equal amounts. Rod 2 was then fully inserted, the other rod positions remaining unchanged, and the negative reactivity determined by measuring the prompt-decay constant. The reactivity worth of a single rod was thus determined to be –0.62 ± 0.05 dollar.

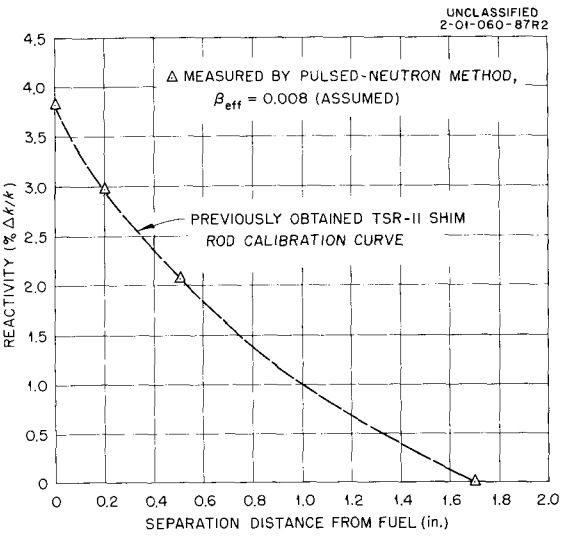

Fig. 2.3.2. TSR-II Rod-Calibration Curve, Showing Pulsed-Neutron-Source Data.

To obtain the total reactivity worth of the entire control system, boron poison was added to the core and to part of the reflector until the reactor was just critical with all rods withdrawn. All rods were then fully inserted and the negative reactivity measured by the pulsed-neutron technique. The reactivity worth of the entire system, from this measurement, is –4.77 ± 0.14 dollars.

Reduced Generation Time (l/β_{eff}) of the TSR-II

The theory on which pulsed-neutron-source measurements of the reduced generation time (l/β_{eff}) are based has been presented elsewhere.[1] The reduced generation time is equal to the inverse of the prompt-neutron decay constant when the reactor is just-critical. The technique employed in this measurement was identical with that of similar measurements for the Bulk Shielding Reactor I. The value obtained for the TSR-II in the present experiment is l/β_{eff} = 6.61 ± 0.20 msec.

Part 3

CRITICAL EXPERIMENTS

3.1 SOLUTION EXPERIMENTS IN A FLUX-TRAP CRITICAL ASSEMBLY: PRELIMINARY STUDY FOR HIGH FLUX ISOTOPE REACTOR

J. K. Fox L. W. Gilley D. W. Magnuson

Introduction

A study of a flux-trap critical assembly has been made, using a solution of $UO_2(NO_3)_2$ enriched to 93.5 wt % in U^{235} and dissolved in mixtures of D_2O and H_2O. This assembly was a preliminary mockup of the proposed High Flux Isotope Reactor (HFIR), and the data was intended to aid in the establishment of design parameters for the HFIR.

The following measurements were made:

1. critical parameters of the assembly with various amounts of neutron absorber in the D_2O reflector;
2. relative flux distribution under various conditions of reflector poison and fissile solution concentration, measured with bare and cadmium-covered miniature U^{235} fission counters;
3. ratio of the absolute thermal flux in the center of the assembly to the power in the fissile solution; and
4. reactivity effect of reduction of the hydrogen density in the central region of the assembly.

In one experiment, the end reflectors were removed in order to obtain a value for the reflector savings.

Experimental Assembly

The apparatus has been described elsewhere.[1] The vessel, shown schematically in Fig. 3.1.1, consisted essentially of four concentric aluminum cylinders, having nominal outside diameters of 6, 16, 32, and 44 in., each with a wall thickness of $\frac{1}{8}$ in. Immediately below the cylinders was a 6-in.-deep compartment, which could be filled with water to achieve an effectively infinite bottom reflector. The compartments, as shown in the figure, were identified as regions I, II, III, IV, and V. Region III was nominally 18 in. high, and above it was a fixed compartment, 12 in. thick. A removable annulus, 12 in. high, could be placed in the upper part of region II, and, with it in place, the height of region II was 17.7 in.

Experiments and Critical Parameters

The experiments were divided into four groups (numbered 1, 2, 3, and 4) on the basis of fuel concentration and boron poison concentration in the D_2O of region III. Table 3.1.1 shows the critical parameters for all experiments.

Group 1 was subdivided into 1*a* and 1*b*, separating the totally reflected experiments, 1*a*, from the experiments without end reflectors, 1*b*. There was an almost negligible difference

[1] C. A. Burchsted, *High Flux Isotope Reactor Critical Experiment – Equipment*, ORNL CF-60-4-120 (Apr. 20, 1960).

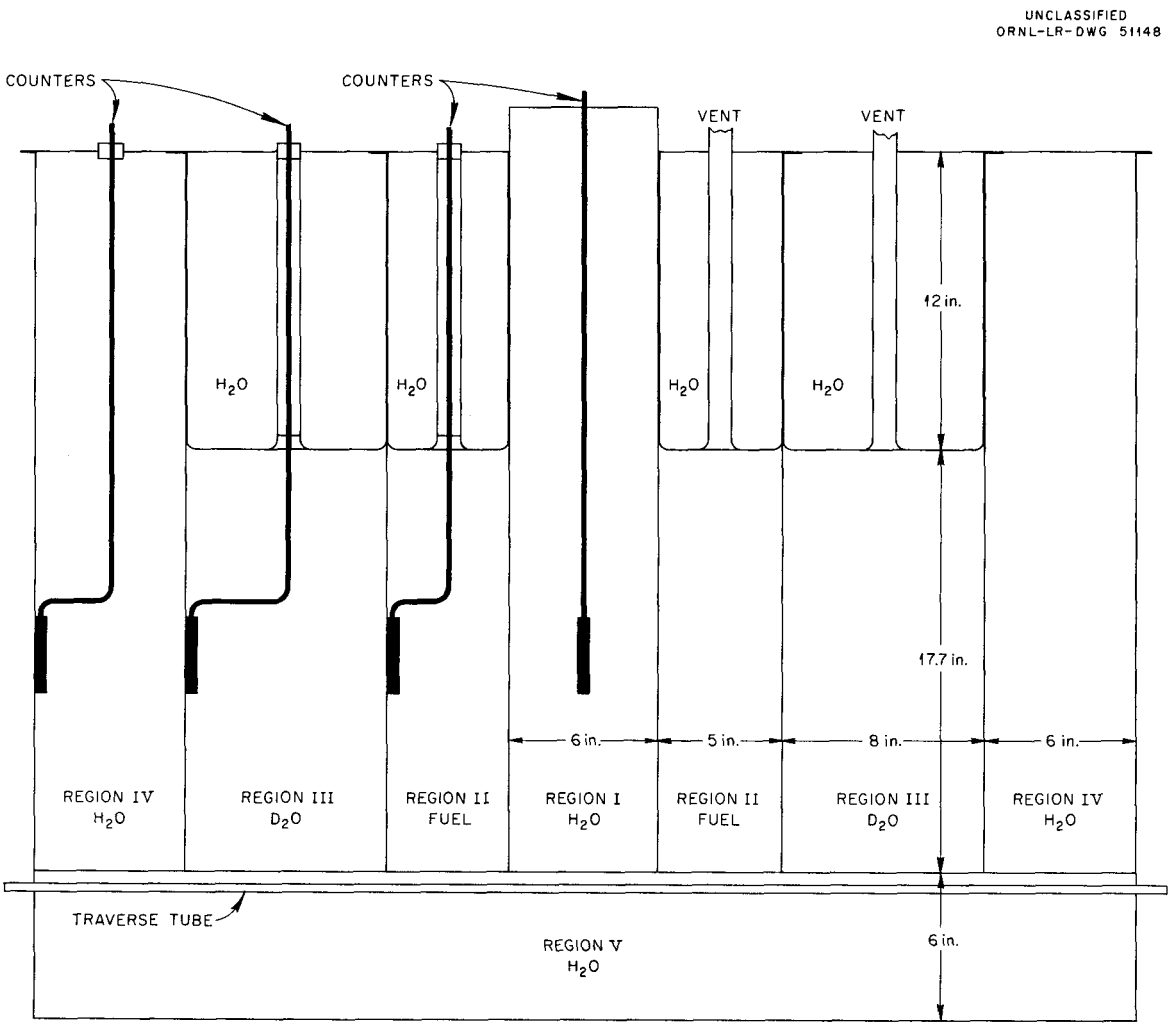

Fig. 3.1.1. Section Through Midplane of Flux-Trap Critical Assembly.

between the chemical analyses of 1*a* (93.17 g of U^{235} per liter) and 1*b* (92.42 g of U^{235} per liter). This stemmed from the necessity of making up additional solution for the 1*b* experiments. The difference in the critical heights of experiments 1*a* and 1*b* gives the reflector savings of 3.2 in. (see Table 3.1.1).

Group 2 of the experiments was divided into 2*a* and 2*b*, with the only difference being the presence of the fission counters in 2*b*. The poisoning effect due to the counters, especially when cadmium-covered, was responsible for the difference in critical height shown in the table.

Additional flexibility for control purposes was obtained from the small positive reactivity gained by permitting the fissile solution to rise in the vent tube and the small clearances around the top reflector of region II.

Table 3.1.1. Critical Parameters of Solutions of 93.5 wt % U^{235}-Enriched $UO_2(NO_3)_2$ in D_2O-H_2O, in the HFIR-Mockup Flux-Trap Assembly

N:U atomic ratio = 2.007

Region-III D_2O reflector = 99.7 at. % D

Experiment Group No.	U^{235} Concentration (g/liter)	Specific Gravity of Solution at 23°C	Assembly Temperature (°C)	H:U^{235} Atomic Ratio	D:U^{235} Atomic Ratio	Deuterium Content (at. %)	Reflector Conditions[a]	Boron Concentration in Region-III D_2O (g/liter)	Critical Height[b] (in.)	Critical Mass (kg of U^{235})	U^{235} Fission Counter Positions
1*a*	93.17	1.2352	21	12.46	258.4	95.4	Totally reflected	0.00	17.68	4.49	No counter present
1*b*	92.54	1.2358	23.5	12.55	260.3	95.4	No end reflectors	0.00	24.08[c]	6.07	No counter present
2*a*	119.7	1.2711		13.08	195.9	93.8	Totally reflected	0.037	17.61	5.75	No counter present
2*b*	119.7	1.2711	23.7	13.08	195.9	93.8	Totally reflected	0.037	17.88	>5.78[d]	Centered in 4 regions
3	137.5	1.2958	23.7	11.33	169.5	93.8	Totally reflected	0.056	17.95	>6.64[d]	Centered in 4 regions
4	105.9	1.2262		70.9	166.3	70.1	Totally reflected	2.35	17.59	5.08	At outer wall of regions II and III, near top

[a]See Fig. 3.1.1 for details of regions.

[b]Vessel is full at 17.7 in. Critical heights reported above this value have excess fuel in vent tubes except for cases with no end reflectors.

[c]H_2O and D_2O in other regions were also at this height.

[d]These are the masses for the just-full vessel.

Relative Flux Distributions

Radial traverses at the vertical midplane, using bare and cadmium-covered miniature U^{235} fission counters, were made in each of the four experiments. All traverse data were normalized to unit bare counting rate at the center of the assembly. Similar, vertical traverses were performed in regions I, II, and III for each of the experiments; but, since the results were the expected simple cosine curves (with some leveling near each end), they are omitted from the present report.

Figures 3.1.2 and 3.1.3 show the bare and cadmium-covered fission-counter traverses, respectively, for experiment 1*a*. Bare-fission-counter radial traverses were also made during this experiment in the bottom H_2O reflector, region V, at distances of 9.62, 12.03, and 14.65 in. below the midplane of the assembly. The results are shown in Fig. 3.1.4.

The radial-traverse data from experiment 2 was almost identical with that from experiment 3, which is shown in Figs. 3.1.5 and 3.1.6; therefore, the data for experiment 2 are not presented.

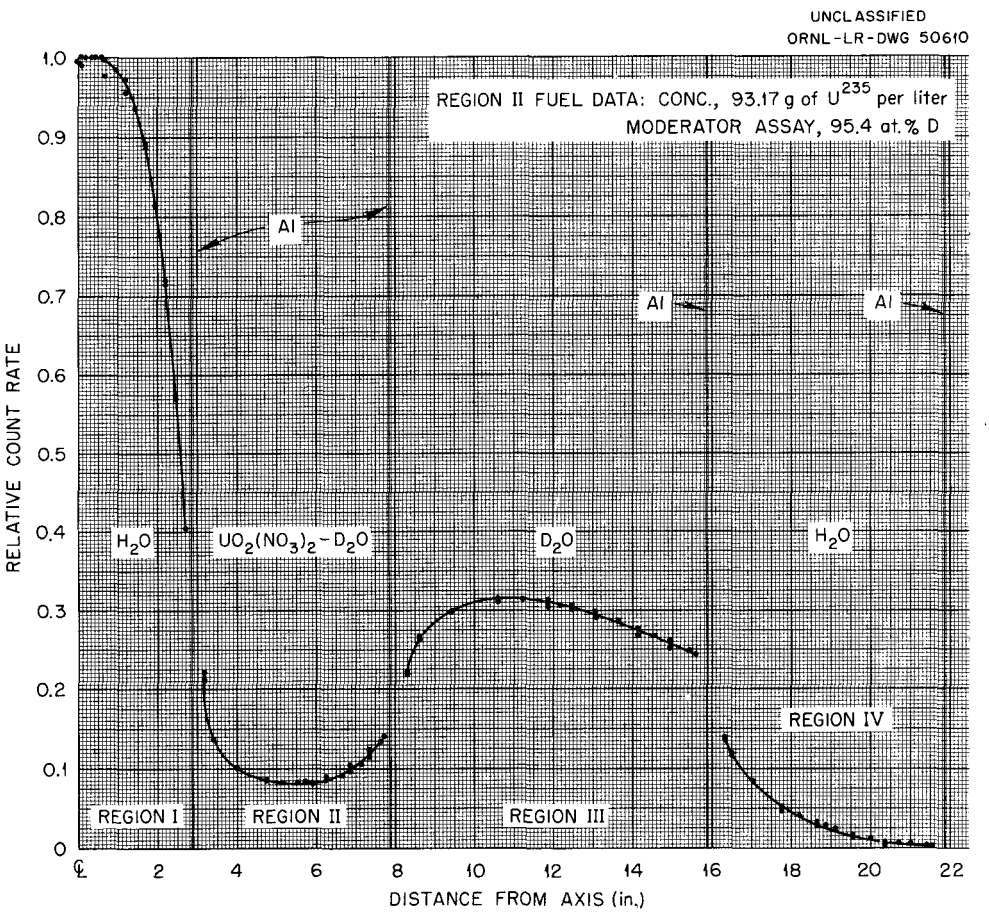

Fig. 3.1.2. Bare U^{235} Fission-Counter Traverse, Radially at Midplane of Experiment 1.

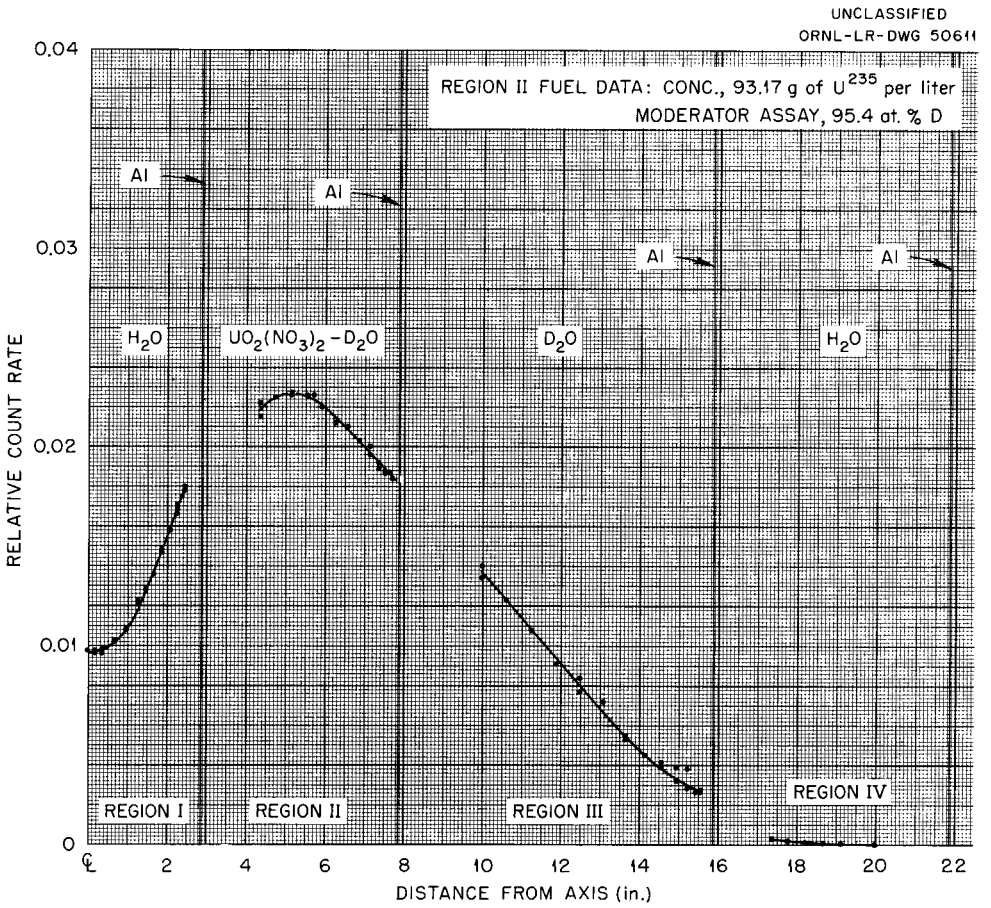

Fig. 3.1.3. Cadmium-Covered U^{235} Fission-Counter Traverse, Radially at Midplane of Experiment 1.

The severe depression of the total flux in the D_2O, caused by the high boron content of region III, is evident in the traverses of experiment 4, as shown in Figs. 3.1.7 and 3.1.8.

Cadmium ratios at the centers of regions I, II, and III were computed for experiments 1, 3, and 4. The computed cadmium ratios for each region are shown below.

Experiment	Region I	Region II	Region III
1	104	3.58	35.6
3	101	2.78	32.6
4	102	7.51	4.38

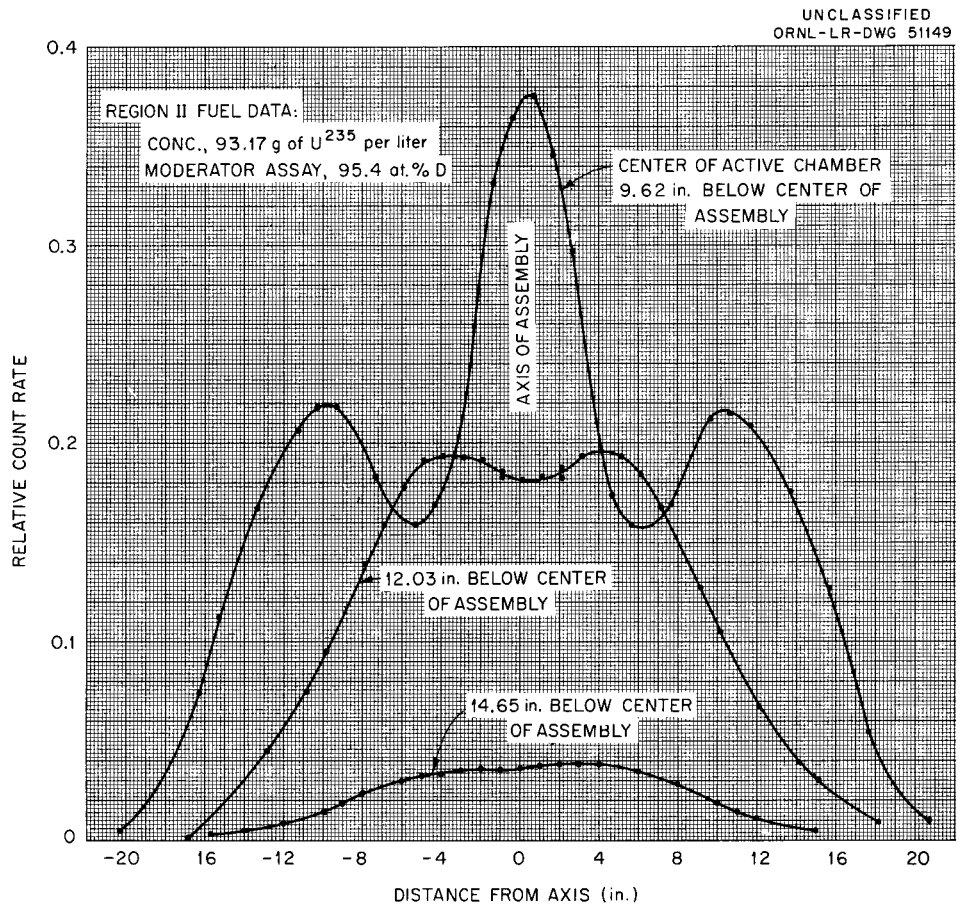

Fig. 3.1.4. Bare U^{235} Fission-Counter Traverse, Radially at Three Levels in Bottom Reflector of Experiment 1.

Ratio of Absolute Thermal Flux at the Center of the Assembly to Power in the Fissile Solution

Two methods were used to evaluate the ratio of the thermal neutron flux in the center of region I to the power in region II. In the first, the thermal neutron flux was measured from the activity induced in bare and cadmium-covered gold foils irradiated at the center of region I. The foils and the counters used in measuring their activity had previously been calibrated against foils irradiated in the ORNL Standard Pile. The power generation in region II was determined from the average fission density of a well-mixed fuel sample after the irradiation of the foils, as measured by radiochemical analysis. In determining the saturated count rate of the foils, corrections were applied for the epithermal absorptions in the cadmium covers; corrections were also made for self-shielding and flux depression by the method of Trubey *et al.*[2] The two

[2]D. K. Trubey, T. V. Blosser, and G. M. Estabrook, *Neutron Phys. Ann. Prog. Rep. Sept. 1, 1959*, ORNL-2842, p 204.

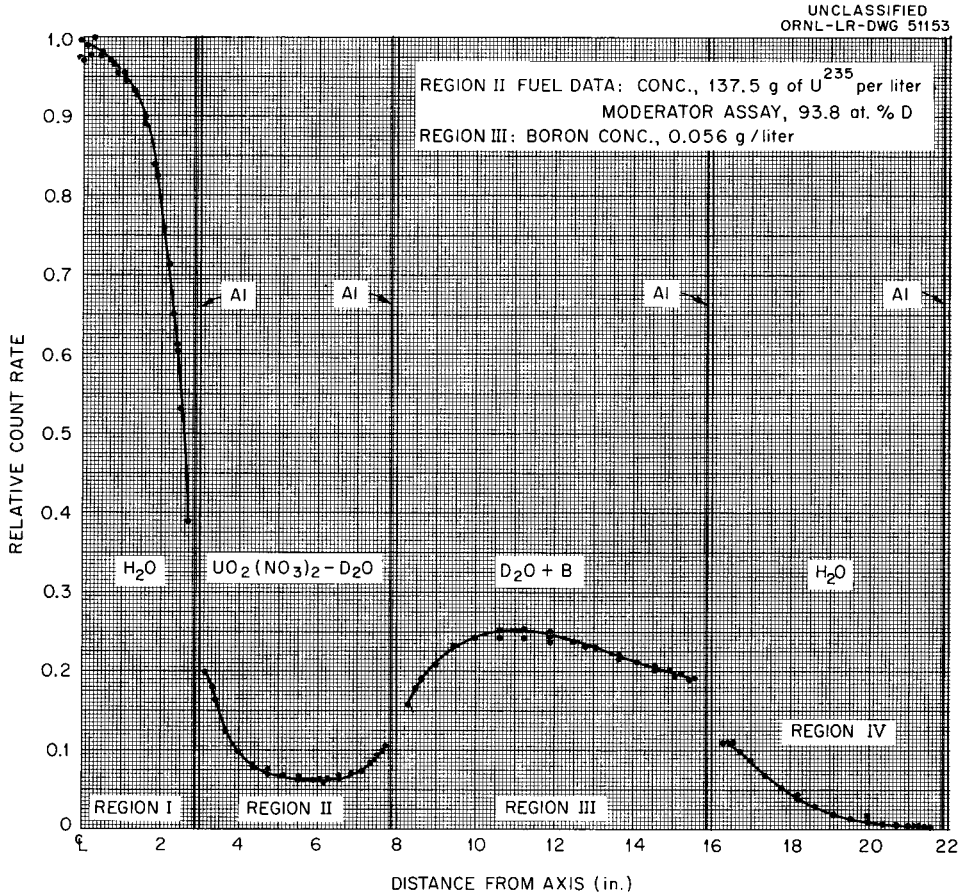

Fig. 3.1.5. Bare U^{235} Fission-Counter Traverse, Radially at Midplane of Experiment 3.

measurements made by this method, using the equivalence 1 w = 3.38×10^{10} fissions/sec, gave results of 5.86×10^7 and 5.79×10^7 neutrons $cm^{-2}\ w^{-1}\ sec^{-1}$.

The second method utilized the results from bare-fission-counter traverses in region II to determine an average count rate which was assumed to be proportional to both the average fission rate and the count rates measured by bare and cadmium-covered counters in the center of region I. The average count rate in the center of region I is

$$R_{\mathrm{I}} = K\left[\int \phi_M \sigma_f(E)\, dE + \int \phi_{\mathrm{epi}} \sigma_f(E)\, dE\right] , \tag{1}$$

the average count rate in region II is

$$R_{\mathrm{II}} = K \int \bar{\phi}_F \sigma_f(E)\, dE \ , \tag{2}$$

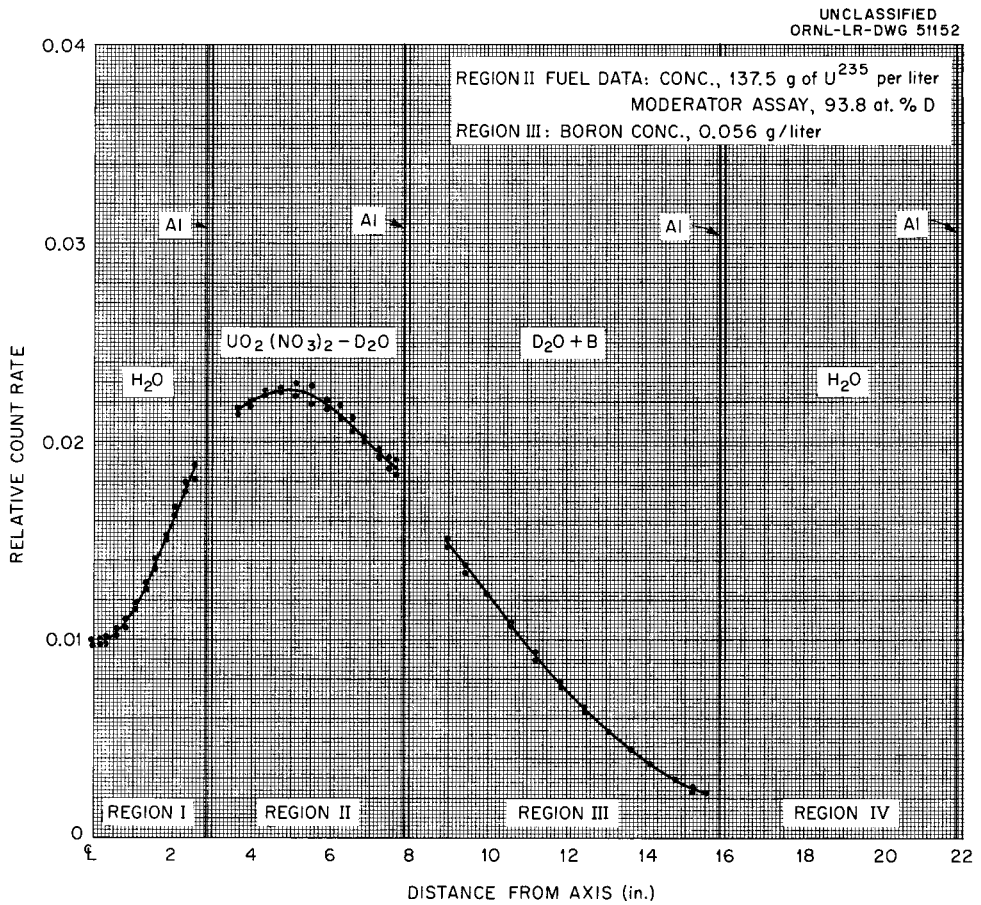

Fig. 3.1.6. Cadmium-Covered Fission-Counter Traverse, Radially at Midplane of Experiment 3.

and the ratio

$$\frac{R_{\mathrm{I}}}{R_{\mathrm{II}}} = 0.886\,\sigma_f(2200)\,\frac{CR}{CR-1}\,\frac{\int \phi_M\,dE}{\int \bar{\phi}_F\,\sigma_f(E)\,dE}\,, \tag{3}$$

where

ϕ_M = Maxwellian thermal flux in region I,

$\bar{\phi}_F$ = flux in fuel, averaged over fuel volume,

$\sigma_f(E)$ = fission cross section,

$\sigma_f(2200)$ = 2200-m/sec fission cross section,

ϕ_{epi} = epicadmium flux in center of region I,

CR = cadmium ratio in center of region I,

K = counter efficiency.

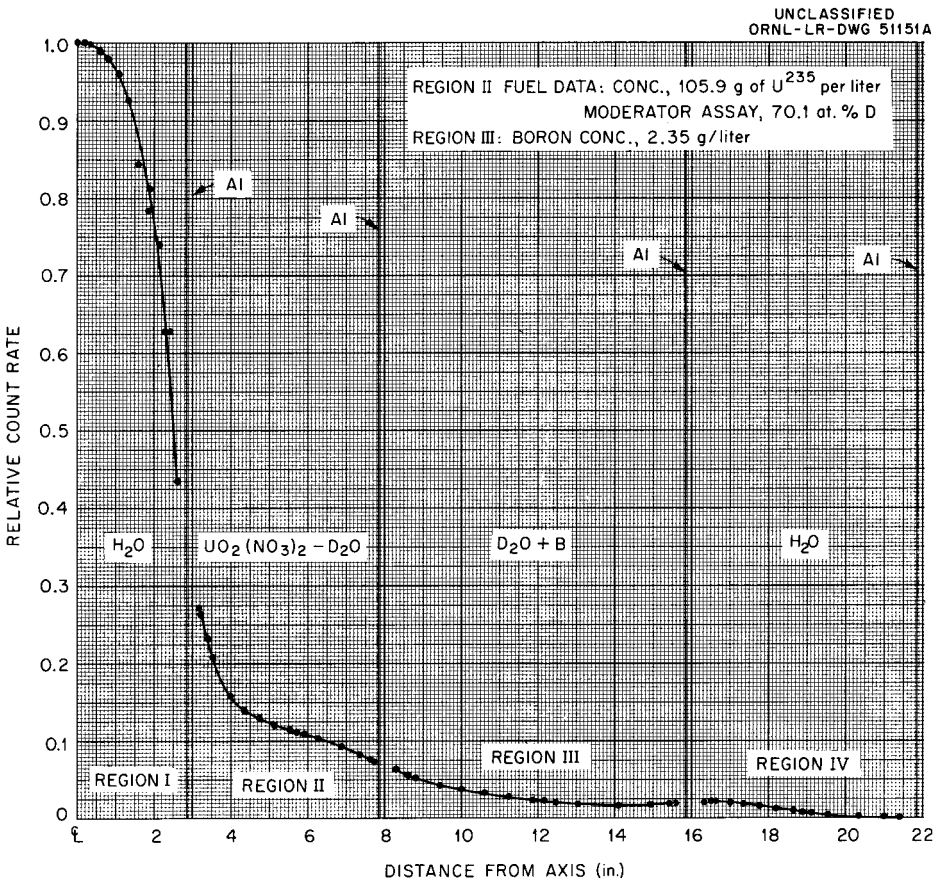

Fig. 3.1.7. Bare U^{235} Fission-Counter Traverse, Radially at Midplane of Experiment 4.

If N_F is the number of fissile atoms in the fuel volume, the ratio of the thermal flux in region I to the total fissions per second is given by

$$\frac{\int \phi_M \, dE}{N_F \int \bar{\phi}_F(E)\sigma_f(E) \, dE} , \tag{4}$$

and therefore

$$\frac{\text{Thermal flux}}{\text{Total fissions per second}} = \frac{R_I/R_{II}}{0.886\sigma_f[CR/(CR-1)]N_F} . \tag{5}$$

The value of this ratio was 5.73×10^7 neutrons cm^{-2} w^{-1} sec^{-1}.

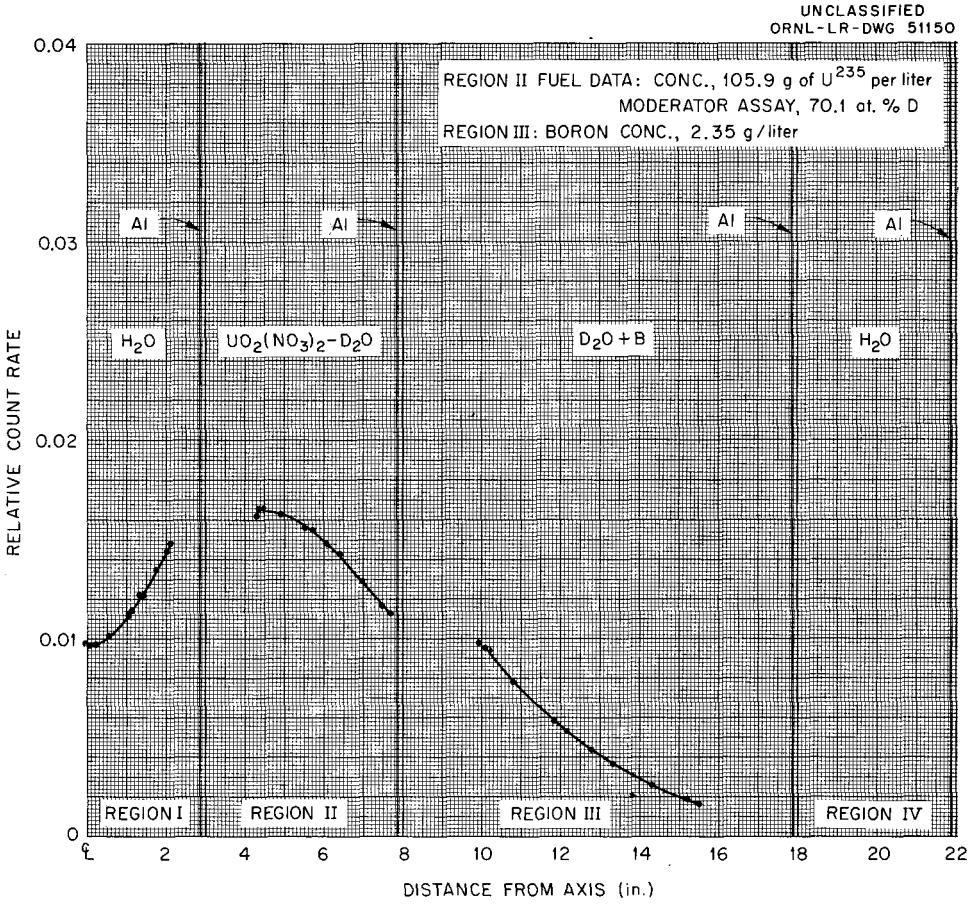

Fig. 3.1.8. Cadmium-Covered Fission-Counter Traverse, Radially at Midplane of Experiment 4.

Reactivity Effect of the Reduction of the Hydrogen Density in the Central Region of the Assembly

Since the water of region I was expected to have a positive void coefficient, the reactivity effects resulting from the displacement of water by air, plastics, and aluminum between the end reflectors of region I were determined during experiment 4. In some experiments the plastics, which had less hydrogen per unit volume than water, were used. In others, larger density changes were introduced by inserting air-filled plastic tubes ($\frac{3}{8}$-in. ID), while the hydrogen density was reduced to zero by displacing the water with air. In the experiments with aluminum, a maximum hydrogen displacement of 73% was achieved.

At critical for each displacement experiment, the assembly was never full; an air void was always present between the fissile solution and the top reflector in region II. The reactivity corresponding to change in height, $\Delta k/\Delta h$, was determined by measuring the positive periods that accompanied small increases in height above critical.

Figure 3.1.9 shows the critical height as a function of the reduction in hydrogen density in region I for the fissile solution and reflector conditions of experiments 2, 3, and 4. The curves show that the critical height decreases for both types of void-causing material until a reduction in hydrogen density of about 60% is reached, then begins to increase. The relative effect of the displacement of water by air is clearly greater than that of the displacement by aluminum. The data for this portion of experiment 4 is shown in Table 3.1.2. The reactivities corresponding to small changes in height from delayed critical were calculated by using the delayed-neutron data of Keepin *et al.*[3] and also by taking into account the additional delayed contribution due to photoneutrons from the (γ,n) reaction in the D_2O, using the data of Bernstein *et al.*[4] The importance of all delayed neutrons was assumed to be the same as that of prompt neutrons in these calculations. Reactivity effects corresponding to three assumptions of efficiency of photoneutron production are shown in the table. A graphical integration from a plot of $\Delta k/\Delta h$ vs critical height for experiment 4 gives a maximum Δk, assuming a photoneutron production efficiency of 50%, of 0.055 for an optimum air void, and 0.040 for the optimum aluminum void. A complete report of this work is being prepared.

[3]G. R. Keepin, T. F. Wimett, and R. K. Zeigler, *Phys. Rev.* **107**, 1044 (1957).

[4]S. Bernstein *et al.*, *Phys. Rev.* **71**, 573 (1947).

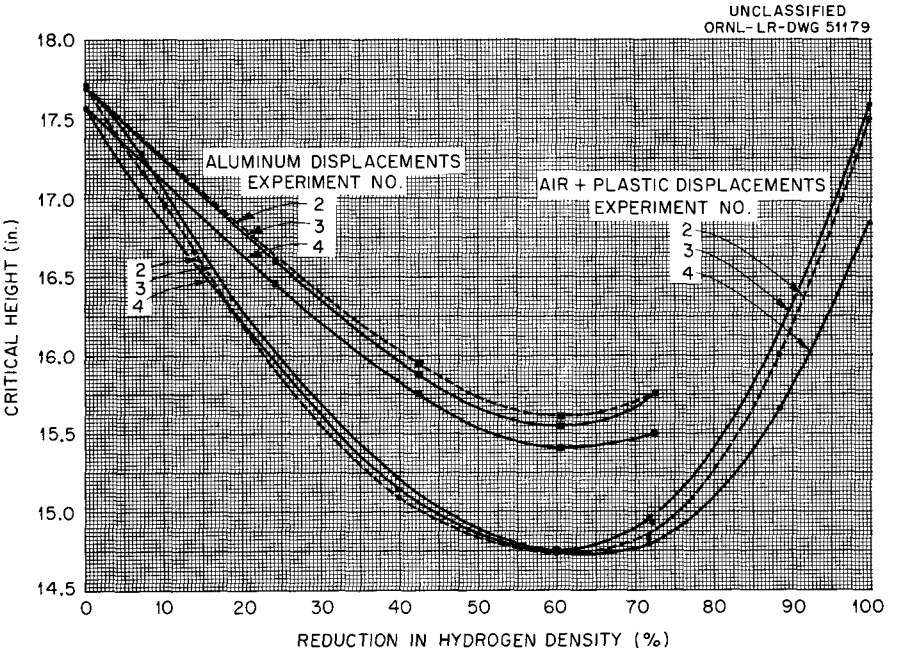

Fig. 3.1.9. Critical Height as a Function of Reduction in Hydrogen Density in Region I of Experiments 2, 3, and 4.

Table 3.1.2. Critical Height and $\Delta k/\Delta b$ for Various Degrees of Reduction of the Hydrogen Density in Region I of Experiment 4 in the HFIR-Mockup Flux-Trap Assembly

U^{235} in region II: 105.9 g/liter
D in region II: 70.1 at. %
B in region III: 2.35 g/liter

Reduction in Hydrogen Density in Region I (%)	Critical Height (in.)	Δb (in.)	Period (sec)	Reactivity ($\Delta k \times 10^4$)			$\Delta k/\Delta b$		
				Zero Photoneutron Efficiency	50% Photoneutron Efficiency	100% Photoneutron Efficiency	Zero Photoneutron Efficiency	50% Photoneutron Efficiency	100% Photoneutron Efficiency
Water Displacement by Plastic + Air									
0	17.59	0.0215	270	2.73	3.45	4.17	0.0127	0.0160	0.0194
7.19	17.02	0.0224	245	2.98	3.74	4.50	0.0133	0.0167	0.0201
18.50	16.31	0.0187	274	2.69	3.42	4.13	0.0144	0.0183	0.0221
39.9	15.14	0.0208	191	3.71	4.55	5.39	0.0178	0.0219	0.0259
59.9	14.74	0.0173	211	3.39	4.20	5.01	0.0196	0.0243	0.0290
71.8	14.79	0.0210	163	4.24	5.15	6.05	0.0202	0.0245	0.0288
88.6	15.67	0.0173	218	3.30	4.05	4.89	0.0191	0.0234	0.0283
100	16.85	0.0173	204	3.50	4.32	5.13	0.0202	0.0257	0.0296
Water Displacement by Aluminum									
24.2	16.46	0.0180	299	2.49	3.18	3.87	0.0138	0.0177	0.0215
42.4	15.76	0.0166	272	2.72	3.44	4.16	0.0164	0.0207	0.0251
60.6	15.42	0.0204	204	3.50	4.32	5.13	0.0172	0.0212	0.0251
72.8	15.50	0.0204	200	3.56	4.39	5.21	0.0175	0.0215	0.0255

3.2 HOMOGENEOUS CRITICAL ASSEMBLIES OF 2% U^{235}-ENRICHED UF_4 IN PARAFFIN

J. T. Mihalczo J. J. Lynn

The program of critical experiments with homogeneous hydrogen-moderated assemblies of 2% U^{235}-enriched UF_4 and paraffin reported previously[1] has been extended to a mixture with an $H:U^{235}$ atomic ratio of 501. This mixture contains 82 wt % UF_4 and has a uranium density of 1.97 g/cc.

The minimum critical masses and minimum critical volumes have been established for bare and reflected cylinders and parallelepipeds and are shown in Figs. 3.2.1 and 3.2.2 along with those for previous UF_4-paraffin mixtures. The reflector material was an effectively infinite thickness of paraffin or of Plexiglas.

[1] J. T. Mihalczo and J. T. Lynn, *Neutron Phys. Ann. Prog. Rep. Sept. 1, 1959*, ORNL-2842, p 85.

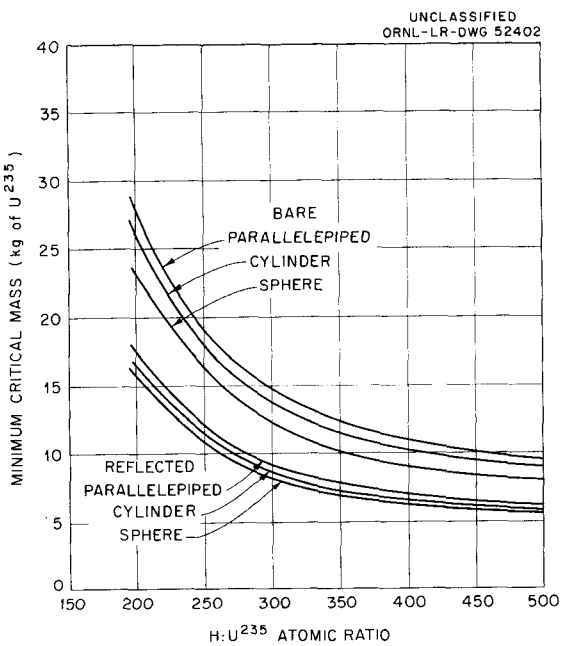

Fig. 3.2.1. Critical Mass of 2% U^{235}-Enriched UF_4–$C_{25}H_{52}$ as a Function of the $H:U^{235}$ Atomic Ratio.

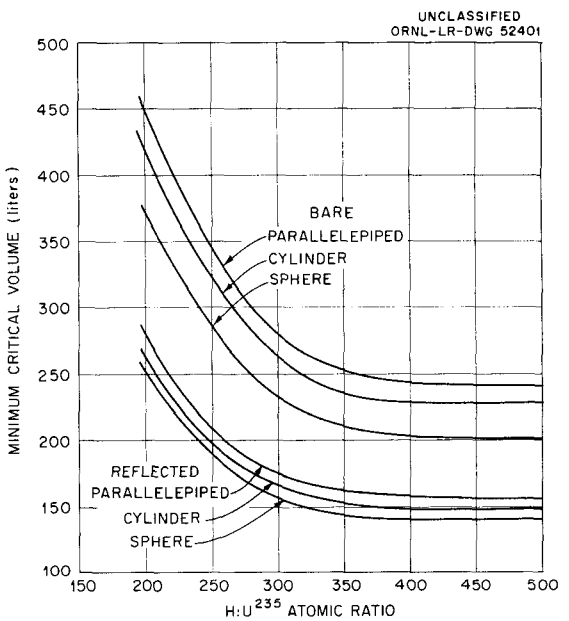

Fig. 3.2.2. Critical Volume of 2% U^{235}-Enriched UF_4–$C_{25}H_{52}$ as a Function of the $H:U^{235}$ Atomic Ratio.

3.3 CRITICAL DIMENSIONS OF RANDOM ARRAYS OF ThO_2-UO_2 PELLETS

J. K. Fox L. W. Gilley

Several current or proposed reactor designs employ the fuel in the form of small, metal-clad pellets of thoria and uranium oxide. Reprocessing of spent fuel will be initiated by chemical dissolution of the pellets after mechanical decladding. As a guide to the design of dissolver equipment, several criticality experiments have been performed with unclad pellets,[1] consisting of a mixture of ThO_2 and UO_2, randomly stacked in 1.6-mm-thick-wall aluminum or steel cylinders. Water was added to the cylinders to serve as a neutron moderator, and the cylinders were surrounded by water reflector for all experiments.

The pellets were nominally 0.66 cm in diameter and 1.32 cm long, although some irregular shapes and fines were included because of breakage during handling. Density of the pellets was 8.3 g/cc, with a uranium content of 5.94 wt % and a U^{235} content of 5.54%; thus, the nuclear properties approximated those of 5% U^{235}-enriched uranium. When pellets were poured into a 38-cm-dia cylinder, the random pattern that was produced resulted in an average concentration of 0.29 g of U^{235} per cubic centimeter of vessel volume. When the pellets were covered with water, the resulting $H:U^{235}$ atomic ratio was 34, severely less than optimum moderation. Approximately 900 kg of pellet material (50 kg of U^{235}) was available for the experiments. Table 3.3.1 displays the results of measurements in cylinders of three diameters.

Table 3.3.1. Experimental Results

Cylinder Material	Cylinder Diameter (cm)	Pellet Depth (cm)	Pellet Mass (kg of U^{235})	k, Multiplication Constant
Stainless steel	38.1	153	50.0	$\ll 1$
Aluminum	44.2	58.2	25.6	~ 1
	50.8	45.7	26.6	1

The critical dimensions of random assemblies of these pellets are extremely sensitive to the degree of moderation. This was demonstrated during experiments preliminary to those described above. The dry ThO_2-UO_2 pellets were delivered to the laboratory in plastic bottles, 13 cm in inside diameter and 116 cm high. The average wall thickness of the bottles was 0.64 cm. When filled to a height of 109 cm, each contained about 4.45 kg of U^{235}. Preliminary experiments utilized the material as received. It was first shown that adding water to a bottle produced little neutron multiplication. A close-packed, body-centered hexagonal array of seven bottles, with water covering the pellets but without external water, was subcritical, and this close-packed array remained subcritical when submerged in water. However, when the seven bottles were

[1] The pellets were supplied by the Babcock and Wilcox Co.

separated a distance 0.6 cm, corresponding to a separation of about 1.9 cm between pellet assemblies, the array became critical upon addition of external water. An increase in the bottle-to-bottle spacing to 1.0 cm increased the reactivity, but a further separation to 1.9 cm caused the array to become subcritical.

3.4 CRITICAL PARAMETERS OF BARE AND REFLECTED 93.4 wt % U^{235}-ENRICHED URANIUM METAL SLABS

J. T. Mihalczo J. J. Lynn

The critical thicknesses of slabs of 93.4 wt % U^{235}-enriched uranium metal have been measured in a series of neutron multiplication experiments. The uranium metal had a density of 18.7 g/cc and was in the form of machined parallelepipeds. The effect of Plexiglas as a neutron reflector was determined, and a limited number of measurements with beryllium and graphite reflectors were made.

The experimental arrangement is shown in Fig. 3.4.1. The separable "split table" apparatus of the ORNL Critical Experiments Facility was modified by mounting on one half of the

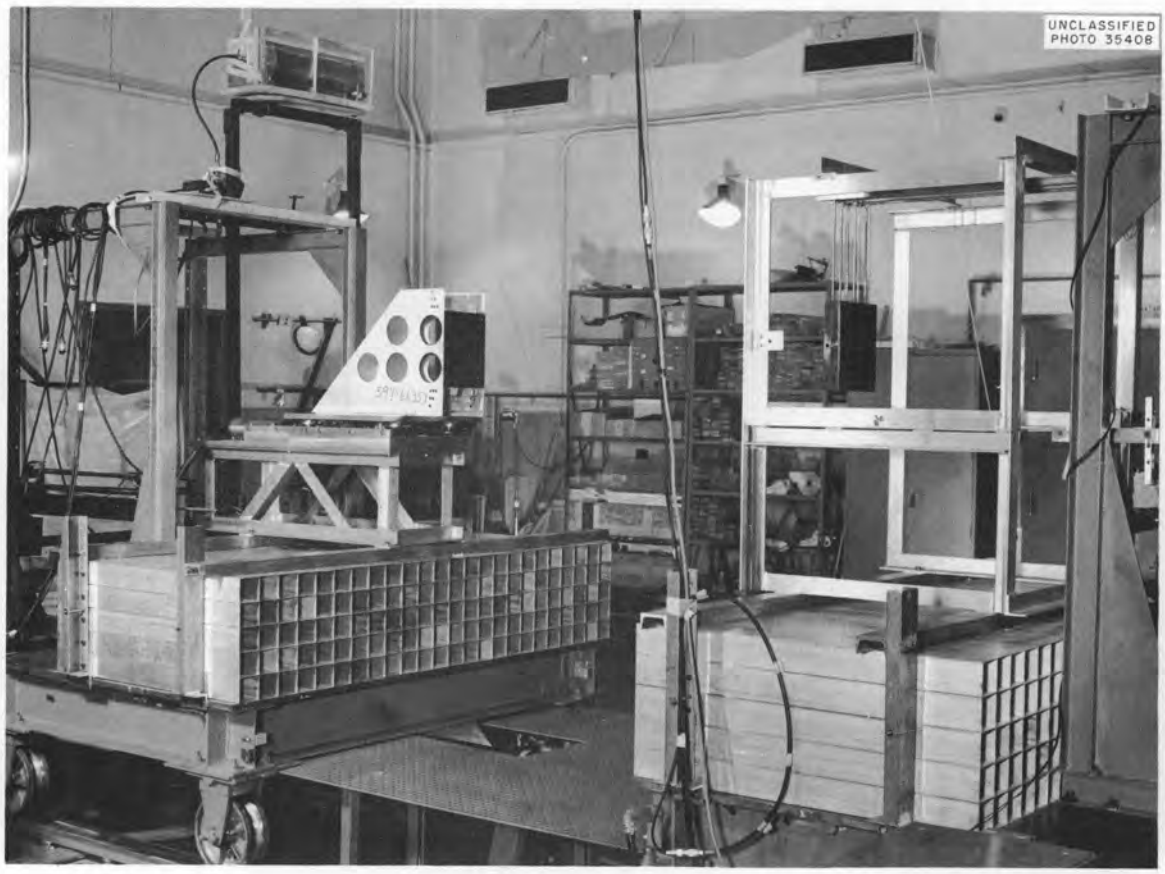

Fig. 3.4.1. Experimental Arrangement.

table a smaller, independently movable, aluminum table. A frame was attached to the other half of the table, and the experimental material divided between small table and frame. Before the assembly was completed by bringing the small table against the frame, a strong spring was compressed against the small table. When the magnets which held the components together were de-energized by a scram signal, the spring repelled the small table at an initial rate of 1 in. in ~60 msec. The rapid initial separation enhanced the safety factor inherent in the use of the divided table.

The strength of the Po-Be neutron source was ~10^7 neutrons/sec. Three BF_3 gas-filled counters placed around the assemblies were used to measure the neutron multiplication. The critical mass of U^{235} as a function of the thickness $/\sqrt{area}$ ratio is shown in Fig. 3.4.2, while Table 3.4.1 gives critical thicknesses and critical masses for reflected and unreflected slabs of

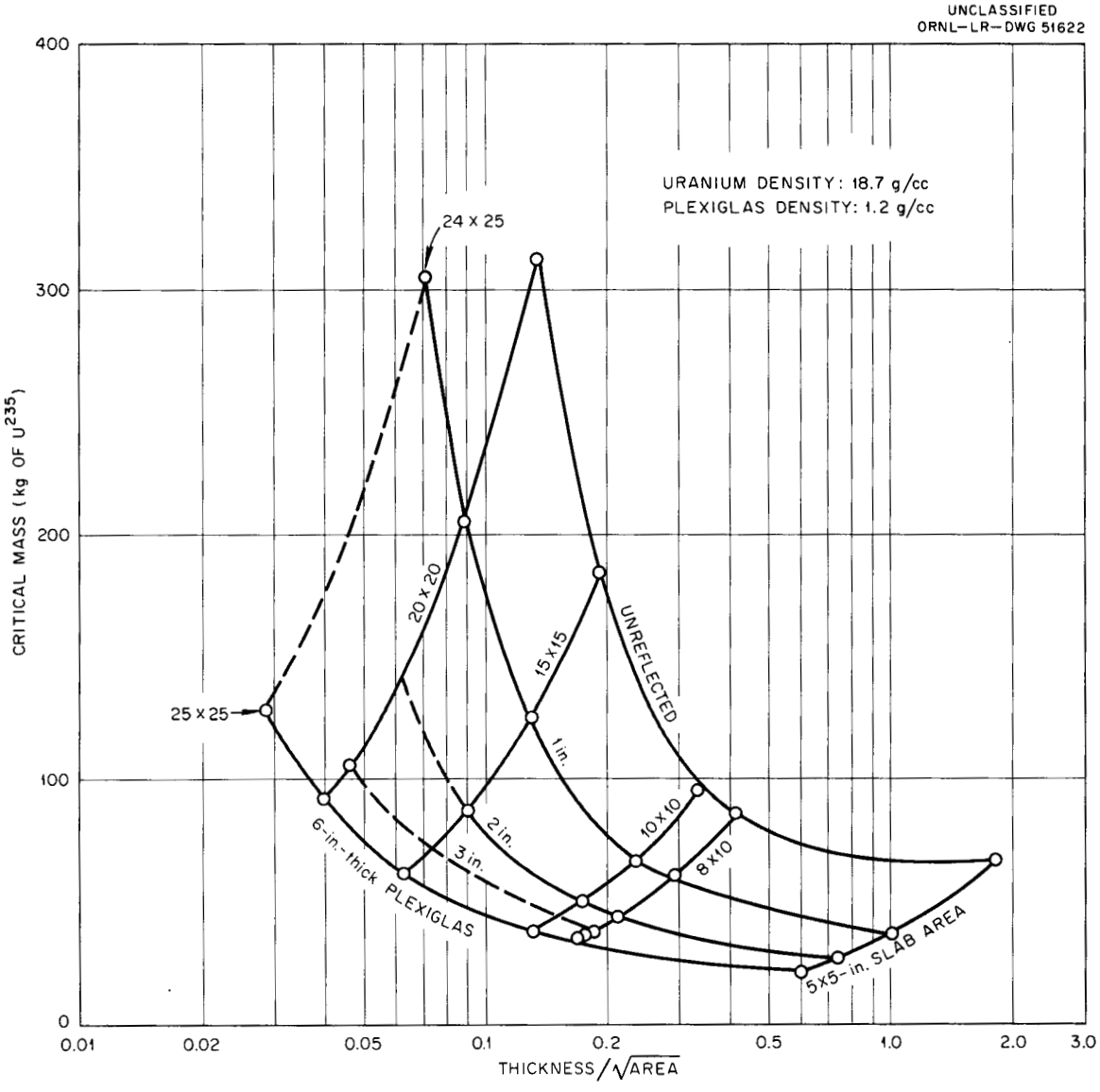

Fig. 3.4.2. Critical Mass of U^{235} as a Function of Parallelepipedal Geometry for Bare and Plexiglas-Reflected Slabs.

Table 3.4.1. Critical Thickness and Critical Mass of Slabs of 93.4 wt % U^{235}-Enriched Uranium Metal Reflected with Plexiglas

Slab Dimensions (in.)	Plexiglas-Reflector Thickness (in.)	Critical Thickness (in.)	Critical Mass (kg of U^{235})	Per Cent of Critical Mass Assembled
5 × 5	0	9.13	65.6	97
	1	4.96	35.5	96
	2	3.70	26.5	98
	6	3.05	21.8	98
8 × 10	0	3.74	85.7	97
	1	2.64	60.5	95
	2	1.89	43.3	93
	3	1.63	37.4	92
	4	1.55	35.5	97
	6	1.53	35.0	98
10 × 10	0	3.32	95.1	98
	1	2.32	65.6	97
	2	1.72	49.3	93
	6	1.30	37.3	96
15 × 15	0	2.87	184.9	96
	1	1.92	123.7	97
	2	1.35	87.0	94
	6	0.95	61.3	92
20 × 20	0	2.72	311.9	92
20 × 20	1	1.79	205.5	98
	3	0.92	105.3	95
	6	0.80	91.7	94
24 × 25	1	1.77	304.5	85
25 × 25	6	0.71	127.1	94
∞	0	2.4*		
	6	0.6*		

*Extrapolated from the above data.

various areal dimensions. Since, for reasons of safety, an exactly critical slab was never assembled, the percentage of critical mass assembled is also given. These data extrapolate to 0.6 in. as the thickness of a critical slab infinite in extent and reflected by 6 in. of Plexiglas. The thickness of a similar but unreflected slab is 2.4 in.

A slab with areal dimensions of 8 × 10 in. was reflected with AGOT graphite (density 1.72 g/cc), and the results are shown in Table 3.4.2. In another test, critical thickness and critical mass of a 5 × 5 in. slab, reflected with 12 in. of beryllium, were found to be 1.4 in. and 10.1 kg of U^{235}. The density of the beryllium was 1.86 g/cc.

Table 3.4.2. Critical Thickness and Critical Mass of 8 × 10 in. Slabs of 93.4 wt % U^{235}-Enriched Uranium Metal Reflected with Graphite

Graphite-Reflector Thickness (in.)	Critical Thickness (in.)	Critical Mass (kg of U^{235})	Per Cent of Critical Mass Assembled
1.43	2.52	57.7	94
2.87	2.11	48.4	95
5.75	1.65	37.8	91
12.0	1.32	30.3	95

3.5 CRITICAL EXPERIMENTS WITH PRNC RESEARCH REACTOR FUEL ELEMENTS

E. B. Johnson K. M. Henry, Jr.

A series of critical experiments, using the first set of fuel elements fabricated for the Puerto Rico Nuclear Center (PRNC) pool-type research reactor, has been completed in the Pool Critical Assembly (PCA) of the Bulk Shielding Facility (BSF). The experiments were requested by the AEC in order to experimentally verify that the calculated[1] loading per fuel element would provide sufficient excess reactivity to meet normal operating requirements. Since two sets of elements were to be fabricated for this reactor, modifications could have been made in the second set had these experiments indicated their desirability. Four configurations, all based on the geometries proposed by the designer,[2] were assembled.

PRNC reactor fuel elements are of the MTR type, having 18 plates per standard element, mechanically joined to the side plates. Core material is a dispersion of U_3O_8 in aluminum, 24 mils thick in the finished plate, with an 18-mil aluminum cladding on each side. The uranium is enriched to 20% in U^{235}. Each standard element contains 192 g of U^{235}, while partial elements, made by decreasing the amount of U_3O_8 in the dispersion, contain 96 g of U^{235}. Each control-rod element contains 96 g of U^{235} in nine fuel-bearing plates.

Nuclear control of the core during the critical experiments was accomplished with four BSF-type B_4C shim-safety rods and a type 347 stainless steel regulating rod, all operating within the PRNC control-rod elements. The location of the five rods in each core was the same, as shown in Fig. 3.5.1, and was that proposed by AMF.[2] In addition to the conventional control rods, boron-impregnated plastic strips were used as fixed poison to counteract the excess reactivity encountered in loadings 3 and 4. The amount and distribution of the boron in these

[1] E. G. Silver and W. Etzel, *Neutron Phys. Ann. Prog. Rep. Sept. 1, 1959*, ORNL-2842, p 6.

[2] *Hazards Summary Report for the University of Puerto Rico Nuclear Reactor*, AMF Atomics (March 1960).

UNCLASSIFIED
2-01-058-0-555

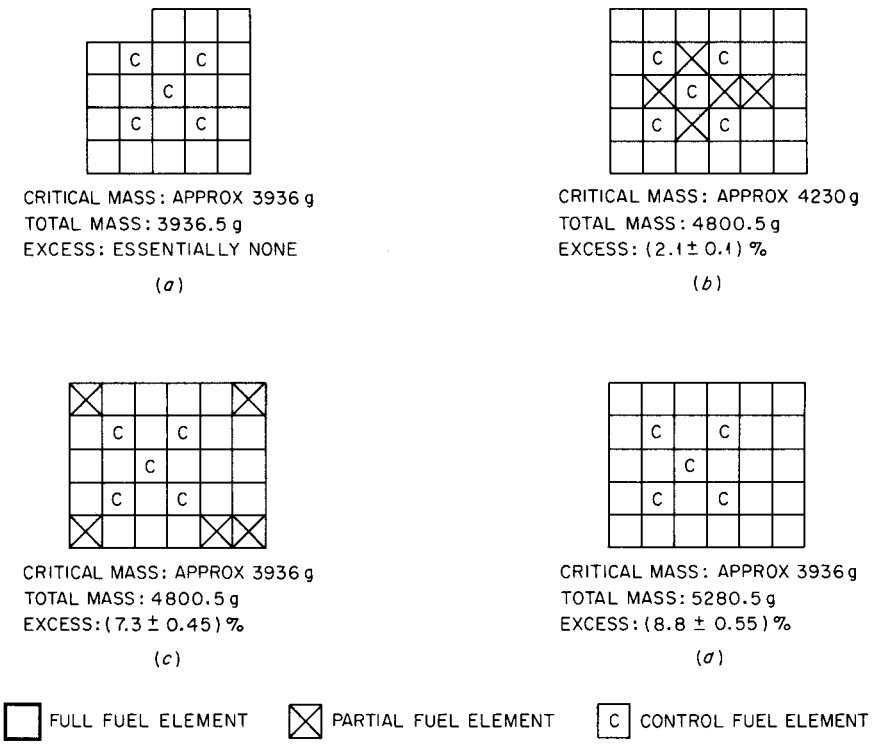

Fig. 3.5.1. Configurations of Puerto Rico Nuclear Center Research Reactor Fuel Elements Assembled in the Pool Critical Assembly of the Bulk Shielding Facility.

strips was not uniform; therefore each strip was individually calibrated by the method of Cagle *et al.*[3] In this method the absorption cross section of the plastic strip is determined by comparison with a material of known cross section (copper), from the ratio between regulating-rod displacements (in the linear portion of the rod) required as the two materials are alternately placed in the same position in a critical core. Some of the strips had previously been calibrated in the LITR; the rest were calibrated in a PCA loading. In order to prevent any strips accidently broken during the experiments from dropping completely through the core, aluminum screens were fitted at the bottom of the fuel plates above the lower end box.

The excess reactivity (the reactivity which the configuration would contain were all control devices completely removed from the core) was measured by a combination of two methods: the positive stable period method and the method of distributed poison. The reactivity corresponding to a measured positive period was calculated from the inhour equation, using Keepin's delayed neutron data[4] and an effective delayed neutron fraction of 0.0079. The positive period measurements were used in the final evaluation of the data only for available reactivities of less than 1%, because of the pronounced effect of rod shading.

[3] C. D. Cagle and R. A. Costner, Jr., *Initial Post Neutron Measurements in the ORR*, ORNL-2559 (May 28, 1959).

[4] G. R. Keepin, T. F. Wimett, and R. K. Ziegler, *J. Nuclear Eng.* **6**, 1 (1958).

The first PRNC fuel-element core assembled in the PCA is shown as (*a*) in Fig. 3.5.1. This was the configuration calculated by Silver[1] and was predicted to have a k_{eff} of 1.0042. The observed excess reactivity was less than 0.05%.

Figure 3.5.1*b* shows the first of the full (5 × 6) element arrays to be assembled, with the five 96-g partial elements located near the center of the core. This is intended to be the initial clean, cold, operating core in the "stall" position (adjacent to the thermal column and beam tubes). After completion of the loading and evaluation of the excess reactivity by positive period measurements, a number of boron-impregnated plastic strips were uniformly distributed throughout the core (except within the control rod elements) to absorb 1.3% of reactivity, based on the calculated (by the methods of ref 1) cross sections of the core. The remaining 0.8% of excess reactivity was measured by the inhour method. Total excess was thus 2.1%.

As the fuel is burned in the operating core, it is proposed to move the partial elements out of the center of the core, replacing them with full elements. This configuration was duplicated with cold, clean elements in the third configuration, shown in Fig. 3.5.1*c*. Poison strips were added to the core until a total reactivity of 6.55% was controlled by this method when loading was completed. Positive period measurements showed 0.75% of available excess reactivity remaining in the final loading. The total excess reactivity in this loading thus was 7.3%, or an increase of 5.2% resulting from moving the partial rods from the central region to the corners.

The final configuration, shown in Fig. 3.5.1*d*, was a 5 × 6 array containing all full fuel elements. Boron strips were added until a total of 8.1% reactivity was controlled by the attached poison. The remaining reactivity was 0.7%, making a total of 8.8% for this loading.

The effects of rod shading noted above became obvious during the calibration of the second loading, from an apparent discrepancy between the inhour calibration of the unpoisoned core and the effect of the addition of calibrated poison. Investigation of the discrepancy in this and the following two loadings showed that the reason lay in the fact that, due to shading by another rod, the apparent worth of a shim-safety rod changed appreciably, even over the limited range of motion available. It should be pointed out that the fourth shim-safety rod, located in the central position, was always fully withdrawn during calibrations.

The probable errors in these experiments are unusually large, both because of the primary purpose of the measurements and also because of the limited time available. The error in the total delayed neutron fraction is quoted by Keepin[4] as ±3.2%. Random errors in period measurements (±2%) and in the calibration of the boron plastic strips (±5%) result in a cumulated error of about ±6% for most of the measurements. It was not possible to realistically estimate the influence of the error due to rod shading on the final measurements, but it is probably greater than 6%.

Part 4

EXPERIMENTAL NUCLEAR PHYSICS

4.1 MEASUREMENTS OF η OF U^{233} AND U^{235} BY A MANGANESE-BATH TECHNIQUE

R. L. Macklin[1] G. deSaussure J. D. Kington W. S. Lyon[2]

The preliminary results of an experiment to determine the absolute thermal values of η of U^{233} and U^{235} by a manganese-bath technique have previously been reported.[3] The experiment has now been completed and all corrections have been applied to the data. The final results obtained for η, corrected to 2200 m/sec, were 2.296 ± 0.010 for U^{233} and 2.077 ± 0.010 for U^{235}.

A detailed description of this experiment, including a complete listing and discussion of the corrections applied to the experimental data, has been published elsewhere.[4]

---

[1]Physics Division.

[2]Chemistry Division.

[3]G. deSaussure, R. L. Macklin, *et al.*, *Neutron Phys. Ann. Prog. Rep. Sept. 1, 1959*, ORNL-2842, p 99.

[4]R. L. Macklin, G. deSaussure, *et al.*, *Manganese Bath Measurements of η of U^{233} and U^{235}*, ORNL CF-60-2-84 (Mar. 15, 1960).

4.2 DETERMINATION OF THE THERMAL VALUE OF η OF U^{233} AND U^{235} BY DIRECT COMPARISON OF CRITICAL PARAMETERS OF AQUEOUS SOLUTIONS

R. Gwin D. W. Magnuson

An experimental determination of the thermal value of η of U^{233} and U^{235}, based on the direct comparison of the critical parameters of unreflected, homogeneous aqueous solutions of the uranyl nitrates of U^{233} and U^{235}, has been completed. The precision achieved by this method is enhanced by the use of dilute solutions in large systems, and in the present investigation the largest volumes consistent with the amount of U^{233} available have been used. Experiments performed with 27- and 48-in.-dia spheres and 5- and 9-ft-dia cylinders have yielded consistent values of η.

The average thermal values of η determined are 2.284 ± 0.015 for U^{233} and 2.074 ± 0.015 for U^{235}. The 2200-m/sec values are the same, since the g factor for η is unity in each case.

A detailed report of this investigation has been published elsewhere.[1]

---

[1]R. Gwin and D. W. Magnuson, *Critical Experiments for Reactor Physics Studies*, ORNL CF-60-4-12 (Sept. 16, 1960).

4.3 THE SPECTRUM OF PROMPT GAMMA RAYS FROM U^{235} FISSION

F. C. Maienschein R. W. Peelle

An experiment has been in progress for some time to determine the spectrum of gamma rays emitted within about 5×10^{-8} sec after the thermal-neutron fission of U^{235}. This spectrum is not only of potential interest for comparison with the predictions of fission theories but of immediate practical interest in the design of efficient radiation shields for fission reactors. In fact, a preliminary analysis[1] of part of the spectral data above 400 kev has already been applied to shield design.[2]

Three spectrometers have been used in the investigation. For the energy range above 400 kev, pair and Compton spectrometers were employed;[1,3] and for the energy range below 400 kev, a single-crystal spectrometer was used[4] together with a time-of-flight technique to exclude unambiguously the neutron-induced backgrounds. Final analysis of all the data is now under way and involves the following steps:

1. the proper combination of all the data runs, including some not available for the earlier analyses;
2. correction of the data for all count-rate-sensitive phenomena;
3. a determination of the absolute efficiencies and the response function for the spectrometers; and
4. the application of this information to the measured pulse-height spectra.

The first two steps have now been completed but will not be discussed here. Step 3, which consists of two phases – the standardization of monoenergetic sources used to calibrate the spectrometers and the determination of the response functions of the spectrometers for these sources – is in progress. The first phase has been completed for all the spectrometers, but the second phase has been completed for the pair spectrometer only. Since most of the work during the past year has been concentrated on step 3, the major portion of the discussion which follows is concerned with this subject, primarily as it has been applied to the pair and Compton spectrometers. Some discussion of the low-energy investigation is also given. [The fourth step listed has not been approached in this investigation, but it has been given considerable study elsewhere (see Sec 8.1).]

---

[1] F. C. Maienschein *et al.*, *Proc. U.N. Intern. Conf. Peaceful Uses Atomic Energy, 2nd, Geneva, 1958* 15, 366–72 (1959).

[2] See, for example, H. Goldstein, *Fundamental Aspects of Reactor Shielding*, p 58, Addison-Wesley, Reading, Mass., 1959; A. W. Casper, *Comparison of Bulk Shielding Reactor Centerline Measurements in Water with Predictions*, APEX-504 (November 1958); A. F. Avery *et al.*, *Methods of Calculation for Use in the Design of Shields for Power Reactors*, AERE R-3216, p 35 (1960).

[3] R. W. Peelle, F. C. Maienschein, and T. A. Love, *Neutron Phys. Ann. Prog. Rep. Sept. 1, 1958*, ORNL-2609, p 45.

[4] R. H. Ritchie, Appendix in ORNL-1142, *Multiple Crystal Gamma-Ray Spectrometer*, by F. C. Maienschein (July 3, 1952).

Source Standardization

Because of difficulties in calculating the absolute efficiencies of the Compton and pair spectrometers[5] from basic cross-section data, it is essential that the efficiencies be determined experimentally at a number of points throughout the 0.4- to 8-Mev energy range. This is done by observing the pulse-height spectra resulting when sources of known disintegration rates are placed in the region normally occupied by the U^{235} fission chamber during the experiment. However, finding sources of known strength was one of the major problems of the investigation.

It was desirable to standardize the sources by absolute counting techniques, using available coincidence equipment; but, for this technique to be applicable the sources could not be too strong. On the other hand, because of the low efficiencies of the pair and Compton spectrometers, convenient spectrometer-efficiency measurements could not be made unless the source strength was of the order of 10^7 gamma rays per second, and sources of this strength, even though they had favorable decay schemes, could not be standardized by absolute counting techniques.[6] Furthermore, it was practically impossible to find radioactive sources with conveniently long decay periods in the important energy region above 2.8 Mev.

In an attempt to overcome these difficulties, several approaches were used. In some cases an initially strong source with a conveniently variable strength was used to study the spectrometer response while the source was strong, and it was later standardized after it became sufficiently weak. High-pressure, 4π ionization chambers having a wide dynamic range were then usually used as monitors to relate the intensities of the weak standardized sources to the strong sources of the same material.

The ion chambers were also used to calibrate sources composed of materials other than those used in any of the absolute standardizations, a procedure which was possible provided that the gamma-ray energy dependence of the response of the ion chambers could be determined.

Absolute Coincidence Measurements. – The various sources which have been standardized by absolute counting are given in Table 4.3.1, the details of the standardizations for several of the sources being the topic of other papers in this report (see Secs 4.4 and 4.6). The sources not discussed elsewhere are the Zn^{65} source, the N^{16} source, and the Sn^{113} source. The Zn^{65} source was counted in the experimental arrangement used for the series of γ-γ coincidence measurements described in Sec 4.4, aiding in the understanding of those measurements. This was possible largely because of the near proximity of the gamma-ray energies from the Sc^{46} and Zn^{65} sources (1.12 and 1.114 Mev, respectively).

---

[5] T. A. Love, F. C. Maienschein, and R. W. Peelle, *Neutron Phys. Ann. Prog. Rep. Sept. 1, 1959*, ORNL-2852, p 93.

[6] The strongest attainable $B^{11}(p,\gamma)C^{12}$ source, for example, had an intensity small enough to allow standardization (see sec 4.4), but a spectrometer response function with only poor statistical accuracy was obtained by counting $\frac{2}{3}$ day.

Table 4.3.1. Summary of Sources Standardized by Absolute Counting

Sources	Gamma-Ray or X-Ray Energy (Mev)	Primary Standardization Method	Approximate Strength of Standardized Source (sec^{-1})	Estimated Relative Standard Deviation	Link to Source Used to Determine Spectrometer Efficiency
Sc^{46}, Co^{60}, Y^{88}, Na^{24}	0.9–1.8	γ-γ coincidence	$\sim 10^5$	0.006	4π ionization chamber
Na^{24}	1.37, 2.75	γ-γ coincidence	10^5	0.01	Direct
$B^{11}(p,\gamma)C^{12}$	4.4, 11.8	γ-γ coincidence	6×10^4	0.015	Direct
Zn^{65}	1.11	Scintillation counter of known efficiency	1.5×10^5	0.011	4π ionization chamber
Hg^{203}	0.28, 0.07	β-γ coincidence, e-x coincidence	5×10^3	0.007	4π ionization chamber and monitor counter ratio
N^{16}	6.1, 7.1	β-γ coincidence	5×10^3	0.045*	Monitor counter ratio
Sn^{113}	0.393, 0.0246	e-x coincidence	10^4	0.05*	4π ionization chamber and monitor counter ratio

*Includes errors from published decay-scheme information.

The N^{16} source, which has a half life of 7 sec and decays to O^{16} with the emission of a 6.1-Mev gamma ray in over 90% of the decays and a 7.1-Mev gamma ray in the remainder, was produced via the $O^{16}(n,p)N^{16}$ reaction occurring when water was pumped through an irradiation cell in the Bulk Shielding Reactor. The water from the irradiation cell was circulated first through a source-mockup cell in the spectrometer and then through a specially constructed 4π, plastic-phosphor beta-ray detector adjacent to a 3 by 3 in. NaI gamma-ray detector. The reactor was operated at a relatively high power to obtain a strong source for the spectrometer measurements and at a low power for the standardization measurements with the beta- and gamma-ray detectors. The beta-ray detector was so constructed that even beta rays from the lowest energy transitions in N^{16} could be detected with high efficiency. The source strength Q of the N^{16} was obtained from

$$Q = Rf(1 + \alpha)\frac{D_\gamma D_\beta}{D_{\beta\gamma}} ,$$

where D_β and D_γ are the singles counting rates for the beta- and gamma-ray detectors, respectively; $D_{\beta\gamma}$ is the coincidence counting rate; R is the ratio of average source strengths during the spectrometer run and the standardization run (determined by gamma-ray counting); and f and α are quantities obtained from (1) the beta-decay branching ratios in the N^{16} decay scheme, (2) the volume ratio of the water in the source cell to that in the beta-ray counter, (3) the average fractional decay of the N^{16} between the source cell and the beta-ray counter, (4) the ratio of the efficiencies of the beta- and gamma-ray counters, and (5) the counter backgrounds. Although this

experiment was carried out with great care, the spectrometer efficiency measurements for the N^{16} gamma rays are inexplicably inconsistent with other measurements (see below).

The Sn^{113} source consisted of a small amount of the K-capture isotope encapsulated in a 0.5-in.-dia by 0.25-in. plastic phosphor. The main decay is through the 1.7-hr metastable 0.393-Mev level of In^{113}, the internal conversion of the 0.393-Mev gamma ray leading to x-ray emission. The source was standardized by measuring coincidences between these x rays (in a neighboring NaI detector) and the corresponding conversion electrons. X rays (average energy of 24.6 kev) are also emitted following the K electron capture, but the long life of the 0.393-Mev level ensured that only the x rays from internal conversion were in coincidence with conversion electrons. The result obtained for the x-ray emission rate depends on literature values of the In^{113} fluorescent efficiency (fraction of K-shell vacancies which lead to x-ray emission) and the relative intensity of K-shell internal conversion of the 0.393-Mev gamma ray to the total internal conversion of that transition. Similarly, the result for the gamma-ray emission rate depends on literature values of the ratio of K capture to L capture in Sn^{113} or the ratio of all Auger electrons to all conversion electrons in In^{113}. Fortunately this isotope has been studied sufficiently to allow calculation of the necessary corrections with the accuracy stated in Table 4.3.1.

4π High-Pressure Ionization Chamber Measurements. – The high-pressure ionization chambers[7] used as secondary standardization instruments were first described by Jones and Overman[8] and have since been improved.[9] Each one consists of a steel right-circular cylinder with a typical dimension of about 8 in., shielded with a 4-in.-thick lead jacket and filled with argon at about 40 atm. Sources for measurement were inserted into a re-entrant thimble which positioned them just below the center of the gas volume, and with the help of a vibrating reed electrometer used as a null indicator, a standard potentiometer, and a series of four resistors ranging from 10^8 to 10^{11} ohms, the ionization current was determined. A collecting potential of 300 v was used, which was inadequate to prevent recombination in the higher regions of source intensity utilized (up to about 1 mc of Co^{60} or the equivalent).

These ionization chambers were used for the determination of source strengths because they were believed to be stable and to have fairly well-known intensity and energy calibrations. In the considerations leading to the final fixing of their calibrations, relative and absolute standardizations were separated, and the former was subdivided into relative calibrations as functions of source intensity, time (drift compensation), and gamma-ray energy.

The intensity calibration of the ion-chamber-current output was based on a series of Co^{60} sources obtained by dilution of a solution which had been standardized by β-γ coincidence measurements. This work was performed by the Radiochemical Analysis Group under S. A.

---

[7]Used through the courtesy of the Analytical Chemistry and Isotopes Divisions of ORNL.

[8]J. W. Jones and R. T. Overman, *The Use and Calibration of a 100% Geometry Ion Chamber*, Mon-C-399 (1948).

[9]Modifications have been designed by the ORNL Instrumentation and Controls Division, especially by R. Abele of the Counter Laboratory.

Reynolds and W. S. Lyon.[10] Since the thickness of the argon in the ion chambers is much less than an attenuation length for all gamma rays capable of penetrating the glass, the plastic, and the steel thimbles surrounding the source, the relative effectiveness of gamma rays of various energies in producing ionization was assumed to be independent of source intensity. For each instrument range corresponding to a "grid" resistor used to measure the ion current, a graph was drawn relating, for any source material, the observed voltage to the nominal strength of a Co^{60} source which would yield the same ionization rate.[11] The internal consistency of this intensity calibration was checked by a thorough month-long series of readings on a pair of gold foils irradiated with thermal neutrons so that their decay covered the entire important intensity range. Since the decay constant of the Au^{198} activity produced is well known, the consistency of the results was considered a good test of the validity of the intensity calibration. The results of the statistical consistency tests indicated that the measurements on the gold samples are consistent with the Co^{60} calibration of the chambers over each sensitivity range, provided that each ion chamber reading is assigned an error of 3 mv or 1%, whichever is larger, except on the highest sensitivity range, where the estimated variances were doubled. (The full-scale reading on each range is 1 v.) However, differences observed between average values from the different ranges suggest an over-all calibration uncertainty of $\sim$1%.

Unfortunately the intensity calibration of each ionization chamber can be time dependent, if for no other causes than those of resistor drifts or gas pressure loss, and in the high-current regions because of fluctuations of the collecting voltage supply. Apparently other causes of drift also exist. In order to counteract the effects of such drifts on ion chamber readings obtained over the course of about three years, the readings obtained over this interval by using radium and Cs^{137} sources of a few intensities were used to normalize the ion chamber readings. Such a procedure is not entirely satisfactory, since the shape of the intensity calibration is assumed to remain constant at least on the range identified with a given "grid" resistor, a poor assumption in the case of drifts caused by fluctuations in the collecting voltage. However, without such corrections, which amount to about ±3% for one chamber and ±2% for the other, it was impossible to analyze the available data in an internally consistent manner.

In order that an ion chamber could be used for sources composed of radioactive material for which no absolute counting calibrations were performed, it was necessary to obtain the average fractional energy loss in the argon of the chamber as a function of gamma-ray energy. Given such

[10]We are greatly indebted to this group, which over the years has provided a set of intensity and energy calibrations of the ion chambers used and has been most cooperative in supplying additional information pertinent to their use.

[11]The procedure used to obtain equivalent Co^{60} source strengths for the ion chamber measurements during the experiment was as follows. A set of measured resistor values was obtained from bridge measurements and the Au^{198} decay data described later. By using these resistor values, the Co^{60} intensity vs ionization-current curves for the two ion chambers were fit on the average with two parameters. For satisfactory interpolation, these analytic fits were used rather than the set of calibration graphs. However, the fits systematically deviated from the raw data in significantly large regions of intensity, so curves were drawn for the small corrections required to provide full agreement between calibration points and fitted curves.

a relationship and the knowledge of the decay scheme of any gamma-ray-emitting nuclide, the response of the ion chamber per gamma-ray emission by the nuclide could be determined. Since the ion chamber intensity calibration was in terms of the equivalent disintegration rate of Co^{60}, for a new isotope the average charge released in the ion chamber per gamma ray relative to that for a gamma ray from Co^{60} (about 1.25 Mev) was really required.

Gamma-ray cross sections were used to calculate the required ion chamber efficiency curve. Experimental points for the curve, or combinations thereof, were available from the series of absolute source standardizations described above. While the final ion chamber efficiency curve based on experiment and calculation has not yet been fixed, the experimental data in the 0.9- to 2.7-Mev region have almost the calculated shape, and the absolute agreement is better than the accuracy to which the argon pressure is known.

Although the absolute calibration of the ion chambers for Co^{60} sources could be based on the work of Reynolds and Lyon, it was difficult for this experiment to determine the proper normalization factors for the drift compensation; therefore, the absolute source strength determined with the aid of the ion chambers will be based entirely upon the γ-γ absolute counting standardization outlined above.

Effects of Source Self-Absorption. – The spiral fission chamber used in all but the low-energy experiments was of such heavy construction that even for 2-Mev fission gamma rays about 10% of those gamma rays directed toward the spectrometer interacted in the fission chamber or its housing. Consequently, for every source used to measure spectrometer efficiency it was necessary to (1) correct for the interaction of gamma rays in the sources during measurements in the 4π ionization chambers, since the total number of emitted gamma rays is required for efficiency determinations, and (2) compensate pulse-height spectra measured with the pair and Compton spectrometers to make the absorption of any source capsule used equivalent to that of the spiral fission chamber.

These two corrections differ mainly because the ion chamber has a nondirectional response, as opposed to the directional response of the spectrometer, and because the roles of scattered photons from Compton interactions are quite different in the two cases. The behavior of the ion chamber efficiency as a function of energy is such that Compton-scattered gamma rays yield more ionization per unit energy than primary gamma rays so that the smallest estimated effective ion chamber transmission was 0.96 (at 0.6 Mev). On the other hand, transmissions for sources measured with the pair and Compton spectrometers are much lower – about 0.88 at 1.8 Mev. In this case, however, the estimated transmissions do not enter directly into the result because most of the calibration sources were contained in a manner similar to that for the fission chamber itself. The calculations, therefore, need only estimate the quotient of the transmissions for the standard source and the fission chamber at each source energy.

Effective transmissions for measurements in the 4π ionization chambers were based on calculations at a few source points along the capsule axes, considered adequate because of the high

Page 88:

Last sentence on page should read: "Thus the over-all effect of the spectrometer, R(i,j), on a gamma-ray spectrum represented by Γ_j photons per unit gamma-ray energy interval may be written as

$$\sum_j R(i,j) \left\{ \Gamma_j \Delta E_\gamma^j \right\} = \sum_j \left\{ P(j)\, \delta_{i,j} + T(i,j) \right\} \Gamma_j \Delta E_\gamma^j = N_i \quad , \qquad (1)$$

where N_i is the measured number of counts in bin i produced by the incident spectrum."

effective transmission. Transmissions for use with pulse-height distributions measured with the pair spectrometer have also been calculated, but in this case integrations were performed over the volumes of the fission chamber and the corresponding source capsules. The interior parts of the fission chamber, which consisted largely of the Teflon insulators and the spiral of aluminum foil with U^{235} plated on it, were homogenized.

Response Matrix Formulation for the Pair Spectrometer

Of the two spectrometers used for the energy region from 0.4 to 8 Mev, the response matrix has been formulated for the pair spectrometer only. The procedure, which is also being used for the other spectrometers, was as follows: Pulse-height spectra obtained from the spectrometer upon exposure to fission gamma rays were corrected for background effects, counts lost due to electronic limitations, and the number of fissions observed during the spectrum accumulation. The resulting distribution of counts as a function of pulse height was then converted to a distribution of counts as a function of electron energy, E_e, where $E_e = E_\gamma - 2m_0c^2$. The spectrometer gain and zero were measured with monoenergetic sources, and corrections for nonlinearity of the pulse-height analyzer were also performed to determine the electron energy corresponding to a given pulse height. For each region of the gamma-ray energy spectrum, several pulse-height spectra were obtained. These were then combined to obtain the number of counts N_i in the energy interval ΔE_e^i or bin i, located at energy E_e^i.

The remaining step in obtaining a gamma-ray energy spectrum is the correction for the efficiency of the spectrometer or the probability that a gamma ray of energy, E_γ^j, will give rise to a count with a pulse height corresponding to a given bin i. An ideal spectrometer would give rise to pulses corresponding to a single bin for a monoenergetic gamma ray, but scintillation spectrometers are far from ideal in this respect, giving rise to a large "tail" of pulses smaller than the "correct" bin and a distribution of pulses in bins adjacent to the "correct" one.

The response of the pair spectrometer was determined experimentally by studying the pulse-height spectra produced upon the sequential exposure of the spectrometer to sources producing a total of 11 gamma rays of different energies. The resulting spectra were analyzed in terms of a "peak" area and a "tail" spectrum (see Fig. 4.3.1). The tail response per source photon, $T(i,j)$, was taken as the number of counts observed in bin i upon exposure to a photon of energy, E_γ^j, in the photon energy interval ΔE_γ^j. The peak area per source photon, $P(j)$, was taken as the sum of the observed responses between electron energy limits c_j and d_j, which depended on the gamma-ray energy E_γ^j and were determined by fitting the observed spectra. The peak area is located in the bin $i = j$, which includes the energy corresponding to the observed center of the peak, m_j. Thus the over-all effect of the spectrometer, $R(i,j)$, on a gamma-ray spectrum represented by Γ_j photons per gamma-ray energy interval, ΔE_γ^j, located at gamma-ray energy E_γ^j, may be written as

$$\sum_j R(i,j)\left\{\Gamma_j \Delta E_\gamma^j\right\} = \sum_j \left\{P(j)\delta_{ij} + T(i,j)\right\}\Gamma_j \Delta E_\gamma^j = N_{ij} \quad , \tag{1}$$

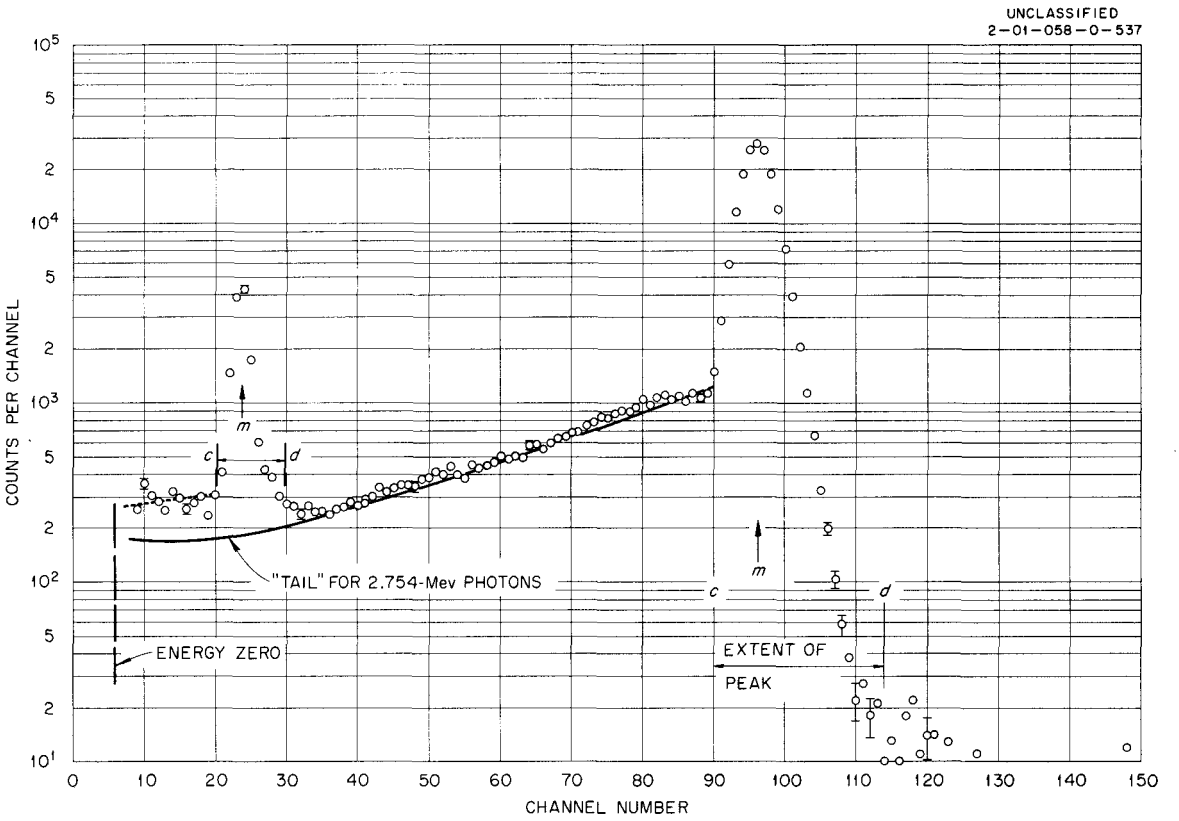

Fig. 4.3.1. Response of the Pair Spectrometer to the Radiation from Na^{24}: $E_\gamma = 1368 \pm 1$ kev and 2754 ± 1 kev. The circles show the experimental data, and the lines represent the predictions from the final tail fits. Three other Na^{24} spectra (2754 kev only) were analyzed for the fitting process. The statistical errors are shown at a few points. The electron energy was equal to approximately 19.25 times the channel number minus 5.9 for this run. Parameters used in the text in defining the peak are shown for both gamma-ray peaks.

where N_{ij} is the measured number of counts corresponding to bin i produced by a gamma ray of energy E_γ^j.

In principle, once the response matrix $R(i,j)$ has been determined, Eq. 1 can be solved for the desired gamma-ray spectrum, Γ_j. Solution of the set of linear equations has been tried in the past, with resulting serious difficulties due to divergent oscillations in the solution for an appropriately large number of energy divisions, i and j (ref 12). It is expected that this type of difficulty will be avoided by solving for a spectrum smoothed by the energy resolution of the spectrometer. For further discussion of this aspect of the problem see ref 2.

It was observed that the tail response of the pair spectrometer for monoenergetic sources could be fit reasonably well with a pair of exponential functions of electron energy. Thus the

[12]Divergent oscillations in matrix inversion procedures have been reported in private communications from W. Zobel of ORNL and N. Scofield of USNRDL.

tail response becomes

$$T(i,j) = P(j)\left\{k_1^j \exp a_1^j(E_e^i - m_j) + k_2^j \exp a_2^j E_e^i\right\}\Delta E_e^i \ , \qquad \text{for } 0 < i < c_j \ , \tag{2}$$
$$= 0 \ , \qquad \text{for } i > c_j \ ,$$

and the total response is

$$R(i,j) = P(j)\left[\delta_{ij} + \left\{k_1^j \exp a_1^j(E_e^i - m_j) + k_2^j \exp a_2^j E_e^i\right\}\Delta E_e^i\right] \ . \tag{3}$$

At this point, the problem was divided into two parts: (1) determining $P(j)$ and (2) determining the parameters k^j and a^j.

Peak Efficiency Measurement. – Values for $P(j)$ were determined by exposing the spectrometer to each of the sources of gamma rays shown in Table 4.3.2. [Derived values for the N^{16} gamma rays (see below) were used because of the uncertainties associated with the experimental values.] For the source measurements, the correction factors for counts lost due to the pair spectrometer electronics varied from 1.066 to 1.000, with errors which were unimportant (<0.006).

Table 4.3.2. Sources Used in Calibration of Pair Spectrometer

Source	Gamma-Ray Energy (kev)	Peak Efficiency (counts/photon)	Total Efficiency* (counts/photon)
		$\times 10^{-7}$	$\times 10^{-7}$
Zn^{65}	1,114	0.00378 ±0.00053	0.0076 ±0.0011
Co^{60}	1,173	0.010 ±0.0015	0.0164 ±0.0030
Na^{22}	1,276	0.0413 ±0.0014	0.0475 ±0.0018
Co^{60}	1,333	0.0682 ±0.0035	0.0868 ±0.0050
Na^{24}	1,368	0.0938 ±0.0014	0.121 ±0.0026
Y^{88}	1,840	0.511 ±0.010	0.566 ±0.011
Na^{24}	2,754	1.396 ±0.009	1.840 ±0.013
C^{12}	4,433	2.07 ±0.09	3.59 ±0.19
N^{16}	6,135	2.32 ±0.09**	4.92 ±0.20**
N^{16}	7,121	2.39 ±0.18**	4.82 ±0.51**
C^{12}	11,810	0.80 ±0.40	6.79 ±0.26

*Proportional to NaI pair cross section.

**After normalization.

In order to define the peak area $P(j)$, values of the constants c_j and d_j had to be obtained as a function of E_γ^j. The position of c_j (see Fig. 4.3.1) was chosen by observation of the mono-energetic response curves and was taken as

$$c_j = m_j - w_j\left\{1.31 - 8.5 \times 10^{-5}(E_\gamma^j - 1022)\right\} \ , \tag{4}$$

where all quantities are in kev, and w_j is the measured resolution, full width at half maximum. The quantity w_j is given approximately as

$$w_j = 2.75(E_\gamma^j - 1022)^{1/2} - 4$$

for energies up to ~2.5 Mev, but for higher energies it increases more rapidly than the above expression due to broadening of the peak by bremsstrahlung losses. The quantity d_j was taken as $m_j + 2w_j$. Large variations in the value of d_j cause only small variations in $P(j)$, as may be seen by studying Fig. 4.3.1.

The values obtained for $P(j)$ are shown in Fig. 4.3.2 as counts/photon divided by a Born approximation[13] to the pair cross section for NaI in cm^2/molecule. Division by this calculated

[13]Obtained by integration of the data given by P. V. C. Hough, *Phys. Rev.* **73**, 266 (1948).

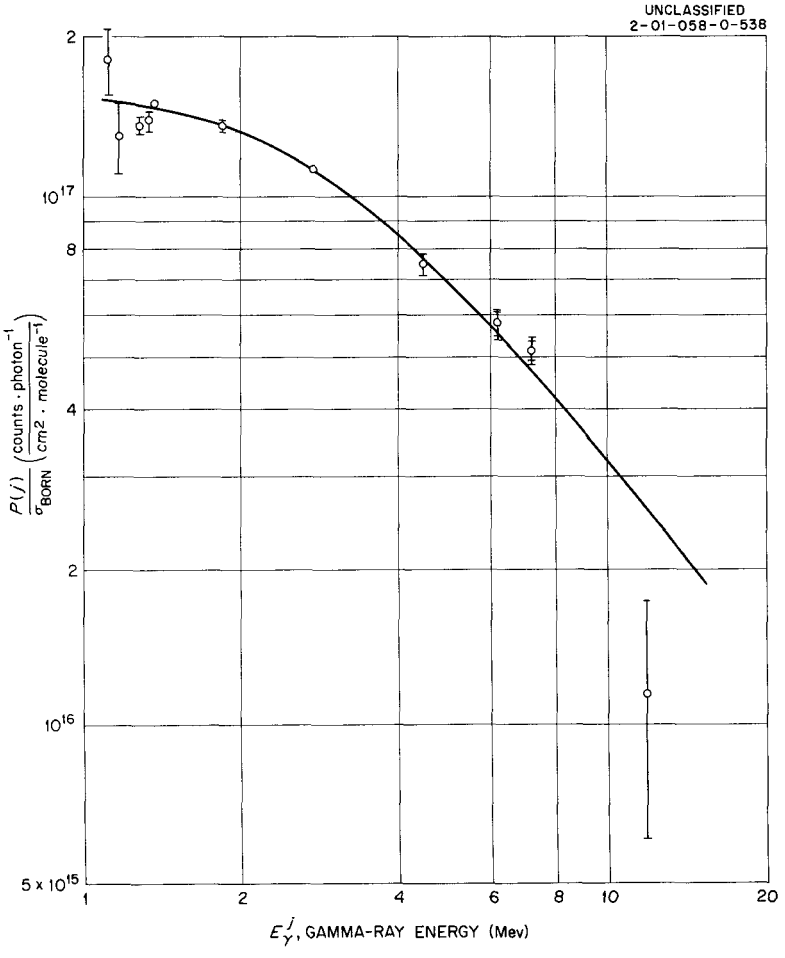

Fig. 4.3.2. Variation of Pair Spectrometer Peak Efficiency with Gamma-Ray Energy. The probability of producing a count in the defined peak $P(j)$ by a photon of energy E_γ^j arising at the point of fission has been divided by the Hough formulation of the Born approximation for the pair cross section of NaI. Two errors are shown for the points at 6.13 and 7.12 Mev. In each case, the larger error is supposed to reflect the effects of the normalization shown in Fig. 4.3.3.

(and incorrect) pair cross section was carried out simply in order to remove the very rapid dependence upon energy and to permit reasonable interpolation.

The value of $P(j)$ decreases with increasing energy relative to the pair cross section because losses from the peak become more important at higher energies. Positrons escape from the center crystal of the pair spectrometer and thus lead to lost counts. Bremsstrahlung losses by the electrons and electron escape give rise to pulses smaller than the peak pulse height. Because of these and perhaps other factors, the tail appears to "swallow up" the peak at the higher energy until the two are virtually indistinguishable at 12 Mev.

Tail-Shape Fitting. – The response curves obtained with eight gamma-ray sources were analyzed to find the tail shapes; these sources were not necessarily of known strength. For most of the gamma-ray energies, multiple runs were available for determination of the values of k_1^j, k_2^j and a_1^j, a_2^j, the magnitudes and slopes respectively, of the exponential fitting functions relative to the peak area. After a weighted combination of the tail constants, an interpolation vs energy was performed for three of the four constants. The fourth was determined by the constraint that the resulting value of $\sum_i T(i,j)/P(j)$ equals the measured value, and then all four parameters were modified by a second iteration. A physical interpretation of the details of the fitting is difficult since the slopes of both exponentials change sign as a function of energy. However, the fit achieved empirically is reasonably good, as indicated in Fig. 4.3.1.

The observed tail for the low-energy (1.368-Mev) gamma ray in Na^{24} was not used in obtaining the tail parameters. The dashed line shown in Fig. 4.3.1 was predicted by the fit.

Experimental Determination of Pair Cross Section for NaI. – Although the experiment was not designed to yield the pair cross section for NaI, it was possible to obtain relative values from the measured efficiencies. This process was carried out in order to promote confidence in the validity of the measured efficiency data. The following types of corrections were applied to the observed pulse-height spectra.

1. The tail response was extrapolated to zero energy before summing to determine the "total" response of the spectrometer. The extrapolated area was only a few per cent of the total.

2. Attenuation of the gamma radiation in the source container was calculated by taking the geometry into account by a combination of analytical and numerical techniques. The geometry was "bad" and thus Compton scattering from the source shell did not remove gamma rays. The attenuation varied from 1 to 14% as a function of gamma-ray energy. This effect cancels approximately in the peak-efficiency determination since the sources were in containers similar to the fission chamber.

3. Attenuation by a lithium neutron absorber (and its stainless steel cover) was in good geometry (attenuation of 13 to 26%). This effect exactly cancels in the peak-efficiency determination because the absorber is present in both fission and calibration data.

4. The energy-dependent attenuation of the gamma-ray beam in the NaI crystal was taken into account (8 to 15%).

5. Annihilation of positrons before slowing down constituted an appreciable effect. Fast annihilation produces either one quantum (unlikely) or two quanta, at least one of which does not have energy equal to m_0c^2, with a partly forward angular distribution with respect to the positron. Thus, fast annihilation will not, in general, lead to a pair spectrometer count. The positron spectrum used to calculate the fast annihilation loss was taken to be intermediate between that predicted by the Born approximation and an assumption that all kinetic energy resides in the positrons, since no exact spectral calculations are available. The loss due to fast annihilation varied from 0 to 19%.

6. Escape of positrons from the center crystal is the most difficult correction to make. If the positron "escapes" from the NaI crystal but is annihilated in the aluminum can, a count may still be recorded in the tail response of the spectrometer. Therefore, attenuation in the can was considered in calculating the positron escape. As an indication of the order of magnitude of positron escape, the positron "range" was taken as a fraction (0.5) of the "Nelms" range[14] and the Born approximation positron spectrum assumed. The positron loss was later treated as a parameter in order to match the existing pair cross-section data. The change required from the above assumptions in order to achieve a fit was $\sim$40%, well within the uncertainties.

7. Finally, the total pair efficiency after correction for items 1–6 was divided by an integral of the Hough formulation of the Born approximation[13] in order to give the relative pair cross section in NaI. The resulting data are shown in Fig. 4.3.3 together with a solid-line fit to other available data.[15,16] The errors for the earlier data are similar to those shown. No points are shown in Fig. 4.3.3 corresponding to the two lowest energy points of Fig. 4.3.2 because the backgrounds for these low-energy sources were too large to permit a meaningful definition of the total efficiency. These backgrounds had a much smaller effect on the peak-efficiency determination. In any event, fission data with the pair spectrometer are not available below E_γ = 1.4 Mev.

The data appear reasonable with the exception of the points at 6.135 and 7.121 Mev, which correspond to N^{16} gamma rays. Clearly an error was made in the determination of the spectrometer efficiencies for this source. Two largely independent determinations led to the indicated efficiencies within errors consistent with that shown in Fig. 4.3.3. Careful re-examination of the data from these experiments has yielded no explanation for the discrepancy. Because the N^{16} experiment and analysis required several months to complete, it was not repeated, but, instead, the apparent pair cross sections (relative to the Born cross section) were revised as shown. Then the peak-to-total ratios for this source were assumed to be correct and the peak efficiencies determined corresponding to the revised pair cross sections. These peak efficiencies are included in Fig. 4.3.2, together with errors estimated to include the uncertainties in normalization of the N^{16} data, as shown in Fig. 4.3.3.

[14] A. T. Nelms, *Energy Loss and Range of Electrons and Positrons*, NBS-577, Table I (July 30, 1958); the ranges given ignore multiple scattering and bremsstrahlung losses.

[15] G. W. Grodstein, *X-ray Attenuation Coefficients from 10 kev to 100 Mev*, NBS Circular 583 (Apr. 30, 1957).

[16] H. West, *Phys. Rev.* 101, 915 (1960).

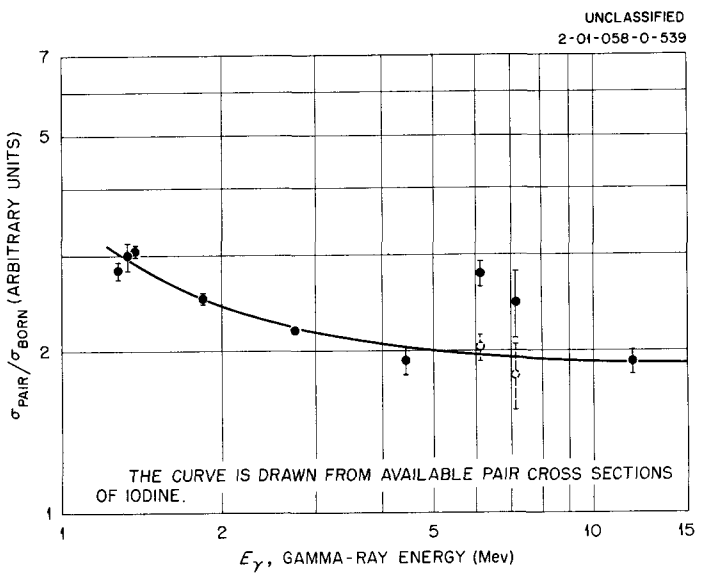

Fig. 4.3.3. Variation of the Relative Pair Cross Section for NaI as Determined from the Measured Total Spectrometer Response. The total pair efficiency has been divided by the Hough Formulation of the Born approximation for the pair cross section as a function of gamma-ray energy, but the absolute values of the ratio have no significance. The solid line represents a fit to the available measured values[15,16] for the pair cross section of iodine, which carry errors comparable to those shown for the present data. The errors shown include all known contributions other than those due to positron escape. The points at 6.13 and 7.12 Mev were adjusted as shown to yield a reasonable variation with energy.

Data for Low-Energy Region

The minimum gamma-ray energy covered by the multiple-crystal spectrometer data was ~0.4 Mev. In order to study lower energies, a single-crystal spectrometer was used to examine the spectrum of gamma rays from fissions in an apparatus of low absorption. A large source-to-detector separation distance was used to permit exclusion of neutron-induced backgrounds by time-of-flight. A preliminary analysis of part of these data[17] demonstrated the presence of peaks in the pulse-height spectra, the most prominent of which could be identified as resulting from x rays emitted by the light and heavy fission fragments. In further analysis, data from several runs for each of the three overlapping energy regions were combined and corrections made for random counts and other backgrounds, lost counts, analyzer nonlinearities, and the observed fission rates. After comparison within the three regions and in the areas of overlap, the data appeared to be consistent.

For the energy calibration required for the fission data combination and for formulation of the single-crystal spectrometer response function, it was necessary to expose the spectrometer to low-energy gamma rays. Twenty gamma rays from fourteen different sources were used, including the x rays from some of these sources. The response function remains to be formulated from these

[17] F. C. Maienschein *et al.*, *Proc. U.N. Intern. Conf. Peaceful Uses Atomic Energy, 2nd, Geneva, 1958* 15, 366–72 (1959).

data. The absolute source strengths required to determine the peak efficiency $P(j)$ were obtained by the methods described above. The efficiency may also be calculated with reasonable confidence. The energies for the x-ray sources were obtained from weighted combinations of energies for the K-shell transitions.

The rather large attenuations in the apparatus used with the multiple-crystal spectrometer led to a careful design of minimum wall thickness for the low-energy spectral measurements. Calculations were made for the attenuation due to 15 layers of material between source and detector. These calculations were equally applicable to either the monoenergetic sources or the fission-chamber radiation, since the sources were exposed at various positions within a replica of the fission chamber. The gamma-ray cross sections used were those of NBS-583 (ref 15) except for uranium, where cross sections from recent experiments are available for the low-energy region.[18] Most of the material was disposed in either "good" or "bad" geometry. For the bad geometries, account was taken of the energy-angle correlation of Compton scattering, and a photon was considered to be removed from the peak response if the energy change exceeded the measured resolution (full width at half maximum).

In order to check the calculated attenuations, eight sources of x rays were placed at various positions within the fission chamber mockup, and the spectrometer response was observed. Comparison of the variation of the measured response with the calculations demonstrated consistency by the usual χ^2 test for all but one of the sources. Since the fission chamber attenuation was dominant, especially for low energies, this check is considered to validate the attenuation calculations.

Remaining Analysis

Two portions of the analysis remain to be completed. First, the response matrix $R(i,j)$ must be formulated for the Compton and single-crystal spectrometers from the response data and the known source strengths. Then Eq. 1 must be solved for the smoothed gamma-ray spectrum and the associated uncertainty. Although they may be stated briefly, these steps are not trivial, especially since no satisfactory solution to the second problem has been demonstrated.

[18] R. B. Roof, Jr., *Phys. Rev.* 113, 824 (1959).

4.4 GAMMA-GAMMA COINCIDENCE STANDARDIZATION OF SOURCES, WITH APPLICATION TO THE $B^{11}(p,\gamma)C^{12}$ REACTION

R. W. Peelle F. C. Maienschein

Introduction

This section describes methods used for gamma-gamma coincidence standardization of a number of radioactive sources. Sources standardized by absolute coincidence counting are often useful in determining the quantitative response characteristics of gamma-ray spectrometers. For instance, the determination of efficiency as a function of energy for the Compton and pair spectrometers used to measure the prompt-gamma-ray spectrum from U^{235} fission[1] depends heavily on the use of calibrated sources, since the efficiency of such spectrometers is difficult to calculate. For gamma-ray energies below 3 Mev, a number of radioactive nuclides suitable for calibration sources are available. Some of these radionuclides have prominent gamma-ray cascades in their decay schemes and are therefore suitable for use in producing sources standardizable by the methods described here. In the higher-energy region it is practically impossible to find suitable radioactive sources; this section therefore includes an extension of gamma-gamma coincidence methods to the standardization of the cascade source of 11.8- and 4.4-Mev gamma rays from the capture of 170-kev protons in B^{11}. The method is worthy of some attention because the efficiency of even a single NaI crystal cannot be well calculated in this energy region, if for no other reason than the uncertainties in the NaI gamma-ray cross sections in the 5- to 10-Mev range.

The basic coincidence method has been described in the literature.[2] In the simplest case we consider a point radioactive source emanating, at constant rate Q, a coincident cascade consisting of a radiation r_1 followed by a radiation r_2, with an isotropic angular distribution between the two. We specify the use of two detectors d_v and d_w, the first sensitive only to radiation r_1, with efficiency v, and the second sensitive only to radiation r_2, with efficiency w. Then if D_v and D_w are the counting rates in the detectors d_v and d_w, respectively, and D_{vw} is the coincidence counting rate, we have

$$D_v = Qv \ ,$$

$$D_w = Qw \ ,$$

$$D_{vw} = Qvw \ ,$$

$$\frac{D_v D_w}{D_{vw}} = Q \ , \text{ the desired source strength.}$$

The power of the method is easily seen to be the independence of the result from experimental parameters which influence the efficiencies v and w. The above simple analysis is not sufficient

[1]See sec 4.3, this report.

[2]J. Barnothy and M. Forro, *Rev. Sci. Instr.* 22, 415 (1951); S. de Benedetti and R. W. Findley, "The Coincidence Method," p 255, vol 45, *Handbuch der Physik* (ed. by S. Flügge), Springer, Berlin, 1958.

for cases where the cascade radiations observed are both gamma rays, since for any bias adjustment at least one of the detectors must be made sensitive to both gamma rays. Meyer *et al.*[3] have proposed the use of a method for gamma-gamma coincidence standardization wherein each detector is made about equally sensitive to each source radiation; in this case the equations again easily simplify, provided v and w are sufficiently small. Meyer shows that the result is insensitive to reasonable errors in the equality of efficiency for the two radiations. His basic approach is used throughout this section, but important modifications have been made, as required by the decay and reaction schemes studied.

The purposes of this section are to illuminate the degree of usefulness of the gamma-gamma standardization method, to develop rather completely the methods of analyzing data from such experiments, and to indicate the degree of success attained with the methods described. Of particular importance are the extensions to include the $B^{11}(p,\gamma)C^{12}$ reaction.

Coincidence Standardization of Radioactive Sources

Coincidence Equations. – Equations for the source strength are derived in this section for the decay scheme shown in Fig. 4.4.1, which is adequate for the analysis of Y^{88} coincidence studies. The schemes for Co^{60}, Na^{24}, and Sc^{46} can be obtained readily as simplifications of this one. The properties of the decay scheme are defined as follows:

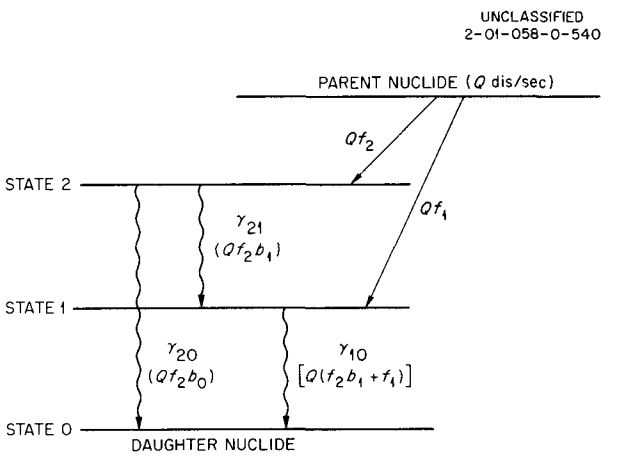

Fig. 4.4.1. Model Decay Scheme for Coincidence Analysis. Expressions in parentheses indicate decay rates of various transitions.

Q = sum of average decay rates of the parent nuclide to the excited states of the daughter;

f_j = fraction of all decays which lead to the excited state j (here $f_0 \equiv 0$);

b_0 = fraction of excitations of the second excited state which decay directly by crossover transition to the ground state;

b_1 = fraction of excitations of the second excited state which decay to the first excited state.

Internal conversion has been ignored because it is insignificant for the nuclides studied. From

[3]K. P. Meyer, P. Schmid, and P. Huber, *Helv. Phys. Acta* 32, 423 (1959).

these definitions the rates of emission of the various gamma rays follow:

$$S_{20} = \text{average emission rate of } \gamma_{20} = Qf_2 b_0 \ ;$$

$$S_{21} = \text{average emission rate of } \gamma_{21} = Qf_2 b_1 = \bar{Q} \ ; \tag{1}$$

$$S_{10} = \text{average emission rate of } \gamma_{10} = Q(f_2 b_1 + f_1) = \bar{Q}(1 + \bar{f}_1) \ . \tag{2}$$

The second equality in Eq. 2 defines $\bar{f}_1$.

The counting rates from the two detectors and the coincidence rate corrected for counting difficulties (random coincidences, counting losses, etc.) are related to the source decay rate in the manner indicated below, provided that each detector is biased to exclude any x rays, bremsstrahlung, scattered gamma rays, or annihilation radiation. It is also assumed that the coincidence circuit has unit efficiency for pulses within the bias interval used for the "singles" counting rate from each detector, and that it has zero efficiency for pulses from outside this range. (Except for the corrections already listed, this assumption is met by the usual two-speed coincidence schemes.) The relationships are:

$$\begin{aligned} D_v &= Q[f_2(b_1 v_{21} + b_0 v_{20}) + (f_1 + f_2 b_1)v_{10} + f_2 b_1 \Delta_v] \\ &= \bar{Q}\left[v_{21}\left(1 + \frac{b_0 v_{20}}{b_1 v_{21}}\right) + v_{10}(1 + \bar{f}_1) + \Delta_v\right] \ , \\ D_w &= \bar{Q}\left[w_{21}\left(1 + \frac{b_0 w_{20}}{b_1 w_{21}}\right) + w_{10}(1 + \bar{f}_1) + \Delta_w\right] \ , \\ D_{vw} &= \bar{Q}\Delta_a \bar{W}(\theta)[v_{21} w_{10} + v_{10} w_{21}] \ , \end{aligned} \tag{3}$$

where

D_v, D_w ≡ observed count rate in detectors d_v and d_w,

D_{vw} ≡ observed coincidence rate,

v_{ij}, w_{ij} ≡ efficiency, including fractional solid angle, of counters d_v and d_w, respectively, for radiation γ_{ij},

$\bar{Q}\Delta_a$ ≡ count rate in detector d_a from pulses caused by simultaneous detection of coincident gammas. The Δ's contain a negative term because the remainder of the expression ignores coincidence summing.

$\bar{W}(\theta)$ ≡ angular correlation function at the angle θ subtended at the source by the two detector centerlines, attenuated to compensate for the finite size of the detectors. This function depends on the source decay scheme. It is normalized so that $\int \bar{W}(\theta)\, d\Omega = 4\pi$.

The above equations can be manipulated to yield S_{10} (Eq. 2) by introducing the quantities δ_v and δ_w, defined by the following relations:

$$w_{21} = w_{10}(1 + \bar{f}_1)(1 + \delta_w) \;; \qquad v_{21} = v_{10}(1 + \bar{f}_1)(1 + \delta_v) \;. \tag{4}$$

The significance of these choices will be discussed later. Also, for simplicity, we define simultaneous detection corrections such that for detector d_v we have:

$$(\mathrm{SDC})_v = \frac{-\Delta_v}{v_{21}[1 + (b_0 v_{20}/b_1 v_{21})] + v_{10}(1 + \bar{f}_1)} \;.$$

The analogous equation holds for d_w, replacing all the v's by the corresponding w's. By substitution in and combination of Eqs. 3,

$$\frac{D_v D_w}{D_{vw}} = \frac{S_{10}[1 - (\mathrm{SDC})_v][1 - (\mathrm{SDC})_w]}{\overline{W}(\theta)(2 + \delta_v + \delta_w)} \left[1 + (1 + \delta_v)\left(1 + \frac{b_0 v_{20}}{b_1 v_{21}}\right)\right]\left[1 + (1 + \delta_w)\left(1 + \frac{b_0 w_{20}}{b_1 w_{21}}\right)\right] \;. \tag{5}$$

The usefulness of this formulation in the present work depends upon a fairly small crossover ratio (b_0/b_1) in the decay scheme and upon the choice of the detector biases to make the δ's small compared to unity. The largest value of b_0/b_1 encountered was about 0.006. Since terms of Eq. 5 in $(b_0/b_1)^2$ and $\delta_v \delta_w (b_0/b_1)$ thus are very small compared to unity, they can be ignored, and if we take $v_{20}/v_{21} \cong w_{20}/w_{21}$, Eq. 5 can be well approximated by the following:

$$\frac{D_v D_w}{D_{vw}} \cong \frac{S_{10}[1 - (\mathrm{SDC})_v][1 - (\mathrm{SDC})_w]}{\overline{W}(\theta)} \left[2 + \frac{\delta_v \delta_w + (b_0 w_{20}/b_1 w_{21})(4 + 3\delta_v + 3\delta_w)}{2 + \delta_v + \delta_w}\right] \;. \tag{6}$$

Since, in practice, values of δ larger than 0.2 were not encountered with radioactive sources, the entire term which includes the effects of efficiency variation and the crossover gamma ray never yielded a correction greater than 3%. Equation 6 can then in practice be used to obtain S_{10} to an accuracy normally determined by the statistical accuracy of the coincidence rate D_{vw}. If the value of S_{21} (Eq. 1) is also desired, the branching ratios of the decay must be known. In the common case, $f_1 = b_0 = 0$ (or $f_2 b_1 = 1$), the above equations simplify.

Evaluation of $\overline{W}(\theta)$ was made on the basis of published information on angular correlation, level spin, and parity obtained from other workers as shown in Table 4.4.1, since in every case the lifetime of the intermediate state seems to be short enough to assure independence of the correlation from the chemical composition of the source. Attenuation of the coefficients to account for the finite detector size was accomplished according to the techniques suggested by Rose[4] and by Feingold and Frankel,[5] use in numerous cases being made of the plots given by Stanford.[6] This correlation was unimportant because of the small detector solid angles used.

[4] M. E. Rose, *Phys. Rev.* 91, 610 (1953).

[5] A. M. Feingold and S. Frankel, *Phys. Rev.* 97, 1025 (1955).

[6] A. L. Stanford, Jr., and W. K. Rivers, Jr., *Rev. Sci. Instr.* 30, 719 (1959).

Table 4.4.1. Summary of Coefficients[a] Used in Angular Correlation Function $W(\theta) = 1 + \alpha_1 P_1(\cos\theta) + \alpha_2 P_2(\cos\theta)$

Isotope	Cascade Decay Scheme	α_1	α_2	Reference
Y^{88}	$3^-(D)\ 2^+(Q)\ 0^+$	−0.0714	0	*b,d*
Na^{24}	$4^+(Q)\ 2^+(Q)\ 0^+$	5/49	4/441	*c,d*
Co^{60}	$4^+(Q)\ 2^+(Q)\ 0^+$	5/49	4/441	*d*
Sc^{46}	$4^+(Q)\ 2^+(Q)\ 0^+$	5/49	4/441	*e*

[a]The given coefficients have not been attenuated to compensate for the finite size of the scintillator.

[b]E. D. Klema, *Phys. Rev.* 102, 449 (1956); C. F. Coleman, *Phil. Mag.* 1, 166 (1956); G. R. Bishop and J. P. Perez Y Jorba, *Phys. Rev.* 98, 89 (1955).

[c]I. V. Estulin, V. S. Popov, and F. E. Chukreev, *Soviet Phys. JETP* 3, 866 (1956).

[d]K. Way *et al.*, *Nuclear Data Sheets*, National Academy of Sciences–National Research Council.

[e]K. Way *et al.*, *Nuclear Level Schemes*, TID-5300 (June 1955).

The SDC's were limited to a fraction of a per cent by the choice of experimental geometry. These small corrections were obtained by a crude numerical integration, over the observed pulse-height distributions, of the probability for simultaneous detection of both γ_{21} and γ_{11} in the same detector. This integration determined the spectrum of summed coincident pulses within the accepted bias interval, and depended upon a separation of the observed singles pulse-height spectrum into contributions from the two gamma rays, as well as upon an approximate source strength derived from Eq. 6 without the final correction terms. In general, there are negative terms in the SDC's (extra observed counts) arising from simultaneous detection of γ_{10} and γ_{21}, which leads to pulse components neither of which alone would have been large enough to be counted without the coincidence summing. The usually larger positive terms (lost counts) arise when there is coincidence summing of components large enough to be counted by themselves. If the summed pulse is counted, only one count is lost, while if the sum is above the range of pulse heights selected for counting, two counts are lost. The general problem can be approached by reference to the limiting case where the integral bias on d_v might be set at very low energy, in which case $(\mathrm{SDC})_v = v_{21}v_{10}/(v_{21} + v_{10})$, if $b_0 = f_1 = 0$. (Meyer *et al.*[3] seem to have accepted this approximate relation even in cases where the integral bias was not set at a low level; this acceptance led to an overestimate of the correction unless an upper bias level was also used.)

Methods for evaluating the δ's depend upon the property of the definitions in Eq. 4 that, if the δ for either detector vanishes, observed singles and coincidence spectra from the other counter become identical in shape, provided pulses from the crossover gamma ray (γ_{20}) have been subtracted. As an example, we derive below an expression for δ_v useful when the energy of γ_{21} is greater than that of γ_{10}. In the $b_0 = 0$ approximation, let $P_w(E)$ be the pulse-height spectrum in counter d_w, and $C_w(E)$ the coincidence spectrum in that counter, both normalized

to one emission of γ_{21} from the source. Let N_{ij}^{w} be the pulse-height spectrum of γ_{ij} per gamma ray counted with d_w. Then from Eqs. 3 and 4 we have

$$P_w(E) = w_{21} N_{21}^{w}(E) + w_{10}(1 + \bar{f}_1) N_{10}^{w}(E) \quad ,$$

while

$$C_w(E) = v_{10} W(\theta) \left[(1 + \delta_v)(1 + \bar{f}_1) w_{10} N_{10}^{w}(E) + w_{21} N_{21}^{w}(E) \right] \quad .$$

It can be seen that by normalizing and subtracting the pulse-height spectrum $N_{21}^{w}(E)$ from the higher-energy gamma ray (γ_{21}), the low-energy portion of which must be estimated from other available data, one obtains:

$$\frac{[C_w(E)/v_{10} \overline{W}(\theta)] - w_{21} N_{21}^{w}(E)}{P_w(E) - w_{21} N_{21}^{w}(E)} = 1 + \delta_v \quad . \tag{7}$$

With data obtained in counter d_v, δ_w is determined in a similar manner. A method based on Eq. 7 is used if the energy of γ_{10} is greater than that of γ_{21}, with the provision that in such a case the contributions from γ_{10} must be normalized. If additional coincidence data with suitably chosen bias levels is available, more precise formulations can be given, based on the same property of the definition of the δ's; these formulations do not depend upon extrapolation of the higher-energy pulse-height distribution into the region of the lower-energy peak.

In the derivation of Eq. 6 it was tacitly assumed that the source was a point, and that the efficiencies and source strength were constants. These restrictions are by no means necessary, as has been indicated to some degree in the literature.[7,3] If the Eqs. 3 are written in the approximation of $f_2 b_1 = 1$ as integrals over the source volume and over the time duration of the run, it can be shown that the usual equations for the source strength hold, on the average, provided that at least one counter is time independent and also that the efficiency of at least one counter is space-independent. ~~efficiencies of both counters are independent of time and space~~. In addition, it can be shown that errors tend to be small even in cases where neither of these conditions holds. Note that gamma-ray scattering and absorption in the source affect only $\overline{W}(\theta)$ and the detector efficiencies, provided a given photon cannot scatter and be counted in both detectors.

Experimental Methods. – Although source standardizations utilizing Eq. 6 have been performed in three geometries, most of the data were obtained with the arrangement shown in Fig. 4.4.2. In addition to routine checks of electronics, the following precautions were taken to ensure accurate results:

1. Source volume dimensions were about 1 mm, and capsules had wall thicknesses less than 0.1 g/cm^2 except in the case of the Y^{88} sources, for which, nevertheless, the scattering effects were found by calculation to be unimportant.

---

[7] J. L. Putnam, *Limitations and Extensions of the Coincidence Method for Measuring the Activity of β-γ Emitters*, AERE-I/M-26 (July 13, 1953).

UNCLASSIFIED
2-01-058-0-541

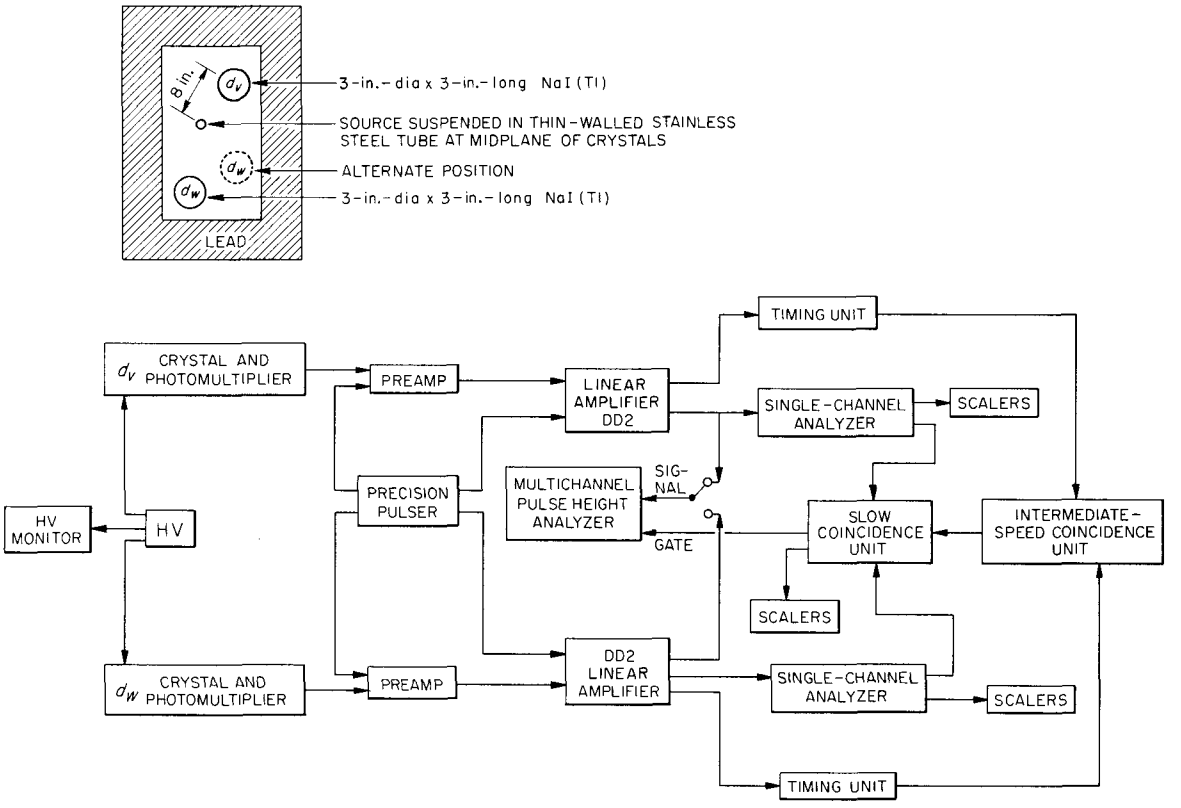

Fig. 4.4.2. Apparatus for Radioactive-Source Coincidence Measurements. Note that the coincidence spectrum or ungated spectrum can be obtained from each detector channel.

2. Pulse-height selection in the slow branch of the coincidence apparatus was adjusted so that neither Compton-scattered gamma rays from the walls of the shield nor annihilation quanta could be counted. Upper bias levels were chosen to minimize detection of any crossover gammas.
3. Care was taken that enough absorber was present to prevent observation of any beta-gamma coincidences. Plastic absorbers placed midway between source and detector were used to check on this effect.
4. Source strengths and detector efficiencies were chosen to balance uncertainties in random coincidence rates and count losses on one side, and high backgrounds and poor counting statistics on the other. For the equipment and geometry used, values of Q just under 10^5 dis/sec were considered ideal.
5. In order to remove any doubt concerning the angular correlations between the coincident gamma rays, all measurements were repeated, using angles $\theta = 94$ and $155°$. The vicinity of $180°$ was avoided because near this angle annihilation radiation from positron emission in Y^{88} would have caused the lower detector-bias settings to be too critical.

For each source nuclide, each detector angle, and each detector, both singles and coincidence data were obtained. Coincidence data from each detector was obtained with two types of bias settings governing the pulses from the other detector, giving counting rates for two efficiencies of the latter. For d_v, for example:

1. The bias of d_w was set so that both γ_{21} and γ_{10} were detected, according to the requirements of Eq. 6 for determining S_{10}.
2. The bias on d_w was reset so that only the pulses from the higher-energy gamma rays (say, γ_{21}) were counted. The resulting spectrum of coincident pulses from d_v then represented only the lower-energy gamma ray, γ_{10}. The results can be used directly to determine the efficiency v_{10}, useful for an independent calculation of δ_v.

In addition, for some cases coincidence spectra were obtained from d_v with the bias on d_w set to accept only those pulses in a narrow window about the peak in the pulse-height distribution corresponding to the lower-energy gamma ray (γ_{10}), thus accentuating the pulses from γ_{21} in the coincidence spectrum. A few random coincidence runs were also made to check the coincidence resolving time.

Results. – Table 4.4.2 summarizes the results obtained during the main series of experiments, and shows the degree of consistency observed between the various values of Q for a given source. In each case the governing contribution to the estimated error was the statistical uncertainty in the number of observed coincidence counts. Other than the consistency of this one series of runs, the only check on the validity of the source strengths measured by the above methods comes from two independent sets of similar measurements on Na^{24} performed with source

Table 4.4.2. Results and Internal Consistency[a] from Gamma-Gamma Coincidence Source Standardization

Source Description	Number of Coincidence Runs	χ^2/ν	$\bar{Q}(1+\bar{f}_1)^b$ (sec^{-1})
Co^{60}	4	11/3	$(7.54 \pm 0.02) \times 10^4$
Sc^{46}	4	4.5/3	$(6.94 \pm 0.03) \times 10^4$
Na^{24}	4	2.7/3	$(5.33 \pm 0.04) \times 10^4$
Y^{88} (larger)	5	1.3/4	$(2.37 \pm 0.01) \times 10^5$
Y^{88} (smaller)	2	4.9/1	$(7.35 \pm 0.13) \times 10^3$

[a]About half the runs for each source were performed at a detector angle of 155° and about half at 94°. A chi-square test combining the results in the third column leads to a probability of about 4% that the combined value of chi square would be greater if the estimated errors are valid. This is taken as evidence that error estimates should probably be increased by about 30% to account for the scatter in the data.

[b]Corrected for decay.

and detector geometries quite different from those in Fig. 4.4.2. These measurements are consistent with each other, based on readings from high-pressure ionization chambers[8] as an independent check on the relative intensities of the three sources.

Coincidence Standardization of a $B^{11}(p,\gamma)C^{12}$ Source

Coincidence standardization of the source of coincident 11.81- and 4.43-Mev gamma rays from proton capture in B^{11} involves a number of difficulties not present with radioactive sources. Such an experiment can be performed by allowing ~200-kev protons from an accelerator to strike a thick B^{11} target in which some protons are captured as they slow down through the 163-kev $J = 2$ resonance. Such a source is not steady in time, but coincidence equations like Eq. 6 yield the correct average over the interval of data collection. However, the erratic time dependence of such a source does require either that the standardization be performed while the source is being used for whatever purpose requires the standardization or that a monitor be used for normalization. Since in the present case the standard source was needed to measure the efficiency of a scintillation pair spectrometer at 4.4 and 11.8 Mev, this spectrometer was operated at the same time the coincidence standardization was being performed by means of an auxiliary detector operated in coincidence with the center (A) crystal of the pair spectrometer.

The nuclear-reaction gamma-ray source is more complex than a radioactive source, since the direction of the proton beam influences the intensity and angular correlation of the coincident gamma rays (the captured protons are not S-wave).

Experimental Methods. – Figure 4.4.3 shows the experimental arrangement utilized to measure the average emission rate from the $B^{11}(p,\gamma)C^{12}$ reaction while the source was being used to calibrate a scintillation pair spectrometer. The Bulk Shielding Facility electrostatic accelerator provided a measured[9] 0.4 ma of charged-particle current on a thick target of B^{11} evaporated on a heavy silver backing. During the ~20-hr run, it was necessary to raise the proton energy from 200 kev to 250 kev, presumably to compensate for carbon buildup on the target.

Figure 4.4.4 is a block diagram of the electronics for this experiment. The lower-voltage detector pulse-height biases for this experiment were adjusted to correspond to about 1.5 Mev, partly to exclude gamma rays from a Co^{60} contamination in the spectrometer housing. The upper bias levels were set just above the 11.8-Mev peak to minimize detection of the 16-Mev gamma rays which also arise in this reaction.

Coincidence Equations. – Figure 4.4.5 shows the energy schematic of the reaction used. Since P-wave protons are captured in the resonance, each of the studied gamma rays has an angular distribution with respect to the beam direction, as well as an angular correlation, which depends on the beam direction, with the other gamma ray. These angular dependencies seriously

---

[8]Courtesy of the Isotopes and Analytical Chemistry Divisions.

[9]The actual proton current is presumed to lie between 0.2 and 0.3 ma.

UNCLASSIFIED
2-01-058-0-542

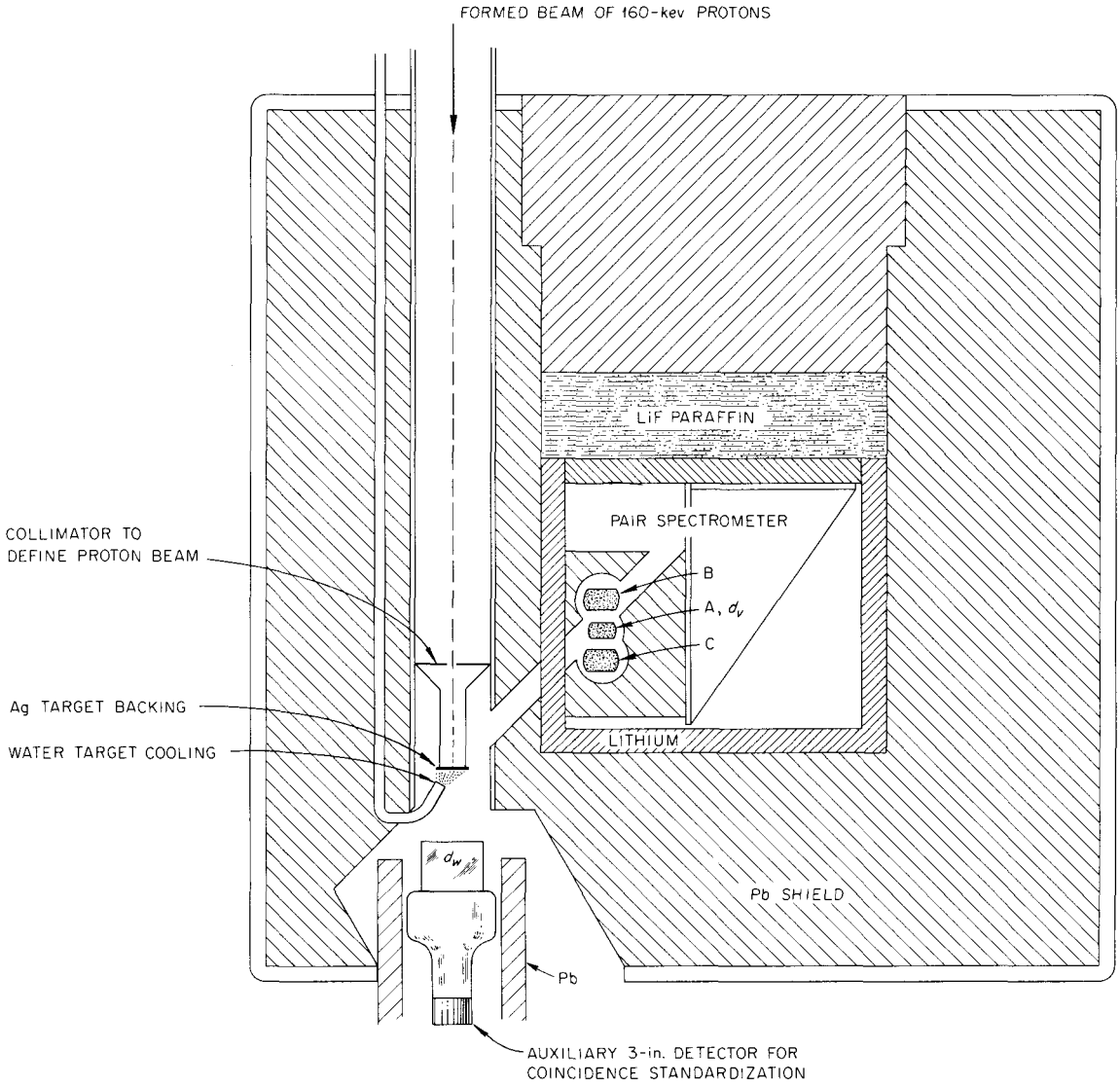

Fig. 4.4.3. Diagram of Apparatus Used for the $B^{11}(p,\gamma)C^{12}$ Experiment.

complicate the equations previously derived. Fortunately this reaction has received both experimental[10] and theoretical[11] study, so that the basic angular functions could be obtained with some uniqueness from earlier work. These functions simplify considerably when one detector (d_w in this case) is coaxial with the beam direction. In the derivations below, the displacement of d_w from the beam axis is handled as a small quantity.

Multiplying Eq. 17 of Biedenharn *et al.*[11] by the factor $\frac{1}{32}$ gives $W(\theta_{21},\theta_{10},\phi)$, which governs the relative probability of emission of γ_{21} and γ_{10} at angles θ_{21} and θ_{10} to the proton beam

[10]See references of Table 4.4.3.

[11]L. C. Biedenharn, G. A. Arfken, and M. E. Rose, *Phys. Rev.* **83**, 586 (1951).

direction. The quantity ϕ is the azimuthal angle between the planes containing the beam direction and the two gamma rays. The quantity W is so normalized that it gives unity when averaged over all directions of emission of each gamma ray. The full expression for $W(\theta_{21},\theta_{10},\phi)$ is simplified below for the cases in which one or the other of the gamma rays is emitted in the direction of the proton beam:

$$W(\theta_{21},0) = \tfrac{1}{4}[3 + 2x + P_2(\cos\theta_{21})] \;; \tag{8}$$

$$W(0,\theta_{10}) = \tfrac{1}{8}\left[(5.2 + 5.6x) + \tfrac{1}{7}(10 + 8x)P_2(\cos\theta_{10}) + \tfrac{48}{35}(1 - 2x)P_4(\cos\theta_{10})\right] \;. \tag{9}$$

Similarly the yield of each gamma ray can be expressed, averaged over the direction of the other photon:

$$Y_{21}(\theta_{21}) = 1 + \tfrac{7}{20}(2x - 1)P_2(\cos\theta_{21}) \;; \tag{10}$$

$$Y_{10}(\theta_{10}) = 1 + \left(\frac{2x - 1}{4}\right)P_2(\cos\theta_{10}) \;. \tag{11}$$

UNCLASSIFIED
2-01-058-0-543

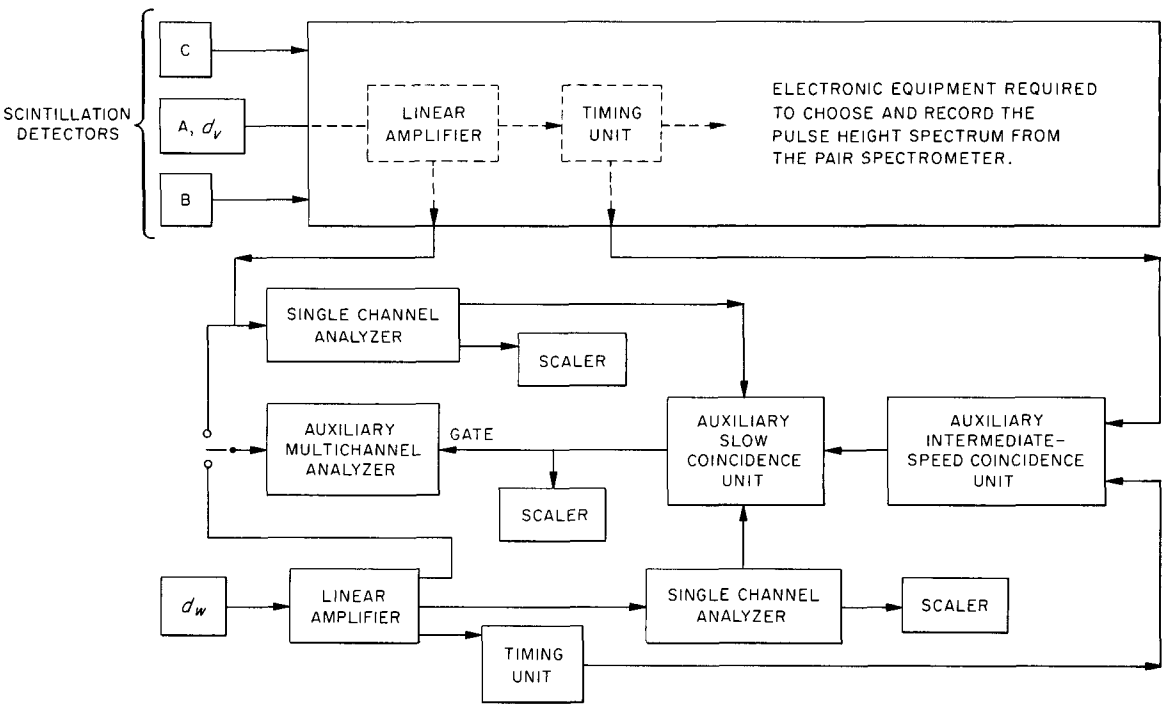

Fig. 4.4.4. Simplified Block Diagram of Electronics Used in Standardization of the $B^{11}(p,\gamma)C^{12}$ Source. The linear amplifier and timing unit of the pair spectrometer circuitry are also used here because the A detector of the pair spectrometer also serves as the d_v detector. Note that this problem requires two coincidence circuits and two multichannel pulse-height analyzers or their equivalent.

In the above equations x is the fractional contribution of channel spin $S = 1$ (ref 12) to the reaction intensity. (Note that the beam direction loses its importance if $x = \frac{1}{2}$.) In practice x is a parameter determined by the experiments of other workers on the angular dependence of radiations from this reaction as well as any other reactions involving the same compound nucleus state. The value chosen for x was (0.69 ± 0.015), where the error is based on scatter between the various experimental results summarized in Table 4.4.3. The validity of Eqs. 8–11 is based on the assumptions of the level properties and radiation multipolarities shown in Fig. 4.4.5 and the assumption that only the 163-kev level is important in producing the observed de-excitation gamma rays.

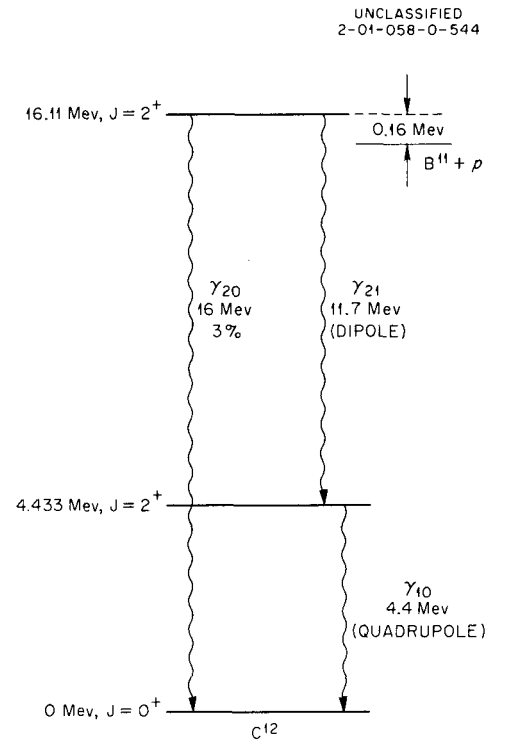

DATA FROM: F. AJZENBERG-SELOVE AND T. LAURITSEN, *NUCLEAR PHS.* 11, 1 (1959)

Fig. 4.4.5. Energy-Level Schematic of the $B^{11}(p,\gamma)C^{12}$ Reaction.

To simplify the derivation of the analog of Eq. 6 for the present case, it is assumed below that the detector counting rates have been corrected for the following:

1. all room and random-coincidence backgrounds, (former 1%, latter $\leqq 0.2\%$);
2. counting losses, both singles and coincidence, ($\sim 0.2\%$);
3. counting of the crossover gamma rays (γ_{20}), [$(1.5 \pm 0.4)\%$ for each detector];
4. simultaneous detection of coincident gamma rays in the d_w detector, (0.7%).

With these simplifications the analogs of Eqs. 1 and 2 are obtained from Eqs. 10 and 11, giving $S_{21}(\theta) = QY_{21}(\theta)$ and $S_{10}(\theta) = QY_{10}(\theta)$, where Q is the rate of emission of coincident gamma-ray cascades. The rate Q can be determined from the experimental data by application of the following analog of Eq. 5:

$$\frac{D_v D_w}{QD_{vw}} = \frac{[(1+\delta_v)Y_{21}(\theta_v) + Y_{10}(\theta_v)][\overline{Y}_{10}(0) + (1+\delta_w)\overline{Y}_{21}(0)]}{(1+\delta_v)\overline{W}(\theta_v,0) + (1+\delta_w)\overline{W}(0,\theta_v)} \quad . \tag{12}$$

The bars on the angle functions indicate that the functions of Eqs. 8–11 have been attenuated properly for the smoothing effect of the finite size of detector d_w. The angle θ_v is the fixed angle between the proton beam direction and the line between source and detector d_v. Because of complications in Eq. 12 the results cannot readily be displayed in a manner which makes

[12]The channel spin is defined as the vector sum of the target (B^{11}) spin and projectile (proton) spin, giving in this case the two possibilities $\frac{3}{2} \pm \frac{1}{2}$.

obvious the small dependence upon δ's. Therefore it is best in this case to evaluate Eq. 12 to determine Q, and then to determine the sensitivity of the result to various errors by obtaining derivatives of the right side of Eq. 12. Table 4.4.4 lists the parameters used for the evaluation of Eq. 12 and the importances of the various sources of error.

Table 4.4.3. Summary of Information Used to Evaluate x, the Fractional Contribution of Channel Spin 1 to the $B^{11}(p,\gamma)C^{12}$ Reaction in the 163-kev Resonance

x	Reaction	Measurement	References
0.70 ± 0.02	$B^{11}(p,\alpha)Be^8$	α angular distribution	*a*
0.69 ± 0.02	$B^{11}(p,\gamma)C^{12}$	$Y_{21}(\theta_{21})$	*b–e*
0.70 ± 0.03	$B^{11}(p,\gamma)C^{12}$	$Y_{10}(\theta_{10})$	*e*
$0.67^{+0.3}_{-0.5}$	$B^{11}(p,\gamma)C^{12}$	$W(\theta_{21},0)$	*b*
0.68 ± 0.18	$B^{11}(p,\gamma)C^{12}$	$W(\theta_{21},\pi/2)$	*b*
0.61 ± 0.14	$B^{11}(p,\gamma)C^{12}$	$W(110°,110°,\phi)$	*f*
0.66 ± 0.02	$B^{11}(p,\gamma)C^{12}$	$Y_{20}(\theta_{20})$	*c*
0.69 ± 0.015[g]			

[a] D. M. Thomson *et al.*, *Proc. Phys. Soc.* (*London*) **A65**, 745 (1952).
[b] T. P. Hubbard, E. B. Nelson, and J. A. Jacobs, *Phys. Rev.* **87**, 378 (1952).
[c] D. S. Craig, W. G. Cross, and R. G. Jarvis, *Phys. Rev.* **103**, 1414 (1956).
[d] G. L. Jenkins *et al.*, *Phys. Rev.* **91**, 915 (1953).
[e] P. J. Grant *et al.*, *Proc. Phys. Soc.* (*London*) **A67**, 751 (1954).
[f] G. M. Lewis, *Phil. Mag.* **43**, 690 (1952).
[g] Used in this analysis (not a direct average).

Table 4.4.4. Evaluation of $K = D_v D_w / 2QD_{vw}$ from Eq. 12, with Uncertainties

Parameter q_i	$q_i \pm \Delta q_i$ (ref *a*)	$(\partial K/\partial q_i)$ (ref *b*)	$\Delta q_i(\partial K/\partial q_i)$
θ_v	$134.5° \pm 0.5°$	-0.14 rad^{-1}	0.0012
θ_w	$1.5° \pm 1.2°$	-0.2 rad^{-1}	0.004
δ_v	0.35 ± 0.05	0.082	0.004
δ_w	0.47 ± 0.07	0.047	0.003
x	0.69 ± 0.015	0.17	0.0025

The above parameters result in $K = 1.000 \pm 0.007$, using Eqs. 8–12 with appropriate attenuation of Legendre coefficients for the finite size of d_w.

[a] Value of parameter plus or minus estimated standard deviation.
[b] Derivatives are evaluated at the listed parameter values.

The values of δ_v and δ_w encountered here were much larger than any observed using radioactive sources. The evaluation of the δ's was also complicated by the angular dependence of the yields from the reaction. It was shown, by using the same logic previously employed, that the analogs of Eq. 7 for this case are:

$$(1+\delta_v) = \frac{\overline{Y}_{10}(\theta_w)}{\overline{Y}_{21}(\theta_w)} \frac{\overline{W}(\theta_w,\theta_v)}{\overline{W}(\theta_v,\theta_w)} \left\{ \frac{[\overline{Y}_{21}(\theta_w)C_w(E)/v_{10}\overline{W}(\theta_w,\theta_v)] - \overline{Y}_{21}(\theta_w)w_{21}N^w_{21}(E)}{[P_w(E) - \overline{Y}_{21}(\theta_w)w_{21}N^w_{21}(E)]} \right\} , \quad (13)$$

$$(1+\delta_w) = \frac{\overline{W}(\theta_v,\theta_w)}{\overline{W}(\theta_w,\theta_v)} \frac{Y_{10}(\theta_v)}{Y_{21}(\theta_v)} \left\{ \frac{[Y_{21}(\theta_v)C_v(E)/\overline{W}(\theta_v,\theta_w)w_{10}] - Y_{21}(\theta_v)v_{21}N^v_{21}(E)}{[P_v(E) - Y_{21}(\theta_v)v_{21}N^v_{21}(E)]} \right\} , \quad (14)$$

where, in the present case, $\theta_w \cong 0$.

Results. – As indicated in Table 4.4.4, errors in the correction terms were not very important in the standardization of the source, since from the counting data $(D_v D_w)/(2D_{vw}) = 6.37 \times 10^4$ $\text{sec}^{-1} \pm 1.2\%$. The final average source strength (6.37×10^4 sec^{-1}) is quoted to a precision of 1.4%, but since the pair spectrometer is much less efficient than its center crystal, the accuracy of the resulting determination of the spectrometer efficiency was governed by statistics in the pair spectrometer pulse-height spectrum. This would not be the case if a single-crystal spectrometer were being studied.

The complexity of the experimental system described in this section limits its usefulness, since the production of an ~0.3-ma beam of protons at a given target point requires equipment frequently unavailable to the gamma-ray spectroscopist. The results, however, have unusual value because absolute sources at this energy are rarely available. In the calibration of a more efficient spectrometer, a disturbing factor would be the simultaneous contribution of the two gamma rays (plus the 3% contribution of the 16-Mev crossover) to the pulse-height spectrum. This difficulty could be relieved by obtaining in the detector of interest the spectrum of pulses from only the 4.4-Mev gamma ray, in coincidence with the 11.7-Mev gamma ray in the auxiliary detector. This approach, which would directly yield the efficiency of the detector under study, was not applicable in the present instance, because of the low efficiency of the pair spectrometer which we desired to calibrate.

Conclusions

The techniques of gamma-gamma coincidence standardization of sources are widely applicable to nuclides from which the most important gamma rays are a cascade of two or more coincident radiations. The most useful techniques were found to be those extending the work of Meyer *et al.*,[13] characterized by the effort to make the coincident spectrum from each gamma-ray detector have approximately the same appearance as the singles spectrum. As long as the source of

[13] K. P. Meyer, P. Schmid, and P. Huber, *Helv. Phys. Acta* 32, 423 (1959).

interest has an appropriate decay scheme and has strength in the appropriate range, it is felt that the method gives highly reliable results, which are rather insensitive to many experimental difficulties. While the method can compete with other absolute counting techniques only for certain isotopes, it has the advantage that an encapsulated source may be studied.

4.5 GAMMA-RAY INTENSITY RATIOS IN THE DECAY OF 105-DAY Y^{88}

R. W. Peelle

Introduction

An experiment to determine the spectrum of gamma rays emitted promptly in the thermal-neutron-induced fission of U^{235} is described in Sec 4.3. The calibration of the efficiency of the pair and Compton spectrometers used in that experiment requires a rather precise knowledge of the decay scheme of Y^{88}, which was one of the most convenient calibration sources for the spectrometers.

Figure 4.5.1 shows the decay scheme of Y^{88} which decays, largely by electron capture, to the excited states of Sr^{88}. Energy measurements for these transitions have been previously reported.[1] Table 4.5.1 summarizes the literature values of the branching ratios defined in Fig. 4.5.1, and includes the values obtained in the present work for the relative intensities of the three gamma rays present. The measurements reported below were obtained with a scintillation pair spectrometer and with coincidence counting techniques which, in this case, seem to give better precision than that previously attained.

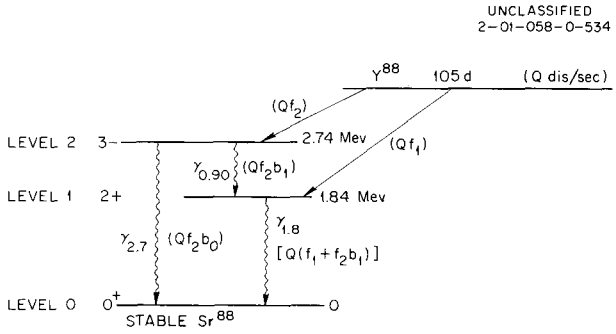

Fig. 4.5.1. Decay-Scheme Definitions for Y^{88}. Expressions in parentheses represent transition rates. Published values indicate that all but a small fraction of the decays to the first excited state of Sr^{88} go by electron capture.

---

[1] R. W. Peelle and T. A. Love, *Scintillation Spectroscopy Measurements of Gamma-Ray Energies from Sources of Y^{88}, Mn^{54}, and Zn^{65}*, ORNL-2790 (1959). The values quoted in this report were 1840 ± 2 and 898.8 ± 1.2 kev.

Table 4.5.1. Literature Values of Gamma-Ray Intensity Ratios in the Decay of Y^{88} to Sr^{88}

$\frac{S_{2.7}}{S_{1.8}}$	$\frac{S_{1.8}}{S_{0.90}}$	Method	Reference
$\times 10^{-3}$			
5 ± 3	1.09 ± 0.05	Calibrated NaI(Tl) scintillator	*a*
$5 \pm ?$	$1.09 \pm ?$	Calibrated NaI(Tl) scintillator	*b*
5.97 ± 0.25		Calibrated scintillation pair spectrometer	Present work
	1.064 ± 0.008	Coincidence scintillation spectroscopy	Present work

[a]N. H. Lazar, E. Eichler, and G. D. O'Kelley, *Phys. Rev.* 101, 727 (1956).
[b]F. M. Tomnovec, *Bull. Am. Phys. Soc.* [2]1, 391 (1956).

Pair Spectrometer Determination of Relative Intensity of Crossover Transition

The pulse-height spectrum of Fig. 4.5.2 is one of those used to determine the crossover[2] intensity with the scintillation pair spectrometer. According to the notation of Fig. 4.5.1, the relative intensities of the two higher energy transitions are given by

$$\frac{S_{2.7}}{S_{1.8}} = \frac{f_2 b_0}{f_1 + f_2 b_1} = \frac{b_0/b_1}{1 + \bar{f}_1} , \tag{1}$$

where

$$1 + \bar{f}_1 = 1 + \frac{f_1}{f_2 b_1} = \frac{S_{1.8}}{S_{0.90}} ,$$

which is further discussed below.

Note that internal conversion coefficients, which have been measured to be less than 0.1%,[3] have been ignored in the above considerations.

The intensity ratio of the higher energy gamma rays can be determined directly from the data of Fig. 4.5.2 provided that the efficiency of the spectrometer has been measured for the energies concerned, because the low over-all efficiency of $\sim 10^{-7}$ makes coincidence summing quite unimportant. Since calibrated sources of the 1.84-Mev Y^{88} gamma ray and the 2.754-Mev Na^{24} gamma rays have been measured with the same spectrometer used here, this efficiency ratio is known. Table 4.5.2 summarizes the available data and the sources of error in the determination. The final value obtained was $S_{2.7}/S_{1.8} = (5.97 \pm 0.25) \times 10^{-3}$.

[2]No attempt was made to precisely measure the energy of the observed transition, but the average of the observed peaks agreed, within the $\sim$10-kev error, with the expected 2.74 Mev. The agreement within data taken over a five-month period gives some assurance of radiochemical purity.

[3]K. Way *et al.*, *Nuclear Data Sheets*, National Academy of Sciences—National Research Council, Washington, 1959.

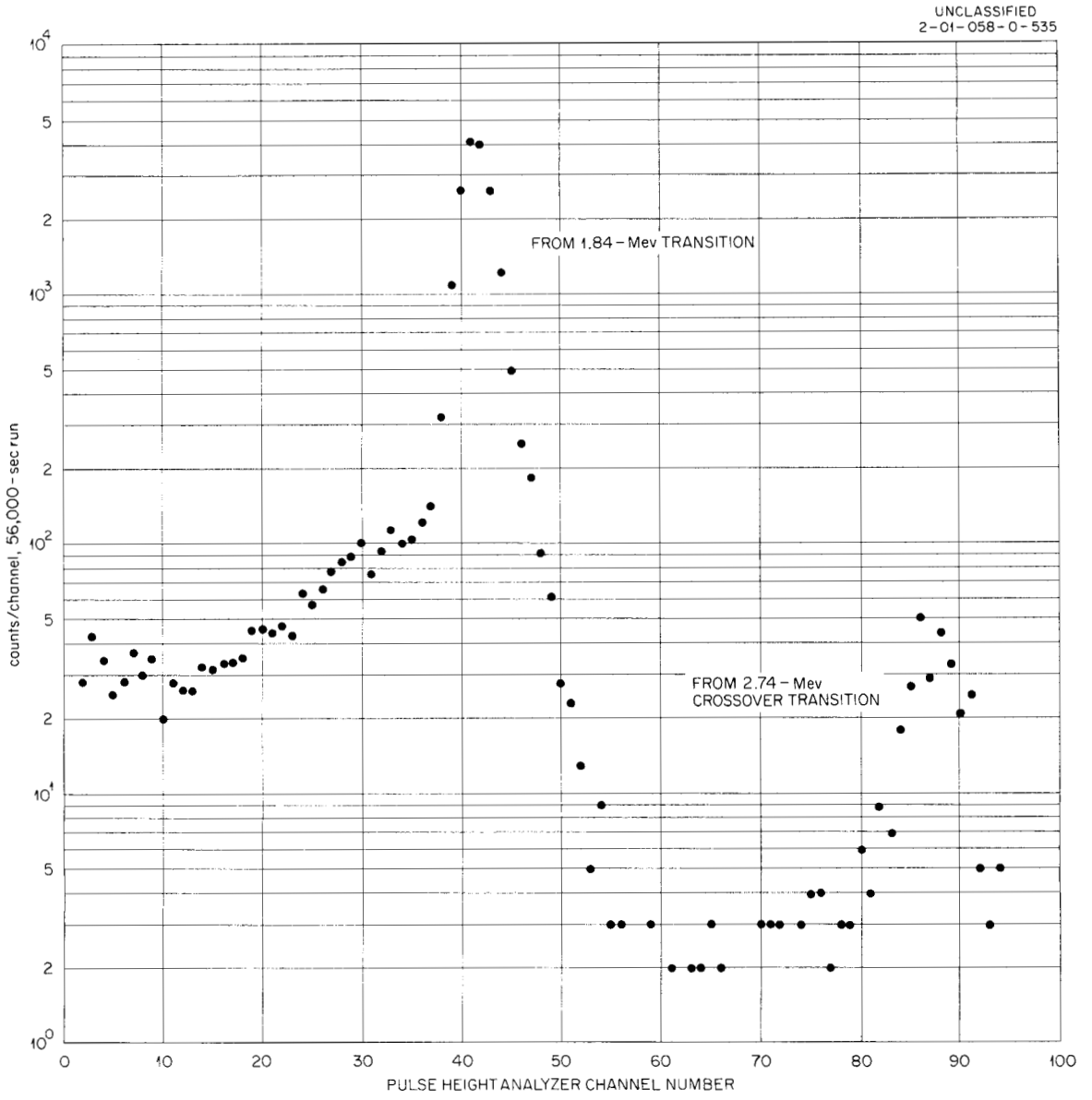

Fig. 4.5.2. Typical Pair Spectrometer Pulse-Height Spectrum from a Y^{88} Source.

Coincidence Measurement of the Relative Intensity of 1.84- and 0.90-Mev Gamma Rays

The value of $1 + \bar{f}_1$ (or $S_{1.8}/S_{0.90}$) may be determined with good precision by coincidence techniques because of the near agreement in energy of the 0.899-Mev Y^{88} transition with the 0.89-Mev transition in the simple 100% cascade decay scheme of Sc^{46} shown in Fig. 4.5.3. It is only necessary to perform the appropriate γ-γ coincidence measurements for each source in the same geometry. Such measurements were performed in conjunction with the γ-γ coincidence studies described in Sec 4.4 of this report. Using the notation of Sec 4.4, wherein d_v and d_w are the two gamma-ray detectors with efficiencies v_E and w_E for gamma-ray transitions of energy E

Table 4.5.2. Summary of Data Yielding $S_{2.7}/S_{1.8}$, the Relative Intensities of the 2.74-Mev Crossover and the 1.84-Mev Ground State Transitions in the Decay of Y^{88}

Date Obtained	$\frac{C_{2.74}}{C_{1.84}}$ [a]	$\left\langle \frac{C_{2.74}}{C_{1.84}} \right\rangle_{av}$	$\left(\frac{\epsilon^b_{1.8}}{\epsilon^b_{2.754}} \right)$ [b]	$f\alpha$ [c]	$\frac{S_{2.7}}{S_{1.8}}$
	$\times 10^{-2}$	$\times 10^{-2}$			$\times 10^{-3}$
February 1958	1.59 ± 0.07	1.61 ± 0.05	0.366 ± 0.007	1.013 ± 0.002	5.97 ± 0.25
April 1958	1.63 ± 0.11				
July 1958	1.62 ± 0.09				

[a] The count ratio in each run was determined according to the observed total counts in the two peaks as defined for peak efficiency in sec 4.3 of this report. The quoted errors in this ratio are based solely on counting statistics.

[b] This peak efficiency ratio is that illustrated in sec 4.3, applying to γ-rays of Y^{88} and Na^{24} averaged over position in the fission chamber utilized in the experiment there described. The error largely originated in the uncertainty in the strength of the Y^{88} source used to obtain the peak efficiency.

[c] The term $f\alpha$ is the correction for the difference in self-absorption between the fission chamber and the source used for these measurements, and for the difference between the crossover transition energy (2.739 Mev) and the calibration gamma-ray energy from Na^{24} (2.754 Mev).

leading to observed counting rates D_v and D_w, one can specialize Eqs. 3 of Sec 4.4 for the case where $w_{0.90} = 0$, that is, where detector d_w is so biased that only the higher-energy gamma rays (1.84 Mev) are detected, with an efficiency defined to be $w^b_{1.8}$. One obtains

$$D_w = \bar{Q}\left[w^b_{1.8}(1 + \bar{f}_1) + \Delta^b_w + \left(w^b_{2.7} b_0/b_1\right)\right],$$
$$D_{vw} = \bar{Q}\bar{W}(\theta) v_{0.90} w^b_{1.8}, \tag{2}$$

where in the notation of Fig. 4.5.1, $\bar{Q} = Qf_2 b_1$, and $\bar{f}_1 = f_1/f_2 b_1$.

Dividing the second equation by the first,

$$\frac{D_{vw}}{D_w} = \frac{\bar{W}(\theta) v_{0.90}}{1 + \bar{f}_1 + \left(w^b_{2.7} b_0/w^b_{1.8} b_1\right) + \left(\Delta^b_w/w^b_{1.8}\right)} = \frac{\bar{W}(\theta) v_{0.90}}{\left[1 + \bar{f}_1 + \left(w^b_{2.7} b_0/w^b_{1.8} b_1\right)\right]\left[1 - (\mathrm{SDC})^b_w\right]}, \tag{3}$$

where $(\mathrm{SDC})^b_w$ is defined under Eqs. 4 of Sec 4.4 or by the above equality. The method used to experimentally determine $1+\bar{f}_1$ follows directly from Eq. 3, assuming that the appropriate counting rates and attenuated angular correlation functions $\bar{W}(\theta)$ are available. Note that in practice the efficiency $v_{0.90}$ corresponds to whatever range of pulse heights is used in determining the coincidence rate D_{vw}, so the spectrum of coincidence counts in d_v was observed and the energy interval

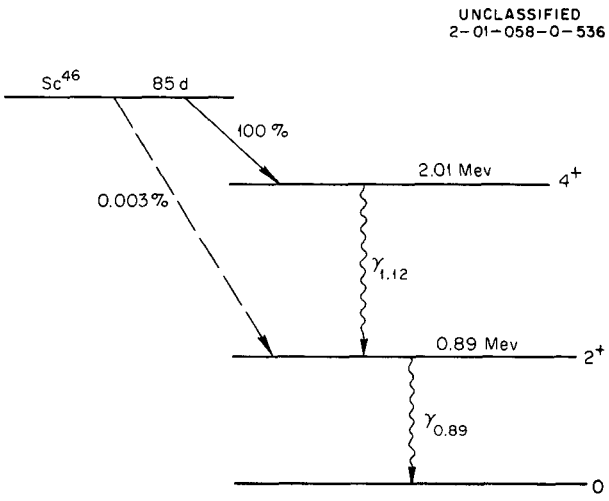

Fig. 4.5.3. Decay Scheme of Sc^{46}. Based on data from: K. Way *et al.*, *Nuclear Level Schemes*, $A = 40 - A = 92$, National Academy of Sciences – National Research Council, Washington (1955).

corresponding to the efficiency $v_{0.90}$ was determined after the experiment. Note that for Sc^{46}, $\overline{f}_1 = b_0 = 0$, so the correction terms in the denominator vanish, yielding a value for $v_{0.89}$. In the case of the Y^{88} source measured in the same geometry, $v_{0.90}$ (Y^{88}) will be almost the same as $v_{0.89}$ (Sc^{46}), and the small correction term in the denominator of Eq. 3 for Y^{88} can be estimated from the results of the first portion of this report and the pulse-height spectra observed with standardized Y^{88} and Na^{24} sources. The quantity $(SDC)^b_w$ is small and is calculated in the manner described in Sec 4.4. Table 4.5.3 summarizes the four sets of values observed using different detectors and geometries. The correction for source self-absorption occurs because the two sources were not encapsuled in the same manner, the more-rugged Y^{88} capsule having a considerably higher self-absorption. The ratio of efficiencies at the two energies, 0.89 and 0.899 Mev, was obtained from the slope of a graph on which were plotted all the measured photopeak efficiencies observed in one fixed detector geometry during the coincidence experiments. The error in this correction stems largely from the 4-kev uncertainty in energy of the 0.89-Mev transition in the decay of Sc^{46}.

The final results, $1 + \overline{f}_1 = 1.064 \pm 0.008$ and $S_{2.7}/S_{1.8} = (5.97 \pm 0.25) \times 10^{-3}$, lead to the branching ratios summarized in the next paragraph, assuming no ground state transitions between Y^{88} and Sr^{88}, ignoring internal conversion, and combining intensities from electron capture and β^+ decay.

In the notation of Fig. 4.5.1, the branching ratios determined in this experiment are: $f_2 = 0.940 \pm 0.007$; $f_1 = 0.060 \pm 0.007$; $b_1 = 0.9937 \pm 0.0003$; and $b_0 = (6.31 \pm 0.27) \times 10^{-3}$. Note that, by definition, $f_1 + f_2 = 1$ and $b_0 + b_1 = 1$.

Table 4.5.3. Summary of Data on $S_{1.8}/S_{0.90} = 1 + \bar{f}_1$

(A chi-square test on the results indicated a probability of ~0.6 that a larger value of chi-square would be observed in another set of data with the same standard deviations.)

Run[a]	$\dfrac{v_{0.90}\, e^{-\mu t}}{1 + \bar{f}_1 + \dfrac{b_0 w_{2.7}}{b_1 w_{1.8}}}$ (from Y^{88} data)[b]	$v_{0.89}$ (from Sc^{46})	$1 + \bar{f}_1 + \dfrac{b_0 w_{2.7}}{b_1 w_{1.8}}$	$1 + \bar{f}_1$
	$\times 10^{-3}$	$\times 10^{-3}$		
1	2.808 ± 0.013[c]	3.16 ± 0.02	1.072 ± 0.008	1.069 ± 0.008
2	2.895 ± 0.026	3.21 ± 0.02	1.055 ± 0.012	1.052 ± 0.012
3	2.708 ± 0.023	3.05 ± 0.04	1.072 ± 0.017	1.068 ± 0.017
4	3.263 ± 0.045	3.63 ± 0.05	1.057 ± 0.021	1.054 ± 0.021
			Av	1.064 ± 0.008[d]

[a]Runs 1 and 3 were measured at a detector angle of 155°, 2 and 4 at an angle of 94°. The first two runs used the efficiency of d_v as indicated, while the latter two were actually based on d_w.

[b]The quantity $e^{-\mu t} = 0.961 \pm 0.003$; $v_{0.90}/v_{0.89} = 0.990 \pm 0.003$; $w_{2.7}/w_{1.8} = 0.6 \pm 0.1$.

[c]Averaged from three independent experiments for which the remainder of the tabulated data remains constant.

[d]A standard error of 0.006 was obtained by combining the errors of runs 1 through 4. The quoted error of 0.008 includes a contribution of 0.005 from uncertainties common to all the above, such as estimated errors in count loss correction, $v_{0.90}/v_{0.89}$, and $e^{-\mu t}$.

4.6 DETERMINATION OF THE INTERNAL CONVERSION COEFFICIENT OF THE 279-kev GAMMA RAY IN Tl^{203} BY ABSOLUTE COINCIDENCE TECHNIQUES

R. W. Peelle

Introduction

The present experiments were performed to determine absolute strengths of sources used to calibrate the NaI(Tl) spectrometer used for measurements of the prompt gamma rays from U^{235} thermal fission in the energy region from 15 to 600 kev. This purpose required a knowledge of the absolute strengths of both 73-kev (average) x rays and 279-kev gamma rays from a source used in conjunction with this spectrometer. This report summarizes measurements on a much smaller source which was eventually compared to the calibration source by a counting experiment in a suitable geometry. The measurements also yield a new value of α_K, the ratio of K-shell internal conversion to gamma-ray emission in the daughter Tl^{203}.

Considerable interest has been shown in measurements of the conversion coefficients in Tl^{203}, largely by the techniques of beta-ray spectroscopy. The simple decay scheme is shown in Fig. 4.6.1. The 279-kev transition is considered to be a mixed ΔL forbidden $M1$-$E2$ transition,[1] which can also be studied by looking at the electromagnetic cascade in the decay of Pb^{203} (refs 2 and 3) or by Coulomb excitation of Tl^{203} (ref 4). Internal conversion in such heavy elements takes on added interest because overlap of the electron wave functions with the nucleus

[1] B. I. Deutch, *Phys. Rev.* **117**, 818 (1960).
[2] T. Lindquist, *Nuclear Phys.* **3**, 367 (1957).
[3] G. J. Nijgh and A. H. Wapstra, *Nuclear Phys.* **9**, 545 (1959).
[4] F. K. McGowan and P. H. Stelson, *Phys. Rev.* **109**, 909 (1958).

UNCLASSIFIED
2-01-058-0-546

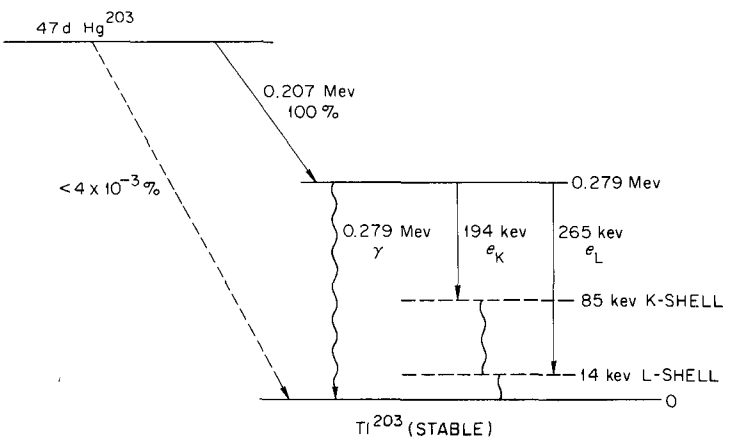

Fig. 4.6.1. The Decay Scheme of Hg^{203}. The solid horizontal lines are nuclear energy levels, while the broken ones represent atomic excitations corresponding to K- and L-shell vacancies produced by internal conversion of the 0.279-Mev electromagnetic transition. Literature values of the probabilities for the various decay modes of the excited state by gamma-ray emission (γ) and conversion electron emission (e_K, e_L, ...) are tabulated in Table 4.6.1.

allows the possibility of observation of nuclear structure effects in the conversion coefficients.[1,3] Table 4.6.1 summarizes the more-precise values from the literature for the internal conversion properties of Tl^{203}. The values of α_K are for comparison with the values obtained from the present work, while the ratios between conversion intensities in the various electron shells are required in the analysis of this experiment. The values actually used in the calculation here are the "best values" chosen by Nijgh and Wapstra.[3]

Table 4.6.1. Summary[a] of Internal Conversion Data for the 279-kev Transition in Tl^{203}

$\alpha_K = \frac{e_K}{\gamma}$	$\frac{e_K}{e_L}$	$\frac{e_L}{e_M + e_N}$	Reference
0.147 ± 0.002	3.29 ± ?		*b*
0.159 ± 0.004	3.24 ± 0.05		*c*
0.15 ± 0.01	3.1 ± 0.3		*d*
0.13 ± 0.01	3.32 ± 0.07		*f*
0.163 ± 0.003	3.39 ± 0.06	3.3 ± 0.1	*g*
0.19 ± 0.01			*h*

[a]Only the most recent values and those with the smaller estimated errors are included. Additional values are listed in: K. Way *et al.*, *Nuclear Data Sheet* 59-2-133, National Academy of Sciences – National Research Council. The last value listed was obtained using a calibrated scintillation spectrometer, while all others utilized the techniques of β-ray spectroscopy.

[b]R. K. Doerner and A. N. Weber, *Phys. Rev.* **99**, 672A (1955).

[c]C. Nordling *et al.*, *Nuclear Phys.* **1**, 326 (1956).

[d]Z. O'Friel, *Phys. Rev.* **101**, 1076 (1956).

[f]J. L. Wolfson, *Can. J. Phys.* **34**, 256 (1956).

[g]G. J. Nijgh and A. H. Wapstra, *Nuclear Phys.* **9**, 528 (1959).

[h]M. K. Ramaswamy and P. S. Jastram, *Nuclear Phys.* **15**, 510 (1960).

The experimental method used rests upon the observation that, for a nuclide which decays by a single beta transition to an excited state of its daughter, the pulses from a 100%-efficient 4π detector of fast electrons can be completely separated into groups which correspond to the emission or nonemission of internal conversion electrons (ignoring the problem of resolution in the detector and presuming that the conversion electrons have about as much energy as the most energetic beta particles). The decay scheme of Hg^{203} meets these requirements.

A suitable experimental device can be produced by encapsulating the source in a plastic scintillator. The pulse-height resolutions achievable in practice permit identification of certain ranges of pulses from the detector as corresponding wholly to beta decay alone (followed by gamma emission), other ranges as corresponding wholly to beta decay followed by conversion electrons. The arrangement is an example of complete coincidence summing which, therefore, thoroughly distorts the familiar spectrum of beta rays and conversion electrons observed in low-efficiency beta-ray spectrometers. If only *K*-conversion electrons were emitted, the appearance

of the pulse-height spectrum in the limit of good resolution would be that of two beta-ray spectra side by side, the second displaced to higher energy by an amount equal to the energy of the conversion electrons and having a relative magnitude given by the internal conversion coefficient.

Experimental Method

The apparatus consisted of a simple two-speed coincidence circuit[5] fed by pulses from two photomultipliers. On one phototube was mounted a $1\frac{3}{4}$-in.-dia by 1-in.-thick NaI(Tl) crystal with an aluminum cover sufficiently thin to allow response to the 11-kev (average) L x rays of Tl^{203}. On the other phototube, stationed 2 to 3 in. away from the photon detector, was placed a small plastic scintillator about 0.25 in. thick and 0.6 in. in diameter. The top 0.1 in. of this scintillator was glued onto the remainder after a weak source of Hg^{203} had been evaporated to dryness within a small cavity in the lower section. The construction of the counter ensured that any electrons with as much as a few tens of kilovolts of energy would give rise to a measurable pulse from the plastic scintillator.

Figure 4.6.2 shows a typical ungated pulse-height spectrum observed in the plastic phosphor, as well as corresponding coincidence spectra for which the bias on the NaI gamma detector was set either to count only the 0.279-Mev gamma rays or to accentuate the K x rays. Similarly, Fig. 4.6.3 shows the ungated spectrum in the NaI scintillator and those coincidence spectra corresponding to nearly pure detection of beta rays and of beta rays plus conversion electrons. Spectra of these types were obtained for two different spacings between detectors and for different gains in the gamma-ray detector channel along with the simultaneously observed counting rates between preset pulse heights in each of the detector channels.

The paragraphs below derive the equations which make possible the reduction of the experimental data to give the source strengths of the gamma and x radiation and finally the desired conversion coefficient. The symbol Q denotes the disintegration rate of the source. The quantities γ, e_K, e_L, e_M, etc., which sum to unity are the probabilities for the 0.279-Mev level of Tl^{203} to decay by emission of gamma rays or conversion electrons from the electron shells denoted by the subscripts. In this notation the K-conversion coefficient $\alpha_K = e_K/\gamma$. Similarly, x_K and x_L are the fluorescent efficiencies for these shells, the probability that a K- or L-shell vacancy will result in the emission of a characteristic x ray rather than Auger electrons. Note that x_L may depend on the relative populations of the L subshells though it will be considered as a constant below.

Detector counting rates (after subtraction of all counting backgrounds) in the formulas below are defined as B^i for the plastic beta-ray detector and G^j for the NaI scintillator, where the superscripts refer to the detector biasing schemes. The j symbols identifying the pulse-height

[5] R. W. Peelle and T. A. Love, *Appl. Nuclear Phys. Ann. Prog. Rep. Sept. 1, 1957*, ORNL-2389, p 249.

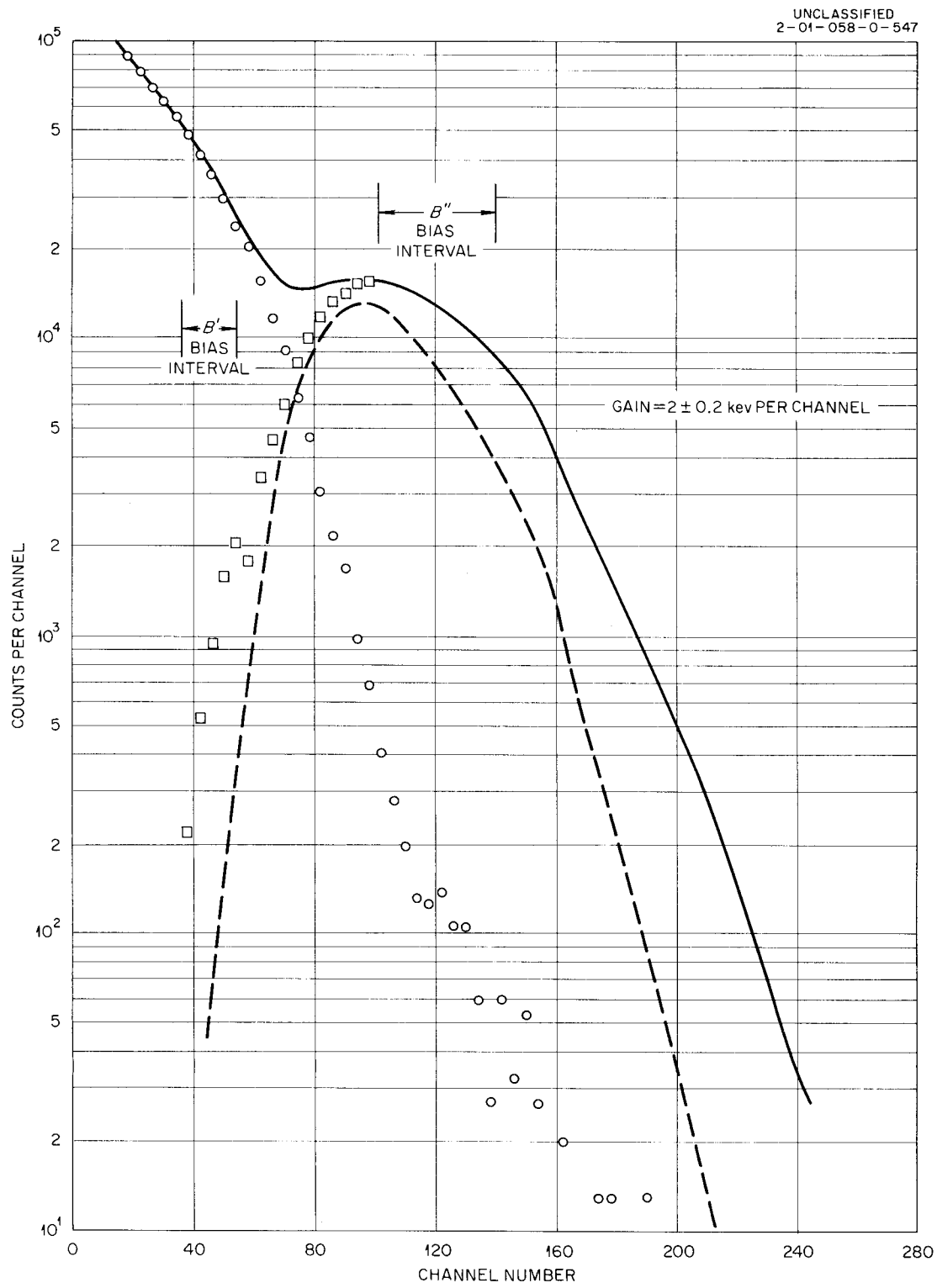

Fig. 4.6.2. Hg^{203} Beta-Ray Spectra as Observed in the Plastic Phosphor. The solid line is the ungated spectrum of pulses from the counter, composed of contributions from the beta rays from the source as well as the spectrum of summed coincidence pulses of beta rays with conversion electrons from the 279-kev transition in Tl^{203} and a small contribution from gamma-ray interactions in the plastic counter. The ordinate scale is determined by this solid curve. The circles represent the visually normalized spectrum of pulses observed in the plastic phosphor in coincidence with 279-kev gamma rays, supposedly from beta rays unaccompanied by conversion electrons. The squares are the difference, and together with the solid line at higher pulse heights, presumably represent the spectrum of coincidence-summed pulses from beta rays and conversion electrons. The dotted line represents the shape of the K conversion plus beta ray spectrum as inferred from the spectrum of pulses in coincidence with K x rays.

Note that independent evidence indicates that the squared points fall at too high a number of counts per channel, presumably because of a small counter gain difference between the two spectra subtracted to yield these points.

The pulse-height intervals indicated (B' and B'') are those corresponding to the two pulse-height intervals employed with the beta-ray detector channel.

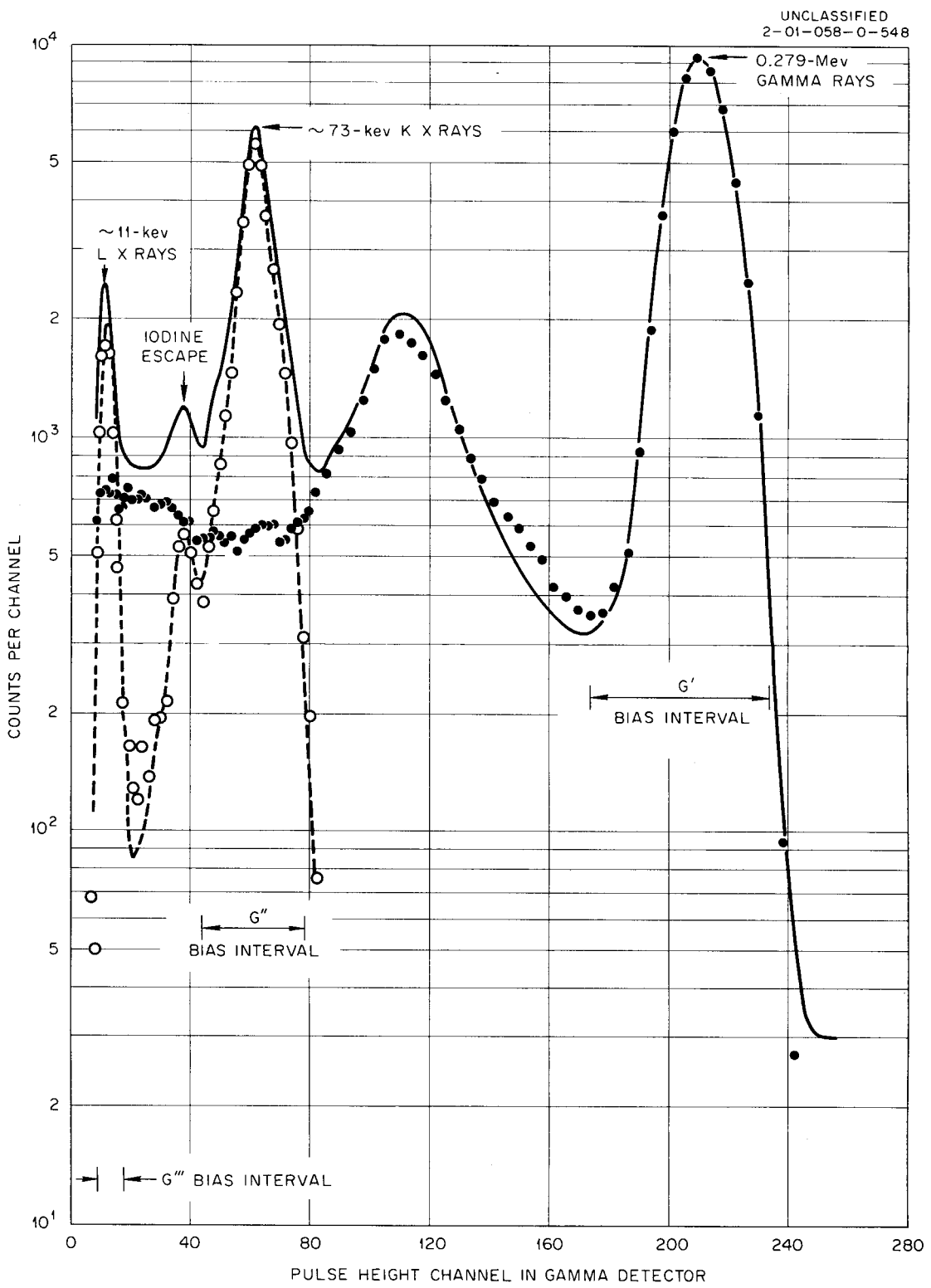

Fig. 4.6.3. Experimental Decomposition of the Photon Spectrum Observed in the NaI(Tl) Detector from the Hg^{203} Source Encapsulated in the Plastic Phosphor. The solid line is the observed ungated spectrum, and the ordinate scale is determined by these data. The solid points, normalized to the ungated spectrum at the pulse-height peaks corresponding to the 0.279-Mev gamma ray, represent the pulse-height spectrum of 0.279-Mev gamma rays alone obtained by observing those pulses in the gamma counter in coincidence with beta rays detected using the type-($'$) bias in the electron counter. The circle points are the difference between these two curves in the x-ray energy region, differences at higher energies presumably being caused by detection of scattered gamma rays. The broken line is the normalized gated spectrum obtained in coincidence with conversion electrons (plus beta rays) detected using the type-($''$) bias in the plastic counter. The small differences between the circle points and the dotted line are explained largely by the relative efficiency of detection for K and L conversion electrons within this bias interval. The pulse-height intervals indicated (G', G'', G''') are those corresponding to the three pulse-height intervals employed with the gamma-ray detector channel.

region for which the gamma-ray detector acceptance was biased are:

- ′ Pulses corresponding to the photopeak of the 279-kev gamma ray
- ″ Pulses from the Tl^{203} K x rays, along with some residual tail from the gamma-ray transition
- ‴ Pulses from Tl^{203} L x rays, along with tail from higher energy transitions

The i symbols identifying the pulse-height region for which the beta-ray detector acceptance was biased are:

- ′ Pulses largely from beta rays not in coincidence with any conversion electrons
- ″ Pulses largely from coincidence-summed beta and conversion electron pulses

Pulse-height regions corresponding to j and i are indicated in Figs. 4.6.2 and 4.6.3. The corresponding lower-case symbols, g^j_γ, g^j_K, g^j_L, etc., are the efficiencies of the gamma-ray detector for the subscript electromagnetic radiations with the superscript bias settings, and b^i_β, b^i_K, b^i_L, etc., the efficiencies for various fast-electron-yielding transitions to be counted in the plastic phosphor. Because these efficiencies include the effect of pulse-height biases, the b^i need not be close to unity. It is implied, for example, that b^i_K is the efficiency of the plastic phosphor for the (true) coincidence summed pulses, each resulting from the absorption of a beta ray chosen at random from the beta-spectral distribution in coincidence with a K-shell conversion electron. Coincidence counting rates are written in the form $\binom{B^j}{G^i}$. The superscript indices for all quantities are denoted with primes as indicated above.

First, consider the equations for the gamma-ray strength based on measurements with type-(′) biasing, for which no x rays are detected in the NaI crystal:

$$\left.\begin{aligned} G' &= Q\gamma g'_\gamma \quad , \\ B' &= Q(\gamma b'_\beta + e_K b'_K + \ldots) \quad , \\ \binom{B'}{G'} &= Q\gamma b'_\beta g'_\gamma \quad . \end{aligned}\right\} \tag{1}$$

In the equation for B' the terms in e_L, etc., have been omitted because the (′) biasing attempts to prevent detection of any conversion electrons, and the L-conversion electrons have an even lower detection probability than the K electrons because of their higher energy. The equations may be combined to yield:

$$\frac{B'G'}{\binom{B'}{G'}} = Q\gamma\left(1 + \frac{e_K b'_K}{\gamma b'_\beta}\right) \quad . \tag{2}$$

In practice, the correction term in Eq. 2 was so small (~0.5%) that any reasonable value of the conversion coefficient e_K/γ yields adequate accuracy for a determination of the gamma-ray strength $Q\gamma$. The value of b'_K/b'_β can be estimated by looking carefully for any evidence of K x rays in the coincidence spectrum obtained using the b' biasing.

To obtain information about the conversion coefficient it is necessary to study the analogs of Eqs. 1 for the type-($''$) bias of the plastic phosphor which accepts only the higher-energy pulses corresponding largely to detection of conversion electrons (plus a beta ray) in this detector. Such pulses can also be produced by simultaneous detection of a beta particle and the associated gamma ray in the plastic counter, and it is assumed in the equations below that this effect has been subtracted as a background along with any residual counts from noncoincident beta rays. For the NaI detector both type-($''$) bias, accentuating the K x-ray detection, and type-($'''$) bias accentuating the L x ray are pertinent. The relations for these quantities follow:

$$B'' = Q(e_K b_K'' + e_{LMN} b_L'') \ , \tag{3}$$

$$G'' = Q(\gamma g_\gamma'' + e_K x_K g_K'') \ , \tag{4}$$

$$G''' = Q[\gamma g_\gamma''' + e_K x_K g_K''' + x_L g_L'''(e_L + e_K C_{KL})] \ , \tag{5}$$

$$\begin{pmatrix} B'' \\ G'' \end{pmatrix} = Q e_K b_K'' x_K g_K'' \ , \tag{6}$$

$$\begin{pmatrix} B'' \\ G''' \end{pmatrix} = Q[x_K g_K''' e_K b_K'' + x_L g_L'''(e_L b_L'' + e_K b_K'' C_{KL})] \ . \tag{7}$$

The e_{LMN} of Eq. 3 is defined to be the total internal conversion probability less e_K. The efficiency for M and N conversion electrons is assumed to be the same as for the L electrons because of the relatively small energy differences between the outer shells. The symbol C_{KL} is defined to be the fraction of K-shell vacancies which produce L-shell vacancies either through x ray or Auger electron emission. Coincidence rates other than those of Eqs. 6 and 7 are defined analogously.

Reduction of Eqs. 3–7 becomes possible after simplifications are introduced. Observation of data such as that of Fig. 4.6.1 suggests that terms including g_K''' can be neglected. Furthermore, terms like $Q\gamma g_\gamma''$ in Eq. 4 and $Q\gamma g_\gamma'''$ in Eq. 5 can be evaluated and subtracted by comparisons such as Fig. 4.6.1 between normalized gated and ungated spectra in the gamma-ray detector. The evaluation and subtraction can be handled numerically by the following relations[6] which also define $\overline{G}''$ and $\overline{G}'''$:

$$G'' - \overline{G}'' \equiv Q\gamma g_\gamma'' = \frac{Q\gamma b_\beta' g_\gamma''}{b_\beta'} = \begin{pmatrix} B' \\ G'' \end{pmatrix} \frac{G'}{\begin{pmatrix} B' \\ G' \end{pmatrix}} \ , \tag{8}$$

and similarly

$$G''' - \overline{G}''' \cong Q\gamma g_\gamma''' = \begin{pmatrix} B' \\ G''' \end{pmatrix} \frac{G'}{\begin{pmatrix} B' \\ G' \end{pmatrix}} \ . \tag{9}$$

---

[6]Note that these relations assume $b_K' = 0$. In practice, a correction of a few per cent must be made for $b_K' \neq 0$.

With the help of Eq. 8, Eqs. 3, 4, and 6 can be combined to yield

$$\frac{B''\bar{G}''}{\begin{pmatrix} B'' \\ G'' \end{pmatrix}} = Qe_K \left[1 + \left(\frac{e_{LMN}}{e_K} \right) \left(\frac{b_L''}{b_K''} \right) \right] \quad . \tag{10}$$

This is the desired result for Qe_K except for the correction term which depends on the relative efficiency of the plastic counter and its detector channel for the K and L conversion electrons. This efficiency ratio is reflected in the relative strengths of the K and L x rays in the coincidence experiments described by Eqs. 6 and 7 compared to the ungated observations described in Eqs. 4 and 5. Therefore information concerning b_L''/b_K'' is contained in the experimental value of the factor F defined below using a combination of these equations:

$$F = \frac{\bar{G}''}{\begin{pmatrix} B'' \\ G'' \end{pmatrix}} \frac{\begin{pmatrix} B'' \\ G''' \end{pmatrix}}{\bar{G}'''} = \frac{e_K C_{KL} + e_L (b_L''/b_K'')}{e_K C_{KL} + e_L} \tag{11}$$

or

$$\frac{b_L''}{b_K''} = F + C_{KL}(F-1)\frac{e_K}{e_L} \quad . \tag{12}$$

Values obtained from Eqs. 12 and 10 may be combined to yield the strength of the K x ray ($Qe_K x_K$) provided a literature value of the K-fluorescent yield (x_K) is adopted and Eqs. 2, 10, and 11 together with an estimate of the small correction b_K'/b_β' yield either the K-shell conversion coefficient $e_K/\gamma = \alpha_K$ or the total conversion coefficient α. All such results depend on literature values of ratios between the conversion coefficients[3] and C_{KL},[7] which is estimated to have the value 0.80 ± 0.025.

Results

The gamma-ray strength of the Hg^{203} source encapsulated in the plastic phosphor was found to be (5750 ± 30) gammas/sec, the average of three fairly independent runs performed over the course of a few days. The quoted error is based on the scatter between the three observations and is larger than that (±17 gammas/sec) derived from counting statistics alone.

Five coincidence runs were made to determine the strength of the conversion electron source using different choices of the range of pulse heights included in the B'' counting rate. Two of these runs were eliminated because the lower bias levels were set so low that large and rather poorly known corrections had to be made to the B'' count rates for detection of beta rays alone and for detection of beta-gamma coincidences in the plastic counter. The remaining three runs are in fortuitous agreement, yielding a value Qe_K = (942 ± 35) electrons/sec. Table 4.6.2 shows

[7] P. R. Gray, *Phys. Rev.* 101, 1306 (1956); A. E. Sandström, p 226, vol 30, *Handbuch der Physik*, Springer, Berlin, 1958.

the values of some of the important quantities for the three runs, and Table 4.6.3 lists the relative errors in the inputs to the calculations and the propagated relative errors in the result for one of these runs. It is clear from Table 4.6.3 that the governing source of error in the conversion electron runs was the uncertainty in $\bar{G}'''$, a corrected ungated counting rate. In fact, the largest error in each of the runs shown in Table 4.6.2 was the uncertainty in the background count associated with G'''.

Table 4.6.2. Experimental Results for the Rate of Emission of Conversion Electrons for the Source Studied[a]

Run No.	$\frac{B''\bar{G}''}{\binom{B''}{G''}}$ (sec^{-1})	F	$\frac{b''_L}{b''_K}$	Qe_K (sec^{-1})	$\delta(Qe_K)$ (ref b) (sec^{-1})
2	1492	1.15	1.50	945	55
3	1417	1.09	1.31	942	50
5	1631	1.28	1.91	940	93

[a]See Eqs. 10, 11, and 12 in text.

[b]Estimated standard deviation: see Table 4.6.3. Note that the errors on the first two runs are highly interdependent because they arise largely from a common value of $\bar{G}'''$ which enters into the result through F.

The final result for the K-shell internal conversion coefficient is $\alpha_K = 0.164 \pm 0.006$ and for the total conversion coefficient, $\alpha = 0.227 \pm 0.008$. The ratio between these is taken from the literature, but as seen from Table 4.6.3, the value of α is much the less influenced should the literature values of the conversion electron intensity ratios prove to be much less accurate than indicated by Table 4.6.1. The doubtful runs (1 and 4) yielded smaller conversion coefficients.

The method used here is capable of producing more dependable results when applied to this isotope. Three obvious steps toward this end could be taken by another experimenter:

1. More care can be exercised in the determination of the quantities which yielded the largest error estimates in this experiment, such as $\bar{G}'''$. During the present experiment it was not realized that the result would be so sensitive to this determination.
2. The plastic counter was much thicker than necessary, with the result that about 5% of the 0.28-Mev gamma rays interacted in the plastic. Such a counter can be designed to lower the gamma sensitivity by at least a factor of 3 while nevertheless stopping all fast electrons emitted by the source. Estimates of any residual effect of the gamma interactions would be aided if the pulse height vs absorbed energy scale in the plastic were more accurately established than in the present case.
3. Steps should be taken to assure radiochemical purity of the source.

Table 4.6.3. Propagation of Errors in the Determination of Qe_K and Qe (ref *a*)

Typical values shown are from run 3 of Table 4.6.2

q_i	$\frac{\delta q_i}{q_i}$ (ref *b*)	$\frac{\partial(Qe_K)}{\partial q_i}\frac{\partial q_i}{Qe_K}$ (ref *c*)	$\frac{\partial(Qe)}{\partial q_i}\frac{\partial q_i}{Qe}$
	$\times 10^{-2}$	$\times 10^{-2}$	$\times 10^{-2}$
B''	0.5	0.5	0.5
$\bar{G}''$	0.6	0.05	0.05
$\begin{pmatrix} B'' \\ G'' \end{pmatrix}$	0.5	0.04	0.04
$\bar{G}'''$	3.4	3.1	3.1
$\begin{pmatrix} B'' \\ G''' \end{pmatrix}$	1.2	1.1	1.1
C_{KL}	3.1	0.2	0.2
$\frac{e_L}{e_K}$	1.5	1.1	0.003
$\frac{e_M + e_N}{e_L}$	3.3	0.26	0.04

[a] $e \equiv e_K + e_L + \ldots \equiv 1 - \gamma$.

[b] The estimated relative error in the quantity labeled q_i.

[c] The relative error in the result for Qe_K or Qe propagated from the estimated relative error in q_i.

The second and third items above would reduce the plausible systematic errors in the determination, while only the first would much affect the error estimate quoted on the result. Note that the discarding of two runs was related to item 2 above.

The method here used depends rather heavily upon the details of the simple decay scheme of Hg^{203}. Few, if any, additional isotopes can be studied using the equations given. However, with additional analysis, it is believed that the requirements on the decay scheme could be slightly relaxed.

The value obtained for α_K for the 279-kev transition agrees with, but has a larger uncertainty than, the accepted value[3] of 0.162 ± 0.003. However, the method employed is independent of the systematic errors which arise in determining the beta-ray counting rate in the usual method. Therefore the confirmation provided by this experiment is considered valuable in the light of the difference[3] between the results of either experiment and calculated conversion coefficients.

Part 5

EXPERIMENTAL REACTOR PHYSICS

5.1 THERMAL-FLUX CALIBRATION IN SLOT 11 OF ORNL STANDARD GRAPHITE PILE

G. M. Estabrook

The ORNL Standard Graphite Pile was last calibrated in 1952.[1] Since then it has twice been dismantled and relocated; thus a recalibration was indicated. Methods and procedures for the present measurement paralleled those reported in 1952.

The thermal-neutron flux in slot 11 was calculated from gamma-ray activities induced in 1¼-in.-dia, 1-mil-thick gold foils as counted on an NaI scintillation counter of known efficiency. The efficiency of the scintillation counter was defined as the ratio of the count rate of an activated gold foil, measured on the NaI counter, to the absolute disintegration rate of the foil, measured in a high-pressure ionization chamber. A series of three foil exposures was made for the thermal-flux determination.

A Maxwellian distribution of neutron velocities with a most-probable velocity, v_0, corresponding to room temperature (2200 m/sec or 0.025 ev) was assumed. The thermal flux was independently calculated for each of the foil activations from the formula

$$nv_0 = \frac{AA_s}{EN_0 m \sigma_a} ,$$

where

A = atomic weight of gold, g/mole,

A_s = thermal saturated activity of the gold foil, dis/sec,

E = efficiency of the NaI counter,

N_0 = Avogadro's number, atoms/mole,

m = mass of gold foil, g,

σ_a = 2200-m/sec absorption cross section of gold, cm^2/atom.

A perturbation correction of 4.2%, computed according to Skyrme's theory,[2] was applied to each gold-foil thermal activity.

The value of the absolute thermal flux for 2200-m/sec (most-probable velocity) neutrons, obtained by averaging the results of all measurements, is $nv_0 = 635 \pm 32$ neutrons cm^{-2} sec^{-1}.

Since there is a range of neutron velocities in the thermal region, and since the thermal cross section for gold is proportional to $1/v$ in this region, one may be interested in the flux for average-velocity neutrons. Kaplan[3] gives for a Maxwellian distribution:

$$\bar{v} = \frac{2}{\sqrt{\pi}} v_0 = 1.128\, v_0 ,$$

---

[1] E. D. Klema, R. H. Ritchie, and G. McCammon, *Recalibration of the X-10 Standard Graphite Pile*, ORNL-1398 (Oct. 17, 1952).

[2] T. H. R. Skyrme, *Reduction in Neutron Density Caused by an Absorbing Disc*, MS-91.

[3] I. Kaplan, *Nuclear Physics*, p 458–64, Addison-Wesley, Cambridge, Mass., 1955.

indicating that the average velocity is ~ 13% higher than the most-probable velocity. Thermal-neutron cross sections are usually given for the most-probable-velocity neutron. Because the gold thermal cross section varies inversely with the velocity, the cross section for average-velocity neutrons will be ~ 13% lower than that for the most-probable velocity. This cross section, usually called the effective cross section, $\bar{\sigma}$, is expressed[4] as

$$\bar{\sigma} = \sigma(\bar{v}) = \frac{\sigma \text{ at most-probable velocity}}{1.128} .$$

The thermal-neutron flux for average-velocity neutrons, sometimes called the "true" thermal-neutron flux, is obtained by using the effective cross section in the calculations or by multiplying the 2200-m/sec flux by the factor 1.128. Application of this factor to the value of nv_0 obtained above gives the thermal-neutron flux for average-velocity neutrons: $n\bar{v} = 716 \pm 36$ neutrons cm^{-2} sec^{-1}. The flux obtained for average-velocity neutrons from the 1952 calibration[1] was $n\bar{v} = 703 \pm 35$ neutrons cm^{-2} sec^{-1}. (The error shown was not reported in ref 1 but was estimated at a later time.)

[4] R. L. Murray, *Nuclear Reactor Physics*, p 30–33, Prentice-Hall, New York, 1957.

5.2 A NEUTRON CHOPPER SPECTROMETER FOR THE BULK SHIELDING FACILITY

V. V. Verbinski

Introduction

The preliminary design of a neutron chopper spectrometer for the Bulk Shielding Facility, to be located underground adjacent to the pool of the Bulk Shielding Reactor (BSR), has been completed. Construction of the spectrometer facility is expected to be completed in late 1961. It will be used for the study of aspects of reactors and shields which cannot presently be treated with adequate confidence by available calculational techniques. The spectral measurements should either substantiate the calculational methods or direct further study. The proposed program of experiment, following initial alignment, will include spectral measurements in pure and mildly borated water, for comparison with existing data from other installations, and measurements of the energy and angular distribution of neutrons diffusing from the shield-air interface of a highly poisoned hydrogenous shield. Spectral measurements within a shield, spectra from several regions of the BSR, and spectra as functions of position in reactor lattices will also be observed.

Design

General. – A schematic diagram of the chopper spectrometer is shown in Fig. 5.2.1. The BSR is shown near the wall of its pool, adjacent to a metal window, through which the neutrons pass into an experimental cell in which a shield sample or a reactor matrix may be positioned. Neutrons penetrating the sample are collimated to a rotating chopper, leave the chopper through an exit collimator to an evacuated drift tube, and finally are intercepted by a stack of BF_3-filled proportional counters. A boral-lined beam-catcher tube, terminated with paraffin to reduce back scattering, catches the neutrons which penetrate the stack of counters. The flight path is about 10 m, which, with 0.065-in. slits in an 18-in.-dia rotor spinning at 10,000 rpm, will give an energy resolution of about 10% at 100 ev, 3% below 10 ev, and 30% at 1000 ev.

Rotating Chopper. – The mechanical chopper, based largely on the design experience obtained with the ORR fast-neutron chopper, was designed to yield maximum transmission of neutrons consistent with the resolutions noted above. Rotor and collimators are made of Monel. A large-diameter Monel rotor will produce a sharp neutron burst over a wide range of neutron energies. A small and reasonably constant value of edge leakage as a function of neutron energy is important for accurate calculation of the chopper transmission function. The rotor is suspended from a thin quill for operation at high speeds, while fixed bearings will be clamped on for low-speed operation to prevent serious resonance oscillations noted in a pilot model.

Instrumentation. – Pulses from the stack of high-pressure BF_3-filled proportional counters terminating the flight path will go to a 256-channel time-of-flight analyzer that is gated "on" with a "start" pulse from the chopper. Each of the 256 channels can have a preselected window width of 2.5, 5, 10, 20, 40, or 80 μsec to cover the time-of-flight range corresponding to a neutron energy range of 0.005 to 1000 ev. The several rotor speeds needed to cover this range can be maintained to better than one part in 500 by a specially designed speed control. The analyzer will have a punched-tape readout coded for the Oracle, which will transform the time-of-flight data to neutron spectra in conformance with the factors discussed below.

The total count rate of all counts entering the analyzer will be monitored. The neutron flux entering the chopper will also be monitored by a small, thin-walled, low-pressure BF_3 counter, and the outputs of the two monitors will be compared to help detect the sources of possible drifts and errors, such as reactor power-level changes and rotor–collimator misalignment. The input monitor will also serve to normalize the several pieces of the spectral curve obtained at the several rotor speeds required.

Energy Spectrum from Time-of-Flight Spectrum

Basic. – The neutron energy E is related to the measured time of flight by

$$E(\text{ev}) = \left(\frac{72.3}{\tau}\right)^2 \frac{\mu\text{sec}}{\text{m}} , \qquad (1)$$

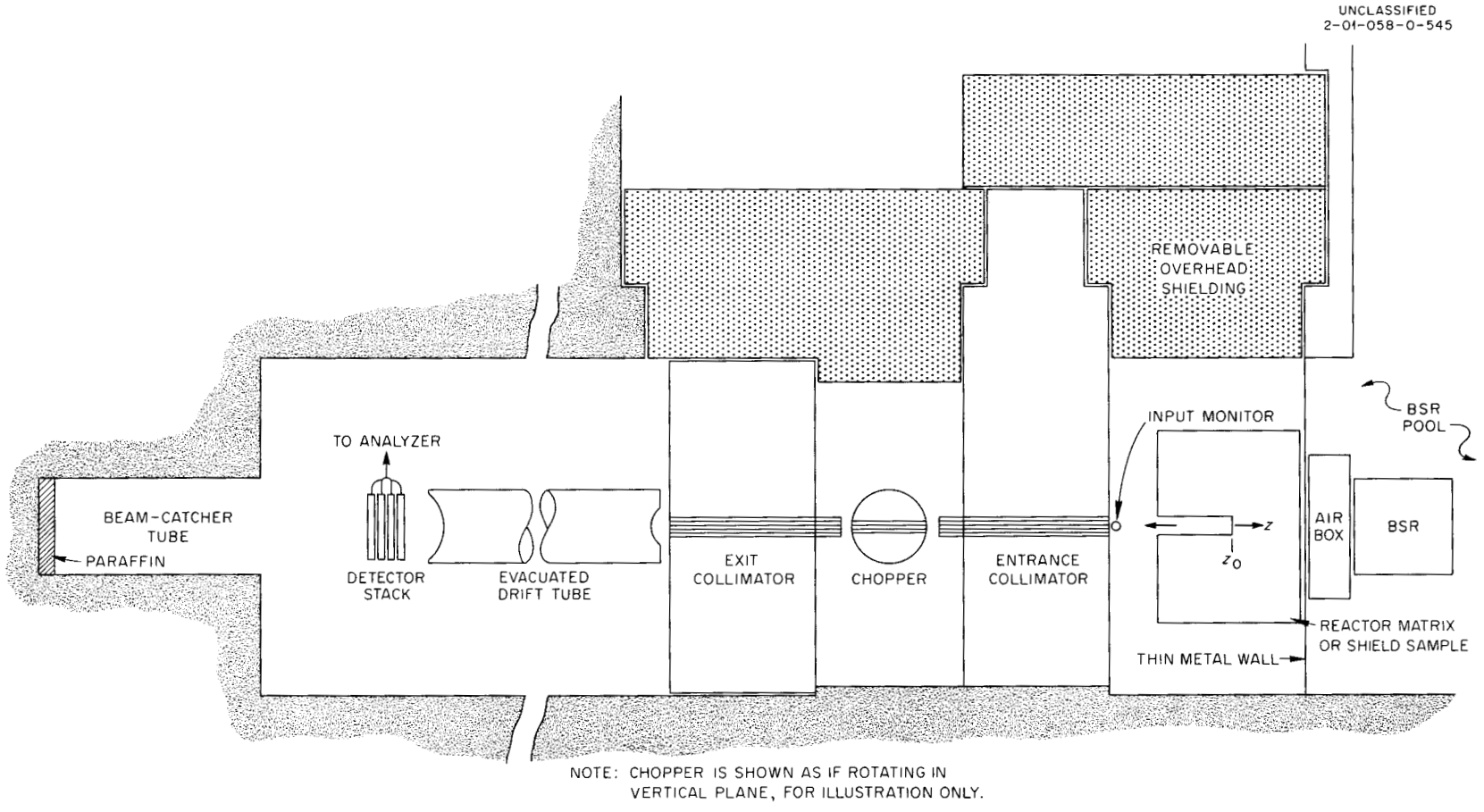

Fig. 5.2.1. Schematic of Proposed Neutron Chopper Spectrometer for the Bulk Shielding Facility.

and if all other factors are constant with energy,

$$\frac{dN}{dE} = \frac{dN}{d\tau}(\text{constant})\tau^3 \quad , \tag{2}$$

where $dN/d\tau$ vs E is the true time-of-flight spectrum.

Energy Dependence of the Detector. – The stack of BF_3 counters will tend to saturate in the thermal-energy region but elsewhere will have a $1/v$ response. The detector stack will be calibrated over the entire energy range with a single, low-pressure BF_3 counter. In the epithermal region, the correction for counter response will be

$$\frac{dN}{d\tau} = \frac{1}{\tau}\frac{dN'}{d\tau} , \tag{3}$$

where $dN'/d\tau$ would be the observed time-of-flight spectrum if the transmission of the rotor were energy independent and if the background counts were properly subtracted.

Chopper Transmission Function. – After the background is properly subtracted, the time-of-flight spectrum $dN''/d\tau$ observed with a $1/v$ detector is related to the true time-of-flight spectrum by

$$\tau C_\tau \frac{dN}{d\tau} = \frac{dN''}{d\tau} , \tag{4}$$

where C_τ is the chopper transmission function. For the forward-directed neutron flux, from Eq. 2,

$$\frac{dN}{dE} = \frac{\tau^2\, dN''}{d\tau}\frac{1}{C_\tau} \tag{5}$$

for a $1/v$ detector. Note that in the region of the spectrum where $dN/dE = (\text{constant})/E = (\text{constant})\tau^2$,

$$(\text{constant})\tau^2 = \tau^2 \frac{dN''}{d\tau}\frac{1}{C_\tau} , \tag{6}$$

or

$$\frac{dN''}{d\tau} = (\text{constant})C_\tau \quad . \tag{7}$$

Thus, under the conditions of a $1/v$ detector response, a forward-directed flux with a $1/E$ energy dependence, and proper background subtraction, the exact shape of C_τ is displayed on the time-of-flight analyzer. Since the conditions can be very nearly obtained, the calculated shape of C_τ can be checked. Final check and adjustment of C_τ will be made by measuring a spectral region at a number of rotor speeds. In general, only the correct shape of C_τ will produce a single-valued curve.

Background. – In a stable system, the background is a periodic function of rotor position because of neutron leakage through the array of rotor slits. As the slits are rotated, the amount

of Monel in the path of the collimated neutron beam will vary. The time dependence of this variation in leakage will be symmetric about the "burst" time (the time when the slits are fully open) if the slit geometry is symmetric about the longitudinal center line of the slit. For this reason, the proposed rotor will have symmetric slits.

The time-of-flight analyzer is gated "on" many channels before the burst time so that the background is displayed. The very fast leakage neutrons, those that traverse the flight path within a burst width, can be subtracted out, channel by channel, counting from the burst time. The bulk of the leakage arises from these neutrons because the rotor is relatively transparent to high-energy neutrons. Slower-neutron leakage can be estimated in many ways, for example, by moving the neutron counters close to the chopper, by inserting a cadmium foil in the beam, or by changing the chopper angular velocity, in each case noting the change of shape of the displayed curve.

Relationship Between the Forward-Directed Flux and the Total Flux. – Consider a reentrant hole in a reactor matrix or a shield slab, as shown in Fig. 5.2.1. The chopper spectrometer measures the forward-directed flux crossing the $z = z_0$ plane at the bottom of the hole. This forward-directed flux is made up of neutrons scattered from various depths z behind the z_0 plane. The directed neutron flux, $\phi(\mu,E,z_0)$, is not, in general, equal to the total flux $\phi(E,z_0)$ at the same point. Where the diffusion theory approximations are valid, the following relationship holds:[1,2]

$$\phi(\mu,E,z_0) = (\text{constant})\ \phi(E,z_0) \left[1 + \frac{\lambda_t(E)}{\phi(E,z_0)} \frac{\partial\phi}{\partial z}(E,z)\bigg|_{z=z_0} \right] , \tag{8}$$

where $\mu = \cos\theta$ and θ is the angle to the normal of the z_0 plane; $\lambda_t(E)$ is the transport mean free path at energy E. Most of the previous time-of-flight measurements were made under conditions where this approximation was valid; z_0 is located near the center of a reactor matrix, near the center of a moderator volume with a pulsed-neutron source also near the center, or the moderator cross section is fairly independent of energy [$\lambda_t(E) \cong$ constant]. Note that such configurations could be used to obtain a $1/E$ forward-directed flux from a $1/E$ total-flux region. This could then be used to obtain $C_{\tau'}$ as discussed earlier.

However, the above relationship is not expected to be valid where a source is located exterior to the shield and where the shield is hydrogenous, with a strong $1/v$ poisoning. Here $\partial\phi/\partial z$ and $\partial\lambda_t(E)/\partial E$ are both large, and the diffusion theory approximations completely break down. Purohit[3] has investigated the problem by using transport theory with the Goertzel-Selengut approximation [$J(E,z') \cong J(E,z)$]. Retaining terms to $\partial^2\phi/\partial z^2$, he obtains

---

[1]R. E. Slovacek and R. S. Stone, *Low-Energy Spectra Measurements*, a paper presented at the Conference on Neutron Thermalization, Gatlinburg, Tennessee, April 1958.

[2]C. G. Campbell *et al.*, *Proc. U.N. Intern. Conf. Peaceful Uses Atomic Energy, 2d, Geneva, 1958*, 15/P/10.

[3]S. Purohit, *Milne Problem with Capture*, ORNL-3005 (Sept. 28, 1960).

$$\phi(\mu,E,z_0) = \phi(E,z_0) + c\,\frac{\partial\phi}{\partial z'}(E,z')\bigg|_{z'=z_0} + d\,\frac{\partial^2\phi}{\partial z^2}(E,z'^2)\bigg|_{z'=z_0} , \tag{9}$$

where

$$c = \frac{1}{\Sigma_t(E)}\,(a - \mu) ,$$

$$d = \frac{1}{\Sigma_t^2(E)}\,[b\,\Sigma_t(E) - a\mu + \mu^2] ,$$

and

$$a = \frac{2}{3}\,\overline{\mu^2}\left[1 - \frac{\Sigma_t(E)}{\Sigma_t(E) - \Sigma_s(E)\,\overline{\mu}_L}\right],$$

$$b = -\frac{\overline{\mu^2}}{\Sigma_t(E) - \Sigma_s(E)\,\overline{\mu}_L} ,$$

$\Sigma_t(E)$ = total macroscopic cross section,

$\Sigma_s(E)$ = macroscopic scattering cross section,

$\overline{\mu}_L$ = average of the cosine of the scattering angle in the laboratory system,

$\overline{\mu^2}$ = average of the square of the cosine of the angle between the z-axis and the directed flux.

The above expression reduces to Eq. 8 if the $\partial^2\phi/\partial z^2$ term is dropped, if the scattering in the sample is symmetric in the laboratory system, and if $\mu = 1$. But for a highly poisoned, hydrogenous medium, the scattering is the least symmetric and the second derivative of the flux is quite strong in the geometric arrangements required.

Since the above relationship contains known functions of μ, E, and the material constants, only the gradient of the flux and its second derivative need be measured to obtain the energy dependence of the total flux from the measured energy dependence of the directed flux. These flux plots are now being made for a mixture of methyl borate and methanol with a value of $C = \Sigma_s/\Sigma_t$ equal to that for LiH.

Hole Perturbation. – A re-entrant hole might be expected to perturb the spectrum at z_0, the bottom of the hole. However, the work done at General Atomic[4] with both poisoned and unpoisoned polyethylene demonstrates that as the hole diameter is increased to several inches no spectral change is observed. Of course, the situation should be somewhat worse with very high poison content because λ_t becomes much smaller at low energies. The effect of hole perturbation can be determined by the "hohlraum" technique, in which the shield is sliced

[4] J. R. Beyster *et al.*, *Measurement of Low Energy Neutron Spectra*, GA-1088 (Nov. 13, 1959).

through the z_0 plane, at the bottom of the re-entrant hole, and a change of spectral shape is looked for as the separation w between the two shield halves is increased. If the spectrum does change with w for small values of w, but then reaches an equilibrium value for larger values of w, one of these larger values will be used for all subsequent measurements. The hohlraum technique is applicable only if the flux in the z_0 plane is constant over a distance of several w's. A gold-wire flux plot will be used to determine the applicability of the technique.

5.3 AN APPLICATION OF THE PULSED-NEUTRON TECHNIQUE TO REACTOR STUDY

R. Perez-Belles G. deSaussure E. G. Silver

Introduction

The pulsed-neutron technique[1] can be used to measure the decay constant, λ, of the fundamental mode of the neutron distribution in an unreflected moderating assembly following the injection of a burst of neutrons. The fundamental mode of the neutron distribution in such an experiment satisfies the Helmholtz equation:

$$\nabla^2 n + k^2 n = 0 \quad , \tag{1}$$

where the lowest eigenvalue k^2 is given by

$$k^2 = \frac{\lambda - \lambda_a}{D} \quad , \tag{2}$$

in which λ_a is the inverse lifetime of the neutrons in the moderator, and D is the diffusion constant. If λ_a and D are known for a particular moderator, the method affords a means to determine the lowest eigenvalue of Helmholtz' equation for a given geometry, and can be applied[2] to the experimental solution of problems in mathematics, acoustics, reactor theory, and other fields.

When applied to reactor theory, Eq. 1 describes the spatial behavior of the neutron density in an all-thermal, critical bare reactor. In this case the lowest eigenvalue is the buckling, B^2, and various methods have been proposed to calculate the change in buckling when a control rod is inserted in the reactor. The pulsed-neutron technique provides a means of experimentally measuring this quantity and thus testing the theoretical models.

---

[1] G. von Dardel and H. G. Sjöstrand, *Progr. in Nuclear Energy Ser. 1* **2**, 183 (1958).
[2] H. G. Sjöstrand, *Arkiv Fysik* **15**, 147 (1959).

Experimental Procedure

The moderating assemblies used for these experiments were rectangular prisms of beryllium, built in several sizes from small 1-in.-high, $2\frac{7}{8}$-in.-square blocks. Each block had a $\frac{3}{16}$-in.-dia hole through its center, so that the completed prisms contained a series of $\frac{3}{16}$-in.-dia channels on $2\frac{7}{8}$-in. centers. Three types of cadmium control rods were used: thin $\frac{3}{16}$-in.-dia rods, which could be inserted in the $\frac{3}{16}$-in. channels; a cruciform-section rod, with four arms or blades each 0.030 in. thick and $1\frac{7}{16}$ in. wide, which could be inserted between a stack of blocks without appreciably distorting the assembly; and hollow "thick" rods, formed of 0.050-in. cadmium sheet with a square $2\frac{7}{8}$- by $2\frac{7}{8}$-in. cross section. Insertion of the thick rod required removal of a stack of beryllium blocks.

In each experiment the decay constant of thermal neutrons was measured in the clean beryllium assembly; then the cadmium rods were inserted and a new decay constant measured. Details of the pulsed-neutron technique employed have been previously reported.[3] The changes in buckling corresponding to the measured changes in the decay constant were obtained from the results of previous work.[3]

Experimental Results and Comparison with Calculations

Thin Cadmium Rods. – Four measurements were made using the $\frac{3}{16}$-in.-dia cadmium rods in a beryllium assembly $20\frac{1}{8}$ by $20\frac{1}{8}$ by 20 in. high. The buckling of this assembly, without rods, was 1.05×10^{-2} cm^{-2}; its decay constant was 1.58 ± 0.02 kc. Rod configurations are shown in Fig. 5.3.1, and the experimental values of the decay constant, the corresponding changes in the buckling, and the change in buckling computed by the Nordheim-Scalettar method[4] are given in Table 5.3.1. Comparison of results shows agreement between experiment and calculation for one-, two-, and four-rod configurations, but for the eight-rod configuration the computed change in buckling is $\sim 20\%$ greater than the experimental result.

Cruciform-Section Rods. – A single experiment was performed with the cruciform-section rod described above. The 20-in.-long rod was placed vertically at the center of a 20-in.-high, $17\frac{1}{4} \times 17\frac{1}{4}$ in. assembly. Without the rod this assembly had a decay constant of 1.875 ± 0.02 kc and a buckling of 1.29×10^{-2} cm^{-2}. With the rod inserted the measured decay constant was 2.58 ± 0.07, corresponding to a buckling of $(1.87 \pm 0.06) \times 10^{-2}$ cm^{-2}, or a change in the buckling due to the rod of $(0.58 \pm 0.06) \times 10^{-2}$ cm^{-2}.

In order to calculate a value for this configuration, the cruciform rod had to be converted to an equivalent cylinder, since the Nordheim-Scalettar method only applies to circular cylinders.

---

[3] G. deSaussure and E. G. Silver, *Determination of the Neutron Diffusion Parameters in Room Temperature Beryllium*, ORNL-2641 (1959).

[4] L. W. Nordheim and R. Scalettar, *Theory of Pile Controls*, MDDC-42 (1946) and *Phys. Rev.* **70**, 115 (1946); see also G. V. Sinyutin and V. M. Semenov, *Proc. U.N. Intern. Conf. Peaceful Uses Atomic Energy, 2d, Geneva, 1958*, 15/P/2469.

UNCLASSIFIED
ORNL-LR-DWG 52287

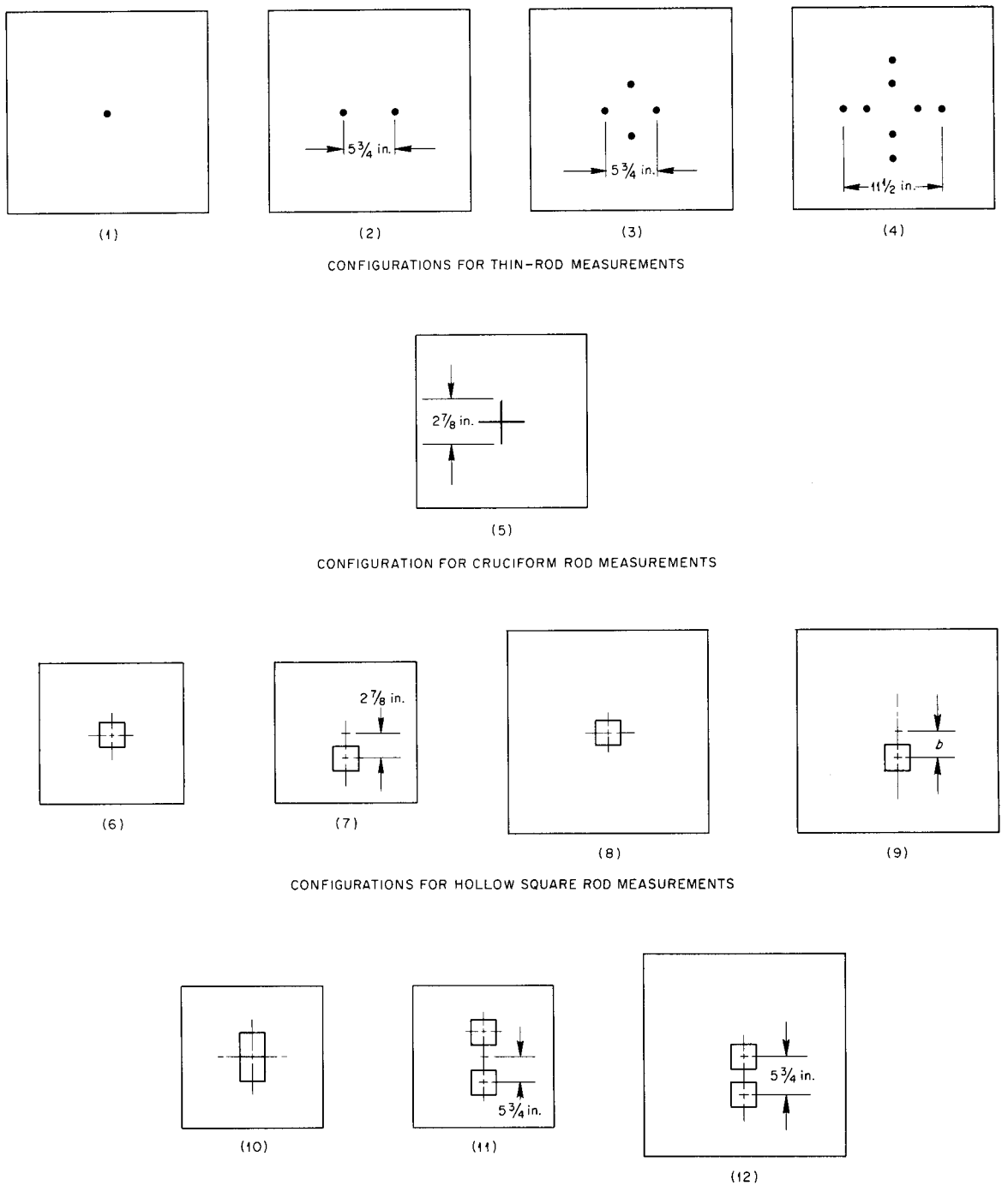

Fig. 5.3.1. Configurations Used in Decay-Constant Measurements with Cadmium Rods in Beryllium Assemblies.

Table 5.3.1. Changes in Decay Constants and Buckling Due to Insertion of Thin Cadmium Rods into a Beryllium Assembly

Configuration*	Decay Constant (kc)	B^2, Buckling (cm^{-2})	Change in B^2 (10^{-2} cm^{-2})	
			Measured	Computed
1	1.70 ± 0.02	0.0114 ± 0.0002	0.093 ± 0.016	0.079
2	1.74 ± 0.02	0.0119 ± 0.0002	0.147 ± 0.014	0.136
3	1.91 ± 0.02	0.0132 ± 0.0002	0.269 ± 0.021	0.269
4	2.06 ± 0.02	0.0144 ± 0.0002	0.392 ± 0.021	0.472

*Configurations are shown in Fig. 5.3.1. All assemblies are 20 in. high and $20\frac{1}{8} \times 20\frac{1}{8}$ in. square. Cadmium rods are $\frac{3}{16}$ in. OD and 20 in. high.

The radius of the required equivalent cylinder was computed by two methods: that of Wheeler[5] and that of Hurwitz and Roe.[6] The change in buckling computed by the Nordheim-Scalettar method, using the radius from the Wheeler prescription, was 0.74×10^{-2} cm^{-2}, a value about 30% higher than the experimental result, and outside the experimental error. On the other hand, using the Hurwitz-Roe recipe for the radius gave a change in buckling of 0.59×10^{-2} cm^{-2}, in excellent agreement with the experiment.

Single Large, Hollow Rods. – Six measurements were made using one of the $2\frac{7}{8}$- by $2\frac{7}{8}$-in. hollow cadmium rods described above. The first two measurements were made with a 16-in.-long rod in a 16-in.-high, $14\frac{3}{8}$- by $14\frac{3}{8}$-in. beryllium assembly. The unpoisoned assembly had a decay constant of 2.565 ± 0.02 kc, giving a buckling of 1.86×10^{-2} cm^{-2}. Of the two measurements made, the first was performed with the cadmium box on the vertical axis of the assembly, the second with the axis of the box displaced $2\frac{7}{8}$ in. from the assembly axis.

The following four measurements with the single large, hollow rod were made with a 20-in.-long rod in a 20-in.-high, $20\frac{1}{8}$- by $20\frac{1}{8}$-in. beryllium assembly. The assembly without control rod had a decay constant of 1.58 ± 0.02 kc and a buckling of 1.05×10^{-2} cm^{-2}. The four measurements were made with the axis of the cadmium box first coincident with the axis of the assembly, then displaced successively $2\frac{7}{8}$, $5\frac{3}{4}$, and $8\frac{5}{8}$ in. from the center line.

For comparison calculations it was again necessary to convert the hollow cadmium box to an equivalent cylinder. Two methods were used. The first, the Hurwitz-Roe recipe, has been noted above. The second was designated as the "weighted equivalent radius" recipe.[7] In this method the radius of the circular cylinder equivalent to the box was obtained by equating the fractional areas of the control rod as box and cylinder, weighting each by the pertinent ratio of the local flux at the location of the control rod to the average flux in the assembly.

[5] J. Wheeler, quoted by H. Etherington, p 8–16 in *Nuclear Engineering Handbook*, McGraw-Hill, New York, 1958.

[6] H. Hurwitz and G. M. Roe, *J. Nuclear Energy* 2, 85 (1955).

[7] This method was suggested by A. Simon.

Table 5.3.2, which summarizes the data from the experiments with single large, hollow cadmium rods, shows that the results obtained by the second method are better, although neither gives good agreement with experiment.

Two Large, Hollow Rods. – Three measurements were made using a pair of $2\frac{7}{8} \times 2\frac{7}{8}$ in. cadmium boxes, with their lengths matched to the height of the particular beryllium assembly. The results, which are given in Table 5.3.3, show disagreement between experiment and calculation. This, of course, was to be expected, from the lack of agreement in the single box results noted above.

Table 5.3.2. Changes in Buckling Due to the Substitution of a Thin-Walled, Rectangular Cadmium Rod for One Stack of Beryllium in a Beryllium Assembly

Configuration[a]	Size of Assembly (in.)	δB^2, Change in Buckling (10^{-2} cm^{-2})			
		Measured	Computed: NS-HR[b]	Computed: NS-WER[c]	Computed: PDQ[d]
7	$16 \times 14\frac{3}{8} \times 14\frac{3}{8}$	1.49 ± 0.03		1.38	1.59
8	$16 \times 14\frac{3}{8} \times 14\frac{3}{8}$	1.35 ± 0.09		0.84	0.77
9: $b = 0$	$20 \times 20\frac{1}{8} \times 20\frac{1}{8}$	0.55 ± 0.02	0.65	0.58	0.67
9: $b = 2\frac{7}{8}$		0.27 ± 0.02	0.40	0.37	0.42
9: $b = 5\frac{3}{4}$		0.07 ± 0.02	0.18	0.17	0.20
9: $b = 8\frac{5}{8}$		0.02 ± 0.01	0.05	0.04	

[a]Configurations are shown in Fig. 5.3.1; b is the distance from the axis of the assembly to the axis of the rod. Rod length was equal to the assembly height.

[b]NS-HR indicates computation by Nordheim-Scalettar method, using Hurwitz-Roe recipe for equivalent cylinder.

[c]NS-WER indicates computation by Nordheim-Scalettar method, using weighted equivalent radius method for equivalent cylinder.

[d]PDQ calculation, x-y geometry.

Table 5.3.3. Changes in Buckling Due to the Substitution of Two Thin-Walled Rectangular Cadmium Rods for Two Stacks of Beryllium in a Beryllium Assembly

Configuration*	Size of Assembly (in.)	δB^2, Change in Buckling (10^{-2} cm^{-2})	
		Measured	Computed: PDQ**
10	$16 \times 14\frac{3}{8} \times 14\frac{3}{8}$	2.24 ± 0.15	1.84
11	$16 \times 14\frac{3}{8} \times 14\frac{3}{8}$	2.34 ± 0.05	2.14
12	$20 \times 20\frac{1}{8} \times 20\frac{1}{8}$	0.65 ± 0.02	0.70

*Configurations are shown in Fig. 5.3.1.

**PDQ calculation, x-y geometry.

PDQ Computations. – Failure of the Nordheim-Scalettar calculation to show agreement with experiment in the case of the large, hollow rods led to a test with the IBM 704 PDQ code for this problem. The code was used to perform x-y geometry calculations, using at the cadmium surface the boundary condition

$$\frac{D\nabla\phi}{\phi} = \frac{\lambda_{tr}}{3d} ,$$

where λ_{tr} is the beryllium transport mean free path and d the extrapolation length, taken as $0.77\lambda_{tr}$. Results, shown as parts of Tables 5.3.2 and 5.3.3, are generally about 10% higher than the values derived from experiment.

In order to investigate the possibility that better results might be obtained from the PDQ code by a change in the boundary condition at the surface of the cadmium box, a series of computations was performed in which the extrapolation length d was varied within wide limits. Results are shown in Table 5.3.4 and indicate that the changes in the buckling calculated by the PDQ code are not sensitively dependent upon the extrapolation length.

Table 5.3.4. Buckling and Change in Buckling Computed by the PDQ Code for the Case of a Thin-Walled Cadmium Rod Inserted in a Beryllium Assembly, for Various Assumed Extrapolation Lengths (Configuration 6)*

d/λ_{tr}	B^2, Buckling (cm^{-2})	δB^2 (10^{-2} cm^{-2})
0.68	0.03508	1.648
0.71	0.03491	1.631
0.74	0.03474	1.614
0.77	0.03456	1.596
0.83	0.03439	1.579

*Configuration is shown in Fig. 5.3.1. The assembly was 16 in. high, and the rod was 16 in. long.

Conclusions

The following conclusions may be made from these experiments: (1) The Nordheim-Scalettar method is adequate for calculations of changes in bucklings associated with one or more absorbing rods of small diameter compared with the transport mean free path in the moderator. (2) The Hurwitz-Roe recipe to convert a cruciform-section rod to an equivalent cylinder gives results that agree with experiment; the Wheeler recipe does not. (3) Both the Nordheim-Scalettar method and the PDQ code fail to predict correctly the buckling of the configurations containing boxlike cadmium rods, the cross-sectional dimensions of which are comparable with the transport mean free path in the moderator.

Both the Nordheim-Scalettar method and the PDQ code are based on diffusion theory and use the concept of extrapolation length to compute the buckling. This model may not be adequate for assemblies containing a large volume of black absorber, although this is somewhat surprising since the model permits very accurate computation of bucklings for cubical assemblies of even only a few mean free paths. Measurements with rods of intermediate sizes might make it possible to determine the point at which diffusion theory becomes inadequate.

A possibility also exists that the discrepancy between experiment and calculation is due to some presently unaccounted for systematic error in the measurements.

5.4 DETECTOR TECHNIQUES USED IN THE MEASUREMENT OF THE SLOWING DOWN OF FISSION NEUTRONS IN WATER

T. V. Blosser D. K. Trubey

Introduction

The experimental arrangement and procedures used in determining the slowing-down distribution of neutrons from the fission of U^{235}, in water, has previously been described.[1,2] Since the experiment is expected to resolve previously existing discrepancies between various experimental measurements and calculations, it has been necessary to minutely examine all factors affecting the final result. One of these factors encompasses the techniques used in detecting and counting the slowing-down density of neutrons in a moderating medium. This factor has not been studied in detail by previous experimenters.

Slowing-Down Detectors

A number of detectors have been proposed for slowing-down measurements, but perhaps the most suitable are thin foils of natural indium, to which either cadmium or boron covers may be added to reduce the response to thermal neutrons. Indium has a large resonance, ~30,000 barns, occurring at 1.45 ev, and from the activated state which is most probable, decays with a half life of 54.2 min, convenient for either beta or gamma counting techniques.

Natural indium is composed of two isotopes, ${}_{49}In^{113}$, in 4.23% abundance, and ${}_{49}In^{115}$, which makes up 95.77%. The first is stable while the second, with a half life of 6×10^{14} yr, decays slowly by beta emission. When natural indium is bombarded by neutrons a number of reactions are possible, the most important of which are given in Table 5.4.1.

[1] T. V. Blosser, D. K. Trubey, and E. P. Blizard, *Neutron Phys. Ann. Prog. Rep. Sept. 1, 1958*, ORNL-2609, p 55.

[2] T. V. Blosser and D. K. Trubey, *Neutron Phys. Ann. Prog. Rep. Sept. 1, 1959*, ORNL-2842, p 109.

Table 5.4.1. Neutron-Induced Reactions in Naturally Occurring Indium Isotopes (Natural Indium: 4.23% In^{113}; 95.77% In^{115})

Reaction	Incident Neutron Energy (Mev)	Cross Section (barns)	Half Life	Reference
${}_{49}In^{113}(n,\gamma){}_{49}In^{114}$	Thermal	~56	49 days 72 sec	*a, b, c*
${}_{49}In^{113}(n,n'){}_{49}In^{113}$	0.34 (threshold)	0.36	4.5 hr	*d, e*
${}_{49}In^{113}(n,2n){}_{49}In^{112}$	9.15 (threshold)		14.5 min	*a, b, c*
${}_{49}In^{115}(n,\gamma){}_{49}In^{116}$	Thermal	145	54.2 min 13 sec	*a, b, c*
${}_{49}In^{115}(n,n'){}_{49}In^{115}$	~0.34 (threshold)	0.36	4.5 hr	*d, e*

[a] I. Pullman, chap. 1.1 in *The Reactor Handbook*, ed. by J. F. Hogerton and R. C. Grass, Technical Information Service, AEC, 1955.

[b] *Activation Handbook for Aircraft Designers*, NARF-57-50T, FZK-9-124 (1957).

[c] D. Strominger, J. M. Hollander, and G. T. Seaborg, *Table of Isotopes*, 2d ed., UCRL-1928 (1958).

[d] G. B. Collins *et al.*, *Phys. Rev.* 55, 507 (1939).

[e] S. G. Cohen, *Nature* 161, 475 (1948).

The principal gamma-ray reaction with indium is ${}_{49}In^{115}(\gamma,\gamma){}_{49}In^{115}$, with a ~1.00-Mev threshold, a 4.5-hr half life, and a cross section of ~ 10^{-10} cm^2 (ref 3).

In the use of indium foils as neutron detectors, the most important of the reactions listed in Table 5.4.1 is the ${}_{49}In^{115}(n,\gamma){}_{49}In^{116}$ reaction, with a cross section of 145 barns. As indicated in the decay schemes of Fig. 5.4.1, however, the decay of In^{116} is not uncomplicated. The principal decay is by beta emission with a half life of 54.2 min, but there is also a 13-sec half-life activity resulting from slow-neutron activation. The latter activity can be minimized by only a 3-min wait before beginning beta counting, or may be ignored if gamma-ray counting techniques are used. A fast-neutron activation of indium, by inelastic scattering, decays in 4.5 hr by emission of 0.335- and 0.338-Mev gamma rays. This activation only becomes important with long exposures of the foils, and, if counting is done by scintillation counting methods, may be excluded by appropriately setting the energy bias.

---

[3] W. C. Miller and B. Waldman, *Phys. Rev.* **75**, 425 (1949).

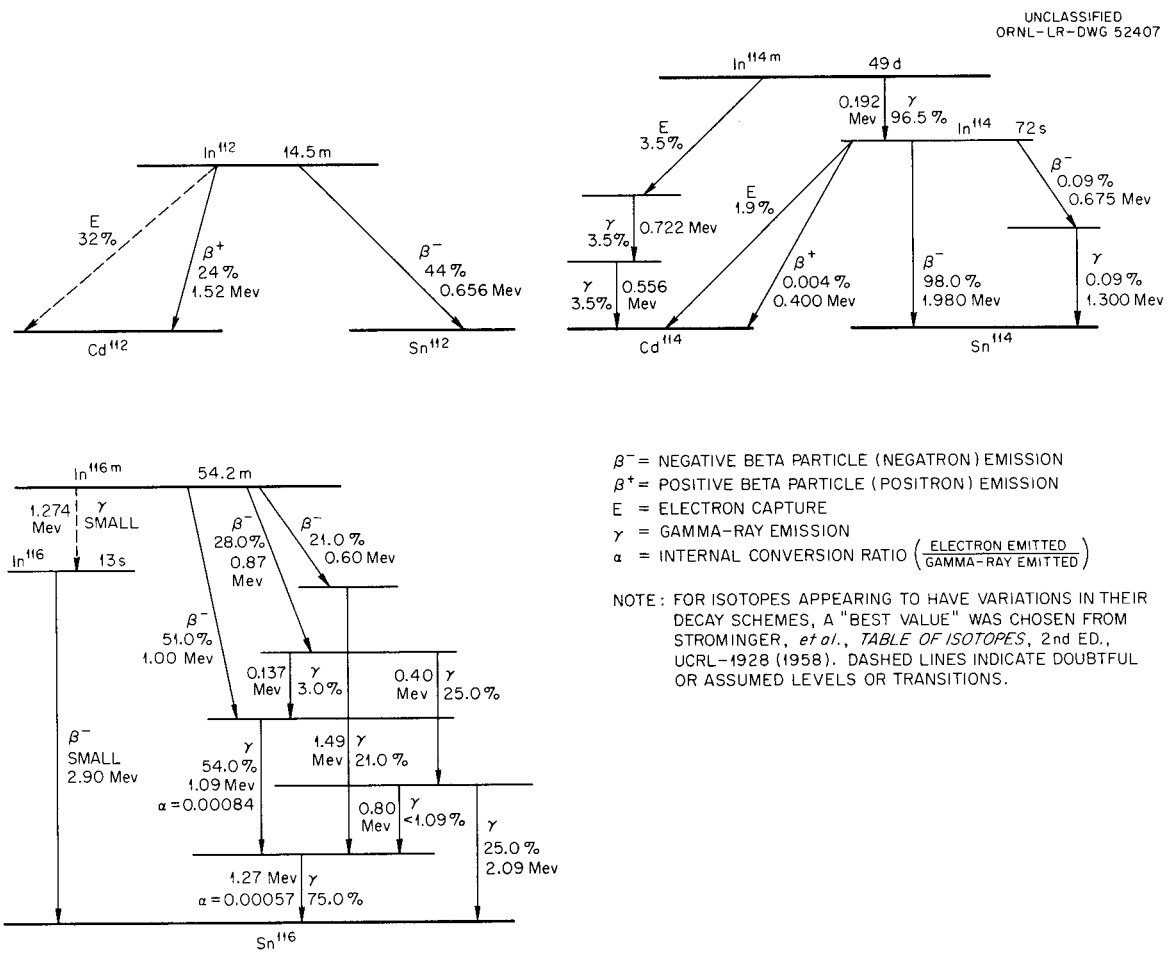

Fig. 5.4.1. Decay Schemes for ${}_{49}In^{112}$, ${}_{49}In^{114m}$, and ${}_{49}In^{116m}$.

Counting Techniques

The activity induced in indium foils by the reactions detailed above may be determined by either beta or gamma-ray counting, each having certain merits. Both have been used in the present experiment.

Beta Counting. – When the beta activity was to be counted, a flow-type beta-proportional counter was used.[4] The counter was reasonably stable and relatively insensitive to gamma radiation. However, since the flux in the experimental volume was not isotropic, and since the foil itself attenuates the emitted beta particle, it was necessary to count both sides of an indium foil.

When used for neutron distribution measurements with beta counting, the sensitivity of an indium foil is importantly affected by its thickness.

In the present work, an optimum indium foil thickness was experimentally determined, and the results are shown in Fig. 5.4.2. From the curve it appears that the sensitivity of the foil increases to a maximum at a foil thickness of ~90–100 mg/cm^2 (roughly 5.4 mils thick) and slowly decreases beyond this point. The decrease may be attributed to internal beta-ray absorption in a thick foil, and to the tendency of an absorber placed in a neutron flux to suppress the neutron density.

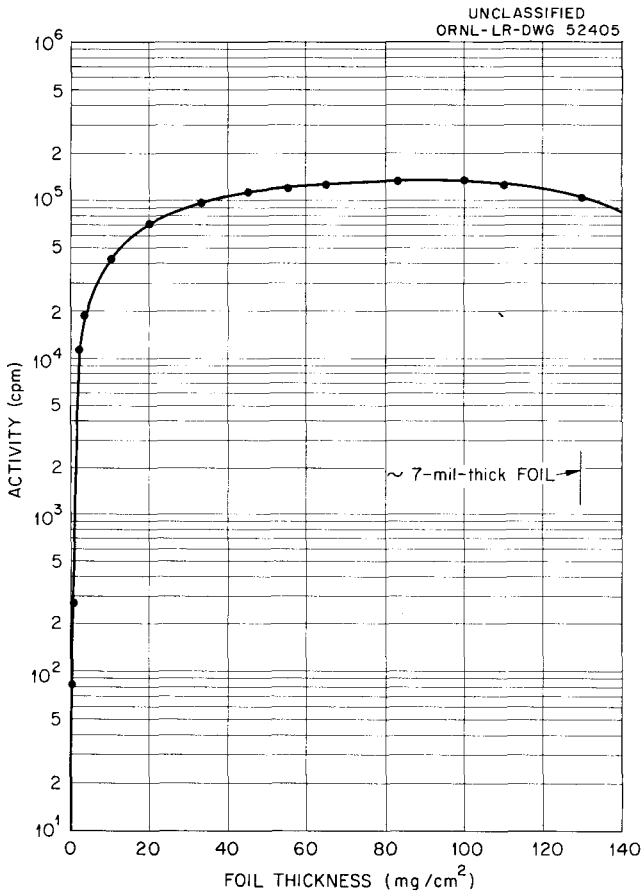

Fig. 5.4.2. Activity of Neutron-Irradiated Natural Indium, Determined by Beta-Counting, as a Function of Indium Thickness.

Gamma-Ray Counting. – Gamma-ray activity induced in an indium foil was observed with a NaI(Tl) scintillation counter, a diagram of which is shown as Fig. 5.4.3. The design ensured reproducible foil placement, and the dual crystal arrangement increased the counting sensitivity. Since the NaI(Tl) crystal is also responsive to beta particles, a thickness of 0.25 in. of aluminum separates the foil from either crystal. This thickness is sufficient to stop an ~3.5-Mev beta particle, while the most energetic beta to be expected from indium, according to the decay schemes shown above, is ~2.90 Mev. The aluminum, however, offers only a few per cent attenuation

[4] D. K. Trubey, T. V. Blosser, and G. M. Estabrook, *Neutron Phys. Ann. Prog. Rep. Sept. 1, 1959*, ORNL-2842, p 204.

to the gamma rays from indium, the bulk of which have energies greater than 0.4 Mev. A foil in counting position appears to the crystal as a finite disk source, with separation equal to the 0.25-in. aluminum thickness.

Figure 5.4.4 shows a typical experimental pulse-height spectrum for indium. Since no corrections have been applied for geometry, scatterings, or contributions from overlapping adjacent energy peaks, the spectrum appears generally smeared. The pulse-height selector was calibrated in terms of energy against previously calibrated Au^{198} and Cs^{137} foils for the purpose of setting an energy bias. Activity of the indium foils was measured by integrally counting the pulses above the energy bias of 0.4 Mev.

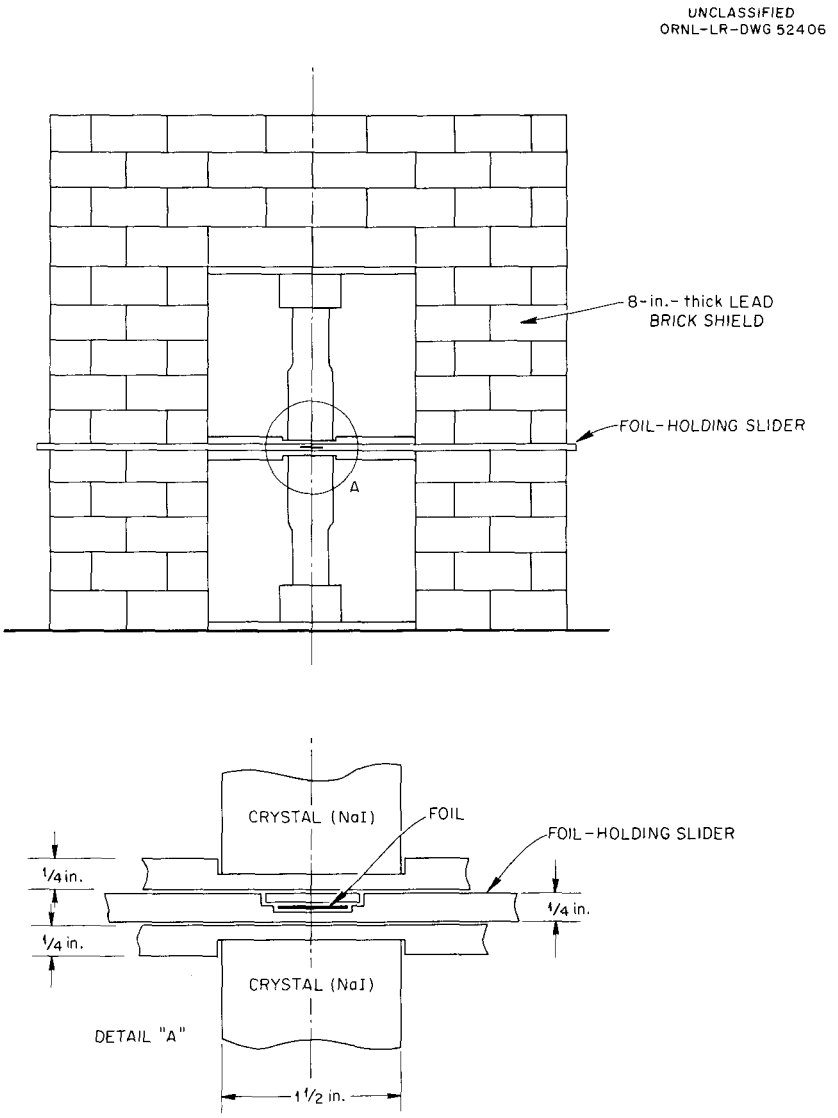

Fig. 5.4.3. Diagram of NaI(Tl) Scintillation Counter Arrangement.

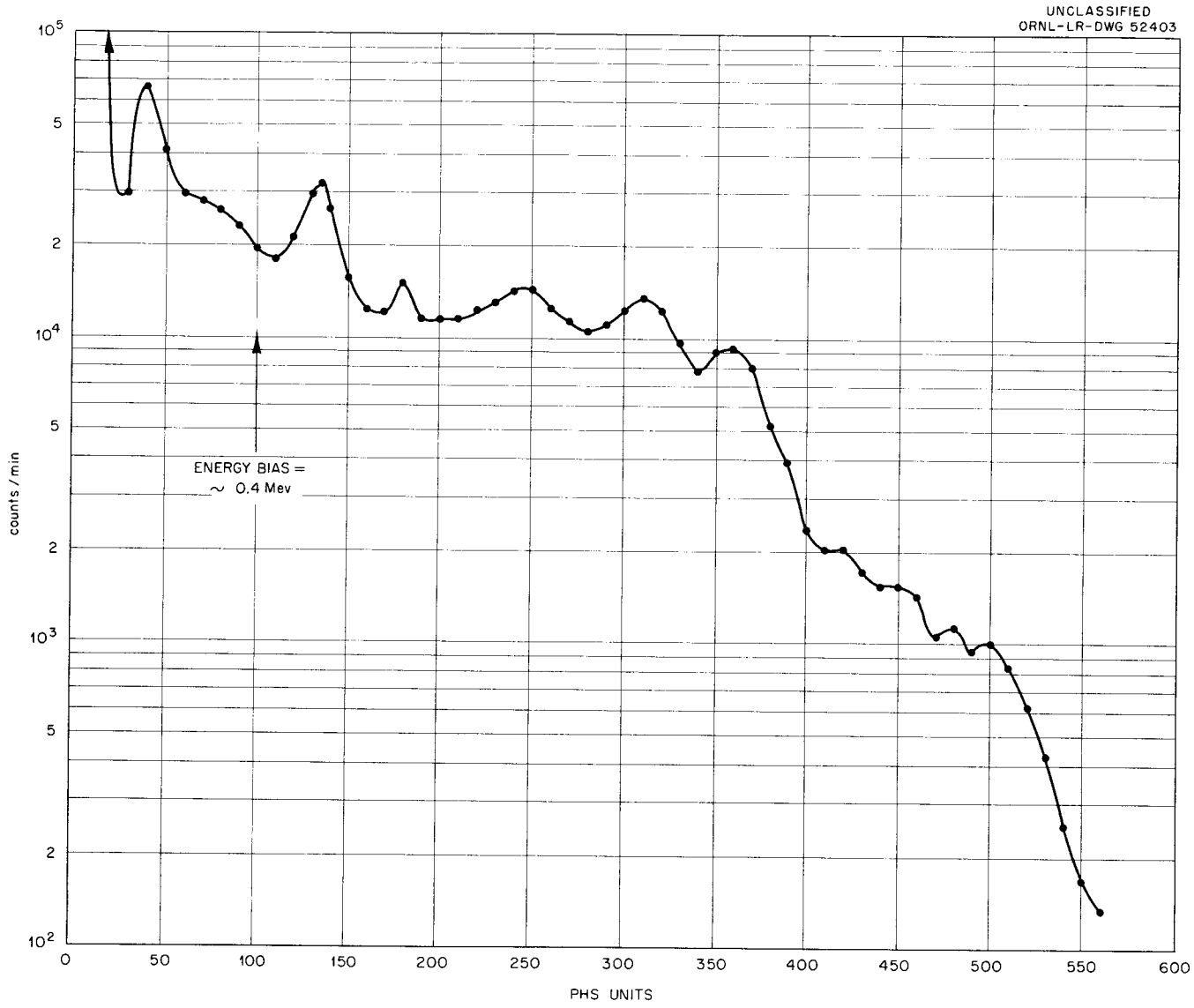

Fig. 5.4.4. Uncorrected Spectrum of Gamma Radiation from a Neutron-Irradiated Indium Foil.

Effect of Higher Resonances

In addition to the principal resonance at 1.45 ev, several strong resonances at energies greater than 1.45 ev appear in the neutron cross section of indium. The contributions to the age due to absorptions in these higher resonances may be readily estimated provided that certain assumptions can be made.

If the slowing-down distribution of fission neutrons in water is Gaussian, then the slowing-down density at each energy may be written as

$$G_i = a_i\, e^{-r^2/4\tau_i} , \tag{1}$$

where

τ_i = age to a particular energy,

a_i = a factor slowly varying with energy,

r = distance from source.

The experimentally measured kernel, G_M, is a sum of such kernels multiplied by the response of each resonance. Thus,

$$G_M = a_0 b_0 e^{-r^2/4\tau_0} + a_1 b_1 e^{-r^2/4\tau_1} + a_2 b_2 e^{-r^2/4\tau_2} + \ldots \tag{2}$$

where b_i is the response of the detector to each resonance; or, if the slow variation of a_i is neglected,

$$G_M \cong G_0 \left[1 + R_1 e^{-(r^2/4)(\tau_1^{-1} - \tau_0^{-1})} + R_2 e^{-(r^2/4)(\tau_2^{-1} - \tau_0^{-1})} + \ldots \right] \tag{3}$$

where R_i is the ratio of the response of the ith resonance to the first (1.45 ev) resonance.

The ratio R_i may be computed from

$$R_i = \frac{\sigma_i f_i \alpha_i}{\sigma_0 f_0 \alpha_0} , \tag{4}$$

where

σ_i = resonance integrals of In^{115},

f_i = self-shielding factor,

α_i = relative importance of 54.2-min activity compared to 13-sec activity.

For In^{115}, the second and third resonance integrals are about 1.5% of the first one, and the rest are negligible. The self-shielding factor is essentially unity except for the first resonance, where its value may drop as low as 0.2 for a 5-mil foil. Experimental values of this factor, measured in water close to a U^{235} source, are shown in Fig. 5.4.5, in which the theoretical curve is from ref 4.

The relative importance of the 54.2-min activity vs the 13-sec activity has been determined for the first two resonances by Domanic and Sailor.[5] The relative importance for the third resonance is probably about the same as for the first.

[5] F. Domanic and V. L. Sailor, *Phys. Rev.* 119, 208 (1960).

Since

$$\tau_i^{-1} - \tau_0^{-1} = \frac{\tau_i - \tau_0}{\tau_i \tau_0} = \frac{\Delta\tau}{\tau_i \tau_0} \ , \quad \text{and } \tau_i \cong \tau_0 \ ,$$

$$\tau_i^{-1} - \tau_0^{-1} \cong \frac{\Delta\tau}{\tau^2} \ . \tag{5}$$

Values of $\Delta\tau$ were obtained from Coveyou and Sullivan.[6] The appropriate factors for 5-mil-thick In^{115} are shown in Table 5.4.2.

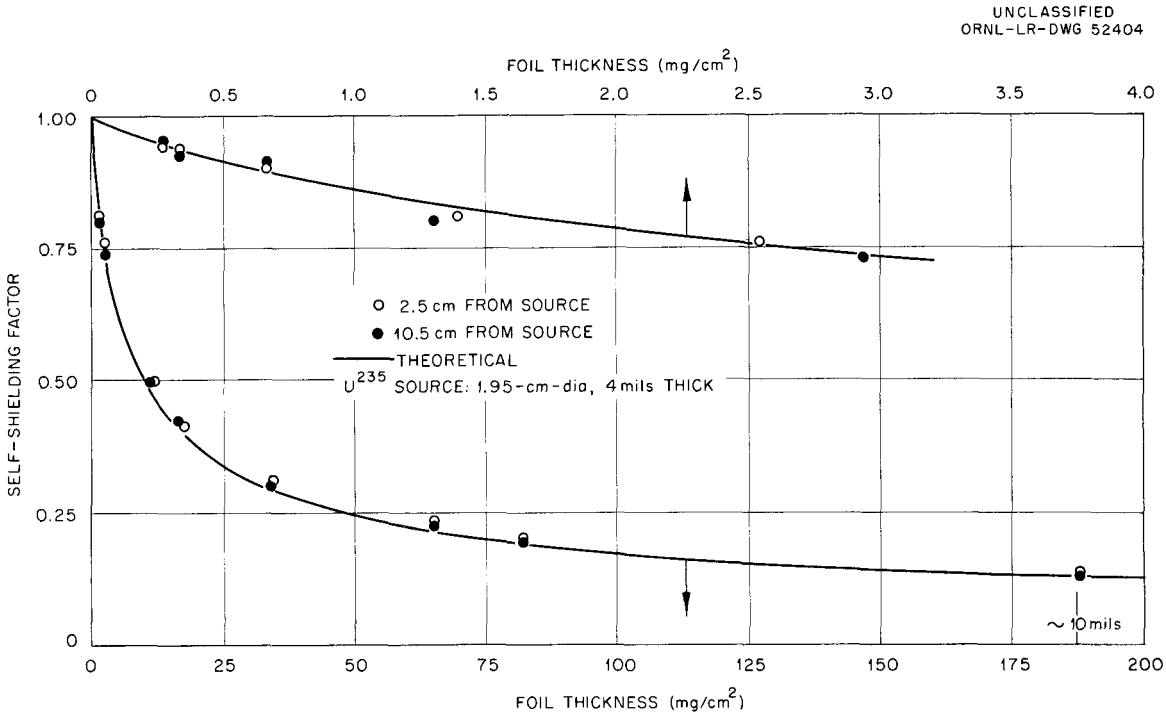

Fig. 5.4.5. Self-Shielding Factor for Indium Foils in Water at Various Distances from a U^{235} Fission Source, as a Function of Foil Thickness.

Table 5.4.2. Factors Required for Solution of Eq. 3

Energy (ev)	σ_i/σ_0	f_i/f_0	α_i/α_0	$\Delta\tau$ (cm^2)	$\Delta\tau/\tau^2$
3.86	0.0156	5	0.3	0.51	0.754×10^{-3}
9.1	0.0150	5	1.0	0.84	1.24×10^{-3}
12.1	0.00056	5			

A computation based on the preceding assumptions shows that for infinite dilution or zero-thickness foils the effect of the higher resonances on the measured kernel G_M/G_0 is only about 1% for distances of from 0 to 100 cm from the source, but is ~ 10% for a 5-mil-thick foil over the same range. The resulting small error in the age can be eliminated by extrapolating to infinite dilution. Unfortunately, the statistics for very thin foil measurements at distances >60 cm, upon which the extrapolation depends, are very poor.

[6] R. R. Coveyou and J. G. Sullivan, *Neutron Phys. Ann. Prog. Rep. Sept. 1, 1958*, ORNL-2609, p 82.

Part 6

REACTOR THEORY

6.1 ON THE VALIDITY OF THE SECOND FUNDAMENTAL THEOREM IN A MEDIUM WITH ANISOTROPIC SCATTERING[1]

L. Dresner

In calculating the criticality of bare, homogeneous reactors one often replaces the finite reactor by an infinite one of identical composition, and adds the requirement that the flux at all energies vanish on the same extrapolated surface. This extrapolated surface is generally located 0.7104 transport mean free path (t.m.f.p.) from the reactor surface, although the value of the extrapolation distance depends somewhat on the composition of the reactor. If the space variation of the flux is taken to satisfy the wave equation, the criticality eigenvalue equation can be solved, and one is able to prove the second fundamental theorem of reactor theory, viz.: the nonescape probability is the Fourier transform of the *infinite-medium* kernel evaluated for the buckling of the extrapolated reactor volume.[2]

The replacement of the finite reactor by an infinite reactor plus an appropriate boundary condition ought not to significantly affect the flux deep in the interior of a large reactor, where the effects of the edge are small. However, when the dimensions of the reactor are comparable to a mean free path, edge effects will be important throughout the reactor and the theorem should fail. A detailed numerical analysis of this problem has been given by Inönü[3] for one-velocity slab reactors with *isotropic* scattering. In this case the relevant kernel both for the *finite* and *infinite* medium is the transport kernel,

$$K(|\mathbf{r}-\mathbf{r}'|) = \frac{\exp(-|\mathbf{r}-\mathbf{r}'|)}{4\pi|r-r'|^2} \quad . \tag{1}$$

Its Fourier transform is

$$K(B) = \frac{\arctan B}{B} \quad . \tag{2}$$

[Here, as in the remainder of this paper, the mean free path (m.f.p.) has been chosen as the unit of length.] Because of the symmetric nature of the finite medium kernel,[2] quite precise values of the nonescape probability, P_{NE}, may be calculated from the following variational expression:[4]

$$P_{NE} = \frac{\int_V \phi(\mathbf{r}) K(|\mathbf{r}-\mathbf{r}'|)\phi(\mathbf{r}')d^3r d^3r'}{\int_V \phi^2(\mathbf{r})d^3r} \quad . \tag{3}$$

---

[1]Summarized from: L. Dresner, *Nuclear Sci. and Eng.* 7, 419 (1960).

[2]A. M. Weinberg and E. P. Wigner, *The Physical Theory of Neutron Chain Reactors*, chap. XII, University of Chicago Press, Chicago, 1958.

[3]E. Inönü, *Nuclear Sci. and Eng.* 5, 248 (1959).

[4]B. Davison, *Neutron Transport Theory*, Oxford University Press, London, 1957.

Comparing nonescape probabilities calculated from Eqs. 2 and 3, Inönü was able to show that the second fundamental theorem held with surprising accuracy for sizes comparable to a mean free path. For example, for a slab reactor of thickness T, equal to 2 m.f.p., Eqs. 2 and 3 differ by less than 2%; for $T = 4$ m.f.p., the relative difference is of the order of 0.2%.

In a reactor with *anisotropic* scattering a procedure exactly analogous to that of Inönü has been followed. In obtaining the approximate nonleakage probability from the second fundamental theorem in a medium with anisotropic scattering, it has proved convenient to avoid directly calculating the infinite medium kernel and then Fourier-transforming it. Instead we have solved the Fourier-transformed integrodifferential form of the transport equation in an infinite medium subject to the condition that the space variation of the angular flux satisfies the wave equation and vanishes on the extrapolated boundary. This procedure will produce directly the approximate nonleakage probability, which, of course, will equal the transformed kernel. To simplify the calculations, and to facilitate comparison with Inönü's work, we have carried out this calculation only in slab geometry. Furthermore, we have only considered the case of linear anisotropy, that is, the case in which only the lowest two moments of the scattering kernel do not vanish. The solution of the Fourier-transformed one-velocity transport equation has been carried out with the B_L-expansion method of Hurwitz and Zweifel.[5] The detailed development of the calculation has been given elsewhere.[6]

In order to test these predictions of the second fundamental theorem, a quite precise solution for the criticality of a bare slab reactor for the case of linearly anisotropic scattering has been obtained by a variational technique. Again the details have been previously presented.[6]

Table 6.1.1 presents the variational estimates of P_{NE}. The accuracy of these estimates is discussed at length in ref 6. In Table 6.1.2 estimates of P_{NE} from the second fundamental

[5] H. Hurwitz and P. F. Zweifel, *J. Appl. Phys.* **26**, 923 (1955); see also H. L. Garabedian, Mon-P-274.

[6] L. Dresner, *Nuclear Sci. and Eng.* **7**, 419 (1960).

Table 6.1.1. Variational Estimates of P_{NE}

T	P_{NE}			
	$\bar{\mu} = 0.0$	$\bar{\mu} = 0.1$	$\bar{\mu} = 0.2$	$\bar{\mu} = 0.3$
0.2	0.2611	0.2589	0.2566	0.2544
0.4	0.3964	0.3924	0.3884	0.3845
1.0	0.6190	0.6125	0.6060	0.5944
2.0	0.7830	0.7761	0.7692	0.7624
4.0	0.9021	0.8972	0.8923	0.8873
8.0	0.9648	0.9623	0.9599	0.9574
20.0	0.9929	0.9923	0.9917	0.9911

Table 6.1.2. Estimates of P_{NE} from the Second Fundamental Theorem

T	P_{NE}			
	$\bar{\mu} = 0.0$	$\bar{\mu} = 0.1$	$\bar{\mu} = 0.2$	$\bar{\mu} = 0.3$
0.2	0.2484	0.2243	0.1679	
0.4	0.3890	0.3667	0.3200	
1.0	0.6174	0.6030	0.5808	0.5350
2.0	0.7828	0.7733	0.7616	0.7451
4.0	0.9021	0.8965	0.8900	0.8820
8.0	0.9649	0.9623	0.9591	0.9553
20.0	0.9929	0.9922	0.9914	0.9905

theorem are given. In the calculation of the results of Table 6.1.2, the dependence of the extrapolated end point on anisotropy and strength of absorption was given by

$$z_0(k,\bar{\mu}) = \frac{z_0(k,0)}{1-\bar{\mu}} , \tag{4}$$

an approximation due to Kofink.[7] The effect of this approximation has also been discussed in ref 6. Case *et al.*[8] have tabulated values of $z_0(k,0)$.

From comparison of Tables 6.1.1 and 6.1.2 it is evident that:

1. In the case of isotropy, that is, where $\bar{\mu} = 0$, the second fundamental theorem gives very accurate values of P_{NE} even for very thin slabs. For example, for $T = 0.2$ the relative error in P_{NE} is –5%, while for $T = 1.0$ it is only –0.25%. Inönü[4] also remarked on this very high accuracy, although his approximate calculations were somewhat cruder in that he did not employ the known dependence of z_0 on k.

2. The accuracy of the second fundamental theorem decreases with increasing anisotropy; for example, for $T = 1.0$ and $\bar{\mu} = 0.3$, the relative error in P_{NE} is about –11%, or almost 45 times the corresponding relative error when $\bar{\mu} = 0$. In particular, the approximate value of P_{NE} decreases too rapidly with increasing $\bar{\mu}$.

On this basis we conclude that the second fundamental theorem is less reliable the more anisotropic the scattering. The absolute accuracy of the procedure presented here (based on Eq. 4), however, is not bad except for the smallest and most anisotropic reactors. This information may nevertheless contraindicate the use of the second fundamental theorem in hydrogenous reactors, where at fission energies the mean reactor dimension is often only a few mean free paths long, and where the scattering is quite anisotropic.

[7] W. Kofink and H. S. Moran, unpublished results quoted in ref 3.

[8] K. M. Case, F. de Hoffman, and G. Placzek, *Introduction to the Theory of Neutron Diffusion*, vol I, USGPO, Washington, D.C., June 1953.

6.2 COMPARISON THEOREMS FOR THE ESTIMATION OF CRITICALITY IN BARE, ONE-VELOCITY REACTORS[1]

L. Dresner[2]

In two previous papers[3,4] the author has proven several theorems for the estimation of average collision probabilities for uniform isotropic volume sources of neutrons in solids of irregular shape by comparison with solids of regular shape for which this quantity is known (e.g., slab, sphere, cylinder, hemisphere, oblate spheroid).

In this summary some quite similar theorems are given for the critical multiplication in a bare, one-velocity reactor with isotropic scattering, a quantity even less well known than the collision probability, exact values being available only for spheres[5] and slabs.[6]

The critical multiplication constant of a homogeneous multiplying body V is defined as the lowest eigenvalue C_0 of the equation

$$\phi(\mathbf{r}) = C\int_V \phi(\mathbf{r}')K(\mathbf{r}-\mathbf{r}')\,d\mathbf{r}' \,, \tag{1a}$$

where

$$K(\mathbf{r}) = \frac{e^{-r}}{4\pi r^2} \,. \tag{1b}$$

Here, as in the remainder of the paper, the unit of length has been chosen to be the mean free path in the body V; $\phi(\mathbf{r})$ is therefore the collision density at $\mathbf{r}$. The smallest number of secondary neutrons emerging from each collision which will make V critical is then C_0. A related quantity is P $(= C_0^{-1})$, the average collision probability of neutrons distributed in V in the lowest persisting flux mode.

Theorem 1. – If a body V_1 can be totally included in another body V_2, then $P(V_1) \leqq P(V_2)$.

Theorem 2. – If a solid V^* is obtained from a solid V by Steiner symmetrization, then $P(V^*) \geqq P(V)$.

Steiner symmetrization is defined with respect to some plane Q as follows: (1) V^* is symmetric with respect to Q, (2) any straight line perpendicular to Q that intersects one of the solids V^* and V intersects the other also (*both intersections have the same length*), and (3) the intersection with V^* consists of just one line segment. It is known that Steiner symmetrization

[1]A complete version of this work has been submitted for publication in *Nuclear Sci. and Eng.*

[2]Work performed while the author was on assignment to the Institut für Neutronenphysik und Reaktortechnik, Kernforschungszentrum, Karlsruhe, Germany.

[3]L. Dresner, *Nuclear Sci. and Eng.* **6**, 63 (1959).

[4]L. Dresner, *Nuclear Sci. and Eng.* **7**, 260 (1960).

[5]M. H. L. Pryce, *Critical Conditions in Neutron Multiplication*, MSP-2A (declassified 1947). Pryce's results and others can be found in: E. Inönü, *Neutron Phys. Ann. Prog. Rep. Sept. 1, 1959*, ORNL-2842, p 134–37.

[6]E. Inönü, *Nuclear Sci. and Eng.* **5**, 248 (1959).

leaves the volume invariant.[7] It is also known that symmetrization in an appropriately chosen infinitude of planes reduces all finite solids to spheres, and symmetrization in an appropriate infinitude of planes, all containing the common axis, reduces all infinite right cylinders to right circular cylinders.[7] It immediately follows, then, that:

Corollary. – *Of all convex solids of a given volume, the sphere has the maximum collision probability (minimum critical multiplication), and of all right cylinders of given base area, the circular cylinder has the maximum collision probability (minimum critical multiplication).*

Theorem 3. – If V is the volume common to (1) two perpendicular slabs, S_1 and S_2, or (2) three mutually perpendicular slabs S_1, S_2, and S_3, or (3) a convex right cylinder C and a slab S, perpendicular to it, then

$$(a) \quad P(V) \geqq P(S_1)P(S_2) \ ,$$

$$(b) \quad P(V) \geqq P(S_1)P(S_2)P(S_3) \ ,$$

$$(c) \quad P(V) \geqq P(C)P(S) \ .$$

Theorem 4. – If $P_1(V)$ is the average collision probability of neutrons distributed uniformly in V, then $P(V) \geqq P_1(V)$.

Theorem 5. – If B is the lowest eigenvalue of the differential equation $\nabla^2\phi(\mathbf{r}) + B^2\phi(\mathbf{r}) = 0$ and boundary condition, $\phi(\mathbf{r}) = 0$ on S, the surface of V, then $P(V) \geqq \arctan B/B$.

Proofs and a discussion of the theorems are contained in the complete version submitted for publication, but can also be found in Arbeits-bericht Nr. 1 (18. Mai 1960) of the Institut für Neutronenphysik und Reaktortechnik, Kernforschungszentrum, Karlsruhe, Germany.

Discussion

As is always the case with such theorems their applicability is limited, and while success is often striking in special cases, in general, the estimates provided are crude. Nonetheless the estimates are interesting in that they are exact although they may be inaccurate, and, in any case when upper and lower bounds are obtained, the maximum possible error is known.

Theorem 1 will give good results in general for $P = C_0^{-1}$ only when the volumes of the solids being compared are not too different, since the critical multiplication is a fairly sensitive function of size. For a similar reason the corollary to theorem 2 provides close overestimates of P only for fairly symmetrical solids (e.g., equilateral cylinders, cubes, etc.), while theorem 3 generally provides fairly close underestimates only if all the P's involved are close to unity. Theorem 4, which is based on a variational estimate with a flat trial function for the flux, will only give a very good underestimate of P for small solids, where the flux has not too high a curvature. Theorem 5, on the other hand, is based on an essentially diffusion-theoretic trial

[7] G. Pólya and G. Szegö, *Isoperimetric Inequalities in Mathematical Physics*, Princeton University Press, Princeton, 1951.

function, and thus gives close underestimates of P only for large solids. These indications, however, apply only in extreme cases, and in general the estimates provided by the various theorems must be compared to see which are best.

6.3 TIME-DEPENDENT THERMAL-NEUTRON ENERGY SPECTRA IN A MONATOMIC HEAVY GAS[1]

S. N. Purohit

The time-dependent thermal-neutron energy spectra for times greater than the slowing-down time were generated in a monatomic heavy gas by means of a multigroup formalism. These spectra were obtained for both infinite and finite media of beryllium and graphite. The behavior of asymptotic energy spectra during the last stage of neutron thermalization and diffusion was studied. The thermalization time constant for the establishment of the final Maxwellian velocity distribution of neutrons, in a monatomic heavy gas, was estimated to be equal to $(1.176\xi\Sigma s_0 v_0)^{-1}$. Total thermalization times for neutrons in beryllium and graphite were found to be equal to 114 and 238 μsec, respectively. The diffusion-cooling coefficient for beryllium was calculated by using the energy-dependent transport mean free path to be equal to 0.890 cm^2. For graphite, under the constant diffusion-coefficient assumption, the diffusion-cooling coefficient was calculated to be equal to 1.922 cm^2.

[1]Summarized from: S. N. Purohit, *Time-Dependent Thermal-Neutron Energy Spectra in a Monatomic Heavy Gas*, ORNL CF-60-7-44 (July 11, 1960).

6.4 HOMOGENEOUS, INFINITE MEDIUM P_1 CODES

W. E. Kinney

Multigroup codes, based on a consistent P_1 approximation to the Boltzmann equation,[1] have been written to calculate neutron ages and Fourier transforms. In addition to supplying important reactor physics data, these codes facilitate rapid investigations to improve the multigroup methods. Effects produced upon the age by changes in group structure or cross sections, the introduction of anisotropic scattering, choice of the slowing-down kernel or method of treating a resonance can all be studied with only a small expenditure of computer time.

A Corn Pone[1] group structure tape and the first three subprograms of Corn Pone prepare input for the Age and Transform Oracle codes. About 5 min is required to compute and punch the ages or transforms for 30 groups.

[1]W. E. Kinney *et al.*, *Appl. Nuclear Phys. Ann. Prog. Rep. Sept. 10, 1956*, ORNL-2081, p 133.

The P_1 Equations

The P_1 equations for a slab with a plane source at the origin are

$$\frac{1}{3}\frac{d}{dx}\phi_0(x,u) + \sum_m \beta_m(u)\phi_1(x,u) + \sum_m \frac{\partial}{\partial u} p_m(x,u) = 0 \quad , \tag{1}$$

$$\frac{d}{dx}\phi_1(x,u) + \sum_m \alpha_m(u)\phi_0(x,u) + \sum_m \frac{\partial}{\partial u} q_m(x,u) - S(u)\delta(x) = 0 \quad , \tag{2}$$

$$\gamma_m \frac{\partial}{\partial u} q_m(x,u) + q_m(x,u) = \xi_m \sigma_m(u)\phi_0(x,u) \quad , \tag{3}$$

$$\rho_m \frac{\partial}{\partial u} p_m(x,u) + p_m(x,u) = \eta_m \sigma_m(u)\phi_1(x,u) \quad , \tag{4}$$

where

x = the distance from the origin,

u = the lethargy,

ϕ_0 = the flux,

ϕ_1 = the current,

α_m = the macroscopic absorption cross section for the mth element,

σ_m = the macroscopic scattering cross section for the mth element,

$\beta_m = \alpha_m + (1 - \bar{\mu}_m)\sigma_m$,

$\bar{\mu}_m$ = the average cosine of the scattering angle in the laboratory system for the mth element,

q_m = the slowing-down density for the mth element,

p_m = the slowing-down current for the mth element,

$\xi = \langle u \rangle$,

$\gamma = \dfrac{\langle u^2 \rangle}{2\langle u \rangle}$,

$\eta = \langle u\mu \rangle$,

$\rho = \dfrac{\langle u^2\mu \rangle}{2\langle u\mu \rangle}$ (the broken brackets indicating an average in all of the above),

$\delta(x)$ = delta function,

S = source.

As shown in ref 1, these equations may be put into group equations of the form, for group i,

$$\frac{d}{dx}\bar{\phi}_0(x) + A(u_i,u_{i+1})\bar{\phi}_1(x) + B(x,u_i,u_{i+1}) = 0 \quad , \tag{5}$$

$$\frac{d}{dx}\bar{\phi}_1(x) + C(u_i,u_{i+1})\bar{\phi}_0(x) - D(x,u_i,u_{i+1}) = 0 \quad , \tag{6}$$

where

$\bar{\phi}_0$ = the average flux in group i,

$\bar{\phi}_1$ = the average current in group i,

u_i = the lower lethargy limit of group i,

u_{i+1} = the upper lethargy limit of group i,

$$B(x,u_i,u_{i+1}) = G(u_i,u_{i+1})\phi_1(x,u_i) - 3\sum_m \frac{1-e^{-\Delta u/\rho_m}}{\Delta u} p_m(x,u_i) \ ,$$

$$D(x,u_i,u_{i+1}) = -l(u_i,u_{i+1})\phi_0(x,u_i) + \bar{S}\delta(x) + \sum_m \frac{1-e^{-\Delta u/\gamma_m}}{\Delta u} q_m(x,u_i) \ ,$$

$$\Delta u = u_{i+1} - u_i \ ,$$

$$q_m(x,u_{i+1}) = q_m(x,u_i)e^{-\Delta u/\gamma_m} + \left(1 - e^{-\Delta u/\gamma_m}\right)\xi[{}^*\sigma_m \bar{\phi}_0(x) + \sigma_m^* \phi_0(x,u_i)] \ , \tag{7}$$

$$p_m(x,u_{i+1}) = p_m(x,u_i)e^{-\Delta u/\gamma_m} + \left(1 - e^{-\Delta u/\gamma_m}\right)\eta[{}^*\sigma_m \bar{\phi}_1(x) + \sigma_m^* \phi_1(x,u_i)] \ , \tag{8}$$

and ${}^*\sigma$ and σ^* are defined in ref 1.

The Age Code

Theory. – To arrive at the multigroup age equation, first define

$$\begin{aligned}
\phi_0^0(u) &= \int_{-\infty}^{\infty} \phi_0(x,u)\, dx \ , \\
\phi_1^1(u) &= \int_{-\infty}^{\infty} x\phi_1(x,u)\, dx \ , \\
\phi_0^2(u) &= \int_{-\infty}^{\infty} x^2\phi_0(x,u)\, dx \ , \\
q_m^0(u) &= \int_{-\infty}^{\infty} q_m(x,u)\, dx \ , \\
p_m^1(u) &= \int_{-\infty}^{\infty} xp_m(x,u)\, dx \ , \\
q_m^2(u) &= \int_{-\infty}^{\infty} x^2 q_m(x,u)\, dx \ .
\end{aligned} \tag{9}$$

Note that

$$\int_{-\infty}^{\infty} x^n \frac{d}{dx} \phi(x)\, dx = -n \int_{-\infty}^{\infty} x^{n-1} \phi(x)\, dx \quad . \tag{10}$$

Integrate Eq. 6 from $-\infty$ to ∞:

$$C(u_i, u_{i+1})\bar{\phi}_0^0 - D^0(u_i, u_{i+1}) = 0 \quad , \tag{11}$$

$$D^0(u_i, u_{i+1}) = -I(u_i, u_{i+1})\phi_0^0(u_i) + \bar{S} + \sum_m \frac{1 - e^{-\Delta u/\gamma_m}}{\Delta u} q_m^0(u_i) \quad . \tag{12}$$

Multiply Eq. 5 by x and integrate from $-\infty$ to ∞:

$$-\bar{\phi}_0^0 + A(u_i, u_{i+1})\bar{\phi}_1^1 + B^1(u_i, u_{i+1}) = 0 \quad , \tag{13}$$

$$B^1(u_i, u_{i+1}) = G(u_i, u_{i+1})\phi_1^1(u_i) - 3 \sum_m \frac{1 - e^{-\Delta u/\rho_m}}{\Delta u} p_m^1(u_i) \quad . \tag{14}$$

Multiply Eq. 6 by x^2 and integrate from $-\infty$ to ∞:

$$-2\bar{\phi}_1^1 + C(u_i, u_{i+1})\bar{\phi}_0^2 - D^2(u_i, u_{i+1}) = 0 \quad , \tag{15}$$

$$D^2(u_i, u_{i+1}) = -I(u_i, u_{i+1})\phi_0^2(u_i) + \sum_m \frac{1 - e^{-\Delta u/\gamma_m}}{\Delta u} q_m^2(u_i) \quad . \tag{16}$$

The average flux age in group i is

$$\tau_\phi = \frac{1}{2} \frac{\bar{\phi}_0^2}{\bar{\phi}_0^0} \quad . \tag{17}$$

The slowing-down age is

$$\tau_q = \frac{1}{2} \frac{\sum_m q_m^2(u_i)}{\sum_m q_m^0(u_i)} \quad . \tag{18}$$

Input. – The input is the same as for a one-region Corn Pone case.

Output. – Output is on paper tape. The group number is punched first as 00*iii*00001, where *iii* is a hex integer. There is then punched in packed decimal floating point the average flux age, the end-point flux age, and the slowing-down age.

Test Results. – The slowing-down age to lethargy 18.0491 (1.45 ev) in constant cross section hydrogen ($\Sigma_s = 1$) from a monolethargic source with average lethargy of 3.9647 ($\sim 1.9 \times 10^6$ ev) was computed to be 13.7526 cm^2. The analytic result[2] of $\Delta u - \frac{1}{3}$ gives 13.7511 cm^2. The flux age to average lethargy 17.9273 was computed to be 14.6354 cm^2. The analytic result[2] of $\Delta u + \frac{2}{3}$ is 14.6293 cm^2.

The slowing-down age from a fission source to 1.45 ev in light water was computed to be 23.3 cm^2 for isotropic scattering in oxygen. Monte Carlo results[3] give 23.8 cm^2.

Additional results are given in Sec 6.7 of this report.

The Fourier Transform Code

Theory. – First define

$$\phi_0(\omega,u) = \int_{-\infty}^{\infty} \phi_0(x,u)e^{-i\omega x}\,dx = \text{the Fourier transform of the flux,}$$

$$\phi_1(\omega,u) = \int_{-\infty}^{\infty} \phi_1(x,u)e^{-i\omega x}\,dx = \text{the Fourier transform of the current,}$$

$$q_m(\omega,u) = \int_{-\infty}^{\infty} q_m(x,u)e^{-i\omega x}\,dx = \text{the Fourier transform of the slowing-down density,} \tag{19}$$

$$p_m(\omega,u) = \int_{-\infty}^{\infty} p_m(x,u)e^{-i\omega x}\,dx = \text{the Fourier transform of the slowing-down current.}$$

Multiply Eqs. 5 and 6 by $e^{-i\omega x}$ and integrate from $-\infty$ to ∞; then

$$i\omega\bar{\phi}_0(\omega) + A(u_i,u_{i+1})\bar{\phi}_1(\omega) + B(\omega,u_i,u_{i+1}) = 0 \ , \tag{20}$$

$$B(\omega,u_i,u_{i+1}) = G(u_i,u_{i+1})\phi_1(\omega,u_i) - 3\sum_m \frac{1-e^{-\Delta u/\rho_m}}{\Delta u}\, p_m(\omega,u_i) \ , \tag{21}$$

$$i\omega\bar{\phi}_1(\omega) + C(u_i,u_{i+1})\bar{\phi}_0(\omega) - D(\omega,u_i,u_{i+1}) = 0 \ , \tag{22}$$

$$D(\omega,u_i,u_{i+1}) = -I(u_i,u_{i+1})\phi_0(\omega,u_i) + \bar{S} + \sum_m \frac{1-e^{-\Delta u/\gamma_m}}{\Delta u}\, q_m(\omega,u_i) \ , \tag{23}$$

where the $p_m(\omega,u_i)$ and $q_m(\omega,u_i)$ are obtained by the same operation on Eqs. 7 and 8.

---

[2]R. E. Marshak, *Revs. Modern Phys.* **19**, 3 (1947).
[3]J. G. Sullivan, unpublished results.

Multiply through by $i\omega$ and eliminate $\bar{\phi}_1(\omega)$ to get

$$\bar{\phi}_0(\omega) = \frac{A(u_i,u_{i+1})D(\omega,u_i,u_{i+1}) + i\omega B(\omega,u_i,u_{i+1})}{A(u_i,u_{i+1})C(u_i,u_{i+1}) + \omega^2} \quad . \tag{24}$$

Then $i\omega\bar{\phi}_1(\omega)$ may be computed from Eq. 22, and $q_m(\omega,u_{i+1})$ may be computed from the transform of Eq. 7.

Input. – The input is the same as for a one-region Corn Pone case. Following this is a list of ω^2, typed in packed decimal floating point, terminated by F100000000.

Output. – Output is on paper tape. First is punched the group number as 00*iii*00001, where *iii* is a hex integer. The transform of the slowing-down density is then punched in packed decimal floating point.

Test Results. – The Fourier transform of the slowing-down density from a fission source in light water at 1.375 ev with isotropic oxygen scattering was computed to be 0.587 for a B^2 of 0.028 cm^2. Monte Carlo results[3] gave 0.590 ± 0.014 at 1.44 ev.

6.5 ANISOTROPIC SLOWING-DOWN PARAMETERS FOR CORN PONE

W. E. Kinney

Introduction

The inclusion in nuclear calculations of anisotropic scattering in the center-of-mass system can produce results differing significantly from results obtained by assuming all scattering isotropic. For example, the calculated age to indium resonance of fission neutrons in light water is increased by 1.4 cm^2 when anisotropic scattering in oxygen is included.[1]

Two codes have been written for the Oracle to compute the slowing-down parameters used by Corn Pone[2] for the case of anisotropic scattering. The two codes permit use of scattering data in either of two commonly furnished forms. A Legendre Polynomial Code employs the coefficients obtained in the expansion of the differential scattering cross section in a series of Legendre polynomials. The Differential Code uses the differential scattering cross section directly.

The Legendre Polynomial Code

The probability of scattering in the center-of-mass system into $d\omega$ about ω can be expressed as

$$\mathcal{P}(\omega)\, d\omega = \sum_{l=0}^{\infty} \frac{2l+1}{2} f_l P_l(\omega)\, d\omega \quad ,$$

[1] J. G. Sullivan, unpublished Monte Carlo results.

[2] W. E. Kinney *et al.*, *Appl. Nuclear Phys. Ann. Prog. Rep. Sept. 10, 1956*, ORNL-2081, p 133.

where

ω = cosine of the center-of-mass scattering angle,

$P_l(\omega)$ = lth Legendre polynomial.

The code uses f_0 through f_8 to average the desired quantities.

Input. – The paper tape input is as follows:

1. A = the scatterer-to-neutron mass ratio. Type in packed decimal floating point.
2. E = the energy for which the expansion coefficients are given, in ev. Type in packed decimal floating point.
3. ω_0 = the initial value of ω (negative). Type in packed decimal floating point.
4. $\Delta\omega$ = the ω interval to be used in the numerical integrations. Type in packed decimal floating point.
5. $\left.\begin{array}{l} a)\ f_0 \\ b)\ f_1 \\ c)\ f_2 \\ d)\ f_3 \\ e)\ f_4 \\ f)\ f_5 \\ g)\ f_6 \\ h)\ f_7 \\ i)\ f_8 \end{array}\right\}$ = the expansion coefficients. Type in packed decimal floating point.

Operating Instructions. –

1. Load the program from paper tape into memory position 000.
2. Put the input tape under the reader.
3. Transfer to the left of memory position 000.
4. For additional cases, repeat 3.

Output. – The output is punched on paper tape in packed decimal floating point as follows:

1. A = the scatterer-to-neutron mass ratio,
2. E = the energy, in ev,
3. $\int_{-1}^{1} \wp(\omega)\, d\omega$,
4. $\langle \mu \rangle$ = the average cosine of the laboratory scattering angle,
5. $\xi = \langle u \rangle$ = the average lethargy gain,
6. $\gamma = \dfrac{\langle u^2 \rangle}{2\,\langle u \rangle}$,
7. $\eta = \langle u\mu \rangle$,
8. $\rho = \dfrac{\langle u^2\mu \rangle}{2\,\langle u\mu \rangle}$.

Results. – Table 6.5.1 lists values of $\langle \mu \rangle$, ξ, γ, η, and ρ for oxygen. The expansion coefficients listed by Troubetzkoy[3] were used in the computation; $\Delta\omega$ was 0.025. These values will be used to compute a Corn Pone anisotropic age in water.

[3] E. S. Troubetzkoy, *Fast Neutron Cross Sections of Iron, Silicon, Aluminum, and Oxygen*, NDA 2111-3 (Nov. 1, 1959).

Table 6.5.1. Values of $\langle \mu \rangle$, ξ, γ, η, and ρ for Oxygen for Energies from 18.0 to 0.284 Mev

Energy (Mev)	$\langle \mu \rangle$	ξ	γ	η	ρ
18.0	0.734	0.0333	0.0498	0.00678	−0.0432
17.1	0.726	0.0343	0.0514	0.00614	−0.0601
16.3	0.721	0.0349	0.0522	0.00580	−0.0698
15.5	0.712	0.0360	0.0542	0.00481	−0.105
14.75	0.705	0.0368	0.0553	0.00429	−0.131
14.0	0.700	0.0375	0.0562	0.00385	−0.161
13.3	0.693	0.0384	0.0572	0.00331	−0.204
12.7	0.687	0.0392	0.0580	0.00290	−0.254
12.1	0.681	0.0399	0.0588	0.00243	−0.324
11.5	0.677	0.0404	0.0588	0.00244	−0.324
10.9	0.672	0.0411	0.0592	0.00222	−0.371
10.4	0.668	0.0416	0.0593	0.00216	−0.387
9.89	0.662	0.0422	0.0593	0.00219	−0.382
9.41	0.658	0.0427	0.0596	0.00203	−0.426
8.95	0.653	0.0434	0.0596	0.00207	−0.416
8.51	0.644	0.0445	0.0601	0.00174	−0.518
8.1	0.636	0.0456	0.0602	0.00176	−0.514
7.7	0.619	0.0476	0.0612	0.00101	−0.966
7.33	0.604	0.0496	0.0626	0.0000222	−48.8
6.97	0.586	0.0518	0.0630	−0.000356	3.10
6.63	0.551	0.0563	0.0650	−0.00216	0.579
6.3	0.510	0.0614	0.0668	−0.00412	0.341
6.0	0.464	0.0670	0.0702	−0.00822	0.219
5.7	0.420	0.0726	0.0717	−0.0106	0.189
5.43	0.373	0.0784	0.0732	−0.0133	0.168
5.16	0.336	0.0831	0.0749	−0.0163	0.155
4.91	0.345	0.0820	0.0750	−0.0162	0.159
4.67	0.414	0.0734	0.0730	−0.0122	0.189
4.44	0.433	0.0709	0.0718	−0.0104	0.209
4.23	0.428	0.0716	0.0707	−0.00927	0.223
4.02	0.404	0.0746	0.0713	−0.0104	0.210
3.82	0.262	0.0924	0.0817	−0.0282	0.143
3.64	0.139	0.108	0.0893	−0.0461	0.131
3.46	0.0851	0.114	0.0923	−0.0544	0.128
3.29	0.130	0.109	0.0895	−0.0468	0.130
3.13	0.172	0.104	0.0861	−0.0390	0.133
2.97	0.160	0.105	0.0840	−0.0359	0.134
2.83	0.129	0.109	0.0820	−0.0338	0.136
2.69	0.0910	0.114	0.0802	−0.0320	0.137

Table 6.5.1 (continued)

Energy (Mev)	$\langle \mu \rangle$	ξ	γ	η	ρ
2.56	0.0390	0.120	0.0814	−0.0362	0.128
2.44	0.0205	0.1226	0.0818	−0.0376	0.127
2.32	0.0966	0.113	0.0847	−0.0400	0.131
2.21	0.0712	0.116	0.0829	−0.0378	0.130
2.1	0.0714	0.116	0.0827	−0.0374	0.130
2.0	0.0713	0.116	0.0828	−0.0375	0.130
1.9	0.0730	0.116	0.0830	−0.0379	0.129
1.81	0.0748	0.116	0.0832	−0.0382	0.129
1.72	0.0813	0.115	0.0835	−0.0384	0.129
1.63	0.0868	0.114	0.0838	−0.0387	0.129
1.55	0.0961	0.113	0.0841	−0.0389	0.130
1.48	0.108	0.112	0.0842	−0.0386	0.130
1.41	0.178	0.103	0.0822	−0.0322	0.134
1.34	0.448	0.0690	0.0650	−0.00262	0.528
1.27	−0.0068	0.126	0.0912	−0.0577	0.127
1.21	−0.0169	0.127	0.0926	−0.0611	0.126
1.15	−0.0332	0.126	0.0936	−0.0622	0.125
1.096	0.00243	0.125	0.0957	−0.0660	0.125
1.042	0.0157	0.123	0.0991	−0.0718	0.124
0.991	0.0237	0.122	0.0977	−0.0686	0.124
0.943	0.0342	0.121	0.0897	−0.0523	0.126
0.897	0.0508	0.119	0.0812	−0.0353	0.130
0.853	0.0680	0.117	0.0790	−0.0306	0.133
0.812	0.0881	0.114	0.0790	−0.0299	0.135
0.772	0.107	0.112	0.0788	−0.0289	0.137
0.734	0.127	0.109	0.0779	−0.0267	0.140
0.699	0.153	0.106	0.0766	−0.0238	0.145
0.666	0.176	0.103	0.0755	−0.0214	0.151
0.632	0.120	0.100	0.0743	−0.0188	0.158
0.601	0.230	0.0963	0.0726	−0.0154	0.172
0.572	0.256	0.0931	0.0711	−0.0126	0.188
0.544	0.319	0.0853	0.0671	−0.00622	0.284
0.518	0.402	0.0749	0.0611	0.00181	−0.559
0.492	0.463	0.0672	0.0560	0.00708	−0.0757
0.468	0.482	0.0648	0.0579	0.00481	−0.178
0.445	0.255	0.0932	0.0790	−0.0244	0.156
0.424	0.149	0.106	0.0842	−0.0367	0.136
0.403	−0.0256	0.128	0.0896	−0.0554	0.123
0.383	−0.165	0.146	0.0918	−0.0681	0.117
0.365	−0.185	0.148	0.0908	−0.0668	0.116
0.347	−0.106	0.138	0.0874	−0.0550	0.119
0.330	−0.0673	0.134	0.0860	−0.0499	0.121
0.314	−0.0182	0.127	0.0840	−0.0437	0.124
0.299	0.0317	0.121	0.0821	−0.0378	0.128
0.284	0.0417	0.120	0.0817	−0.0366	0.129

The Differential Code

The Differential Code breaks the ω interval (ω again being the cosine of the center-of-mass scattering angle) from -1 to $+1$ into subintervals of widths $\Delta\omega$ and uses specified values of the average differential scattering cross section over the subintervals to perform the required integrations numerically.

Input. – The paper tape input is as follows:

1. A = the scatterer-to-neutron mass ratio. Type in packed decimal floating point.
2. E = the energy, in ev, at which the differential cross section is given. Type in packed decimal floating point.
3. ω_0 = the initial value of ω (negative). Type in packed decimal floating point.
4. $\Delta\omega$ = the ω subinterval to be used in the numerical integration. Type in packed decimal floating point.
5. N = the number of values of the differential scattering cross section which follow. Type as a hex integer.
6. Type the N values of the differential scattering cross section in packed decimal floating point. Type in order of increasing ω.

Operating Instructions. – Operating instructions are the same as for the Legendre Polynomial Code.

Output. – The output is punched on paper tape in packed decimal floating point as follows:

1. A = the scatterer-to-neutron mass ratio.
2. E = the energy, in ev.
3. $\sum_{i=1}^{N} \overline{\sigma_i}\,\Delta\omega$, where $\overline{\sigma_i}$ = the average differential scattering cross section in the ith interval.
4. $\langle\mu\rangle$
5. ξ
6. γ
7. η
8. ρ

Symbols have same meanings as previously given.

Results. – Table 6.5.2 lists values of $\langle\mu\rangle$, ξ, γ, η, and ρ for beryllium. Cross sections were obtained from the angular distributions given by Häfele;[4] $\Delta\omega$ was 0.05.

---

[4] W. Häfele, *The Fast Multiplication Effect of Beryllium in Reactors*, ORNL-2779 (Sept. 8, 1959).

Table 6.5.2. Values of $\langle \mu \rangle$, ξ, γ, η, and ρ for Beryllium for Energies from 1 to 7 Mev

Energy (Mev)	$\langle \mu \rangle$	ξ	γ	η	ρ
1	0.240	0.170	0.131	−0.0292	0.302
1.21	0.250	0.167	0.132	−0.0305	0.304
1.5	0.300	0.156	0.126	−0.0205	0.366
1.75	0.201	0.178	0.135	−0.0374	0.274
2.15	0.165	0.186	0.150	−0.0641	0.242
2.44	0.0614	0.209	0.165	−0.100	0.224
2.6	0.133	0.193	0.159	−0.0822	0.226
3.5	0.426	0.128	0.135	−0.0278	0.320
4.1	0.432	0.127	0.136	−0.0279	0.324
5.0	0.536	0.104	0.122	−0.00934	0.612
6.0	0.576	0.0945	0.120	−0.00719	0.720
7.0	0.635	0.0814	0.111	0.000629	−5.96

6.6 ADDITIONS AND CHANGES TO CORN PONE

W. E. Kinney

Introduction

The method of homogenizing heterogeneous reactor cells and thereby defining disadvantage factors has long been known.[1,2] A version of Corn Pone[3] has been assembled which incorporates codes to compute and use disadvantage factors.

The boundary conditions on a void have been changed to conform to the assumption of isotropic currents entering the void.

Disadvantage Factors

The disadvantage factors as used in the code are defined as

$$DF_{ij} = \frac{\bar{\phi}_{ij}}{\bar{\phi}_{\mathrm{cell}_i}}, \tag{1}$$

[1] S. Glasstone and M. C. Edlund, *The Elements of Nuclear Reactor Theory*, Van Nostrand, New York, 1952.

[2] A. M. Weinberg and E. P. Wigner, *The Physical Theory of Neutron Chain Reactors*, University of Chicago Press, Chicago, 1958.

[3] W. E. Kinney *et al.*, *Appl. Nuclear Phys. Ann. Prog. Rep. Sept. 10, 1956*, ORNL-2081, p 133.

where

DF_{ij} = disadvantage factor in the ith group, jth region,

$\bar{\phi}_{ij}$ = average flux in the ith group, jth region,

$\bar{\phi}_{\text{cell}_i}$ = average flux in the cell in the ith group.

Disadvantage factors are computed in each group for a cell of 19 or fewer regions.

Application of Disadvantage Factors

To apply the disadvantage factors, conservation of events between the homogeneous and heterogeneous case is required. That is,

$$\sum_j \Sigma_{ij} \bar{\phi}_{ij} V_j = \bar{\phi}_{\text{cell}_i} V_{\text{cell}} \sum_j \Sigma_{ij} \ , \tag{2}$$

where

Σ_{ij} = macroscopic cross section for some event in the ith group, jth region,

V_j = volume of the jth region,

V_{cell} = volume of the cell.

The homogenized cross section is, then,

$$\sum_j \Sigma_{ij} = \sum_j \Sigma_{ij} f_j (DF)_{ij} \ , \tag{3}$$

where f_j = the volume fraction of the jth region = V_j/V_{cell}.

The input to the homogeneous calculation for each element in the central region is the nuclear density multiplied by the volume fraction. In addition, the set of disadvantage factors which is to be applied to the element is specified. The absorptions, fission, and productions in each element, properly disadvantaged, may be punched on paper tape and printed on the Oracle curve plotter if desired.

Void Boundary Conditions[4]

If the currents entering a void are assumed to be isotropic, then the following boundary conditions hold:

$$r_2^g j_+(r_2) = r_1^g j_+(r_1) + r_2^g j_-(r_2) \left(1 - \frac{r_1^g}{r_2^g} \right) \ , \tag{4}$$

$$j_-(r_1) = j_-(r_2) \ , \tag{5}$$

[4]The method employed was suggested by L. G. Alexander of the Reactor Projects Division.

where

$j_{\pm}(r)$ = the $\begin{Bmatrix}\text{positive}\\ \text{negative}\end{Bmatrix}$ partial current at radius r,

r_1 = the inner radius of the void,

r_2 = the outer radius of the void,

g = a geometry factor = 0, 1, 2 for a slab, cylinder, or sphere, respectively.

Since

$$j_{\pm}(r) = \frac{1}{4}\phi_0(r) \pm \frac{1}{2}\phi_1(r) \ ,$$

where

$\phi_0(r)$ = the flux at r,

$\phi_1(r)$ = the current at r,

the boundary conditions may be put into the form

$$\left(\frac{r_1}{r_2}\right)^g \phi_1(r_1) = \phi_1(r_2) \ , \tag{6}$$

$$\left(\frac{r_1}{r_2}\right)^g \phi_0(r_1) = \left(\frac{r_1}{r_2}\right)^g \phi_0(r_2) + 2\left[1 - \left(\frac{r_1}{r_2}\right)^g\right]\phi_1(r_2) \ . \tag{7}$$

Since the average flux in a cell is needed for the computation of disadvantage factors, an expression for the flux within the void must be obtained.

Applying Eqs. 6 and 7 to a surface of radius r within the void gives immediately

$$\phi_0(r) = \phi_0(r_1) - 2\left[1 - \left(\frac{r_1}{r_2}\right)^g\right]\phi_1(r_1) \ . \tag{8}$$

Integrating from r_1 to r_2 gives

$$\bar{\phi}_0 V = \phi_0(r_1)\frac{r_2^{g+1} - r_1^{g+1}}{g+1} + 2\phi_1(r_1)\left[r_1^g(r_2 - r_1) - \frac{r_2^{g+1} - r_1^{g+1}}{g+1}\right] , \tag{9}$$

where

$$V = \int_{r_1}^{r_2} r^g \, dr \ ,$$

$\bar{\phi}_0$ = the average flux in the region.

These boundary conditions have been put into Corn Pone.

6.7 AN EXAMINATION OF SOME FEATURES OF CORN PONE, A MULTIGROUP, MULTIREGION REACTOR CODE

W. E. Kinney

Introduction

In the design of Corn Pone,[1,2] the P_1 multigroup, multiregion, one-dimensional reactor code for the Oracle, a considerable degree of refinement and flexibility was introduced. The difference equations are good to fourth order in the lattice spacing, rather than to second order,[2] as is more common, and a linear lethargy variation of flux over a group has been assumed in the calculation of group events – scatterings, absorptions, etc. Inclusion of these features involved considerable additional effort, and therefore some studies have been made to evaluate their worth.

Slowing-down may be treated with age (Fermi), Wigner, or Goertzel-Greuling kernels,[3,4] and by setting the slowing-down current equal to zero, P_1 theory may be reduced to diffusion theory. Since more computing time is required for P_1 theory than for diffusion theory, and for Goertzel-Greuling kernels than for age (Fermi) kernels, comparisons have been made between the two theories and the two slowing-down models.

Fourth-Order vs Second-Order Approximations

The fourth-order approximations are developed in ref 1, and may be compared to the second-order approximations given in ref 3. For a comparison case, an infinite-slab reactor, moderated and reflected with light water, was calculated. The core had a half thickness of 14 cm, and contained 3.1×10^{20} atoms of U^{235} per cm^3. The reflector thickness was 10 cm. The first set of cases, using the first 18 groups of the group structure given in Table 6.7.1, was run until the fractional change in the multiplication constant from one iteration to the next was less than 0.0001. The second set, using 31 groups, was run one iteration. The comparison of results is given in Table 6.7.2. It is evident that the use of numerical approximations to derivatives good to fourth order does not yield results greatly different from those obtained by using the simpler second-order approximations. Although there certainly exist systems for which the differences between second- and fourth-order results are greater, the slight improvement offered by the fourth-order approximation is far outweighed by the ease of coding and inherently faster running time of the second-order equations.

---

[1] W. E. Kinney *et al.*, *Appl. Nuclear Phys. Ann. Prog. Rep. Sept. 10, 1956*, ORNL-2081, p 133.

[2] W. E. Kinney, R. R. Coveyou, and J. G. Sullivan, *Neutron Phys. Ann. Prog. Rep. Sept. 1, 1958*, ORNL-2609, p 84.

[3] H. Soodak, F. Adler, and E. Greuling, chap. 1.3, p 368 in *The Reactor Handbook*, vol 1, AECD-3645 (1955).

[4] G. Goertzel and E. Greuling, *Nuclear Sci. and Eng.* 7, 1 (1960).

Table 6.7.1. The 31-Group Structure

Group	Lower Energy Limit (ev)	Group	Lower Energy Limit (ev)
	10^8	16	9.214×10^{-1}
1	10^7	17	6.176×10^{-1}
2	6.065×10^6	18	4.140×10^{-1}
3	3.679×10^6	19	2.775×10^{-1}
4	2.231×10^6	20	2.272×10^{-1}
5	1.353×10^6	21	1.860×10^{-1}
6	8.208×10^5	22	1.523×10^{-1}
7	1.832×10^5	23	1.247×10^{-1}
8	9.118×10^3	24	1.021×10^{-1}
9	4.54×10^2	25	8.358×10^{-2}
10	1.12×10^2	26	6.843×10^{-2}
11	3.372×10^1	27	5.603×10^{-2}
12	1.515×10^1	28	4.587×10^{-2}
13	1.016×10^1	29	3.756×10^{-2}
14	4.564×10^0	30	3.075×10^{-2}
15	1.375×10^0	31	2.518×10^{-2}
			Thermal

Table 6.7.2. Comparison of Fourth-Order Approximation Results with Second-Order Results

Order	Core Points	Reflector Points	Multiplication Constant	Core Absorptions	Core Escapes	Reflector Absorptions	Reflector Escapes
			Set 1 (18 Groups)				
Fourth	37	26	1.49107	0.837524	0.162480	0.0440251	0.118449
Second	37	26	1.49109	0.837535	0.162468	0.0440193	0.118462
Fourth	16	11	1.49105	0.837516	0.162582	0.0440214	0.118409
Second	16	11	1.49117	0.837583	0.162534	0.0439943	0.118512
Fourth	13	9	1.49104	0.837511	0.162698	0.0440182	0.118360
Second	13	9	1.49123	0.837612	0.162414	0.0439788	0.118544
			Set 2 (31 Groups)				
Fourth	16	11	1.57390	0.848267	0.151767	0.0900343	0.0616666
Second	16	11	1.57343	0.848016	0.151431	0.0898242	0.0617169

A serious disadvantage of the fourth-order equations for use in a production code is the limitation they impose on the size of the lattice spacing. Some of the coefficients of the difference equations may reverse sign if the lattice spacing is too large (e.g., P_k and R_k of Eq. 20 in ref 1). This reversal cannot occur for the coefficients of the second-order equations.

The Linear Flux Assumption. – If the flux is assumed to vary linearly with lethargy over a group as

$$\phi(u) = \phi(u_i) + \frac{\phi(u_{i+1}) - \phi(u_i)}{u_{i+1} - u_i}(u - u_i) \quad , \tag{1}$$

where

u = the lethargy,

u_i = the lower lethargy limit of group i,

u_{i+1} = the upper lethargy limit of group i,

then

$$\frac{1}{u_{i+1} - u_i}\int_{u_i}^{u_{i+1}} \sigma(u)\phi(u)\, du = {}^{*}\sigma\bar{\phi} + \sigma^{*}\phi(u_i) \quad , \tag{2}$$

where

$$\begin{aligned} {}^{*}\sigma &= \frac{2}{(u_{i+1} - u_i)^2}\int_{u_i}^{u_{i+1}} \sigma(u)(u - u_i)\, du \quad , \\ \sigma^{*} &= \frac{1}{(u_{i+1} - u_i)^2}\int_{u_i}^{u_{i+1}} \sigma(u)(u_{i+1} + u_i - 2u)\, du \quad , \end{aligned} \tag{3}$$

$\bar{\phi}$ = the group average flux = $\dfrac{\phi(u_i) + \phi(u_{i+1})}{2}$.

If either the flux, $\phi(u)$, or the cross section, σ, is constant over the group,

$${}^{*}\sigma = \bar{\sigma} = \text{average cross section} \quad , \qquad \sigma^{*} = 0 \quad .$$

The constant or "flat" flux assumption is made in most multigroup formulations for the purpose of computing group events.

Two fourth-order P_1 calculations, using Goertzel-Greuling kernels for both the slowing-down density and current, were made on the test reactor of the previous paragraphs. The first calculation assumed a linear variation of the flux over the groups, while the second assumed the flux to be flat. Multiplication constants, absorptions, and escapes are compared in Table 6.7.3.

Table 6.7.4 compares the age of fission neutrons to 1.375 ev in various media, computed with Goertzel-Greuling kernels for the linear- and flat-flux assumptions. Isotropic scattering was assumed throughout.

Table 6.7.3. Multiplication Constants and Events for a Light-Water-Moderated Reactor, Computed Under Linear- and Flat-Flux Assumptions

Flux Assumption	Multiplication Constant	Core Absorptions	Core Escapes	Reflector Absorptions	Reflector Escapes
Linear	1.56474	0.856657	0.143343	0.102882	0.0404612
Flat	1.56523	0.858170	0.141829	0.101917	0.0399123

Table 6.7.4. Results of Linear- vs Flat-Flux Assumption in a Goertzel-Greuling–P_1 Calculation of the Age of Fission Neutrons to 1.375 ev in Four Media

Medium	Age to 1.375 ev, τ (cm^2)	
	Linear-Flux Assumption	Flat-Flux Assumption
H_2O	22.88	22.56
D_2O	108.06	108.12
Beryllium	62.34	61.45
Carbon	300.93	302.31

The differences between the linear- and flat-flux results are not large enough to warrant the use of the linear-flux assumption.

The Slowing-Down Models

The slowing-down density for a single scatterer may be defined as

$$q(r,u) = \int_0^u \sigma(u')\phi_0(r,u')\,du' \int_u^\infty K_0(u' \to u'')\,du'' \quad , \tag{4}$$

where

$\sigma(u')$ = the macroscopic scattering cross section,

$\phi_0(r,u')$ = the flux per unit lethargy,

$K_0(u' \to u'')\,du''$ = the probability of scattering from u' to du'' about u'',

u = the lethargy.

Age theory expands the scattering density about u and keeps only the first term to give the proportionality of slowing-down density to flux:

$$q(r,u) = \xi\sigma(u)\phi_0(r,u) \quad . \tag{5}$$

Goertzel-Greuling theory retains the first two terms in the expansion to obtain a differential equation relating the slowing-down density and the flux,

$$\gamma \frac{\partial}{\partial a} q(r,u) + q(r,u) = \xi\sigma(u)\phi_0(r,u) \quad , \tag{6}$$

where

$$\xi = \langle u \rangle \quad ,$$

$$\gamma = \frac{\langle u^2 \rangle}{2\xi} \quad ,$$

and $\langle \quad \rangle$ indicates average.

In an infinite medium distant (in lethargy) from a uniform source,

$$\frac{\partial}{\partial u} q(r,u) = -\alpha(u)\phi_0(r,u) \quad , \tag{7}$$

where $\alpha(u)$ = the absorption cross section.

Substituting Eq. 7 into Eq. 6 gives a modified age equation:

$$q(r,u) = [\xi\sigma(u) + \gamma\alpha(u)]\phi_0(r,u) \quad . \tag{8}$$

The slowing-down current for a single scatterer is defined as

$$p(r,u) = \int_0^u \sigma(u')\phi_1(r,u')\, du' \int_u^\infty K_1(u' \to u'')\, du'' \quad , \tag{9}$$

where

$\phi_1(r,u)$ = the current per unit lethargy per unit volume,

$K_1(u' \to u'') = \mu(u',u'')K_0(u' \to u'')$,

$\mu(u',u'')$ = the cosine of the laboratory scattering angle.

Diffusion theory sets $p(r,u) = 0$.

P_1-age theory expands the current scattering density about u and keeps only the first term to give:

$$p(r,u) = \eta\sigma(u)\phi_1(r,u) \quad . \tag{10}$$

P_1–Goertzel-Greuling theory expands the current scattering density about u and retains the first two terms to obtain a differential equation relating the slowing-down current and the current:

$$\rho \frac{\partial}{\partial u} p(r,u) + p(r,u) = \eta\sigma(u)\phi_1(r,u) \quad , \tag{11}$$

where

$$\eta = \langle u\mu \rangle \quad ,$$

$$\rho = \frac{\langle u^2\mu \rangle}{2\eta} \quad .$$

In an infinite medium,

$$\frac{\partial p(r,u)}{\partial u} = -\beta(u)\phi_1(r,u) \quad , \tag{12}$$

where $\beta(u)$ = the transport cross section.

Substituting Eq. 12 into Eq. 11 gives a modified P_1-age expression:

$$p(r,u) = [\eta\sigma(u) + \rho\beta(u)]\phi_1(r,u) \quad . \tag{13}$$

In summary, Goertzel-Greuling–P_1 theory uses Eq. 6 for the slowing-down density and Eq. 11 for the slowing-down current. Age-P_1 theory uses Eq. 8 for the slowing-down density and Eq. 13 for the slowing-down current. Goertzel-Greuling–diffusion theory uses Eq. 6 for the slowing-down density and sets the slowing-down current equal to zero. Age-diffusion theory uses Eq. 8 for the slowing-down density and sets the slowing-down current equal to zero.

Comparison of P_1 and Diffusion Slowing-Down Models

A number of calculations were performed to investigate the differences in results obtained from the use of P_1 vs diffusion-theory slowing-down models. Only for slowing in light water was much difference evident.

The results of a Corn Pone infinite-medium age code (Sec 6.4) computation of the age of fission neutrons in light water are plotted in Fig. 6.7.1 as a function of terminal energy. Isotropic oxygen scattering was assumed. For comparison, Monte Carlo results,[5] using identical

[5] D. J. McGaff *et al.*, *RETRACE, A Monte Carlo Code for Characterizing the Slowing Down of Neutrons in an Infinite Homogeneous Medium*, Memorandum EPS-S-389, MIT Engineering Practice School (Nov. 13, 1958).

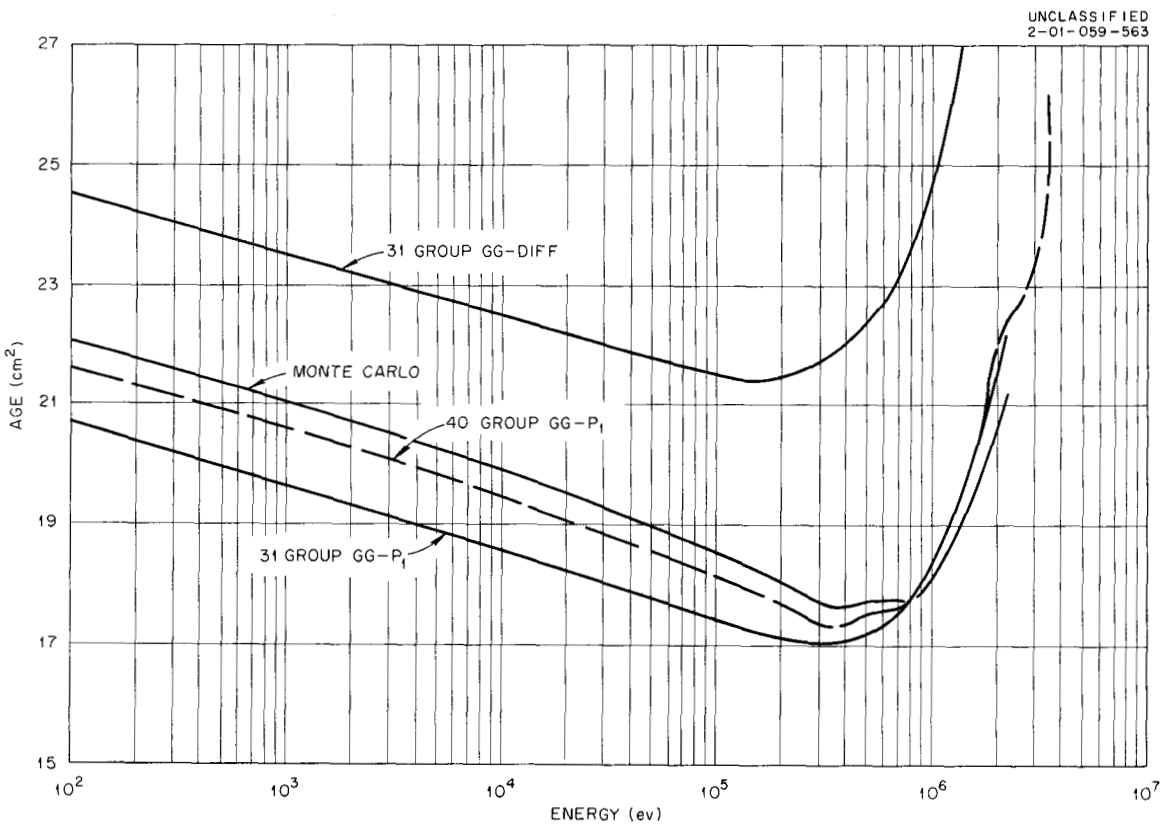

Fig. 6.7.1. Age of Fission Neutrons in Light Water with Isotropic Scattering as a Function of Final Energy.

basic cross sections, are also shown. It is clear that the P_1 results are in better agreement with Monte Carlo. The departure of the P_1 result from Monte Carlo occurs in the region of the 0.43-Mev oxygen scattering resonance. Use of a more-detailed group structure, containing 39 groups from 100 to 10^7 ev, with several groups in the oxygen resonance, produced better agreement with Monte Carlo than did the 31-group structure, which contained but ten groups in the range 100 to 10^7 ev. The slowing-down age to 1.375 ev for the various calculations is: 31-group Goertzel-Greuling–diffusion, 26.32 cm^2; 31-group Goertzel-Greuling–P_1, 22.56 cm^2; 40-group Goertzel-Greuling –P_1, 23.58 cm^2; and Monte Carlo, 23.93 cm^2.

Figure 6.7.2 is a plot of the Fourier transform (see Sec 6.4 of this report) of the fission source slowing-down density at thermal energy (0.025 ev) vs buckling, for light water. Results for both P_1 and diffusion theory are plotted.

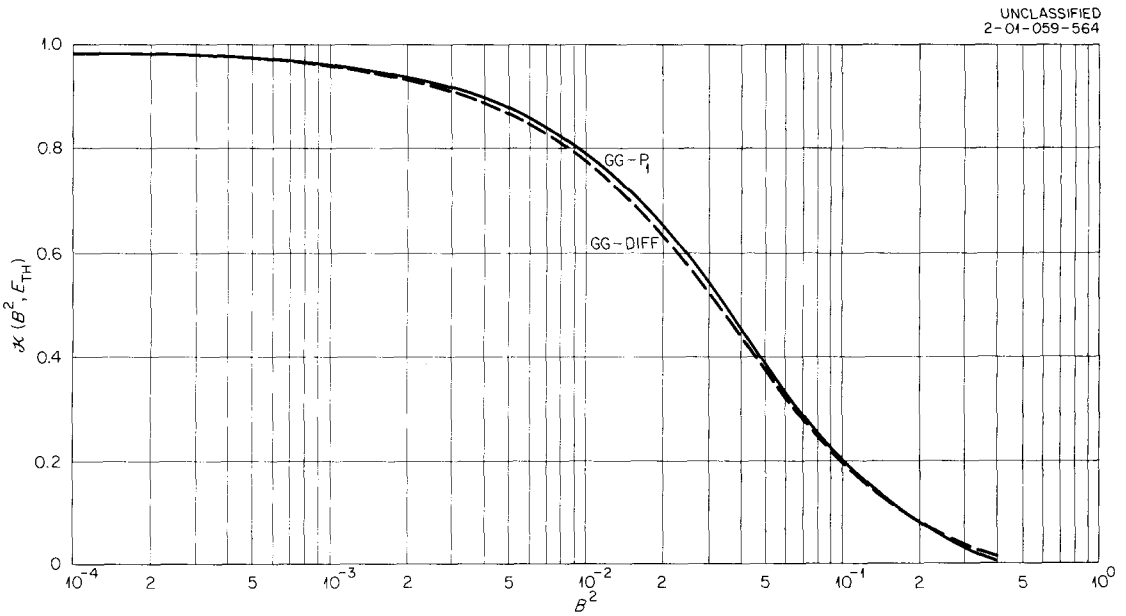

Fig. 6.7.2. $\mathcal{K}(B^2, E_{th})$ vs Buckling for Fission Neutrons in Light Water with Isotropic Scattering.

Figure 6.7.3 is a plot of the computed Lid Tank thermal fluxes in water for both P_1 and diffusion theory. The experimental curve[6] (not shown) lies about midway between the two curves. Both calculations were done with isotropic oxygen scattering, and it is expected that when the anisotropy is included, the P_1 curve will come into good agreement with experiment.

Table 6.7.5 compares P_1 and diffusion theory calculations of multiplication constants, absorptions, and escapes for bare spheres moderated by light water, heavy water, beryllium, and carbon. Only the calculations for light water show an appreciable difference.

---

[6]D. W. Cady and E. A. Warman, *Appl. Nuclear Phys. Ann. Prog. Rep. Sept. 1, 1957*, ORNL-2389, p 180–84.

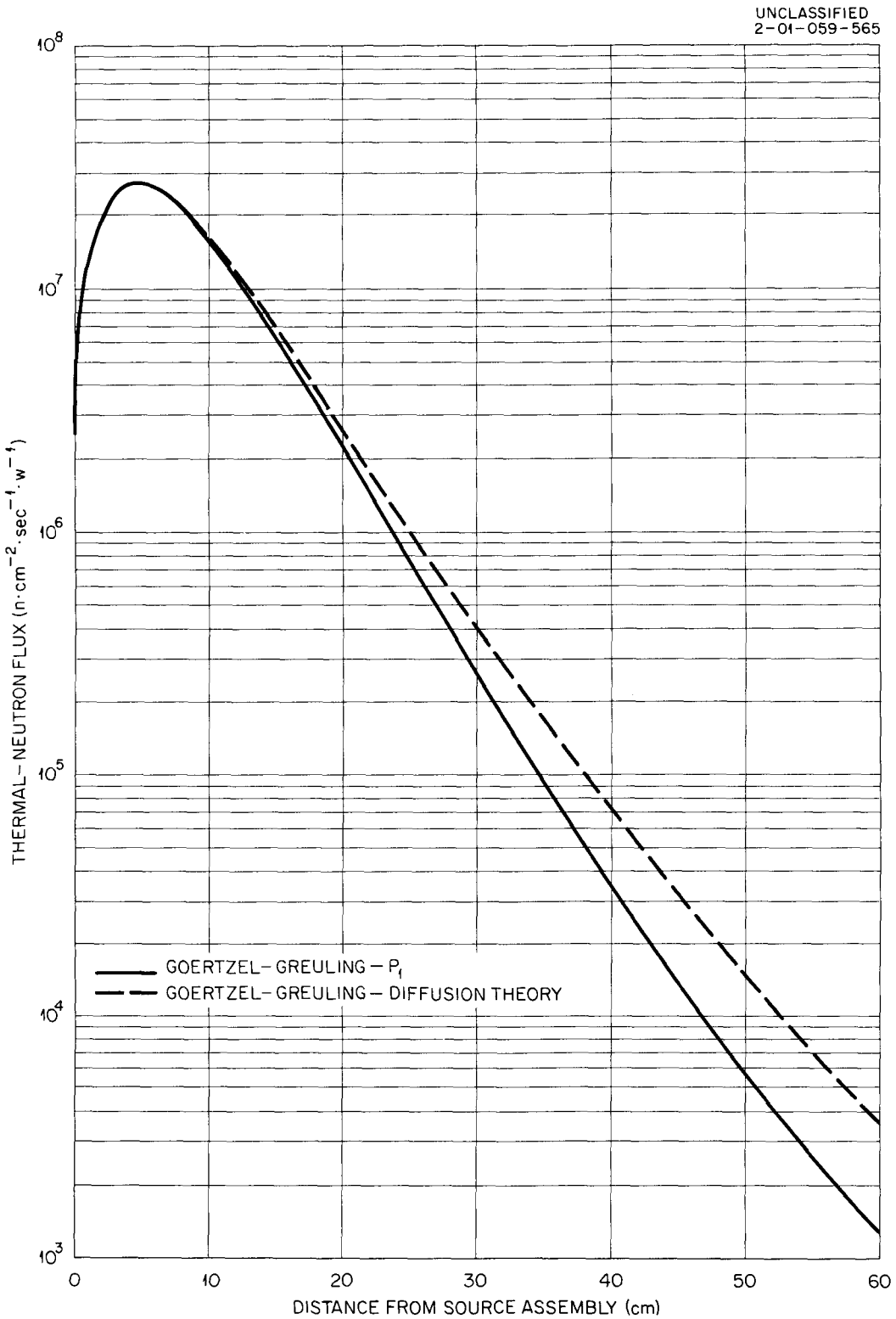

Fig. 6.7.3. Computed Thermal Flux in Light Water as a Function of Distance from the ORNL Lid Tank Source Plate.

Table 6.7.5. Comparison of Goertzel-Greuling–P_1, Goertzel-Greuling–Diffusion, and Age-Diffusion Results for Bare Spheres with Various Moderators

Model	Sphere Radius (cm)	Multiplication Constant	Fast Absorptions	Fast Escapes	Thermal Absorptions	Thermal Escapes
			H_2O Moderator			
GG-P_1	19.5	0.998800	0.075091	0.328257	0.565874	0.030782
GG-diffusion	19.5	0.979750	0.073352	0.342225	0.555246	0.029177
			D_2O Moderator			
GG-P_1	90	1.06109	0.020108	0.131467	0.489601	0.358825
GG-diffusion	90	1.06132	0.020117	0.131122	0.489701	0.359061
Age-diffusion, linear	90	1.07377	0.016483	0.125010	0.495423	0.362883
Age-diffusion, flat	90	1.06948	0.017613	0.127081	0.493573	0.361678
			Beryllium Moderator			
GG-P_1	40	1.01826	0.084962	0.351700	0.409555	0.153785
GG-diffusion	40	1.02005	0.085189	0.350016	0.410210	0.154589
Age-diffusion, linear	40	1.05109	0.088165	0.341483	0.422492	0.176584
Age-diffusion, flat	40	1.04484	0.086844	0.334118	0.420622	0.158279
			Carbon Moderator			
GG-P_1	100	1.01434	0.053792	0.276669	0.433776	0.235799
GG-diffusion	100	1.01520	0.053868	0.276121	0.434117	0.235897
Age-diffusion, linear	100	1.02751	0.054958	0.266563	0.439043	0.239436
Age-diffusion, flat	100	1.02431	0.054354	0.268602	0.438021	0.239004

It is interesting to note that the inclusion of the slowing-down current is more important for elements of mass number from 3 to 80 than for deuterium. If Eq. 11 is integrated over a group extending from lethargy u_i to u_{i+1}, and if it is assumed that

$$\int_{u_i}^{u_{i+1}} \sigma(u)\phi(u)e^{u/\rho}\,du = \bar{\sigma}\bar{\phi}\int_{u_i}^{u_{i+1}} e^{u/\rho}\,du \quad , \tag{14}$$

then

$$p(r,u_{i+1}) = p(r,u_i)e^{-\Delta u/\rho} + (1 - e^{-\Delta u/\rho})\eta\bar{\sigma}\bar{\phi} \quad . \tag{15}$$

Figure 6.7.4 plots $(1 - e^{-\Delta u/\rho})\eta$ vs mass number for $\Delta u = 0.5$, assuming isotropic scattering. The term is largest for hydrogen but reaches a minimum for a mass number of 6. The term does not rise to the deuterium value until the mass number is 80.

Figures 6.7.5, 6.7.6, and 6.7.7 compare P_1 and diffusion theory ages for heavy water, beryllium, and carbon.

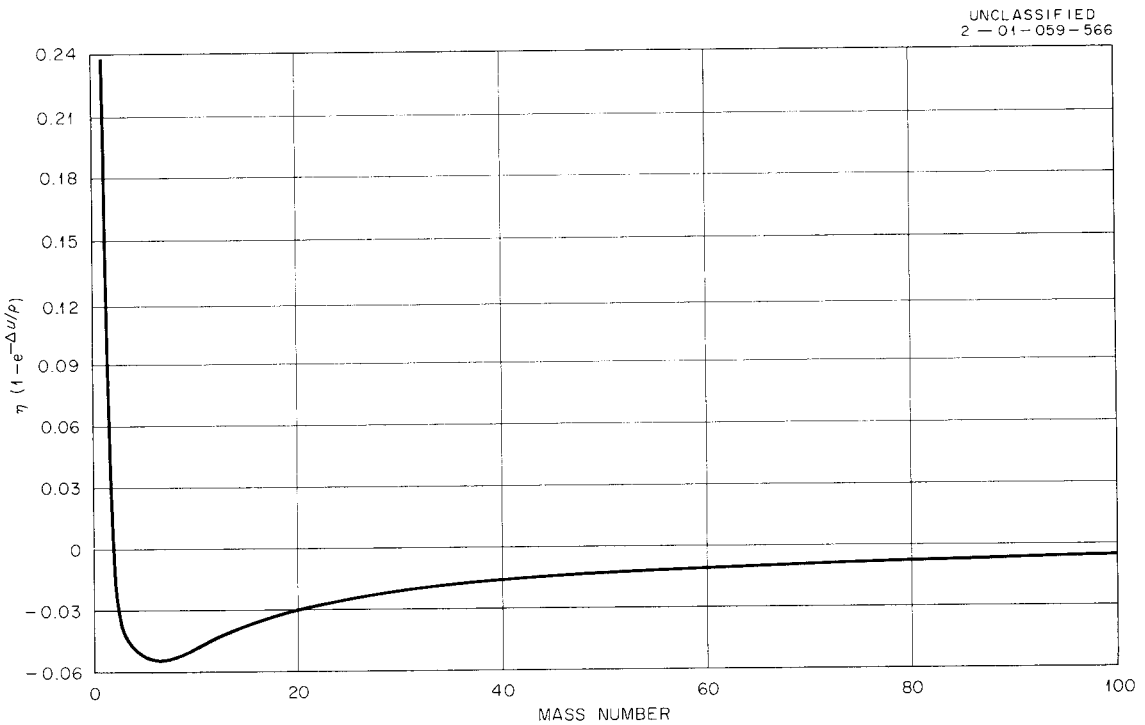

Fig. 6.7.4. $\eta(1 - e^{-\Delta u/\rho})$ **vs Mass Number for** $\Delta u = 0.5$**; Isotropic Scattering in the Center-of-Mass System.**

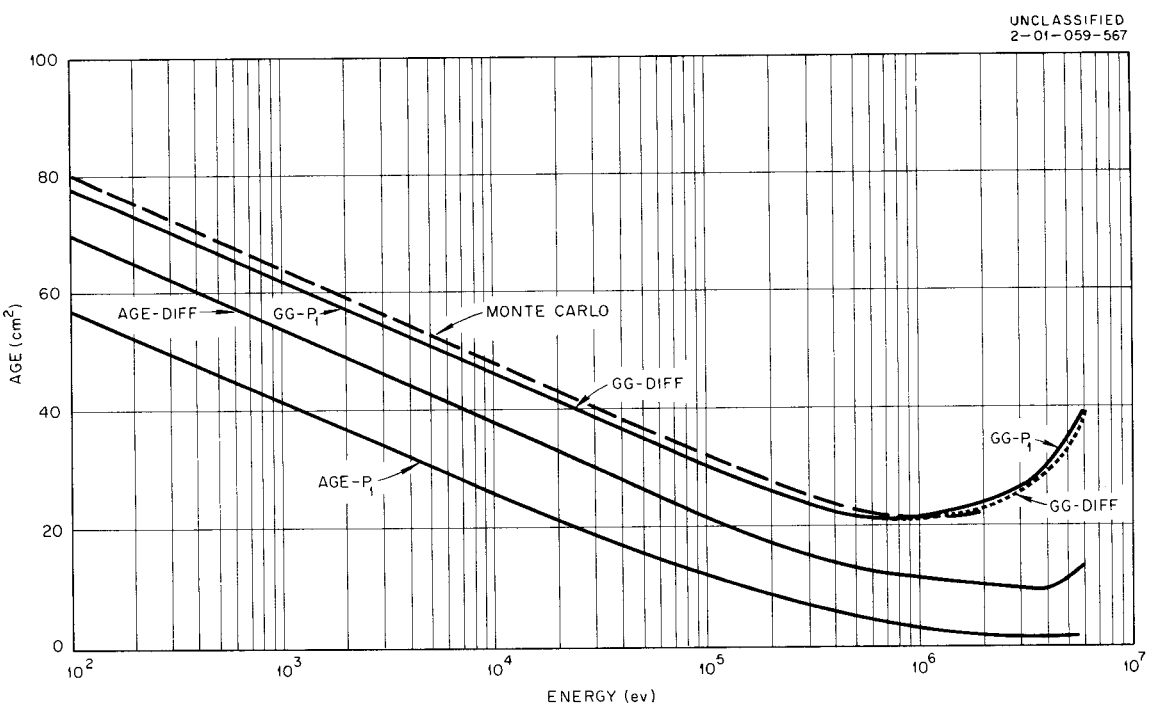

Fig. 6.7.5. Age of Fission Neutrons in Heavy Water as a Function of Energy; Isotropic Scattering by Oxygen.

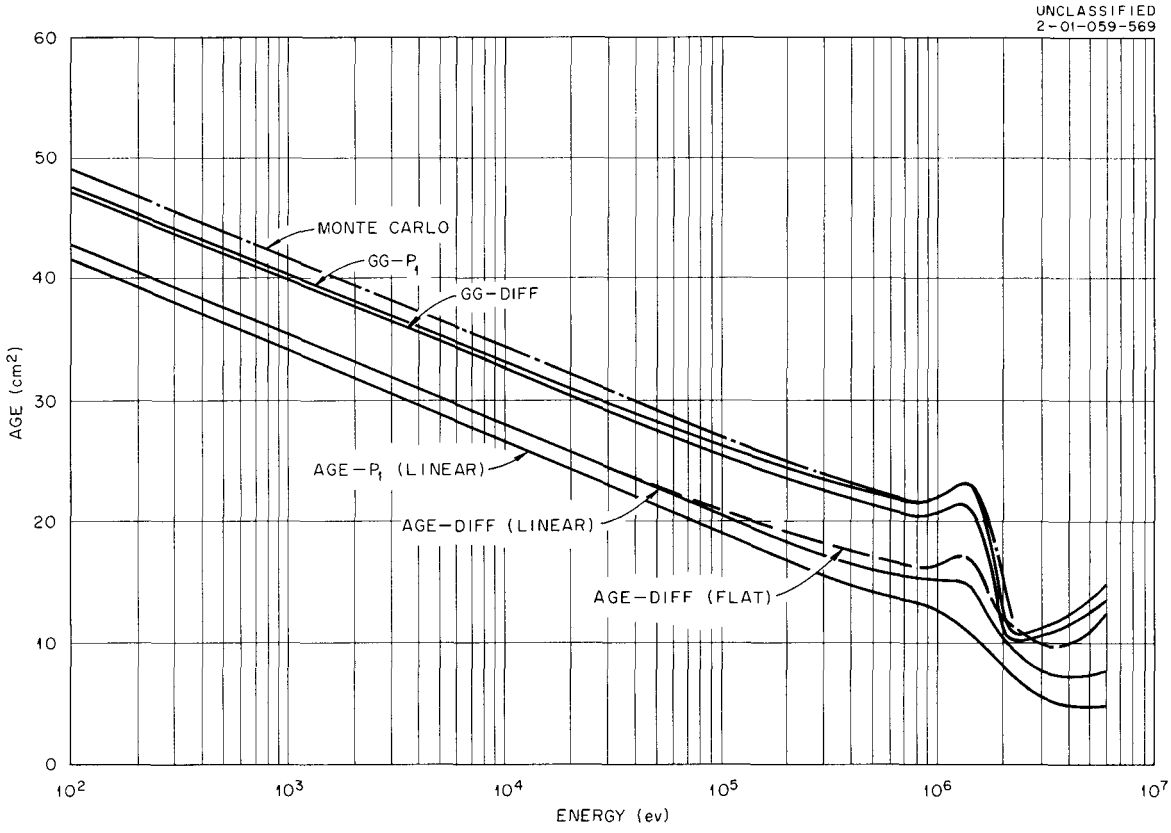

Fig. 6.7.6. Age of Fission Neutrons in Beryllium as a Function of Energy.

Comparison of Goertzel-Greuling–Diffusion and Age-Diffusion Theory

In addition to the comparison between P_1 and diffusion theory noted above, Figs. 6.7.5, 6.7.6, and 6.7.7 also show the results obtained from the use of various slowing-down models, plus Monte Carlo results, for slowing in heavy water, beryllium, and carbon, respectively. Figures 6.7.8, 6.7.9, and 6.7.10 display the Fourier transform of the thermal slowing-down density as a function of buckling for both Goertzel-Greuling–diffusion and age-diffusion models for the same three moderators. Ages to 1.375 ev computed by the various methods are shown in Table 6.7.6. The differences between Goertzel-Greuling and age theory slowing-down in heavy water are in agreement with the findings of Levine *et al.*[7]

The ages computed according to the Goertzel-Greuling theory are in much better agreement with Monte Carlo results than are the age-theory ages, even for carbon. This suggests the construction of an alternative age theory slowing-down model, simpler than the one usually used, yet more nearly correct. Consider the following:

---

[7]M. M. Levine *et al.*, *Nuclear Sci. and Eng.* **7**, 14 (1960).

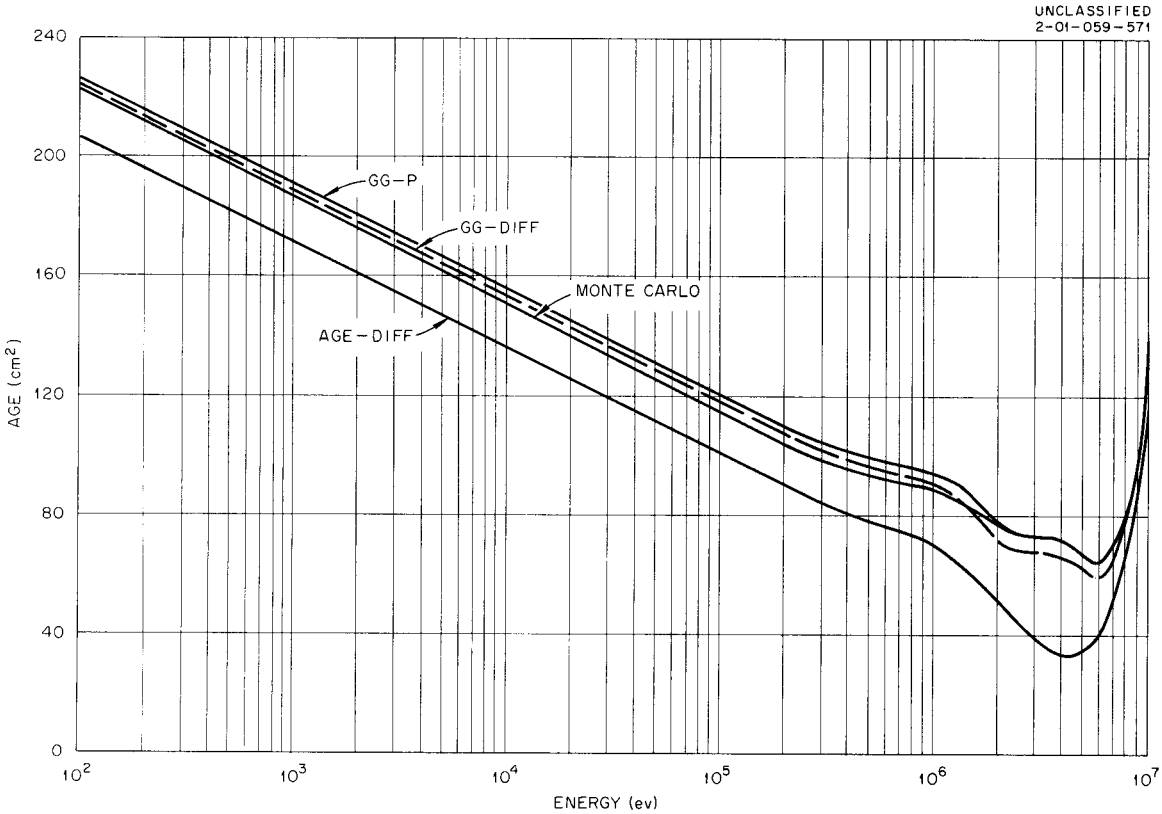

Fig. 6.7.7. Age of Fission Neutrons in Carbon as a Function of Energy.

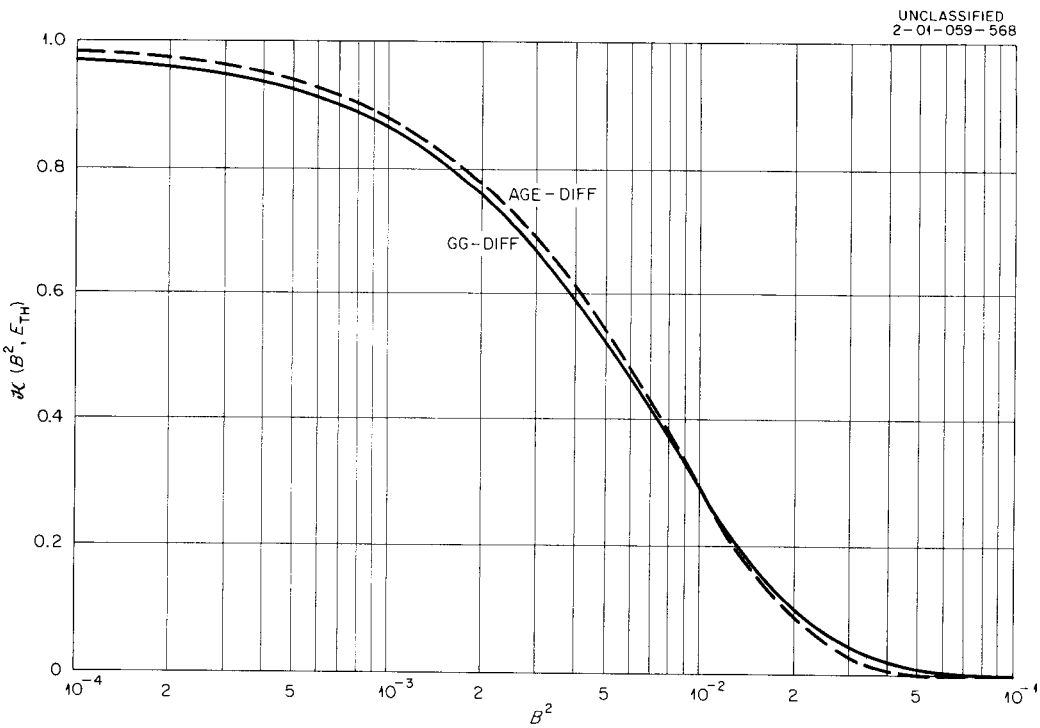

Fig. 6.7.8. $\mathcal{K}(B^2, E_{th})$ vs Buckling for Fission Neutrons in Heavy Water; Isotropic Scattering.

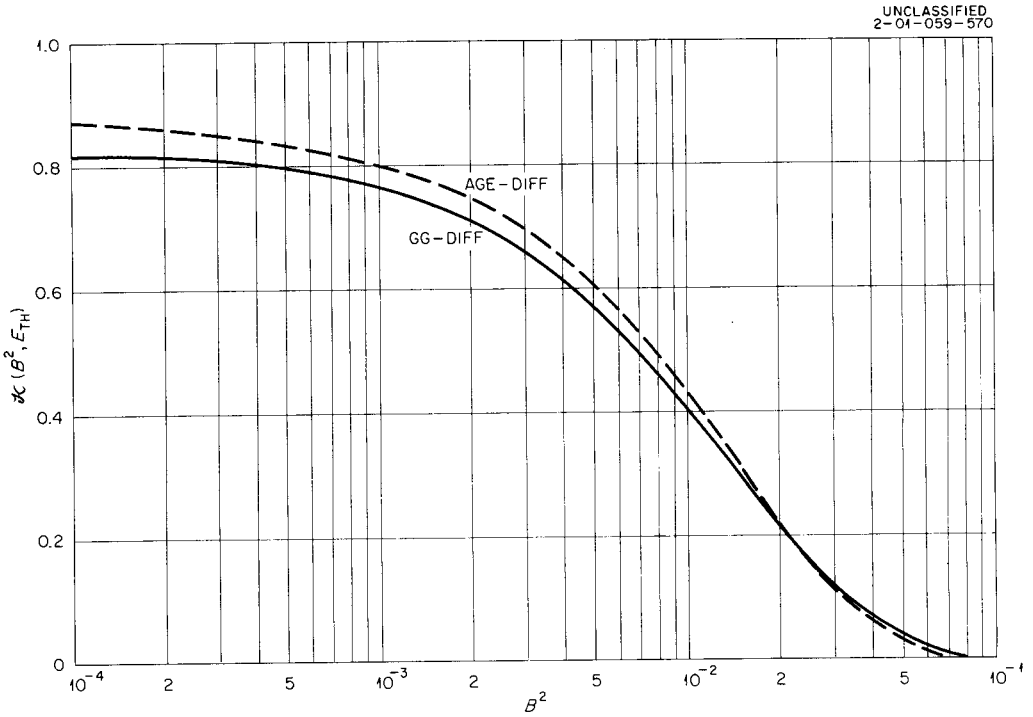

Fig. 6.7.9. $\mathcal{K}(B^2, E_{th})$ **vs Buckling for Fission Neutrons in Beryllium.**

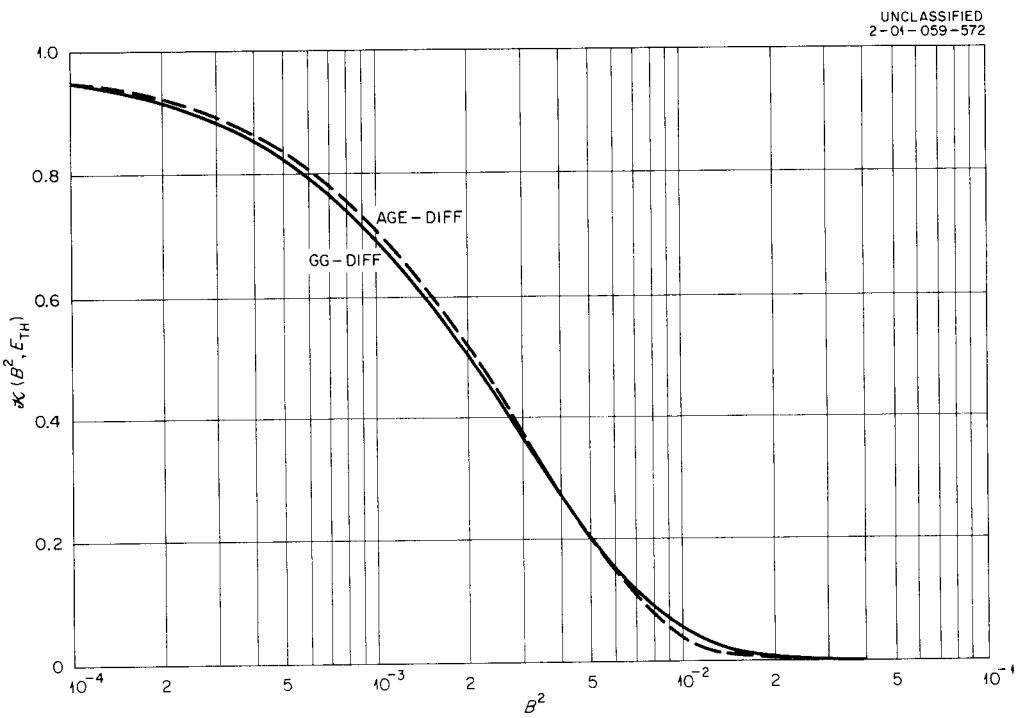

Fig. 6.7.10. $\mathcal{K}(B^2, E_{th})$ **vs Buckling for Fission Neutrons in Carbon.**

Table 6.7.6. Age of Fission Neutrons to 1.375 ev, in Heavy Water, Beryllium, and Carbon, Computed by Various Methods

Method	Age to 1.375 ev (cm^2)		
	D_2O	Be	C
Goertzel-Greuling–P_1	108.12	61.45	292.7
Goertzel-Greuling–diffusion	107.62	60.83	290.5
Age-diffusion	99.73	56.48	273.6
Monte Carlo	109.9 ± 0.6	62.8 ± 0.8	289 ± 2
Eq. 18–diffusion		61.66	292.0

We integrate Eq. 6 over a group extending from lethargy u_i to u_{i+1}, and assume that

$$\int_{u_i}^{u_{i+1}} \sigma(u)\phi(u)e^{u/\gamma}\,du = \bar{\sigma}\bar{\phi}\int_{u_i}^{u_{i+1}} e^{u/\gamma}\,du \ . \tag{16}$$

Then

$$q(r,u_{i+1}) = q(r,u_i)e^{-\Delta u/\gamma} + (1 - e^{-\Delta u/\gamma})\xi\bar{\sigma}\bar{\phi} \ . \tag{17}$$

But, for a Δu of 0.5, $e^{-\Delta u/\gamma}$ is 0.03 for beryllium and 0.01 for carbon. One may say, then, that for these moderators

$$q(r,u_{i+1}) \approx \xi\bar{\sigma}\bar{\phi} \ . \tag{18}$$

That is, the slowing-down density out of a group is equal to ξ times the *average* scattering cross section for the group times the *average* flux in the group. The common practice in the past has been to let the flux vary linearly over the group for slowing-down density purposes and to use the upper lethargy end-point value of the cross section in the computation of the slowing-down density. The use of Eq. 18 will simplify multigroup codes by eliminating the computation of the end-point fluxes and the storage of the end-point cross sections. Ages computed with diffusion theory and by requiring Eq. 18 to hold exactly are compared with ages computed with the other methods in Table 6.7.6.

Table 6.7.5 includes comparisons between Goertzel-Greuling–diffusion and age-diffusion results for bare spheres of heavy water, beryllium, and carbon. Two assumptions were made in the age-diffusion calculations on the end-point fluxes. The linear assumption let the flux vary linearly over the group so that the average flux was the average of the upper and lower end-point fluxes. The flat assumption set the upper lethargy end-point flux equal to the average flux. The linear assumption leads to oscillations from group to group in some cases where the flat assumption does not. Ages from the two assumptions are compared for beryllium in Fig. 6.7.6.

Conclusions

Difference equations good to second order in the lattice spacing rather than fourth order should be used for multigroup codes. The linear-flux assumption for computing group events does not result in a significant improvement over the flat-flux assumption. For a coarse group structure (31 groups), and for isotropic scattering, only light water shows a significant difference between P_1 and diffusion theory.

Goertzel-Greuling theory gives better results than does age theory even for heavy moderators. For a coarse group structure (31 groups), the use of a slowing-down density of

$$q(r, u_{i+1}) = \xi \bar{\sigma} \bar{\phi}(r)$$

for moderators heavier than deuterium should give results nearly equivalent to Goertzel-Greuling results and will reduce code storage requirements and computing time.

6.8 AN IBM 704 CODE FOR THE CALCULATION OF MOMENTS

I. M. Happer W. E. Kinney

Introduction

The moments of a plane source neutron distribution, or the moments of a gamma-ray source distribution, have wide application in reactor and shielding calculations. For example, the second moment of such a neutron distribution in an infinite medium is proportional to the age,[1] while the higher moments may be used to reconstruct the flux. The moments may also be used to check the results of Monte Carlo calculations such as those given by the O5R code.[2] The method of moments has also been extensively applied to gamma-ray attenuation calculations.[3]

A code is nearing completion for the IBM 704 computer which uses the moments method[3,4] to compute the even moments, from the zeroth to the tenth, of the flux and the slowing-down distribution. The main code solves the group moment equation for the moments of the flux. Slowing-down density moments may be obtained by summing the scattering sources below the energy of interest. The portion of the code which computes and stores the kernels has been written and tested. The main code has been written but not yet tested.

---

[1] A. M. Weinberg and E. P. Wigner, *The Physical Theory of Neutron Chain Reactors*, p 322, University of Chicago Press, Chicago, 1958.

[2] R. R. Coveyou, J. G. Sullivan, and H. P. Carter, *Neutron Phys. Ann. Prog. Rep. Sept. 1, 1958*, ORNL-2609, p 87.

[3] H. Goldstein and J. E. Wilkins, Jr., *Calculations of the Penetrations of Gamma Rays, Final Report*, NDA-15C-41 or NYO-3075 (1954).

[4] L. V. Spencer and U. Fano, *Phys. Rev.* 81, 464 (1951).

Theory

We begin with the Boltzmann equation for a plane isotropic source, and expand the flux and scattering kernel in a series of Legendre polynomials. Integration over the solid angle and taking the moments of the flux expansion coefficients gives the moments equation:[4]

$$\Sigma_T(E)\phi_{n,l}(E) = \delta_{0l}\delta_{0n}\chi(E) + \frac{l+1}{2l+1} n\phi_{n-1,l+1}(E) + \frac{l}{2l+1} n\phi_{n-1,l-1}(E) +$$

$$+ \sum_m \int_E^{E_0} \Sigma_s^m(E')\phi_{n,l}(E')K_l^m(E' \to E)\, dE' + \int_E^{E_0} \Sigma_s^H(E')\phi_{n,l}(E')K_l^H(E' \to E)\, dE' \quad , \qquad (1)$$

$$\phi_{n,l}(E) = \int_{-\infty}^{\infty} \phi_l(x,E)x^n\, dx \quad , \qquad (2)$$

where

$\Sigma_T(E)$ = macroscopic total cross section,

E = energy,

E_0 = highest energy of interest,

$\phi_l(E)$ = lth expansion coefficient of the flux,

δ_{nl} = Kronecker delta; $\delta_{nl} = 0$, $n \neq l$; $\delta_{nn} = 1$,

$\chi(E)$ = source spectrum,

$\Sigma_s^m(E)$ = macroscopic scattering cross section for the mth element in the medium,

$K_l^m(E' \to E)$ = lth expansion coefficient of the scattering kernel for the mth element in the medium,

$\Sigma_s^H(E)$ = macroscopic scattering cross section for hydrogen,

$K_l^H(E' \to E)$ = lth expansion coefficient of the scattering kernel for hydrogen,

x = distance from the origin, which is taken at the source.

Hydrogen is treated separately, since it may scatter neutrons to the entire energy range.

We divide the energy range into groups. The scattering integrals on the right of Eq. 1 may then be approximated as:

$$\int_E^{E_0} \Sigma_s^m(E')\phi_{n,l}(E')K_l^m(E' \to E)\, dE' = \sum_j \bar{\Sigma}_{s_j}^m \bar{\phi}_{n,l_j} K_l^m(j \to E) \quad , \qquad (3)$$

where

$$K_l^m(j \to E) = \int_{E_j}^{E_{j-1}} K_l^m(E' \to E)\, dE' \quad ,$$

E_j = the lower energy limit of group j,

E_{j-1} = the upper energy limit of group j,

and the bar indicates average.

After integration of Eq. 1 over the ith group and division by the energy width of the group,

$$\bar{\Sigma}_{T_i}\bar{\phi}_{n,l_i} = \delta_{0l}\delta_{0n}\bar{\chi}_i + \frac{l+1}{2l+1}n\bar{\phi}_{n-1,l+1_i} + \frac{l}{2l+1}n\bar{\phi}_{n-1,l-1_i} +$$

$$+ \sum_{j=1}^{i}\sum_{m}\bar{\Sigma}^m_{s_j}\bar{\phi}_{n,l_j}K^m_l(j\to i) + \sum_{j=1}^{i}\bar{\Sigma}^H_{s_j}\bar{\phi}_{n,l_j}K^H_l(j\to i) \quad , \tag{4}$$

where

$$K^m_l(j\to i) = \frac{1}{\Delta E_i}\int_{E_i}^{E_{i-1}} K^m_l(j\to E)\,dE \quad ,$$

E_i = lower energy end point of group i,

E_{i-1} = upper energy end point of group i,

$\Delta E_i = E_{i-1} - E_i$.

Now

$$K^m_l(j\to i) = K^m_0(j\to i)P_l(\mu) \quad , \tag{5}$$

$$K^m_0(j\to i) = \frac{1}{1-\alpha}\ln\frac{E_{j-1}}{E_j}\sum_{l=0}^{8}(2l+1)\bar{f}_{l_j}P_l(\omega) \quad , \tag{6}$$

where

μ = the cosine of the laboratory scattering angle going from group j to group i

$$= \frac{1}{2}(A+1)\sqrt{\frac{\bar{E}_i}{\bar{E}_j}} - \frac{1}{2}(A-1)\sqrt{\frac{\bar{E}_j}{\bar{E}_i}} \quad ,$$

ω = the cosine of the center-of-mass scattering angle going from group j to group i

$$= 1 - \frac{(A+1)^2}{2A}\left(1 - \frac{\bar{E}_i}{\bar{E}_j}\right) ,$$

$$\bar{E}_i = \frac{E_i + E_{i-1}}{2} \quad ,$$

$$\bar{E}_j = \frac{E_j + E_{j-1}}{2} \quad ,$$

$$\alpha = \left(\frac{A-1}{A+1}\right)^2 \quad ,$$

A = the ratio of scatterer mass to neutron mass,

$\bar{f}_{l_j}$ = the average lth expansion coefficient for the jth group in an expansion of the differential scattering cross section in the center-of-mass system,

P_l = the lth Legendre polynomial.

When the end of the range for scattering from group j lies in group i, there are four special cases which must be considered; $K_0(j\to i)$, $\bar{E}_j$, and $\bar{E}_i$ are given for these cases in Table 6.8.1.

Table 6.8.1. Expressions for $(1-\alpha)K_0(j \to i)\,\Delta E_i$, $\bar{E}_j$, and $\bar{E}_i$ for Special Cases

Case	$(1-\alpha)K_0(j \to i)\,\Delta E_i$	$\bar{E}_j$	$\bar{E}_i$
$\alpha E_{j-1} > E_{i-1} > \alpha E_j > E_i$	$E_{i-1} \ln \frac{E_{i-1}}{\alpha E_j} - \alpha\left(\frac{E_{i-1}}{\alpha} - E_j\right)$	$\frac{\left(\frac{E_{i-1}}{\alpha} - E_j\right)\left[E_{i-1} - \frac{\alpha}{2}\left(\frac{E_{i-1}}{\alpha} + E_j\right)\right]}{(1-\alpha)K_0(j \to i)}$	$\frac{E_{i-1} + \alpha E_j}{2}$
$\alpha E_{j-1} > E_{i-1} > E_i > \alpha E_j$	$E_{i-1} \ln \frac{E_{i-1}}{E_i} - (E_{i-1} - E_i)\left(1 - \ln \frac{E_i}{\alpha E_j}\right)$	$\frac{\frac{E_{i-1} - E_i}{\alpha}\left[E_{i-1} - \frac{1}{2}(E_{i-1} + E_i) + E_i - \alpha E_j\right]}{(1-\alpha)K_0(j \to i)}$	$\frac{E_i + E_{i-1}}{2}$
$E_{i-1} > \alpha E_{j-1} > E_i > \alpha E_j$	$E_{i-1} \ln \frac{\alpha E_{j-1}}{E_i} - \alpha\left(E_{j-1} - \frac{E_i}{\alpha}\right) + (E_{i-1} - E_i) \ln \frac{E_i}{\alpha E_j}$	$\frac{E_{i-1}\left(E_{j-1} - \frac{E_i}{\alpha}\right) - \frac{\alpha}{2}\left(E_{j-1}^2 - \frac{E_i^2}{\alpha^2}\right) + (E_{i-1} - E_i)\left(\frac{E_i}{\alpha} - E_j\right)}{(1-\alpha)K_0(j \to i)}$	$\frac{E_i + E_{i-1}}{2}$
$E_{i-1} > \alpha E_{j-1} > \alpha E_j > E_i$	$E_{i-1} \ln \frac{E_{j-1}}{E_j} - \alpha(E_{j-1} - E_j)$	$\frac{(E_{j-1} - E_j)\left[E_{i-1} - \frac{\alpha}{2}(E_{j-1} + E_j)\right]}{(1-\alpha)K_0(j \to i)}$	$\frac{E_{i-1} + \alpha E_j}{2}$

Code Description

The energy range between a specified E_0 and a specified cutoff energy E_c is first divided into N major groups whose limits differ by a factor of 2 in energy. The major groups are further subdivided into n minor groups equally spaced in energy. There may be a total of 1600 minor groups. Cross sections and expansion coefficients are first averaged over the specified group structure. There may be four scatterers in addition to hydrogen.

The order of the last moment desired is specified and must be even and not greater than 10. The $K_l^m(j \to i)$ are computed and summed over the elements and stored on tape. There may be scattering from group j to 512 groups below. This is sufficient to treat deuterium with 128 minor groups per major group. The hydrogen kernel is not stored but is computed in the main code, assuming isotropic scattering.

The source is isotropic, and its spectrum may be the fission spectrum or may be specified.

Acknowledgment

We wish to thank R. R. Coveyou for his suggestion of the problem.

6.9 A TREATMENT OF TIME-DEPENDENT SLOWING-DOWN OF NEUTRONS, USING GROUP THEORY

E. Guth E. Inönü

Wigner has developed a method using group theory for those problems of multiple scattering in which the elementary scattering law is invariant under a group of transformations.[1] The integral transforms, used in more standard treatments for the reduction of convolutions, come in here naturally through the representations of the groups of transformations. We have applied this method to the treatment of the time-dependent slowing-down of neutrons through elastic collisions. In this case of time and energy dependence there appears a group of linear transformations which does not yield orthogonality. Nevertheless it is possible to determine all positive time moments of the distribution functions and from them the distribution function itself. The conditions for the existence of the group are the following: (1) the differential scattering cross section in the center-of-mass system may have any angular dependence, but is independent of energy; (2) the total scattering cross section is proportional to v^γ (γ being any real number); (3) either the absorption cross section varies as $1/v$ or the ratio of absorption to scattering cross section is constant (including zero). For the special case of no absorption

[1] E. P. Wigner, *Phys. Rev.* 94, 17 (1954).

and spherically symmetric scattering in the center-of-mass system, our solution reduces to Waller's exact expression.[2]

As a further generalization, we have discussed the group which, with the same assumptions about the cross sections, exists for the case of time-energy-space-direction dependence. Here also the group-theoretical method yields naturally all positive moments of the distribution functions.

A detailed report has been published elsewhere.[3]

[2] I. Waller, *Proc. U.N. Intern. Conf. Peaceful Uses Atomic Energy, 2nd, Geneva, 1958* **16**, 450 (paper P/153) (1958).

[3] E. Guth and E. Inönü, *Group-Theoretical Treatment of Time- and Energy-Dependent Multiple Scattering, with Application to the Slowing-Down of Neutrons*, ORNL-3010 (Oct. 7, 1960); also submitted to *Journal of Mathematical Physics*.

6.10 THE EFFECT OF THE BOUNDARY REGION IN THE DETERMINATION OF THE EXTRAPOLATION LENGTH FROM EXPERIMENTS WITH CRITICAL CYLINDERS[1]

E. Inönü

During the experiments of R. Gwin and D. W. Magnuson with bare, homogeneous critical assemblies of aqueous U^{235} solutions,[2] a series of flux traverse measurements were made along the vertical axes of two critical cylinders, 19 and 42 in. high, with U^{235}, cadmium-covered U^{235}, and U^{238} fission chambers.

When these data were fitted with the usual cosine functions, the extrapolation lengths obtained for the three distributions corresponding to thermal, epithermal, and fast neutrons appeared to differ from each other. In particular, the difference between fast and thermal extrapolation lengths in the measurements in the 19-in.-high cylinder was definitely outside the limit of statistical error.

The apparent disagreement with the first fundamental theorem of reactor theory, which predicts the same spatial dependence for all energies in an interior region of a bare, homogeneous reactor, however, is not real.

This has been demonstrated by excluding from the experimental data all points within 3 in. of the boundaries, and fitting the remainder to a cosine distribution. The new extrapolation lengths which are obtained by this process are then consistent, within statistical errors, with a unique value. This value is $\delta_{ex} = 2.9 \pm 0.1$ cm. (The indicated error is only an order-of-magnitude estimate.)

[1] Summarized from: E. Inönü, *The Analysis of Flux Traverse Measurements in the Gwin-Magnuson Critical Experiments*, ORNL CF-59-12-2 (Dec. 1, 1959).

[2] R. Gwin and D. W. Magnuson, *Critical Experiments for Reactor Physics Studies*, ORNL CF-60-4-12, in press.

A similar analysis of flux distributions obtained from Corn Pone calculations by Gwin, Magnuson, and Kinney[3] yields other and more striking demonstrations of the important role played by the boundary region in the determination of the extrapolation length by an over-all fit to the data. The analysis of these data indicates clearly that an energy-independent extrapolation length may be obtained only by excluding data within about 3 to 3.5 in. of the boundary.

[3]D. W. Magnuson, R. Gwin, and W. E. Kinney, *Neutron Phys. Ann. Prog. Rep. Sept. 1, 1959*, ORNL-2842, p 151.

6.11 ON RANDOM WALK INTERPRETATION OF LINEAR BOLTZMANN EQUATIONS[1]

E. Guth E. Inönü

Although many special problems of multiple scattering have been treated in the past by using recurrence relations,[2] the exact connection between the recurrence relations which define random walks and the linear Boltzmann integrodifferential equations does not seem to have been clearly established.

A random walk consists of a succession of "elementary events" which change the state of the system and are statistically independent of each other. For multiple scattering of particles, the elementary event may be taken, in general, as a collision and subsequent traversal of a free path. It changes the state of the system from the one in which it was before a collision to the state in which it is before the next one.

The probability distribution $f_n(s)$ for the "state" s reached by a "random walker" after n steps satisfies the recurrence relation

$$f_{n+1}(t) = \int f_n(s)P(s,t)\, ds \quad , \tag{1}$$

where the nonnegative $P(s,t)$ is the elementary probability for a transition from s to t per "unit interval" around t and the integration is over the whole many-dimensional region reached by the "random walker." On the other hand, for the multiple scattering of particles, the Boltzmann theory gives a distribution function $f(s)$, regardless of the number of steps taken to reach s. Thus,

$$f_{\text{Boltzmann}} = \lim_{n\to\infty} \sum_{k=0}^{n} f_k(s) \quad . \tag{2}$$

Clearly, $f_n(s)$ contains more information than $f(s)$. However, $f_n(s)$ is nothing but the nth term in

[1]E. Guth and E. Inönü, *Phys. Rev.* 118, 899–900 (1960).

[2]See, e.g., W. Bothe, *Z. Physik* 54, 161 (1929); S. Goudsmit and J. L. Saunderson, *Phys. Rev.* 57, 24 and 58, 36 (1940); C. C. Grosjean, dissertation, Columbia University, 1951 (unpublished) and *Physica* 19, 29 (1953); E. P. Wigner, *Phys. Rev.* 94, 17 (1954).

the iteration series solution of the linear Boltzmann equation and therefore can also be obtained directly from a generating Boltzmann distribution $f_\lambda(s)$ by means of the relation

$$f_n(s) = \frac{1}{n!}\left[\frac{d^n f_\lambda(s)}{d\lambda^n}\right]_{\lambda=0} , \tag{3}$$

where $f_\lambda(s)$ is the solution of the equation

$$f_\lambda(t) = f_0(t) + \lambda \int f_\lambda(s) P(s,t)\, ds , \tag{4}$$

where $f_0(t)$ is the given source distribution and λ is a parameter.

As an example of the close connection between the two methods, the well-known integral Boltzmann equation for neutron transport in a nonmultiplying infinite medium has been derived from a $P(s,t)$ which involves a transition in a seven-dimensional phase-time space. The details have been published elsewhere.[1]

Besides neutron transport, the above connection between recurrence relations and linear Boltzmann equations applies also to Brownian motion, Rayleigh's problem (which is related to neutron thermalization), and many other problems.

6.12 SOLUTION OF THE MONOENERGETIC BOLTZMANN EQUATION IN AN INFINITE HOMOGENEOUS MEDIUM WITH LINEARLY ANISOTROPIC SCATTERING FOR AN ISOTROPIC POINT SOURCE

E. Inönü

It is well known that the monoenergetic Boltzmann equation in an infinite homogeneous medium with isotropic scattering and an isotropic point (or plane) source can be solved exactly by the method of Fourier transforms.[1] That the same method may be applied to the case of anisotropic scattering is also a matter of general knowledge;[2] however, due to algebraic complications, the results in this case do not seem to have been published anywhere. Following a suggestion of E. P. Wigner, the relatively simple case of linearly anisotropic scattering has been treated in detail. The results will be published in a separate report. One conclusion worth noticing is that in the expression for the asymptotic flux the so-called effective source strength (the coefficient β in the expression 9.27*b* of ref 1) turns out to be equal to that for isotropic scattering to first order in Σ_a/Σ, where Σ_a/Σ is the ratio of the absorption to the total cross section.

---

[1]Cf., e.g., A. M. Weinberg and E. P. Wigner, *The Physical Theory of Neutron Chain Reactors*, p 236 ff., University of Chicago Press, Chicago, 1958.

[2]See, e.g., the remarks of B. Davison, *Neutron Transport Theory*, p 243, Oxford University Press, London, 1957.

6.13 MILNE PROBLEM WITH CAPTURE

S. N. Purohit[1]

The neutron flux and the emergent angular distribution of neutrons in the Milne problem with capture were calculated by an approximate method. This involves the representation of the nonasymptotic flux by a single exponential. Placzek[2] used this representation for the non-absorption case. Total neutron flux in an absorbing medium is written as follows:

$$\phi(z) = J(0) \sqrt{\frac{2\nu^2(1-\nu^2)}{\alpha(\nu^2-\alpha)}} \left[\sinh \nu(z+z_0) + Ae^{-Bz}\right] . \tag{1}$$

The first term represents the asymptotic flux. The ratio of absorption to total cross sections is α, z_0 is the extrapolated distance measured in total mean free path, and z is the distance from the boundary inside the medium; $J(0)$ is the total neutron current at the boundary; A and B are the parameters which characterize the nonasymptotic flux; and the quantity ν is the real root of the following transcendental equation:

$$(1-\alpha)\frac{\tanh^{-1}\nu}{\nu} = 1 . \tag{2}$$

Values of z_0 and ν are known for various values of α. In order to determine A and B, we iterate Eq. 1, using the following integral equation:

$$\phi(z) = \frac{1-\alpha}{2}\int_0^\infty \phi(z')E_1(|z-z'|)\,dz' . \tag{3}$$

To the zeroth iteration, as given by Eq. 1, and to the first iteration, the following integral condition at the boundary is applied:

$$\phi(0) = J(0)\sqrt{\frac{\nu^2}{\alpha}} . \tag{4}$$

From these two equations A and B were determined for different values of α. These are given in Table 6.13.1.

Neutron flux and the emergent angular distribution corresponding to Eq. 1 were calculated for

---

[1]Present address: Brookhaven National Laboratory.

[2]G. Placzek, *The Neutron Density near a Plane Surface*, MT-16 (1944).

a large number of cases. The results were compared with those of LeCaine[3] obtained by a variational method and were found to be in excellent agreement.

In addition to the above problem, the general relation between angular neutron flux measured with a neutron chopper and the total neutron flux for the case of linear anisotropic scattering in a highly absorbing medium is discussed in detail in a complete report to be published later.

[3]J. LeCaine, *Can. J. Research* A28, 242 (1950).

Table 6.13.1. Values of A and B

α*	$-A$	B
0.1	0.0784	3.4259
0.2	0.1194	3.2692
0.3	0.1621	3.0616
0.4	0.2115	2.8860
0.5	0.2778	2.7934
0.6	0.3893	2.4035
0.7	0.6491	1.6261
0.8	1.8360	1.3939

*Ratio of absorption to total cross section.

6.14 NEUTRON THERMALIZATION AND DIFFUSION IN PULSED MEDIA[1]

S. N. Purohit[2]

A general formalism for determining the lower time eigenvalues associated with a decaying pulse of neutrons in a finite multiplying or nonmultiplying medium has been developed. The eigenvalues are expressed in terms of the energy transfer moments of the scattering kernel of the medium, weighted by a Maxwellian distribution. The formalism is general and avoids the concept of neutron temperature. It is based upon the following expansion:

$$\phi(E,r,t) = \sum_p \phi_p(r) \sum_i e^{-\lambda_{ip} t} \sum_n A_{n_{ip}} E e^{-E} L_n^{(1)}(E) \ , \tag{1}$$

where

$\phi(E,r,t)$ = neutron flux,

$\phi_p(r)$ = pth spatial mode,

λ_{ip} = eigenvalue associated with the pth spatial mode and ith energy mode,

$L_n^{(1)}(E)$ = associated Laguerre polynomial of first order,

E,r,t = energy, space, and time variables.

The first eigenvalue, λ_1, for the infinite nonabsorbing medium, obtained using only two Laguerre polynomials, is related to the diffusion cooling coefficient, C_0, in the following

[1]Summarized from: S. N. Purohit, *Neutron Thermalization and Diffusion in Pulsed Media*, ORNL CF-60-7-32 (July 11, 1960).

[2]Present address: Brookhaven National Laboratory.

manner, for the case of a constant diffusion coefficient D:

$$\lambda_1 = \frac{2}{3\pi} \frac{D^2 v_0^2}{C_0} \quad . \tag{2}$$

In an infinite, nonabsorbing medium, the reciprocal of λ_1 is the thermalization time constant for the establishment of the Maxwellian distribution. Thermalization time constants were estimated for various moderators, using the following relation:

$$t_{th} = \frac{3}{2} \frac{\sqrt{\pi}}{M_2 v_0} f_t \quad . \tag{3}$$

In the above equation M_2 is the second energy transfer moment, weighted by the Maxwellian distribution. The correction factor f_t due to higher energy transfer moments was found, for a monatomic heavy gas, to be equal to 1.133 and 1.182, using three and four Laguerre polynomials, respectively. It was assumed that f_t can be given adequately by the monatomic heavy gas model. For the heavy gas case, t_{th} was estimated to be equal to $(1.274\xi\Sigma_{s0}v_0)^{-1}$, using four polynomials.

The importance of the first eigenvalue in the establishment of the final asymptotic energy distribution in finite as well as in infinite media is discussed at length in the paper of which this report is a summary.

For the case of a multiplying medium, an analysis of an experiment using a U^{235} plus water mixture[3] was carried out. The age of fission neutrons to thermal energy in water was shown to increase by about 8% when the nonleakage probability was replaced by the Laplace-Fourier transform instead of the Fourier transform of the slowing-down kernel for the infinite medium.

[3]E. C. Campbell and P. H. Stelson, *Phys. Semiann. Prog. Rep. Sept. 10, 1956*, ORNL-2204, p 34.

6.15 THE O5R CODE: A GENERAL-PURPOSE MONTE CARLO CODE FOR THE IBM 704

R. R. Coveyou J. G. Sullivan

The basic features of the O5R code, the Oak Ridge Random Research Reactor Routine, for the IBM 704 computer have previosuly been detailed.[1] This Monte Carlo code was prepared for three general tasks. The first was to perform specific reactor calculations, up to and including studies of entire reactors. The second was to examine the capabilities of the Monte Carlo method for reactor calculations, while the third was to furnish results suitable for use as comparison standards in evaluating other methods of computation. Mainly because of the third

[1]R. R. Coveyou, J. G. Sullivan, and H. P. Carter, *Neutron Phys. Ann. Prog. Rep. Sept. 1, 1958*, ORNL-2609, p 87.

requirement, great care was taken to assure an adequate representation of neutron cross-section data. Cross sections may be specified at as many as 10^4 energy points.

The O5R code has now been rather thoroughly tested with a variety of problems. Initial tests, run on manufactured problems in which the answers were known, served to define the accuracy and limitations of the code. Neutron ages in a number of media were then computed, and compared with the results given by a simpler code using the same cross-section data. Finally, several practical problems were run, and the results appeared to be satisfactory. A simple model for thermal effects is presently being used, but two successively more exact models are being developed.

The Health Physics Division is now using a version of the O5R code in studies involving a plane monoenergetic neutron source parallel to the axis of a right circular cylinder of tissue components. Total energy loss, energy deposition in thicknesses of cylinder material toward the source, amount of absorption, amount of (n,γ) and (n,α) activity produced, and number of thermal collisions are being calculated. In addition to their primary information value, these results will also serve to suggest potential improvements in the code.

The IBM 7090 computer is expected to be operable in December 1960, and it is expected that the main portions of the O5R code, now written for the 704, will be unaffected by the change. The more accurate models for thermal effects, noted above, will be introduced, and the versatility of the code increased to allow a larger number of media and more flexible geometry routines than are presently available.

Part 7

SHIELDING RESEARCH

7.1 LID TANK SHIELDING FACILITY MEASUREMENTS BEHIND THE ML-1 SHIELD MOCKUP

A. D. MacKellar

Introduction

An experimental evaluation of the ML-1 reactor shield design was performed at the Lid Tank Shielding Facility (LTSF) at the request of Aerojet-General Corp. Thermal-neutron flux, fast-neutron dose, and gamma-ray dose were measured behind slab mockups of the proposed shield and several possible variations, and the postshutdown decay characteristics of a mockup were determined.

Experimental Procedure

The shield mockups were placed in the steel configuration tank of the LTSF, as close to the source plate as possible. A list of the configurations tested is given in Table 7.1.1. A "probe distance," defined as the distance from the source plate to the center-of-detection of the measuring instrument used, less the distance from the instrument wall to the center-of-detection, was measured by moving the instruments until they touched the front of the 25- or 31-in. aluminum tank within which the measurements were made. The probe distance was used to compute the experimentally unavoidable air gaps in the configuration. The air gap was simply equal to the probe distance less the thicknesses of the $\frac{1}{8}$-in. boral and $\frac{1}{16}$-in. aluminum plates covering the source plate, the 2.23-cm air-bag thickness,[1] the $\frac{3}{8}$-in. aluminum window, and the thicknesses of the various components of the mockup.

Thermal-neutron fluxes were measured with U^{235} fission chambers and BF_3 counters and were normalized to 2200 m/sec. Fast-neutron doses were measured by Hurst-type dosimeters, and gamma-ray dose measurements were made with an anthracene crystal scintillation counter or a 50-cc ionization chamber. All data were normalized to a per-watt basis by dividing by 5.22 w, the nominal source plate power.

Results

The configuration identified as I-0 in Table 7.1.1 was the first experimental setup and represents the types and thicknesses of materials proposed in the ML-1 original reference design except that it contained tap water instead of water mixed with ammonium pentaborate (APB). Thermal-neutron, fast-neutron, and gamma-ray measurements made behind the I-0 and I-8 configurations, which are identical except that I-8 contains a 7.5 wt % solution of APB in water instead of the tap water of I-0, are compared in Figs. 7.1.1, 7.1.2, and 7.1.3. The addition of the boron to the water reduced the thermal flux by a factor of between 10 and 100, while reducing the fast-neutron dose by only about 10%. The gamma-ray dose rate was diminished by a factor of about 2.

[1]The general arrangement of the LTSF is well known. The 2.23-cm-thick air bag is used to exclude the water in the Lid Tank from the region between the source plate and the configuration tank.

Table 7.1.1. Description of Configurations

Configuration Number	Components in Order of Location from Front of Configuration Tank	Probe Distance (cm)	Boron Content (%)
I-0	2 in. lead, 1/4 in. aluminum, 2 in. Hevimet, 1/4 in. aluminum, 1/4 in. Lucite, 1/4 in. type 347 stainless steel, 1/8 in. boral, 3 3/4 in. lead, 1/8 in. stainless steel	43.67	0.0
	5-in. stainless steel tank containing 1/8 in. stainless steel, 5 in. dry APB,* 1/8 in. stainless steel		
	1/8 in. boral		
	25-in. aluminum tank containing 1/8 in. aluminum, 25 in. water, 1/8 in. aluminum		
I-8	2 in. lead, 1/4 in. aluminum, 2 in. Hevimet, 1/4 in. aluminum, 1/4 in. Lucite, 1/4 in. type 347 stainless steel, 1/8 in. boral, 3 3/4 in. lead, 1/8 in. stainless steel	43.67	1.52
	5-in. stainless steel tank containing 1/8 in. stainless steel, 5 in. dry APB, 1/8 in. stainless steel		
	1/8 in. boral		
	25-in. aluminum tank containing 1/8 in. aluminum, 25 in. 7.5 wt % APB, 1/8 in. aluminum		
III-8-(1/2)	2 in. lead, 1/4 in. aluminum, 2 in. Hevimet, 1/4 in. aluminum, 1/4 in. Lucite, 1/4 in. type 347 stainless steel, 1/8 in. boral, 3 1/4 in. lead	42.32	1.52
	5-in. stainless steel tank containing 1/8 in. stainless steel, 5 in. 7.5 wt % APB, 1/8 in. stainless steel		
	1/2 in. lead, 1/8 in. stainless steel, 1/8 in. boral		
	25-in. aluminum tank containing 1/8 in. aluminum, 25 in. 7.5 wt % APB, 1/8 in. aluminum		
III-8-1	2 in. lead, 1/4 in. aluminum, 2 in. Hevimet, 1/4 in. aluminum, 1/4 in. Lucite, 1/4 in. type 347 stainless steel, 1/8 in. boral, 2 3/4 in. lead	42.42	1.52
	5-in. stainless steel tank containing 1/8 in. stainless steel, 5 in. 7.5 wt % APB, 1/8 in. stainless steel		
	1 in. lead, 1/8 in. stainless steel, 1/8 in. boral		
	25-in. aluminum tank containing 1/8 in. aluminum, 25 in. 7.5 wt % APB, 1/8 in. aluminum		

Table 7.1.1 (continued)

Configuration Number	Components in Order of Location from Front of Configuration Tank	Probe Distance (cm)	Boron Content (%)
III-8-2	2 in. lead, ¼ in. aluminum, 2 in. Hevimet, ¼ in. aluminum, ¼ in. Lucite, ¼ in. type 347 stainless steel, ⅛ in. boral, 1¾ in. lead 5-in. stainless steel tank containing ⅛ in. stainless steel, 5 in. 7.5 wt % APB, ⅛ in. stainless steel 2 in. lead, ⅛ in. stainless steel, ⅛ in. boral 25-in. aluminum tank containing ⅛ in. aluminum, 25 in. 7.5 wt % APB, ⅛ in. aluminum	42.42	1.52
IV-8-0	2 in. lead, ¼ in. aluminum, 2 in. Hevimet, ¼ in. aluminum, ¼ in. Lucite, ¼ in. type 347 stainless steel, ⅛ in. boral, 3¾ in. lead, ⅛ in. stainless steel, ½ in. boral 31-in. aluminum tank containing ⅛ in. aluminum, 21 in. 7.5 wt % APB, ⅛ in. aluminum	29.88	1.52
IV-8-(½)-5	2 in. lead, ¼ in. aluminum, 2 in. Hevimet, ¼ in. aluminum, ¼ in. Lucite, ¼ in. type 347 stainless steel, ⅛ in. boral, 3¼ in. lead, ⅛ in. stainless steel, ½ in. boral 31-in. aluminum tank containing ⅛ in. aluminum, 5 in. 7.5 wt % APB, ½ in. lead, 25½ in. 7.5 wt % APB, ⅛ in. aluminum	35.75	1.52
IV-8-(½)-10	2 in. lead, ¼ in. aluminum, 2 in. Hevimet, ¼ in. aluminum, ¼ in. Lucite, ¼ in. type 347 stainless steel, ⅛ in. boral, 3¼ in. lead, ⅛ in. stainless steel, ½ in. boral 31-in. aluminum tank containing ⅛ in. aluminum, 10 in. 7.5 wt % APB, ½ in. lead, 20½ in. 7.5 wt % APB, ⅛ in. aluminum	48.45	1.52
IV-8-(½)-18	2 in. lead, ¼ in. aluminum, 2 in. Hevimet, ¼ in. aluminum, ¼ in. Lucite, ¼ in. type 347 stainless steel, ⅛ in. boral, 3¼ in. lead, ⅛ in. stainless steel, ½ in. boral 31-in. aluminum tank containing ⅛ in. aluminum, 18 in. 7.5 wt % APB, ½ in. lead, 12½ in. 7.5 wt % APB, ⅛ in. aluminum	61.13	1.52

*Ammonium pentaborate.

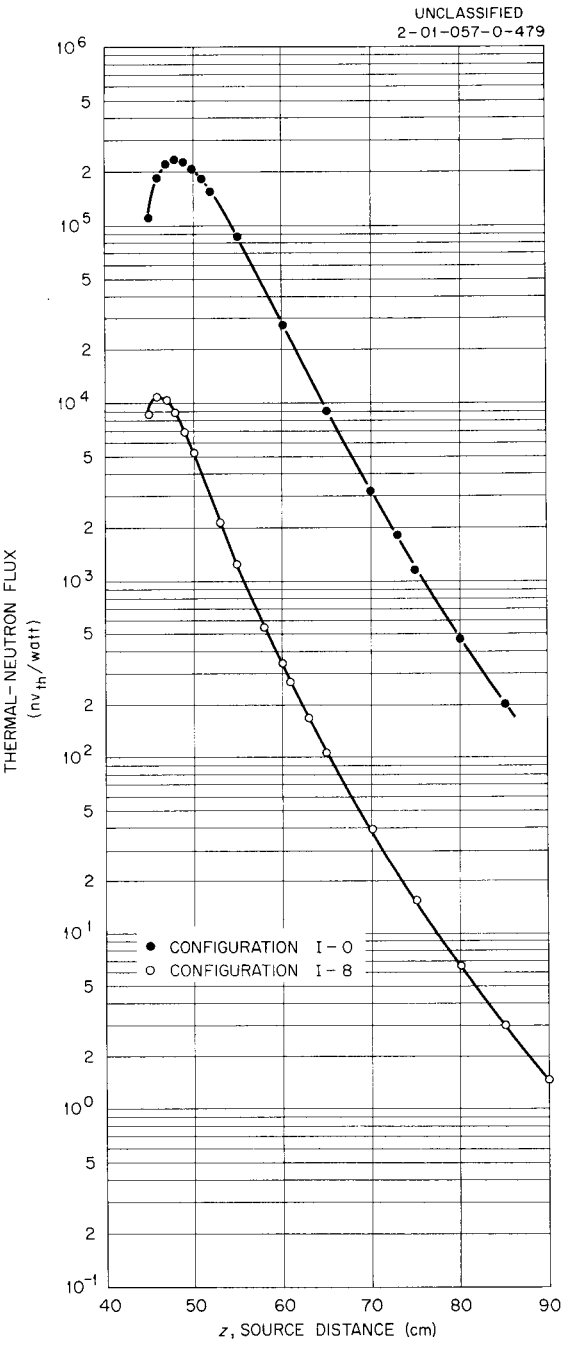

Fig. 7.1.1. Thermal-Neutron Flux as a Function of Distance from Source, Measured Behind Configurations I-0 and I-8.

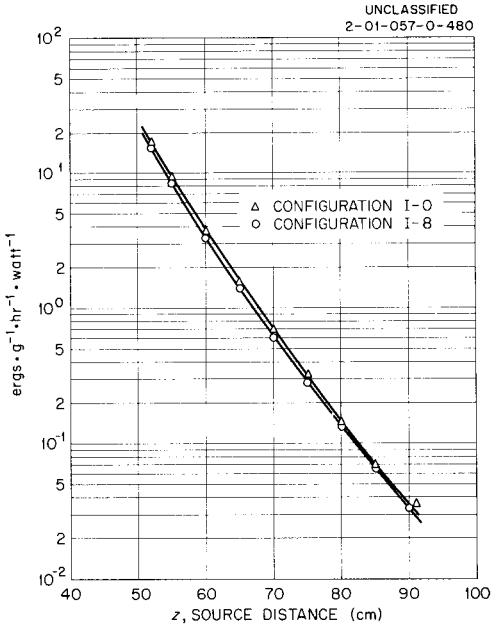

Fig. 7.1.2. Fast-Neutron Dose Rate as a Function of Distance from Source, Measured Behind Configurations I-0 and I-8.

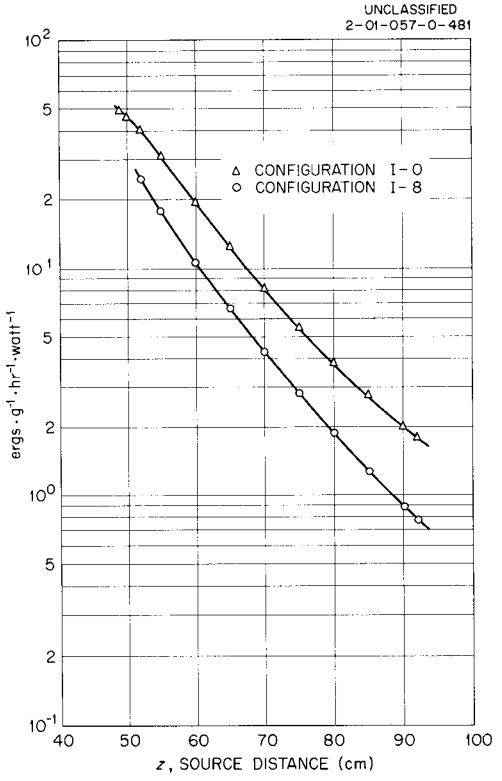

Fig. 7.1.3. Gamma-Ray Dose Rate as a Function of Distance from Source, Measured Behind Configurations I-0 and I-8.

Since the decay characteristics of this reactor shield were of particular importance, the gamma-ray dose rate behind configuration I-0 was measured as a function of time after power shutdown. The results are shown in Fig. 7.1.4.

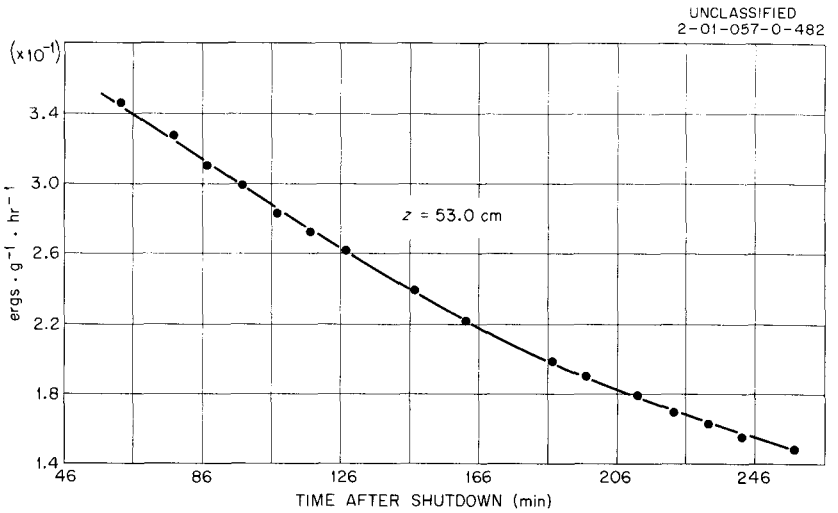

Fig. 7.1.4. Gamma-Ray Dose Rate Behind Configuration I-0 as a Function of Time After Power Shutdown.

The preferred distribution of a constant total thickness of lead in front of and behind the 5-in.-thick, $\frac{1}{8}$-in.-wall stainless steel tank containing the 7.5 wt % APB solution was examined by means of three configurations which differed only in the lead placement. The measurements demonstrated that the lead was more effective as a gamma-ray shield when placed behind the 5-in. tank. Configuration III-8-1, in which $2\frac{3}{4}$ in. of lead preceded the tank, with 1 in. behind, gave dose rates in the 25-in. tank of APB about a factor of 1.8 lower than those given by III-8-($\frac{1}{2}$), in which $3\frac{1}{4}$ in. of lead preceded the tank and only $\frac{1}{2}$ in. followed. Configuration III-8-2, which had 2 in. of lead behind the tank and $1\frac{3}{4}$ in. of lead before, gave dose rates about a factor of 3.2 lower than doses from III-8-($\frac{1}{2}$). These results are shown in Fig. 7.1.5. Since the placement of the lead in front of or behind the 5-in. tank should not affect the dose rate unless the gamma rays originate in the tank, it is clear that the contribution to the gamma-ray dose from capture gamma rays originating in the stainless steel tank walls was quite significant.

The effect of placing lead behind various thicknesses of 7.5 wt % APB solution was measured with configurations IV-8-0, IV-8-($\frac{1}{2}$)-5, IV-9-($\frac{1}{2}$)-10, and IV-8-($\frac{1}{2}$)-18. In Fig. 7.1.6 the gamma-ray dose rates are plotted for no lead in the 31-in. tank of 7.5 wt % APB, then for $\frac{1}{2}$ in. of lead behind 5, 10, and 18 in. of 7.5 wt % of APB solution. The $\frac{1}{2}$ in. of lead behind 5 in. of solution resulted in about a 50% decrease in gamma-ray dose rate, compared with the results from the configuration with no lead. At 90 cm from the source plate, the configuration with 10 in. of APB solution in front of the $\frac{1}{2}$ in. of lead showed an additional 10% decrease in dose rate. A further increase to 18 in. of APB gave a drop of 17% below the dose from the configuration containing 5 in. of APB before the lead. These data indicate that placing the lead behind

a greater thickness of APB solution reduces the dose rate by shielding the capture gamma rays born in the APB solution. A detailed report of this work is to be published elsewhere.[2]

[2] A. D. MacKellar, *Lid Tank Shielding Facility Measurements Behind ML-1 Shield Mockup*, to be published as an ORNL CF Memorandum.

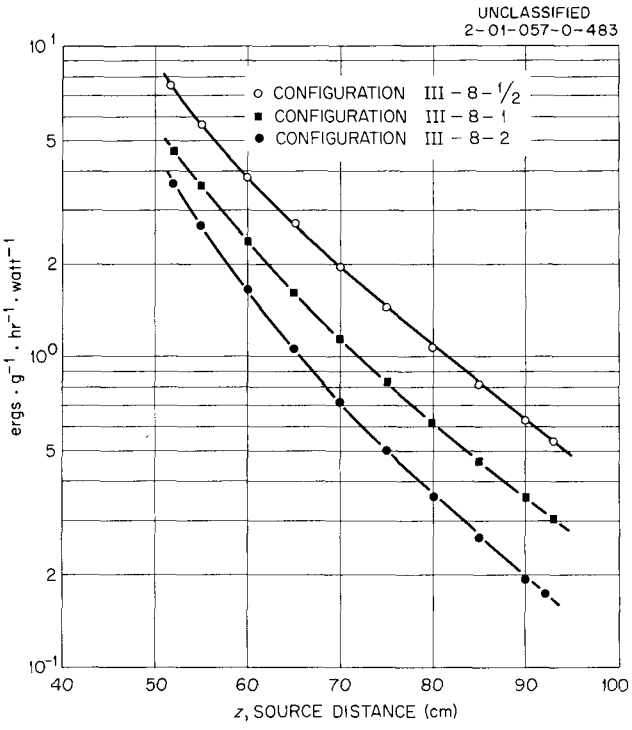

Fig. 7.1.5. Gamma-Ray Dose Rate as a Function of Distance from Source, Measured Behind Configurations III-8-(½), III-8-1, and III-8-2.

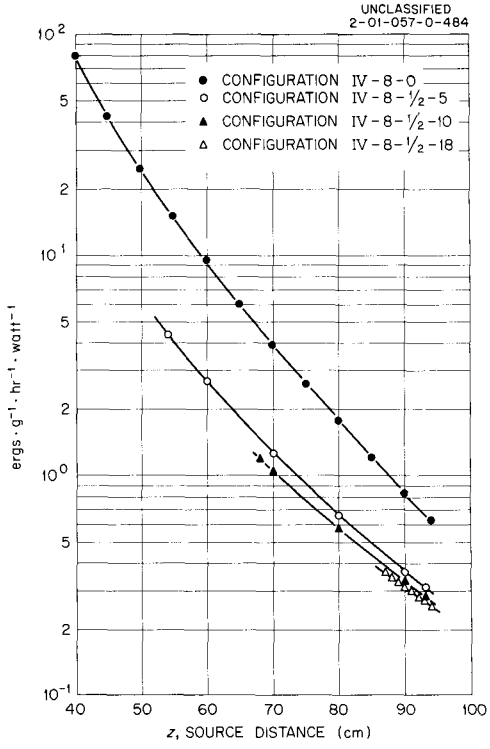

Fig. 7.1.6. Gamma-Ray Dose Rate as a Function of Distance from Source, Measured Behind Configurations IV-8-0, IV-8-(½)-5, IV-8-(½)-10, and IV-8-(½)-18.

7.2 ANGULAR DISTRIBUTION OF NEUTRONS EMERGING FROM PLANAR SURFACES OF DIFFUSING MEDIA

V. V. Verbinski

The design of a reactor shield would be greatly facilitated by a knowledge of the energy and angular distributions of the neutrons being transmitted through the shield. For example, the energy details of the flux within a shield are necessary for the calculation of neutron-induced gamma-ray fluxes in the shield materials, and the energy and angular distributions of the neutrons at the surface of a shield are required for calculations of gamma-ray doses resulting from neutrons captured outside a shield. Unfortunately, the problem of neutron diffusion near a

boundary in a scattering and absorbing medium does not easily lend itself to an analytical solution, especially when the medium is hydrogenous and contains a strong poison. Slowing down is difficult to factor in, and strong flux gradients presumably make diffusion theory approximations completely invalid. Two calculational methods now being developed for the problem are the NIOBE Code (Direct Numerical Integration of the Boltzmann Equation) at NDA and a Monte Carlo Code at ORNL.

In addition to the calculations, the problem will be attacked experimentally by use of a neutron chopper now under construction at ORNL (see Sec 5.2). In order to guide the design of the chopper and at the same time to obtain information for comparison with calculations already performed, a preliminary experiment has been performed at the Bulk Shielding Facility to measure the angular distribution of low-energy neutrons emerging from slab shields.

Because of the current interest in high-performance neutron shields, the experiment included several measurements on poisoned and unpoisoned hydrogenous slabs. The review article by Bethe[1] gives an angular distribution of $\phi(\mu) = 1 + \sqrt{3}\,\mu$ for pure paraffin (or water) calculated by the diffusion theory approximation, and this has already been verified somewhat at thermal energies by Fink.[2] One goal in this experiment was to determine whether this angular distribution is also valid in hydrogenous shields at other energies and to investigate how it varies with the addition of poison, the thickness of the sample, and the angle of incidence of the input neutrons. If the angular distribution were found to be independent of the angle of incidence, it could be assumed that the Milne problem[3] is correctly mocked up. This is of particular interest since many calculations use the Milne geometry (semi-infinite medium with the source at $-\infty$).

In order to investigate the angular distribution of neutrons in non-slowing-down media, a group of measurements was also made on poisoned and unpoisoned lead slabs. These were compared with calculations which have been made by Case *et al.*[4] with the one-velocity transport theory.

Description of Experiment

The apparatus, as positioned adjacent to the reactor, is shown in Fig. 7.2.1. Neutrons from the reactor pass through a 10-in.-dia air-filled collimator to the shield sample where, after some diffusion, the attenuated neutron flux emerges into an air chamber. Some of the neutrons pass into the air-filled beam tubes and to the detector foils. Neutrons not captured by the foils mostly strike the end of the air-filled beam-catcher cap.

---

[1]H. A. Bethe, *Revs. Mod. Phys.* **9**, 132–33 (1937).

[2]G. A. Fink, *Phys. Rev.* **50**, 738 (1936).

[3]See, for example, F. T. Adler and C. Mark, *Milne Problem with Capture*, MT-66, Chalk River.

[4]K. M. Case, F. de Hoffmann, and G. Placzek, *Introduction to the Theory of Neutron Diffusion*, p 147, USGPO, Washington 25, D.C., 1953.

UNCLASSIFIED
2-01-058-567

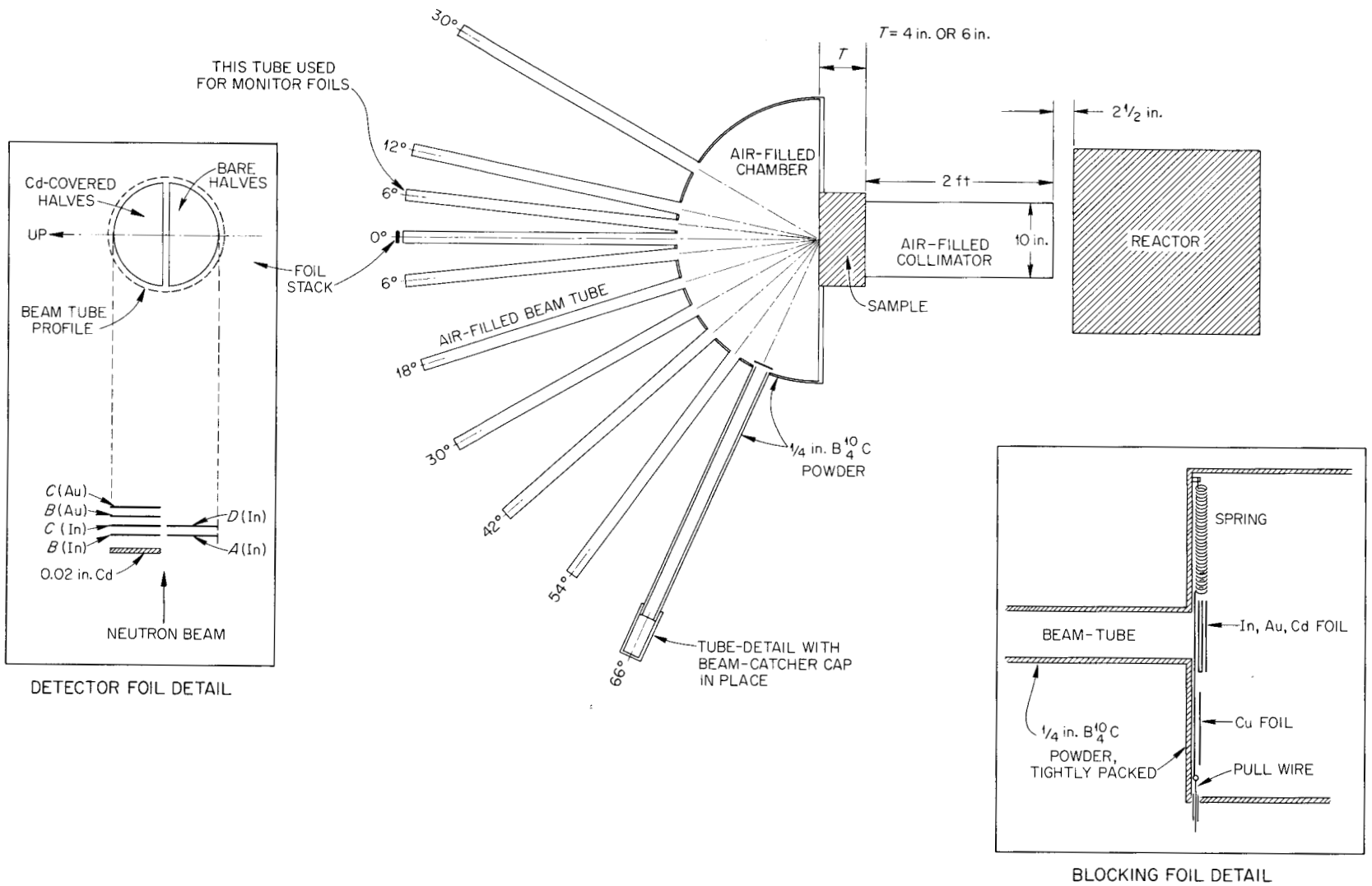

Fig. 7.2.1. Apparatus for Measuring Angular Distributions of Neutrons Diffusing Through a Plane Parallel Slab of Material.

Except for the section adjacent to the shield sample, the air chamber was lined with a ¼-in. thickness of well-packed $B_4^{10}C$ powder to minimize scattering within the chamber. The beam tubes and the beam-catcher caps were also lined with the $B_4^{10}C$. In order to investigate the effect of the angle of incidence of the input neutrons, an air-filled adapter tilted 30° with respect to the normal in the horizontal plane was placed between the shield sample and the 10-in.-dia collimator. The shield sample, the air chamber, and the beam tubes were thereby tilted 30° with respect to the input neutrons.

The circular detector foils were divided into half-disks as shown in the foil detector detail in Fig. 7.2.1. One stack of half-disks was cadmium covered (20-mil thickness), and the other stack was bare. With this arrangement several difference measurements were possible. With the gold foils, for example, the difference in neutron activation between the B-foil and the C-foil gave a measure of the gold-resonance neutron flux. The B-foil was black to most of the gold-resonance neutrons but only about 3% absorptive to thermal neutrons. With the indium foils, the differences between the B- and C-foil activations (called the $B-C$ activity) gave a measure of the indium-resonance flux. The $D-C$ activity gave a measure of the thermal-neutron flux.

Each angular distribution determination (each run) was made with two foil exposures. In one exposure, gold, indium, and cadmium blocking foils were inserted at the air-chamber end of the beam tubes (good geometry), as shown in the blocking foil detail of Fig. 7.2.1. This exposure determined the background activity of the detector foils. After removing and counting the detector foils, the exposure was repeated with the gold and indium blocking foils replaced by a copper foil of equal scattering probability. The detector foil activity in the second exposure thus was the foreground activity. The background $B-C$ gold foil activity was then subtracted from the foreground $B-C$ activity to obtain the net activity.

Each group of detector foils was always removed within about 15 min after exposure and counted three times so that erratic counts could be eliminated by "voting out" the bad count. Counting errors were somewhat infrequent. A 20-channel analyzer stored the photopeak counts from a 3- by 3-in. NaI detector. After corrections for foil decay and foil-weight variations were made, the data were normalized-plotted as $\phi(\mu)/\phi(1)$ vs μ, where $\mu = \cos\theta$ and θ is the angle from the normal.

Results

The plots of $\phi(\mu)/\phi(1)$ vs μ are presented in Figs. 7.2.2 and 7.2.3, each column of graphs representing one run with the exception of the last column of Fig. 7.2.3 where runs 9 and 10 are combined. Most columns have three graphs, the top graph presenting thermal-neutron data, the middle graph indium-resonance (1.44-ev) data, and the bottom graph gold-resonance (4.9-ev) data.

The samples used in runs 1 through 3 (Fig. 7.2.2) were 6-in.-thick hydrogenous slabs with boron poisoning of σ_0 = 0, 4.66, and 72 barns, respectively. [The symbol σ_0 = poisoning per

hydrogen atom at thermal energy. The corresponding poisoning for each energy region is given by the C value shown on each graph where $C = \Sigma_s/(\Sigma_a + \Sigma_s)$.] The angular distributions for all these runs are strikingly similar and seem to follow the $\phi(\mu) = 1 + \sqrt{3}\,\mu$ angular dependence (shown by solid lines in graphs) for a nonpoisoned hydrogenous medium given by Bethe.[1] In run 4 the 6-in.-thick slab used in run 3 was reduced to 4 in., and the angular distribution was found to be identical to that obtained in run 3, within the accuracy of these measurements. The curved, dashed lines in runs 3 and 4 are from one-velocity calculations by Case *et al.*[4] for the C values given in each graph. (The thermal data for these runs were statistically meaningless and therefore deleted; reruns are being made.) Runs 5 through 7 (Fig. 7.2.3) were identical with runs 1 through 3 except that the angle of incidence of the input neutrons was 30°. Again no change in $\phi(\mu)$ was observed.

The samples used in runs 8 through 10 consisted of 6-in. thicknesses of powdered lead, unpoisoned in runs 8 and 9 and poisoned with B_4C in run 10 ($C = 0.17$ for thermal neutrons). The powder density was 7.14 g/cc. In run 8 the input neutrons entered at an angle of 30°, while for runs 9 and 10 they were normally incident. It is observed that in lead the angular distribution for the 30° input neutrons did not peak at $\mu = 1$ and also that the neutrons emerging from the lead samples had a memory of their input direction. Yet in runs 8 and 9 the "good-statistics" thermal-neutron data suggest an approximate $\phi(\mu) = 1 + 2\,\mu$ dependence for angles far from the angle of input of the neutrons, as the one-velocity ($C = 1$) calculation predicts. The run-10 data superposed on the run-9 data in Fig. 7.2.3 show that there is indeed more forward peaking for the poisoned lead than for pure lead. The dashed curves with these plots represent the one-velocity calculations of Case *et al.* for the poisoned sample. A crude fit is attempted at larger angles (small μ). Certainly, these "one-velocity" runs must be repeated using a heavier slab of lead.

Conclusions

The experiments with hydrogenous materials agree with the angular distribution of $\phi(\mu) = 1 + \sqrt{3}\,\mu$ given by Bethe[1] for nonpoisoned hydrogenous media and also show that the angular distribution is unaffected by poisoning for the range of poisoning investigated ($1 \geqq C \geqq 0.75$). Furthermore, a comparison of runs 3 and 4 shows that $\phi(\mu)$ is not affected by varying the sample thickness from 4 to 6 in. This observed constancy with thickness is to be expected once spectral equilibrium is reached, and it can be assumed that spectral equilibrium was reached in this material since Beyster *et al.*[5] have shown that the spectrum is constant in a much more weakly poisoned hydrogenous material (polyethylene) at thicknesses above 2 in. These experiments indicate then that after the neutron energy spectrum becomes stabilized, the angular distribution of neutrons in typical hydrogenous materials, both poisoned and unpoisoned, is constant. This being true, the angular distribution given here can be used in shielding calculations for a poisoned hydrogenous material, and the energy spectrum need be determined for

[5] J. R. Beyster *et al.*, *Measurement of Low Energy Neutron Spectra*, GA-1088 (Nov. 13, 1959).

UNCLASSIFIED
2-01-058-568

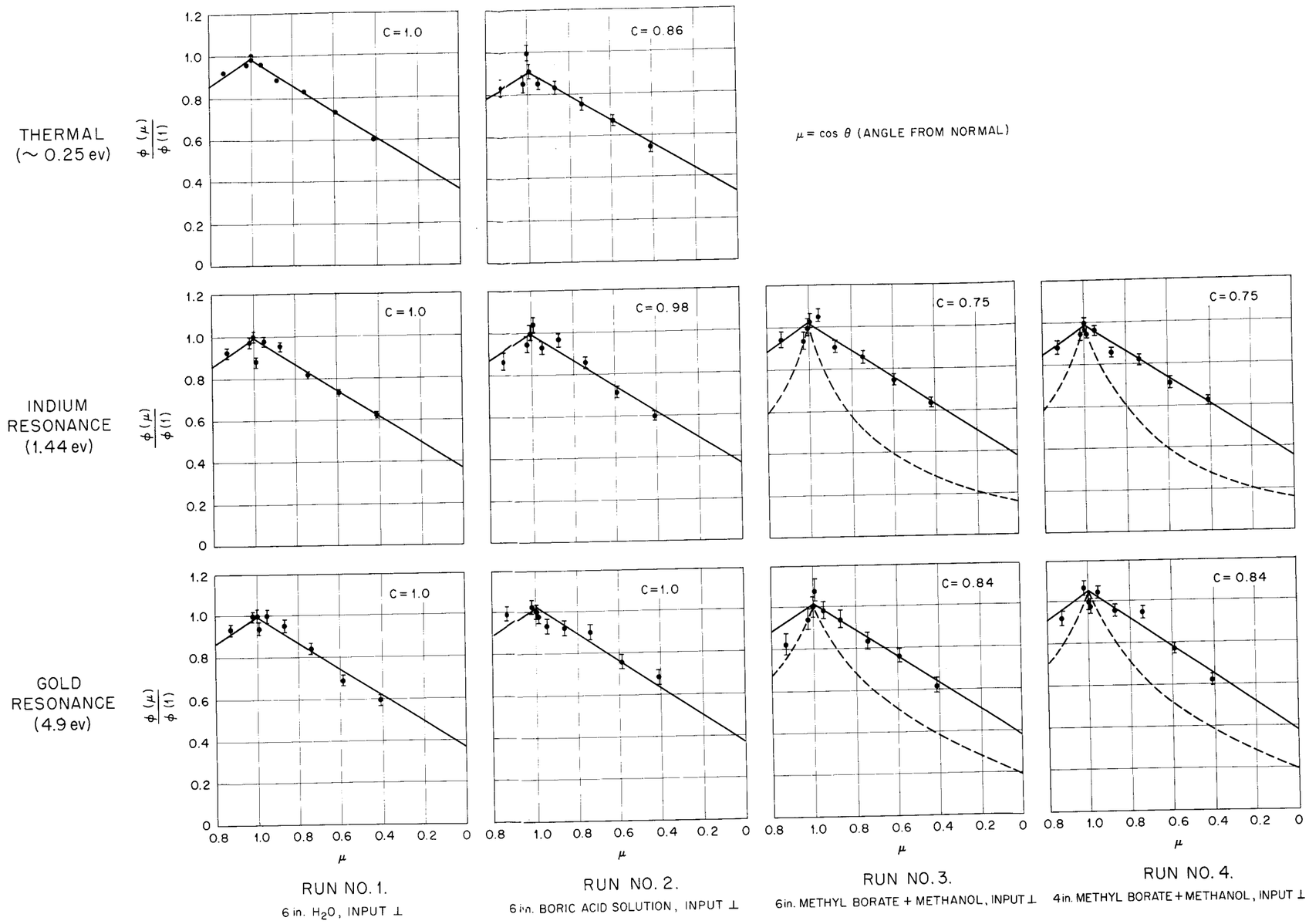

Fig. 7.2.2. Angular Distributions of Neutrons Emerging from Poisoned Hydrogenous Slabs with Thermal, Indium Resonance, and Gold Resonance Energies. The solid lines represent the $\phi(\mu) = 1 + \sqrt{3}\,\mu$ angular dependence given by Bethe for a nonpoisoned hydrogenous medium. The dashed lines give $\phi(\mu)$ values from one-velocity calculations by Case *et al.* for the specified C values. Error bars indicate statistical uncertainties only.

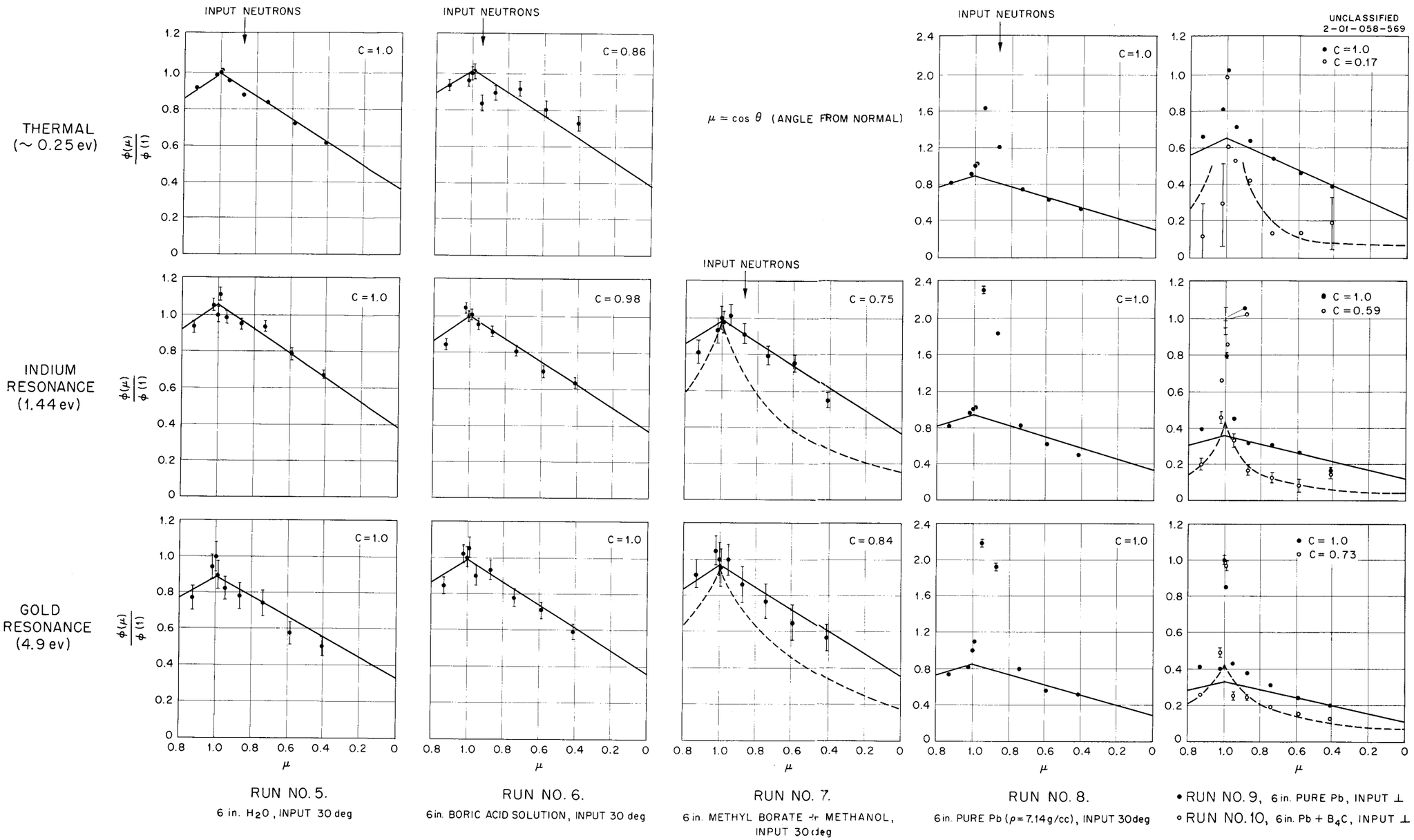

Fig. 7.2.3. Angular Distributions of Neutrons Emerging from Poisoned Hydrogenous and Lead Slabs with Thermal, Indium Resonance, and Gold Resonance Energies. The solid lines in runs 5, 6, and 7 represent the $\phi(\mu) = 1 + \sqrt{3}\,\mu$ angular dependence given by Bethe for a nonpoisoned hydrogenous medium. The solid lines in runs 8, 9, and 10 represent the $\phi(\mu) = 1 + 2\,\mu$ dependence expected for pure lead ($C = 1$). The dashed lines give $\phi(\mu)$ values from one-velocity calculations by Case *et al.* for the specified C values. Error bars indicate statistical uncertainties only.

only one thickness of the material, provided that the thickness is greater than 2 in. This will greatly simplify the shielding problem since calculations for this energy region are difficult because of crystal structure and molecular binding effects.

The experiments with the lead slabs qualitatively agree with the one-velocity calculations of Case *et al.*, that is to say, according to the superposed plots of runs 9 and 10, the poisoned lead certainly shows stronger forward peaking than the unpoisoned lead. However, the fact that the angular distribution is affected by the angle of incidence of the neutrons shows that the Milne problem was not properly mocked up and precludes further discussion until additional measurements with thicker lead slabs are made.

7.3 EXAMINATION OF THE RANGE OF APPLICABILITY OF CONDITIONAL MONTE CARLO TO DEEP-PENETRATION PROBLEMS

S. K. Penny C. D. Zerby

The difficulties involved in the application of the straightforward Monte Carlo method to problems involving deep penetrations are well known.[1] These difficulties are sometimes alleviated when an importance-sampling scheme is used,[1] but importance sampling requires parameters obtained by trial and error, as well as some prior assumptions concerning the results sought. A recent application by Drawbaugh[2] of the conditional Monte Carlo sampling method of Trotter and Tukey[3] to a one-velocity transport problem with isotropic scattering suggests that the conditional sampling technique is potentially very suitable for application to the deep-penetration problem. Drawbaugh obtained remarkably accurate estimates of the flux at distances up to 20 mean free paths, but since his example was only a one-dimensional phase-space problem it was not established that the accuracy of the flux estimates could be maintained for problems involving several phase-space variables. For this reason the conditional sampling technique has here been applied to the spatial part of a Monte Carlo calculation of the energy spectra and angular distributions from an isotropic point source of gamma rays in an infinite medium in which energy degradation was permitted. This particular problem was chosen because it presents geometric complications affording a rigorous test of the conditional sampling technique and because moments-method results were available for determining the accuracy of the estimates obtained.

---

[1] H. Kahn, *Applications of Monte Carlo*, AECU-3259 (April 1954).

[2] D. W. Drawbaugh, "On the Solution of Transport Problems by Conditional Monte Carlo," to be published in *Nuclear Sci. and Eng.*

[3] H. F. Trotter and J. W. Tukey, *Symposium on Monte Carlo Methods* (ed. by H. A. Meyer), Wiley, New York, 1956.

The general mathematical development of the conditional sampling method has been elsewhere presented.[2-5] The development for the particular problem at hand is also to be presented elsewhere.[6] The methods used to sample the momentum space were standard and conform to the examples given by Kahn.[1]

The results are presented as differential energy spectra and differential angular distributions. That is to say, let $n(r,\omega,E)$ be the number of collisions per unit volume, steradian, unit energy, and unit time, of particles of energy E moving in a direction such that ω is the cosine of the angle between that direction and the radius vector whose magnitude is r, the distance from the source. The energy flux is given by

$$\phi(r,\omega,E) = n(r,\omega,E)\,\frac{E}{\mu(E)}\ , \tag{1}$$

where μ is the linear absorption coefficient.

The differential energy spectrum is

$$\phi(r,E) \equiv 2\pi \int_{-1}^{1} d\omega\ \phi(r,\omega,E)\ . \tag{2}$$

The differential angular distribution is

$$\phi(r,\omega) \equiv 2\pi \int_{0}^{E_0} dE\ \phi(r,\omega,E)\ , \tag{3}$$

where E_0 is the source energy.

Two cases were calculated for comparison with moments-method results. The first considered a 1-Mev source in water, a weakly absorbing medium, and the second an 8-Mev source in lead, a strongly absorbing medium. The separation distances in both media ranged from one to 20 mean free paths (mfp).

All the Monte Carlo results are given as histograms, where the quantities plotted are those given by Eqs. 2 and 3, scaled by $4\pi r^2 e^{\mu_0 r}$, where $\mu_0 = \mu(E_0)$.

Figure 7.3.1 shows the differential energy spectra for a 1-Mev source in water, while Fig. 7.3.2 gives the angular distributions for the same case. The angular distributions for separations of 10 and 20 mfp are not shown because they were noticeably irregular. Figure 7.3.3 shows the differential energy spectra for the 8-Mev source in lead, and Fig. 7.3.4 the angular distributions for the 8-Mev source in lead. In Figs. 7.3.1 and 7.3.3 the smooth curves are the comparable moments-method results.

Figure 7.3.5 shows the differential energy spectrum of the 8-Mev source in lead at 20 mfp as computed in three fashions. The solid-line histogram is the result shown in Fig. 7.3.3;

---

[4] J. M. Hammersley, *J. Assoc. Comput. Mach.* 3, 73 (1956).

[5] J. Spanier, *Monte Carlo Methods and Their Application to Neutron Transport Problems*, WAPD-195 (July 1959).

[6] S. K. Penny and C. D. Zerby, "Examination of the Range of Applicability of Conditional Monte Carlo to Deep Penetration Problems," to be submitted to *Nuclear Sci. and Eng.*

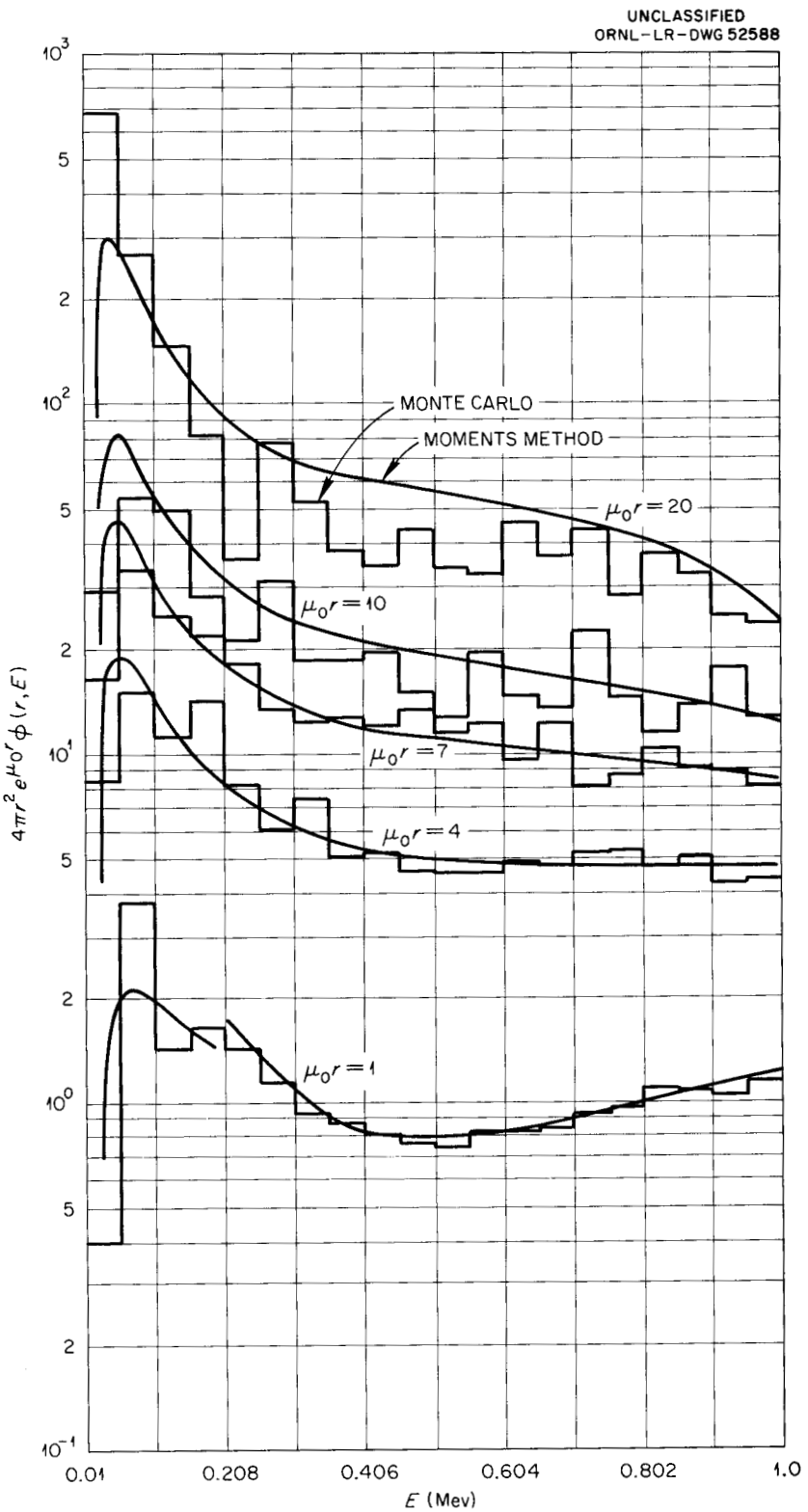

Fig. 7.3.1. Differential Energy Spectra for a 1-Mev Isotropic Point Source in Water.

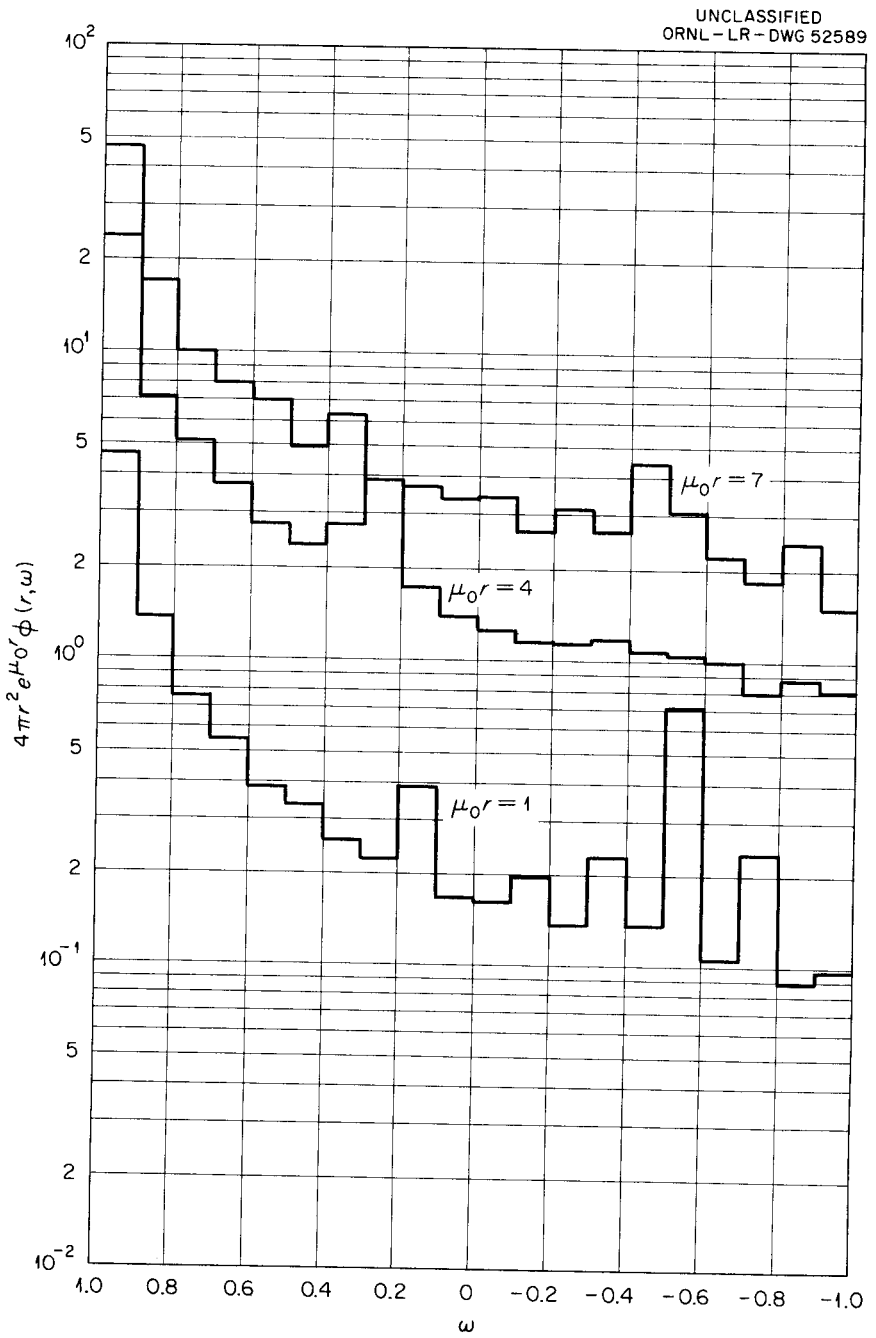

Fig. 7.3.2. Differential Angular Distributions for a 1-Mev Isotropic Point Source in Water.

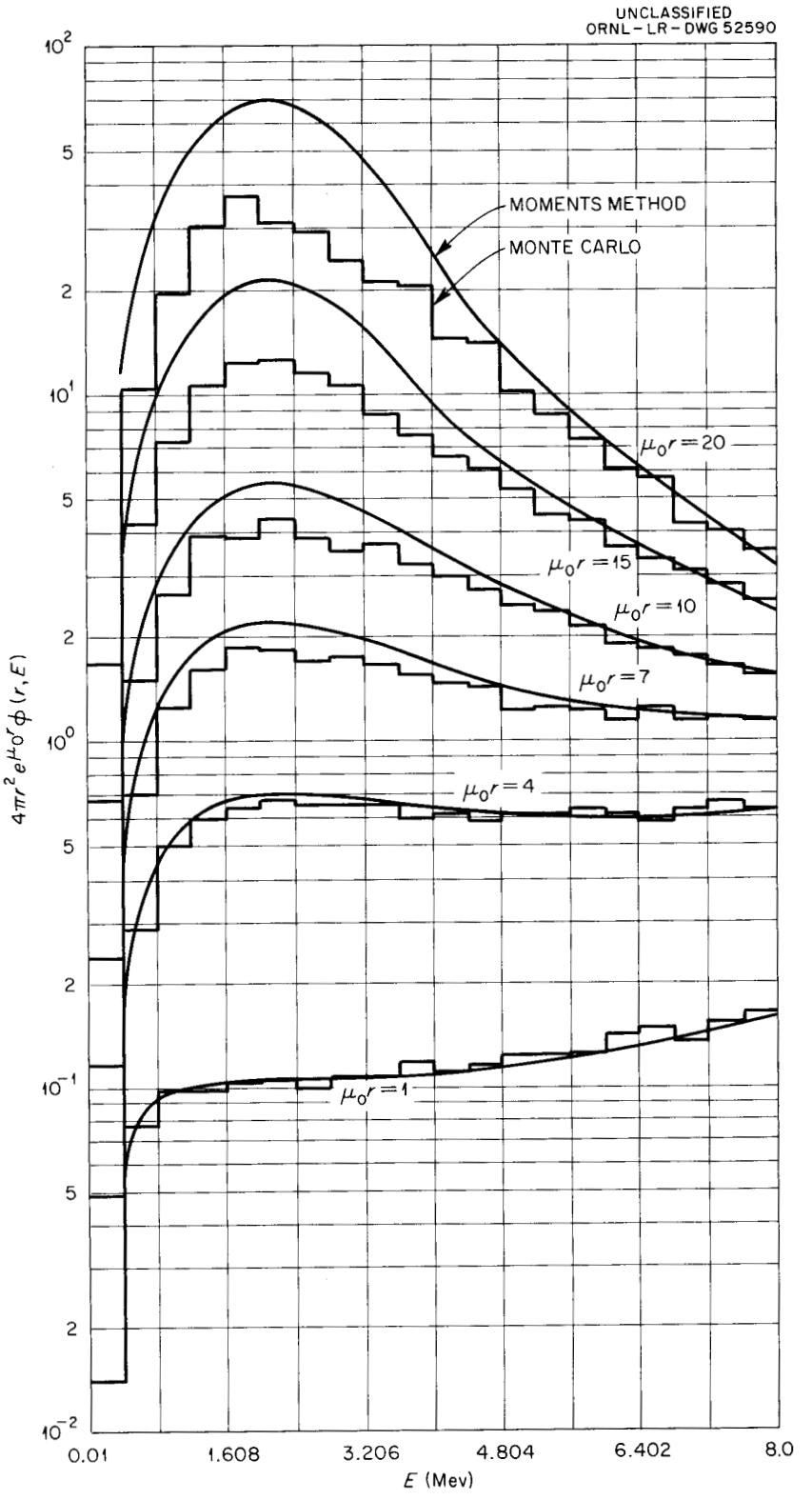

Fig. 7.3.3. Differential Energy Spectra for an 8-Mev Isotropic Point Source in Lead.

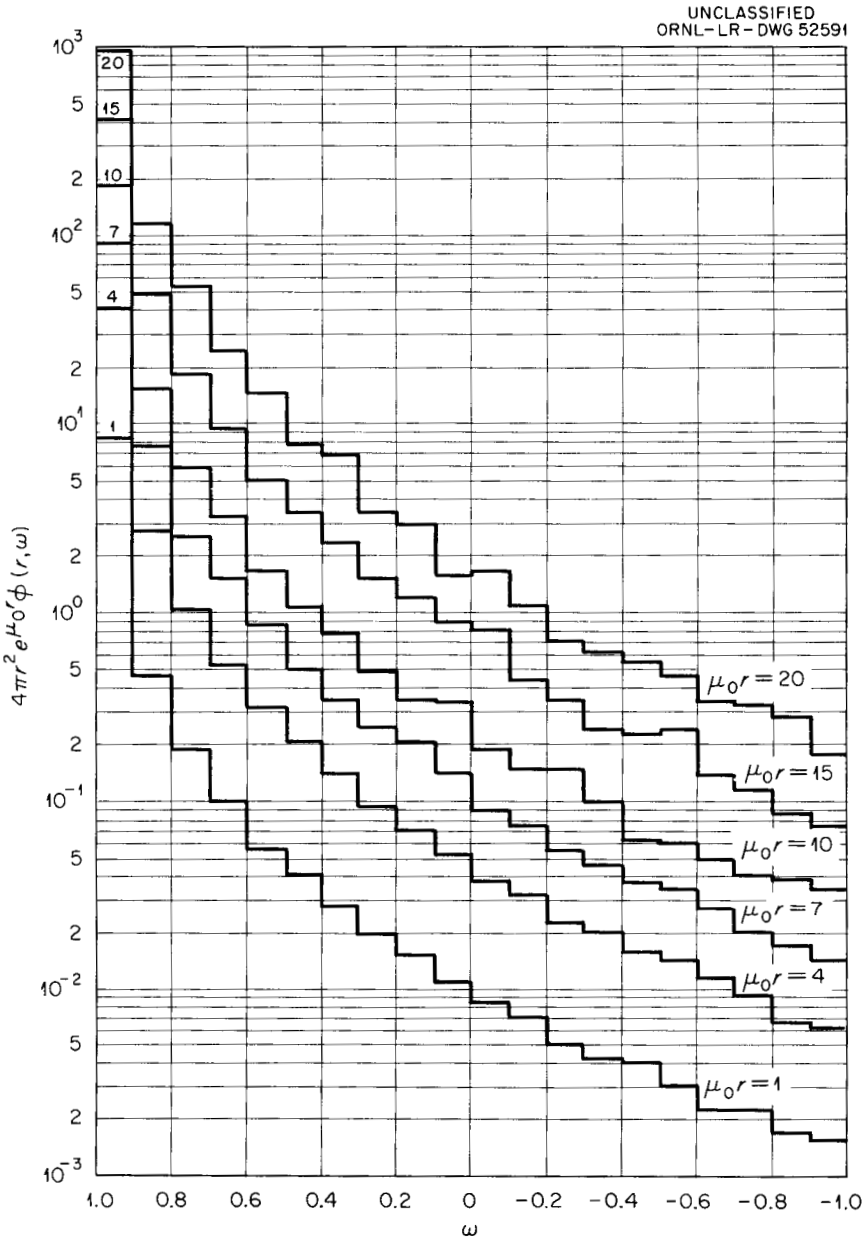

Fig. 7.3.4. Differential Angular Distributions for an 8-Mev Isotropic Point Source in Lead.

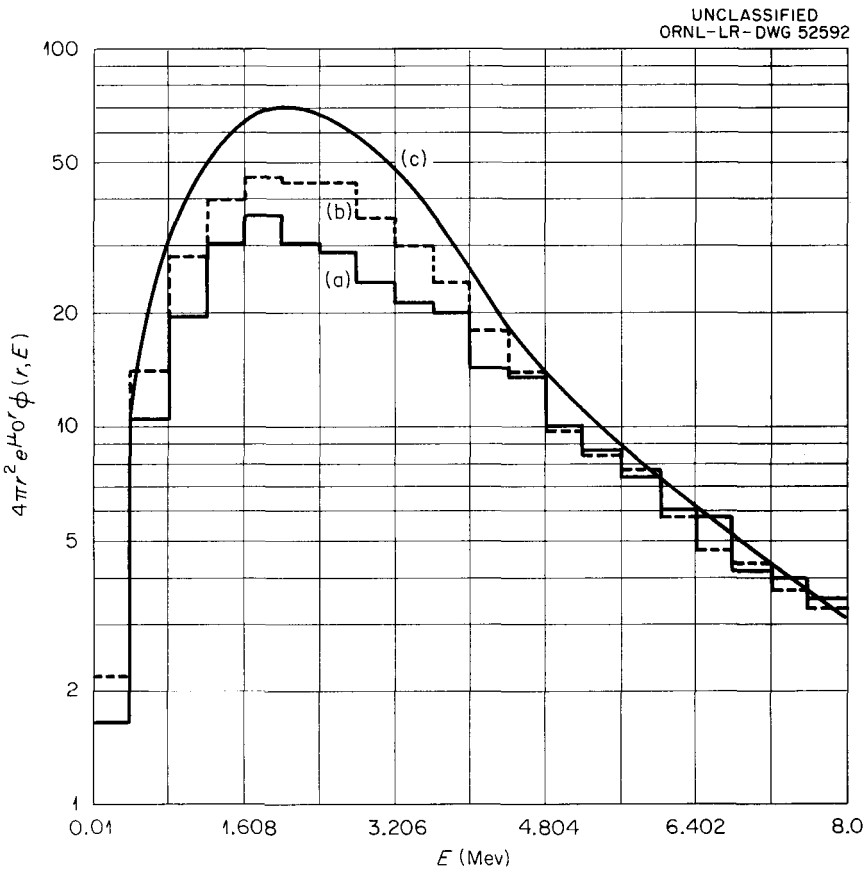

Fig. 7.3.5. Comparison of the Differential Energy Spectra for an 8-Mev Isotropic Point Source in Lead Calculated (*a*) by Monte Carlo, Using Most Recent Absorption Coefficients, (*b*) by Monte Carlo, Using Coefficients Used in Moments Method Calculations, and (*c*) by Moments Method.

the broken-line histogram the Monte Carlo results obtained using the moments-method absorption coefficients reported in ref 7; and the smooth curve the moments method results. Figure 7.3.6 displays the angular distribution for the 8-Mev source in lead at 20 mfp, the solid-line histogram being taken from Fig. 7.3.4 and the broken-line histogram again the result of using moments-method absorption coefficients. Table 7.3.1 is a comparison of the two sets of absorption coefficients.

Figure 7.3.7 shows the buildup factors[7] for both the 1-Mev source in water and the 8-Mev source in lead, computed from Monte Carlo and moments methods. The buildup factor is the result of dividing the area under the differential energy spectrum curve by the source energy and adding unity.

The data presented are averages of repeated computations, each with a relatively small number of histories compared with the total number of histories in the average. The differential

[7]H. Goldstein and J. E. Wilkins, Jr., *Calculations of the Penetrations of Gamma Rays, Final Report*, NDA 15C-41 or NYO-3075 (1954).

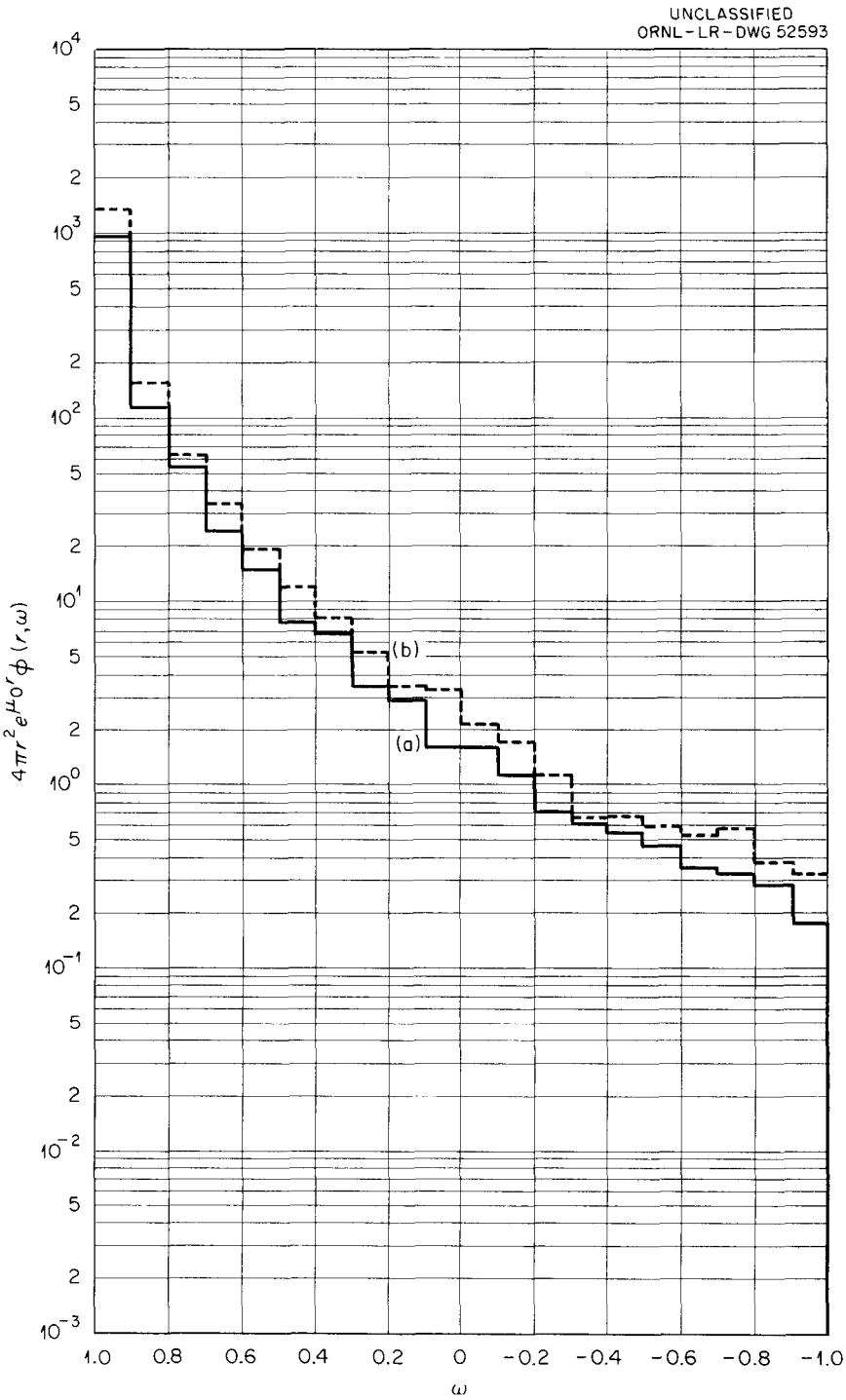

Fig. 7.3.6. Comparison of the Differential Angular Distributions for an 8-Mev Isotropic Point Source in Lead, Calculated (*a*) by Monte Carlo, Using Most Recent Absorption Coefficients, and (*b*) by Monte Carlo, Using Coefficients Used in Moments-Method Calculations.

Table 7.3.1. Comparison of Most Recent* Linear Absorption Coefficients for Lead with Those Used in Moments-Method Calculations**

Energy (Mev)	μ, Linear Absorption Coefficient		(1)/(2)
	(1) Most Recent	(2) Used in Moments-Method Calculations	
0.4	2.35	2.41	0.975
0.5	1.63	1.66	0.982
0.6	1.29	1.28	1.01
0.8	0.944	0.929	1.02
1	0.771	0.755	1.02
1.5	0.575	0.575	1.00
2	0.517	0.513	1.01
3	0.475	0.466	1.02
4	0.474	0.471	1.01
5	0.481	0.489	0.984
6	0.493	0.506	0.974
8	0.518	0.531	0.976

*G. W. Grodstein, *NBS Circular 583* (Apr. 30, 1957).

**H. Goldstein and J. E. Wilkins, Jr., *Calculations of the Penetrations of Gamma Rays, Final Report*, NDA 15C-41 or NYO-3075 (1954).

data showed some fluctuation between repetitions, with the lead data much more stable than the water data, but the integrals of the data fluctuated much less.

All the water data were computed with approximately 4000 histories per histogram, except for the 20-mfp results, which were obtained from 13,000 histories. The lead data utilized approximately 12,000 histories per case except for the 15- and 20-mfp computations, in which 40,000 histories were used. The larger numbers of histories in the lead calculations arise because the histories are terminated much more quickly in lead than in water, and the running time per problem was approximately the same for the lead and water cases.

The results obtained in this test indicate that the conditional sampling technique applied to the spatial part of the problem gave fairly accurate results for distances up to about 10 mfp. It is emphasized that no importance sampling, etc., was performed to obtain samples in the momentum space.

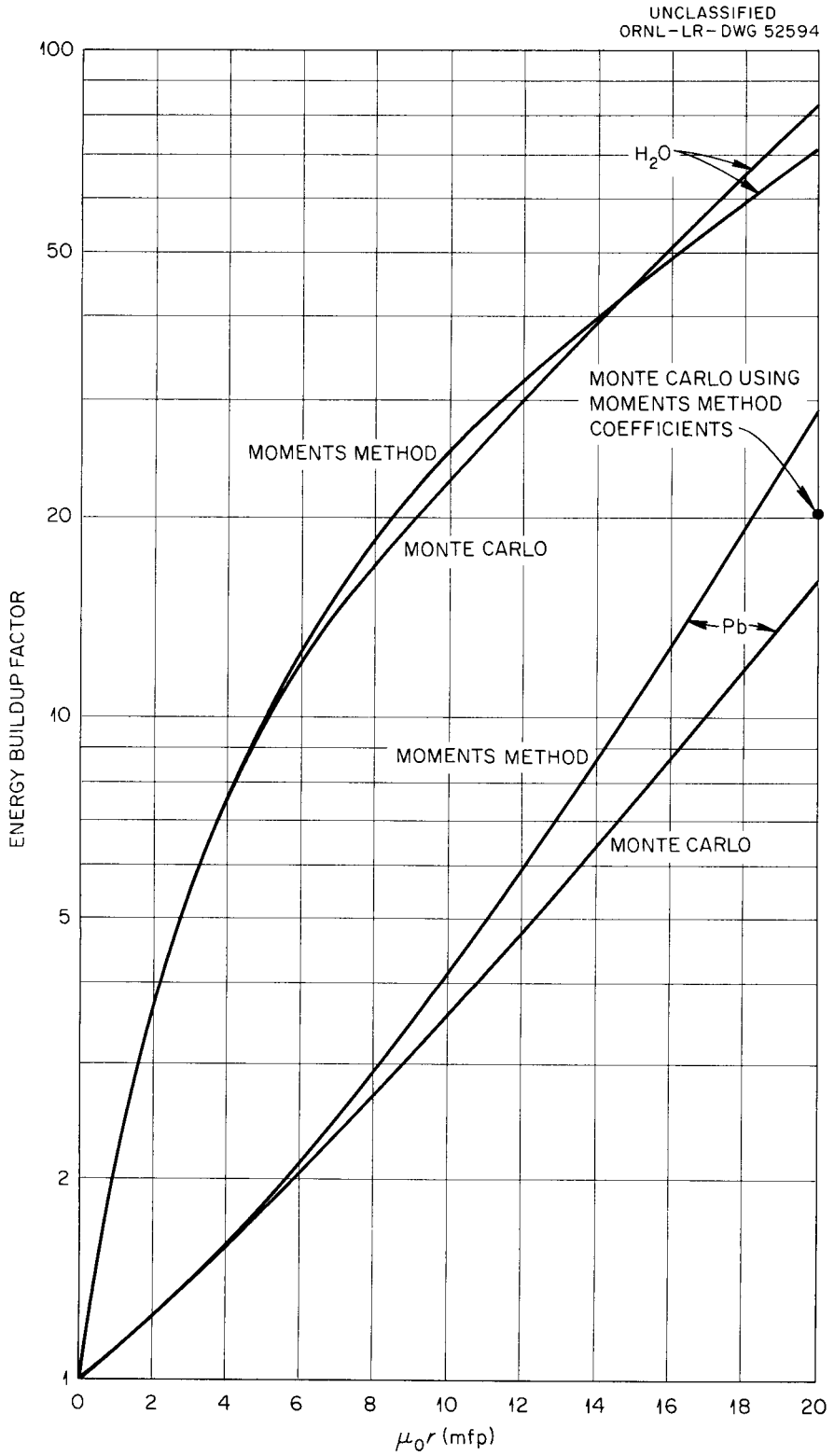

Fig. 7.3.7. Comparison of Buildup Factors Calculated by Monte Carlo and Moments Method for a 1-Mev Isotropic Point Source in Water and an 8-Mev Isotropic Point Source in Lead.

7.4 DESIGN OF A SHIELD FOR THE OAK RIDGE RESEARCH REACTOR SOUTH FACILITY (GCR LOOP NO. 2)

D. K. Trubey

Introduction

A test loop, to be used for evaluation of gas-cooled-reactor fuel elements and designated as GCR Loop No. 2, is soon to be installed at the South Facility of the Oak Ridge Research Reactor (ORR). This installation has required the design of a movable shield suitable for both equipment and personnel protection. Experimental and theoretical programs assisting in this design are in progress.

The proposed arrangement of the GCR Loop No. 2 is shown in Fig. 7.4.1, in which the principal feature of the shield, a 6-ft-long water beam catcher, is clearly evident.

Experimental Program

Experimental measurements performed at the ORR HB-2 facility are described in Sec 7.5 of this report. These measurements provided a means of estimating the ORR leakage, including the neutron spectrum, as well as the attenuation characteristics of the ORR radiation through various shield materials. An analysis of the data is in progress. An additional experiment was performed at the ORR HS-1 facility, a 10-in.-dia beam hole, at a reactor power of 24 kw. The gross features of the GCR Loop No. 2 were mocked up with a 50-lb perforated slab of stainless steel, simulating the elbow in the GCR loop, and a large tank of water, simulating the beam catcher noted above. Measurements of radiation scattered out the sides of the tank and back-scattered from the front of the tank were obtained. These data are to be published elsewhere.[1]

Theoretical work has employed four IBM 704 computer programs. The first, called Grinder, is described in Sec 7.6 of this report. It calculates, anywhere in the cell, the scattered gamma-ray dose rate and energy flux resulting from a beam of gamma rays incident upon the end of the beam catcher. Some results have been obtained and are being analyzed.

The second program is the O5R code,[2] which generates neutron histories and writes the details of each collision on magnetic tape. This code is now able to follow a history after a neutron has been thermalized.

The remaining two programs have been written by FORTRAN[3] to process the O5R data. The first, called "O5R Statistical Estimation," computes the fast-neutron dose rate and energy distribution at various points in the cell by statistical estimation, with the assumption that the scattering is isotropic in the center-of-mass system. For each collision, the contributions to the

---

[1] D. K. Trubey *et al.*, *A Measurement of the Radiation Streaming Through Beam Tube HS-1 at the ORR*, to be published as an ORNL CF Memorandum.

[2] R. R. Coveyou, J. G. Sullivan, and H. P. Carter, *Neutron Phys. Ann. Prog. Rep. Sept. 1, 1958*, p 87, ORNL-2609.

[3] FORTRAN is an automatic coding system for the IBM 704 data processing system, jointly developed by IBM, R. A. Hughes, and R. Nutt.

UNCLASSIFIED
2-01-059-575

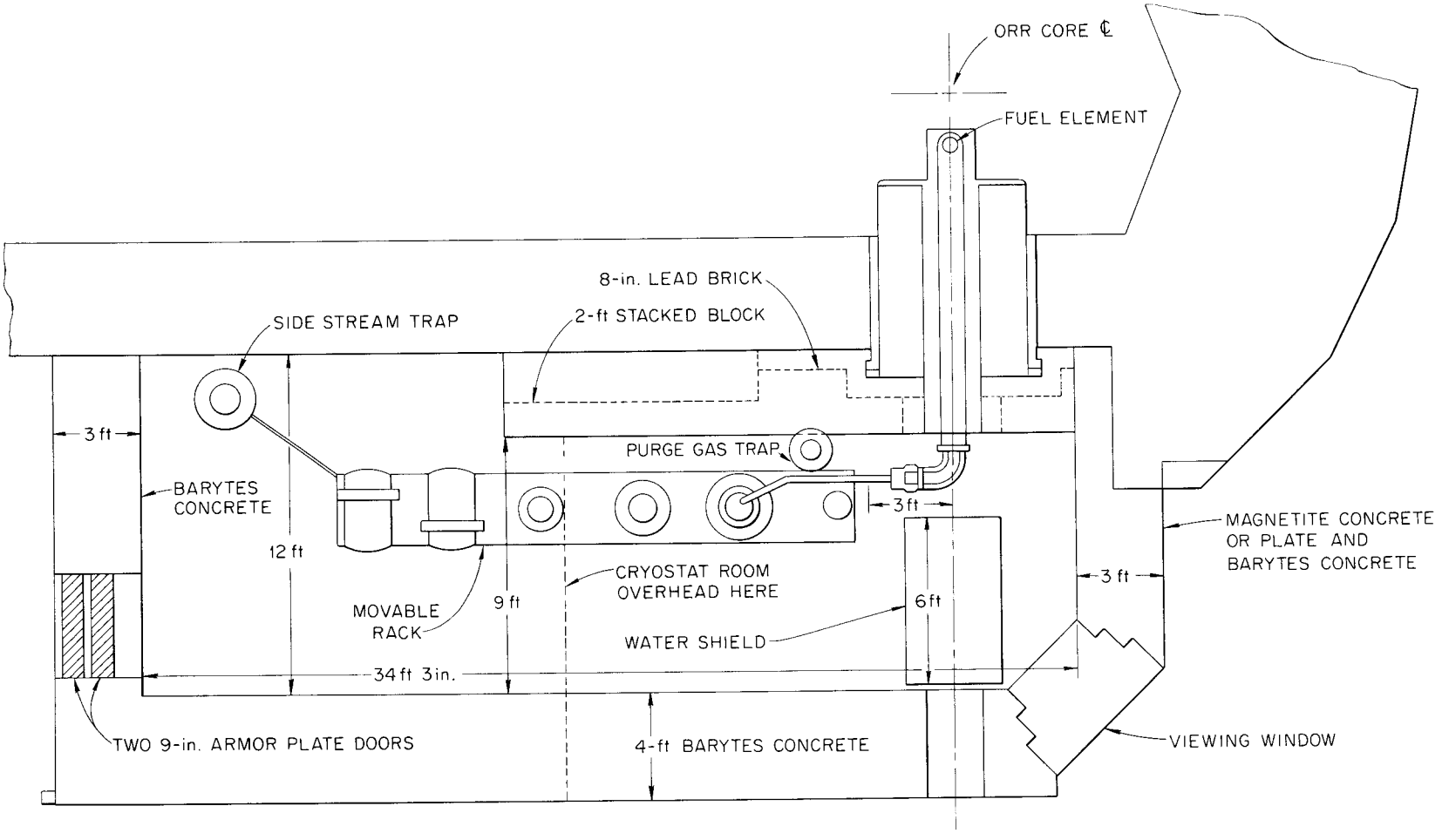

Fig. 7.4.1. ORR South Facility (HS-1) with the GCR Loop No. 2 in Place.

detector from scattering by oxygen and by hydrogen are separately considered. The second FORTRAN program, the "O5R Capture Gamma-Ray Code," estimates the dose rate at various detectors within the cell from secondary gamma rays resulting from thermal absorptions in the water tank. Buildup factors are utilized to account for multiple scattering in results for both pure and borated water.

7.5 DESIGN OF A SHIELD FOR THE ORR SOUTH FACILITY: EXPERIMENTAL PROGRAM AT BEAM HOLE HB-2

F. J. Muckenthaler T. V. Blosser

Introduction

The previous paper (see Sec 7.4) has outlined experimental work and calculations performed in support of the design of a shield for the South Facility of the ORR. The requirements for this shield are rather stringent since it must be placed in a prescribed volume, must be light, readily mobile, and so designed that there be a minimum amount of scattered radiation. During operation of the GCR Loop No. 2 the shield will serve as protection for the electronic equipment located near the emergent beam and for the personnel. During shutdown it will serve as a shield for personnel working inside the permanent shield.

The experimental data required for the shield design included fast-neutron and gamma-ray dose rate measurements for the unattenuated beam, plus measurements behind a variety of shield configurations. Also, since little data existed concerning the fast-neutron and gamma-ray spectra from the ORR core, it was decided to make spectral measurements. It would have been desirable to make the experimental measurements at HS-1, a 10-in.-dia beam hole at the South Facility; however, an external shield surrounding the hole would have been required, and none was readily available. Since time was important, and because the fabrication of a shield would have been unjustifiably costly for just a short-term experiment, a substitute location was sought. Beam hole HB-2, which has a permanent concrete personnel shield, was available. It was felt that the spectra from this smaller-diameter hole would closely approach those from the 10-in.-dia hole, and, therefore, the experimental data were obtained at beam hole HB-2. The permanent concrete shield includes a cavity in the middle, which was used for placement of shielding samples, and air ducts running vertically up from the cavity, which were utilized for some scattering measurements.

The data obtained consists of neutron spectra, both unattenuated and after passing through various shield configurations, and gamma-ray and fast-neutron dose rate measurements behind various combinations of iron, lead, barytes concrete, polyethylene, and borated polyethylene.

An attempt was made to determine the relationship of the scattered component of a beam to the transmitted component for both neutrons and gamma rays by measuring the scattered dose in a duct at right angles to the shield coffin. These measurements were made as functions of both absorber thickness and detector position within the duct.

Experimental Arrangement

Shield test samples, uniformly 12 × 12 in., were positioned in the air gap located in the middle of the permanent shield. Streaming around the samples was minimized by surrounding the slabs with a concrete coffin whose inside surfaces were a machine fit to the sample edges. The coffin had no shielding on the ends; so, measurements could be made directly behind the configurations. Gamma-ray dose rate measurements employed a 50-cc ion chamber, and all neutron measurements were made with a Hurst-type dosimeter except for the foil data reported below.

Results

Neutron Data. – Thermal and fast-neutron fluxes were observed in the unattenuated beam and through a number of shield configurations. Thermal-neutron measurements used bare and cadmium-covered gold foils; fast-neutron measurements were made with fission foils and sulfur pellets. The fission foils, Pu^{239}, Np^{237}, and U^{238}, were arranged in that order inside a boron ball during irradiation so that thermal-neutron activation could be prevented. The sulfur pellets were irradiated independently, since the required irradiation period was much longer than for the foils. The results of the neutron flux measurements are shown in Fig. 7.5.1, in which the number of neutrons with energy greater than the reaction threshold is shown as a function of energy for various thicknesses of concrete. Thermal-neutron data is also plotted.

A 2-in. thickness of concrete in the beam caused a sharp reduction in the relative intensity of thermal and low-energy neutrons, but increased thicknesses greater than 6 in. appeared to have little effect on the spectral shape. The attenuation in the high-energy region gave a relaxation length of about 8 cm.

Figure 7.5.2 shows fast-neutron dose rates as a function of concrete shield thickness. Dose rate was calculated from fast-neutron spectra and normalized to correspond to the dose rate that would have been measured with a Hurst-type dosimeter. The shape of the curve is as expected: data from small and large concrete thicknesses lie above the straight-line portion of the curve due to scattering in the personnel shield surrounding the foils during exposure.

Since a complete compilation of the fast-neutron dose rate data will be published in a later report, only a few general observations of shield performance are given at this time.

A shield composed of 10 in. of iron and 14 in. of borated polyethylene gave a reduction in fast-neutron dose rate three times greater when the iron faced the beam than when the polyethylene led. The same amount of iron and borated polyethylene used as alternating slabs was not as effective as the shield with all the iron facing the beam. A shield composed of 6 in. of lead in front of 11 in. of concrete gave about a factor of 6 greater attenuation than the same

shield with the concrete facing the beam, and, in fact, gave about the same attenuation as 16 in. of concrete backed by 6 in. of lead. However, a 2-in. thickness of lead in front of 21 in. of concrete was only about 10% more effective than when the shield was reversed.

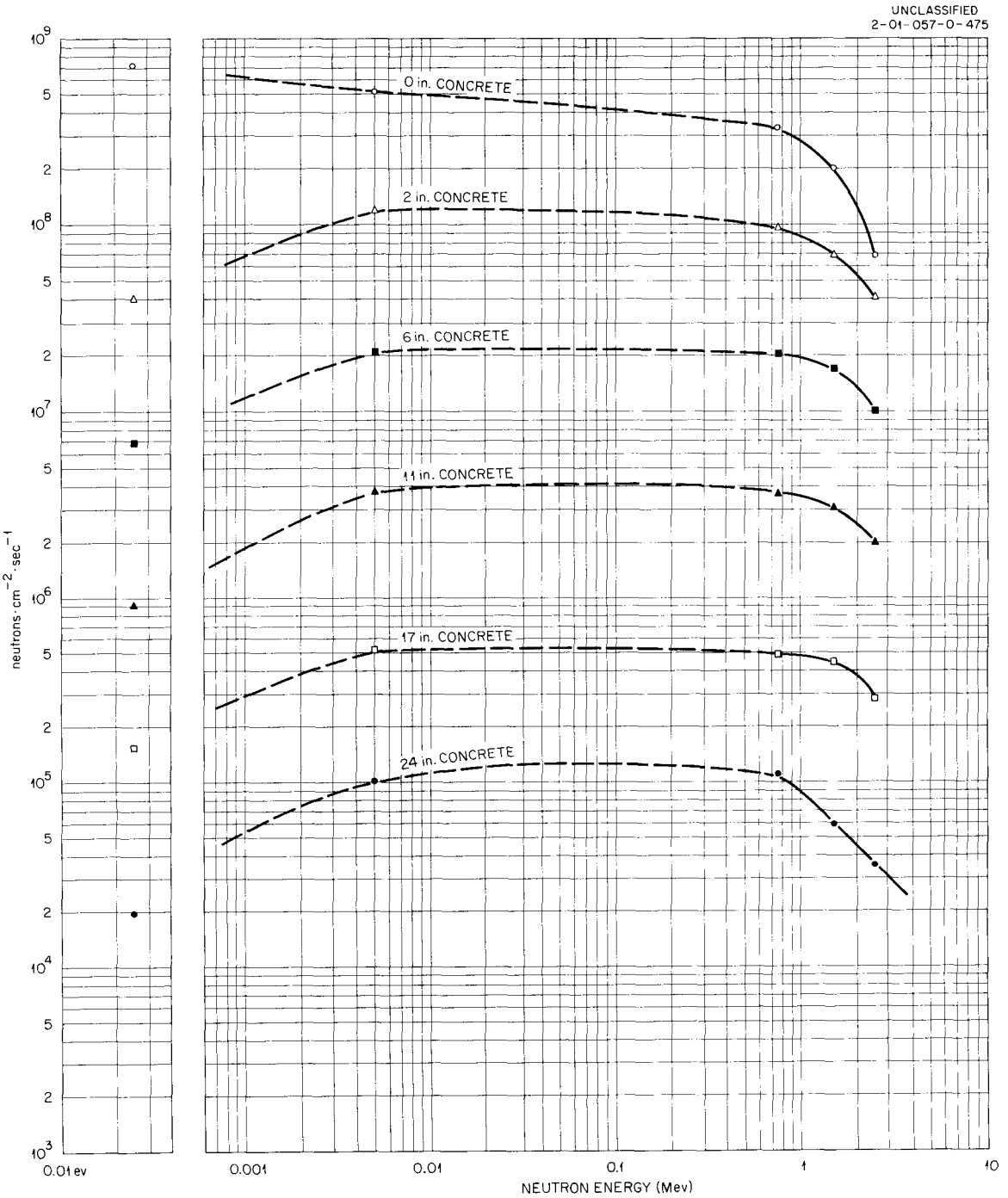

Fig. 7.5.1. Neutron Flux from ORR HB-2 as a Function of Neutron Energy for Various Thicknesses of Concrete Shield.

Along with the dose measurements behind various shield configurations, an attempt was made to measure the scattered dose rate from the shield in a duct at a right angle to the beam axis. Since the measured dose rate included an unknown contribution from neutrons scattered from areas other than those directly below the duct and penetrating the duct walls, precise values were not obtained. Despite the error, however, some general observations were made. It was concluded that scattering was more severe from lead than from iron, and both scattered more than concrete. Scattering from polyethylene was about a factor of 10 less than from iron or lead, and about a factor of 5 less than from concrete.

Gamma-Ray Data. – Figure 7.5.3 shows the gamma-ray dose rate from beam hole HB-2 as a function of thickness of concrete shield. The relaxation length is about 10 cm, as expected. The addition of a $\frac{3}{8}$-in. thickness of Plexibor to the beam side of the 17- and 24-in. concrete shields made no difference in the dose rate behind the thicker shield, and only about a 10% difference behind the thinner shield.

During the experiments with various thicknesses of concrete shields, a few measurements were made of the scattered gamma-ray dose rate in the air duct which extended vertically from

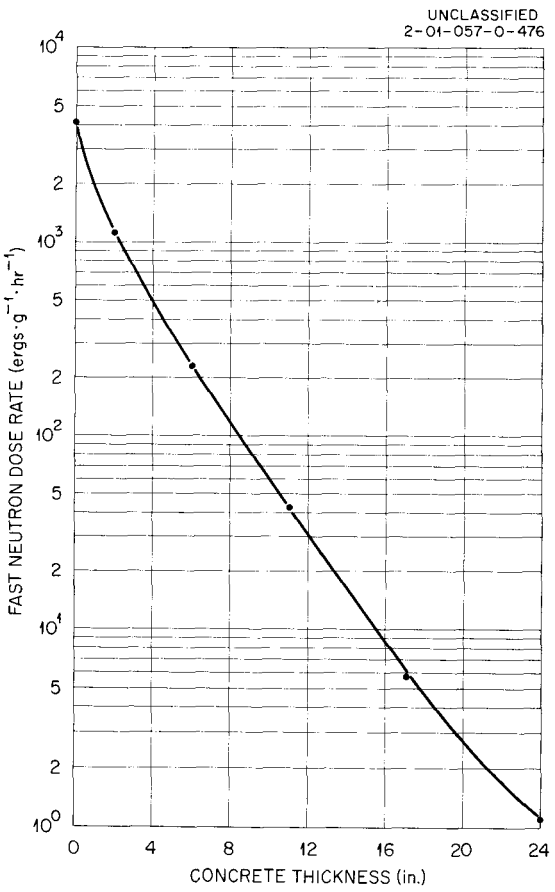

Fig. 7.5.2. Fast-Neutron Dose from ORR HB-2 as a Function of Thickness of Concrete Shield.

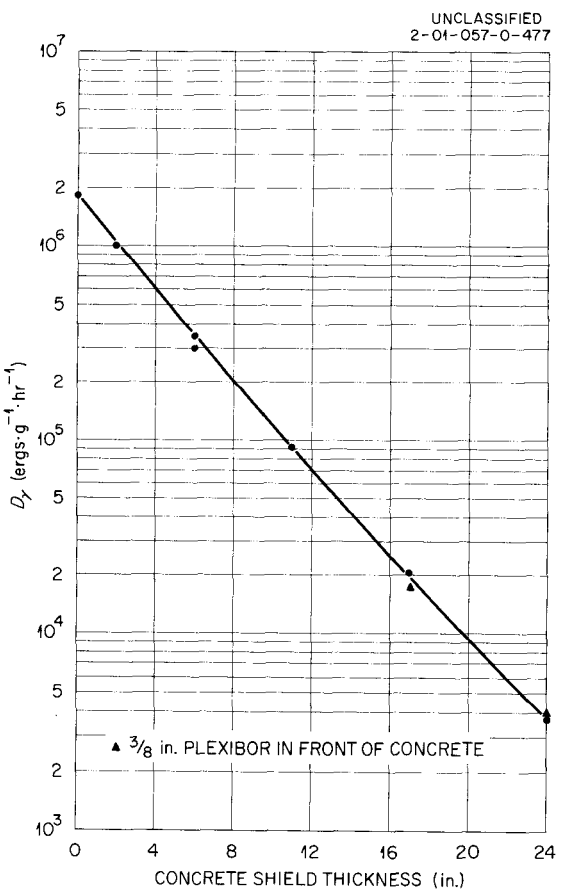

Fig. 7.5.3. Gamma-Ray Dose Rate from ORR HB-2 as a Function of Thickness of Concrete Shield.

On Fig. 7.5.2, exponents on dose rate scale should be increased by 2 (i.e., 10^2 becomes 10^4, etc.)

the shield coffin. The maximum dose was observed when the front face of the shield, regardless of its thickness, was located at the rear edge of the duct. For neutrons, the maximum dose had been observed when the front face of the shield was at the front edge of the duct. Plexibor placed in front of the concrete shield caused a factor-of-two reduction in the scattered dose when the face of the shield was located at the front of the duct. The Plexibor, however, had no effect when an additional 7 in. of concrete was placed at the front of the shield.

Figure 7.5.4 shows the gamma-ray dose rate behind various shield configurations, plotted as a function of total shield thickness. When the lead thickness is varied behind a constant 16-in. thickness of borated polyethylene, the dose rate behaves as expected, decreasing by a factor of 10 for each 2 in. of lead added. When the thickness of borated polyethylene preceding a fixed thickness of lead is varied, a sharp initial drop in dose rate with the first addition of borated polyethylene is noted. This results mainly from a decrease in neutron captures in the lead, combined with a decrease of gammas resulting from neutron scattering in the lead. When various thicknesses of concrete precede a fixed thickness of lead, the initial drop in dose rate appears to be much smaller than in the borated polyethylene case, but since no data point was obtained in this region, the exact shape is not known.

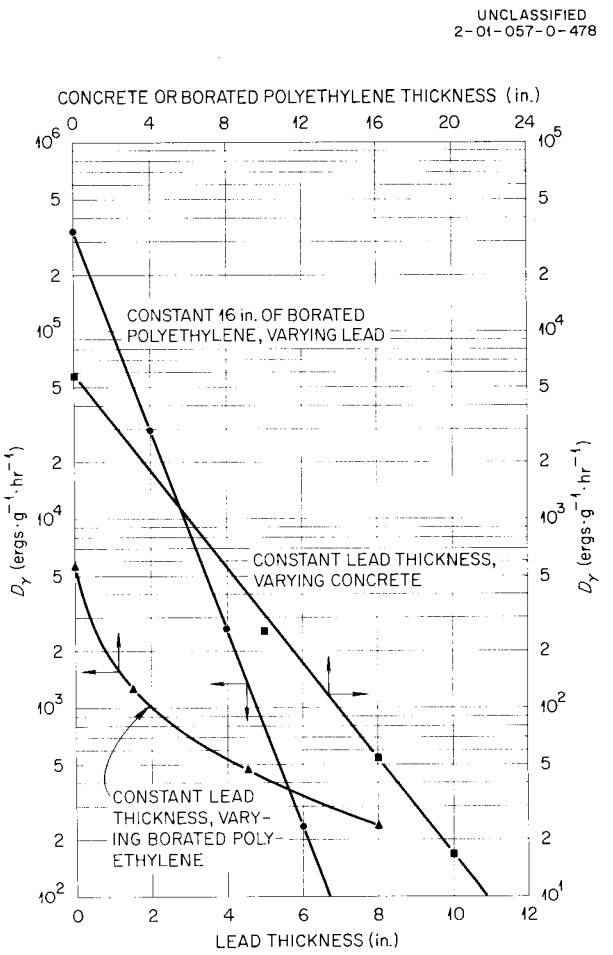

Fig. 7.5.4. Gamma-Ray Dose Rate from ORR HB-2 as a Function of Shield Thickness for Several Shield Configurations.

A $\frac{3}{8}$-in. thickness of Plexibor placed in front of a 16-in. polyethylene–6-in. lead shield caused a reduction in dose behind the shield of about 7%. An additional 8% decrease was noted when both the Plexibor and the polyethylene were replaced by borated polyethylene.

A check was made on the preferred distribution of 10 in. of iron and 14 in. of borated polyethylene in a shield. The maximum dose rate was observed when the full thickness of borated polyethylene faced the beam. Reversing the shield, so that the full 10 in. of iron faced the beam, reduced the dose rate by 20%. A shield in which the iron and borated polyethylene were in alternate layers, with a 4-in. layer of borated polyethylene facing the beam, gave dose rates

halfway between those for the two shields noted above.

In a shield composed of 2 in. of lead and 21 in. of concrete, the order of the materials was unimportant as long as either arrangement was preceded by Plexibor. However, when the Plexibor was not used, a dose rate measured behind 6 in. of lead followed by 11 in. of concrete was 40% greater than when 10 in. of concrete was followed by 6 in. of lead.

A more detailed presentation of the data obtained in these experiments will be made at a later date. Final analysis of the data and application to the design of the South Facility shield is being done by other members of the Neutron Physics Division.

7.6 GRINDER: AN IBM 704 MONTE CARLO PROGRAM FOR ESTIMATING THE SCATTERING OF GAMMA RAYS FROM A CYLINDRICAL BEAM CATCHER

D. K. Trubey S. K. Penny

Introduction

A Monte Carlo program has been written for the IBM 704 data-processing machine for the computation of energy spectra and dose rates of gamma rays scattered from within a homogeneous right circular cylinder to various positions outside the cylinder. The gamma-ray beam is incident upon the end of the cylinder, and, as the program is presently written, is coaxial with the cylinder. A small change in the present code would permit the beam to strike the end surface at any angle. The energy and radius of the incident gamma-ray beam, the dimensions and composition of the cylinder, and the detector positions (limited to 20) are specified in the input. An important feature of the program is that the computing time, rather than the number of histories, is an input parameter.

The photon histories are traced by a strictly analog procedure,[1] that is, no biasing techniques are employed. The contributions to the detectors are computed by statistical estimation,[1] that is to say, the contribution in each detector is the probability that a photon will scatter toward the detector and arrive there uncollided. Thus each collision makes a contribution to each detector. The usual difficulty in statistical estimation arising from scatterings that occur very close to a detector is not met with in Grinder, since all detectors are outside the scattering medium.

The energy spectrum at each detector position is given in histogram form in units of energy flux per unit incident photon flux per unit energy. There are 20 equal energy intervals of width $(E_0 - 0.01 \text{ Mev})/20$. The energy spectra are multiplied by dose-conversion factors and added to yield an estimate of the dose rate (tissue) in rads per hour per unit incident photon flux. Included in the output are: the number of case histories, the number of collisions, the number of

[1] H. Kahn, *Applications of Monte Carlo*, AECU-3259 (April 1954).

histories degraded below the energy and weight cutoffs, the energy albedo, the energy transmitted, the energy leaking from the lateral surface, the time used for the computation, the initial and final random numbers, and the input parameters. The output is on magnetic tape for off-line printing.

Calculational Procedure

The initial position of the photon is uniformly picked from a circle by uniformly choosing the Cartesian coordinates x and y and rejecting if the particle lies outside the beam radius. The history is then traced by means of subroutines developed by one of the authors for another program (see Sec 7.3). The weight is reduced at each collision to account for absorption. At each collision the energy flux at each detector is computed from

$$\frac{P(E,\theta)WE'e^{-\mu_t(E')fR}}{R^2} ,$$

in which

$P(E,\theta)$ = probability of scattering in the direction of the detector through the angle θ per unit solid angle

$$= \frac{N\, d\sigma/d\Omega\ (E,\theta)}{\mu_t(E)} ,$$

N = electron density,

$\mu_t(E)$ = total absorption coefficient,

W = photon weight,

$d\sigma/d\Omega\ (E,\theta)$ = Klein-Nishina scattering cross section,

R = distance to detector from collision,

E' = photon energy after scattering through the angle θ with initial energy E,

f = fraction of the path length that lies within the cylinder.

This quantity is accumulated in the 20 energy intervals to form a histogram which is normalized at the end of the calculation to unit particle flux incident on the cylinder per unit energy. The dose rate is then obtained by multiplying each histogram quantity by an energy-flux-to-dose conversion factor. These factors are an estimate of

$$\int_{E_1}^{E_2} T(E)\, dE ,$$

in which the $T(E)$ are the energy-flux-to-tissue-dose-rate conversion factors listed by Blizard[2] for energies above 0.1 Mev and by Rockwell[3] for energies less than 0.1 Mev. The function

[2] E. P. Blizard, sec 7.3 of *Nuclear Engineering Handbook*, ed. by H. Etherington, McGraw-Hill, New York, 1958.

[3] T. Rockwell III (ed.), *Reactor Shielding Design Manual*, TID-7004 (March 1956).

$T(E)$ is assumed to be an exponential between listed values. This gives a fairly good representation in the region where the function descends rapidly between 0.01 and 0.06 Mev, and a good representation elsewhere.

When the photon escapes the cylinder, and also when computing f, the surface penetrated must be determined. This is known immediately for some detector positions, but for others a test must be made. After this is determined, f is computed from

(a) $f = -z/R_z$, reflected,

(b) $f = (L - z)/R_z$, transmitted,

(c) $f = \sqrt{(b/a)^2 + (c/a)} - (b/a)$, side leakage,

in which

x, y, z = coordinates of collision,

L = length of cylinder,

R_x, R_y, R_z = components of R,

$a = R_x^2 + R_y^2$,

$b = xR_x + yR_y$,

c = (radius of cylinder)$^2 - (x^2 + y^2)$.

Tests of the Code

Transmission results have been compared with values computed by the Oracle program of Auslender.[4] The computed albedo has been compared with the results of Berger.[5] The expected result in the highest energy for a detector position at the rear may be determined analytically, as follows.

To be in the highest energy box, for a narrow cylinder, nearly all the particles must have collided only once and must have been scattered through an angle less than θ (see Fig. 7.6.1). The average Klein-Nishina macroscopic cross section from θ to π is $\bar{\mu}$. The contribution in the highest energy box is then

$$\phi(E_0, \mu_t L) e^{\mu_t L} \cong \int_{x=0}^{L} \int_{\rho=0}^{x \tan \theta} \frac{2\pi\rho \, d\rho \, dx}{\Delta E R^2},$$

in which

μ_t = total absorption coefficient,

x, L, ρ, R are dimensions shown in Fig. 7.6.1,

[4] S. Auslender and D. K. Trubey, *Instructions for the Operation of an Oracle Code for Monte Carlo Solution of the Transport Problems for Gamma Rays Incident on a Slab*, ORNL CF-60-10-37 (to be published).

[5] M. J. Berger and D. J. Raso, *Backscattering of Gamma Rays*, NBS 5982 (Feb. 8, 1960).

ΔE = energy width into which the scattered photon falls after scattering through an angle less than θ,

E_0 = initial energy.

$$\phi(E_0,\mu_t L)e^{\mu_t L} \cong \frac{2\pi\bar{\mu}}{\Delta E}\int_{x=0}^{L}\int_{R=x}^{x\sec\theta}\frac{R\,dR}{R^2}\,dx = \frac{2\pi\bar{\mu}}{\Delta E}\,L\ln\sec\theta\ ,$$

but, for small angles,

$$\ln\sec\theta = \sec\theta - 1 \cong 1 - \cos\theta\ .$$

For $0.95E_0 \leqq E \leqq E_0$ (where the energies are in Mev),

$$0.95 = \frac{1}{1 + \dfrac{E_0}{0.511}(1-\cos\theta)}\ ,$$

$$1 - \cos\theta = \frac{0.05}{1.859E_0} = \frac{0.0269}{E_0}$$

$$\cong 0.027 \text{ for } E_0 = 1 \text{ Mev}\ .$$

UNCLASSIFIED
2-01-059-576

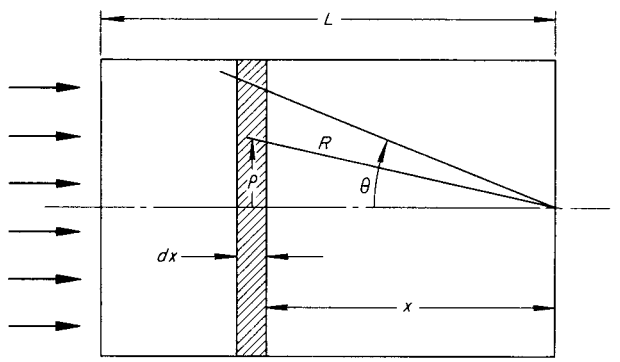

Fig. 7.6.1. Geometry for Calculation of Highest-Energy Contribution.

Thus, for one mean free path in water, and E_0 = 1 Mev,

$$\bar{\mu} = 0.025\ \text{cm}^{-1}$$

$$\phi(1,1)e^1 \cong \frac{2\pi(0.025)14.1(0.027)}{0.05} = 1.20\ .$$

With 15 min of computing (20,000 collisions, two detectors), Grinder yielded a value of 1.15 for the highest energy interval and an average value of 1.32 for the two highest intervals. The energy albedo was calculated to be 0.027, to be compared with a value of 0.046 for a semi-infinite medium[5] and in good agreement with a value of 0.031 computed by the Auslender Oracle program.[6]

Application

Grinder is being used for the estimation of energy distributions and dose rates of gamma rays scattered within the cell of the ORR South Facility (see Sec 7.4), from water and from stainless steel. Grinder, as contrasted to many programs which give only an albedo in infinite geometry, is particularly suited for estimation of reflected dose rates under finite-geometry conditions.

---

[6]Unpublished result of calculations described by L. A. Bowman and D. K. Trubey, *Neutron Phys. Ann. Prog. Rep. Sept. 1, 1958*, ORNL-2609, p 110, 115.

7.7 THE SINGLE-SCATTERING APPROXIMATION TO THE GAMMA-RAY AIR SCATTERING PROBLEM

D. K. Trubey

It has been hypothesized that a good approximation to the scattered flux (or dose rate) in air is the single-scattered flux (or dose rate) with exponential attenuation and buildup neglected. Such a simple method, if sufficiently accurate, would be useful in computing skyshine from a reactor or other source. Neglect of attenuation, of course, tends to compensate for neglect of buildup.

This approximation previously was demonstrated to be satisfactory in the case of neutrons scattered in air isotropically in the center-of-mass system. The results were in good agreement with those of a Monte Carlo calculation.[1] Since Monte Carlo calculations also exist[2] for the air-scattered flux and dose rate for gamma rays, a comparison of results obtained from the gamma-ray single-scattering approximation with Monte Carlo results has been made.

The problem considers a line beam of monoenergetic gamma rays emitted from a point source in a uniform, infinite medium of air. The resulting dose rate at a distance x from a source of energy E and emitting photons at an angle ψ from the source-detector axis is conveniently given by

$$\text{Dose}(E,x,\psi) = \frac{N}{x}\,\frac{C(E)D(E,\psi)}{\sin\psi}\,,$$

where N = the electron density per cm^3, and the functions $C(E)$ and $D(E,\psi)$ (a fraction) are defined by

$$\int_{\psi}^{\pi} \frac{d\sigma}{d\Omega}\,(E,\theta)T(E,\theta)d\theta = C(E)D(E,\psi)\,,$$

where

θ = angle through which the photons are scattered,

$\frac{d\sigma}{d\Omega}$ = Klein-Nishina scattering cross section,

T = conversion factor (given in ref 2).

The product, $C(E)D(E,\psi)$, was computed numerically on the Oracle.

The scattered flux was obtained by a similar method, which will not be detailed here.

---

[1] F. L. Keller, C. D. Zerby, and J. Hilgeman, *Monte Carlo Calculations of Fluxes and Dose Rates Resulting from Neutrons Multiply Scattered in Air*, ORNL-2375 (1958).

[2] R. E. Lynch *et al.*, *A Monte Carlo Calculation of Air-Scattered Gamma Rays*, ORNL-2292, vol I (1958).

The results of the calculations and the comparison with the Monte Carlo data are to be published elsewhere.[3] They show, however, that the simple dose rate approximation gives very good results for all angles and photon energies, while the flux approximation gives good results to about 60° for distances up to 100 ft. If the detector is shielded in any way, however, these results probably are not valid, since energy and angular distribution at the shield are important.

[3]D. K. Trubey, *The Single-Scattering Approximation to the Gamma-Ray Air-Scattering Problem*, ORNL-2998 (1960); also to be submitted to *Nuclear Sci. and Eng.*

7.8 DEVELOPMENT OF AN IBM 704 ANALYTICAL CODE FOR ANALYSIS OF AXIALLY SYMMETRIC REACTOR SHIELDS

F. B. K. Kam H. E. Stern

Introduction

A series of automatic data processing machine programs, applicable to the preanalysis of typical Tower Shielding Facility (TSF) experiments and to general shield design, are being developed. Codes intended to calculate the various components of dose inside a shielded crew compartment are being written for the IBM 704.

Primary Neutron Program

An axially symmetric reactor shield configuration is assumed and neutron dose rate is computed for a detector point on the axis of symmetry. The reactor core is defined as either a homogeneous sphere or a homogeneous spherical shell. The surrounding shield is defined as a series of concentric, homogeneous spherical shells plus an outer, shaped region. A single shadow shield may be embedded in the outer region, the inner surface of which must be spherical and the thickness of which may be a function of polar angle. A more general arrangement, which will permit three such shadow shields, is also being worked on.

The fuel region is divided into annular sections for computation purposes, and the dose rate to any point on the axis of symmetry is calculated on a line-of-sight basis. The calculation of distance traversed in each shield region has been coded as a FORTRAN subprogram and can be used in other main programs of this study if required.

The material attenuation in the hydrogenous portion of the shield is assumed to be of point kernel form, such as that given for moments-method calculations.[1,2] In practice, the logarithm of the expression $4\pi^2 D(r)$, in which $D(r)$ is the dose rate at a distance r from a point source of neutrons, is fitted with a polynomial, and the coefficients are fed in as input data.

[1]R. Aronson *et al.*, *Penetration of Neutrons from a Point Isotropic Fission Source in Water*, NYO-6267, NDA 15C-42 (Sept. 22, 1954).

[2]R. Aronson, J. Certaine, and H. Goldstein, *Penetration of Neutrons from Point Isotropic Monoenergetic Sources in Water*, NYO-6269, NDA 15C-60 (Dec. 15, 1954).

The calculation of the attenuation in the heavy materials in the shield is based on removal cross section data. Attenuation through the rear of the crew compartment is lumped with that of the reactor shield.

Provision is made in the code for a maximum of 15 reactor shield regions. The dimensions of each region, the increment of the angular variable, the angular thickness functions for shaped portions of the shield, and the radial power density function of the active core are all treated as input data.

Primary Gamma Rays

The same basic code designed to compute fast-neutron dose rates is also used to calculate primary gamma-ray dose rates. Capture gamma rays resulting from thermal-neutron captures within the limits of the Tower Shielding Reactor II reactor tank are included in the primary contribution. A volume integration over the source region is carried out, and attenuation along each line-of-sight path is computed using the product of an exponential times the buildup. Values of the buildup factor are taken from the data for water given by Goldstein,[3] based on the total number of mean free paths traversed.

Gamma-Ray Buildup Code

A FORTRAN subprogram utilizing the dose rate buildup factors for water given by Goldstein [3] has been written for the IBM 704 to provide a polynomial approximation to the buildup. A fit of the cube root of the buildup as a function of the number of mean free paths, for fixed energy, was determined using third-degree polynomials, and the various coefficients fitted in turn, using fourth-degree polynomials. The resulting expressions give values within 5% of the published experimental data over the entire energy range from 0.255 to 10 Mev, and from 0 to 20 mean free paths. The machine time required to obtain a single value of the buildup is approximately 8.4 msec.

Status

The gamma-ray buildup code and the subprogram for calculation of distance traveled in each shield region have been coded and debugged. The remainder of the programs described above have been coded and are in the process of debugging.

---

[3] H. Goldstein and J. E. Wilkins, *Calculations of the Penetration of Gamma Rays, Final Report*, NYO-3075 (June 30, 1954).

7.9 DESIGN OF A REACTOR SHIELD

H. E. Stern F. B. K. Kam

The shields designed for nuclear-powered aircraft are of two general types. The first is the unit shield in which the attenuating material is placed around the reactor; the second is the divided shield in which the shielding material is divided between the source and the receiver. Although the unit shield can be expected, in general, to be "shaped" less severely than the divided shield, there is still much to be gained in weight savings in both cases through efficient design. Accordingly, a study has been initiated of some of the problems in the specification of reactor shield systems and of calculational methods for obtaining optimum configurations. The systems considered utilize two basic materials: a light, hydrogenous material, primarily to attenuate neutrons, and a dense material of high atomic weight, primarily to attenuate gamma rays. The detector shield, if any, is assumed fixed.

Preliminary studies have been directed toward a better understanding of the gamma-ray problems and to the design and placement of heavy materials within the light neutron-shielding material surrounding the reactor core. The gamma-ray dose at the detector position is essentially composed of gamma rays born in the core plus gamma rays resulting from neutron interactions in the shield. Most of the work thus far has been a study of the gamma rays born in the core, which were subdivided into photons that penetrate all the layers of heavy material, photons that scatter "favorably" in the light shield material so as to bypass at least part of the heavy material, and photons that escape the reactor without penetrating all the layers of heavy material, scatter favorably in the surrounding air, and reach the detector.

A simple model was chosen which enables the approximate calculation of each of these components. The computations were carried out for a shadow shield fixed in location with respect to the source of gamma rays, of uniform thickness and variable half angle. Total dose rates at an unshielded detector, as well as shield weight, were obtained as a function of shadow-shield half angle. By means of a Lagrange multiplier approach, the optimum half angle and corresponding relative dose rate were obtained as a function of assumed shadow-shield thickness.

Because of the assumptions involved, the results should be most realistic for thicknesses of the order of several centimeters and half angles greater than, say, 30°. The work thus far has served principally to give some insight into the relative magnitudes of the quantities involved and to test a simple optimization scheme. In future work more realistic problems will be considered that involve variable-thickness shadow shields and include secondary gamma-ray contributions.

7.10 ELECTRON CASCADES: STATUS REPORT

C. D. Zerby H. S. Moran

The shielding problem connected with the currently intensive development of high-energy particle accelerators operating in the Bev energy region[1] has stimulated interest in high-energy electron cascades. When a high-energy beam of electrons from an accelerator is stopped by a shield, the resulting electron-photon cascade must be contained for protection of personnel and equipment. As the beam energy is increased, the size of the shield must be increased, and its dimensions and cost are of considerable importance when energies reach 10 to 45 Bev, such as are projected for the Stanford University Linear Accelerator.

The containment of the cascade itself, however, is not the only problem, since coupled with it is the problem of containment of the photoneutrons born within the shield. The shielding of these neutrons presents a different type of problem, which in fact may cause an important increase in shield dimensions and cost. Since most photoneutron cross sections reach a maximum in the 15- to 20-Mev energy range, it is particularly important to determine the intensities and spatial distributions of gamma rays in the shower over this range, in order to establish the strengths and source distribution of the photoneutrons.

In an effort to provide all data that may be of interest from an electron-photon cascade, a calculation utilizing a Monte Carlo technique is being prepared for solution by an automatic computer. A review of available experimental and theoretical data relating to the cascade has been made for the wide span of energies of interest. Most of the basic theoretical knowledge is contained in an article by Bethe and Ashkin.[2] All physical processes believed to be of importance in the various stages of the cascade will be taken into consideration.

Particularly difficult to evaluate and include in the calculation, because of lack of information, are the effects of some of the very high energy processes, such as inelastic collisions of electrons with nuclei. Such collisions may lead to release of other particles into the shower and also to an enhancement of the gamma-ray spectrum. Although these processes will be examined as well as possible to determine their contributions, for the first calculations inelastic interactions with the nucleus will be ignored.

Most of the cross-section data required for the calculation have been prepared in such a way that the cascade can be calculated for an arbitrarily chosen material. Codes for determining the cross sections, as well as random selection techniques for determining the angles of scattering from the differential cross sections, have been prepared. The final assembly of the cascade problem is now in the process of development.

---

[1] *Major Activities in the Atomic Energy Programs, January–December 1959*, p 148 ff, USGPO, January 1960.

[2] H. A. Bethe and J. Ashkin, "Passage of Radiation Through Matter," *Experimental Nuclear Physics* (ed. by E. Segrè), vol I, p 166, Wiley, New York, 1953.

7.11 CALCULATION OF THE DIFFERENTIAL INELASTIC CROSS SECTION FOR COMPLEX NUCLEI

H. Bertini C. D. Zerby

Introduction

In order to calculate the penetration of high-energy particles through the radiation shielding associated with high-energy accelerators or rockets, it is necessary to have detailed information about the reactions that these particles can have with complex nuclei. Although some of the cross-section data for these reactions have been obtained experimentally, they are insufficient for a comprehensive shielding calculation. An experimental program to obtain all the necessary data would be prohibitively long and expensive. For this reason it is necessary to rely on calculations to supply the missing information. The program described here has the objective of calculating those cross sections that will be necessary for future shielding calculations.

The problem is to calculate the differential energy and angular cross section for the emission of particles from complex nuclei when the latter are bombarded by pions or nucleons in the energy range from 50 Mev to 30 Bev. The calculation is being developed in steps, starting with an incident energy range from 50 to 300 Mev, which will be extended first to 2 Bev and finally to 30 Bev. The reason for this is that production processes complicate the problem at the higher energies; thus, appropriate production models will have to be incorporated as the incident energy increases. At present the lower-energy phase of the program is nearing completion and will form the basic program for the calculation at all incident energies. The isobar model[1] for pion production will be included in the basic program to extend it into the intermediate energy range, and a statistical production model, such as that given by Hagedorn,[2] will be included in order to reach the highest energy range.[3]

Method of Calculation

In the range of energies considered in this problem, the wavelength of the incident particle is small compared with the internucleon distances (1.3×10^{-13} cm) within the nucleus. For this reason, the inelastic interaction of the incident particle with the complex nucleus can be considered to be the result of a series of direct interactions with the individual nucleons. A convenient method of estimating the results of these multiple interactions is the Monte Carlo method of calculation. It is expected that this method will be effective in its simplest form because of the fortuitous degree of opacity of the nucleus, which makes it at most four or five mean free path lengths across, at the source energies considered. The complete problem is being coded

---

[1] S. J. Lindenbaum and R. M. Sternheimer, *Phys. Rev.* **106**, 1107 (1957); **105**, 1874 (1957); **109**, 1723 (1958); *Phys. Rev. Letters* **5**, 24 (1960).

[2] R. Hagedorn, *Nuovo cimento* **15**, 434 (1960).

[3] The suggestion of using Hagedorn's model in the high-energy range was made by T. A. Welton.

for computation on an IBM 704 and will be suitably modified for computation on the IBM 7090 when this machine becomes available.

Nuclear Model

In order to account for the variation of the nucleon density inside the nucleus and yet keep the mechanics of the calculation as simple as possible, the nucleon density was assumed to be constant in each of three concentric spherical sections. The variation of the density from one section to the next and the radii of the sections were taken in such a way that the step model approximated the charge-density distribution obtained from electron-scattering experiments.[4] For simplicity the density distribution of neutrons was taken to have the same form as that for protons.

A potential well was assumed to exist in each of the spherical sections of the step model of the nucleus. The depth of the well in each case was taken to be equal to the sum of the binding energy of a nucleon and the Fermi energy of a zero-temperature Fermi gas which had a density equal to that of the nucleons in the corresponding section. In general there was a different well depth for the neutrons and protons in each section, since the densities of these nucleons are not necessarily the same in any given isotope. The well depth has the effect of increasing the kinetic energy of an incident particle with respect to the nucleons in the nucleus and will alter the effective cross section that must be used. That there are two well depths in each section means only that the way the cross section is altered in each section for collisions with neutrons will be slightly different from the way it is altered for collisions with protons.

The same potential well as described above was used for the nucleus in the case of incident nucleons and incident pions. The justification for using this well for pions is that it is comparable in depth with the average value obtained from the analysis of pion scattering data using an optical model.[5]

Although the well depth was determined in part by the Fermi energy of a zero-temperature Fermi gas, the protons and neutrons in each section of the step model of the nucleus were assumed to have a momentum distribution which includes a high-momentum tail. For convenience a Gaussian momentum distribution was taken with a $1/e$ value at 15 Mev. The latter value was chosen from the recommended values appearing in the literature,[6–9] which range from approximately 12 to 20 Mev.

---

[4] R. Hofstadter, *Revs. Modern Phys.* 28, 214 (1956).

[5] A rather complete list of references to the analysis of pion scattering data has been given by W. F. Baker, J. Rainwater, and R. E. Williams, *Phys. Rev.* 112, 1763 (1958).

[6] J. D. Dowell *et al.*, *Proc. Phys. Soc. (London)* 75 (Pt. 1), 24 (1960).

[7] L. S. Azhgirey *et al.*, *Nuclear Phys.* 13, 258 (1959).

[8] J. M. Wilcox and B. J. Moyer, *Phys. Rev.* 99, 875 (1955).

[9] E. M. Henley, *Phys. Rev.* 85, 204 (1952).

The present nuclear model differs from that used in previous calculations of this type.[10] Some of these differences are most easily pointed out by listing a few features of the model used in the previous calculations.

1. The previous model assumed a single region of uniform density.
2. The pions were unaffected by the potential well.
3. A zero-temperature Fermi-gas momentum distribution for the nucleons in the nucleus was used.

The changes effected in the model for the present calculation were made in order to obtain better agreement with experimental results.

Cross Sections

Because the transport of the incident particle through the nucleus is assumed to proceed by way of direct interactions with the nucleons, most of the required cross sections can be obtained from the literature on fundamental-particle interactions. Several partial compilations are available,[11-13] and other data are scattered throughout the literature. The experimental cross section data was included in the calculation in tabular form, with intermediate values obtained by linear interpolation.

The differential p-p scattering cross section is assumed to be isotropic in the center-of-mass system up to 500 Mev. From 500 Mev to 1 Bev the cross section is represented by

$$\frac{d\sigma}{d\Omega} = A + B\mu^3 \ , \qquad \mu = \cos\theta \ , \qquad 0 \leqq \mu \leqq 1 \ ,$$

and is assumed to be symmetric about $\mu = 0$; θ = scattering angle in the center-of-mass system. The quantities A and B are energy dependent and are tabulated at every 20-Mev interval.

The differential n-p scattering cross section for $0 \leqq E \leqq 300$ Mev is represented by

$$\frac{d\sigma}{d\Omega} = C + C_1\mu^4 \ , \qquad -1 \leqq \mu \leqq 0 \ ,$$

$$= C + D_2\mu^3 \ , \qquad 0 \leqq \mu \leqq 1 \ ,$$

and for 300 Mev $\leqq E \leqq$ 740 Mev by

$$\frac{d\sigma}{d\Omega} = C + C_3\mu^6 \ , \qquad -1 \leqq \mu \leqq 0 \ ,$$

$$= C + C_2\mu^3 \ , \qquad 0 \leqq \mu \leqq 1 \ .$$

---

[10] N. Metropolis *et al.*, *Phys. Rev.* 110, 185, 204 (1958).

[11] For total p-p and n-p cross sections, see F. F. Chen, C. P. Leavitt, and A. M. Shapiro, *Phys. Rev.* 103, 211 (1956).

[12] For differential p-p and n-p cross sections, see W. N. Hess, *Revs. Modern Phys.* 30, 368 (1958).

[13] For pion nucleon cross sections, see S. J. Lindenbaum, *Ann. Rev. Nuclear Sci.* 7, 317 (1957).

All the constants were chosen to adequately fit the experimental differential cross section data, where available. A plot of each coefficient vs energy was made, and a smooth curve was drawn between the points to obtain the value of each coefficient at all desired energies.

The pion nucleon scattering is somewhat complicated because charge exchange scattering, such as the reaction

$$\pi^- + p \longrightarrow \pi^0 + n \quad ,$$

represents a very large fraction of the scattering cross section at these energies. If one assumes that the pion nucleon scattering at these energies is governed by S- and P-wave scattering and that the isotopic spin dependence of the phase shifts is determined by the total isotopic spin quantum number[14] T, then, by application of simple scattering theory, one can demonstrate the equality of the cross sections for the following reactions:

$$\frac{d\sigma}{d\Omega}(\pi^+ + p) = \frac{d\sigma}{d\Omega}(\pi^- + n) \quad ,$$

$$\frac{d\sigma}{d\Omega}(\pi^0 + p) = \frac{d\sigma}{d\Omega}(\pi^0 + n) \quad ,$$

$$\frac{d\sigma}{d\Omega}(\pi^- + p) = \frac{d\sigma}{d\Omega}(\pi^+ + n) \quad .$$

Another result that follows directly from this is the equality of the charge exchange cross sections for the following reactions: $\pi^- + p$, $\pi^0 + p$, $\pi^0 + n$, and $\pi^+ + n$. Thus, if one knows the total $\pi^- + p$ scattering cross section, one can calculate the fraction of this cross section which is charge exchange scattering and use this to calculate the total $\pi^0 + p$ cross section. It is necessary to know the value of the π^0 + nucleon cross section because the half life of the π^0 (of the order of 10^{-15} sec) is not sufficiently short to permit the assumption that it decays inside the nucleus before making any collisions.

For the assumptions listed above, the differential scattering cross section for both direct and charge exchange scattering is of the form

$$\frac{d\sigma}{d\Omega} = \lambda\!\!\!^{-2} (A + B \cos\theta + C \cos^2\theta) \quad .$$

The coefficients A, B, and C were calculated at each 20-Mev interval from zero to 340 Mev, for all of the listed reactions, from the phase shifts given by Orear.[15]

---

[14] H. L. Anderson *et al.*, *Phys. Rev.* **91**, 155 (1953).

[15] J. Orear, *Phys. Rev.* **100**, 288 (1955).

These coefficients had values such that there was no obvious and simple way to sample from the above distribution. So, instead of tabulating A, B, and C, the solution to

$$\int_{-1}^{\mu} (A + B\mu' C\mu'^2)\, d\mu' = R$$

is to be tabulated at 20-Mev intervals for random numbers R, which range from zero to 1, in steps of 0.05. This will greatly facilitate the sampling from the distribution.

In the energy regions being considered here, pion absorption is an important process. Pion absorption, treated in the customary fashion,[7,16] gives rise to two nucleons. Isotopic spin considerations indicate that the π^0 absorption cross section should be one half the charged-pion absorption cross section. These cross sections are listed in tabular form as before.

General Features of the Calculation

The general flow of the calculation is very much an analog of the sequence of physical processes that are expected to occur in the nucleus. Each process is simulated by the usual Monte Carlo techniques, and, effectively, each source particle or member of the resulting cascade in the nucleus is traced through its history until it is lost from the nucleus, is absorbed, or is trapped, leaving the residual nucleus in an excited state. The exclusion principle was incorporated by forbidding those collisions where the final energy of a nucleon was below the Fermi energy of the nucleons in the nucleus. In practice all collisions were simulated as if there were no restriction and then rejected if the energy state of the scattered nucleon had an energy below the Fermi level.

To properly simulate a collision of a particle with a nucleon in the nucleus, in the history of any given particle, it is necessary to randomly select the vector momentum of the struck nucleon from a probability distribution function. In order to obtain the correct form of the distribution function one must take into account the momentum distribution of the particles inside the nucleus, the change in the cross section with the relative incident energy, and the relativistic effects in going from the laboratory system to the system in which the struck particle is at rest. By taking these effects into account, an expression is obtained which turns out to be sufficiently complicated to take about 1.5 min of machine time to evaluate. This situation is intolerable, for the expression has to be evaluated for each of thousands of collisions for each case. A simplifying assumption, which becomes more accurate at high energy, was made to avoid this situation. The assumption was that the vector momentum of the struck particle should be obtained directly from the momentum distribution itself. One can partially compensate for the small errors introduced in this way by using total cross sections which are averaged over the momentum distribution inside the nucleus, taking into account all the effects mentioned

[16] R. M. Frank, J. L. Gammel, and K. M. Watson, *Phys. Rev.* **101**, 891 (1956).

above. For this reason average cross sections were calculated for pions and nucleons of various incident energies and compared with the cross section at the incident energy. At all energies where the average cross section was different from the cross section at the incident energy by more than 10%, the average cross section was used. As expected, it was only necessary to use the average cross section in the regions where the cross section varies rapidly.

Initial Results

The results of some calculations of the total nuclear inelastic cross section for several reactions are given in Tables 7.11.1–7.11.3. The inelastic cross section defined here includes all incoherent effects. The symbols used are: σ_c, the calculated inelastic cross section; σ_x, the experimental inelastic cross section; and σ_g, the geometric cross section. Both σ_c and σ_g were calculated from the model of the nucleus described above. All cross sections are in millibarns. The quantity E is the incident laboratory energy of the designated particle.

The results so far indicate the general validity of the approach, although there were discrepancies in some of the cases listed. Attempts made to change the shape of the density distributions did not improve the agreement in general.

The results for the angular and energy distribution of the emitted particles for the first phase of the calculation will be available soon.

Table 7.11.1. Total Inelastic Cross Sections for Pi Mesons Incident on Various Elements at Various Energies

E	Material	σ_c (mb)	σ_x (mb)	σ_g (mb)
		Negative Pi Mesons		
225 Mev	Al	607	596 ± 30^a	769
	Sn	1392	1550 ± 70^a	1540
	Pb	1905	2290 ± 90^a	2045
970	Al	422	442 ± 20^b	
	Sn	1119	1199 ± 52^b	
	Pb	1589	1690 ± 100^b	
1.5 Bev	Cu	249	240 ± 14^c	552
	Fe	718	705 ± 37^c	1068
	Pb	1642	1600 ± 95^c	2045
		Positive Pi Mesons		
270 Mev	C	325	$296 \pm {}^{35}_{28}{}^d$	552

[a] V. G. Ivanov *et al.*, *Soviet Phys. JETP* **4**, 922 (1957).
[b] J. W. Cronin, R. Cool, and A. Abashian, *Phys. Rev.* **107**, 1121 (1957).
[c] T. Bowen *et al.*, *Nuovo cimento* **9**, 908 (1958).
[d] W. Kan-Chang *et al.*, *Soviet Phys. JETP* **35**, 625 (1959).

Table 7.11.2. Total Inelastic Cross Sections for Neutrons Incident on Various Elements at Various Energies

E	Material	σ_c (mb)	σ_x (mb)	σ_g (mb)
84 Mev	Al	536	500 ± 50[a]	769
	Cu	892	910 ± 50[a]	1138
	Pb	1768	1850 ± 180[a]	2045
765 Mev	Al	470	435 ± 10[b]	
	Cu	821	822 ± 23[b]	
	Pb	1700	1923 ± 62[b]	
1.4 Bev	Al	480	410[c]	
	Cu	832	670[c]	
	Pb	1713	1730[c]	

[a] G. P. Millburn *et al.*, *Phys. Rev.* **95**, 1268 (1954).
[b] N. E. Booth, G. W. Hutchinson, and B. Ledley, *Proc. Phys. Soc. (London)* **71**(3), 293 (1958).
[c] T. Coor *et al.*, *Phys. Rev.* **98**, 1369 (1955).

Table 7.11.3. Total Inelastic Cross Sections for Protons Incident on Various Elements at Various Energies

E	Material	σ_c (mb)	σ_x (mb)	σ_g (mb)
185 Mev	Al	440	408[a]	769
	Cu	782	746[a]	1136
	Pb	1652	1550[a]	2045
900 Mev	Al	469	370 ± 29[b]	
	Cu	812	740 ± 52[b]	
	Pb	1670	1660 ± 50[b]	
2.8 Bev	C	258[c]	230 ± 12[d]	552
	Fe	730[c]	690 ± 28[d]	1068
	Pb	1650[c]	1630 ± 75[d]	2045

[a] G. P. Millburn *et al.*, *Phys. Rev.* **95**, 1268 (1954).
[b] N. E. Booth *et al.*, *Proc. Phys. Soc. (London)* **70**(3), 209 (1957).
[c] The calculated cross sections are for $E = 2.53$ Bev.
[d] T. Bowen *et al.*, *Nuovo cimento* **9**, 908 (1958).

7.12 NEUTRON YIELDS FROM (α,n) REACTIONS

F. S. Alsmiller G. M. Estabrook

Isotopes decaying by alpha emission and certain light-element impurities may frequently be present in uranium and plutonium materials in sufficient concentrations to give a substantial neutron yield from (α,n) reactions. Several calculations of (α,n) yields, performed in support of a Chemical Technology Division investigation of hazards associated with fabrication of fuel elements from metallic U^{233} and its alloys or compounds, are reported here.

The (α,n) cross section $\sigma_\nu(E)$ for the νth reacting element is generally an increasing function of the alpha-particle energy E. If the dimensions of the moderating medium, for example uranium, are much greater than the range of an alpha particle, account must be taken of the alpha energy-loss rate in the medium, $-dE/dx = N_\eta \epsilon_\eta(E)$. Here, ϵ_η is the energy-dependent alpha-particle stopping cross section per atom or molecule in medium η, and N_η is the number of atoms or molecules of material η per unit volume.

The neutron yield is conveniently computed as a function of time, t, by summing the contributions of all members of any decay chain of isotopes, denoted by μ, whose first member is present at $t = 0$ in known amount, and which has an alpha-decay rate given by $\lambda_1 = \lambda_\mu$.

Accordingly, the yield $R^\eta_{\mu\nu}(t)$, the number of neutrons produced by element ν in medium η per second per gram of μth isotope present initially, is given by

$$R^\eta_{\mu\nu}(t) = \lambda_\mu \frac{L}{AW_\mu} \frac{N_\nu}{N_\eta} \sum_j F_{j\mu}(t)\, Y^\eta_{j\nu} \ , \tag{1}$$

where

j = the index identifying a daughter in the series,

L = Avogadro's number,

AW_μ = atomic mass of μth isotope,

N_ν = number density of the νth element,

$F_{j\mu}(t) = \lambda_j N_j(t)/\lambda_\mu N_\mu(0)$,

$Y^\eta_{j\nu} = \sum_k P_{kj} \int_0^{E_K} \sigma_\nu(E)\, dE/\epsilon_\eta(E)$,

P_{Kj} = fraction of alpha particles from jth isotope which are emitted at initial energy E_K.

The ratios $F_{j\mu}(t)$ are easily computed from the equations of radioactive decay; the integrals $Y^\eta_{j\nu}$ were evaluated by a graphical method.

No experimental information concerning the ranges or stopping cross sections of 2- to 10-Mev alpha particles in uranium or plutonium was found. The stopping cross sections were obtained by following a suggestion of Lindhard and Scharff.[1] A least-squares determination of the

[1] J. Lindhard and M. Scharff, *Kgl. Danske Videnskab. Selskab, Mat.-fys. Medd.* **27**(15) (1953).

parameters a and b in the empirical formula

$$\epsilon = 10^{a}\left(\frac{Z}{E}\right)^{0.5+b} \times 10^{-15}\ \text{ev cm}^2 \qquad (E \text{ in Mev}) \tag{2}$$

was carried out, using all available data[2] for $Z > 20$ in the alpha-particle energy range from 2 to 10 Mev. The results are:

$$a = 1.271\ ; \qquad \sigma(a) = 4.5 \times 10^{-3} = \sqrt{\text{Var } a}\ ,$$

$$b = 4.84 \times 10^{-3}\ ; \qquad \sigma(b) = 2.03 \times 10^{-3} = \sqrt{\text{Var } b}\ .$$

Since b is small, with a large relative uncertainty, the approximation $b = 0$ was used for the sake of simplicity. The probable percentage error in ϵ due to statistical uncertainty in a and neglect of b should not exceed 6%; the experimental error for much of the data used was 8%.

Typical yields computed from Eq. 1 are presented in Tables 7.12.1–7.12.3. The greatest restriction on the accuracy of these and further calculations is the lack of complete information concerning the energy dependence of the (α,n) cross sections.

This work will be described in detail in other reports now being prepared for publication.

[2] W. Whaling, *Handbuch der Physik*, vol 34, p 202 (ed. by S. Flügge), Springer, Berlin, 1958.

Table 7.12.1. Neutron Yields from $Be^9(\alpha,n)C^{12}$ Reactions[a] in Uranium Metal

Time Interval (days)	Yield (neutrons sec^{-1} g^{-1}) for Various Isotopic Constituents[b]					
	Th^{228}	U^{232}	U^{233}	U^{234}	U^{235}	U^{236}
	$\times 10^9\ N_{Be}/N_U$	$\times 10^6\ N_{Be}/N_U$	$\times 10^3\ N_{Be}/N_U$	$\times 10^3\ N_{Be}/N_U$	$\times N_{Be}/N_U$	$\times N_{Be}/N_U$
1	0.69	7.4	1.9[c]	1.1[c]	0.26[c]	9.1[c]
3	1.3	7.4				
7	2.1	7.6				
14	2.7	8.1				
30	2.8	9.2				
60	2.7	11				
120	2.6	15				
180	2.4	19				
240	2.3	23				
360	2.0	29				

[a] The $Be^9(\alpha,n)C^{12}$ cross section in the range $2.6 \leqq E \leqq 8.2$ Mev was taken from J. H. Gibbons and R. L. Macklin, *Phys. Rev.* **114**, 571 (1959); extrapolations to lower energies [I. Halpern, *Phys. Rev.* **76**, 248 (1949); T. W. Bonner *et al.*, *Phys. Rev.* **102**, 1348 (1956)] and higher energies account for ~15% of the total yield.

[b] An over-all uncertainty of 15 to 25% in the results is estimated.

[c] These values remain the same over the entire time interval.

Table 7.12.2. Neutron Yields from $Be^9(\alpha,n)C^{12}$ and $Al^{27}(\alpha,n)P^{30}$ Reactions in Plutonium and Aluminum Metals*

Isotopic Constituent μ	R, Yield (neutrons sec^{-1} g^{-1})		
	$R^{Pu}_{\mu,Be}$	$R^{Pu}_{\mu,Al}$	$R^{Al}_{\mu,Al}$
	$\times N_{Be}/N_{Pu}$	$\times N_{Al}/N_{Pu}$	
Pu^{238}	7.1×10^6	1.1×10^5	3.4×10^5
Pu^{239}	1.9×10^4	2.4×10^2	6.9×10^2
Pu^{240}	7.1×10^4	8.7×10^2	2.5×10^3
Pu^{242}	1.0×10^3	9.5×10^0	2.8×10^1
Am^{243}	6.3×10^4	8.4×10^2	2.6×10^3
Cm^{244}	4.0×10^7 (1 day) 3.9×10^7 (1 yr)	7.8×10^5 (1 day) 7.5×10^5 (1 yr)	2.3×10^6 (1 day) 2.2×10^6 (1 yr)

*The yields, except for the yield from the Cm^{244} source, are independent of time up to one year. The $Al^{27}(\alpha,n)P^{30}$ cross section for energies up to 5.3 Mev was taken from I. Halpern, *Phys. Rev.* **76**, 248 (1949) and M. M. Shapiro, *Phys. Rev.* **90**, 171 (1953); extrapolation to higher energies was necessary for Cm^{244} and Pu^{238}. An uncertainty of 15 to 25% in the above results is estimated.

Table 7.12.3. Neutron Yields from $Be^9(\alpha,n)C^{12}$ and $Al^{27}(\alpha,n)P^{30}$ Reactions Stemming from the Pu^{241} Isotope in Plutonium and Aluminum Metals*

Time Interval (days)	R, Yield (neutrons sec^{-1} g^{-1})		
	$R^{Pu}_{241,Be}$	$R^{Pu}_{241,Al}$	$R^{Al}_{241,Al}$
	$\times 10^3\ N_{Be}/N_{Pu}$	$\times 10^2\ N_{Al}/N_{Pu}$	$\times 10^2$
1	1.4	0.14	0.42
3	1.8	0.20	0.61
7	2.5	0.33	0.98
14	3.9	0.55	1.6
30	7.0	1.0	3.1
60	13	2.0	6.0
120	24	3.8	12
180	35	5.7	17
240	47	7.5	22
360	69	11	33

*The $Al^{27}(\alpha,n)P^{30}$ cross section for energies up to 5.3 Mev was taken from I. Halpern, *Phys. Rev.* **76**, 248 (1949) and M. M. Shapiro, *Phys. Rev.* **90**, 171 (1953). An uncertainty of 15 to 25% in the above results is estimated.

7.13 A STUDY OF CONCRETE SAMPLES TAKEN FROM THE TOP SHIELD OF THE ORNL GRAPHITE REACTOR

W. J. Grantham

In the summer of 1959, two additional experiment holes, 70 and 71, were drilled in the top shield of the ORNL Graphite Reactor. The locations of these holes, relative to the center lines of the reactor, are shown in Fig. 7.13.1. For approximately 48 in. from the top surface of the reactor the holes have a nominal diameter of 8 in.; for the remaining 36 in. their nominal diameter is 6 in. Samples taken during the course of the drilling have been studied to determine the present condition of this portion of the shield. At the time the drilling was begun, the accumulated total power developed by the reactor was approximately 4.3×10^8 kwhr. If the radiation intensities quoted by Blosser *et al.* [1] are assumed, the integrated doses were: thermal neutrons, 1.9×10^{19} neutrons/cm^2; fast neutrons, 2.5×10^7 rads (tissue); and gamma rays, 2.5×10^9 rads (tissue).

Hole 70 was wet-drilled, yielding samples suitable only for strength analysis. Hole 71, however, was dry-drilled, at a very slow rate, and samples from this drilling were analyzed for water content as well as for compressive strength. Samples taken from Hole 71 were kept in polyethylene bags from the time they were removed from the hole until water-content determinations were completed. The elapsed time before analysis was of the order of ten months, during which time the induced radioactivity of the concrete decayed from a level of several r/hr to a maximum of 40 mr/hr.

The original samples were redrilled before testing to obtain standard specimens $1\frac{3}{4}$ in. in diameter (twice the maximum aggregate size) and 4 in. long. The standard specimens were then capped on both ends with neat cement. The water content analysis, however, was made before the samples were redrilled.

The results of the water-content analyses are shown in Fig. 7.13.2. The weight percentages were determined by weight loss during heating to 200°C and by water evolved (in nitrogen atmosphere) during heating from 200 to 600°C. The water content of the barytes-haydite portion of the concrete shield shows good agreement with the 10% anticipated.[2]

Compression tests, following the method prescribed by ASTM specification C42-49, were made on samples taken from both holes. The results are shown in Fig. 7.13.3, in which the data points represent the averages of results from several specimens from approximately the same location. No distinction has been made between samples from the two holes. As is evident from the plot, the compressive strengths of both the ordinary and the barytes-haydite concretes fall well below the design strength of 2.5 ksi.[2]

---

[1] T. V. Blosser, *et al.*, *A Study of the Nuclear and Physical Properties of the ORNL Graphite Reactor Shield*, ORNL-2195 (1958).

[2] T. Rockwell III, *Physical Tests on Core Drillings from the Graphite Reactor Shield*, ORNL-241 (1949).

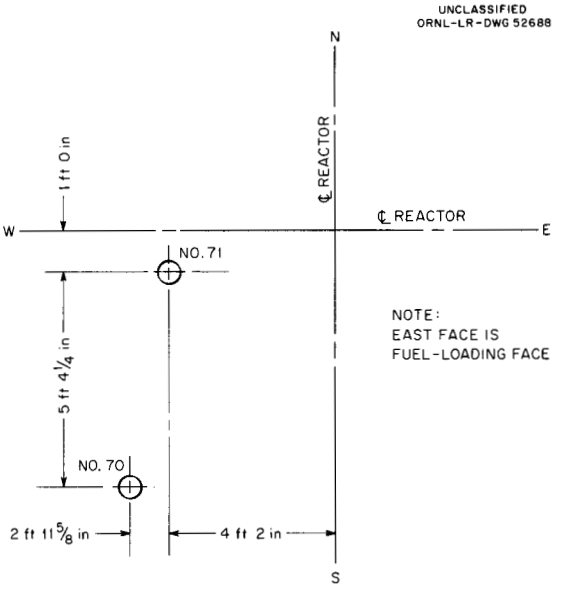

Fig. 7.13.1. Location of Experiment Holes 70 and 71 in the ORNL Graphite Reactor.

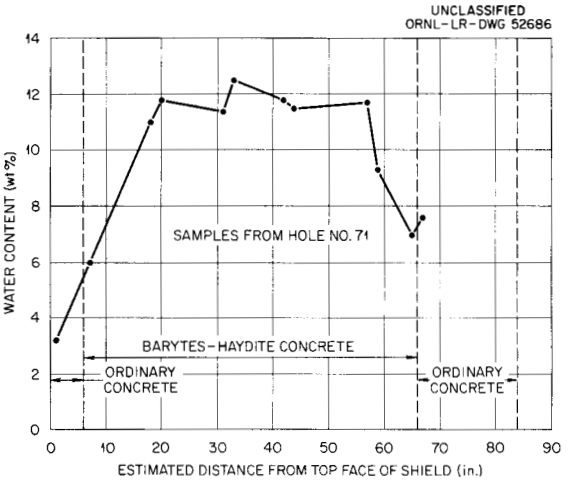

Fig. 7.13.2. Water Content of the Top Shield of the ORNL Graphite Reactor as a Function of Distance from the Top Face.

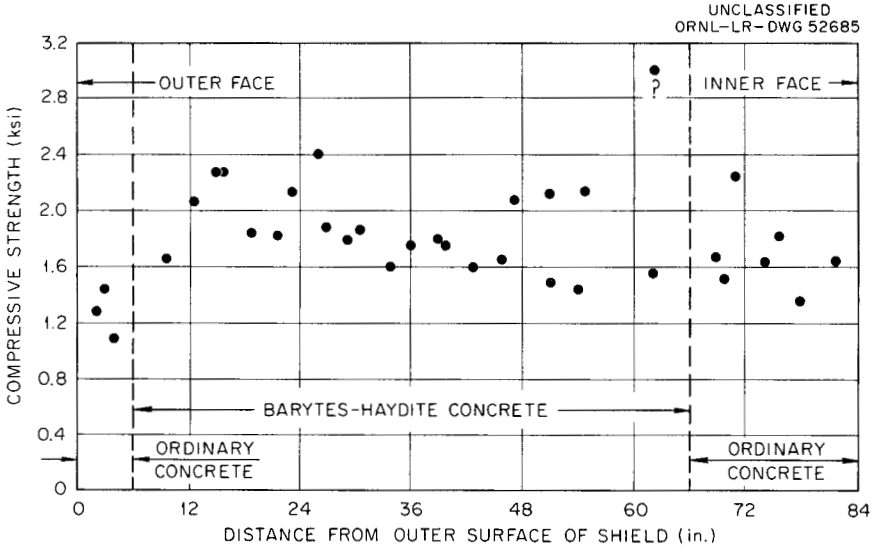

Fig. 7.13.3. Compressive Strength of Concrete Samples from the ORNL Graphite Reactor Shield as a Function of Location in the Shield.

Part 8

RADIATION-DETECTOR STUDIES

8.1 UNSCRAMBLING OF SCINTILLATION SPECTRA

R. O. Chester[1] W. R. Burrus

Introduction

The experimental data from the observation of a gamma-ray spectrum with a scintillation crystal spectrometer is obtained in the form of a distribution or spectrum of pulse heights. However, the intensities of the scintillation pulses within the crystal are not directly related to the energies of the incident gamma-ray photons, but rather to the energies of the electrons resulting from the complicated photon interactions with the crystal. Additionally, statistical "smearing" is introduced into the results by the always nonideal components of the spectrometer system. For these reasons the experimental data must always be "unscrambled" in order to obtain a useful gamma-ray energy spectrum. A method, which requires no prior assumptions concerning the spectrum being analyzed, is under development to perform such unscrambling with the aid of the IBM 704 computer.

In principle, the incident photon energy spectrum can be obtained from the measured pulse-height distribution by setting up and solving a system of simultaneous linear equations, relating the incident spectrum to the measured pulse-height distribution. These equations have the form

$$\begin{array}{c} a_{11}x_1 + a_{12}x_2 + \dots + a_{1n}x_n = b_1 \\ a_{21}x_1 + a_{22}x_2 + \dots + a_{2n}x_n = b_2 \\ \cdot \qquad \cdot \qquad \cdot \qquad \cdot \\ \cdot \qquad \cdot \qquad \cdot \qquad \cdot \\ \cdot \qquad \cdot \qquad \cdot \qquad \cdot \\ a_{m1}x_1 + a_{m2}x_2 + \dots + a_{mn}x_n = b_m \end{array} \tag{1}$$

or, in matrix notation, $Ax = b$. In this system, the components of b represent the measured data, the pulse-height distribution from a multichannel analyzer. The components of x represent the unknown number of photons within corresponding energy intervals. Thus, for monoenergetic radiation, the pulse-height distribution is given by a certain column of the matrix A. For a particular spectrometer, A is the response matrix which describes its response to simple monoenergetic radiations. Physical reality demands that the elements of x and b be nonnegative (one cannot have a minus number of photons nor a minus number of counts). The matrix A is not symmetric for scintillation spectrometers.

There are two conspicuous difficulties involved in setting up and solving the formal matrix equation for the unknown elements of x. The first is that n^2 elements of the matrix must be

---

[1] Instrumentation and Controls Division.

determined (if n is the number of unknown elements of x), and n must be quite large (50 to 300 for typical gamma-ray spectrometers) in order to avoid obscuring fine spectral detail by the discreteness of the matrix. It is virtually impossible to measure all these n^2 elements. At best, a few calibration spectra are measured with nominal accuracy. These data must be extended and augmented by some sort of interpolation, based on their physical interpretation, to provide sufficient information to permit the solution to proceed.

The second difficulty is that large-order systems of equations (assuming that they can be formulated and solved at reasonable expense) lead to results which are inordinately sensitive to small, statistical errors in the experimental data. For example, in a typical 100 by 100 system, statistical errors are often larger by a factor of 10^{10} than the desired solution.

One solution to these difficulties lies in reducing the order of the system to a more modest value. However, this method leads to an unwanted coarseness if n is chosen too small relative to the inherent resolution of the spectrometer. Another approach involves the calculation of a few parameters of the solution, for example, the moments, the first few terms in a series expansion, etc. The latter method may cause some shift in the position of a peak, or may introduce "overshoots" into the result.

The methods described below reduce the above difficulties and also give an estimate of the spectrum directly.

Matrix Generation Method

A program has been initiated to obtain a complete set of response functions for a spectrometer consisting of a 3 × 3 in. NaI(Tl) crystal supplying a 256-channel pulse-height analyzer, with a full-scale energy calibration of 2 Mev. Such a spectrometer is typical of those used for analysis of radiations from reactors and from isotopes, and techniques developed for its use should be adaptable with little change to other spectrometers. Standard spectra have at present been obtained[2] for eight isotopes, ranging from Au^{198} to Y^{88}.

Each standard spectrum has been fitted to the following semiempirical function:

$$y = b_1 \left(\frac{1 + b_2^2 \exp\left[(x - b_3)/b_4\right]}{\exp\left[(x - b_3)/b_4\right] + \left\{1 - b_2 \exp\left[(x - b_3)/b_4\right]\right\}^2} \right)^{1/2} + b_5 \left(\frac{x - b_6}{b_7}\right) \exp\left[\left(\frac{x - b_6}{b_7}\right) - 1\right] + \sum_{\substack{\text{photopeaks and} \\ \text{escape peaks}}} b_i \exp\left[-\left(\frac{x - b_i}{b_k}\right)^2\right], \qquad (2)$$

where y = total counts, x = channel number, and b_k are fit parameters.

---

[2]Standard spectra are being obtained by ~~G. B. Kelley et al.~~ G. D. O'Kelley of the Chemistry Division.

Each photopeak or escape peak is assumed Gaussian. The Compton distribution is fitted by the first function in Eq. 2, the gain function (vs frequency) of a shunt-compensated video amplifier. The second function in Eq. 2 is a "fill-in" for the valley between the photopeak and the Compton distribution. The well-known energy relationships between the positions of the photopeak and the escape and other peaks were not used in the fitting, since it was desired to avoid any detailed assumptions concerning the relation between energy and channel number. Additionally, the first 20 analyzer channels were excluded from the analysis because of instrument nonlinearity.

The parameters shown have been fitted to empirical functions of either the photopeak position or the Compton position, and the Compton position has also been fitted as a function of photopeak position. It is thus possible to reconstruct a standard spectrum by specifying the channel number of the photopeak center. Also, if the channel number is known as a function of energy, then specification of the energy of the incident photon will determine the response-function shape.

Figure 8.1.1 shows a comparison of a response function, reconstructed by specifying the channel number of the photopeak center, with the experimental spectrum. Thus, a complete set of elements for a response matrix can be generated from channel 20 to 200 or more. Such a matrix is being used as a "representative" matrix for testing the methods described below.

Equation Solution Methods

Several techniques are being studied which circumvent the traditional difficulties involved in straightforward matrix inversion. An error analysis shows that the large spurious components in the traditional results are due to rapidly fluctuating eigenvalues of A, which appear statistically with large amplitudes. One of the authors has pointed out[3] that this difficulty can be alleviated by solving, not for the unknown x, but for $x^* = Sx$, where S is a smoothing matrix with a "smoothing width" comparable to the resolution of the experimental apparatus.

The smoothed solution is obtained directly from the original set of equations by replacing the matrix A by AS^{-1}. A method is being studied which may give the matrix AS^{-1} as a modification of the matrix-element fitting procedure without actually computing the inverse of S.

Another error-reducing technique recently tested applies the physical requirement of the nonnegativity of the elements of x. This technique automatically avoids spurious components which would have resulted in negative excursions, and it reduces the errors from $\sim 10^{10}$ larger than the desired solution to something of the order of the desired solution.

In essence, these methods use a programming technique[4] to obtain approximate solutions to the equation

$$Ax - b = \mathbf{r} \ , \qquad x \geqq 0 \ , \qquad (3)$$

[3] W. R. Burrus, *IRE Trans. on Nuclear Sci.* NS-7(2–3), 102 (1960).

[4] S. I. Gass, *Linear Programming, Methods and Applications*, McGraw-Hill, New York, 1958.

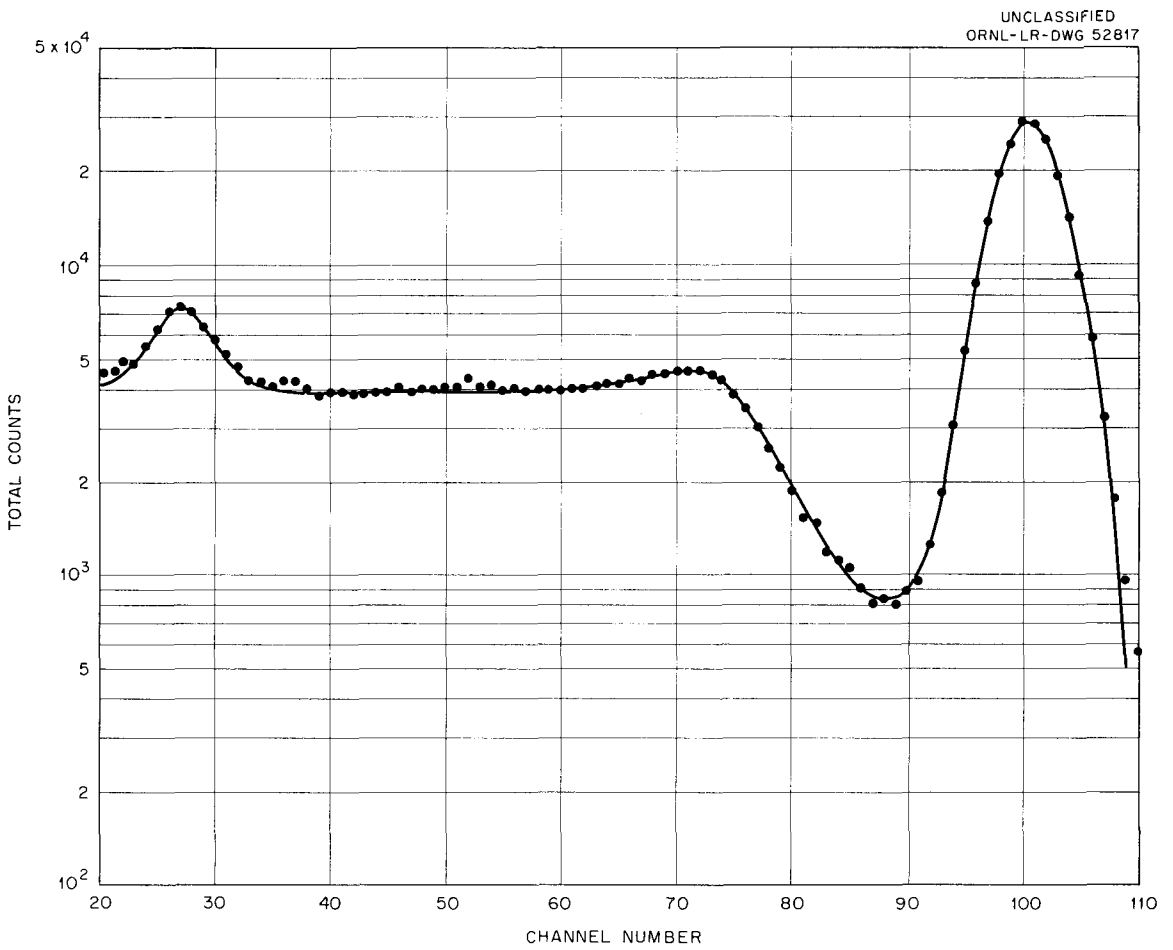

Fig. 8.1.1. Comparison of Experimental and Reconstructed Spectra for Mn^{54}.

such that some function of the residual vector, r, is a minimum. In other words, by allowing some small residual, consistent with the statistical accuracy of the data, an approximate solution is obtained which has no physically impossible negative values. It is possible to formulate the problem as one of linear programming, such that a function of the following form is minimized:

$$F = \sum_i w_i |\mathbf{r}_i|^k \ , \qquad k = 1,\ 2,\ \text{or}\ \infty \ . \tag{4}$$

[For limitingly large values of k, the largest weighted residual $w_i \mathbf{r}_j$ (or residuals) receive all the weight; thus $k = \infty$ corresponds to minimizing the largest residuals such that all the weighted residuals lie within a band of $\pm w_i \mathbf{r}_j$ which is as small as possible.] The weight factors, w_i, are chosen according to the statistical errors of the ith element of b.

Experimental Results

Experiments are in progress with synthetic test cases, using the SCROL (ref 5) code for linear programming with the IBM 704. A 19 by 19 matrix of the form

$$\begin{bmatrix} \frac{1}{2} & \frac{1}{4} & & & & & & \\ \frac{1}{4} & \frac{1}{2} & \frac{1}{4} & & & & & \\ & \frac{1}{4} & \frac{1}{2} & \frac{1}{4} & & & & \\ & & \cdot & \cdot & \cdot & & & \\ & & & \cdot & \cdot & \cdot & & \\ & & & & \cdot & \cdot & \cdot & \\ & & & & & & \frac{1}{4} & \frac{1}{2} \end{bmatrix}^{3}$$

which is known to be very poorly conditioned, has been used in a preliminary test. Table 8.1.1 shows a comparison of the result of the usual matrix inversion technique with the result of the programming technique with $k = \infty$, for a simple, assumed spectrum. An error of 0.01% was artificially introduced in the tenth element of b. This example dramatically shows the extreme sensitivity of the usual inversion technique to such a small (from an experimentalist's standpoint) error. It is also evident from the example that the sensitivity to small errors is reduced to a reasonable value by the use of the programming technique. Because of the highly artificial nature of the test, however, it is not necessarily indicated that similar behavior may be expected in actual practice. In fact, with $k = 1$, the programming method was fortuitously completely insensitive to the error shown in Table 8.1.1. (The $k = \infty$ case is at a disadvantage compared to $k = 1$ or 2, since the solution with $k = \infty$ may be slightly nonunique because of the freedom of "play" between the upper and lower bounds of the weighted residuals. The 17th element of x in Table 8.1.1 shows this effect.)

At present the smoothing technique and the programming method are being combined. Tests using a "more representative" NaI(Tl) response matrix are being prepared.

Acknowledgments

Valuable contributions to the formulation of the linear programming problems and in the numerical computations have been made by M. Davis and J. Replogle of the Central Data Processing Section, ORGDP.

[5] W. Orchard-Hays, *SCROL, A Comprehensive Operating System for Linear Programming on the IBM-704*, C-E-I-R, Inc., Washington, D.C.

Table 8.1.1. Comparison of Matrix Inversion Technique with the Linear Programming Method ($k = \infty$) for a Simple Synthetic Test Case

Element No.	x	$b = Ax$ (exact value)	b^*	$x = A^{-1}b^*$	x (programming method)
1	0	0	0	−6,680.0	0
2	0	1,000.0	1,000.0	13,200.0	0
3	0	6,000.0	6,000.0	−19,403.2	0
4	0	16,000.0	16,000.0	25,139.2	0.66
5	64,000.0	26,000.0	26,000.0	33,732.8	63,998.13
6	0	30,000.0	30,000.0	34,659.2	2.34
7	64,000.0	26,000.0	26,000.0	25,796.8	63,998.56
8	0	16,000.0	16,000.0	40,806.4	0.12
9	0	6,000.0	6,000.0	−42,398.4	0.33
10	0	1,000.0	1,000.1[a]	42,934.4	0
11	0	0	0	−42,398.4	0
12	0	0	0	40,806.4	0
13	0	0	0	−38,203.2	0
14	0	0	0	34,659.2	0
15	0	0	0	−30,267.2	0
16	0	0	0	25,139.2	0
17	0	0	0	−19,403.2	0.11
18	0	0	0	13,200.0	0
19	0	0	0	−6,680.0	0

[a]An error of 0.01% is here artificially introduced.

8.2 GAMMA-RAY RESPONSE OF LARGE NaI(Tl) CRYSTALS

G. T. Chapman T. A. Love

The unquestioned advantages of large NaI(Tl) crystals for gamma-ray spectroscopy have encouraged the continuation of the program of experiment[1] initiated in 1957 at the Bulk Shielding Facility. Recent investigations have centered upon the 8-in.-dia by 8-in.-long composite crystal

[1]G. T. Chapman and T. A. Love, *Appl. Nuclear Phys. Ann. Prog. Rep. Sept. 1, 1957*, ORNL-2389, p 233; also, G. T. Chapman and T. A. Love, *Neutron Phys. Ann. Prog. Rep. Sept. 1, 1958*, ORNL-2609, p 133.

described previously[2] and have been greatly assisted by the availability of the IBM 704 Monte Carlo codes developed by Zerby and Moran[3] for the calculation of NaI response functions.

The experimental data reported below were obtained from the composite crystal mentioned above, using an array of three 3-in.-dia photomultiplier tubes to observe the light pulses. The electronic systems followed conventional patterns.

Figure 8.2.1 shows the pulse-height distribution obtained from the 0.662-Mev gamma ray of Cs^{137}. Curves are shown for (*A*) the calculated distribution, in histogram form; (*B*) the experimental distribution from the 8-in. crystal; and (*C*) the anticoincidence distribution for the 8-in. crystal taken with the gamma rays collimated through a ½-in.-dia hole along the axis of an additional 4-in.-dia by 2-in.-thick crystal mounted on the end of the large crystal. The curves are individually normalized to unit area and then normalized in amplitude at 0.662 Mev.

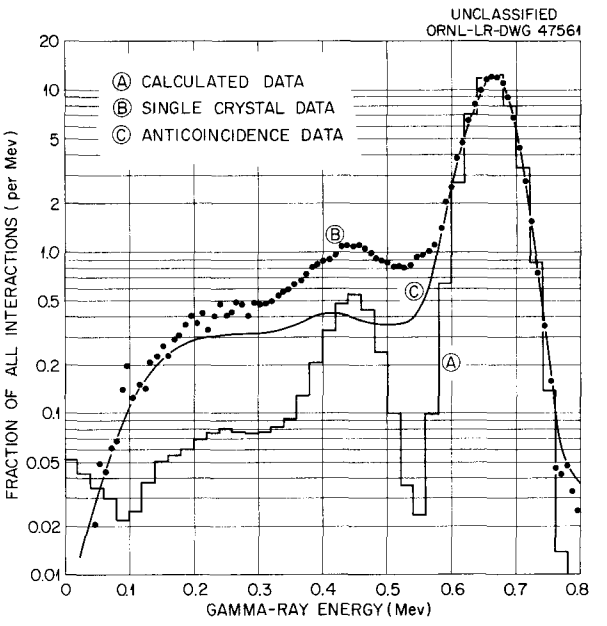

Fig. 8.2.1. Comparison of the Experimental and Calculated Responses of an 8-in.-dia by 8-in.-long NaI(Tl) Crystal to Collimated 0.662-Mev Gamma Rays from Cs^{137}.

The shape of the experimental curves below 0.2 Mev is due to the electronics. The use of the anticoincidence arrangement has nearly eliminated the small backscatter escape peak at 0.45 Mev, implying that a well in the end of the large crystal would improve the peak-to-total ratio. The discrepancy between calculation and experiment evident below 0.6 Mev may be explained by postulating that the tail of the measured distribution is greatly increased by the contributions of gamma rays degraded in energy by scattering in the source container and in the walls of the shield before reaching the crystal. This distribution would not appear in the calculations. The explanation is strengthened by the fact that in other comparisons, involving uncollimated source gammas rather than the collimated gamma rays of the present case, the discrepancy has not occurred.[4]

Figure 8.2.2 shows the measured response of the 8-in.-dia crystal for the 1.368- and 2.754-Mev gamma rays from Na^{24}, again compared with calculation. Normalization was made as noted

[2] G. T. Chapman, T. A. Love, and R. W. Peele, *Neutron Phys. Ann. Prog. Rep. Sept. 1, 1959*, ORNL-2842, p 191.

[3] C. D. Zerby and H. S. Moran, *Neutron Phys. Ann. Prog. Rep. Sept. 1, 1959*, ORNL-2842, p 185; also sec 8.6, this report.

[4] C. D. Zerby, private communication.

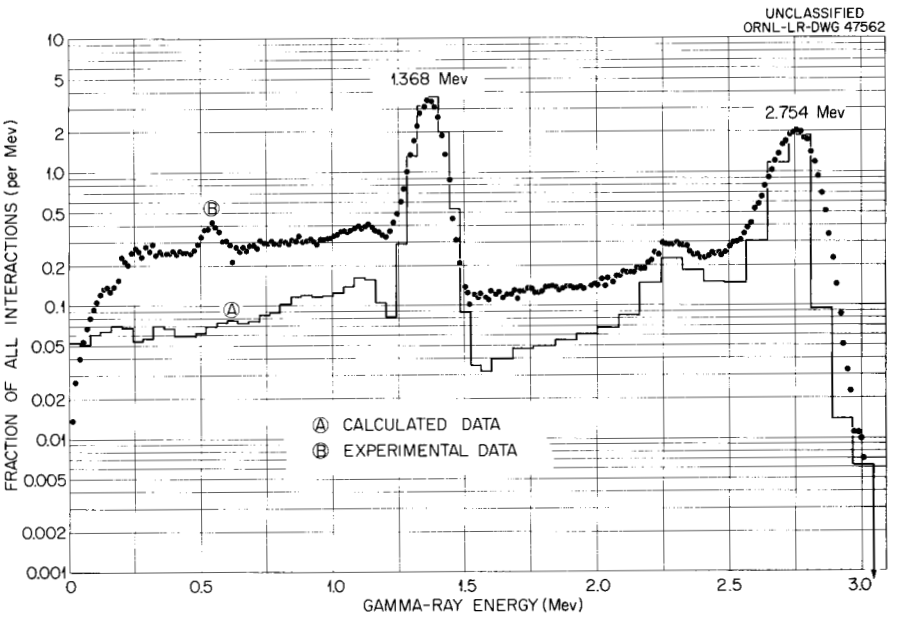

Fig. 8.2.2. Comparison of the Experimental and Calculated Responses of an 8-in.-dia by 8-in.-long NaI(Tl) Crystal to Collimated 1.368- and 2.754-Mev Gamma Rays from Na^{24}.

above. The effect of the gamma rays degraded in energy by scattering is again very prominent. The small peak in the experimental data (curve B) is probably due to annihilation radiation from the lead of the collimator and shield wall and, of course, does not appear in the calculation.

Table 8.2.1 lists the measured resolution of the experimental crystal for various energies, as well as a comparison of measured vs calculated photofractions. It is, of course, impossible under any circumstance to obtain the calculated values under experimental conditions, because of the idealizations inherent in the calculation.

Table 8.2.1. Comparison of Experimental and Calculated Results for the Response of an 8-in.-dia by 8-in.-long NaI(Tl) Crystal

Photon Energy (Mev)	Measured Resolution (%)	Measured*,** Photofraction (%)	Calculated Photofraction* (%)
0.662	11.8	75	92.4
0.899	8.8	66	
1.368	8.6	61	82.7
1.840	7.3	60	
2.754	6.3	52	68.3

*Photofraction is defined as the ratio of the area under the total absorption peak to the total area under the pulse-height distribution curve.

**Values of the measured photofractions are reproducible to within <3%.

The results obtained with the 8-in.-dia by 8-in.-long composite crystal have been much more satisfactory than those from any of the previous approaches. Additional study is required concerning possible effects of the interface between the parts of the composite and concerning the effectiveness and placement of reflecting materials in the crystal package. The comparisons with calculated responses invite further study leading to optimization of collimators and shields.

8.3 THE EFFECTS OF SCINTILLATOR DIMENSIONS ON PULSE-HEIGHT SPECTRA ESTIMATED BY MONTE CARLO FOR LARGE NaI CRYSTALS

R. W. Peelle

A previously reported[1] calculation of the effects of scintillator dimensions on the response of large NaI crystals to gamma rays was handicapped by the then incomplete state of the IBM 704 Monte Carlo code used. The code at that time ignored secondary effects, thus placing a limit of ~2 Mev on the incident energy. An essentially perfected code, taking into account annihilation radiation and bremsstrahlung, now is available[2] and has been used to predict pulse-height spectra for large NaI crystals varying in shape, diameter, length, and in whether axial wells had been included in the end of the crystal. Some results are discussed below. The code, because of the idealized geometry adopted in its construction (in effect, the crystal floats unsupported in a vacuum), is unable to exactly reproduce an experimental spectrum. The contribution to the tail of the experimental spectrum due to gamma rays degraded in energy by scattering in the walls of the collimator and source container is conspicuously absent from the computed spectra. Nevertheless, the calculations may usefully serve as benchmarks by which the experimenter may gage the progress of his efforts to reduce the magnitude of the effects due to scattering. For parameter studies such as the present one, the code is extremely useful.

Figure 8.3.1 shows the calculated results for 2.75- and 7.5-Mev monoenergetic gamma rays incident on a 9-in.-dia, 10-in.-long NaI crystal. This crystal was chosen as the nominal size around which variations were made in these calculations. The results have been smoothed by the use of a Gaussian smoothing function derived from experimental observation. Each curve represents the sum of the points which correspond to the Gaussian full-energy peak, plus the histogram lines which represent the predicted tail spectrum. Because of the smoothing, the tail extends above the full gamma-ray energy in each case. The low intensity of the spectrum at low energies suggests that such a tail would not be experimentally observable. The heavy

---

[1] R. W. Peelle *et al.*, *Neutron Phys. Ann. Prog. Rep. Sept. 1, 1959*, ORNL-2842, p 187.

[2] Section 8.6, this report.

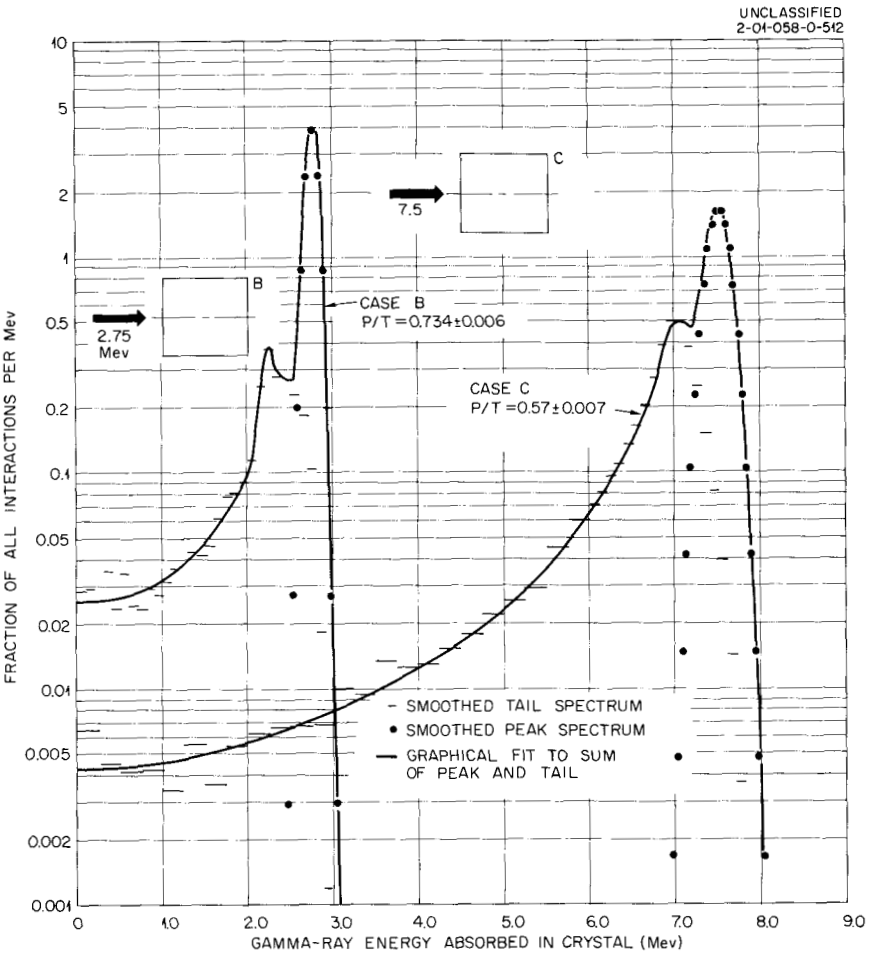

Fig. 8.3.1. Estimated Smoothed Pulse-Height Spectra.

arrow adjacent to the diagrams indicates the position and direction of the incident collimated beam, chosen to be 2 cm in diameter for all the work discussed herein. Figure 8.3.2 displays the 2.75-Mev case from the previous figure, plotted on a linear scale to give an idea of area. The solid lines represent the same smoothed peak and tail spectra shown on the previous figure, while the broken lines are the sum of the smoothed peak and tail. Interestingly, the intensity of the predicted tail under the photopeak is enough to raise the peak ~2%. This increment would not be experimentally identified because it occurs so close to the full energy. The contribution of the smoothed tail also slightly shifts the apparent position of the photopeak. The small rectangles shown on the figure represent the unsmoothed, calculated energy-loss spectrum, the height of the rectangle representing the estimated standard deviation calculated by the code. Such features as the single escape peak at ~2.2 Mev show very clearly in such a presentation, and therefore the results to follow have been presented as unsmoothed spectra. The large block shown centered around the photopeak has an area equal to that of the photopeak and is intended to assist in comparison of tail and peak fractions. The primary purpose in

presenting Figs. 8.3.1 and 8.3.2 has been to clarify the graphical nomenclature, which will be consistent in the rest of the presentations of results.

Figure 8.3.3 compares the predicted pulse-height spectra from the "standard" case shown in Fig. 8.3.2 with that from a 9-in.-dia, 10-in.-long crystal having a truncated conical end. This shape was characteristic of the large crystals earlier supplied and was a result of the

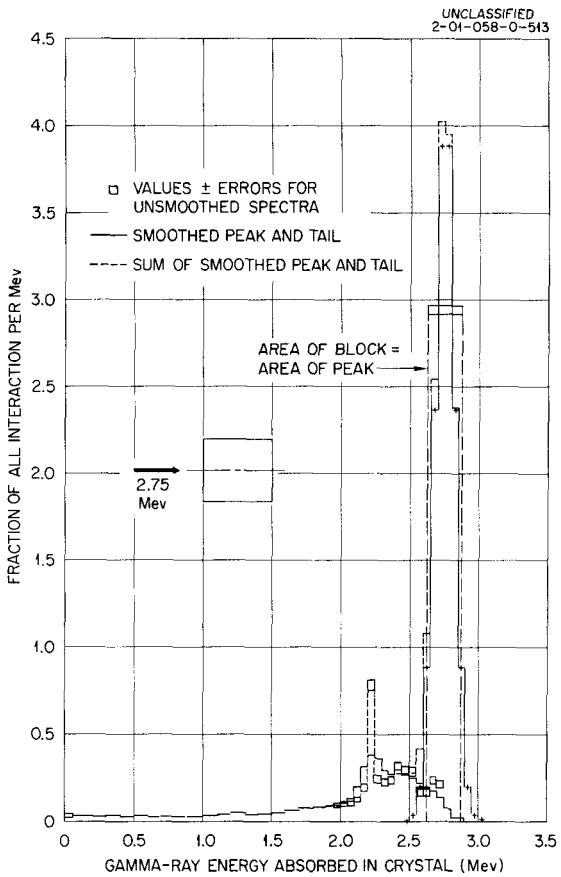

Fig. 8.3.2. Smoothed and Unsmoothed Estimated Spectra.

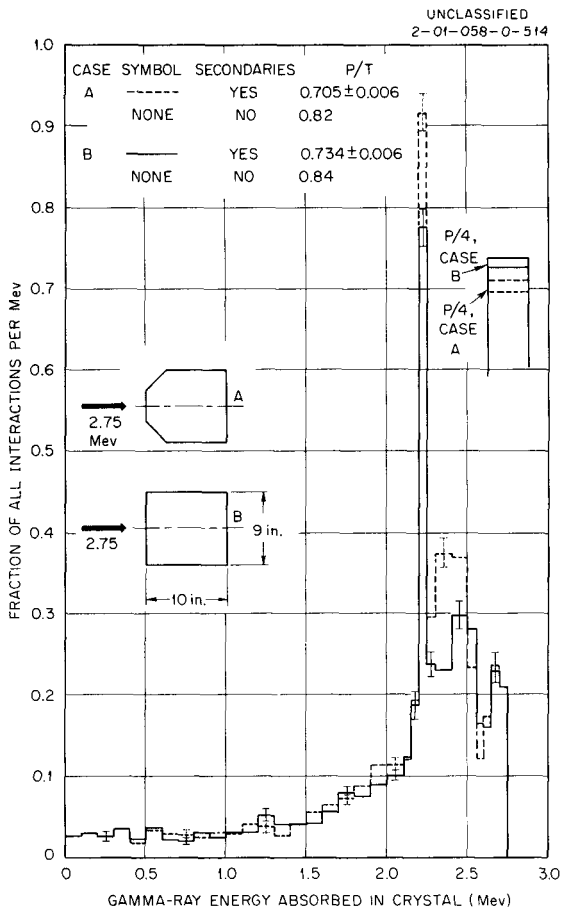

Fig. 8.3.3. Estimated Effect of Truncated Conical End for 2.75 Mev.

method of growing. The difference between the photofractions for the two cases is only 3%. The difference between the two tail spectra is all in the absorbed-energy region above 2 Mev. It can be interpreted that the difference represents the escape from the conical region of crystal *A* of annihilation radiation and Compton radiation scattered through angles between 90 and 180°.

Calculated photofractions are shown on the figure. "No secondaries" indicates that the calculation assumed zero bremsstrahlung and considered pair production processes as pure absorption.

Experimental difficulties in the use of these conically ended crystals are expected to eliminate their use; thus, the small improvement in photofraction is probably of purely academic interest.

Figure 8.3.4 demonstrates the effect of a well in the crystal into which the beam enters. The length of the path of the gamma rays through the crystal is the same. The first point of interest shown here is the comparison between the "no secondaries" cases. Although the curves agree at low energies, it is clear that the use of a well has a strongly marked effect on the section of the spectrum just below the photopeak, even when annihilation radiation and bremsstrahlung are not considered. The difference is satisfactorily interpreted, both in approximate magnitude and in energy, as arising from the escape from the crystal of radiation Compton-scattered through angles near 180° by material close to the surface of the crystal.

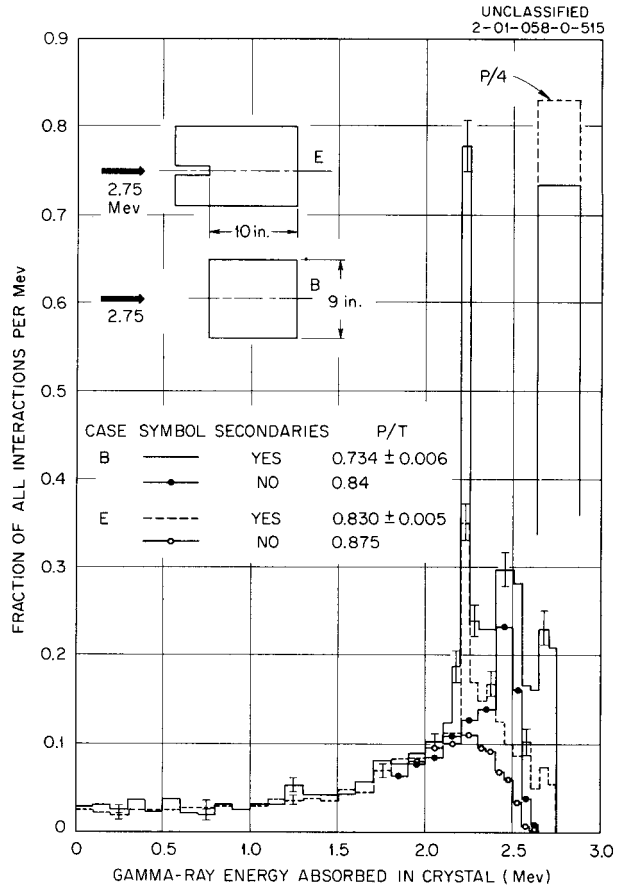

Fig. 8.3.4. Estimated Effect of Well on Energy Loss Spectra for 2.75-Mev Photon.

The histograms calculated by including secondaries also demonstrate the marked influence of the well, the photofraction increasing from 73 to 83% with the inclusion of the well. Again the differences are all above 2 Mev, the curves mingling at low energies. The reduction in the single escape peak is especially noteworthy.

When a similar set of cases is calculated for 7.5-Mev gamma rays, as shown in Fig. 8.3.5, rather than for the 2.75-Mev gamma rays of the preceding example, it is immediately clear that the "no secondaries" condition produces a very bad estimate. The well again produces a sizable improvement in the histograms calculated with all secondaries, the photopeak value increasing from 57 to 70%.

Figure 8.3.6 illustrates the effect of changing crystal length. Crystal E is the same size as those previously discussed, with 10 in. of material for the beam to penetrate. Crystal G has only 6 in. of material. Both have wells. Crystal B, of course, is the standard crystal discussed earlier. When the spectrum from crystal E is compared with that from crystal G, a slight difference is noted in the region near the full energy of 2.75 Mev, but the major difference occurs at low energies, where the 6-in.-penetration-length crystal yields a much higher predicted intensity. This is precisely what is expected from the "analytic zero" concept. The analytic zero, or analytically calculated zero-energy intercept of the pulse-height spectrum, may be

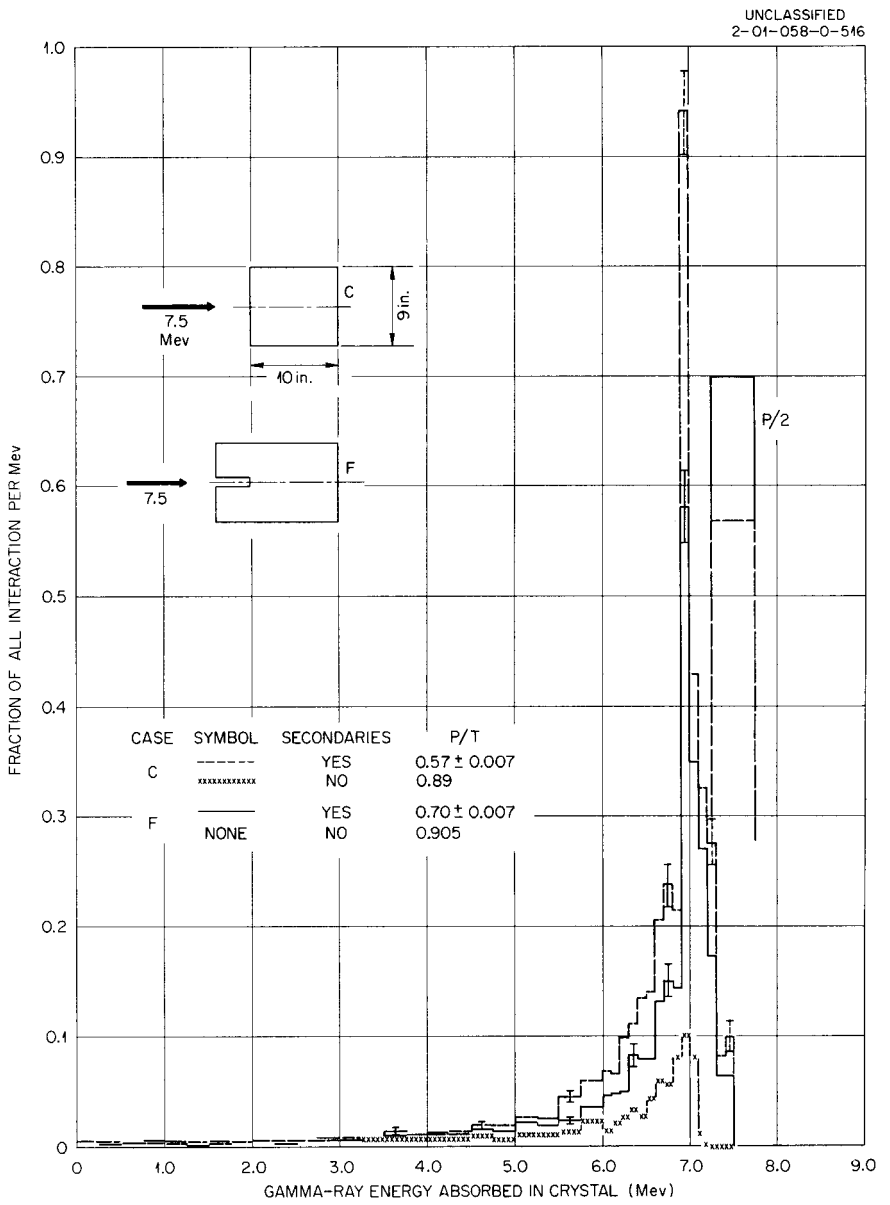

Fig. 8.3.5. Effect of a Well on Estimated Energy Loss Spectrum for 7.5-Mev Photons.

calculated by considering the escape, out of the far end of the crystal, of Compton gamma rays scattered through very small angles, since this is the only process in idealized geometry by which one can get such a small amount of energy deposited in the crystal. For the simple case of an axially collimated beam, the analytic zero is just

$$\Gamma(0) = \frac{(1-\epsilon)}{\epsilon} 2 n_e l \pi r_0^2 \frac{m_0}{E_0^2} , \tag{1}$$

where

ϵ = intrinsic crystal efficiency $= 1 - e^{-\mu l}$,

l = path length of gamma-ray beam through crystal,

n_e = electron density of the crystal,

r_0 = classical electron radius,

m_0 = electron mass,

E_0 = energy of incident gamma ray,

$\Gamma(0)$ = zero-energy intercept of curve representing the fraction of all interacting gamma rays per energy interval.

Since, for these large crystals, ϵ is close to unity, at a given energy the dependence of the intercept goes as $(1 - \epsilon)l$.

Another interesting comparison is shown in Fig. 8.3.6. When crystal G is compared with crystal B, the standard case, it is evident that the two crystals require the same amount of NaI and would therefore cost the same, were it not for the additional cost of drilling the well in G. Crystal G, however, has only a 6-in. penetration length, whereas B has the full 10 in. The spectrum from B falls much lower in the low-energy region than that from G, but is much higher in the region close to the full energy peak. The contributions exactly cancel each other, so that the photofractions are both equal to 73%. It is clear, then, that a well does not change the photofraction, but the inclusion of the well has shifted the counts which would normally occur near the full energy peak to a rather uniform distribution over the lower energies. In a practical case, the well would be drilled only 2 in. deep rather than 4, and the photofraction obtained would be higher than for either of the two cases discussed.

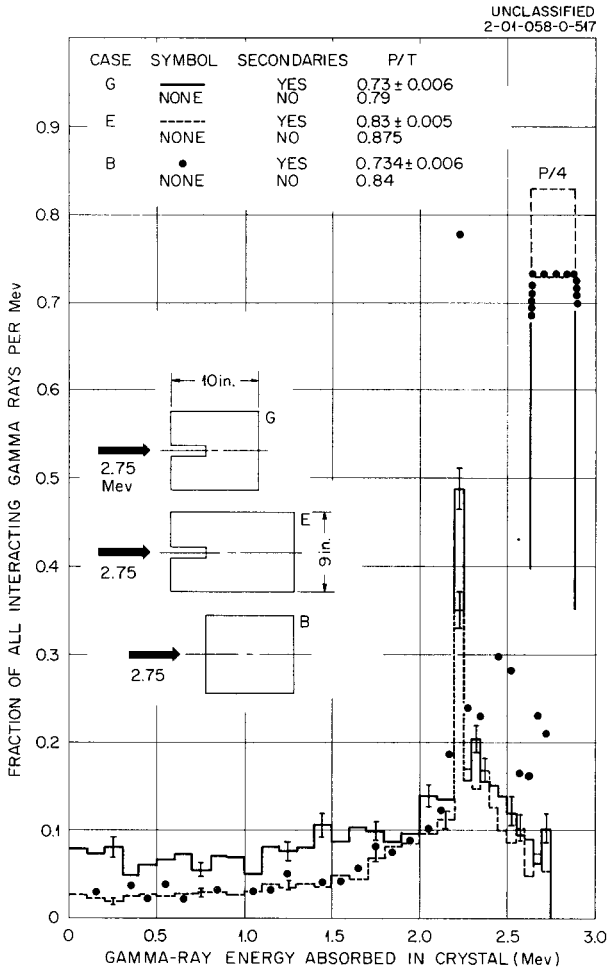

Fig. 8.3.6. Effect of Crystal Length on Estimated Energy Loss Spectra.

Figure 8.3.7 shows the result of varying crystal diameter while retaining a uniform, 10-in. penetration length. As the diameter is increased from 6 to 12 in., the photofractions increase from 70 to 88%. As expected, because the intrinsic efficiency and the path length have not changed, there is no difference at low energies. Although the relevant cases have not been run, for higher gamma-ray energies the effect of changing crystal diameter is expected to be confined to that region of the spectrum fairly close to the full peak.

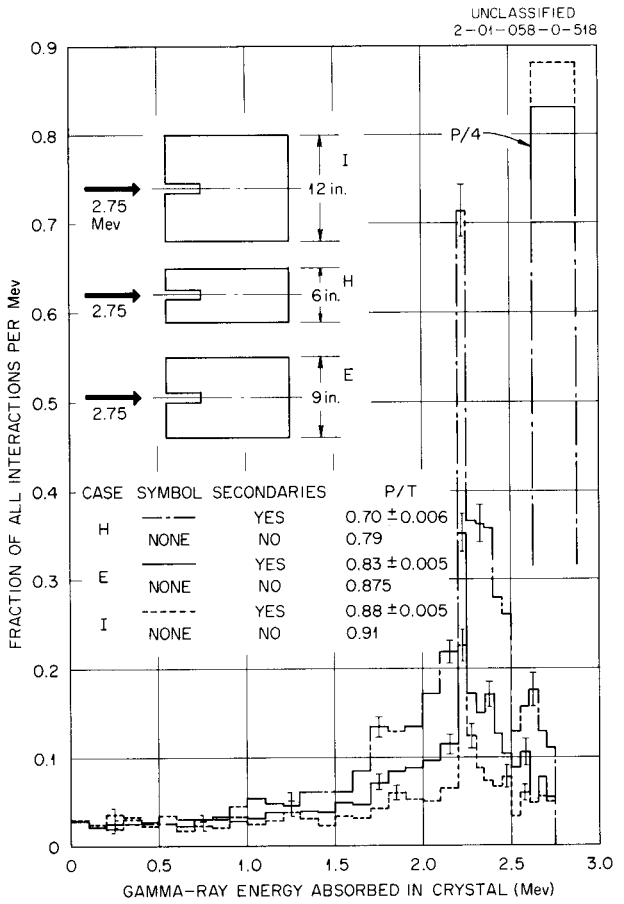

Fig. 8.3.7. Effect of Crystal Diameter on Estimated Energy Loss.

The present work demonstrates clearly that a definite amount of control over the photofraction and over the shape of the tail spectrum can be obtained by care in the choice of crystal dimensions. Efficient design of spectrometers would seem to dictate taking advantage of calculations similar to the above, perhaps altered to fit the region of parameters appropriate to a given problem.

8.4 THE MODEL IV GAMMA-RAY SPECTROMETER: STATUS REPORT

G. T. Chapman

Assembly of the Bulk Shielding Facility (BSF) model IV gamma-ray spectrometer[1] has been completed, with only final calibration of the positioner and readout system[1] yet to be accomplished.

A series of preliminary investigations of the system performance is now in progress, utilizing a special loading, No. 32, shown in Fig. 8.4.1, of the Pool Critical Assembly. This long, thin slab of cold elements is expected to provide a spectrum containing a minimum of scattered gamma rays, and the ultimate goal of the experimental program is the measurement of the gamma-ray spectrum of this configuration. The preliminary program, designed to optimize the performance of the model IV spectrometer, will investigate:

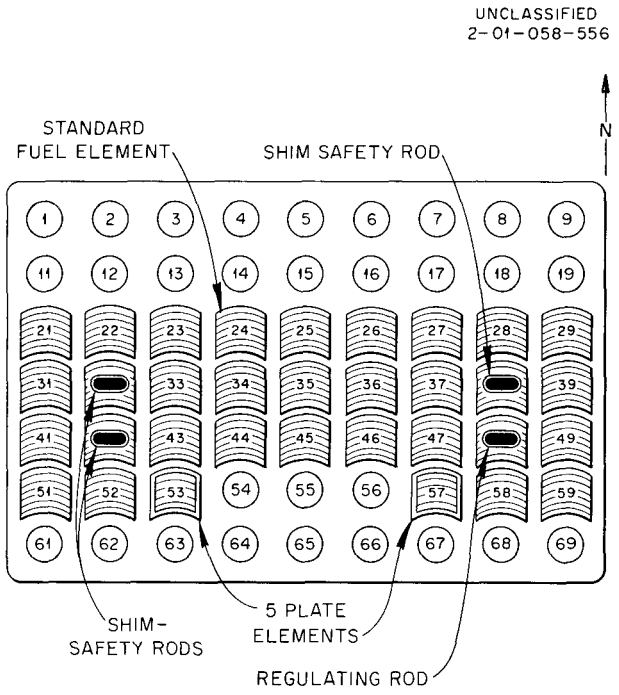

Fig. 8.4.1. Loading No. 32 of the Pool Critical Assembly.

1. backgrounds, with a large NaI(Tl) scintillation detector within the spectrometer shield, in a mixed field of radiation;
2. the relative effect of neutrons entering the shield through the collimator;
3. the effects of collimator size and geometry, in order to make the final experimental result independent of these factors and to minimize the tail of the pulse-height distribution caused by scattering in the collimator;
4. the possible necessity for and effect of an exterior, conical void as a part of the collimator system, in order to remove the large lead shield from the region where gamma rays enter the detector;
5. the reproducibility of the data taken with the multiphototube arrangement necessary with the large crystal;
6. methods of exactly reproducing a particular power level in the reactor used for calibration.

The $9\frac{3}{8}$-in.-dia NaI(Tl) scintillator which was to have been used in the spectrometer was broken while being returned from the manufacturer. It had been shipped to him for modifications designed to improve its response. (Such modifications are not made at the BSF because of the

[1] G. T. Chapman and T. A. Love, *Neutron Phys. Ann. Prog. Rep. Sept. 1, 1958*, ORNL-2609, p 133.

lack of suitable facilities.) However, a new crystal has been obtained and is currently in use. The new crystal is a composite formed by joining a 9-in.-dia, 7-in.-long crystal with another, 9 in. in diameter and 5 in. long. The final configuration is a right cylinder, 9 in. in diameter and 12 in. long. The connection between the two crystals is accomplished by an optically consistent medium. Gamma rays are collimated into a 1-in.-dia, 2-in.-deep well drilled axially in one end. A slightly smaller composite crystal of this type has previously been tested at the BSF.[2] Such a crystal dispenses with the conical end which characterized the $9\frac{3}{8}$-in.-dia crystal, and which was proved to be detrimental to its response, producing double-peaked distributions for monoenergetic gamma rays of energy as low as 1 Mev.[3]

Figure 8.4.2 shows a typical response curve obtained with the 9-in.-dia, 12-in.-long composite crystal. The measured pulse-height distribution is shown for the 2.73-, 6.13-, and 7.12-Mev gamma rays resulting from the decay of N^{16}. Contamination of the distribution is evident in the peak at 0.511 Mev, an annihilation gamma ray originating in the lead of the spectrometer housing, and in the peak at 1.36 Mev, from the decay of $_8O^{19}$ in the water of the pool.

A detailed study of the response of the crystal as a function of energy has not been performed, but resolution is ~11.5% at 0.662 Mev, with a peak-to-total ratio (photofraction) of ~78% at the same energy. This resolution is better than that attained with the earlier, conically ended crystal, while the peak-to-total ratio is somewhat lower than the value of 92% computed by a Monte Carlo calculation.[3] This is to be expected, since the experimental distribution is probably strongly influenced by those gamma rays degraded in energy by scattering in the collimator and source before entering the crystal.

---

[2]G. T. Chapman, T. A. Love, and R. W. Peelle, *Neutron Phys. Ann. Prog. Rep. Sept. 1, 1959*, ORNL-2842, p 191.

[3]T. A. Love and G. T. Chapman, *Gamma-Ray Response Measurements of Large NaI(Tl) Crystals*, a paper presented at the Total-Absorption Gamma-Ray Spectrometer Symposium, Gatlinburg, Tennessee, May, 1960.

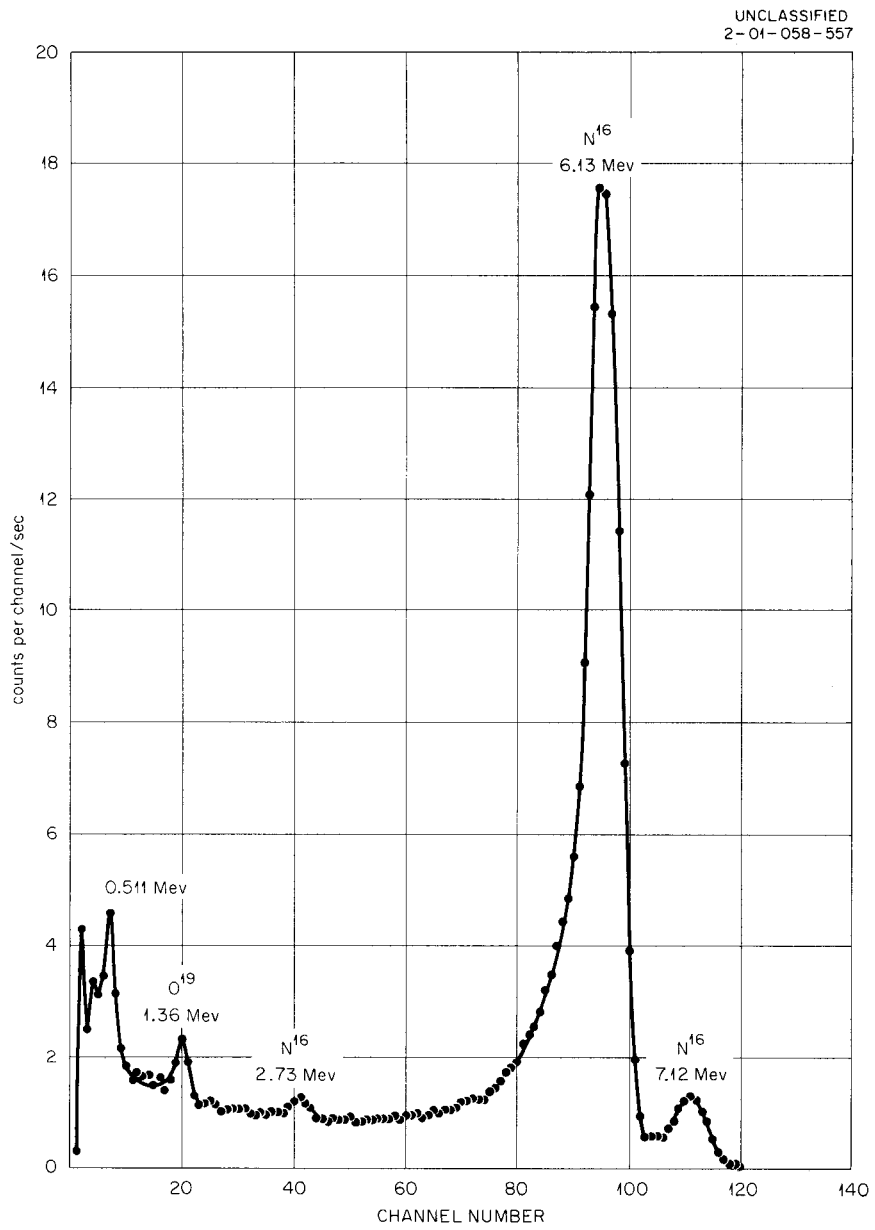

Fig. 8.4.2. Response of a 9-in.-dia, 12-in.-long NaI(Tl) Crystal to Gamma Rays from the Decay of $_7N^{16}$.

8.5 EXPERIMENTAL DETERMINATION OF FLUX DEPRESSION AND OTHER CORRECTIONS FOR GOLD FOILS EXPOSED IN WATER

W. Zobel

The initiation of an experimental program intended to determine suitable correction factors applicable to the use of thin gold foils for thermal-neutron flux measurements has previously been reported.[1] At that time a preliminary value deduced from experiment was reported and was compared to values derived from several calculational prescriptions.

Additional work has been done on this problem, with the experimental attack following that described previously. Foils ranging in thickness from 40 $\mu g/cm^2$ to 493 mg/cm^2 were exposed in the water-filled configuration tank of the Lid Tank Shielding Facility (LTSF) at a position in the LTSF at which the flux was isotropic, as required by the theoretical model. The isotropy was experimentally verified by exposing foils at this position, both parallel and perpendicular to the plane of the source plate. In each of these orientations a foil had one face, only, covered with cadmium. The activities of the foils so exposed agreed to within less than 1%, thus demonstrating isotropy.

Foils were exposed at the end of a 66.5-cm-long Lucite rod, $^9/_{16}$ in. square in section, with a positioning accuracy of ±0.5 mm. Since the flux at the point of exposure is essentially flat, changing by less than 3% over a distance of 1 cm, the error introduced into the measurement by the positioning error was negligible.

Figure 8.5.1 shows the experimental data obtained with thin (<1.7 mg/cm^2) foils, which were prepared by evaporating the gold onto a Mylar backing. The mass of the gold deposited was determined by spectrophotometric analysis, to an accuracy of ±5%. Each data point is the average of four or five measurements. The data were fitted with straight lines, using the method of least squares. The shaded band represents the cadmium difference, with the width of the band

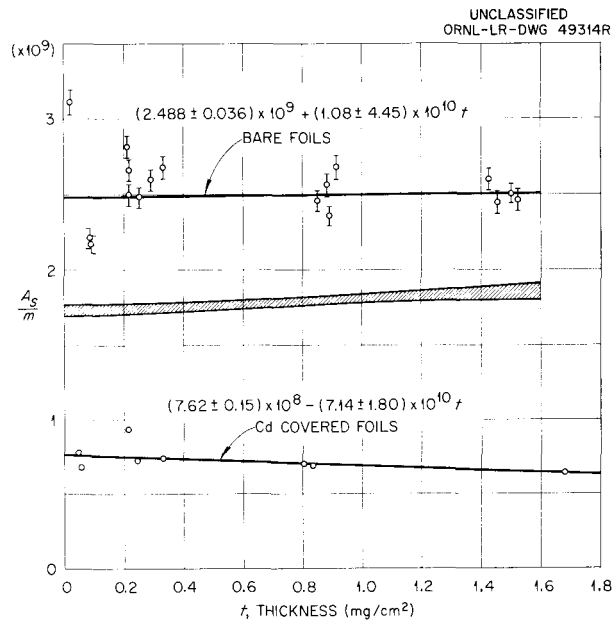

Fig. 8.5.1. Saturated Activity Divided by Foil Mass as a Function of Foil Thickness for Very Thin Gold Foils. Cadmium differences are shown as the shaded band, its width indicating the standard error.

[1] W. Zobel, *Neutron Phys. Ann. Prog. Rep. Sept. 1, 1959*, ORNL-2842, p 202.

indicating the standard error. The quantity of interest is the intercept at zero thickness, $(1.726 \pm 0.039) \times 10^9$.

Figure 8.5.2 shows the data obtained with thicker (< 500 mg/cm^2) foils, which were cut from sheets of the desired thickness, with the mass determined by weighing. The percentage accuracy here, in general, was better than for the thin foils, since the weight was determined to ±0.1 mg.

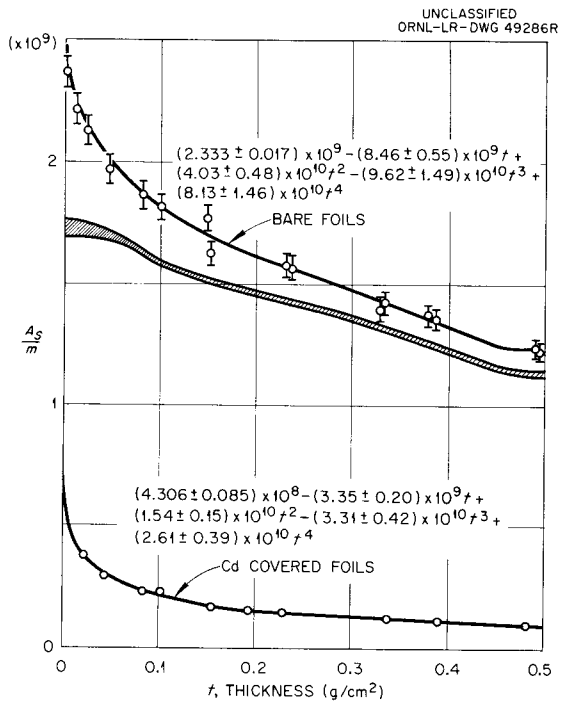

Fig. 8.5.2. Saturated Activity Divided by Foil Mass as a Function of Foil Thickness. Cadmium differences are shown as the shaded band, its width indicating the standard error.

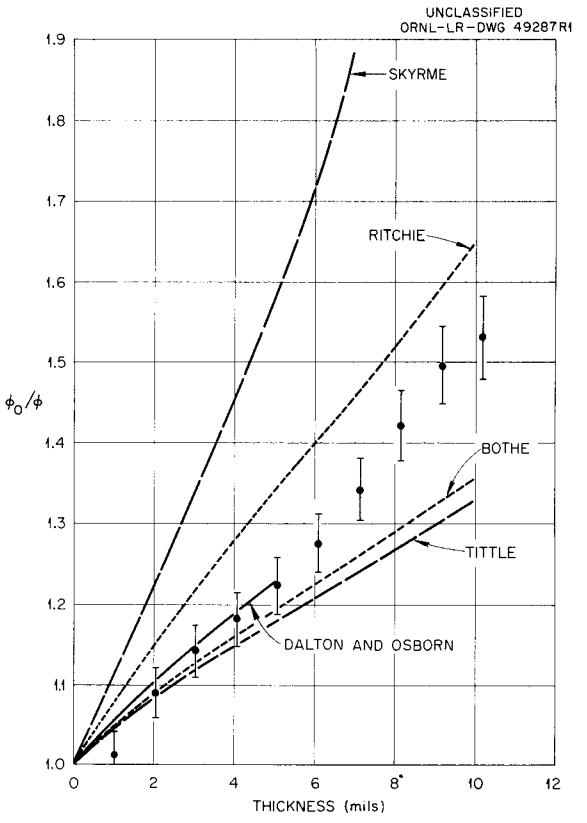

Fig. 8.5.3. Flux Depression and Self-Shielding Correction Factor for Gold Foils as a Function of Foil Thickness: Comparison of Experiment with Theory.

Again the points plotted are the average of four or five measurements. In the case of the thick foils, the data have been fitted to fourth-order polynomials by a least-squares technique, employing the Oracle. The band again indicates the cadmium difference, with the zero-thickness intercept taken from the extrapolated thin-foil data.

Figure 8.5.3 shows the experimentally determined correction factor ϕ_0/ϕ, where $\phi_0 = k(A_s/m)_0$ is determined by the intercept of Fig. 8.5.1, and $\phi = k(A_s/m)$ is determined for the appropriate thickness from Fig. 8.5.2. The constant k is a proportionality constant whose value is the same for both sets of data. The error associated with the points is ~3%.

Since this experiment was begun, a new calculational approach to the problem was made by Dalton and Osborn.[2] In this method the Boltzmann equation describing the perturbed neutron

[2]G. R. Dalton and R. K. Osborn, *Trans. Am. Nuclear Soc.* 3, 284 (1960).

population is converted into an integral equation. The angular integrations are performed analytically, and the spatial integrations are carried out numerically with the aid of the IBM 704. From the curve of Fig. 8.5.3, which also displays the results of the older recipes of Skyrme,[3] Ritchie,[4] Bothe,[5] and Tittle,[6] the results of Dalton and Osborn appear in best agreement with the experiment. An extension of Dalton's work to regions of greater thicknesses is now in progress.

[3]T. H. R. Skyrme, *Reduction in Neutron Density Caused by an Absorbing Disc*, MS-91.

[4]R. H. Ritchie, *H-P Ann. Prog. Rep. July 1, 1958*, ORNL-2806, p 133.

[5]W. Bothe, *Z. Physik* 120, 437 (1943).

[6]C. W. Tittle, *Nucleonics* 8(6), 5 (1951); *Nucleonics* 9(1), 60 (1951).

8.6 CALCULATION OF PULSE-HEIGHT RESPONSE FUNCTIONS FOR GAMMA-RAY SCINTILLATION COUNTERS

C. D. Zerby H. S. Moran

Introduction

The design and development of three IBM 704 Monte Carlo codes for the calculation of pulse-height response functions for gamma-ray scintillation counters has previously been reported.[1] At that time, the codes did not take into account the losses from the detector from secondary annihilation radiation and bremsstrahlung, although treatment of the primary radiation was essentially complete. The codes have now been improved to include the effects noted,[2] so that they now represent an effectively complete description of all the significant physical processes taking place within the crystal. Crystal configurations and source configurations remain as previously described. Codes for NaI, CsI, and xylene, along with complete operating instructions, have been prepared and are available to those interested.[3]

Idealizations and Assumptions

In the design of the codes it was obviously necessary to make certain simplifying idealizations and approximations in order to keep the problem within manageable limits. The basic idealization was that of suspending the scintillator in a vacuum. Background effects, which in any case are effectively unique for a particular experimental arrangement, are thus completely

[1]C. D. Zerby and H. S. Moran, *Neutron Phys. Ann. Prog. Rep. Sept. 1, 1959*, ORNL-2842, p 185.

[2]The bremsstrahlung spectrum was obtained from C. D. Zerby and H. S. Moran, *Bremsstrahlung Spectra in NaI and Air*, ORNL-2454 (Feb. 25, 1958).

[3]C. D. Zerby and H. S. Moran, *An IBM-704 Code for Predicting the Response of Gamma-Ray Scintillation Counters*, ORNL CF-60-5-72 (May 19, 1960).

eliminated. The difference between calculation and experiment produced by this assumption is expected to be significant only in the region of low pulse height.

In the calculation of the photon cascade, the coherently scattered radiation, which is usually confined to an angular distribution peaked in the forward direction except for low energies, was assumed to scatter straight ahead in all cases. This approximation is usual, and its effect has never been detected in other penetration problems.

Electron losses from the counter were ignored, an approximation which should have no significant effect except for very small counters.

In including the effect of the bremsstrahlung and annihilation radiation, it was assumed that the electrons ejected by a Compton, photoelectric, or pair-production event slow down in a region close to where they were ejected from the atom. In effect, the bremsstrahlung and annihilation radiation are assumed to be created at the electron-ejection site. This can only affect pulse-height spectra resulting from the higher of the source energies allowed in the problem.

Comparison with Experiment

Shown in Figs. 8.6.1 through 8.6.7 are comparisons of the calculation with various experimental results for a 3- by 3-in. NaI crystal for source energies from 0.478 to 7.48 Mev. In all these figures the pulse height is given in Mev and the calculated data are normalized to a total response of one count. Figures 8.6.1 and 8.6.2 show the experimental results of McGowan.[4] In his experiments the counter was suspended in the middle of a room by a minimum support in order to reduce background effects, and the resultant pulse-height spectrum was adjusted to take into account the little background that remained. The calculated data were normalized to these data at the photopeak. The calculated data show a deeper dip just below the photopeak and deviate to a certain extent at the smaller pulse heights. This deviation can be partially accounted for by background effects which were not taken into consideration in the experiment, and partially by the poorer statistical accuracy of the calculation in this region.

In order to help determine the shape of the curve at small pulse heights, the contribution at zero pulse height was calculated analytically and is shown in each of the figures as the "analytic zero value."

At source energies above 1 Mev, shown in Figs. 8.6.3 through 8.6.7, the deviation between calculation and experiment persists at small pulse heights with a definitely increasing trend with increasing source energy. Probably the major portion of this difference can be accounted for as background effects which are not considered in the calculation.

Of some interest is the comparison of the calculation with the experimental data obtained with a source of Na^{24} gamma rays, because of the way the calculated data were generated.

[4] F. K. McGowan, private communication.

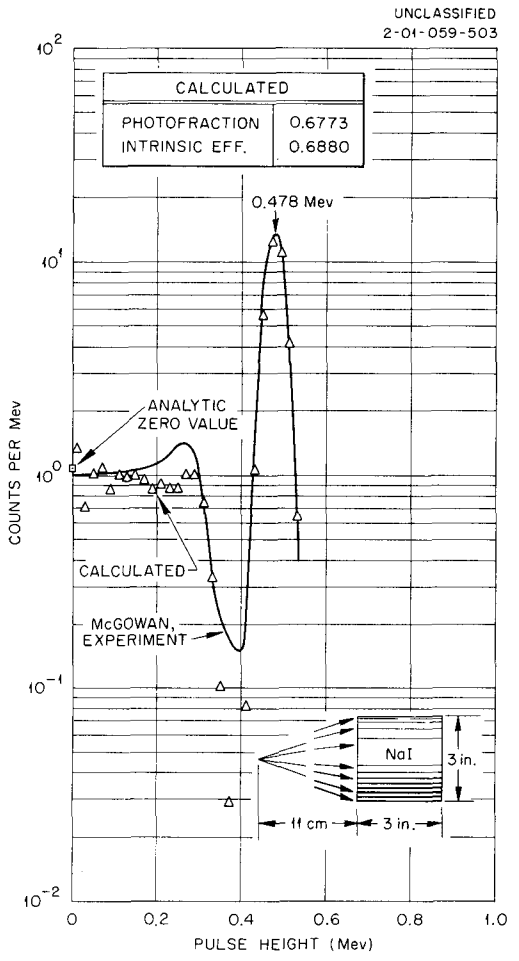

Fig. 8.6.1. Comparison of Calculated Pulse-Height Spectrum with Experimental Values of McGowan for Be^7 Gamma Rays Incident on a 3- × 3-in. NaI Scintillation Counter. Calculated values normalized to a total response of one count.

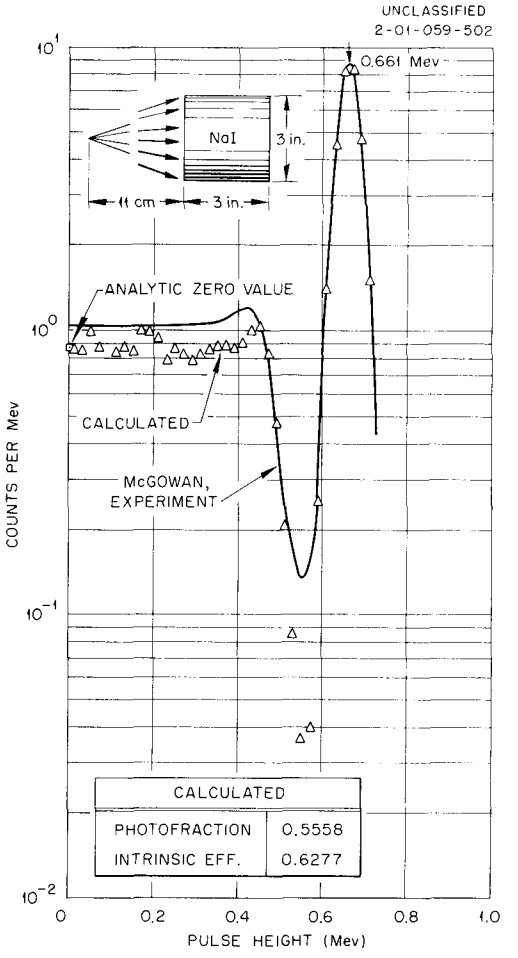

Fig. 8.6.2. Comparison of Calculated Pulse-Height Spectrum with Experimental Values of McGowan for Cs^{137} Gamma Rays Incident on a 3- × 3-in. NaI Scintillation Counter. Calculated values normalized to a total response of one count.

This comparison is shown in Fig. 8.6.4. The problem was calculated two times, once for a 1.38-Mev source and again with a 2.76-Mev source. The resultant pulse-height spectra from these calculations were then compounded to give the final curve, which was normalized to the experimental data at the 2.76-Mev total absorption peak. The fact that the calculated data for the 1.38-Mev peak also lie on the experimental data indicates that the calculation is giving reasonably accurate results.

At the larger pulse-height values for source energies of 3.13 and 4.43 Mev, shown in Figs. 8.6.5 and 8.6.6, the calculation agrees remarkably well with experiment. The total absorption peak and two escape peaks calculated in each case duplicated the experimental values almost exactly.

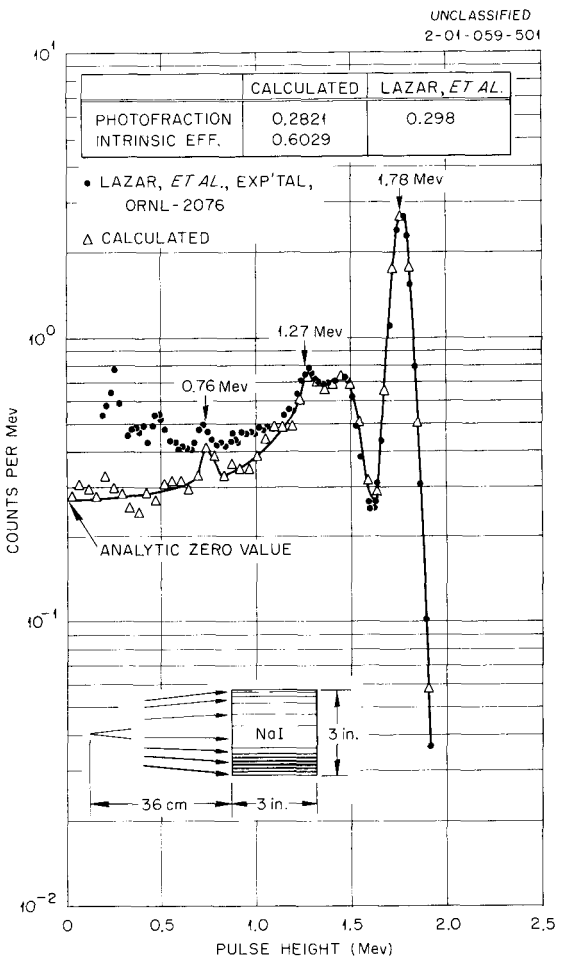

Fig. 8.6.3. Comparison of Calculated Pulse-Height Spectrum with Experimental Values of Lazar and Willard for 1.78-Mev Gamma Rays Incident on a 3- × 3-in. NaI Scintillation Counter. Calculated values normalized to a total response of one count.

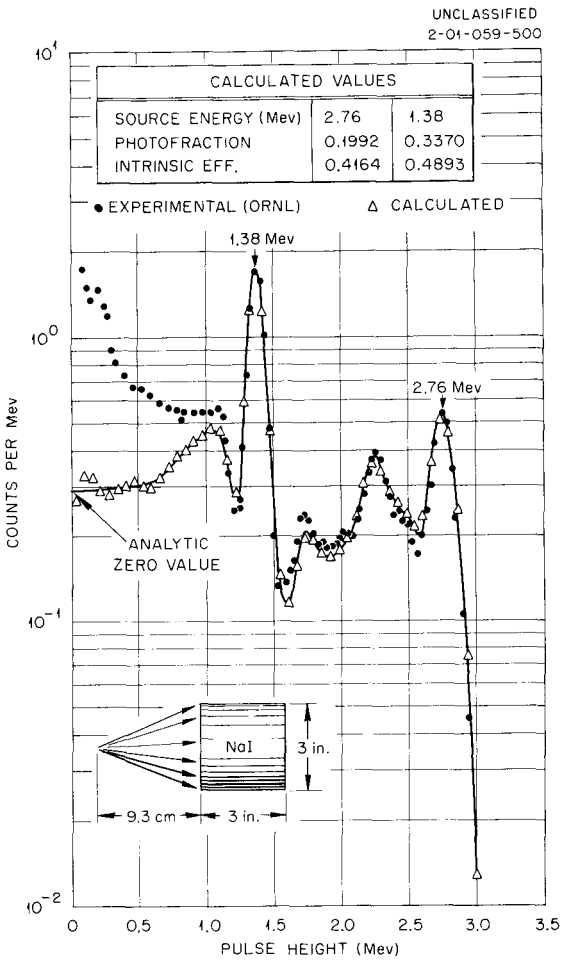

Fig. 8.6.4. Comparison of Calculated Pulse-Height Spectrum with Experimental Values Obtained at ORNL for Na^{24} Gamma Rays Incident on a 3- × 3-in. NaI Scintillation Counter. Calculated values normalized to a total response of one count.

Figure 8.6.7 shows a comparison of the calculation with the experimental values of Lazar and Willard[5] for a source energy of 7.48 Mev. In this case the calculated points are not shown; rather, a smooth curve through the data is presented. This was done in order to simplify the figure and show some additional data indicating the effect of secondary radiation on the pulse-height spectrum. The curve labeled "no secondaries" was calculated by neglecting completely the potential energy losses by annihilation radiation and bremsstrahlung. The curve labeled "only annihilation radiation included as secondaries" neglected the energy loss due to bremsstrahlung, and, finally, the "all secondaries" curve took into account the annihilation radiation

[5]N. H. Lazar and H. B. Willard, *Phys. Semiann. Prog. Rep. Mar. 10, 1956*, ORNL-2076, p 55.

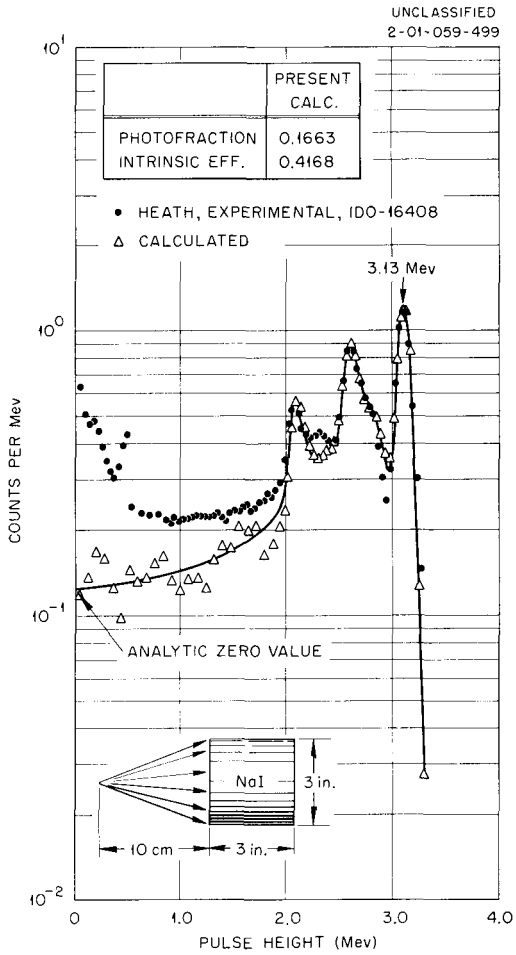

Fig. 8.6.5. Comparison of Calculated Pulse-Height Spectrum with Experimental Values for S^{37} Gamma Rays Incident on a 3- × 3-in. NaI Scintillation Counter. Calculated values normalized to a total response of one count.

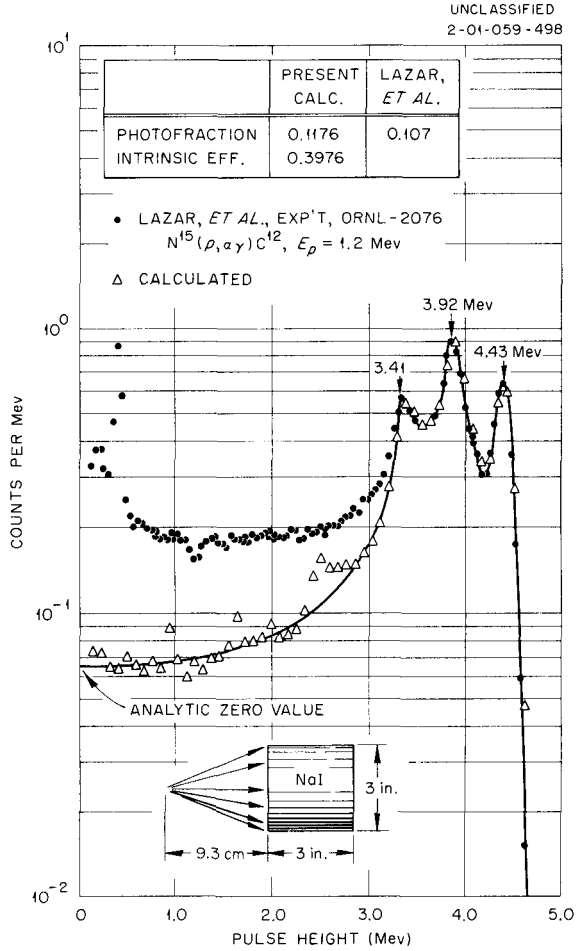

Fig. 8.6.6. Comparison of Calculated Pulse-Height Spectrum with Experimental Values of Lazar and Willard for 4.43-Mev Gamma Rays Incident on a 3- × 3-in. NaI Scintillation Counter. Calculated values normalized to a total response of one count.

energy losses as well as the bremsstrahlung energy losses. As would be expected, the curve neglecting all secondary effects does not agree with the experiment at all. The curve including the annihilation radiation would agree with the experiment fairly well if it were normalized to the experimental data at the total absorption peak; however, the relative heights of the two escape peaks do not agree with experiment until one includes all secondary effects. The curve including the effects of all secondary radiation was normalized to the experimental data at the total absorption peak. One can observe that the two escape peaks lie slightly below the experimental data in this case. This does not necessarily indicate that the calculation is incorrect, because the difference could be accounted for by an apparently large amount of background appearing in the experiment. If the calculated data were normalized to the experimental

data at the first escape peak, for example, the calculated total absorption peak would be approximately 10% higher.

Comparison with Other Calculations

The results of the present calculation have been compared with calculated results of Miller and Snow[6] for several source energies. For the lower source energies agreement is good. For higher source energies, however, a definite disagreement is noted, particularly at the higher-energy pulse heights. This is shown in Fig. 8.6.8, which displays the results of the two calculations for a 6.13-Mev source incident on a 6 × 6 in. NaI crystal with perfect resolution. (The lower-energy pulse heights are not shown, since they disagree only slightly.) As an aid in analysis of the differences, a curve calculated by neglecting effects of all secondary radiations is also shown. This curve was obtained from the present calculation.

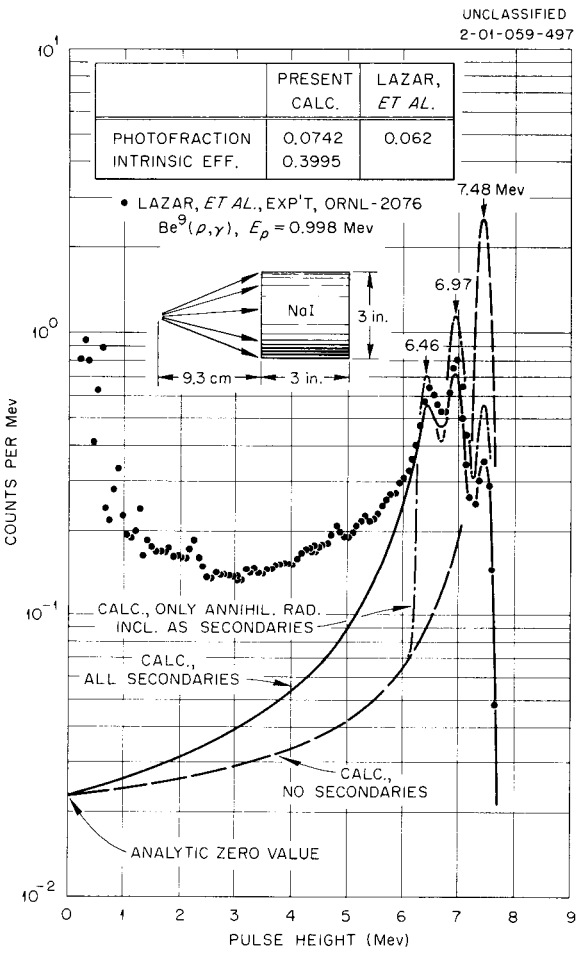

Fig. 8.6.7. Comparison of Present Calculation with Experimental Pulse-Height Spectrum of Lazar and Willard for 7.48-Mev Gamma Rays Incident on a 3- × 3-in. NaI Scintillation Counter. Calculated curves show the effects of secondaries and are normalized to a total response of one count.

It is evident that the results of Miller and Snow follow the curve neglecting secondary effects, up to the second escape peak. At this point there is a discontinuity in the spectrum, as well as another at the first escape peak. The data from the present calculation, in contrast, present a smooth curve, generally above the Miller-Snow results. The effect of the discrepancy is a 50 or 30% difference in the peak-to-total ratio (photofraction), depending upon which data are used as a basis of comparison.

The difference between the two calculations appears to be almost entirely due to the difference in the contribution of the secondary bremsstrahlung. The data from the Miller-Snow calculation show little or no bremsstrahlung effects below the second escape peak, yet show some effect immediately above that peak. There does not seem to be a reasonable explanation for this or for the discontinuity at the first escape peak.

[6] W. F. Miller and W. J. Snow, *Rev. Sci. Instr.* 31, 39 (1960).

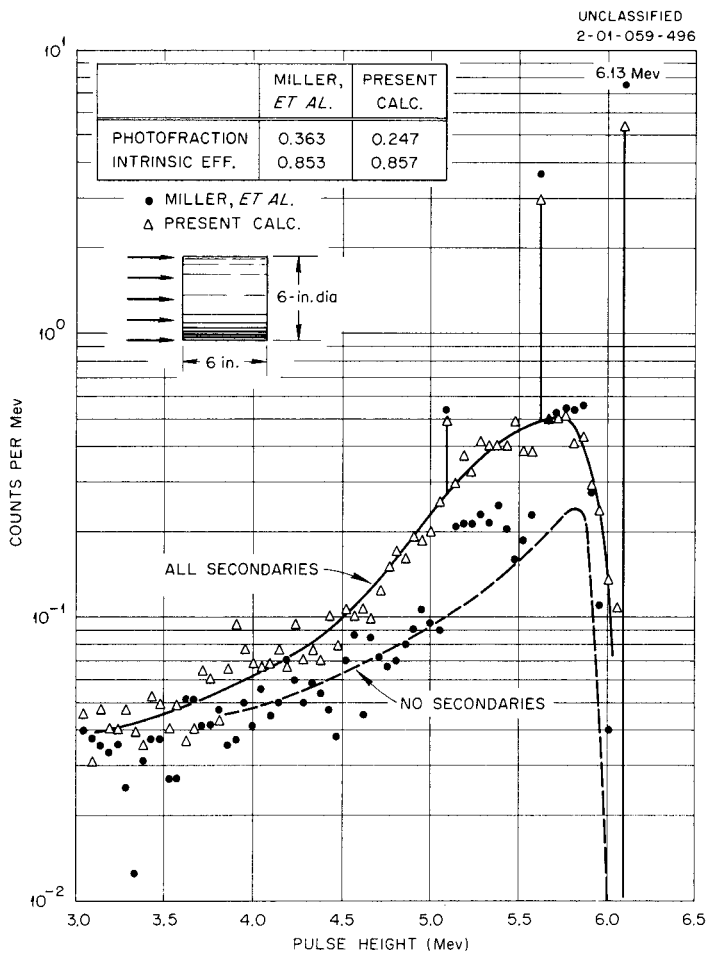

Fig. 8.6.8. Comparison of Present Calculation of Pulse-Height Spectra with That of Miller and Snow for 6.13-Mev Gamma Rays Incident on a Zero-Resolution NaI Scintillation Counter. Curves normalized to total response of one count.

8.7 SCINTILLATION RESPONSE OF ACTIVATED IONIC CRYSTALS TO CHARGED PARTICLES

A. Meyer R. B. Murray

Introduction

The scintillation response of activated inorganic crystals to various charged particles has been reported in a number of investigations. The most widely used inorganic scintillation crystals are the thallium-activated alkali iodides, notably NaI(Tl), CsI(Tl), and KI(Tl). In reviewing the experimental results on these crystals, it is clear that they behave similarly in

their response to different particles. Those features which are common include: a maximum scintillation efficiency to protons and deuterons with an essentially linear response in light intensity vs energy; a decreasing scintillation efficiency to heavier charged particles, with departures from a linear response in energy; and a nearly linear response to electrons, but with a scintillation efficiency less than that to protons. An illustration of these properties for the particular case of CsI(Tl) is given in Fig. 8.7.1, in which the scintillation efficiency is plotted

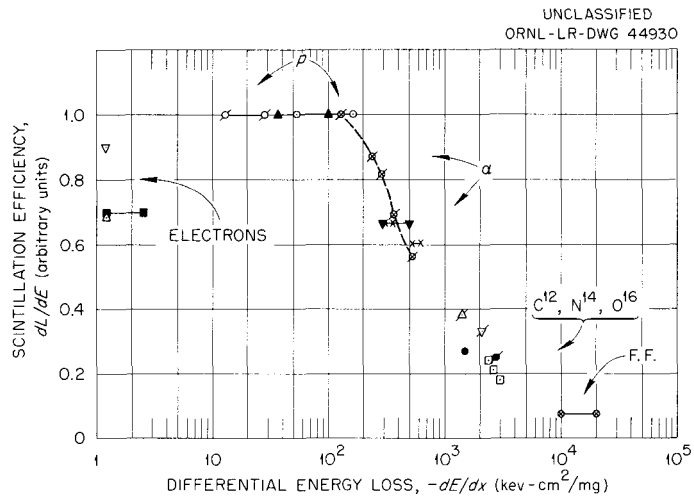

Fig. 8.7.1. CsI(Tl) Experimental Data.

as a function of stopping power for charged particles ranging from electrons through fission fragments. Scintillation efficiency is here defined as dL/dE, the slope of a pulse-height-vs-energy plot. The stopping power, dE/dx, of CsI for light charged particles of a particular energy has been calculated on the basis of the known stopping cross sections for elements near Cs and I in atomic number, based on a recent comprehensive summary by Whaling.[1] For heavier ions (C^{12}, N^{14}, O^{16}), the stopping power is estimated from studies of the ionic charge as a function of velocity during the slowing-down process,[2] combined with the above calculation of dE/dx for protons in CsI. The stopping power for CsI to fission fragments is taken from Fulmer.[3] The points in Fig. 8.7.1 have been taken from numerous experiments.[3–9] In order to compile these

[1] W. Whaling, *Handbuch der Physik* (ed. by S. Flügge), vol XXXIV, p 193, Springer, Berlin, 1958.

[2] A. Papineau, *Compt. rend.* **242**, 2933 (1956); see also, H. H. Heckman *et al.*, *Phys. Rev.* **117**, 544 (1960).

[3] C. B. Fulmer, *Phys. Rev.* **108**, 1113 (1957).

[4] T. R. Ophel, *Nuclear Instr.* **3**, 45 (1958).

[5] R. S. Storey, W. Jack, and A. Ward, *Proc. Phys. Soc. (London)* **72**, 1 (1958).

[6] M. L. Halbert, *Phys. Rev.* **107**, 647 (1957).

[7] A. R. Quinton, C. E. Anderson, and W. J. Knox, *Phys. Rev.* **115**, 886 (1959).

[8] A. Galonsky, C. H. Johnson, and C. D. Moak, *Rev. Sci. Instr.* **27**, 58 (1956).

[9] S. Bashkin *et al.*, *Phys. Rev.* **109**, 434 (1958).

results in a single figure, it has been necessary to normalize one set of data with respect to another; this has usually been done with reference to protons or alphas. The scintillation efficiency with respect to protons in the Mev region is arbitrarily normalized to unity. An attempt to synthesize the results of many experiments, as in Fig. 8.7.1, is clearly subject to considerable uncertainty, and rather large errors should be associated with any single point. The principal feature to be observed is the over-all trend, which seems to be well established and suggests that a continuous function describes the scintillation efficiency over a range of many decades in dE/dx. This hypothesis is further supported by the construction of a similar plot for NaI(Tl), which is found to be indistinguishable from Fig. 8.7.1. Finally, we may note a study of protons, deuterons, and alphas on KI(Tl).[10] The results of this experiment, when plotted as in Fig. 8.7.1, are well fitted by a smooth function and clearly indicate a maximum for protons and deuterons.

Formulation of Model

The scintillation process in activated alkali iodides may be considered in three essentially distinct steps: (1) slowing-down of the incident charged particle, with its energy going into the formation of electrons and holes, either free or bound together as an exciton; (2) the transport of at least part of this energy to activator sites, raising the activator to an excited state; and (3) radiative decay of the excited state. For the purpose of the following treatment it will be assumed that the light output is directly proportional to the number of energy carriers arriving at activator centers, with no further consideration given to the decay process itself. We thus deal only with parts (1) and (2) of the scintillation process. Following the studies of Enz and Rossel[11] and Van Sciver,[12] we assume that both an electron *and* a positive hole must be captured by the activator, either in succession or as an associated pair (exciton). Thus, the electrons and holes produced by the incident primary particle must recombine to stimulate an activator site. To be specific, we will consider in detail the case of recombination in the wake of the particle, followed by diffusion of excitons.

Recombination of n_e pairs of particles (per unit path length) in the wake of an incident particle produces a number of energy carriers n_o, where

$$n_o = \frac{\alpha n_e^2}{1 + \alpha n_e} \tag{1}$$

---

[10] W. T. Link and D. Walker, *Proc. Phys. Soc. (London)* **A66**, 767 (1953).

[11] H. Enz and J. Rossel, *Helv. Phys. Acta* **31**, 25 (1958).

[12] W. J. Van Sciver, *IRE Trans. on Nuclear Sci.* **NS-3**, 39 (1956).

and α is a recombination parameter. The migration of carriers to activator sites is described by a one-velocity diffusion equation,

$$\frac{\partial n}{\partial t} = D\nabla^2 n - nv(N_l\sigma_l + N_a\sigma_a) \quad , \tag{2}$$

where

n = density of carriers = $n(r,t)$,

v = velocity of carriers = constant,

D = diffusion constant,

N_a = density of unoccupied activator sites = $N_a(r,t)$,

N_l = density of lattice trapping sites = constant,

σ_a = cross section for capture of a carrier at an activator site = constant,

σ_l = cross section for capture of a carrier at a lattice trapping site = constant.

The lattice absorption term may be understood to include all trapping mechanisms available in the lattice other than the activators themselves. The initial source strength, $n(t = 0)$, is a delta function at $r = 0$ whose area is n_o. Since the carrier density may be large, and N_a small, we consider the possibility of saturating the unoccupied activator sites and write an additional equation:

$$\frac{\partial N_a}{\partial t} = -nvN_a\sigma_a \quad . \tag{3}$$

These equations can be solved by utilizing the inherent cylindrical symmetry of the diffusion of carriers from the track of the primary particle. The solution can be obtained analytically with the use of a straightforward approximation which reduces a nonlinear differential equation to a set of Bessel's equations. The solution yields the scintillation efficiency (in arbitrary units) as a function of n_e. Assuming that $n_e = K(dE/dx)$, it is then possible to plot a theoretical curve of scintillation efficiency vs dE/dx, with K to be determined by a best fit to the experimental data. Such a plot is shown in Fig. 8.7.2, superposed on the CsI(Tl) experimental points. The choice of K fixes a value for the diffusion length of the energy carriers; in this case, the diffusion length is found to be of order 20 A. It may be pointed out in connection with Fig. 8.7.2 that the decreasing characteristic for high values of dE/dx (above $\sim$50 kev-cm^2/mg) is due to the saturation of luminescence centers. (An activator concentration of 0.1 mole % has been assumed.) The rising characteristic for low dE/dx, however, arises entirely from the recombination term and comes about because the carrier-formation probability goes as n_e^2 for small values of n_e (hence small dE/dx); see Eq. 1.

The theoretical curve of Fig. 8.7.2 can now be employed to predict pulse height vs energy for various particles. An example of such a calculation is given in Fig. 8.7.3 and is compared with the experimental data of Bashkin *et al.*[9] Since the ordinate of Fig. 8.7.2 is in arbitrary units, it is necessary to normalize the theoretical curves at some point in Fig. 8.7.3; the alpha curve of Fig. 8.7.3 was normalized to the experimental points between 1 and 2 Mev. Having

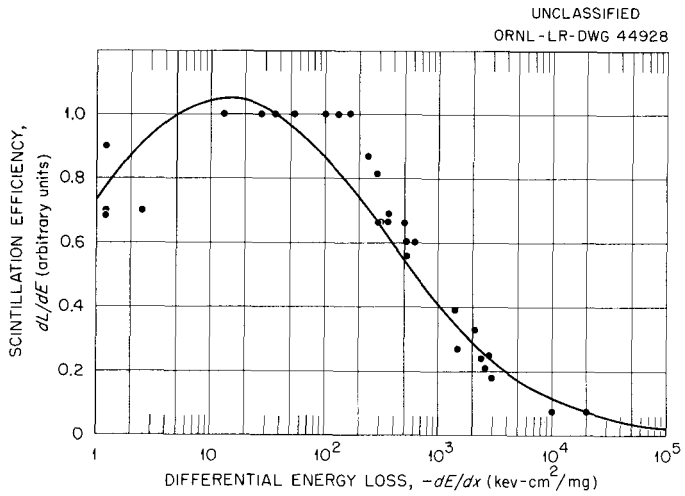

Fig. 8.7.2. Comparison of Calculated Curve and Data Points for CsI(Tl).

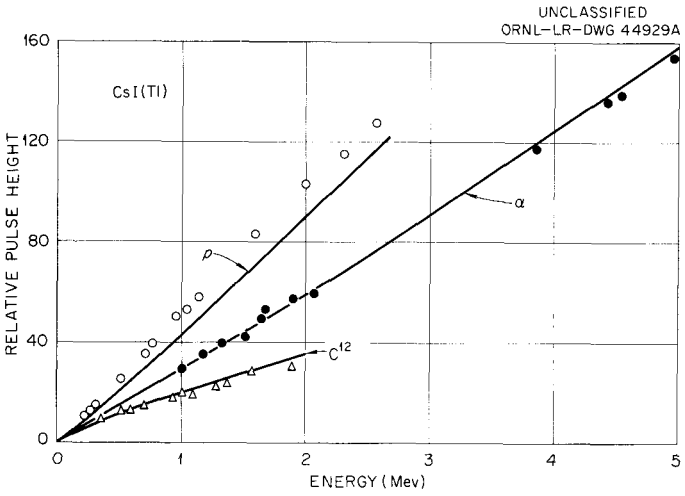

Fig. 8.7.3. Comparison of Calculated Curves with Experimental Data for Various Particles Incident on CsI(Tl).

chosen this one point, the shape and position of each of the theoretical curves of Fig. 8.7.3 is uniquely fixed by the curve of Fig. 8.7.2. It is seen that the agreement with experiment is good for alpha particles and C^{12} ions, but the calculated proton curve is some 10 to 15% lower than the experimental points. This is a consequence of the fact that the theoretical curve of Fig. 8.7.2 does not fall as steeply as the experimental data.

A further point which may be mentioned is that the present model contains the activator concentration as one of the initial parameters (Eq. 2); the results of this model thus contain the concentration as a parameter and predict concentration-dependent effects which are found to be in reasonable accord with theory.

To summarize, the model presented here represents an attempt to interpret the response of activated inorganic crystals to charged particles in terms of the formation, transport, and

capture of energy carriers. The basic assumptions are that the energy carriers are formed by the recombination of electrons and holes and that the density of carriers is a smooth function of dE/dx; these assumptions appear to be justified by experiment. The model predicts scintillation efficiency as a function of dE/dx, concentration-dependent effects, and a diffusion length. The model is a phenomenological one and is greatly simplified; for example, no account is taken of the formation of delta rays or of the slowing down of the diffusing particles. A more detailed description of this work is being prepared for publication.

8.8 USE OF SILICON SURFACE-BARRIER COUNTERS IN FAST-NEUTRON DETECTION AND SPECTROSCOPY

T. A. Love R. B. Murray J. J. Manning H. A. Todd[1]

Introduction

This paper describes recent experiments directed toward the development of a semiconductor counter which may be suitable for certain types of fast-neutron spectral measurements in which the time-of-flight technique is not feasible. A neutron-sensitive semiconductor detector has been constructed by depositing a thin layer of Li^6F between two silicon-gold surface-barrier counters. Neutrons are detected by observing the α + T pair resulting from the $Li^6(n,\alpha)T$ reaction; pulses from the two counters are added and the sum pulse is amplified and recorded on a multichannel analyzer. Since the sandwich arrangement permits simultaneous detection of both reaction products, the magnitude of the resulting sum pulse should be proportional to the energy of the incident neutron plus the reaction Q value (4.78 Mev).

Silicon-gold surface-barrier counters have been used as alpha-particle spectrometers with extremely good energy resolution, for example, within a quarter of a per cent for collimated alpha particles with energy of about 5 Mev (ref 2). The pulse-height distribution to be expected from monoenergetic neutrons on a sandwich detector of the type described here will exhibit a much broader peak, however, since the α + T reaction products are subject to energy loss in the Li^6F and gold layers before reaching the sensitive volume of silicon. The energy loss in a particular event depends on the angle at which the reaction products are emitted; since the α and T may be emitted at any angle, the energy loss is a variable from some minimum value up to the total energy available. In a practical counter, with an Li^6F layer of given thickness,

---

[1] Instrumentation and Controls Division.

[2] J. L. Blankenship and C. J. Borkowski, *Silicon Surface-Barrier Nuclear Particle Spectrometer*, paper presented at the Seventh Scintillation Counter Symposium, Washington, D. C., February 1960 (to be published in *IRE Trans. on Nuclear Sci.*, 1960).

this variable energy loss will govern the width of a monoenergetic neutron peak, with a much smaller contribution from the inherent line width of the silicon counter.

The results presented herein summarize principally construction features of these devices and the results of first experiments with monoenergetic neutrons. Considerably more work remains to be done with other neutron sources and in the study of various background effects.

Counter Construction

The silicon surface-barrier counters were supplied by J. L. Blankenship and R. E. Zedler of this Laboratory. The method of preparation of these detectors has been described elsewhere.[2] The counters used in the present work differ only in that they were not cast in an epoxy resin mold. The edges of the silicon wafer were painted for protection, however, with a thin coat of polystyrene in toluene prior to evaporation of the gold layer. The n-type silicon starting material in the counters used in this work was of nominal 3600 ohm-cm resistivity.

Figure 8.8.1 is a schematic diagram of a sandwich counter. The device consists essentially of two silicon counters seated in thin fluorothene sheets which are in turn mounted in light aluminum rings. A layer of Li^6F, of nominal thickness 150 $\mu g/cm^2$, is vacuum-evaporated on one of the counters prior to assembly. The two counters are brought close together, adjusted to make the faces parallel, and rigidly clamped by means of three clamping nuts and three positioning screws as shown. In practice, it is desirable to separate the counters by as small a distance as possible in order to avoid losing counts from an "edge effect" to be described below. An attempt is made to achieve a separation of about 0.001 in., at the same time taking extreme care that the counters do not touch and thereby produce small scratches on the delicate gold face.

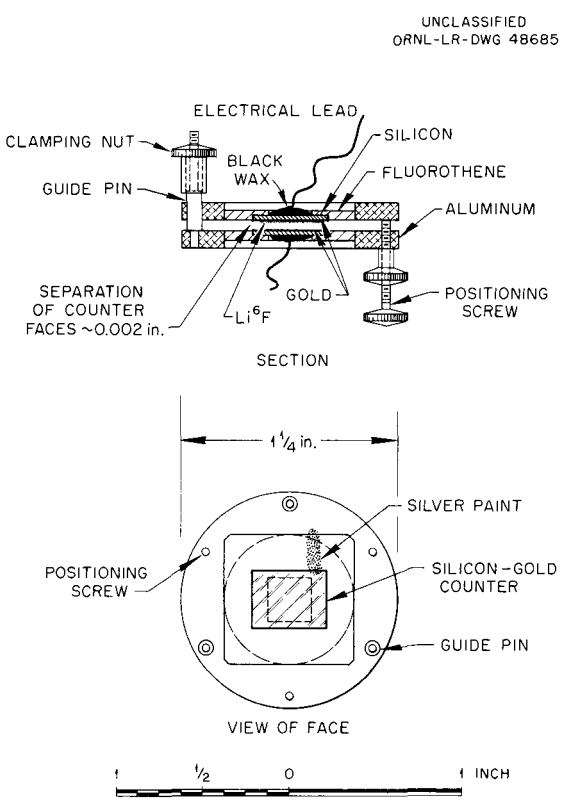

Fig. 8.8.1. Construction Details of a Sandwich Counter.

A schematic diagram of the electrical connections and pulse-analyzing equipment is shown in Fig. 8.8.2. Electrical contact to the gold surface of each counter was made by a narrow streak of silver paint leading from the periphery of the gold surface to the aluminum ring (see Fig. 8.8.1). The aluminum rings were then electrically grounded. The reverse bias, about 30 v, was applied through a 500,000-ohm resistor, and the signal was

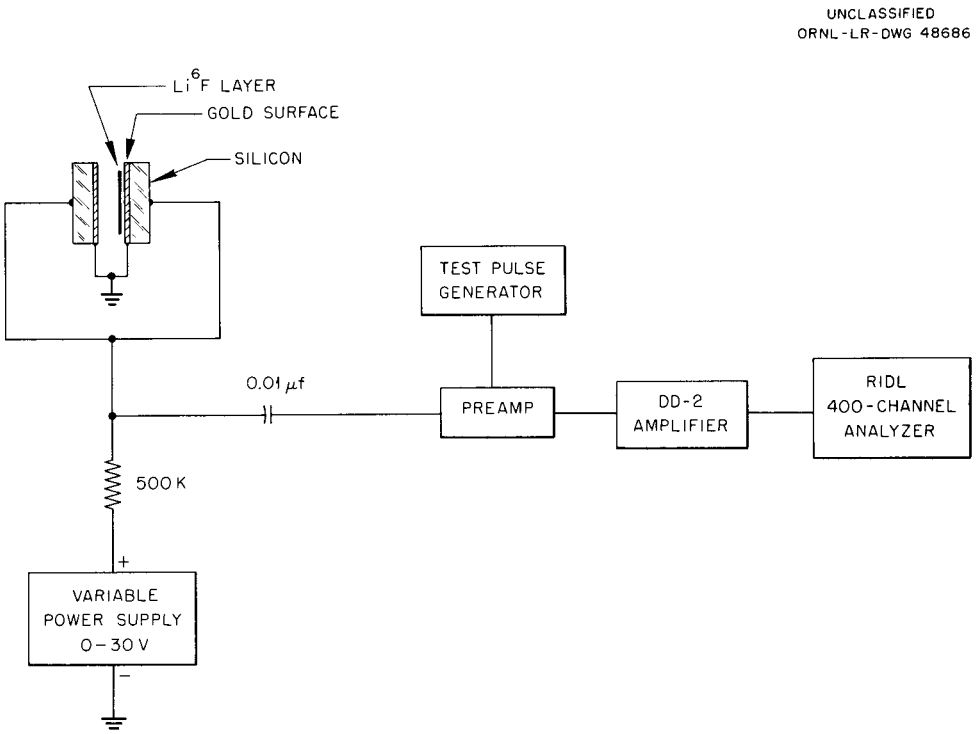

Fig. 8.8.2. Electrical Connections to Counter, and Pulse Circuitry.

fed through a coupling capacitor to a low-noise preamplifier. The signal was then fed to a DD-2 double-delay-line amplifier with a 1.2-μsec clipping time. The amplified signal was analyzed in an RIDL 400-channel analyzer. The linearity and zero position of the analyzing equipment were checked between experimental runs with a mercury-relay test-pulse generator whose signal was fed to the preamplifier input.

Experimental Pulse-Height Spectra and Discussion

T(p,n)He^3 Neutrons. – Pulse-height spectra have been recorded from neutrons incident on several sandwich detectors. In the first set of experiments, neutrons of known energy were produced by the T(p,n)He^3 reaction, using the ORNL 5-Mv Van de Graaff generator to accelerate the incident protons. The target consisted of a layer of ZrT, of nominal thickness 1 mg/cm^2, which had been evaporated on a platinum backing. The sandwich counter in all cases was placed at 0° with respect to the proton beam and was located about 1 in. in front of the target. The plane of the Li^{6}F layer was perpendicular to the direction of the proton beam. Neutron energies were calculated from published tables,[3] taking into account the energy loss of protons passing through the ZrT layer. The full energy spread of neutrons incident on a sandwich counter, arising from both proton energy loss and the angular acceptance of the counter, was

[3] J. L. Fowler and J. E. Brolley, Jr., *Revs. Mod. Phys.* **28**, 103 (1956).

small compared with the neutron-peak width in the pulse-height spectra. Slow neutrons (thermal and epithermal) were obtained by moderating fast neutrons, obtained from the $T(p,n)He^3$ reaction or from a Po-Be source, by blocks of paraffin.

A typical pulse-height spectrum from slow neutrons on counter 1 is shown in Fig. 8.8.3. The full width at half maximum is measured as 0.27 Mev. An approximate calculation of the slow-neutron pulse-height spectrum, based on the energy loss of the charged particles in Li^6F and gold, indicates that the slow-neutron peak should occur at a pulse height corresponding to 4.6 Mev (rather than the Q value of 4.78 Mev). The percentage spread in the slow-neutron peak is thus 0.27/4.6 = 5.9%. The shape of the slow-neutron (or fast-neutron) peak is expected to be non-Gaussian and asymmetric by virtue of the energy-loss processes responsible for the peak width. A low-energy tail is expected in all cases, contributing counts in the spectrum from the peak down to zero pulse height.

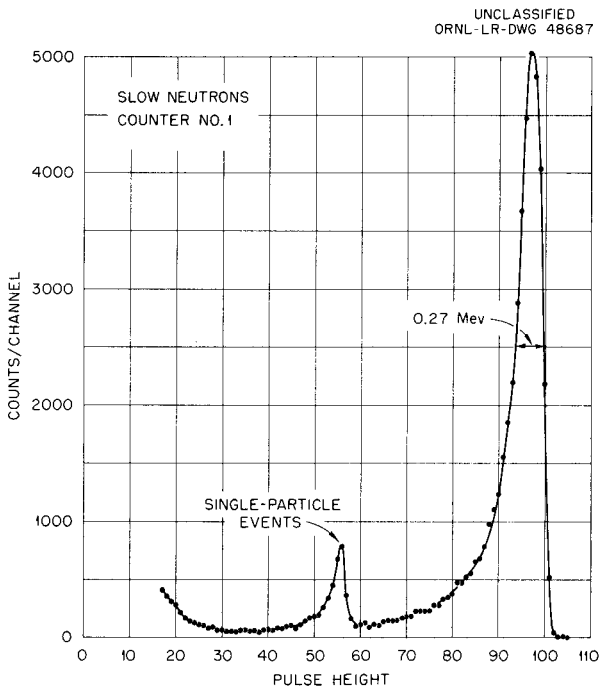

Fig. 8.8.3. Pulse-Height Spectrum from Slow Neutrons on Counter 1.

Figures 8.8.4 through 8.8.8 present pulse-height spectra for neutrons ranging from 0.59 to 3.50 Mev taken with counter 1. In every case a well-defined fast-neutron peak is observed, whose full width at half maximum is indicated on the spectrum. A subsidiary slow-neutron peak is also observed in the spectrum and arises from the presence of a small number of degraded, low-energy neutrons. These low-energy neutrons apparently are slowed in the immediate vicinity of the counter itself, since the relative intensities of the fast- and slow-neutron peaks were essentially unaffected upon surrounding the counter with a cadmium shield. A possible neutron moderator is a blob of Apiezon wax on the back of each counter, securing the pigtail lead. An additional

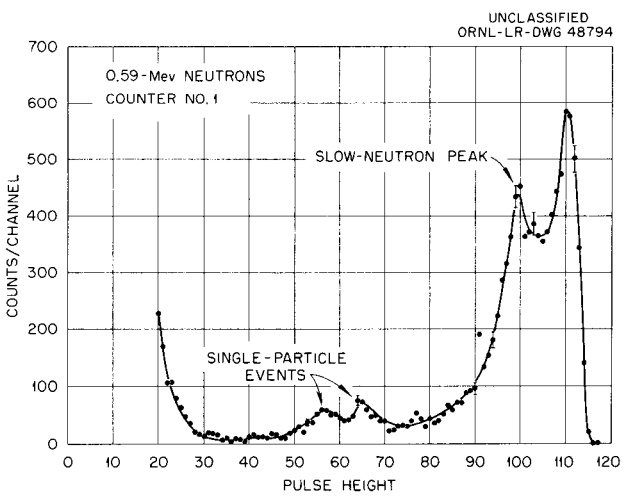

Fig. 8.8.4. Pulse-Height Spectrum from 0.59-Mev Neutrons on Counter 1.

effect to be noted in the fast-neutron spectra is a very large and steep background below the slow-neutron peak. The energy corresponding to the cutoff of this background is very closely correlated with the incident neutron energy, indicating that this effect is due to recoil protons following (n,p) scattering. Additional experiments have confirmed that this is the case and that the source of recoil protons is the thin peripheral band of polystyrene previously described. Both the wax and polystyrene layer have been eliminated in later counters by substituting fluorocarbon materials, resulting in the elimination or reduction of these background effects.

In Fig. 8.8.3 a clearly defined hump occurs below the slow-neutron peak and is labeled "single-particle events." Similar maxima may be observed in the fast-neutron spectra. These maxima arise from events predominantly occurring near the edge of the Li^6F layer. As a result of the finite separation distance between the two counters, there is a certain probability that an event will occur in which the alpha and triton are emitted at a small angle to the plane of the Li^6F layer such that one of the particles will be counted while the other escapes entirely. Thus the pulse-height spectrum from monoenergetic neutrons should in principle display three peaks: one due to the simultaneous capture of

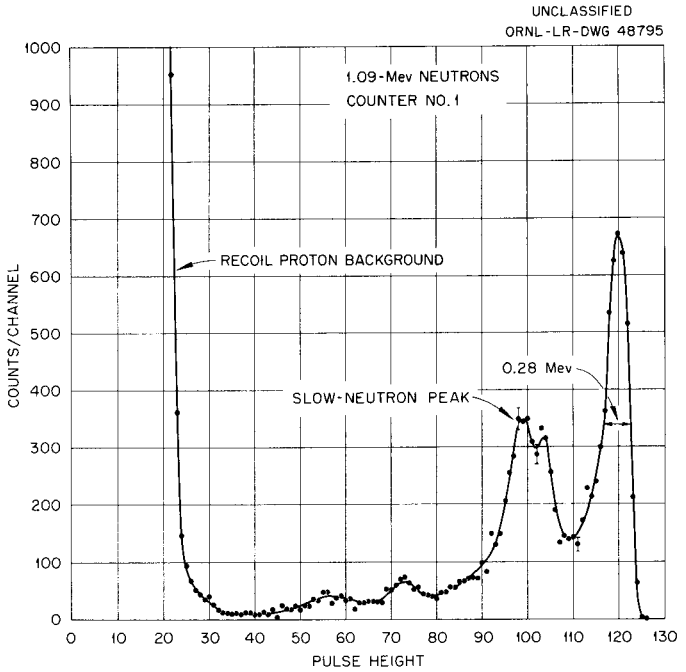

Fig. 8.8.5. Pulse-Height Spectrum from 1.09-Mev Neutrons on Counter 1. Small hump at pulse height 104 is probably due to 0.25-Mev resonance in $Li^6(n,\alpha)T$ cross section.

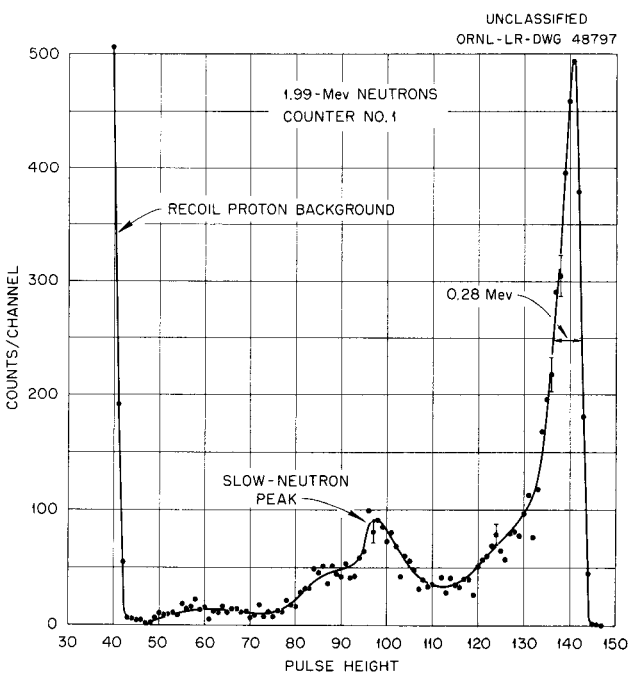

Fig. 8.8.6. Pulse-Height Spectrum from 1.99-Mev Neutrons on Counter 1.

both alpha and triton to give the full-energy peak, one due to capture of the alpha with escape of the triton, and one due to capture of the triton with escape of the alpha. In practice, however, the peak due to alpha capture with escape of the triton is expected to occur at a low pulse height and to be very broad and smeared; this follows from the large energy loss of the alpha in penetrating the Li^6F and gold at small angles. In a practical case then, one would expect to observe only two distinct peaks, as in Fig. 8.8.3. It can be seen in Fig. 8.8.3 that the slow-neutron peak, equivalent to 4.6 Mev deposited, occurs at pulse height 97; the triton-capture peak, equivalent to slightly less than 2.73 Mev, should occur just below pulse height 58, in agreement with experiment. The alpha-capture peak is not observed. The "edge effect" discussed here can be minimized in two ways: (1) by minimizing the separation distance of the two counters, and (2) by evaporating the Li^6F layer over an area less than that of the silicon counter, leaving a blank strip around the border. Both techniques were employed with later counters used in the present study.

$D(d,n)He^3$ and $T(d,n)He^4$ Neutrons. – In a second set of experiments neutrons were produced by either the $D(d,n)He^3$ or the $T(d,n)He^4$ reaction; deuterons were accelerated in a 200-kv Cockcroft-Walton accelerator onto a thick target of either ZrD or ZrT. In these experiments the silicon counters were constructed with fluorocarbon compounds

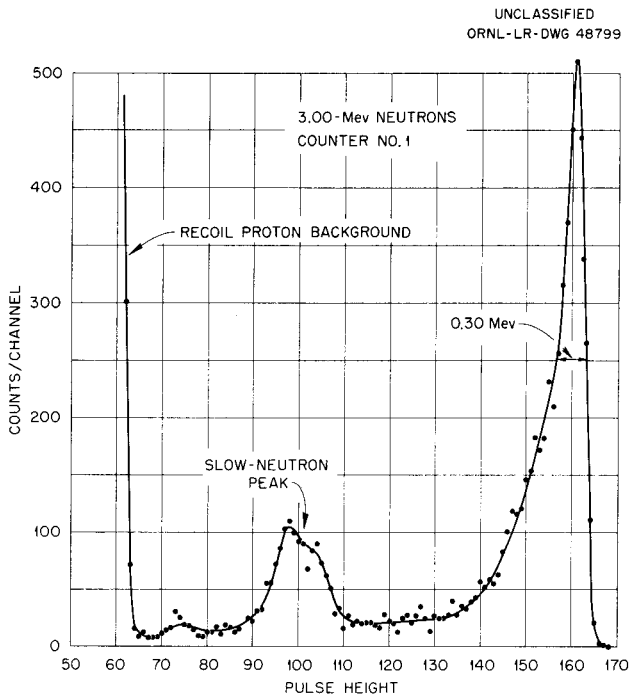

Fig. 8.8.7. Pulse-Height Spectrum from 3.00-Mev Neutrons on Counter 1.

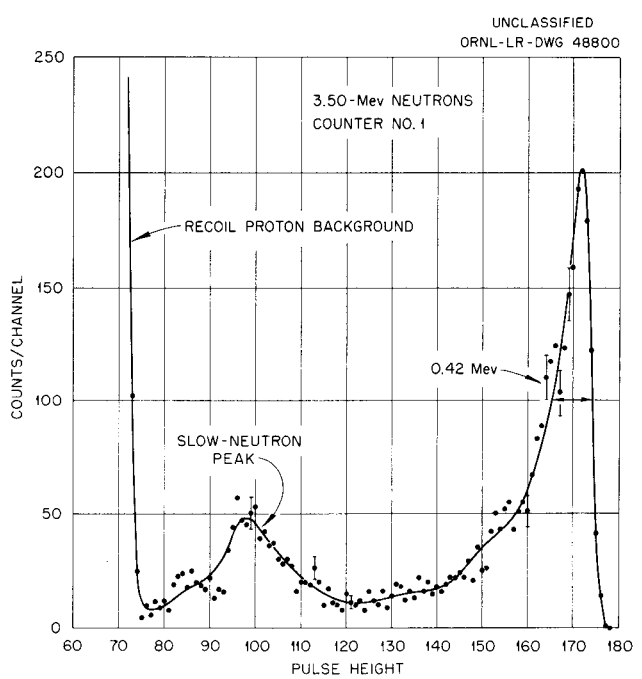

Fig. 8.8.8. Pulse-Height Spectrum from 3.50-Mev Neutrons on Counter 1.

instead of the polystyrene and Apiezon wax in earlier counters. An additional feature was the use of a fast-coincidence circuit (resolving time, 0.1 μsec) requiring simultaneous events in the two counters comprising a sandwich, thus recording $Li^6(n,\alpha)T$ events in which the alpha and triton are stopped in separate counters, but eliminating those cases (largely due to background effects) in which an event occurs in only one counter. A coincidence count was recorded only for those events in which the pulse amplitude from each counter corresponded to an energy deposition of 1.6 Mev or more.

Figure 8.8.9 presents pulse-height spectra resulting from $D(d,n)He^3$ neutrons of energy 2.95 Mev. The spectra shown were measured both with and without the coincidence requirement,

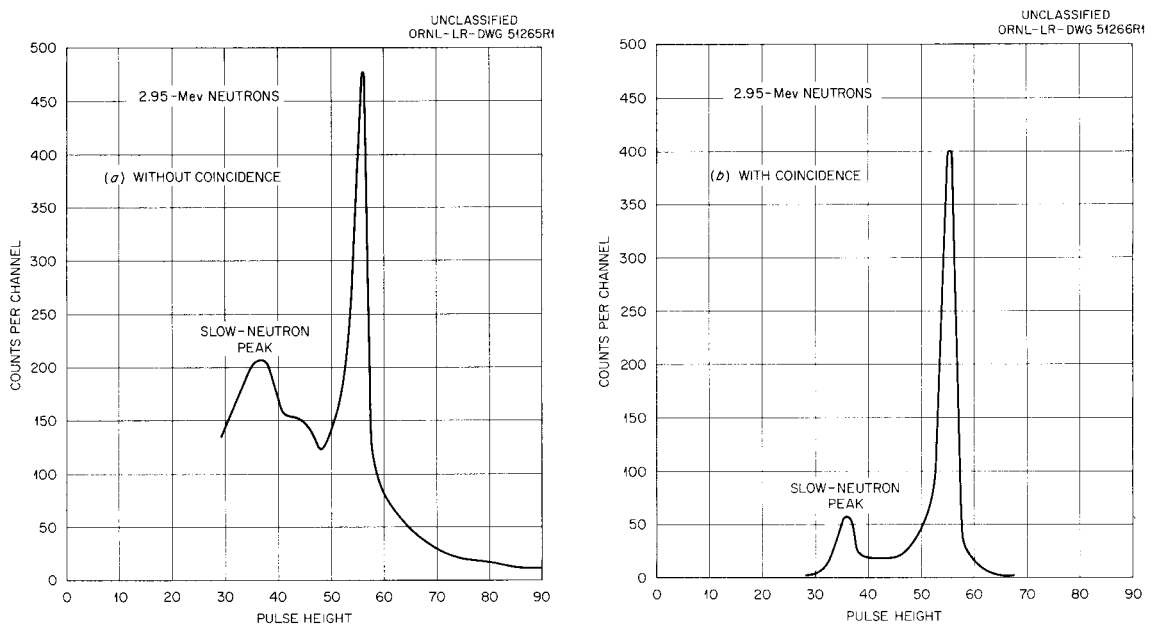

Fig. 8.8.9. Pulse-Height Spectra from 2.95-Mev Neutrons, With and Without Coincidence Circuit.

as indicated on the figure. The continuous background observed in Fig. 8.8.9*a*, without coincidence, is attributed to events resulting from 14-Mev neutrons which arise from the $T(d,n)He^4$ reaction due to a small amount of tritium present as a contaminant in the target and beam tube. In particular, the background observed above the $D(d,n)He^3$ peak must be due to higher-energy neutrons, since the (n, charged particle) reactions in the counter which might contribute to a background are generally endothermic and could not give counts at such a high pulse height. The pulse-height spectrum with coincidence (Fig. 8.8.9*b*) is seen to be much cleaner, indicating that the background events of Fig. 8.8.9*a* occur predominantly in one counter only.

Figure 8.8.10 presents pulse-height spectra resulting from $T(d,n)He^4$ neutrons, of energy 14.7 Mev. In this case, the spectrum is seen to be significantly different from those obtained

with lower-energy neutrons in that the $Li^6(n,\alpha)T$ fast-neutron peak represents only a small fraction of the total counts recorded. Two pulse-height spectra are shown in Fig. 8.8.10, one from a sandwich counter with the Li^6F layer, and one from a sandwich counter without Li^6F. The two counters were otherwise essentially identical in construction and were exposed to the same number of neutrons during the recording of the pulse-height spectra. Clearly, the very large background below the $Li^6(n,\alpha)T$ peak arises from (n, charged particle) events in the silicon and gold and is not associated with the Li^6F. Furthermore, the spectra of Fig. 8.8.10 were recorded with the coincidence requirement, so that the observed background counts must correspond to simultaneous events in both counters. There are a number of (n, charged particle) reactions in both silicon and gold which are energetically possible at 14 Mev and which can contribute to the background, for example, (n,p) and (n,α) reactions. The magnitude of the observed background indicates that the major contribution must arise from silicon, since it constitutes the bulk of the counter. The results of Fig. 8.8.10 indicate that this type of detector is of limited use for neutrons in this energy range.

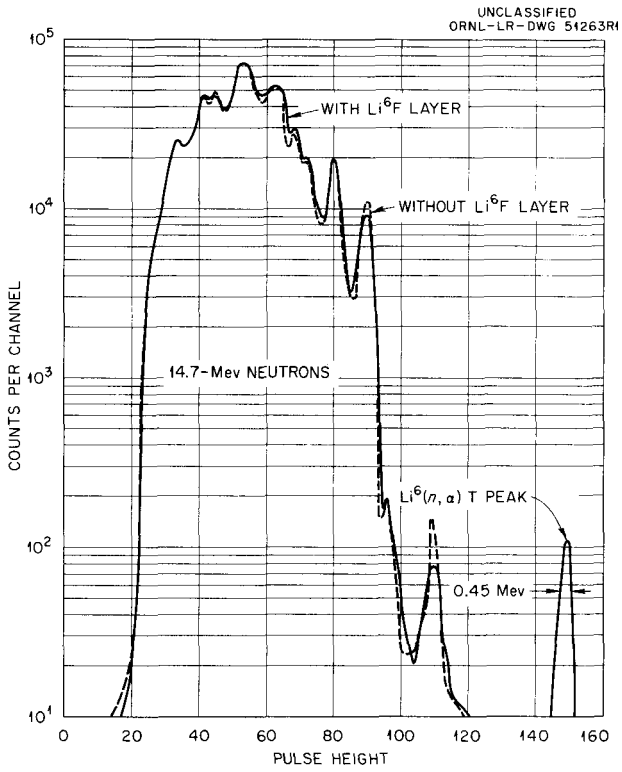

Fig. 8.8.10. Coincidence-Pulse-Height Spectra from 14.7-Mev Neutrons from Counters With and Without an Li^6F Layer.

Referring now to Figs. 8.8.4 through 8.8.10, it is seen that the full width at half maximum ranges from 0.28 to 0.45 Mev. These figures should not be taken exactly, as they are derived from only one set of runs with relatively few total counts in each spectrum. The important points to note are that the neutron-energy spread is relatively constant, of the order of 300 kev, and that the neutron-energy resolution improves rapidly with increasing energy. The fractional width $\Delta E_n/E_n$ decreases from ~30% at 1 Mev to ~10% at 3 Mev and to 3% at 14 Mev. It is of interest to calculate the shape and width of the fast-neutron peak to determine whether the experimentally observed peak width approaches the theoretical value. Such a calculation has been initiated by F. S. Alsmiller and is reported in Sec 8.9.

The pulse-height-vs-energy relationship, according to the present results, is apparently linear or very nearly so, as expected. It is not possible to determine this relationship precisely on the basis of the present work since the total energy deposited in the counters by a neutron of energy E_n is not simply $E_n + Q$ but is less than this by an amount which depends on

the thicknesses of the Li^6F and gold layers and on the angular distribution of the reaction products. As indicated previously, thermal neutrons result in the deposition of about 4.6 Mev. In the absence of detailed calculations for fast-neutron cases, one does not know accurately the energy deposited in a fast-neutron event. As a first approximation, however, a plot of pulse height vs (E_n + 4.6 Mev) can be reasonably fitted with a straight line through the origin, including the 14-Mev point.

Finally, preliminary experiments were carried out to examine the effect of gamma-ray backgrounds on the neutron-counting properties of these detectors. A counter was placed adjacent to a paraffin block in which a Po-Be source had been placed, and the pulse-height spectrum from slow neutrons was recorded. The slow-neutron peak was centered at channel 100 with a fractional width of about 6%. A 0.6-curie Co^{60} gamma-ray source was then placed 5 in. from the detector and the spectrum was rerun. No significant change was observed in the pulse height, width, or count rate in the slow-neutron peak. A steep background occurred, however, at low pulse heights, cutting off at about channel 20. On the basis of this experiment, it is tentatively concluded that these counters offer rather strong discrimination against gamma-ray backgrounds. The large positive Q value of the $Li^6(n,\alpha)T$ reaction, of course, provides a built-in bias against any background event up to 4.6 Mev.

Conclusions

The experiments summarized here indicate possible future application of sandwich counters of this type to certain problems involving the detection and spectroscopy of fast neutrons. The principal advantages of such a counter appear to be its simplicity of construction and operation, its small size, and a reasonably good resolution for neutrons above 1–2 Mev. A further advantage is that the counter accepts neutrons from any direction, eliminating the need for neutron collimation. The detection efficiency is limited by the thickness of the Li^6F layer. A layer 150 $\mu g/cm^2$ thick, as used in the present counters, offers a detection efficiency of 3.4×10^{-3} for thermal neutrons and 0.94×10^{-6} for 2-Mev neutrons, assuming normal incidence of the incoming neutron. These efficiencies are, of course, rather low and limit the use of this technique to experiments with sufficiently high neutron intensities. The efficiency can be increased by the use of thicker Li^6F layers at the expense of broadening the peak width. Another possibility for increasing efficiency is that of stacking, say, 5 to 10 counters together.

8.9 THE DISTRIBUTION IN ENERGY OF ALPHA-TRITON PAIRS RESULTING FROM NEUTRON BOMBARDMENT OF LITHIUM FLUORIDE

F. S. Alsmiller

The employment of paired silicon-gold surface-barrier counters (with an intervening Li^6F layer) to record the sum of the energies of the triton and alpha particle produced in an $Li^6(n,\alpha)T$ reaction, as a measure of the incident neutron energy, has been described in Sec 8.8.

In this paper we consider the problem of calculating the shape and width of the distribution in total energy $N(W)$ of the pairs reaching the silicon. Preliminary results are reported.

A uniform beam of neutrons of energy E_n is assumed incident in the z direction normal to the plane of the Si-Au-LiF-Au-Si sandwich. The (n,α) reaction takes place at some point, $z(0 \leqq z \leqq T)$, in the LiF layer of thickness T. In the laboratory system the total energy available, E_n plus the reaction Q value, and the angle of emergence of the triton, ψ, determine the initial energies, E_{α_0} and E_{t_0}, of the alpha particle and the triton as well as the angle of emergence of the alpha particle χ. Figure 8.9.1 depicts the geometry of the problem. The particles are assumed to travel in straight-line paths in their initial directions, with a continuous rate of energy loss $-dE/dr = N\epsilon(E)$, where N is the density of stopping-material atoms or molecules and $\epsilon(E)$ is the stopping cross section for the charged particle of interest. (Subscripts t or α will be used to denote tritons or alpha particles and L or A the stopping materials, LiF or Au.)

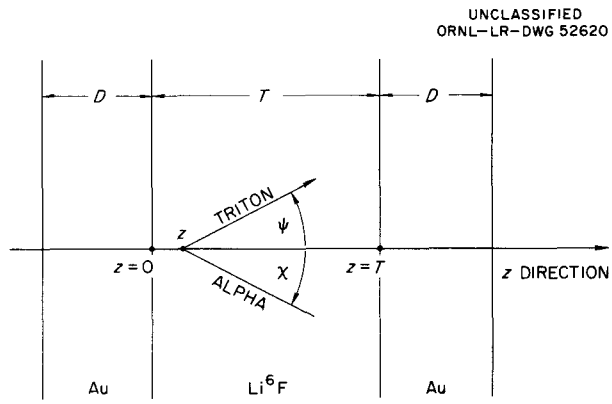

Fig. 8.9.1. Geometry for Calculation of Distribution in Energy of Alpha-Triton Pairs Resulting from Neutron Bombardment of Lithium Fluoride.

The simplest set of equations which does not completely ignore the energy dependence of the stopping cross section is obtained by approximating ϵ for each particle in each medium by its value at the appropriate initial energy, $E_{\alpha_0}(\psi)$ or $E_{t_0}(\psi)$. With this understanding, the energy loss for the triton is

$$\Delta E_t = E_{t_0} - E_{t_{\text{final}}}$$

$$= \frac{N_L \epsilon_{tL}(T - z) + N_A \epsilon_{tA} D}{\cos \psi} \tag{1a}$$

if ψ is in the first quadrant, and

$$\Delta E_t = \frac{N_L \epsilon_{tL} z + N_A \epsilon_{tA} D}{|\cos \psi|} \tag{1b}$$

if ψ is in the second quadrant. The energy loss for the alpha particle can be similarly written:

$$\Delta E_\alpha = E_{\alpha_0} - E_{\alpha_{\text{final}}}$$

$$= \frac{N_L \epsilon_{\alpha L}(T - z) + N_A \epsilon_{\alpha A} D}{\cos \chi} \tag{2a}$$

if χ is in the first quadrant, and

$$\Delta E_\alpha = \frac{N_L \epsilon_{\alpha L} z + N_A \epsilon_{\alpha A} D}{|\cos \chi|} \tag{2b}$$

if χ is in the second quadrant.

In Eqs. 2*a* and 2*b*,

$$E_{\alpha_{\text{final}}} = W - E_{t_{\text{final}}} \quad ,$$

where W is the total energy of the pair when each particle has reached a silicon layer. The total energy loss is

$$\Delta W = \Delta E_t + \Delta E_\alpha = E_n + Q - W \quad . \tag{3}$$

Differentiating yields

$$\left.\frac{dz}{dW}\right)_\psi = \frac{\cos \psi}{N_L} \left(\epsilon_{\alpha L} \frac{\cos \epsilon}{\cos \chi} + \epsilon_{tL} \right)^{-1} \quad . \tag{4}$$

Let σ_L be the differential cross section for lithium atoms in the laboratory system for the $Li^6(n,\alpha)T$ reaction so that $N_L \sigma_L |dz|$ is the fraction of alpha-triton pairs born in the distance interval $|dz|$ per unit triton solid angle. Then $N(W)$, the fraction of pairs detected at energy W, per unit energy range, is given by

$$N(W) = N^{(1)}(W) + N^{(2)}(W) \quad ,$$

where

$$N^{(i)}(W) = 2\pi N_L \int_{\psi^{(i)}_{\min}(W)}^{\psi^{(i)}_{\max}(W)} \sigma_L(\psi) \left| \left.\frac{dz}{dW}\right)_\psi \right|_{(i)} \sin \psi \, d\psi \quad , \quad (i = 1, 2) \; . \tag{5}$$

The term $N^{(1)}(W)$ is computed with triton angles restricted to the first quadrant and alpha-particle angles to the second; $N^{(2)}(W)$ is computed with the quadrants reversed.

The kinematically possible case in which both particles emerge in the forward hemisphere is excluded because only events in which both counters are activated are recorded. Also excluded, for the same reason, are "single-particle" events in which one particle is completely stopped before reaching a silicon layer.

The limiting angles depend on the range of the final energy W. It is obvious that in each quadrant of ψ values, there exist both a minimum energy loss, $\Delta W_{min}^{(i)}$, and a most-probable energy loss, $\Delta W_p^{(i)}$, at which the corresponding partial distribution $N^{(i)}(W_p)$ has its maximum value. Table 8.9.1 summarizes the prescriptions for obtaining these losses, as well as $\psi_{min}^{(i)}$ and $\psi_{max}^{(i)}$ above and below $W_p^{(i)}$, while Table 8.9.2 lists computed values of the minimum and most-probable energy losses for several values of the incident neutron energy.

It is clear that the maximum of the total distribution will fall somewhere between the two partial maxima, which thus serve to bracket it.

Figure 8.9.2 shows the shape of the calculated total distribution curve, near its peak, for the case of purely thermal neutrons ($E_n = 0$) and the assumption of an isotropic reaction cross section, σ_L. The maximum occurs at an energy loss of 210 kev for a gold thickness of 50 $\mu g/cm^2$ and an Li^6F thickness of 150 $\mu g/cm^2$. The width at half-maximum is 220 kev.

Calculations of $N(W)$ for higher-energy neutrons are in progress and will be reported, along with a more detailed discussion of the entire problem, in another paper.

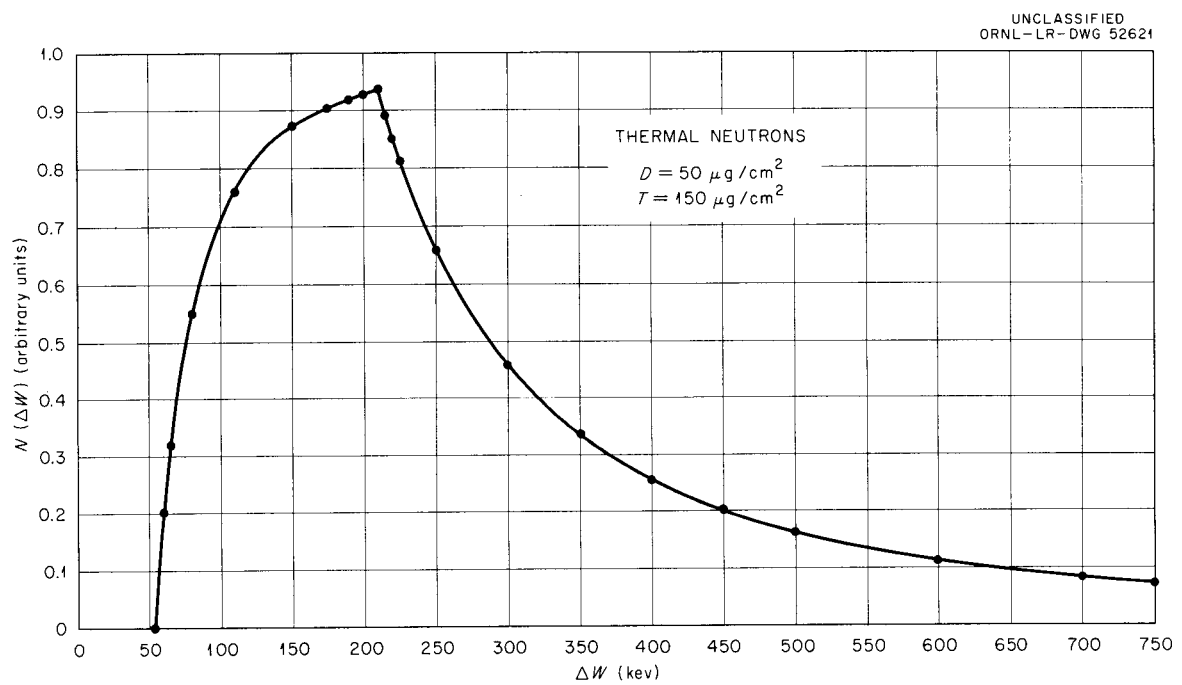

Fig. 8.9.2. Calculated Energy Loss Distribution for Thermal Neutrons Incident on a Silicon Diode Detector.

Table 8.9.1. Summary of Procedures to Determine Limiting Triton Angles in Various Energy Ranges

Case	Range of ΔW			$i = 1$ $0 \leqq \psi < \psi_c$*	$i = 2$ $\pi/2 < \psi < \pi$
I		$(\Delta W)_{min}$	determined by Eqs. 1, 2, and 3 if	$z = 0;\ \psi = 0$	$z = T;\ \psi = \pi$
II	$(\Delta W)_p \geqq \Delta W \geqq (\Delta W)_{min}$	$\psi_{min}(W)$ or corresponding z		$\psi_{min} = 0$	$z = T$
		$\psi_{max}(W)$ or corresponding z		$z = 0$	$\psi_{max} = \pi$
III		$(\Delta W)_p$		$z = T;\ \psi = 0$	$z = 0;\ \psi = \pi$
IV	$(\Delta W)_a \geqq \Delta W \geqq (\Delta W)_p$	$\psi_{min}(W)$		$z = 0$	$z = T$
		$\psi_{max}(W)$		$z = T$	$z = 0$
V		$(\Delta W)_a$		$z = T;\ \Delta E_\alpha = E_{\alpha_0}(\psi)$	$z = 0;\ \Delta E_\alpha = E_{\alpha_0}(\psi)$
VI	$(\Delta W)_b \geqq \Delta W \geqq (\Delta W)_a$	$\psi_{min}(W)$		$z = T$	$\Delta E_\alpha = E_{\alpha_0}(\psi)$
		$\psi_{max}(W)$		$\Delta E_\alpha = E_{\alpha_0}(\psi)$	$z = 0$
VII		$(\Delta W)_b$		$z = 0;\ \Delta E_t = E_{t_0}(\psi)$	$z = T;\ \Delta E_t = E_{t_0}(\psi)$
VIII	$(E_n + Q) \geqq \Delta W \geqq (\Delta W)_b$	$\psi_{min}(W)$		$\Delta E = E_{t_0}(\psi)$	$\Delta E_\alpha = E_{\alpha_0}(\psi)$
		$\psi_{max}(W)$		$\Delta E_\alpha = E_{\alpha_0}(\psi)$	$\Delta E = E_{t_0}(\psi)$

*For $\psi_c(E_n) \leqq \psi < \pi/2$), both particles emerge in the forward hemisphere; that is to say, $0 < \chi \leqq \pi/2$.

Table 8.9.2. Calculated Values of the Minimum and Most-Probable Energy Losses for Various Neutron Energies

Neutron Energy (Mev)	Minimum Energy Loss		Most-Probable Energy Loss	
	$\Delta W^{(1)}$ (kev)	$\Delta W^{(2)}$ (kev)	$\Delta W^{(1)}$ (kev)	$\Delta W^{(2)}$ (kev)
Au Thickness, 50 $\mu g/cm^2$; Li^6F Thickness, 150 $\mu g/cm^2$				
0	53.6	53.6	210	210
0.60	49.1	54.1	236	167
2.00	43.4	51.2	239	135
8.00	31.5	39.3	210	80.0
14.00	25.8	32.5	179	59.7
Au Thickness, 75 $\mu g/cm^2$; Li^6F Thickness, 150 $\mu g/cm^2$				
0	63.9	63.9	220	220
0.60	60.7	63.1	247	176
2.00	54.0	59.1	250	142
8.00	41.0	45.0	219	85.6
14.00	34.2	37.3	187	64.5

8.10 LIGHT OUTPUT OF CsI(Tl) UNDER EXCITATION BY GAMMA RAYS

R. Gwin R. B. Murray

Introduction

A series of experiments designed to investigate the light output of CsI(Tl) under excitation by monoenergetic gamma rays has been essentially completed. These experiments represent the first portion of a program investigating the fundamental scintillation properties of CsI(Tl), with particular emphasis on the investigation of the nature of the energy transport process in the crystal.

A theoretical model, relating the light output of an activated inorganic scintillator to its stopping power for particles of a given energy, and to the density of activator sites, has been proposed by Meyer and Murray (see Sec 8.7, this report). Their theory predicts that the light output of the alkali halides under excitation by charged particles is not a linear function of the particle energy. Such nonlinearity has been observed for gamma rays incident on NaI(Tl) by Engelkemeir[1] and Managan.[2] [Zerby *et al.* (see Sec 8.12) correlate the nonlinearity of the

[1] D. Engelkemeir, *Rev. Sci. Instr.* 27, 589 (1956).

[2] W. W. Managan, in *Applied Gamma-Ray Spectrometry* (ed. by C. E. Crouthamel) p 56, Pergamon Press, New York, 1960.

response to gamma rays with the nonlinear response of the crystal to the electrons produced in the crystal by the gamma rays.] In order to examine the prediction of the theory that such behavior is characteristic of other members of the alkali halide group, CsI(Tl) was chosen for these experiments.

Experimental Method

The fundamental scheme of the experimental program consisted in the measurement of the light output of CsI(Tl) for gamma rays of various energies *relative* to the output for a standard gamma ray, chosen to be the 662-kev gamma from the decay of Cs^{137}. The CsI(Tl) crystal was grown by Harshaw Chemical Co. and contained about 0.1 wt % thallium. A 3-mm-thick, 2.5-cm-dia slice cut from the ingot was coupled through a Lucite light pipe to an RCA C-7261 photomultiplier tube.

The current output of the photomultiplier was integrated, the resulting voltage pulse amplified by a DD-2 amplifier, and then analyzed by a 20-channel analyzer. In order to measure the pulse heights developed in the experimental measurement with a minimum of dependence on calibration of electronics, the following method was employed: The shape of the pulse generated by a mercury relay pulse generator was closely matched to the shape of the pulse developed by the experimental system. The generator pulse was then introduced into the electronic system at the preamplifier and the generator voltage adjusted until the pulse appeared in the desired analyzer channel. The generator voltage was then measured by a Rubicon precision potentiometer. This scheme was used to measure pulse heights developed by the photomultiplier and, in particular, the height corresponding to the maximum of the pulse-height spectrum. The experimental data, then, are the count rates as a function of pulse height, where the pulse height is precisely evaluated by comparison with the pulse from the pulse generator. The pulse height at the peak of the count-rate distribution is then taken to be characteristic of the gamma ray under observation. A unit experiment involves these measurements for the given gamma-ray source and for the 662-kev Cs^{137} standard source. The data obtained are thus relative to the standard source and are completely independent of the high voltage applied to the photomultiplier, the amplifier gain, and the analyzer zero. The main sources of experimental uncertainty inherent in the measuring equipment then are short-term drifts. Since the gain of a photomultiplier tube is extremely sensitive to the voltage applied to the cathode, the output of the high-voltage supply was continuously monitored. Drifts were negligible over the duration of an experiment. The intensities of the individual gamma-ray sources were such that the anode current was always less than 0.05×10^{-6} μamp, in order to minimize dynode fatigue effects in the photomultiplier.

Ideally, the gamma-ray source used in experiments of this type should be completely monoenergetic. Unfortunately, in the low-energy region the usual gamma sources are largely K x-ray sources. Since K x-ray sources are in general composed of four monoenergetic x rays, each of

which gives rise to an individual Gaussian distribution of pulse height vs count rate, an uncertainty exists in the definition of an average energy. The superposition of Gaussians yields an asymmetric peak in the pulse-height spectrum, with the detailed shape dependent on instrument resolution.

The approach taken in this work was to locate the peak of the asymmetric distribution and then to assign an average energy to this peak in the manner described below. For photons whose energies are close together, as in the K x-ray series, the over-all instrument resolution is very nearly the same, and it can be shown that the peak of a K x-ray distribution is given by the transcendental equation

$$V_M = \frac{\sum_i N_i V_i e^{-\alpha^2 (V_M - V_i)^2}}{\sum_i N_i e^{-\alpha^2 (V_M - V_i)^2}} , \tag{1}$$

where

V_M = pulse height at which the maximum of the composite curve occurs,

V_i = pulse height at the maximum of the individual Gaussian distribution from a monoenergetic gamma ray of energy E_i,

α = constant, determined by the experimental resolution,

N_i = relative number of transitions yielding an x ray of energy E_i.

Since the magnitude of the pulse developed by the photomultiplier assembly is proportional to the product of the light output per unit incident energy, $L(E_\gamma)/E_\gamma$, times the gamma-ray energy, E_γ, Eq. 1 can be written

$$\frac{L_M(\bar{E})}{\bar{E}} \bar{E} = \frac{\sum_i N_i [L(E_i)/E_i] E_i e^{-\alpha^2 (V_M - V_i)^2}}{\sum_i N_i e^{-\alpha^2 (V_M - V_i)^2}} , \tag{2}$$

and, if $L(E)/E$ is nearly constant over the energy range considered,

$$\bar{E} = \frac{\sum_i N_i E_i e^{-\alpha^2 [L(\bar{E})/\bar{E}]^2 (\bar{E} - E_i)^2}}{\sum_i N_i e^{-\alpha^2 [L(\bar{E})/\bar{E}]^2 (\bar{E} - E_i)^2}} . \tag{3}$$

This value was used for an average E whenever a K x-ray source was used.

Results and Conclusions

The experimental results, encompassing a range of gamma-ray energies from 10 kev to 2.6 Mev, are shown in Fig. 8.10.1, where the pulse height per unit energy, $L(E_\gamma)/E_\gamma$, is plotted as a function of E_γ. From these results the nonlinearity of the light output of CsI(Tl) as a function of energy for gamma-ray excitation has clearly been demonstrated. The magnitude of the departure from linearity has been measured for the particular crystal employed, although somewhat different results may be obtained for crystals of other sizes. The data will permit a calculation of the light output per unit energy, $L(E_e)/E_e$, for CsI(Tl) in the same fashion as that performed for NaI(Tl) by Zerby *et al.*, described in Sec 8.12 of this report.

Page 296:

Replace Fig. 8.10.1 with new figure below.

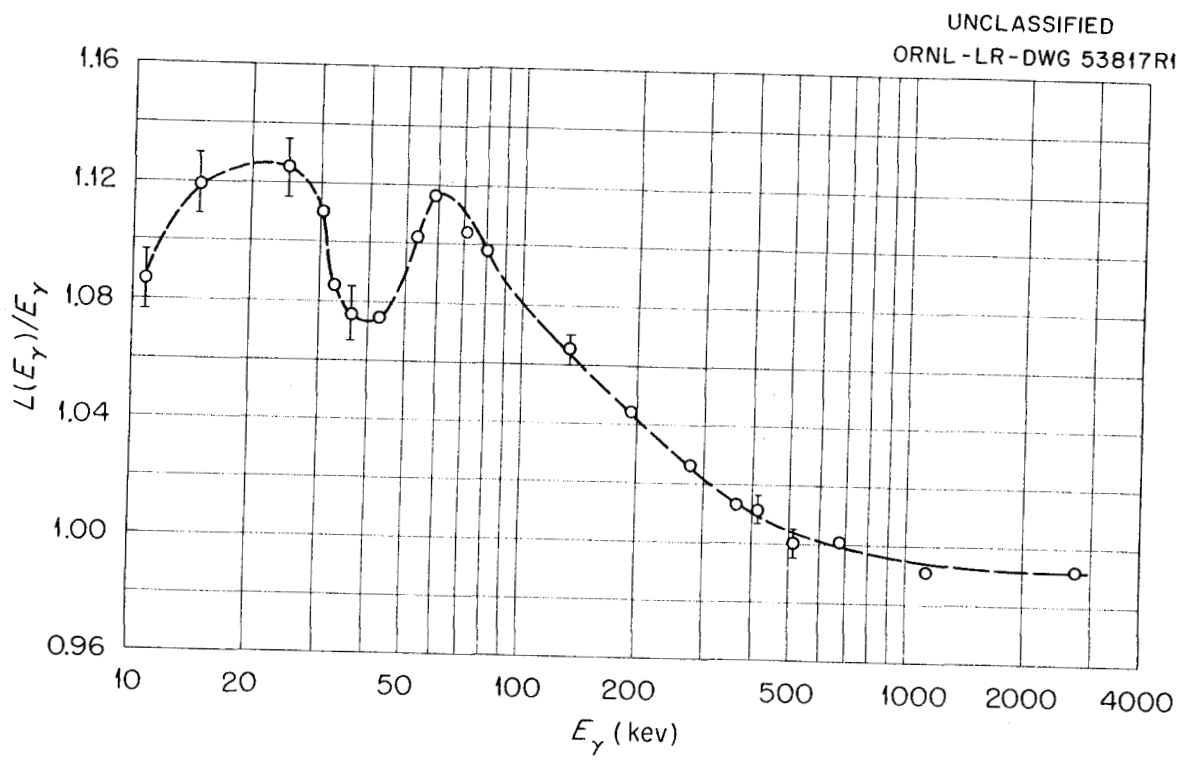

8.11 COMPARISON OF CALCULATIONS OF SCINTILLATION-COUNTER RESPONSE FUNCTIONS FOR CsI WITH NaI CALCULATIONS AND CsI EXPERIMENTS

H. S. Moran C. D. Zerby

Introduction

There has been considerable interest evinced recently in the possibility of achieving better-defined pulse-height spectra by the use of CsI rather than NaI as a scintillator. In order to compare the two materials, calculations of their response functions have been made, using the IBM 704 codes described by Zerby and Moran.[1] In a second comparison, calculated CsI spectra have been compared with experimental results.

Comparison of Calculated Results

For the first comparison, that of calculated results for CsI vs calculated results for NaI, the two crystals were assumed to have linear dimensions that were inversely proportional to the crystal densities, which are in the ratio of 1.227 (ref 2). On this basis, the volume of the CsI crystal is 0.665 that of the NaI crystal, and the weight of the CsI is 0.816 that of the NaI.

Figure 8.11.1 shows a comparison of the calculated responses of the two crystals to 0.662-Mev gamma rays. The CsI crystal, shown in solid outline, was assumed to be 5 in. in diameter by 3 in. long. The corresponding NaI crystal is indicated by the dashed outline. The source was assumed to be point isotropic at a distance of 12 in. from the crystal, with the gamma rays collimated to impinge on a ½-in.-dia circle centered on the face of the crystal. Both curves are normalized to one source photon, rather than at the photopeak, as one might suspect at first glance. The intrinsic efficiencies and photofractions are seen to be very nearly equal, with a very slight edge favoring CsI. Both cases were run with 2000 source particle histories. The broadening coefficients for both cases were obtained from experimental data for the two materials.

The calculated responses of the CsI and NaI crystals to the combined energies of 1.368- and 2.754-Mev gamma rays, which are the energies of the gamma rays from the decay of Na^{24}, are shown in Fig. 8.11.2. In this case, the CsI crystal was taken to be 5 in. in diameter by 3½ in. long. Again, the same proportionality exists between the CsI and the NaI dimensions. The source geometry is here the same as for Fig. 8.11.1. As before, both curves are normalized to one source photon. The intrinsic efficiencies are seen to be in close agreement. Since the two discrete source energies were run separately for each material and the spectra then normalized and compounded, the photofractions for the combined spectra cannot be shown; however, at each of the two energies the CsI photofraction was 6% higher than that for NaI.

---

[1] C. D. Zerby and H. S. Moran, *Neutron Phys. Ann. Prog. Rep. Sept. 1, 1959*, ORNL-2842, p 185; see also sec 8.6, this report.

[2] This basis for comparison was suggested by G. T. Chapman.

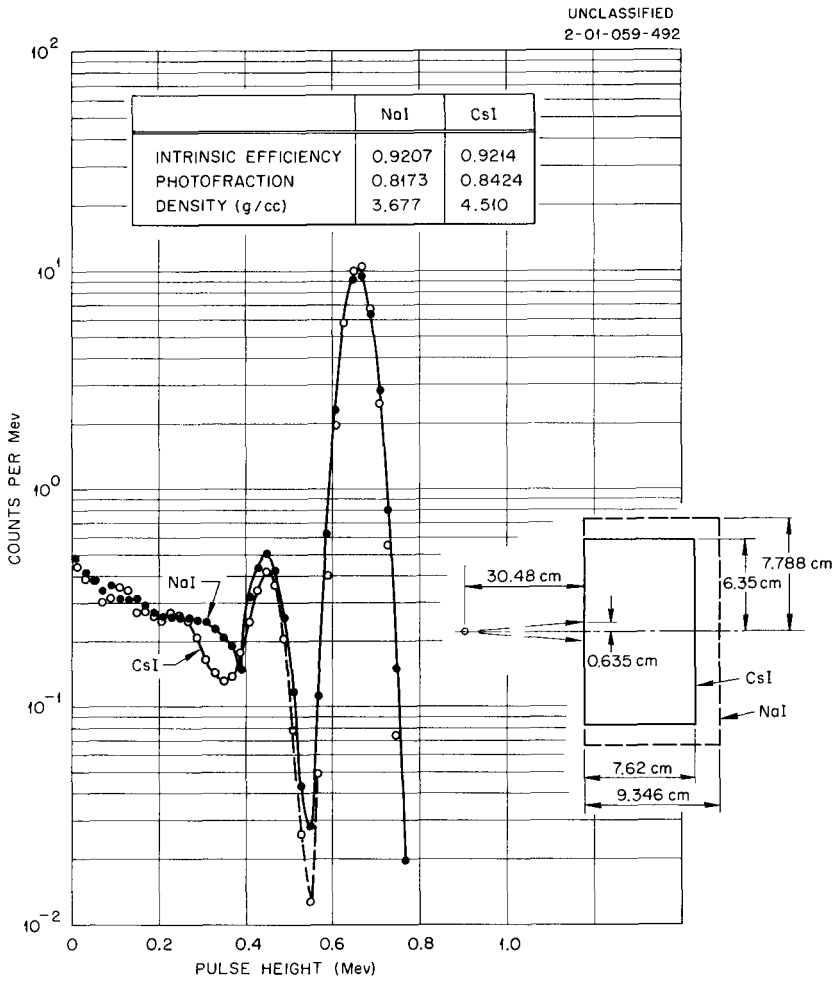

Fig. 8.11.1. Comparison of Calculated NaI and CsI Pulse-Height Spectra, Normalized to One Source Photon, at 0.662-Mev Source Energy.

It is apparent from Figs. 8.11.1 and 8.11.2 that the pulse-height spectra for the two scintillators are in reasonable agreement. Although the electron density and the photoelectric and pair cross sections are greater for CsI than for NaI, neither an increased height of photopeak and escape peak nor a lowering of the low-energy end of the Compton tail for CsI was indicated by these comparisons. The calculations demonstrate that the use of CsI instead of NaI offers comparable intrinsic efficiency and a slight improvement in photofraction, along with a decrease of about one-third in volume and 20% in weight for the crystals and geometries calculated. However, from a practical viewpoint the greater cost of CsI crystals at present may negate these advantages.

Figure 8.11.3 shows a similar comparison at a higher energy, 8.0 Mev. Source and crystal geometries are as before, and the normalization is unchanged. Here the low-energy end of the Compton tail is not shown, as the statistics were poor. The analytic-zero pulse-height values[1] were 1.05×10^{-2} for NaI and 9.2×10^{-3} for CsI, and the data appear to terminate at these

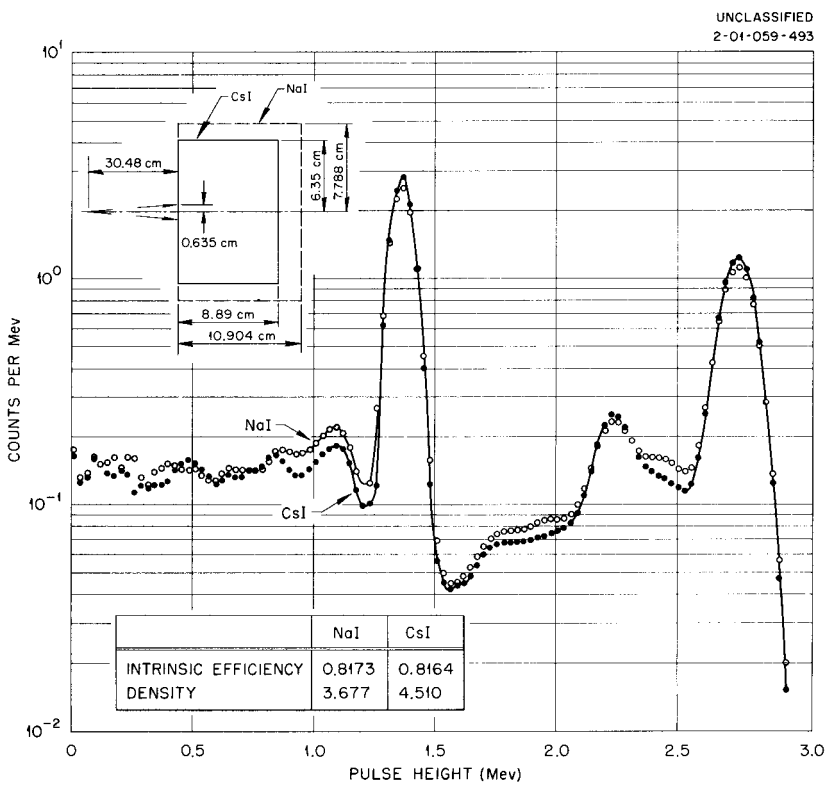

Fig. 8.11.2. Comparison of Calculated NaI and CsI Pulse-Height Spectra, Normalized to One Source Photon, at 1.368- and 2.754-Mev Source Energies.

points. This calculation was performed using the NaI bremsstrahlung, which is believed to be a considerable underestimate for CsI at all energies >3 Mev; thus, the figure also shows the pulse-height distribution with bremsstrahlung omitted in order to display the magnitude of the bremsstrahlung contribution. With the use of the correct CsI bremsstrahlung in the present code, one would expect the low-energy portion of the CsI "all secondary" curve to be somewhat higher, with corresponding slight degradations of the peaks. In order to achieve the agreement shown in the lower-energy comparisons, therefore, the relative size of the CsI crystal would have to be increased, which in turn will increase both the intrinsic efficiency and the photofraction and bring the peak efficiencies of CsI and NaI into closer agreement. The size increase has not been calculated, but the CsI is still expected to be smaller than the NaI.

Calculation vs Experiment

A comparison between calculational and experimental results simultaneously serves two purposes. First, it serves to measure the utility of the code, and second, the comparison aids in evaluating the background effects nonexistent in the code but nevertheless inherent in experiment. The experimental values used here were taken from work of Chapman, Love, and Schmidt,[3] at ORNL. The CsI crystal was 5 in. in diameter and 3½ in. high.

[3] C. Schmidt of Harshaw Chemical Co., which supplied the CsI crystal.

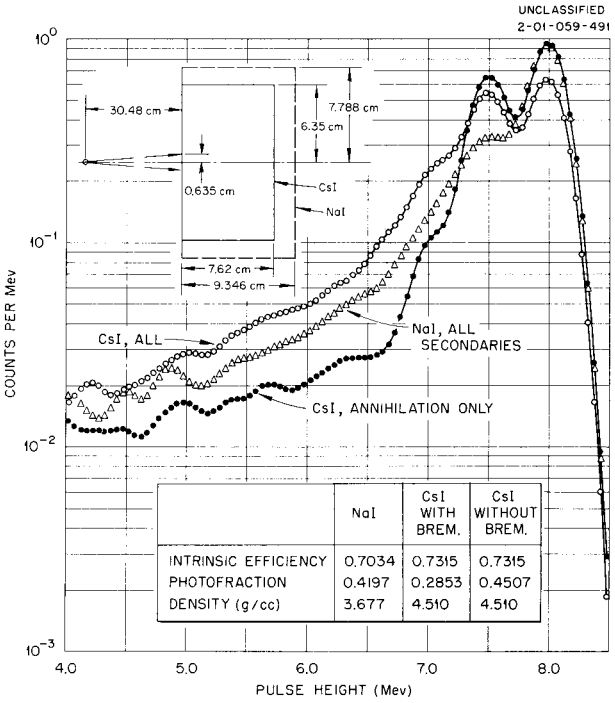

Fig. 8.11.3. Comparison of Calculated NaI and CsI Pulse-Height Spectra, Normalized to One Source Photon, at 8.0-Mev Source Energy.

Figure 8.11.4 shows a comparison between calculation and experiment for the Cs^{137} source at 0.662 Mev. Crystal and source geometries are as indicated; the curves were normalized at the photopeak. The area between the two indicates the experimental background effects attributed to backscattering and collimator effects.

Figure 8.11.5 shows a similar comparison for the Na^{24} source, with the same crystal and source geometries. Pulse-height spectra for the two energies were calculated separately, both normalized to one source photon and then added together. The compounded, calculated spectrum was then normalized to the experimental spectrum at the higher of the two photopeaks. As before, the

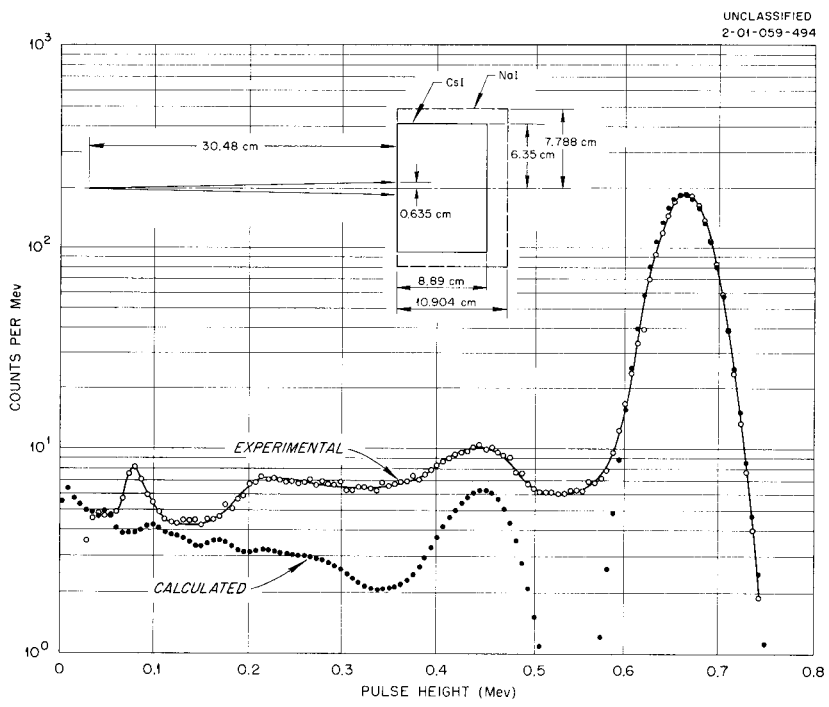

Fig. 8.11.4. Comparison of Calculated and Experimental CsI Pulse-Height Spectra, Normalized at the Photopeak, at 0.662-Mev Source Energy.

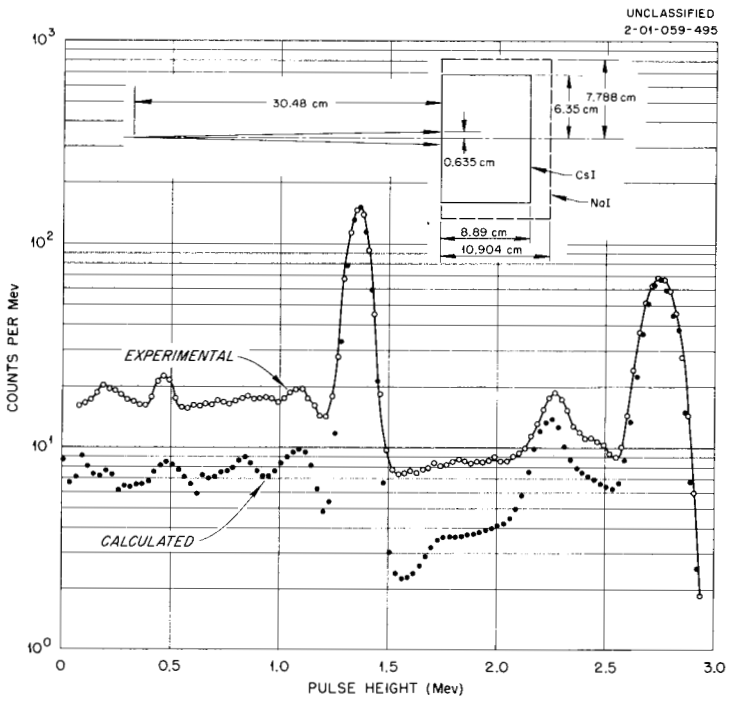

Fig. 8.11.5. Comparison of Calculated and Experimental CsI Pulse-Height Spectra, Normalized at the Photopeaks, at 1.368- and 2.754-Mev Source Energies (Na^{24}).

background effects can clearly be seen. The hint of a maximum on the calculated curve at 1.73 Mev corresponds to the second escape peak below 2.754 Mev, while the maximum at 0.86 Mev shows the first escape peak below 1.368 Mev. The peak at 0.5 Mev on the calculated curve is spurious and can be attributed to a random high point in the unbroadened spectrum. The corresponding peak in the experimental data is a background effect.

It is felt that these last two figures support the belief that the IBM 704 codes produce valid results and that they will prove useful for future contemplated crystal-parameter studies.

8.12 INTRINSIC LINE WIDTH IN NaI(Tl) GAMMA-RAY SPECTROMETERS

C. D. Zerby A. Meyer R. B. Murray

Introduction

In the use of NaI(Tl) scintillation crystals for gamma-ray spectroscopy it is of considerable importance to achieve a minimum line width in the pulse-height spectrum resulting from monoenergetic gamma rays. Much attention has been devoted to the various factors contributing to the line width of the full-energy peak; reviews of this subject are available elsewhere.[1,2]

Briefly stated, the over-all line width is the sum of two contributions. The first is the statistical fluctuation in the production of photons in the scintillation crystal by the incident gamma ray and in their escape to the cathode of the photomultiplier tube. The second is the fluctuation in the production of photoelectrons at the photomultiplier cathode and their subsequent multiplication in the dynode string of the photomultiplier. It is possible to separate the contribution of the photomultiplier from that of the scintillator by experiments in which the photomultiplier cathode is illuminated by an external, pulsed light source. Results[1-3] indicate that the contribution from the scintillator is surprisingly large and cannot be reasonably accounted for on the basis of inhomogeneities in the crystal, optical coupling, etc. For example, in one experiment[3] the over-all line width of 0.661-Mev gamma rays was 7.7%, composed of a 4.0% contribution from the photomultiplier and a 6.6% contribution from the scintillator. (Line width is expressed here as $\Delta E/E$, where ΔE is the full width at half maximum of a peak occurring at pulse-height E.)

The origin of the line broadening from the scintillation crystal has been in question for some years. It is the purpose of this paper to point out that the nonlinear response of NaI(Tl) to electrons results in an intrinsic broadening of the gamma-ray line and that the magnitude of this effect is such that it results in a significant contribution to the total line width.

Scintillation Response of NaI(Tl) to Gamma Rays

The pulse-height-vs-energy relationship for gamma rays on NaI(Tl) has been shown in numerous routine experiments to be a nearly linear function over a wide range of gamma-ray energies. A determination of the exact behavior of this relationship, however, requires very careful experimental methods, with special attention to the behavior of the electronic system used in recording pulse-height spectra. Detailed studies of this nature have been reported recently by Engelkemeir[4] and by Managan.[5] Their results, based on different sets of experiments

[1] W. E. Mott and R. B. Sutton, *Handbuch der Physik*, ed. by S. Flügge, vol 45, p 86, Springer, Berlin, 1958.

[2] C. E. Crouthamel (ed.), *Applied Gamma-Ray Spectrometry*, chap. 2, Pergamon Press, New York, 1960.

[3] G. G. Kelley *et al.*, *IRE Trans. Nuclear Sci.* NS-3, 57 (1956).

[4] D. Engelkemeir, *Rev. Sci. Instr.* **27**, 589 (1956).

[5] W. W. Managan, paper 5.10 of *Proc. Sixth Tripartite Instr. Conf.*, AECL-805 (1959); see also ref 2.

using basically different techniques, are in quite good agreement and indicate a distinct nonlinearity in the pulse-height-vs-energy relationship. This nonlinear behavior is most pronounced at energies below several hundred kev. An illustration of this nonlinearity is shown in Fig. 8.12.1, in which the pulse height per unit energy, L/E_γ, is plotted vs E_γ. The ordinate is

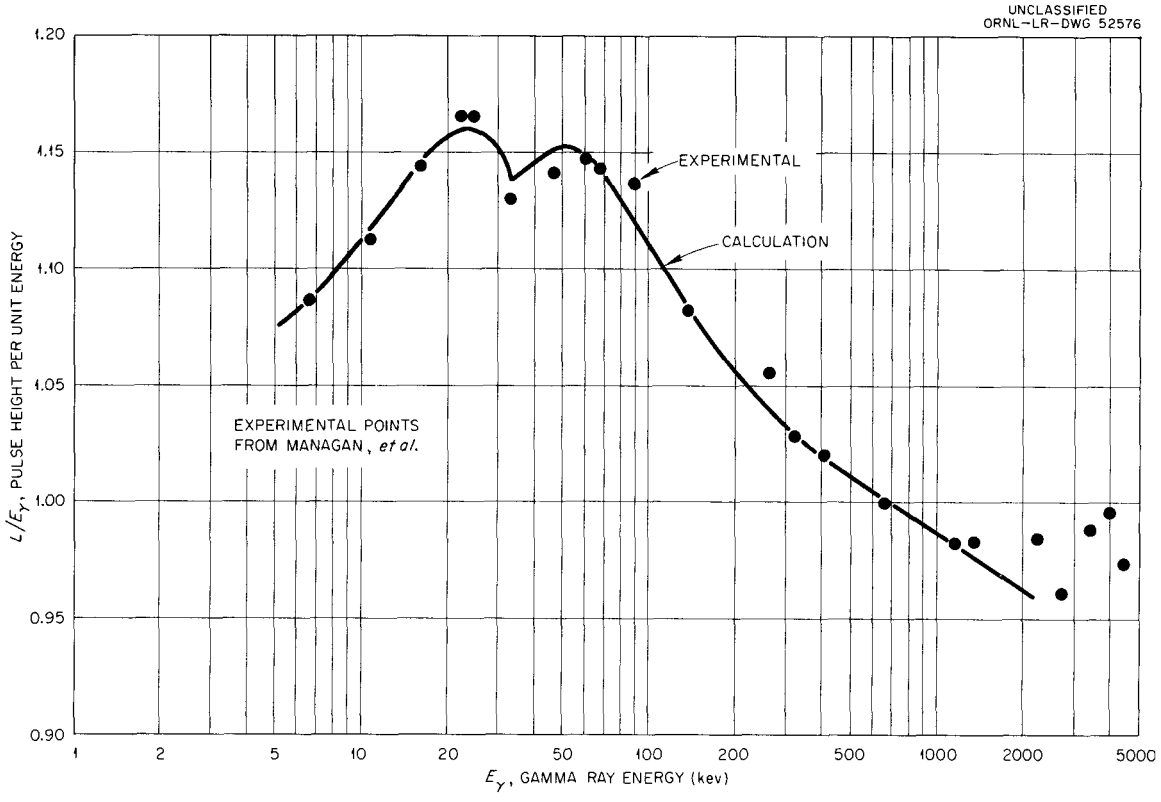

Fig. 8.12.1. Comparison of Calculated and Experimental Values of the Pulse-Height Response of a 2.5-in.-dia by 2-in.-high NaI(Tl) Crystal to Gamma Rays.

arbitrarily normalized to unity at 661 kev. The data points of Fig. 8.12.1 are unpublished results of experiments at Argonne National Laboratory.[6] The three lowest-energy data points are to be considered as tentative pending further experiments. The smooth curve of Fig. 8.12.1 is calculated as described below.

Scintillation Response of NaI(Tl) to Electrons

The scintillation response of NaI(Tl) to incident gamma rays results from the interaction of the gamma rays with the atomic structure to eject electrons which are subsequently stopped in the crystal. For this discussion it is important to obtain the dependence of the response of the crystal on the energy of these electrons. Since the observed nonlinear response to gamma rays

[6]Unpublished results of W. W. Managan, I. S. Sherman, S. I. Baker, and A. J. MacKay, Argonne National Laboratory.

can be accounted for by a nonlinear response to electrons, it is possible to deduce the required data, which is not directly obtainable from experiment.

For high-energy gamma rays the multiplicity of the interactions possible within the crystal can produce an energy spectrum of electrons which may vary considerably from one mono-energetic gamma ray to another. In the gamma-ray energy range below 100 kev, however, the main features of the gamma-ray response curve can be attributed to the response of the crystal to photoelectrons ejected by the first collisions of the incident photons and the subsequent electrons that appear as a result of the photoelectric event. The uncomplicated nature of the response induced by low-energy gamma rays makes it relatively easy to use the experimentally observed low-energy gamma-ray data to calculate the response of the crystal to low-energy electrons. In order to do this, a simplified model to account for the transitions that take place as a result of a photoelectric event must be adopted.

In the model chosen, the iodine atom was assumed to possess three electron levels, with the K-shell binding energy = 33 kev, the L-shell binding energy = 5 kev, and the M-shell binding energy = 1 kev. The transitions accompanying an L-shell photoelectric event initiated by a photon of energy E_γ were then assumed to take place in the following way: An electron, with energy (E_γ – 5 kev) is ejected from the L shell, with subsequent emission of two photons, one of energy 4 kev and another of energy 1 kev, resulting from electron transitions from the M to the L shell and from the continuum to the M shell, respectively. The 4-kev photon then initiates an M-shell photoelectric event, ejecting an electron of energy 3 kev accompanied by a 1-kev photon, emitted as a result of the electron transition from the continuum to the M shell. The two 1-kev photons are assumed to be converted to 1-kev electrons to complete the transitions. The total number of electrons resulting is: one electron with energy (E_γ – 5 kev), one with energy 3 kev, and two 1-kev electrons. In a similar manner one arrives at the following group of electrons as a result of the ejection of a K-shell electron in a photoelectric event: one of energy (E_γ – 33 kev), one with 23 kev, two with 3 kev, and four 1-kev electrons. Now, for gamma-ray energies above the K edge but below 100 kev we assume that the shape of the gamma-ray pulse-height-vs-energy curve results from the nonlinear response of all the electrons that appear from a photoelectric event with K-shell electrons. Below the energy of the K-edge but above the L-edge energy, the shape of the gamma-ray pulse-height curve is attributed to the electrons that appear from a photoelectric event with an L-shell electron. Under these assumptions a set of simultaneous equations can be set up to determine the pulse height per unit energy for each of the electrons that appears in the conversion after a photoelectric event by selecting values of E_γ and using the data from the L/E_γ-vs-E_γ curve as the total light output. The light output for all other electron energies up to approximately 70 kev can then be obtained from the L/E_γ curve by using the assumed model of photoelectric interactions and varying E_γ. Since the experimental data has some error and since the model of photoelectric interactions

was particularly simple, the resulting light output as a function of electron energy had a spread of values which depended on whether they were derived from gamma-ray energies above or below the K edge.

A smooth fit to the data was made, however, and is shown in Fig. 8.12.2 for $1 \leqq E_e \leqq 70$ kev. For $E_e > 70$ kev, the curve was first drawn in an arbitrary fashion and then adjusted by calculations described below. The ordinate of the final L/E_e-vs-E_e curve was arbitrarily normalized to unity at 3 Mev.

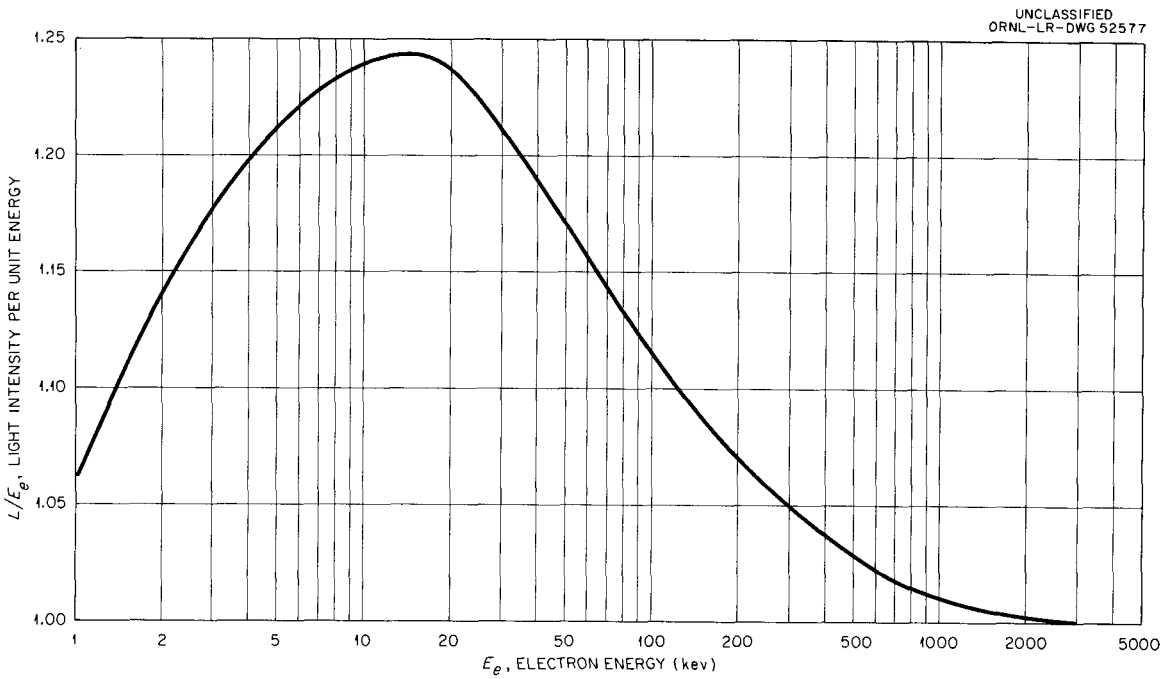

Fig. 8.12.2. Response of NaI(Tl) to Electrons, Deduced from Gamma-Ray Data.

Calculations of the Intrinsic Line Broadening and Pulse Height per Unit Energy for Gamma Rays

From the result of the previous discussion, it is now possible to demonstrate that the nonlinear response of NaI(Tl) to electrons results in an intrinsic broadening of a monoenergetic gamma-ray line. We assume for the moment that all electrons originating in the crystal are stopped and consider only those monoenergetic gamma rays which enter the crystal with an energy somewhat greater than 100 kev and terminate their history in a photoelectric event. Since the histories of the gamma rays vary considerably, the accumulated light output will vary from one gamma ray to another, because of the nonlinear response to the different Compton electrons and photoelectrons generated in each history. The variation in the accumulated light output is reflected in the spread in the pulse-height spectrum of totally absorbed, monoenergetic gamma rays.

In order to calculate the intrinsic broadening, an existing Monte Carlo code which was written to calculate the pulse-height response of NaI(Tl) to gamma rays (Sec 8.6, this report) was altered to include the nonlinear response to the electrons. For gamma-ray energies below the pair-production threshold, the total light output from each gamma ray was the accumulation of the responses of all the Compton electrons and photoelectric events. In the altered code, the light output from a photoelectric event was calculated by using the model described above. For gamma-ray energies above the pair-production threshold the additional complication of including the effects of the pair electrons was accomplished by first selecting the distribution of excess energy between the pair of electrons according to the Born approximation and then calculating the response to each member of the pair.

From the calculation the pulse-height spectrum was obtained in two forms. The first was a spectrum accounting only for the nonlinear response of the electrons, and the second was a version of the first which had been altered to include the broadening resulting from photomultiplier statistics. The full width at half maximum of the photomultiplier broadening was assumed to be given by $\Delta L = A\sqrt{L}$, where L is the pulse height, and A is a constant chosen according to typical experimental values. For a good photomultiplier, $\Delta L/L$ may be about 4% for the case of 661-kev gammas on NaI(Tl); in the calculation described here, A was chosen such that $\Delta L/L$ was 3.83% at 661 kev.

The final electron-response curve shown in Fig. 8.12.2 was the result of an iterative procedure in which a trial function, L/E_e vs E_e, was first introduced into the Monte Carlo code. The resulting L/E_γ-vs-E_γ curve was then compared with experiment; departures of the calculated curve from experiment dictated changes in the L/E_e curve to yield a second trial function, etc. The calculated gamma-ray response curve shown in Fig. 8.12.2 is the result of the last iteration.

The calculated pulse-height spectrum for the total absorption peak for 661-kev gamma rays is shown in Fig. 8.12.3. The histogram indicates the extent of the intrinsic broadening, and the smooth curve shows the same peak after the photomultiplier broadening has been folded in. Although the histogram is ragged, to a certain extent, because of the statistical nature of Monte Carlo calculations, the general features of the data can be easily explained. Of particular interest is the leading peak at the lower pulse-height values which is contributed by first-collision photoelectric events. The second peak is caused by the buildup of second-collision photoelectric events, and the valley between is real and not a result of statistics.

A measurement of the contribution of the intrinsic broadening to the total line width cannot be obtained directly from the histogram presented in Fig. 8.12.3, since it does not have a Gaussian shape. However, its effective resolution can be calculated from the expression $R_I = (R^2 - R_p^2)^{1/2}$, where R = 5.48% is the resolution of the line including photomultiplier broadening shown in Fig. 8.12.3, and R_p = 3.83% is the resolution of the photomultiplier broadening alone. The result is an intrinsic resolution of 3.92%. By similar means, the

intrinsic resolution has been calculated for other gamma-ray energies up to 2.5 Mev and is found to go through a maximum in the 400–500 kev region, reaching a value slightly above 5%. The intrinsic resolution is about 2.7% at 0.15 Mev and 1.5% at 2.5 Mev.

Finally, it is of interest to note that the electron response function L/E_e of Fig. 8.12.2 is simply related to the scintillation efficiency, dL/dE, discussed in Sec 8.7 of this report. In fact, the curve of Fig. 8.12.2 can be used to calculate the scintillation efficiency vs dE/dX for electrons in NaI(Tl). The results of this calculation, which are not shown here, are in good agreement with the behavior of the scintillation efficiency curve shown in Fig. 8.7.2 of Sec 8.7.

It may further be noted that, on the basis of the scintillation model of Meyer and Murray (Sec 8.7), the nonlinear response of NaI(Tl) to electrons arises as a fundamental aspect of the luminescence process in inorganic scintillators and may be expected in other alkali iodides such as CsI(Tl) or KI(Tl).

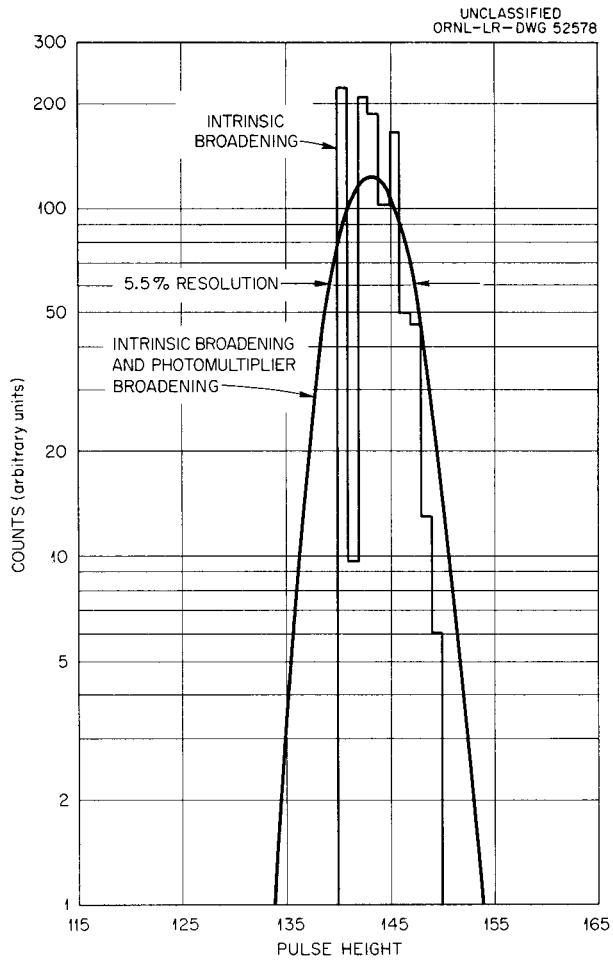

Fig. 8.12.3. Pulse-Height Spectrum in the Region of the Total Absorption Peak for a 661-kev Gamma-Ray Incident on a 2.5-in.-dia by 2-in.-high NaI(Tl) Crystal. Source-to-crystal distance = 10 cm.

Conclusions

The principal feature of this work is the demonstration that the nonlinear response of NaI(Tl) to electrons results in an intrinsic broadening in the line width when NaI(Tl) is used as a gamma-ray spectrometer. The calculated intrinsic line width may be combined with a semiempirical function describing the broadening due to photomultiplier statistics, permitting a calculation of the over-all line width due to these two effects. The line width so calculated represents a minimum value in that no account is taken of broadening due to an imperfect scintillation crystal and imperfect optical effects in the transport of scintillation photons to the photocathode. At 661 kev, the calculated minimum line width is found to be 5.5% for a 2.5-in.-dia by 2-in.-high crystal with the source 10 cm from the crystal face, which is to be

compared with experimental values of the over-all line width in the range 6–8%. It should be pointed out, however, that the intrinsic broadening must depend on the source configuration and crystal dimensions. This dependence has not been investigated, and it is difficult to estimate how sensitive the above results will be to changes in the crystal size and source-to-crystal separation distance without further calculations. A study of these effects will be made in the future.

Part 9

PLASMA PHYSICS THEORY

9.1 FOKKER-PLANCK COEFFICIENTS FOR A PLASMA INCLUDING RADIATION

A. Simon E. G. Harris

The pair-correlation equations, obtained from a generalization of the Rostoker-Rosenbluth expansion to include radiation, have been solved exactly in one special case: for a plasma whose zero-order distribution is static, uniformly distributed in space, and with no external magnetic or electric fields. The results are directly interpretable as coefficients of the Fokker-Planck equation.

The resulting coefficients consist of two terms. One corresponds to direct particle interaction via the Coulomb field. The second is due to interactions via transverse electromagnetic waves. The second term represents an additional contribution which is numerically small except for relativistic particles or under special resonant conditions.

A detailed paper describing this work is being prepared for publication elsewhere.

9.2 DISPERSION RELATIONS FOR PLASMA WAVES IN A FINITE CYLINDRICAL MEDIUM

P. B. Burt[1]

Consider a cylindrical shell of plasma with initial ion and electron density $N_0\ e(r)$, where $e(r)$ is a step function in the radial variable. The external magnetic field B_0 is in the negative z direction and is uniform. Initially the ions have velocities $r\omega_i$ in the θ direction, where ω_i is the ion Larmor frequency, and the electrons are stationary. We derive a dispersion relation for perturbations of this configuration.

The problem is formulated in a manner first employed by Langmuir and Tonks.[2] As a simplification we neglect the perturbed magnetic field.

In order to solve the coupled differential equations given in ref 2, we take an $\exp(i\omega t + ikz + il\theta)$ variation for all quantities and obtain coupled total differential equations in r only. The frequency ω can be complex. The dispersion relation subsequently obtained for a cylindrical shell of inner radius r_1, outer radius r_2, is

---

[1] Summer research participant; permanent address, University of Tennessee, Knoxville.

[2] I. Langmuir and L. Tonks, *Phys. Rev.* 33, 195 (1929). The author was advised of this treatment by E. G. Harris.

$$\left[I_l(kr) \frac{dI_L(pr)}{dr} - \frac{I_l(kr) I_L(pr)}{r} (A + l\alpha) - I_L(pr) \frac{dI_l(kr)}{dr} \right]_{r=r_1} \times$$

$$\times \left[K_L(pr) \frac{dK_l(kr)}{dr} - K_l(kr) \frac{dK_L(pr)}{dr} + \frac{K_l(kr) K_L(pr)(A + l\alpha)}{r} \right]_{r=r_2}$$

$$- \left[\frac{dK_L(pr)}{dr} I_l(kr) - \frac{I_l(kr) K_L(pr)(A + l\alpha)}{r} - K_L(pr) \frac{dI_l(Kr)}{dr} \right]_{r=r_1} \times$$

$$\times \left[I_L(pr) \frac{dK_l(kr)}{dr} - K_l(kr) \frac{dI_L(pr)}{dr} + \frac{K_l(kr) I_L(pr)(A + l\alpha)}{r} \right]_{r=r_2} = 0 .$$

Here I and K are Bessell functions of imaginary argument. The parameters are:

$$\omega_e = \text{Larmor frequency for electrons,}$$

$$\omega_{pi}^2 = 4\pi N_0 \frac{e^2}{m} = \text{plasma frequency of ions,}$$

$$\omega_{pe}^2 = 4\pi N_0 \frac{e^2}{m} = \text{plasma frequency of electrons,}$$

$$W^2 = 1 - \frac{\omega_{pi}^2}{(\omega + l\omega_i)^2} - \frac{\omega_{pe}^2}{\omega^2 - \omega_e^2} ,$$

$$p^2 = k^2 \left[1 + \frac{\omega_{pe}^2 \omega_e^2}{\omega^2(\omega^2 - \omega_e^2) W^2} \right] ,$$

$$2A = \frac{\omega_{pi}^2 l\omega_i}{(\omega + l\omega_i)^3 W^2} ,$$

$$L = \sqrt{l^2 + A^2} ,$$

$$\alpha = \frac{1}{W^2} \left[\frac{\omega_{pe}^2 \omega_e}{\omega(\omega^2 - \omega_e^2)} + \frac{\omega_{pi}^2 \omega_i}{(\omega + l\omega_i)^2} \right] .$$

Unfortunately, this dispersion relation does not exhibit any apparent simplifications.

9.3 EFFECT OF PLASMA POTENTIAL ON DCX STEADY STATE

T. K. Fowler

The effect of a plasma potential on the DCX steady state after burnout has been treated.[1] Because electrons are scattered out of the system more readily than ions, the plasma charges positively to a potential difference between the plasma interior and the machine walls of the order of the mean energy of the electrons, in order to prevent the escape of most of the electrons. This has the consequence that, in comparison with earlier results neglecting the potential, cold electrons flowing through the system drain much less energy from hot ions by collisions.

[1]T. K. Fowler, *Effect of Plasma Potential on DCX Steady State*, ORNL-2914 (1960); see also *Thermonuclear Project Semiann. Rep. July 31, 1960*, ORNL-3011 (to be published).

9.4 A THEORY ON OBTAINING SHORT BURSTS OF IONS FROM A BEAM OF IONS

T. K. Fowler W. M. Good[1]

Through special cases and a general theorem, the authors have in a recent paper[2] shown that, in all methods of obtaining short ion bursts by sweeping a steady beam across an aperture, shorter bursts are obtained at some cost in beam quality, particularly energy spread. For example, given a monoenergetic beam of width Δy and angular divergence corresponding to transverse momentum spread Δp, it is found that the energy spread ΔE in a burst chopped out of this beam and the burst duration Δt satisfy the complementary relation $\Delta E \Delta t = \Delta p \Delta y$, so that ΔE goes up as Δt goes down. This energy spread in turn places qualifications on further shortening the pulses by leading them through "bunching" fields. All results are subject to the assumptions that collective effects, such as space charge, are negligible and that the sweeping process employs only Hamiltonian forces (e.g., electric and magnetic fields).

[1]Physics Division.

[2]To be published in *Nuclear Instruments and Methods*.

9.5 DENSITY OF IONS OUTSIDE A MAGNETICALLY CONFINED ARC

R. G. Alsmiller, Jr.

The nonlinear equations governing the diffusion of ions out of a magnetically confined vacuum arc have been studied.[1] In the case of a single ion species, the equations may be solved in a linear geometry, but only approximate limiting solutions have been obtained in a cylindrical one. No results have been obtained in the case of more than one ion species.

Since the only available experimental data concerns cylindrical carbon arcs containing several ion species, no valid comparison between theory and experiment can be made.

[1]R. G. Alsmiller, Jr., *Thermonuclear Project Semiann. Rep. Jan. 31, 1960*, ORNL-2926, p 64.

Part 10

THEORETICAL NUCLEAR PHYSICS

10.1 THE ELECTROMAGNETIC PRODUCTION OF PION PAIRS

C. D. Zerby

The Pauli-Weisskopf[1] theory of the electromagnetic production of pion pairs has been investigated with the objective of including in it the strong pion-nucleus interaction which ultimately leads to an enhancement of the cross section. This was accomplished by the semiphenomenological method of including the interaction into the rigorous theory in the form of an optical model, a method first suggested by Landau and Pomeranchuk.[2]

In the Pauli-Weisskopf theory an essential element was the assumption that the pair production took place in the presence of an infinitely heavy charged nucleus, where the resulting Coulomb field provided a means of interaction between the meson field and the nucleus to transmit linear momentum, thereby obtaining conservation of energy and momentum. However, the Coulomb field is not the only method of interaction, since there exists a strong, nonelectromagnetic interaction between the meson field and the nucleon field, which can be introduced into the theory by means of an optical potential. Pomeranchuk[3] first examined the effects of the strong interaction on pair production, using a black-nucleus model. Later, Vdovin[4] used the optical model of Fernbach, Serber, and Taylor[5] to improve the theory in a high energy limit, neglecting the Coulomb field.

The optical model of Fernbach, Serber, and Taylor is based on the hypothesis that a complex optical potential can be introduced into the equations of motion of the pions. Although Vdovin did not explicitly display the dependence, it is a necessary step to further improvement of the theory and for further exact calculations. An examination of the field equations reveals that one can indeed explicitly display the optical potentials in the field equations if the imaginary part of the potential is introduced as a time component of a four-vector and the real part as a world scalar. The imaginary part of the potential leads to absorption which includes true absorption as well as all inelastic events that leave the nucleus in an excited state; the real part of the potential, on the contrary, introduces the coherent scattering of the pions from the nucleus as a whole. This means the resulting pair production cross section with these potentials included is for a residual nucleus in the ground state.

To obtain the cross section in the experimentally attainable region just above threshold (279-Mev photon energy) the matrix element for pair production,

$$M = -ie \int \vec{A}_q \left(\psi^*_{k_+} \vec{\nabla} \psi^*_{k_-} - \psi^*_{k_-} \vec{\nabla} \psi^*_{k_+} \right) d^3x \quad , \tag{1}$$

---

[1] W. Pauli and V. Weisskopf, *Helv. Phys. Acta* **7**, 709 (1934).

[2] L. D. Landau and Iu. Ia. Pomeranchuk, *Zhur. Eksptl. i Teoret. Fiz.* **24**, 505 (1953); English Translation: *Proc. CERN Symposium* **11**, 159 (Service d'Information; CERN, 1956).

[3] Iu. Ia. Pomeranchuk, *Doklady Akad. Nauk SSSR* **96**, 265 (1954); English translation: *Proc. CERN Symposium* **11**, 167 (Service d'Information; CERN, 1956).

[4] Yu. A. Vdovin, *Doklady Akad. Nauk SSSR* **105**, 947 (1955).

[5] S. Fernbach, R. Serber, and T. B. Taylor, *Phys. Rev.* **75**, 1352 (1949).

must be solved numerically. This form of the matrix element was arrived at by using first-order perturbation theory, where the interaction was between the pion field and the electromagnetic field, and ψ_{k_+} and ψ_{k_-} are the exact final-state wave functions of the π^+ and π^- mesons, respectively. The form of the final-state wave functions can be resolved unambiguously in the case where a complex potential is present and the equations can be conveniently solved in a spherical coordinate system.

The differential energy spectra for the pion pair production that result from the calculations when a distributed nuclear charge and complex square-well optical potential are present are shown in Fig. 10.1.1. The cross sections are in units of αR^2, where $\alpha = e^2/\hbar c$ is the fine structure constant and $R = e^2/Mc^2$ is the classical pion radius.

The square-well optical-potential parameters were taken from meson-nucleus scattering experiments and had values of −16 Mev for the real part and −5 Mev for the imaginary part. The charge-density distribution was assumed to conform with that obtained from the electron-nucleus scattering experiments and had the form of a Fermi-type distribution function:

$$\rho(r) = \frac{\rho_0}{1 + \exp\left[(r - c)/z_1\right]} \quad , \qquad (2)$$

where ρ_0, c, and z_1 are constants.

Figure 10.1.1 shows the enhancement of the low-energy π^- spectrum (high-energy π^+ spectrum) which is accounted for by the Coulomb force. This differs considerably from the symmetric spectrum about $v = (E - Mc^2)/(E_0 - Mc^2) = 0.5$

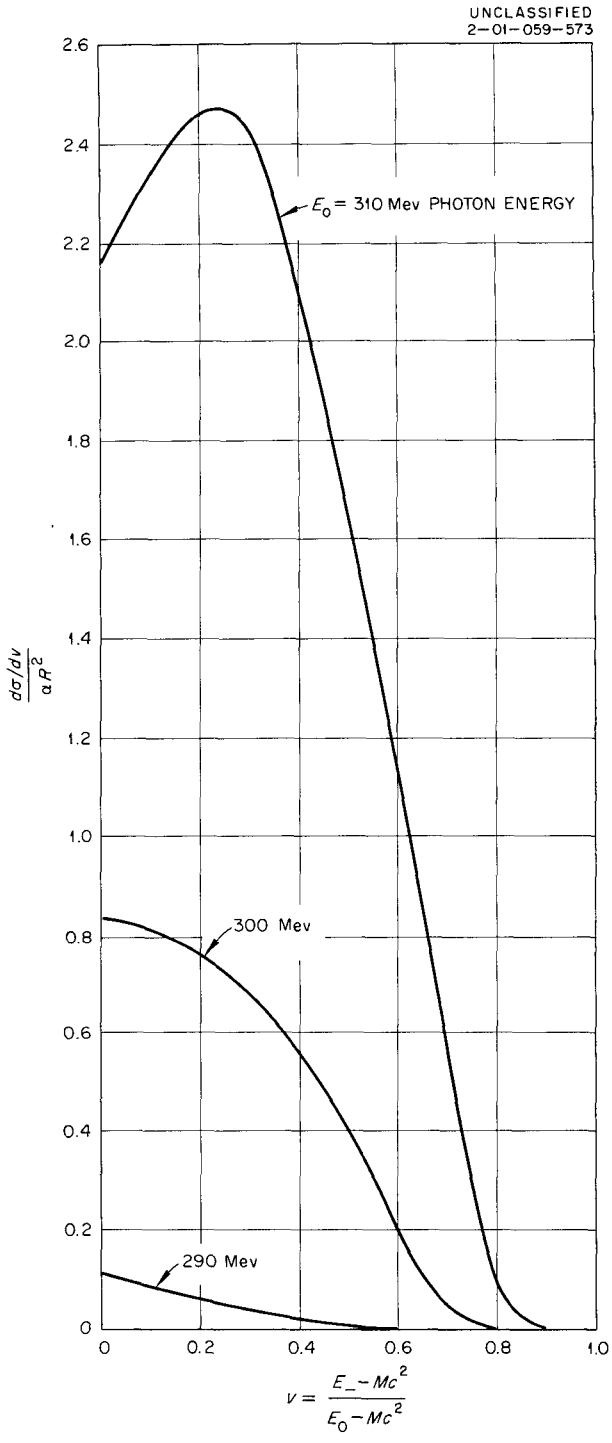

Fig. 10.1.1. Differential Pion Pair Production Cross Section.

which would be obtained if the Coulomb potential were neglected.

The total pion pair production cross section that results from integrating the differential energy spectrum data is shown in Fig. 10.1.2.

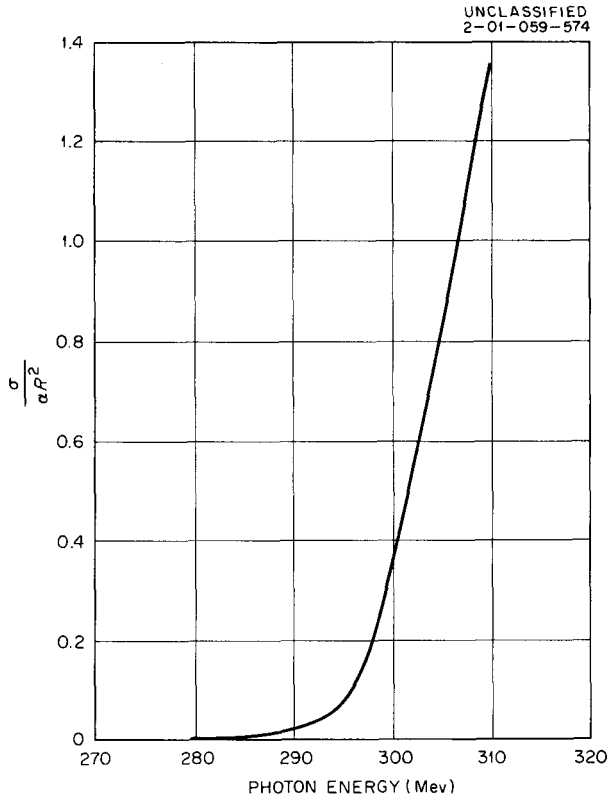

Fig. 10.1.2. Total Pion Pair Production Cross Section.

10.2 A STATISTICAL MODEL FOR NUCLEAR LEVEL SPACINGS

L. Dresner E. Inönü

Wigner's simple formula for the distribution of nuclear level spacings is known to agree very well with the nuclear data. Numerical experiments have shown that it also agrees with the distribution of spacings between adjacent eigenvalues of random symmetric matrices of large order.[1] With the purpose of understanding better the reasons for this success, we have investigated analytically the effects of a slight generalization on the model.

Wigner had pointed out that when two levels are very close together, the probability of finding a given spacing s between them is proportional to s itself, a fact which can be proved by using perturbation theory. By assuming, rather arbitrarily, that this proportionality extends

[1]For previous work on this problem, see L. Dresner, *Neutron Phys. Ann. Prog. Rep. Sept. 1, 1959*, ORNL-2842, p 229, and the references cited therein.

to all spacings, he then derived the spacing distribution:

$$p_w(s) = \rho s e^{-(1/2)\rho s^2} \quad , \tag{1}$$

where ρ is the proportionality constant. A deficiency of this model lies in its lack of information on the correlation between successive spacings. One way to correct this deficiency may be to argue as follows: again using perturbation theory, one can show that, for very small spacings, the joint probability of having N energy levels $\lambda_1, \lambda_2, \ldots, \lambda_N$ is proportional to the product $\prod_{i<j=2}^{N} (\lambda_j - \lambda_i)$, assuming that the λ_i's are chosen in increasing order. We now define a stochastic process by which N levels, λ_i, can be marked on the real axis successively in such a way as to ensure this proportionality for small spacings. The process is defined by saying that the conditional probability of finding the kth level at $d\lambda_k$ around λ_k is proportional to the product of its distances to all previous levels, that is, to $\prod_{j=1}^{k-1} (\lambda_k - \lambda_j)$. Limiting ourselves to the case $N = 3$, we then obtain an equation for $P(s/t)$, the conditional probability for having a spacing larger than s, given the preceding spacing t:

$$-\frac{\partial P(s/t)}{\partial s} = \rho' s(s+t) P\left(\frac{s}{t}\right) \quad , \tag{2}$$

where ρ' is another proportionality constant. Equation 2 and the boundary condition, $P(\rho/t) = 1$, determine $P(s/t)$. The spacing distribution $p(s)$ is then obtained from the integral equation as follows:

$$p(s) = \int_0^\infty -\frac{\partial P(s/t)}{\partial s} p(t)\, dt \quad . \tag{3}$$

Equation 3 is readily solved by iteration. The resulting distribution is plotted in Fig. 10.2.1, together with the Wigner distribution given by Eq. 1, where both are normalized to unit mean spacing. The two curves show the same qualitative behavior and are, even quantitatively, very close to each other. Thus the influence of t on s seems to be very small, which is a partial explanation of the success of Wigner's model. The correlation coefficient of adjacent level

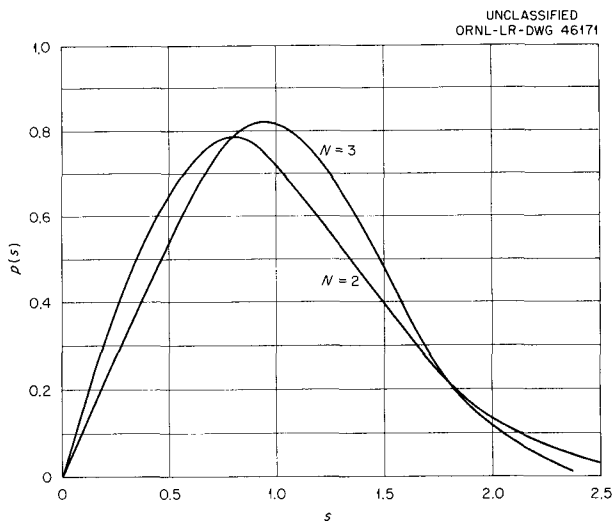

Fig. 10.2.1. Spacing Distributions for $N = 2$ (Wigner) and $N = 3$.

spacings, defined as

$$c = \frac{\overline{(s-\bar{s})(t-\bar{t})}}{\overline{(s-\bar{s})^2}} \quad , \tag{4}$$

is calculated to be −12% for the distribution given by Eqs. 2 and 3. It must be remarked[2] that the joint probability distribution $p(s,t)$ of two adjacent spacings, obtained from the relation

$$p(s,t) = -p(t)\,\frac{\partial P(s/t)}{\partial s} \quad , \tag{5}$$

turns out to be not symmetric in s and t. This is an unsatisfactory feature and shows that Eq. 2 is too simple a way to account for the correlation correctly. However, since the asymmetry is very slight (e.g., one obtains $\overline{st^2} = 2.50$, compared with $\overline{s^2t} = 2.52$), this simple approach should be useful in estimating the effect of the correlation on Wigner's distribution.

We have also attempted to compare the distribution (Eq. 3) and its correlation coefficient with the experimental data, in particular with the recent data of Rosen[3] on slow neutron resonances in U^{238}. Unfortunately, the smallness of the sample size, together with the uncertainty introduced by the possible existence of p levels, makes it impossible to draw definite conclusions in favor of one or the other of the proposed distributions.

The details are given in a separate report, to be published soon.

[2]We would like to thank E. P. Wigner for calling our attention to this point.

[3]J. L. Rosen, *Neutron Resonances in U^{238}*, thesis, Columbia University, CU-185 (1959).

10.3 AN ANALYSIS OF INELASTIC SCATTERING IN U^{238} BELOW 1 Mev[1]

L. Dresner[2]

For the design of fast breeder reactors which use U^{238} as fertile material, a knowledge of the interaction cross sections of U^{238} with fast neutrons is important. Because the five published measurements[3–7] of the partial inelastic scattering cross sections (see Table 10.3.1)

[1]A more detailed report will soon be published as a Kernforschungszentrum INR Arbeitsbericht.

[2]Work performed while the author was on assignment to the Institut für Neutronenphysik und Reaktortechnik, Kernforschungszentrum, Karlsruhe, Germany.

[3]R. C. Allen, *Nuclear Sci. and Eng.* 2, 787 (1957).

[4]R. Batchelor, *Proc. Phys. Soc. (London)* A69, 214 (1956).

[5]J. R. Beyster, M. Walt, and E. W. Salmi, *Phys. Rev.* 104, 1319 (1956).

[6]M. Walt and H. Barschall, *Scattering of 1-Mev Neutrons by Uranium*, TID-5157 (1953).

[7]L. Cranberg and J. S. Levin, *Phys. Rev.* 109, 2063 (1958).

Table 10.3.1. Comparison of Measured Inelastic Scattering Cross Sections for U^{238}

Bombardment Energy (kev)	Inelastic Scattering Cross Section (mb) by Excitation Level				Total	Source
	44 kev	146 kev	300 kev	730 kev		
150	440 ± 200^{a}				440 ± 200^{b}	1
250	$190 \pm 100^{a,c}$	290 ± 150^{a}			580 ± 180^{b}	1
500	$180 \pm 100^{a,c}$	490 ± 250^{a}			670 ± 270^{b}	1
					$800 \pm 200^{a,c}$	2
550	$1430 \pm 200^{f,i}$	$290 \pm 60^{f,j}$			1730 ± 210^{b}	3
1000	$900 \pm 250^{c,f,h}$	$600 \pm 190^{f,h}$	$90 \pm 50^{f,h}$	$520 \pm 80^{f,h}$	2100 ± 330^{b}	3
					$1400 \pm 200^{d,e}$	1
					$1350 \pm 200^{a,e}$	4
					$1200 \pm 700^{a,e,g}$	5
					$1100 \pm 200^{a,e}$	2

[a]Sphere transmission value. Correction for radiative capture made with an assumed value of $\sigma(n,\gamma)$.

[b]Sum, not a directly measured value.

[c]Lower limit due to poor resolution.

[d]Value obtained from measured total and differential elastic scattering cross sections and an assumed value of $\sigma(n,\gamma)$.

[e]Without excitation of the levels at 44 and 146 kev.

[f]Time-of-flight value.

[g]Error estimate by L. Cranberg. See report No. LA-2177.

[h]4π times differential inelastic scattering cross section at 90°.

[i]Differential inelastic scattering cross section measured.

[j]145°:90° scattering ratio = 1.00 ± 0.2.

[1]R. C. Allen, *Nuclear Sci. and Eng.* **2**, 787 (1957). Also includes results of R. C. Allen *et al.*, *Phys. Rev.* **104**, 731 (1956), and R. C. Allen, *Phys. Rev.* **105**, 1796 (1957).

[2]R. Batchelor, *Proc. Phys. Soc. (London)* **A69**, 214 (1956).

[3]L. Cranberg and J. Levin, *Phys. Rev.* **109**, 2063 (1958).

[4]H. R. Beyster, M. Walt, and E. W. Salmi, *Phys. Rev.* **104**, 1319 (1956).

[5]M. Walt and H. Barschall, TID-5157 (1953).

are in disagreement,[8] a semiphenomenological calculation was undertaken to clarify the situation.

The method employed is the well-known one of Hauser and Feshbach,[9] improved, however, in the following important respects:

1. The strength functions were not determined from the optical model[10] but rather were taken as free parameters to be determined by experiment. Angular momenta up to $l = 4$ were

[8]L. Cranberg and J. S. Levin, *Neutron Scattering by U^{235}, Pu^{239}, and U^{238}*, LA-2177 (June 22, 1959).

[9]W. Hauser and H. Feshbach, *Phys. Rev.* **87**, 366 (1952).

[10]H. Feshbach, C. E. Porter, and V. F. Weisskopf, *Phys. Rev.* **96**, 448 (1954).

considered, giving, therefore, five such free parameters. The strength functions for $l = 0$, 2, and 4 were all set equal[11] and determined from the published resonance parameters of Rosen.[12] The p-wave and f-wave strength function were determined from the two measured partial inelastic scattering cross sections at 550 kev (see Table 10.3.1) which are considered by the author to be essentially correct. The values of the strength functions employed were:

$$\frac{\gamma_{n0}^2}{D} = \frac{\gamma_{n2}^2}{D} = \frac{\gamma_{n4}^2}{D} = 0.025 \ , \qquad \frac{\gamma_{n1}^2}{D} = 0.075 \ , \qquad \frac{\gamma_{n3}^2}{D} = 0.135 \ ,$$

at zero neutron-bombarding energy.

2. A correction was made for the energy dependence of the strength function arising from the interference of resonances of the compound nucleus.[13,14]

3. A correction was made for effects of statistical distribution of the neutron widths.[11,15]

4. For the calculation of the inelastic scattering cross sections, the spin and energy dependences of the average level spacing D_J are unimportant. For the calculation of the radiative capture cross section, which has also been done, they are, however, important.[14] We have therefore assumed a J-(spin-) dependence proportional to $(2J + 1)^{-1}$ (ref 16), and an energy dependence as given by Lang and Le Couteur.[16] According to Rosen,[12] at zero bombarding energy, $D_{J=1/2} = 18$ ev (Γ_γ, incidentally, = 0.025 ev).

5. In order to complete Hauser-Feshbach calculations it is necessary to know the spins and parities of all the levels involved, as discussed in the remainder of this paper.

In U^{238}, four known excited states which lie at 44, 146, 300, and 730 kev[3-7] are important below 1 Mev. The ground state is 0^+, since U^{238} is an even-even nucleus; the 44-kev state has been clearly identified by Coulomb excitation as 2^+ (ref 17). The energies of the first three excited states are in the ratio 3:10:21, which characterizes a rotational band.[18] Thus we expect these states to be, respectively, 2^+, 4^+, and 6^+ states. Further states of this band may be neglected.

---

[11] L. Dresner, thesis, Princeton University, 1959, chap. 11; published in *Resonance Absorption of Neutrons in Nuclear Reactors*, ORNL-2659 (Mar. 10. 1959).

[12] J. L. Rosen, thesis, Columbia University, New York, June 5, 1959, published in *Neutron Resonances in U^{238}*, CU-185 (May 6, 1959).

[13] R. G. Thomas, *Phys. Rev.* **97**, 224 (1955).

[14] A. M. Lane and J. E. Lynn, *Proc. Phys. Soc. (London)* **A70**, 557 (1957).

[15] L. Dresner, "Proceedings of the International Conference on the Neutron Interactions with the Nucleus," Sept. 9, 1957; published in TID-7547, ed. by W. W. Havens, Jr.

[16] J. M. B. Lang and K. J. Le Couteur, *Proc. Phys. Soc. (London)* **A67**, 586 (1954).

[17] N. P. Heydenburg and G. M. Temmer, *Phys. Rev.* **96**, 90 (1954); A. S. Devatia, *Phys. Rev.* **100**, 1266 (1955).

[18] A. Bohr and B. R. Mottelson, *Kgl. Danske Videnskab. Selskab, Mat.-fys. Medd.* **27**(16) (1953).

For the state at 730 kev there are several possibilities. Collective oscillations of the quadrupole β and γ type[18] imply, respectively, 0^+ and 2^+ for spin and parity. Collective oscillations of the octupole type[19,20] imply negative parity states, of which the 1^- state has already been observed.[20]

Through comparison with the level scheme of Pu^{238} the choice 1^- for the 730-kev state has been made, although calculations for the choices 0^+ (β vibration) and 2^+ (γ vibration) have also been carried out. For each of these choices further rotational states were assumed; that is to say, a band beginning at 730 kev was assumed. The results of these calculations are summarized in Table 10.3.2, together with results taken from ref 11. (The latter have been corrected

Table 10.3.2. Calculated Inelastic Scattering Cross Sections for U^{238}

Bombardment Energy (kev)	Inelastic Scattering Cross Section (mb) by Excitation Level					Total	$\sigma(n,\gamma)$ (mb)
	44 kev	146 kev	300 kev	730 kev	805 kev		
150	810					810	180
550	1430*	290*				1720	140
1000	1380	720	80	395 (1^-)**	245 (3^-)**	2820	140
	1390	725	80	190 (0^+)	400 (2^+)	2785	150
	1320	600	70	480 (2^+)	290 (3^+)	2820	140

*Normalization.

**Choice of spins and parities.

for some small changes in γ_{n0}^2/D.) In the last two entries in column six, corresponding respectively to β and γ oscillations, the levels actually lie at 775 kev rather than at 805 kev, but the perturbation resulting from assuming them to be at the higher energy is not large. In addition, the next level of each of these bands is a 4^+ level, lying respectively at 880 and 835 kev. We have estimated their respective cross sections at 1 Mev to be 100 and 125 mb. The next level in the rotational band, of which the 1^- and 3^- levels are the first two, is a 5^- lying at 940 kev. Its cross section at 1 Mev is very small and can be neglected.

A comparison of the calculated cross sections with those measured by Cranberg[7] at 1 Mev shows quite good agreement in the cases of the 1^- and 0^+ spin assignments for the 730-kev level. To make this comparison we have assumed that Cranberg's reported result for the 730-kev level is the sum of the excitation cross sections we have calculated for all the levels of the upper rotational band. With this assumption, agreement between theory and experiment is relatively good, except in the case of the 44-kev state. There Cranberg's value is too low,

[19] S. Moszkowski, *Handbuch der Physik*, Band XXXIX (1957).

[20] K. Alder *et al.*, *Revs. Modern Phys.* **28**, 432 (1956).

which is almost certainly a consequence of the inability of his apparatus to completely distinguish between neutrons which have excited the 44-kev state and elastically scattered neutrons. In the case of the 2^+ spin assignment for the 730-kev level, the sum of the excitation cross sections of the upper rotational band is much too large, and this assignment is consequently ruled out.

No decision is possible with respect to the first two spin choices (1^- or 0^+) for the 730-kev state on the basis of the reported data, although if the contributions of the *individual* states of the upper rotational band could be determined, such a decision would be easy. Finally, the calculated values of the (n,γ) cross section are in good agreement with the values reported in BNL-325.[21]

---

[21] D. J. Hughes and R. B. Schwartz, *Neutron Cross Sections*, BNL-325, 2d ed. (1958).

ORNL-3016
UC-34 – Physics and Mathematics
TID-4500 (15th ed.)

INTERNAL DISTRIBUTION

1. C. E. Center
2. Biology Library
3. Health Physics Library
4–6. Central Research Library
7. Reactor Experimental Engineering Library
8–50. Laboratory Records Department
51. Laboratory Records, ORNL R.C.
52. A. M. Weinberg
53. L. B. Emlet (K-25)
54. J. P. Murray (Y-12)
55. J. A. Swartout
56. G. E. Boyd
57. R. A. Charpie
58. W. H. Jordan
59. A. H. Snell
60. C. E. Winters
61. D. S. Billington
62–86. E. P. Blizard
87. F. L. Culler
88. J. L. Fowler
89. J. H. Frye, Jr.
90. C. S. Harrill
91. A. Hollaender
92. A. S. Householder
93. C. P. Keim
94. M. T. Kelley
95. S. C. Lind
96. R. S. Livingston
97. K. Z. Morgan
98. M. L. Nelson
99. H. E. Seagren
100. E. D. Shipley
101. E. H. Taylor
102. E. Guth
103. P. F. Kasten
104. A. J. Miller
105. L. C. Oakes
106. G. D. O'Kelley
107. V. K. Pare
108. D. Phillips
109–110. P. M. Reyling
111. W. M. Good
112. M. J. Skinner
113. G. C. Williams
114. R. S. Cockreham
115. L. S. Abbott
116. M. N. Alam
117. F. S. Alsmiller
118. R. G. Alsmiller, Jr.
119. H. Bertini
120. T. V. Blosser
121. B. Buck
122. W. R. Burrus
123. V. R. Cain
124. A. D. Callihan
125. G. T. Chapman
126. R. R. Coveyou
127. D. F. Cronin
128. G. deSaussure
129. L. Dresner
130. J. F. Ellis
131. G. M. Estabrook
132. T. K. Fowler
133. J. K. Fox
134. R. M. Freestone
135. W. A. Gibson
136. L. W. Gilley
137. J. K. Grant
138. R. Gwin
139. K. M. Henry
140. L. B. Holland
141. J. L. Hull
142. L. Jung
143. E. B. Johnson
144. F. A. Khan
145. F. B. K. Kam
146. R. J. Kerr
147. J. D. Kington
148. W. E. Kinney
149. M. E. LaVerne
150. J. Lewin
151. T. A. Love
152. J. J. Lynn
153. A. D. MacKellar
154. R. J. Mackin
155. R. E. Maerker
156. D. W. Magnuson
157–159. F. C. Maienschein
160. J. J. Manning

161. J. T. Mihalczo
162. J. M. Miller
163. H. S. Moran
164. F. J. Muckenthaler
165. T. Mustafa
166. R. B. Murray
167. A. Meyer
168. R. W. Peelle
169. S. K. Penny
170. F. Perey
171. E. R. Rohrer
172. Y. Shima
173. E. G. Silver
174. A. Simon
175. K. M. Simpson
176. H. E. Stern
177. J. G. Sullivan
178. J. T. Thomas
179. D. K. Trubey
180. W. C. Tunnell
181. V. V. Verbinski
182. D. R. Ward
183. J. H. Wilson
184. H. K. Wimmell
185. L. W. Weston
186. C. D. Zerby
187. W. Zobel
188. E. G. Harris
189. R. L. Macklin
190. W. S. Lyon
191. C. A. Preskitt
192. P. F. Gast (consultant)
193. H. Goldstein (consultant)
194. L. W. Nordheim (consultant)
195. R. F. Taschek (consultant)
196. T. J. Thompson (consultant)
197. ORNL – Y-12 Technical Library, Document Reference Section

EXTERNAL DISTRIBUTION

198. Division of Research and Development, AEC, ORO
199–809. Given distribution as shown in TID-4500 (15th ed.) under Physics and Mathematics category (75 copies – OTS)